Investigation of the mantle source, magma evolution and sulphide mineralisation of the Phalaborwa Complex

Submitted by Dora Kavecsanszki to the University of Exeter as a thesis for the degree of Master of Philosophy in Geology in August, 2021

I certify that all material in this thesis which is not my own work has been identified and that no material has previously been submitted and approved for the award of the degree by this or any other University

Signature

Abstract

The economically significant Phalaborwa complex is well investigated but significant gaps remain in the petrogenetic model. The present study focuses on the mantle source characteristics, the genetic relationships between the lithologies and the nature of the sulphide mineralisation, and discusses the relative roles of mantle and crustal processes.

Comprehensive textural and geochemical (SEM, EPMA) studies of carbonatites, phoscorite, and silicate lithologies were combined with in situ LA-ICPMS analyses of trace element (PGE, noble metal, metalloid, Bi, Cd) distributions. Sulphide assemblages and trace element compositions in the magmatic system were differentiated from those representing re- mobilisation by hydrothermal and supergene processes. The S/Se ratiosand S/Se vs. PGE ratios helped to separate (mantle-derived) magmatic and crustal signatures of the sulphides. Sulphide minerals with magmatic and magmatic-hydrothermal textures and compositions formed at the maximum of 600-700 ^{o}C. A later stage hydrothermal stage (≤ ~400) involving Cu-rich fluids formed abundant bornite-formation and secondary sulphides (e.g. valleriite), and altered non-sulphide phases. The cooling of the deposit is manifested in the formation of series of late stage, low temperature (<100 ^{o}C) Cu-S phases (e.g. djurleite, anilite).

The in situ measurement of S/Se ratios showed mixed mantle-crustal ratios in the sulphides, with the majority showing the presence of crustal sulphur. The in situ trace element analyses showed a general depletion in PGE, noble metals and metalloids in solid solution and that these elements were remobilised and showed relatively elevated levels in secondary phases. PGM and metalloids readily formed microinclusions with other metals (Ag, Au, Bi, Zn, Co, Ni). PGM were found more frequently in secondary sulphides of serpentinised olivine phlogopitite suggesting remobilisation from either sulphides or silicates by high fO_2, neutral fluids.

Crustal processes have obscured the nature of primary mantle-derived processes so that modelling was used as to investigate the range of possible parental magmas. Natural xenoliths from the Kaapvaal craton (Phlogopite wehrlite, eclogite MARID) were used to approximate the composition of the possible Phalaborwa metasomatised/veined mantle source region. Possible parental melts were derived as a function of starting mantle composition and fractional melting plus mixing, and described in terms of their major and trace element characteristics. The results were interpreted in terms of possible genetic relationships between the Phalaborwa lithologies, particularly magma chamber processes (cumulate formation, immiscibility).

The mantle melting path of carbonated phlogopite wehrlite and eclogite mantle evolves from carbonatite to silicate magma, with intermediate compositions including silicocarbonatites. The model silicocarbonatite composition overlaps with the composition of melt inclusions hosted in phoscoritic olivine, representing an early pre-phoscoritic magma composition (Aldous, 1980). The primary melts of MARID mantle became SiO_2 rich too rapidly to produce such silicocarbonatite compositions. There is no compositional pathway reconstructed from the silicocarbonatite or pre-phoscoritic melt to phoscorite rock. The trace element models showed best match with phlogopite wehrlite and eclogitic sources. The modelling showed that it is possible to approximate mantle compositions more precisely than the “metasomatised heterogeneous mantle” usually used for carbonatites.

The Phalaborwa lithologies do not represent the primary magma compositions but are the results of multiple stages of magma differentiation We interpret that cumulate formation and/or immiscibility play a major role in carbonatite and phoscorite formation (respectively), from a primary silicocarbonatite parent.

Contents

List of Figures

boundaries. Dolomite formed around and between the crystals. e: (xN) serpentine after cumulus olivine, fractured and partly re-crystallised apatite with undulatory extinction and interstitial carbonate. f: (xN) cumulus olivine with starting serpentinisation along the fractures, phlogopite with undulatory extinction. xN: under cross polarised light, BSE: backscattered electron image, phl: phlogopite, di: diopside, ap: apatite, ol: olivine, se: serpentine, cal: calcite, mgt: magnetite, il: ilmenite, mon: monazite, bd: baddeleyite.

Figure 3.3.7. Photographs. Silicate rock hand specimens described in the study. a: Feldspathic clinopyroxenite cumulate containing diopside with lesser amount of apatite, phlogopite and interstitial microcline b-e: Clinopyroxenite (b) and micaceous clinopyroxenite (c-e) cumulates with diopside as the most abundant phase, followed by apatite and phlogopite. Phlogopite can form regular bands in the micaceous clinopyroxenites (c). f: Pegmatoid rock with large, pegmatitic phlogopite and apatite crystals. g: Glimmerite rock, where the phlogopite proportion exceeds partially serpentinised diopside. Apatite and calcite are major constituents. The rock is crosscut by a carbonate vein which contains dark-gray coloured streaks of sulphide, magnetite and silicate phases. h: The sample represents two olivine-rich rock types with abundant magnetite-ilmenite and interstitial calcite. In olivine–glimmerite The olivine is strongly serpentinised. In the other rock type, the olivine and phlogopite proportion is roughly the same. The olivine is serpentinised. The contact of the two rock types is marked by a carbonate vein di: diopside, phl: phlogopite, ap: apatite, carb: carbonate (calcite/dolomite), serp: serpentine, mgt: magnetite: int: interstitial, sulph: sulphide 123.

Figure 3.3.8. Transmitted light photomicrographs (xN). Sample Box3-1 representing feldspathoid rocks of Phalaborwa. The interstitial feldspar is microcline (a, c, e). The microcline can display its characteristic cross-hatched twinning (a). The diopside crystals are primarily subhedral with well-developed crystal faces and abundant twinning (a,c ,d, e). Both diopside and apatite can show near- polygonal, adjusted crystal edges (d). Large apatite crystals can display strong fracturing, irregular edges and undulatory extinction (b, d, f), and subgrain formation and recrystallisation at the crystal contacts (b). Subhedral or close to euhedral apatite crystals also occur (a, e), often inside diopside (c, e). Phlogopite form subhedral, often bent laths of various sizes, crosscutting the cumulate phases and each other (a, b, f). xN: under cross polarised light, phl: phlogopite, di: diopside, ap: apatite, mi: microcline 125.

cobalt pentlandite; sig: siegenite; sphl: sphalerite; *mi*: microinclusion; M: marker, TRC:transgressive carbonatite.

Figure 6.2.4. The edited micro-photographs (a.1, b.1, c.1) of the sulphide grains show the analysis lines (AL) that produced the TRA diagrams for each individual lines. a: Cobalt pentlandite with siegenite rim around it (a.1). The analysis produced nonstoichiometric composition due to the AL including two phases and the chalcopyrite contact. The TRA diagrams (a.2-4) show the changes in the composition from the centre towards the edges and at one point in the centre where the AL crossed a siegenite patch. The results show that siegenite is more enriched in Ag, Bi and Pb then the cobalt pentlandite. b: Cobalt pentlandite in troilite-rich TRC gave nonstoichiometric result. As occurred in solid solution (b.4), but generally the phase was depleted in trace elements. Troilite in troilite-rich TRC gave stoichiometric compositions, based on the TRA diagrams (c.2-4) it is depleted in trace elements. bo: bornite; chp: chalcopyrite, cub: cubanite; co-ptl: cobalt pentlandite; sig: siegenite; to: troilite; M: marker, TRC: transgressive carbonatite. 212.

Figure 6.2.5. The edited micro-photographs (a.1, b.1) of the sulphide grains show the analysis lines (AL) that produced the TRA diagrams for each individual lines. a: Sulphide grain in olivine glimmerite with complex intergrowth of Cu-Fe-S phases. The analysis of the mixed phases gave nonstoichiometric results as expected. The TRA diagrams (a.2-4) showed the presence of PGE at the edges of the grain. The PGE formed microinclusions with As (Pt, Ir) or Au (Pd). The former was associated with Co-Ni sulphide grain. b: Sulphide grain in phoscorite with complex Cu-Fe-S phases and Co-Ni sulphide grain. The grain is strongly resorbed at the edges. The analysis produced nonstoichiometric composition as the AL included different phases. Ag-Bi microinclusion occurred in the Co-Ni sulphide grain.: co-ptl: Co-Ni sulphide grain; val: valleriite M: marker, *mi:* microinclusion. 213.

Figure 6.2.6. The diagrams show the trace element compositions of the stoichiometric sulphide phases from the studies Phalaborwa lithologies. Stoichiometric chalcopyrites were found in the transgressive and banded carbonatites, phoscorite and in the olivine glimmerite. Stoichiometric bornite was analysed in the transgressive and banded carbonatites and in the phoscorite, while sphalerite was found in the transgressive carbonatite. The trace elements are presented as chondrite normalised values (Anders and Grevesse, 1989) on a log-scale. 221.

Figure 6.2.7. Sulphide trace element composition of the different transgressive carbonatite (TRC) types including bornite-rich, 223.

(2009); (7) Wang and Becker (2013); (8) Eckstrand and Hulbert (1987).

Figure 6.3.2. The Phalaborwa sulphides were depicted on a S/Se vs Pt+Pd diagram. The S/Se ratio ranges of the different mantle derived samples, primitive mantle and the average mantle S/Se are also indicated. The diagram shows that the majority of the sulphides fall into the S-rich side of the diagram when compared to the average mantle range, which indicate crustal S-enrichment. The other mantle derived samples may represent different mantle sources. (1) Palme and O'Neill (2003); (2) McDonough and Sun (1995); (3) Hutchinson et al. (2015); (4) Hughes et al. (2021); (5) Mackie et al. (2009); (6) Paton et al. (2009); (7) Wang and Becker (2013); (8) Eckstrand and Hulbert (1987). 240.

Figure 6.3.3. The sulphide S/Se ratios (log scale) of the different transgressive carbonatite types depicted together with S/Se ratios of different mantle-derived samples that represent different mantle sources. The average S/Se mantle ratios are indicated on the axis of the diagram. (1) Palme and O'Neill (2003); (2) McDonough and Sun (1995); (3) Hutchinson et al. (2015); (4) Hughes et al. (2021); (5) Mackie et al. (2009); (6) Paton et al. (2009); (7) Wang and Becker (2013); (8) Eckstrand and Hulbert (1987). *: nonstoichiometric analyses were included, which did not change the interpretations. 241.

Figure 6.3.4. The S/Se ratios (log scale) of the banded carbonatite stoichiometric and nonstoichiometric sulphides depicted together with S/Se ratios of different mantle-derived samples that represent different mantle sources. The average S/Se mantle ratios are indicated on the axis of the diagram. (1) Palme and O'Neill (2003); (2) McDonough and Sun (1995); (3) Hutchinson et al. (2015); (4) Hughes et al. (2021); (5) Mackie et al. (2009); (6) Paton et al. (2009); (7) Wang and Becker (2013); (8) Eckstrand and Hulbert (1987). 243.

Figure 6.3.5. The (stoichiometric and nonstoichiometric) S/Se ratios (log scale) of the phoscorite sulphides depicted together with S/Se ratios of different mantle-derived samples that represent different mantle sources. The average S/Se mantle ratios are indicated on the axis of the diagram. (1) Palme and O'Neill (2003); (2) McDonough and Sun (1995); (3) Hutchinson et al. (2015); (4) Hughes et al. (2021); (5) Mackie et al. (2009); (6) Paton et al. (2009); (7) Wang and Becker (2013); (8) Eckstrand and Hulbert (1987). 244.

Figure 6.3.6. The (stoichiometric and nonstoichiometric) S/Se ratios (log scale) of the olivine glimmerite sulphides depicted together with S/Se ratios of different mantle-derived samples that 245.

determined under different conditions and used for calcite and dolomite in this study.

Figure 7.3.1. Primary magma composition, as a function of increasing melt fraction (F) from three different metasomatic mantle source regions. Squares denote (+model number) denote veined mantle starting compositions: (a) Veined phlogopite wehrlite source; (b) Veined eclogite model; (c) MARID. Triangle denote melt composition for fraction F, where colour of symbols tie starting compositions to melt fractions. Melt fractions ranged from 1% (F1) up to 50% (F11). The reference compositions for rocks and minerals are: Phalaborwa phoscorite and average banded carbonatite (BC) compositions (Hanekom et al. 1965); Examples for transgressive carbonatite compositions (TRC1-4) (Milani et al. 2027a); average composition of phoscoritic melt inclusions hosted in olivine (n=15; after Aldous, 1980); Phlogopite- Wehrlite (Gregoire et al. 2002); mineral compositions (Huang et al., 2014), where dunite = olivine. Compositions are listed in Table 7.3.1.a-c. The chemical compositions were recalculated for the system SCM+CO_2 where S: SiO_2 (+TiO_2+Al_2O_3), C: CaO (+Na_2O+K_2O +Ce_2O_3+ La_2O_3), M: MgO (+FeO+MnO+Cr_2O_3) and CO_2: CO_2 (+P_2O_5) (See Appendix 3 for the full list of modal and major element compositions). 280.

Figure 7.3.2. Composition differences between the melt fractions produced by a: 15% (F4) melting and b: 30% melting (F7) of the veined phlogopite wehrlite. The diagrams include nineteen different composition models. The grey and red dashed-circled numbers denote veined phlogopite wehrlite starting compositions. Triangles denote melt composition for fraction F4 (a.) and F7 (b.) representing 15 and 30% melting, respectively. The colour of triangles tie starting compositions to melt fractions. The variograms c-f contrast the S/CO_2 and C/M ratios of melt fraction F4 (c, d) and F7 (e, f) (See Appendix 3 for the full list of modal and major element compositions).TRC1-4: transgressive carbonatite compositions (Milani et al., 2017a), BC: average banded carbonatite composition (Hanekom et al., 1965), Phosocorite: average Phalaborwa phoscorite composition (Hanekom et al., 1965), Melt inclusion composition from Aldous (1970). The chemical compositions were recalculated for the system SCM+CO_2 where S: SiO_2 (+TiO_2+Al_2O_3), C: CaO (+Na_2O+K_2O +Ce_2O_3+ La_2O_3), M: MgO (+FeO+MnO+Cr_2O_3) and CO_2: CO_2 (+P_2O_5) 282.

Figure 7.3.3. Composition differences between the melt fractions produced by a: 15% (F4) melting and b: 30% melting (F7) of the veined eclogite. The black numbers denote starting compositions. The triangles denote melt composition for fraction F4 and F7, 284.

where colour of the triangles tie starting compositions to melt fractions. The variograms c-f contrast the S/CO_2 and C/M ratios of melt fraction F4 (c, d) and F7 (e, f) (See Appendix 3 for the full list of modal and major element compositions). TRC1-4: transgressive carbonatite compositions (Milani et al., 2017a), BC: average banded carbonatite composition (Hanekom et al., 1965). Phoscorite: average Phalaborwa phoscorite composition (Hanekom et al., 1965), Melt inclusion composition from Aldous (1970). The chemical compositions were recalculated for the system $SCM+CO_2$ where S: SiO_2 ($+TiO_2+Al_2O_3$), C: CaO ($+Na_2O+K_2O+Ce_2O_3+La_2O_3$), M: MgO ($+FeO+MnO+Cr_2O_3$) and CO_2: CO_2 ($+P_2O_5$)

Figure 7.3.4. Composition differences between the melt fractions produced by a: 15% (F4) melting and b: 30% melting (F7) of the veined MARID. The original composition of AJE281 is shown by a blue square. The black numbers denote the veined starting compositions. The triangles denote melt composition for fraction F4 and F7, where the colour of the triangles tie starting compositions to melt fractions. The variograms (b-e) contrast the S/CO_2 and C/M ratios of melt fraction F4 (b, c) and F7 (d, e). TRC1-4: transgressive carbonatite compositions (Milani et al., 2017a), BC: average banded carbonatite composition (Hanekom et al., 1965), Phoscorite: average Phalaborwa phoscorite composition (Hanekom et al., 1965); Melt inclusion composition from Aldous (1970). (See Appendix 3 for the full list of modal and major element compositions). The chemical compositions were recalculated for the system $SCM+CO_2$ where S: SiO_2 ($+TiO_2+Al_2O_3$), C: CaO ($+Na_2O+K_2O+Ce_2O_3+La_2O_3$), M: MgO ($+FeO+MnO+Cr_2O_3$) and CO_2: CO_2 ($+P_2O_5$). 285.

Figure 7.3.5. Ce partitioning behaviour (Cl/Co) and calculated liquid concentrations (Cl) during the melting of phlogopite wehrlite (a, b), eclogite (c, d) and MARID (e, f) mantles. The respective Cl/Co ratios and Cl are depicted against melt fractions (F) up to 25% melting. The legends show the included non-veined and veined model names. 286.

Figure 7.3.6. Gd partitioning behaviour (Cl/Co) and calculated liquid concentrations (Cl) during the melting of phlogopite wehrlite (a, b), eclogite (c, d) and MARID (e, f) mantles. The respective Cl/Co ratios and Cl are depicted against melt fractions (F) up to 25% melting. The legends show the included non-veined and veined model names. 288.

Figure 7.3.7. Y partitioning behaviour (Cl/Co) and calculated liquid concentrations (Cl) during the melting of phlogopite wehrlite (a, b), eclogite (c, d) and MARID (e, f) mantles. The respective Cl/Co ratios and Cl are depicted against melt fractions (F) up 290.

List of Tables

List of Appendices

Chapter 1: General Introduction

1.1 Introduction to the Phalaborwa Igneous Complex

The Phalaborwa Complex (South Africa, Letaba District, Northeastern Transvaal) is unique amongst carbonatites as it hosts a large multi-commodity deposit. The main commodities are copper (reserves: 35Mt at 0.54% grade), magnetite (reserves: 9.6 Mt at 55.1% Fe), vermiculite and apatite (PorterGeo Database - Ore Deposit Description). Economic by-products include silver, arsenic, gold, bismuth, lead, antimony, selenium, tellurium, platinum-group elements (PGE) and sulphur (as sulphuric acid). Recently, the deposit was also studied for its rare earth element (REE) mineralisation prospects (Milani et al., 2017b; Giebel et al., 2017).

The formation of the highly variable magmatic rocks of Loolekop (the carbonatitic portions of the Phalaborwa Complex) are coeval – pegmatitic pyroxenite: 2060+/-4 Ma, phoscorite: 2062+/-2 Ma, banded carbonatite: 2060+/-2 Ma, transgressive carbonatite: 2060+/-1 Ma, syenite plugs: 2068+/-17, and mafic dykes outside of the main complex: 2062+/-53 Ma (Wu et al., 2011).

Authors agree that the Phalaborwa carbonatite has mantle origin – isotopic studies have shown that the parental magmas are derived from a heterogeneous, metasomatised lithospheric mantle (Eriksson, 1989; Wu et al., 2011). The Rb-Sr and Sm-Nd isotopic characteristics of the deposit were extensively studied and interpreted as the result of the mixing of different magmas with distinctive initial Nd and Sr values which were derived from a heterogeneous metasomatised mantle (Eriksson, 1989; Yuhara et al., 2003). Based on the isotopic evidence, the magmatic rocks were emplaced simultaneously during the same magmatic event, but the magmatic evolution and the source of the magmatism are complex. Although Phalaborwa has been widely investigated due to its economic significance and unique nature, the deposit's petrogenetic model has not yet been fully developed.

The heterogeneous metasomatised nature of the Phalaborwa mantle is well established, but there is no specific information about the nature of the source region. Plume characteristics

were suggested by Wu et al. (2011) and Bolhar et al. (2020). The proposed carbonatite parental magma was Al, Nb, and Zr-poor with extremely high Sr-levels and K: Na ratios (e.g., Aldous, 1980; Eriksson, 1989; Giebel et al., 2019). Mixing of different (at least two) carbonatite magmas shaped the isotopic characteristics of the complex (Eriksson, 1989; Wu et al., 2011).

Several authors investigated and discussed the genetic relationships between the different lithologies (e.g., Aldous, 1980; Eriksson, 1989; Wu et al., 2011; Milani et al., 2017a, b; Giebel et al., 2019). No evidence was provided for the genetic relationship between the clinopyroxenites and the phoscorite-carbonatite suite. Based on isotopic evidence, formation via fractionation and liquid immiscibility was ruled out (Erikson, 1989). It was suggested that carbonatites are not genetically related to spatially related ultramafic silicate rocks (Harmer, 2000). Around 10% of the known carbonatites are associated with ultramafic silicate rocks (Woolley and Kjarsgaard, 2008), showing that this is not an uncommon rock association. Therefore, a shared evolutionary path is worth considering, especially in the case of Phalaborwa, where the silicate and phoscorite-carbonatite rocks were emplaced synchronously (Wu et al., 2011).

The relationship between phoscorite and carbonatites was considered either liquid immiscibility (Giebel et al., 2019) or fractionation (Milani et al., 2017b). Giebel et al. (2019) proposed liquid immiscibility and shared parental magma based on analogous trends in the mica chemical compositions and mutual geochemical evolution in the banded carbonatite and phoscorite. A fractional crystallisation relationship was proposed based on the REE profile of the two rocks (Milani et al., 2017). Aldous (1980) found primary silicocarbonatite melt inclusions in the phoscoritic olivine with a carbonate component of 40-60 vol% and silicate component of 30-45 vol%. The melt inclusions represented either the earliest carbonatite melt or an immiscible melt coexisting with the silicate melt, which produced the olivine (Aldous, 1980). The transgressive carbonatite, although emplaced last, shows the more primitive (less enriched) REE profile (Milani et al., 2017). Furthermore, orthomagmatic phlogopite with high Ba and Al occurs only in this lithology, suggesting that the magma was enriched in Al and Ba, possibly via crustal contamination (Giebel et al., 2019). The transgressive carbonatite was considered to be the product of a different evolutionary path or parental magma than the phoscorite and the banded carbonatite (Milani et al.,

2017; Giebel et al., 2019). This concurs with the suggestion that the Phalaborwa carbonatites crystallised from multiple magma batches with different compositions and sources (Eriksson, 1989; Wu et al., 2011).

The origin of the Phalaborwa sulphide mineralisation was considered magmatic and magmatic-hydrothermal (e.g., Mitchell and Krouse, 1975; Aldous, 1980; Bolhar et al., 2020; Le Bras et al., 2021) or late-stage hydrothermal (e.g., Hanekom et al., 1965; Rudashevsky et al., 2004; Bolhar et al., 2020; Le Bras et al., 2021).Finally, Phalaborwa is also considered an iron-oxide-copper-gold (IOCG) deposit by various authors (e.g., Groves and Vielreicher, 2001; Chen, 2013), more precisely, the end member of the Olympic Dam type IOCG deposits. The suggestion is based on the similarities between the two deposits: pipe-like nature with abundant breccias, ore mineralisation (Fe- oxide, Cu-sulphides, noble metals), structure-controlled mineralisation and emplacement. It has been suggested that in the case of Phalaborwa, the sulphur was derived from the magmatic assimilation of metasedimentary units (Chen, 2013), contradicting other sulphur isotope and trace element studies that indicated mantle origin (Mitchell and Krouse, 1975; Bolhar et al., 2020; Le Bras et al., 2021).

Although the sulphide assemblage can be interpreted as low-temperature late-stage mineralisation, the presence of a Cu-sulphide phase in carbonatitic melt inclusions of phoscoritic olivines indicates that the Cu-sulphides were present in the carbonatite magma before emplacement (Aldous, 1980). Furthermore, most economic sulphide mineralisation is lithology-bound, which may indicate a genetic relationship with the transgressive carbonatite. Recently, Bolhar et al. (2020) presented the S and Pb isotope compositions of sulphide minerals in the carbonatites and phoscorite. The $\delta^{34}S$ ratios varied widely and intersected the typical mantle values. Their work concluded that the S in the sulphide mineralisation represented asthenospheric S, derived from a subducted slab in the mantle. The Cu-sulphide trace element study of Le Bras et al. (2021) also concluded a magmatic sulphide origin with crustal influence.

The noble metal and metalloid characteristics of the Phalaborwa sulphides were investigated by Rudashevsky et al. (2004), who gave a comprehensive account of the phases occurring in the carbonatites. Their study used mineral

concentrates, and consequently, the samples lost their textural and lithological context.

1.2 The aim of the study

Phalaborwa is a well-studied complex, so the present study aims to concentrate on the gaps in knowledge about the possible mantle sources, parental magma, evolutionary paths of the different lithologies, the complexity of the sulphide mineralisation and the trace element characteristics in a textural and lithological context.

With a comprehensive textural and geochemical study of the sulphide mineralisation in the transgressive and banded carbonatites, the phoscorite and the minor sulphide phases in the silicate rocks, the research aims to separate the different phases of sulphide formation and establish the sulphide petrogenetic sequence across the lithologies.

Using in situ analyses of trace elements (Os, Ir, Ru, Rh, Pt, Pd, Ag, Au, As, Se, Sb, Te, Cd, Bi,) the study aims to characterise the different processes (magmatic, hydrothermal, supergene) that formed the trace element profile of the sulphide phases across the lithologies. By using S/Se ratios determined in the sulphide phases, the study aims to identify magmatic and late-stage effects in the sulphide mineralisation. The study also compares the S/Se ratios of different mantle xenoliths to the Phalaborwa sulphides. The study discusses the reliability of the method and the information the sulphide mineralisation can provide about the mantle domains when using S/Se ratios.

By modelling major and trace element compositions of the melt fractions during mantle melting, the study will investigate the potential mantle sources, parental magmas, and melt evolutionary pathways of the Phalaborwa lithologies and the genetic relationships between them. The modelling exercise is linked to the sulphide studies by including mantle composition types used in the S/Se studies.

1.3 Introduction to carbonatites: classification and petrogenesis

1.3.1 Carbonatite classification

Carbonatites are carbonate-rich, metasomatised mantle-derived igneous rocks. Oldoinyo Lengai is the only known active carbonatite volcano, producing unusual natrocarbonatite lavas. Carbonatites are thought to be non-polymerised ionic liquids with very low viscosity (0.15 P) and density (1.15-2.17 g/cm3) (e.g., Treiman and Schedl, 1983). Less than 200 carbonatite occurrences were known by the 1960s worldwide. However, due to the rapidly increasing knowledge of carbonatite magmatism, the number of known occurrences reached 527 by 2006 (Woolley and Kjarsgaard, 2008).

Two carbonatite classification systems were developed. The IUGS system (Le Maitre, 2002) relies solely on composition to differentiate between the carbonatite types. Mitchell's (2005) classification system focuses on the genetic relationships between the carbonatite and the associated silicate rocks. He emphasised that although the IUGS system works well for common rocks, it is not suitable for rock types that are modally different but genetically related and have the same parental magma type (e.g., lamproite and kimberlite).

The IUGS system suggests, based on Streckeisen (1978, 1979), that a plutonic or a volcanic rock should contain more than 50% modal carbonates to classify as carbonatite. The classification is based on the mineralogy of the rocks that can be plutonic or volcanic. Calcite-carbonatite contains calcite as the main carbonate constituent. The coarse-grained calcite-carbonatites can also be called sövite and alvikite in the case of medium-fine-grained rocks. Dolomite-carbonatites contain dolomite as the main carbonate mineral and can be called beforsite. Carbonatites, where Fe-rich carbonates are dominant, are called Ferrocarbonatites. Natrocarbonatites are unusual rock types, described only from Oldoinyo Lengai (Tanzania) and composed of sodium, potassium and calcium carbonates.

In the case of finer-grained rocks, determining the modal composition is difficult. Further problems are correctly identifying and separating the different carbonate species or the common presence of complex intergrowths (Woolley and Kempe, 1989). The classification of carbonatites based on whole-rock chemistry is used to solve these problems. The chemical classification of carbonatites with SiO_2 <

20 wt% is based on their MgO-CaO-(FeO_t+MnO) wt% ratio. Carbonatite rocks with >20% SiO_2 are called silicocarbonatites, where the silicates can include sodic carbonates and amphiboles, biotite, phlogopite, olivine and feldspars (Mitchell, 2005). The Phalaborwa carbonatites are coarse-grained; therefore, the USGS classification can easily be applied.

Mitchell (2005) discussed that a significant problem of the IUGS classification system is that determining carbonatites only by their modal composition can lead to incorrect petrogenetic models. During the magmatic evolution of an igneous complex, several modally different rocks can form in close proximity to each other. The IUGS classification does not express that these rocks were produced at different stages of the same magmatic process. It puts plutonic and late-stage magmatic rocks into the same category. However, it excludes rocks that belong to the same magmatic process but have lower carbonate or higher silica content, such as silicocarbonatites (Mitchell, 2005). Mitchell (2005) wished to express in his classification system that during the magmatic differentiation of a carbonatite-forming magma, the modal carbonate content of the produced rocks can be highly variable. This concept is relevant in the case of Phalaborwa, where the carbonatite is associated with clinopyroxenites and phoscorites, and the genetic relationship between these rocks has been the subject of investigation of several works (e.g., Eriksson, 1987; Harmer, 2000; Milani et al., 2017b).

Mitchell (2005) defined rocks with greater than 30 vol% primary carbonate as carbonatite without considering the SiO_2 content and emphasised that these rocks are derived from the same parental magma and belong to the same petrological clan. The carbonatite classification system comprises two main groups: the primary carbonatite group and the carbothermal residua and pseudocarbonatite group. The primary carbonatite group includes primary calcite and dolomite carbonatites, which are genetically related to mantle-derived magmas.

The carbothermal residua group includes rocks with a large variety of parental magmas. The term carbothermal represents low-temperature fluids that originated from CO_2-dominated fractionated magma with variable H_2O and F contents (Mitchell, 2005). Pseodocarbonatites include calc-silicate scarns formed by the anatectic melting of crustal rocks and have no connection to mantle-derived rocks. The primary carbonatite group includes six different petrological

clans and associations: (i) nephelinite-clan carbonatites, (ii) melilitite-clan carbonatites, (iii) kimberlite-calcite kimberlites, (iv) alikite-carbonatite association; (v) peralkaline nephelinite- natrocarbonatite association; and (vi) carbonatites without associated silicate rocks. In addition to Mitchell's (2005) categories, Woolley and Kjarsgaard (2008) note carbonatite associations with lamprophyre, olivine-pyroxene ultramafic rocks, olivine-pyroxene ultramafic rocks +syenite, and pyroxene+syenite.

1.3.2 Carbonatite petrogenesis

The consensus is that carbonatite magma is derived from the metasomatised lithospheric mantle; however, the process of the carbonatitic magma formation is still debated. Questions of the carbonatite formation involve the composition of parental melts, the evolution and relationship between the carbonatite and the silicate rocks, the reconstruction of the mantle source or sources from which these rocks are derived, and the determination of how and when the separation of the carbonatite magma takes place and finally, the role of the silicate cumulate formation which often accompanies carbonatites. There are three main models that are used to reconstruct the carbonatite petrogenesis:

1. Fractional crystallisation of mantle-derived parental magma under crustal pressures
2. Carbonatite liquid separation from silicate liquid caused by liquid immiscibility in the upper mantle or crust.
3. Direct melting of carbonated, metasomatised mantle producing primary carbonatite magma.

Numerous studies showed that all three listed processes can produce carbonatite magma under certain conditions. However, the uncertainties around experiment-based models that aim to describe natural systems remain. The geochemical models need to agree with the isotopic and trace element compositions of the natural rocks, the geophysical characteristics of the investigated localities (e.g., geotherm, crust thickness) and the physical properties of the magma types (e.g., magma rheology, density).

All three models are well established and supported by petrological evidence and experimental studies; however, all three have their weaknesses as well. As it was summarised in Brooker and Kjarsgaard (2011), liquid immiscibility experiments

could not reproduce the most common alkali-free carbonatite magma compositions. The primary carbonatitic mantle melt models might not be able to explain how the carbonatite melt can pass through thermal barriers in the mantle, while fractional crystallisation might produce cumulates with physical properties that make a magmatic intrusion process challenging to explain.

1.3.2.1 Carbonatite formation by carbonate-silicate liquid immiscibility

During carbonate-silicate liquid immiscibility, a primary carbonated silicate magma exsolves a silicate and a carbonate liquid at crustal or upper mantle conditions. Given that most carbonatite deposits are associated with magmatic silicate rocks, the immiscibility model is usually considered a possible path of magma evolution. The model is used to reconstruct the formation of several carbonatites, including Oldoinyo Lengai (Freestone and Hamilton, 1980), Kerimasi (Guzmics et al., 2012) and the Gardiner complex (Nielsen, 1980).

Petrological evidence for liquid immiscibility under upper mantle conditions includes mantle xenoliths containing quenched carbonatite melts of primary magnesium-rich carbonatite magma origin (Kogarko et al., 1995; Ionov et al., 1996). Several melt inclusion studies also provided evidence for carbonate-silicate immiscibility. Solovova et al. (2005) observed. Apatite which was derived from phonolitic nephelinite rocks of the Vulture alkaline igneous complex (Italy) contained primary melt inclusions of clearly separated silicate and carbonate liquids. Solovova and Girnis (2012) studied carbonate-silicate melt inclusions from the carbonatites of the Dunkeldyk alkaline complex (Tajik Republic). Their results indicate immiscibility between the two liquids at high temperatures (>1100 ^{o}C) during the evolution of the primary magma. A study of melt inclusions in perovskite, nepheline and magnetite from a clinopyroxene- and nepheline-rich rock (the rock was determined as afrikandite by the authors, but afrikandite does not contain nepheline and clinopyroxene as it was shown in Dunworth and Bell, 1998, and based on this study the rock is closer to turjaite) from the Kerimasi volcano (Tanzania) showed carbonate-silicate-sulphide immiscibility at crustal pressures (0.5-1 GPa) and 1050 ^{o}C (Guzmics et al., 2012).

Several experimental studies were carried out to reconstruct the immiscibility processes between carbonatite and silicate melts in the SiO_2-Na_2O-Al_2O_3-

$CaO+CO_2$ (+/- H_2O) system (e.g., Wyllie, 1978; Kjarsgaard and Hamilton, 1989; Freestone and Hamilton, 1980) and according to Le Bas (1989), most of the carbonatite deposits formed this way. Nephelinite-carbonatite is the most common silicate-carbonatite association (Mitchell, 2005), and it was used to demonstrate immiscibility in several experimental investigations. The fractionation of nephelinite magma results in a liquid with a composition that moves towards phonolitic magma and an exsolved carbonatitic melt with different (Na_2O+K_2O)/CaO ratios (Le Bas, 1989). Immiscibility occurs at 7.6 kbar (Freestone and Hamilton, 1980; Le Bas, 1989). Kjarsgaard and Hamilton's (1989) experiments showed immiscibility at 5 kbar and 1250 ^oC. Lee et al. (1994) pointed out that rounded crystals commonly observed in run products might have been mistakenly interpreted as immiscible globules in a low-alkali experimental system. These globules were probably carbonate phases that crystallised rapidly during the experiments. To overcome this problem, Veksler et al. (1998) used centrifuge separation of the immiscible melts. They found that the technique helped to separate equilibrium immiscible liquids from quench phases. The results of Veksler et al. (1998) agreed with earlier experiments that used similar compositions (e.g., Freestone and Hamilton; Kjarsgaard and Hamilton, 1989).

Although all of the experimental studies above were able to produce immiscible carbonate and silicate liquids at crustal PT conditions, it was indicated by Brooker and Kjarsgaard (2011) that there is a significant difference in the alkali content used in the different experimental systems that ultimately affected the final compositions of the immiscible melts. Experimental studies with moderate-high alkali content (e.g., Koster van Groos and Wyllie, 1963; Watkinson and Wyllie, 1969, 1971) resulted in a carbonatite melt with high alkaline content, which does not occur naturally, while experiments which used more components were able to produce two immiscible liquids at a lower alkali content (Brooker and Kjarsgaard, 2011). Experimental studies using low alkali bulk compositions in the SiO_2-Na_2O-Al_2O_3-$CaO+CO_2$ system reported the expansion of the two liquid field up to 2.5 GPa (Lee and Wyllie, 1998). Experiments of Keshav and Gudfinnsson (2013) in the alkali-free SiO_2-Al_2O_3-MgO-CaO + CO_2 system showed the existence of two liquids at 2.0-2.6 GPa. Other experiments indicated a decrease of the two-liquid field at higher pressure (~2.5 GPa), and it was concluded that the increasing MgO content caused the reduction of the two-liquid fields (Lee and Wyllie 1998). Brooker and Kjarsgaard's (2011) experimental study at a pressure

of 0.1-2.5 GPa and 1225-1700 °C temperature also showed liquid immiscibility at 5 wt.% alkali content. Furthermore, this study showed that at high pressure (>1.0 GPa), the process requires high partial pressure of CO_2. Due to this observation, they suggested that liquid immiscibility is probably not a common process in the mantle. It most likely occurs at lower pressure (<1.0 GPa) where the process does not require such high CO_2 pressure, for example, in crustal or mantle magma chambers in tectonic environments where the lithosphere is relatively thin. Parental magmas of immiscible carbonatites are considered to be silica-undersaturated alkaline magmas such as olivine nephelinite or olivine melilitite which were derived from a carbonated mantle source (Wallace and Green, 1988; Brooker and Kjarsgaard, 2011). In summary, carbonate-silicate liquid immiscibility was reconstructed by several experimental studies showing that the PT conditions, alkali content, MgO content, and partial pressure of CO_2 control the occurrence of liquid immiscibility. Liquid immiscibility can occur in a crustal or shallow mantle magma chamber where a carbonated mantle-derived silica-undersaturated magma can exsolve immiscible carbonate and silicate melts. Alongside the experimental studies, the melt mentioned above inclusion studies also support carbonate-silicate immiscibility.

1.3.2.2 Primary carbonatite magma formation

Small degree partial melting of a carbonated peridotite produces carbonatitic melt (e.g., Wallace and Green, 1988; Dalton and Wood, 1993; Harmer and Gittins, 1998; Lee and Wyllie, 1998, 2000). The melts have a dolomitic composition with a high Mg-number (Mg#= MgO/(MgO+FeO+Fe2O3), and their alkali content is dependent on their source composition (e.g., Wallace and Green, 1998; Dalton and Wood, 1993; Sweeney, 1994). The melt composition remains dolomitic from ~2 GPa to at least 7 GPa (Dalton and Presnall, 1998). These carbonatite melts are essential agents of mantle metasomatism. As summarised in Harmer and Gittins (1998), the first carbonatite melts are eliminated by reaction with the mantle host, changing the mantle composition from lherzolite to wehrlite, according to the reaction below:

$$CaMg(CO_3)_2 + 4MgSiO_3 \rightarrow CaMgSi_2O_6 + 2Mg_2SiO_4 + 2CO^2 \quad (1)$$

carbonate melt + orthopyroxene (lherzolite) à clinopyroxene(metasomatic) + olivine (metasomatic) + CO_2 (fluid)

Progressive metasomatism of the mantle rocks allows the carbonatite melt to reach crustal levels (Harmer and Gittins, 1998). At shallower depths than ~70 km, carbonatite magmas can only be produced from carbonate-wehrlite (Lee and Wyllie, 2000). Experiments at pressure ≤ 2.5 GPa showed that equilibration of dolomitic carbonatite melts with wehrlite will drive the carbonatitic melt towards more calcitic compositions (Dalton and Wood, 1993; Lee and Wylie, 1998). In the experiment of Dalton and Wood (1993), a carbonate melt coexisted with magnesian calcite-containing wehrlite (2.8-3 GPa). Yaxley and Green (1996) (2.2 GPa) reported sodic dolomitic carbonatite melt compositions in equilibrium with harzburgite and lherzolite due to a reaction between wehrlite and CO_2. As Lee and Wyllie (2000) summarised, between appropriate pressure and temperature in the mantle (70-40 km), the calcite component of the carbonatite melt can reach 89%, while the silicate component can increase from 11% to 18%, and liquids deriving from greater depths can have even higher $SiO_2/CaCO_3$ ratios. Harmer and Gittins (1998) argue that dolomitic carbonatite complexes where isotopic evidence does not support a liquid immiscibility origin (i.e., Spitskop in South Africa, Buhera in Zimbabwe, Napak in Uganda, Kerimasi in Tanzania) are the product of primary mantle-derived carbonatite magmas. Petrological evidence for mantle-derived carbonatites includes mantle xenoliths and xenocrysts found in some extrusive carbonatites (Bailey, 1993; Woolley, 2003).

1.3.2.3 Carbonatite formation by fractional crystallisation

Several authors proposed that carbonatite magma can be generated by fractional crystallisation from CO_2-rich silicate magma (e.g., Watkinson and Wyllie, 1971; Lee and Wyllie, 1998). Watkinson and Wyllie (1969) showed that carbonate-rich residual liquid cannot be generated by fractionating silica-saturated magmas at crustal pressures and that the assimilation of carbonate-rich material cannot produce alkaline magma. Watkinson and Wyllie (1971) showed that fractional crystallisation of a silica-undersaturated magma can result in a carbonate-rich melt in the system $NaAlSiO_4$-CaO-CO_2-H_2O. The work reconstructed the formation of mineral assemblages: “(1) nepheline; (2) melilite + nepheline; (3)

hydroxy-haüyne + melilite; (4) cancrinite + melilite and (5) calcite + cancrinite + melilite" which were crystallising continuously at 1 kbar and 600-960 ^{o}C. These mineral assemblages are not abundant components of carbonatite complexes but do occur in okaite, which was considered to be a late-stage product of ijolite or carbonatite magma crystallisation (Gittins, 1989). Formation of sövites of silicate-carbonate complexes by fractional crystallisation is suggested by Kjarsgaard (1998), based on experiments which were carried out at 0.2 and 0.5 GPa and 900-1040 ^{o}C for a carbonated high-CaO nephelinite and it was concluded that phlogopite- olivine-dominated fractionation can result in a carbonate-rich residual liquid. With experiments, Lee and Wyllie (1998) demonstrated that dolomitic magmas can form by fractionating calcite carbonatites. Gittins (1989) disagrees that fractional crystallisation is a substantial process in carbonatite formation, firstly because natural nephelinite magmas are unlikely to contain enough CO_2 for this process, and secondly because of the lack of any known rock with intermediate composition between nephelinite and carbonatite and finally, the fractionation cannot explain the exceptionally high Nb and REE content of some carbonatites. In contrast, fractional crystallisation was thought to have played a significant role in forming the Kola Alkaline Province (Korobienkov et al., 1998; Bell and Rukhlov, 2004; Downes et al., 2005).

1.3.3 Tectonic environment and lithospheric structures of carbonatites

Although the mantle origin of carbonatites is proven, the driving forces of the magmatism are still debated. There are two main views: one holds that the lithospheric processes control carbonatite magmatism and the other is that it is controlled by plume activity.

Advocates of lithospheric control (e.g., Bailey, 1964; 1983; 1992; Woolley and Bailey, 2012) suggest that large-scale tectonic events like plate motions control igneous activity through the formation of tectonic zones in the lithosphere, which work as migration channels for fluids and magmas. The theory is supported by the observations that the location of carbonatite deposits coincides with tectonic structures. Woolley and Bailey (2012) listed twenty-nine alkaline, kimberlite and carbonatite occurrences linked to regional tectonic activities in the African

continent. Woolley (1989) summarised the tectonic structures in which carbonatite occurrences were noted, including rift valleys, major faults, lithosphere-domes, major tectonic lineaments, orogens and plate margins. Examples of graben-related carbonatites include the occurrences in the East African Rift System and the Kaiserstuhl carbonatite in the Rhinegraben, Germany (Woolley, 1989). Carbonatites linked to rift and fault system intersections include the Chilwa Province carbonatites in southern Malawi that formed at the junction of the Zambezi Rift and the East African Rift. Further significant tectonic structures are the swells and domes of the lithosphere that formed along structural weaknesses, and their formation is linked to pre-drift-related faulting and rifting (Woolley and Bailey, 2012). Carbonatite formation can be periodic along the structures discussed above (e.g., Woolley and Bailey, 2012), and this made many researchers believe that the behaviour of the lithosphere is the primary driving force of carbonatite magmatism. Carbonatite deposits occur in both orogenic and anorogenic tectonic environments. According to Bailey and Woolley (2012), no evidence exists for the connection between dome formation and plume activity. The repetition of carbonate and alkaline magmatism in rift systems during large-scale plate movements supports the lithospheric control theory.

According to another view, the spatial and temporal associations between carbonatites, plumes and flood basalts combined with isotopic data suggest that mantle plume activity plays a major role in carbonatite formation (e.g., Bell, 2001; Bell and Tilton, 2001; Wu et al., 2011). Several carbonatite intrusions such as Cape Verde, Canary Islands, Kola Peninsula (e.g., Afrikanda, Khibiny, Kovdor) and the carbonatites of the East African Rift System in Uganda (e.g., Bukusu, Napak, Fort Portal), Kenya (e.g., Buru Hill, Homa Mountain, Shombole) and Tanzania (e.g., Kerimasi, Oldoinyo Lengai, Mosonik) are considered to be plume-related, and many other localities are associated with large igneous provinces (LIP). Examples are summarized in Ernst and Bell (2010) and include the formation of the Paranà- Etendeka LIP (~130 Ma), which is linked to the formation of the Jacupiranga and Messum carbonatites. Likewise, the ~250 Ma old Siberian LIP is linked to the Maimecha-Kotui alkaline province, which contains several carbonatite intrusions. The formation of the Kola Alkaline Province (~370 Ma) was coeval with the extended basaltic magmatism in the East European craton. The Deccan flood basalt in west-central India (~66 Ma) is associated with Amba

Dongar, Sarnu-Dandali (Barmer) and Mundwara carbonatites. The carbonatites of the Superior craton in Canada are associated with the Keweenawan LIP (1114-1085 Ma) and the pan-Superior (1085 Ma) mafic-ultramafic magmatism of the area. Likewise, the formation of the Phalaborwa carbonatite complex on the Kaapvaal craton is linked to the Bushveld LIP (2055 Ma) (Ernst and Bell, 2010; Wu et al., 2011). Ernst and Bell (2010) suggest that LIPs and carbonatites might be parts of the same system but are derived from different depths and sources with different isotopic compositions and fluid content. They also suggest that those carbonatites not linked to LIPs could be derived from plumes that could not produce flood basalts because of their deeper position. Observations of Bell and Rukhlov (2004) at the Kola Alkaline Province support the thermally and compositionally zoned plume model and suggest that carbonatite magma might be generated at the distal, volatile-rich part of the plume, while flood basalts are generated at the centre.

1.3.4 Mantle source characteristics of carbonatites

A large number of isotopic studies proved that carbonatites are derived from heterogeneous metasomatised sublithospheric mantle (e.g., Eriksson, 1989; Simonetti et al., 1995; Wu et al., 2011;). Carbonatite and alkaline magmas are considered to be derived from small degree fractional melting of the mantle (Kramm and Kogarko, 1994; Stevenson et al., 1997). The geological settings of carbonatite magmatism were considered to be any anorogenic, rifted, or subduction-related tectonic environments (e.g., Simonetti et al., 1995; Kogarko et al., 2010). The source of the carbonatite magma was suggested to be lithosphere modified by plumes (e.g., Simonetti et al., 1995; Graham et al., 2004) and a non-convective subcontinental lithospheric mantle (SCLM) with continuous metasomatism which can provide the initial trace element enrichment (Smith et al., 2016).

1.4 Introduction to phoscorite rocks: classification and petrogenesis

1.4.1 Phoscorite classification

Phoscorite is a significant constituent of the Phalaborwa Igneous Complex, which was the first location where the rock type was described by Russel et al. (1954). Phoscorites are magmatic rocks consisting mainly of apatite, magnetite and olivine or diopside and phlogopite (e.g., Krasnova et al., 2002; Krasnova et al., 2004; Wall and Zaitsev, 2004). It is considered a relatively rare rock type, with only 21 occurrences reported worldwide (e.g., Krasnova et al., 2004) which number is a possible underestimation considering that phoscorites might not have been classified as such at certain localities (Krasnova et al., 2004).

The IUGS classification system describes phoscorite as “a magnetite, olivine, apatite rock usually associated with carbonatites” (Le Maitre, 2002). Krasnova et al. (2004) described two classification methods for phoscorites (the methods of Yegorov, 1993 and Krasnova et al., 2002), and none of these was considered in the IUGS classification systems for igneous rocks (Le Maitre, 2002). Yegorov’s (1993) classification scheme applies to rocks dominated by forsterite or diopside, magnetite and apatite. Based on the relative proportion of the mentioned minerals, nine phoscorite types were differentiated, as it is shown in Figure 1.1. a. Another type of classification is the RHA method, described in Krasnova et al. (2004) and more detail in Krasnova et al. (2002). As Krasnova et al. (2004) describe, “RHA is a general procedure designed for the description, grouping and systematic study of any objects and for the creation of database retrieval systems”. In this case, the RHA method was used for ordering mineralogical and chemical data. Krasnova et al. (2004) used approximately 1260 chemical analyses from various sources, including the author’s unpublished data and published data from several works, covering numerous phoscorite occurrences worldwide (the used literature and locations are listed in Krasnova et al., 2004). The geochemical ordering method combined with normative calculation of the molecular % of the rocks’ mineral components yielded the classification diagram depicted in Figure 1.1.b. Krasnova et al. (2004) state that the RHA method is not an alternative classification system for other traditional methods but can be used as an additional aid to describe phoscorites. The advantages of the method include the ability to describe all phoscorite variants, including the continuous series through carbonatite and related rocks. Disadvantages include the

necessity of geochemical data and specific computer software and that the calculation might result in false modal proportions (Krasnova et al., 2004).

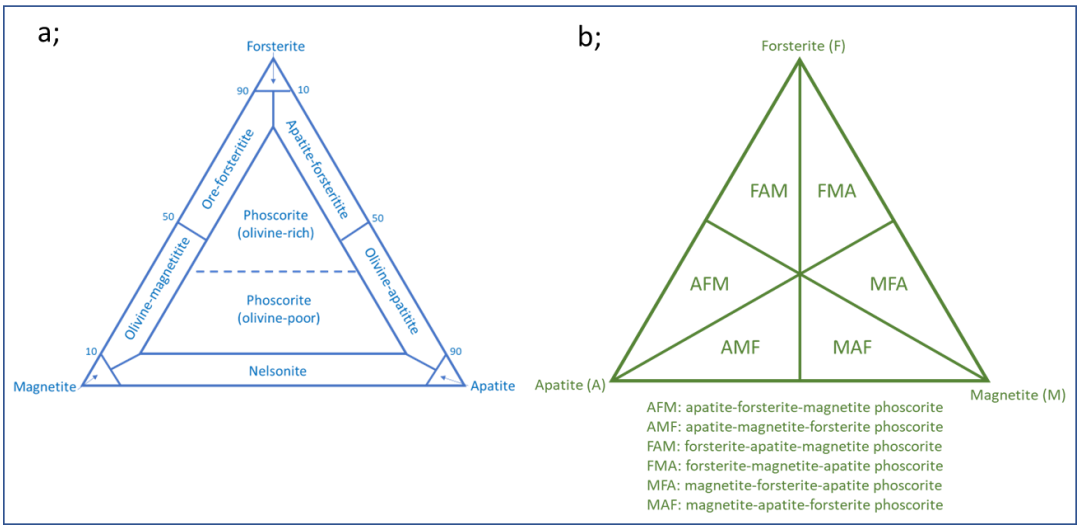

Figure 1.1. Alternative phoscorite classification systems (non-IUGS) by Yegorov (1993) (a) and Krasnova et al. (2002) (b).

1.4.2 Phoscorite petrogenesis and mantle origin

The association with carbonatite rocks and the mineralogical and chemical similarities suggest a strong petrogenetic link between the two rock types (e.g., Zaitsev and Bell, 1995; Krasnova et al., 2004; Cordiero et al., 2010; Rass et al., 2020). In contrast, Dunworth and Bell (2001; 2003) found that the silicate, carbonatite and phoscorite rocks of the Turiy Complex (Kola Alkaline Province, Russia) show Sr and Nd isotope differences, suggesting that these coeval rocks were not generated from the same parental magma but were derived from multiple magma batches of heterogeneous mantle source and evolved via multi-stage differentiation processes. Cordiero et al. (2010) argued that regardless of the radiogenic isotope signature of the source, petrological, mineralogical, and geochemical evidence and the fact that phoscorites occur only in carbonatite-related areas provide a strong case for a common phoscorite-carbonatite parental magma.

Phoscorite (and associated carbonatite) petrogenesis models include gravity settling of heavy minerals (forsterite, magnetite, apatite) (Vartiainen, 1980), separation of light carbonate-rich cumulates (carbonatites) by crystal

fractionation (e.g., Gittins, 1989; Lee and Wyllie, 1998; Veksler et al., 1998; Kogarko et al., 1997; Rass et al., 2020) and liquid immiscibility (e.g., Verwoerd, 1967; Le Bas, 1981; Lee et al., 2004; Rass et al., 2020). Petrological evidence for silicate-carbonate liquid immiscibility included the orbicular and spherulitic carbonatites and phoscorites (representing carbonate globules in silicate matrix or silicate globules in carbonate matrix) listed by Krasnova et al. (2004) from various locations. While studying the carbonatites and phoscorites of the Sokli complex (Finland), Lee et al. (2004) found no geochemical continuum between the phoscorites and carbonatite rocks. Furthermore, zoning patterns of micas and pyrochlores from the phoscorites indicated a more extended crystallisation history than in the carbonatites (cores were similar, but the margins were more developed and more evolved in the phoscorites), suggesting that cumulate and residual liquid origin for the phoscorites and carbonatites respectively was unlikely. The authors concluded that mineralogical equivalence between the two rock types is restricted to the early stages of crystallisation and proposed an immiscibility process between Fe-Ti-rich and carbonatite-rich melts that required further experimental testing. Early crystallisation of olivine, mica and magnetite before segregation would explain the presence of these minerals with the same compositions in both carbonatites and phoscorites (Lee et al., 2004). Rass et al. (2020) studied the carbonatite-phoscorite complex in the southwestern part of the Kovdor massif (Russia). They concluded that both crystal fractionation and liquid immiscibility occurred during the rocks' evolution. Evidence for the former included similar tendencies in compositional changes in both phoscorites and carbonatites from the earlier to late varieties and mineral zoning in both rock types. Differences in trace element (Sr, Zr, Hf) compositions of the carbonatite and phoscorite rocks, however, could not be explained by crystal fractionation only and prompted the authors to consider (in agreement with Lee et al., 2004) liquid immiscibility between phosphate (or Fe-rich phosphate) and carbonatite-proper magmas. Mikhailova et al. (2018) proposed that Kovdor phoscorites and carbonatites were fractionated directly from a single alkaline-ultramafic magma based on the rocks' gradual chemical and mineralogical composition variations. The 3D mineralogical mapping of the Kovdor pipe revealed a gradual zoning defined by the forsterite-hydroxilapatite-magnetite-calcite crystallisation sequence where the alkalinity of the minerals progressively increases with depth (Mikhailova et al., 2016). Rass et al. (2020) pointed out that the results and

conclusions of Mikhailova et al. (2018) are inconsistent both with earlier (Russian) and their own results. Both liquid immiscibility (Giebel et al., 2019) and crystal fractionation (Milani et al., 2017b) were proposed for the origin of the Phalaborwa phoscorites and carbonatites, as it was mentioned in Section 1.1. Carbonate-silicate liquid immiscibility and fractionation and the conditions of their occurrence were discussed in sections 1.3.2.1 and 1.3.2.3.

The strong petrogenetic link between phoscorites and mantle-derived carbonatites also suggests mantle origin for the phoscorites. Sr-Nd isotopic compositions of phoscorites, silicates and carbonatite rocks from the Kola Alkaline Province suggest a complex evolution of these rocks where multiple magma batches evolved from a heterogeneous mantle or mixing of different mantle components (Zaitsev and Bell, 1995; Verhulst et al., 2000; Dunworth and Bell, 2001). Zaitsev and Bell (1995) suggested the mixing of three different mantle components to explain the Sr-Nd isotopic characteristics of the phoscorites and carbonatites of the Kovdor massif. Similarly, a heterogeneous mantle source was proposed in the case of the Phalaborwa Complex (e.g., Eriksson, 1989; Wu et al., 2011).

Crystallisation temperatures for phoscorite mineral constituents included 750-900 ^{o}C for forsterite and 700-900 ^{o}C for apatite in the Kovdor phoscorite (e.g., Kharlamov et al., 1981), while from the Phalaborwa phoscorites apatite showed 850-870 ^{o}C (Solovova et al., 1998).

Chapter 2: Geological background and previous research

2.1 The Kaapvaal craton

2.1.1 The structure of the craton

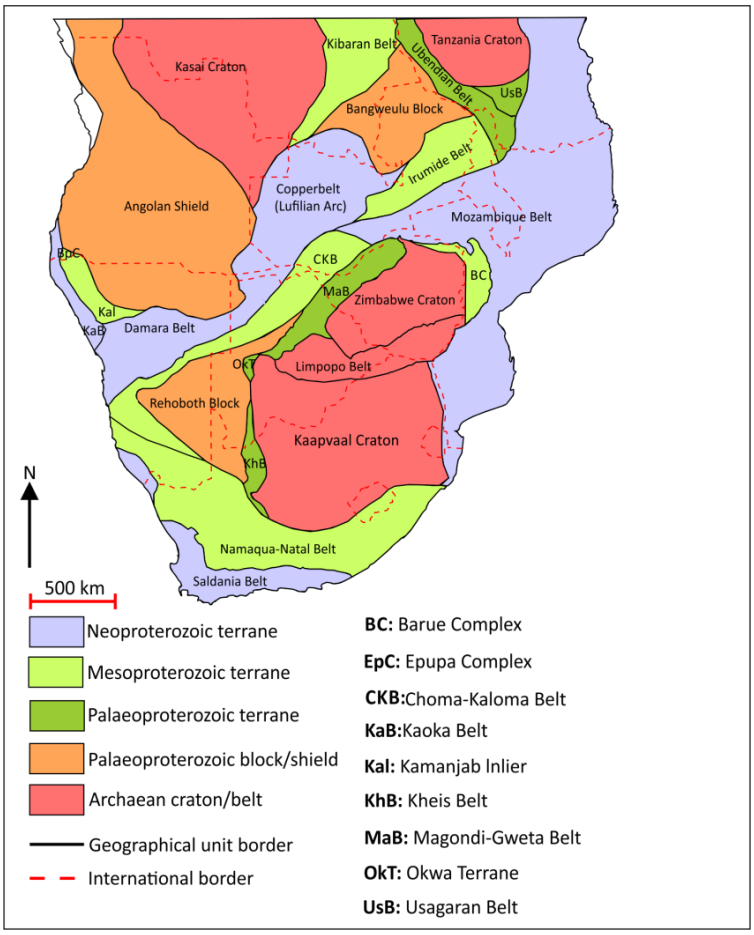

Figure 2.1.1. Structural units of Southern Africa (after McCourt et al., 2013).

The Kaapvaal craton is situated in the southern corner of the African continent and geographically extends to South Africa, Botswana, Zimbabwe, Swaziland, Mozambique and Lesotho. The surface area of the craton is approximately 1,200,000 km2. The northern borders of the Kaapvaal craton include the Limpopo Belt, which connects it to the Zimbabwe craton, and the Okwa block (Fig.2.1.1). From south and southwest it is bordered by the Namaqua-Natal Belt and the Kheis Belt while on the east it connects to the Mozambique Mobile Belt (Fig.2.1.1) (McCourt et al., 2013).

The Kaapvaal craton comprises four different units, which in the literature are referred to as either terranes, blocks or units; the present work will use the former. The four terranes include the Kimberley terrane in the western part of the craton, the Swaziland terrane that forms the southeastern part, the Witwatersrand terrane in the central part, and the Pietersburg terrane in the north. In the literature (e.g., Eglington and Armstrong, 2004), the names Southeastern, Central, Western and Northern terrane (or domain, block, unit) also appear occasionally.

The Witwatersrand terrane connects to its western neighbour, the Kimberley terrane, along the Colesberg lineament or Colesberg Magnetic Anomaly (e.g., Eglington and Armstrong, 2004). in the north, it joins the Pietersburg terrane along the Thabazimbi-Murchison lineament and the Swaziland terrane to the south by the Barberton lineament.

The Kimberley terrane is much younger than the Swaziland terrane and consists of primarily gneisses between the ages of 2.8 Ga and 3.0 Ga, 2.65-Ga granitoids and narrow greenstone belts formed between 3.0 and 3.1 Ga (Griffin et al., 2004). However, harzburgitic diamonds from Kimberley kimberlites associated with the formation of the Western craton nucleus showed an age of 3.2 Ga (Richardson et al., 2004). Eclogitic diamonds from the same source gave an age of 2.9 Ga, representing subduction events during the amalgamation of the western and eastern parts of the Kaapvaal craton (Richardson et al., 2004). A collision between the Western terrane and other parts of the Kaapvaal craton occurred at the end of the Archaean (2.65 Ga). This event resulted in the formation of the 2.46-Ga Buffelsfontein Group (Donnelly et al., 2011), representing an active continental margin. The western part of the terrane was amalgamated into the craton during the Early Proterozoic (Donnelly et al., 2011).

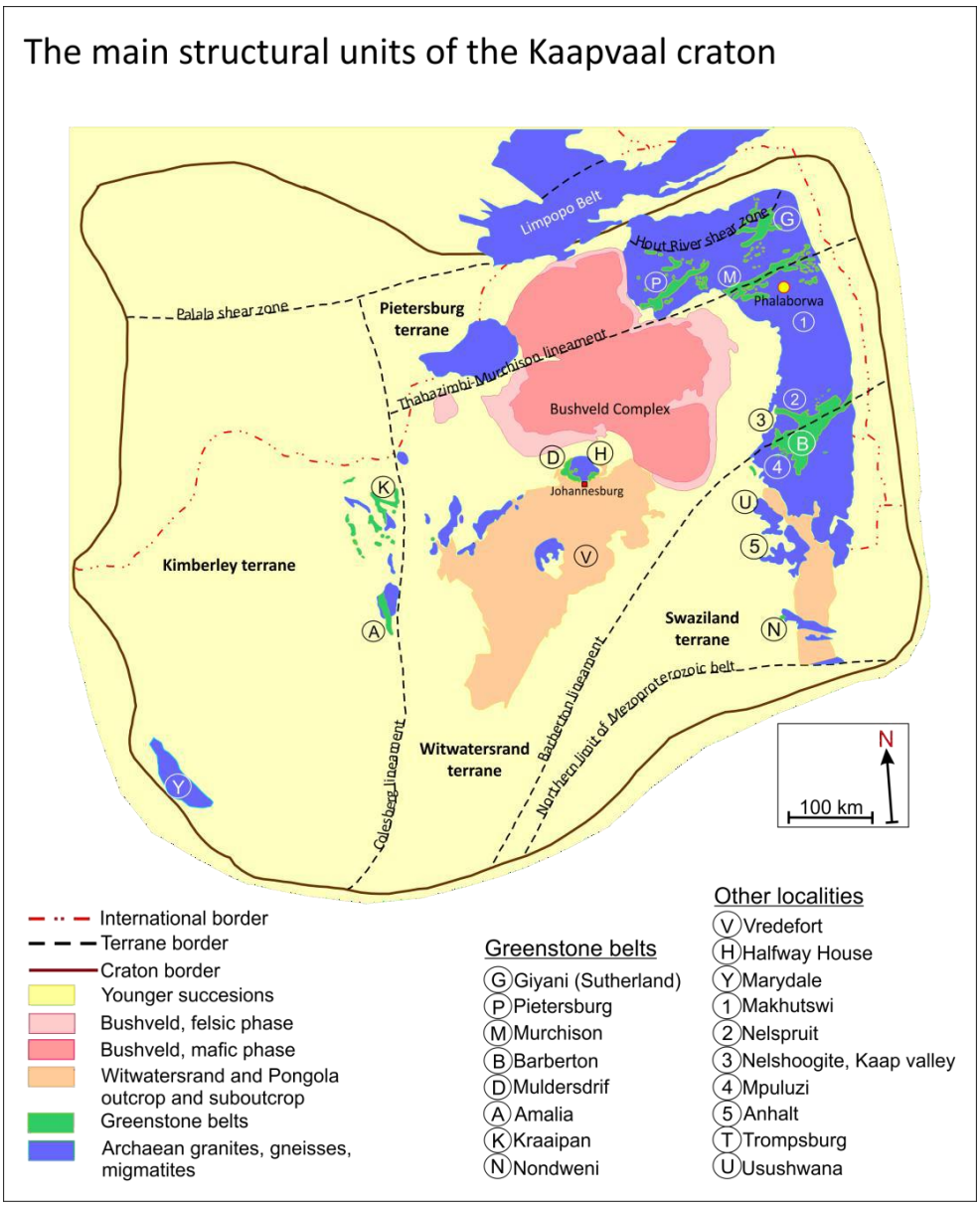

Figure 2.1.2. Structural units of the Kaapvaal craton (after Eglington and Armstrong, 2004)

2.1.2 The evolution of the Kaapvaal craton (from the proto-craton formation until the intrusion of the Phalaborwa Complex)

The structural units of the Kaapvaal craton are shown in Figure 2.1.2. Main phases of the tectonic evolution of the Kaapvaal craton are summarised in Figure 2.1.3. As Eglington and Armstrong (2004) described, the early nucleus of the Kaapvaal craton includes the area between southern Swaziland and the southern Barberton Greenstone Belt and started its evolution with the formation of the Ancient Gneiss Complex (~3350 Ma to 3985 Ma). Other authors suggested that

the proto-craton nucleus extended further south to the Nondweni Greenstone Belt (Wilson and Carlson, 1989; De Wit et al., 1992; Carlson et al., 2000).

Eglington and Armstrong (2004) note that zircons from the Ventersdorp lavas located on the Witwatersrand terrane may suggest the possible extension of the proto-Kaapvaal craton further west.

Detrital zircons from the Ancient Gneiss Complex of Swaziland (Ngwane and Dwalile gneisses) gave the oldest dates of the Kaapvaal craton (and southern Africa), showing ages of 3702 ± 1 Ma, 3683 ± 10 Ma and 3644 ± 4 Ma (Compston and Kröner, 1988; Kröner et al., 1996). More recently, Donnelly et al. (2011) dated the tonalite-trondjhemte-granodiorite (TTG) gneisses of the area and gained ages of 3.68-3.2 Ga, which is consistent with the ages mentioned above. Eglington and Armstrong (2004) note that a significant volcanic episode occurred in the Ancient Gneiss Complex between ~3.6 and ~3.5 Ga. Similarly old detrital grains were dated in the central zone of the Limpopo Belt (Beit Bridge Complex), giving an age of 3709 ± 3 Ma (Kröner et al., 1996).

The next significant event was the onset of the Onverwacht Group volcanism between 3.55 and 3.45 Ga (Kröner et al., 1996), which terminated the proto-nucleus stage of the Kaapvaal craton. The Onverwacht Group volcanism includes the formation of the Theespruit and Komati Formations with an age of ~3.47-~3.48 Ga (Armstrong et al., 1990). Eglington and Armstrong (2004) note that many formations of the Onverwacht Group showed an age of ~3.45 Ga, the same as the tonalite-trondjhemte-granodiorite plutons of the southern Barberton Greenstone Belt with a suggested genetic relationship between the Onverwacht Group and the latter (De Ronde and De Wit, 1994).

The southward expansion of the proto-Kaapvaal craton over the next 200 million years was suggested by Wilson and Carlson (1989), De Wit et al. (1992) and Carlson et al. (2000). The suggestion was based on the age data obtained from the Nandweni Greenstone Belt, giving dates of ~3.2 Ga. However, magmatic zircons yielded ages older than 3.4 Ga, giving the reason for the reconsideration of the area of the proto-Kaapvaal carton and extending it down to Nandweni (Wilson and Carlson, 1989; De Wit et al., 1992 and Carlson et al., 2000).

The next major episode of the craton evolution occurred around ~ 3.23 Ga during the amalgamation of the northwestern and southeastern parts of the Barberton

Mountain Land (De Ronde and De Wit, 1994; Lowe, 1999) and regional suture formation between the Swaziland and Witwatersrand terranes (De Wit et al., 1992).

Eglington and Armstrong (2004) noted that between 3.37 and ~3.24 Ga, two igneous episodes can be separated based on detrital, crystallisation and metamorphism dates. One igneous episode occurred around ~3.3 Ga while the other around ~3.25 Ga. The igneous activity spread from the south-east towards the west and reached the centre of the craton and the Pietersburg terrane. Most activity were concentrated in the Barberton area, forming granitoid intrusions around the greenstone belt. However, it was also significant in the Swaziland and Witwatersrand terranes, forming the Vredefort dome. In the Pietersburg terrane, the volcanism affected the Guyani Greenstone Belt, the central part of the Limpopo Belt. High-grade metamorphism (> ~500 ^{o}C) affected the southern part of the Barberton Greenstone Belt (~3.24 Ga) and the Vredefort dome (~3.2 Ga) (Eglington and Armstrong, 2004). The igneous period was represented by several granitoid intrusions with the age up to ~3.1 Ga. These granitoids occur at the Johannesburg dome (Halfway House granitoids), Kaap Valley tonalite, Nelshoogite gneiss, Anhalt leucotonalites and the eastern margin of the Kaapvaal craton represented by the Mpuluzi granite, Nelspruit and Makhutswi granitoids. This long and extensive igneous period in this area was terminated by the deposition of the Moodies Group sediments, the final part of the Barberton Greenstone Belt (Eglington and Armstrong, 2004).

The igneous activity lasted longer in the Witwatersrand terrane, forming the Dominion Group around ~3.1 Ga. During the same period, greenstone belt formation took place in the Kimberley terrane (Kaapian) and the Pietersburg terrane (Murchison), followed by volcanic activity around ~2.95 Ga in the latter (Eglington and Armstrong, 2004).

Between ~3.04 and ~2.88 Ga, granitoid intrusions were emplaced at the contact of the Witwatersrand and Kimberley terranes. This was the time of the formation of the Colesberg magnetic anomaly. The origin of the magnetic anomaly line was explained by either the juxtaposition of the two terranes or the intrusion of magnetic formations at shallow crustal levels (De Wit and Tinker, 2004).

The large sedimentary basins and successions of the Kaapvaal craton, such as the Witwatersrand Supergroup and the Pongola Supergroup, formed from ~2.91 Ga until ~2.71Ga. During the same period, the Ventersdorp volcanic group formed in major extensional grabens (Tinker et al., 2002; Eglington and Armstrong, 2004), and late to post-tectonic granite plutons were emplaced throughout the craton (Eglington and Armstrong, 2004). The igneous activity continued in the Swaziland and Witwatersrand terranes until 2.61 Ga and concentrated at the northern and western margins of the craton (Eglington and Armstrong, 2004).

The accretion of the Kimberley and Witwatersrand terranes took place about 300 million years before the ~2.75 Ga igneous activity in the Amalia Greenstone Belt, and the creation of the current form of the craton finished by this time (Eglington and Armstrong, 2004). High-grade metamorphism occurred between ~2.75 Ga and ~2.65 Ga, and Eglington and Armstrong (2004) note that this was the first period when extensive geochronological evidence for metamorphism was preserved. The period between 2.65 and 2.6 Ga was characterised by the development of proto-basins for the Transvaal Supergroup and the extensive syn-tectonic granitoid formation associated with the Limpopo orogeny. Granitoid volcanism in the Limpopo Belt continued until 2.5 Ga (Eglington and Armstrong, 2004).

Between ~2.4 Ga and ~2.1 Ga, siliciclastic sediments (Pretoria and Postmasburg Groups) and extensive igneous formations (e.g., Hekpoort andesite) were emplaced as constituent parts of the Transvaal Supergroup. The process was terminated by extensive Rooiberg Group, the formation of Dullstroom Formation, and the intrusion of granite and mafic rocks of the Bushveld Complex at ~ 2.06 Ga. At the same time, extensive, high-grade metamorphism affected the whole craton except its southeastern part (Eglington and Armstrong, 2004).

The Phalaborwa Igneous Complex was formed at the northeastern part of the Witwatersrand terrane, around 20 km south-east from the Thabazimbi-Murchison lineament, which has been repeatedly re-activated during the evolution of the craton (Harmer, 2000). The formation of the Phalaborwa Igneous Complex was coeval with the Bushveld Complex (Wu et al., 2011).

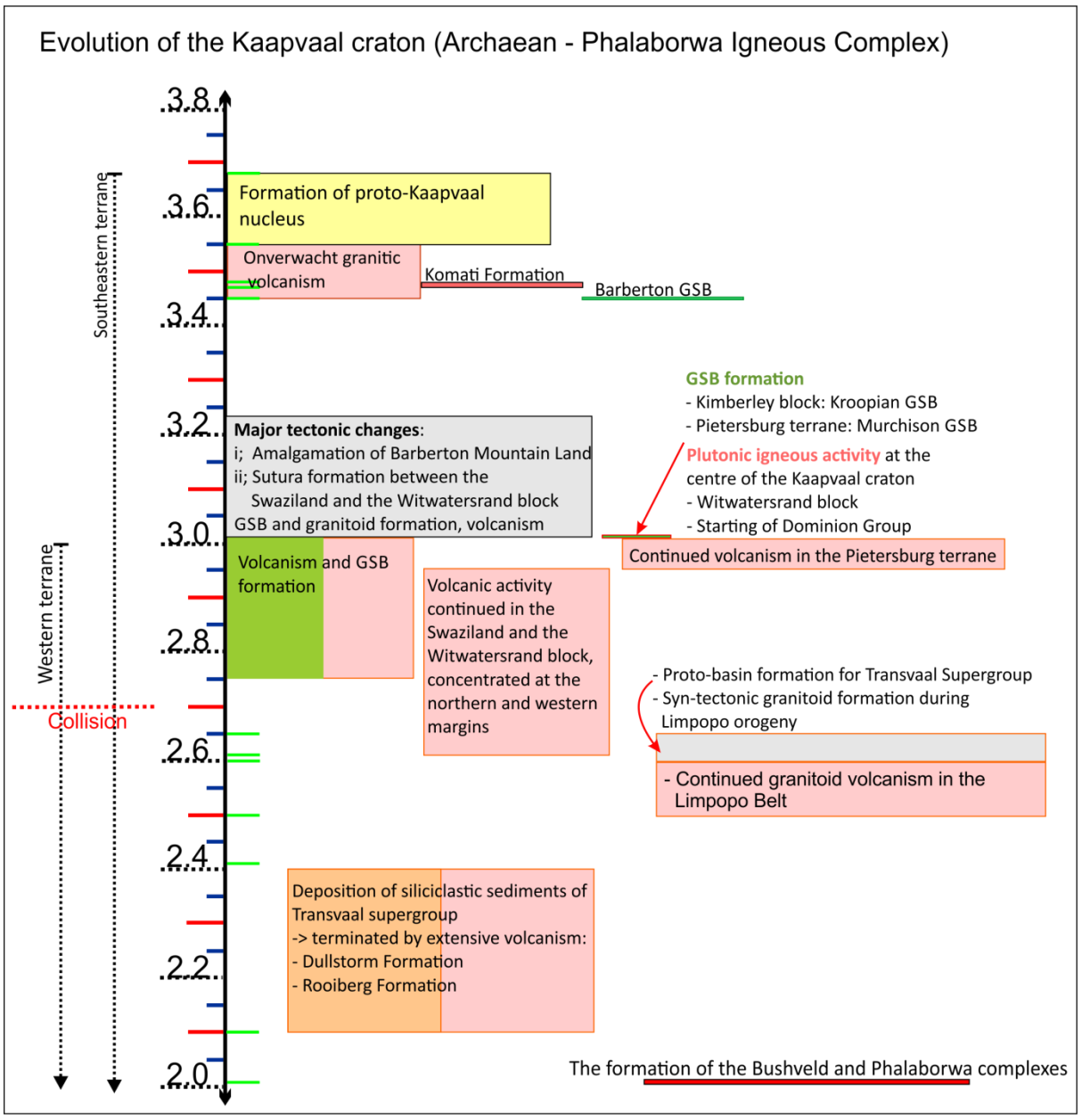

Figure 2.1.3. Main events of the tectonic evolution of the Kaapvaal craton between the Archaean proto-nucleus stage and the formation of the Phalaborwa Igneous Complex (after Eglington and Armstrong, 2004; De Wit and Tinker, 2004. Wu et al., 2011)

2.2 The geology of the Phalaborwa Igneous Complex

The geological description of the Phalaborwa Igneous Complex in the present study relies majorly on the work of Hanekom et al. (1965) who provided the most detailed report.

2.2.1 Location and the general characteristics of the complex

The Phalaborwa Igneous Complex (Fig.2.2.1-2) is a north-south elongated, kidney-shaped body with a surface area of approximately 15-18 km^2. It is situated in Letaba District, northeastern Transvaal (Longitude 31^o 07' East and latitude 24^o 00' South). The best geographical indicator of the location is the merging point of the Olifants and Ga-Selati Rivers right at the southern edge of the complex. Phalaborwa town is located on the northern side of the complex, hosting the Phalaborwa Gate of the Kruger National Park. The large-scale mining operation takes place south from the town and extends over the entire area of the complex.

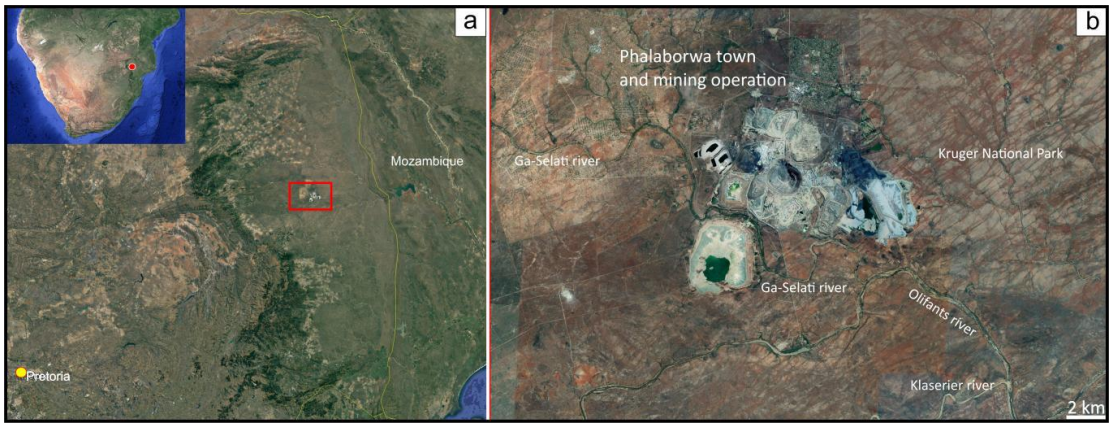

Figure 2.2.1. Location of the Phalaborwa Igneous Complex

The deposit is mined by Palabora Mining Company Ltd. The primary commodities are copper (probable reserves: 35Mt at 0.54% grade), magnetite (probable reserves: 9.6 Mt at 55.1% Fe), vermiculite and apatite. By-products of electrorefining processes (so-called anode slime) are recovered and processed for Ag, As, Au, Bi, Pb, Sn, Se, Te, PGE and sulphuric acid (Palabora Mining Company Annual Report 2012, Rio Tinto; (PorterGeo Database - Ore Deposit Description). The copper and other types of sulphide mineralisation are hosted by carbonatites, mainly by the transgressive carbonatite. The average proportion of sulphides in the carbonatites is 2-3 wt%. Magnetite is recovered from both the carbonatites and the phoscorite, while apatite and vermiculite are mined from the phoscorite and clinopyroxenite.

The Phalaborwa Igneous Complex intruded into an Archaean granite-gneiss complex. The most prominent rock type is clinopyroxenite, with variable modal compositions. The centre of the clinopyroxenite body is intruded by an east-west-trending elongated phoscorite-carbonatite body called Loolekop, which divides the clinopyroxenite into northern and southern units. The phoscorite and the carbonatites form a typical ring complex structure. The carbonatites are calcite carbonatites and can be separated into older banded carbonatite, younger banded carbonatite and the youngest transgressive carbonatite, emplaced in the core of the complex. Small syenite intrusions are common in the area; these are coeval with the Phalaborwa complex (Wu et al., 2011) and form separate, plug-like bodies inside the granite-gneiss complex. Dolerite dykes that crosscut the intrusion in the NE-SW direction are Paleoproterozoic in age (Wu et al., 2011).

Fenitisation of the granite-gneiss was observed at the clinopyroxenite contact. Syenite veinlets and carbonate veinlets and dykes traverse the main clinopyroxenite body. The carbonatite veinlets and dykes spread radially from the carbonatite core of Loolekop and can be found even in the far northern part of the complex. Based on the calculated crystallisation pressure of fluorapatite (4-4.5 kbar), a shallow emplacement depth was suggested (Solovova et al., 1998).

Vermiculitisation is a process that largely affected and created significant economic value in the Phalaborwa complex. As Hanekom et al. (1965) summarised, vermiculite formed by the hydration and alkali loss from phlogopite and biotite. Serpentinisation is also widespread in the Phalaborwa pegmatoid bodies. Hanekom et al. (1965) suggested that magmatic fluids caused the initial stage of olivine serpentinisation, and it was continued by meteoric water close to the surface.

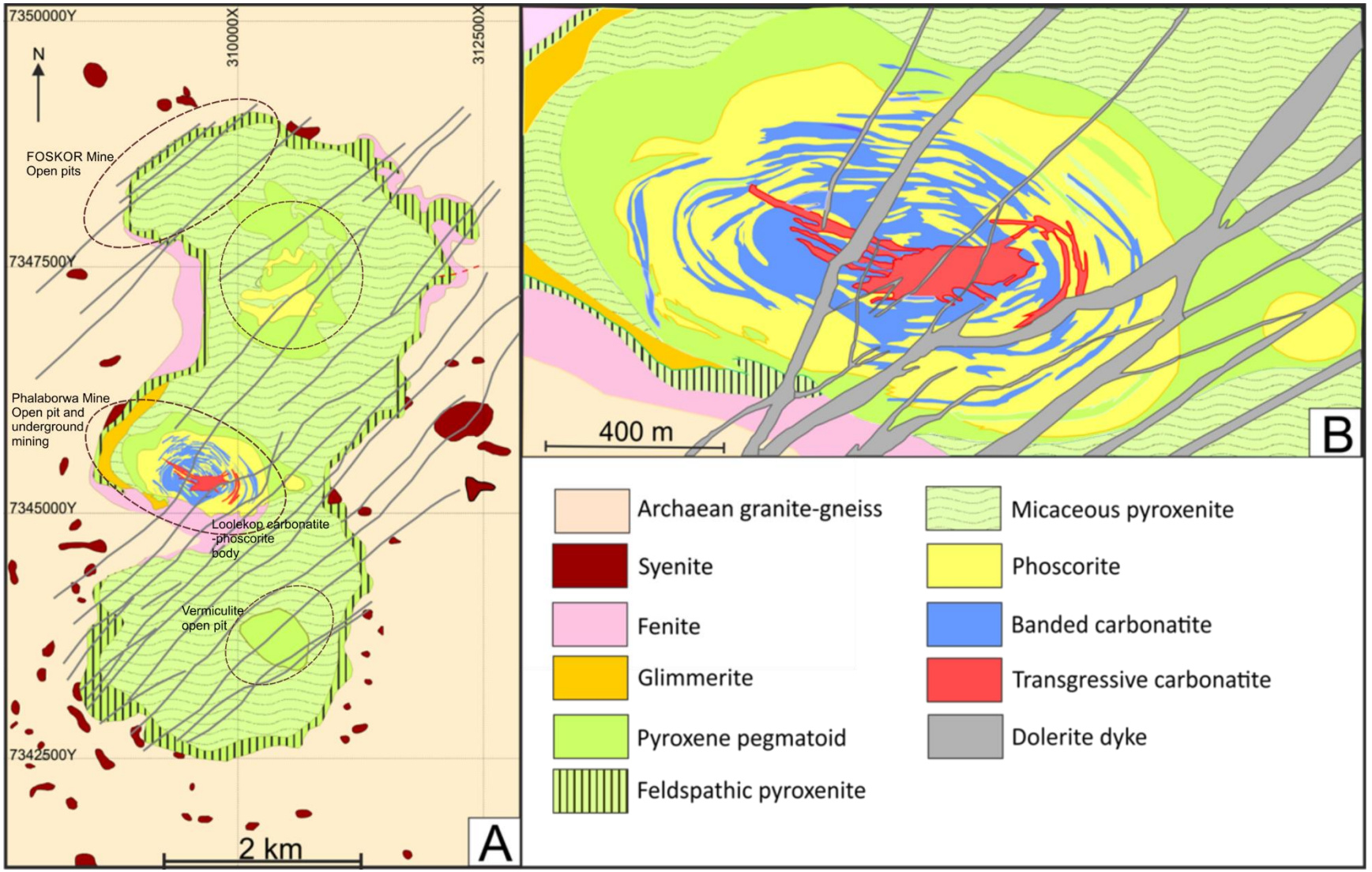

Figure 2.2.2. Geological map and the mining areas of the Phalaborwa Igneous Complex (A) and the Loolekop carbonatite (B) (After Hanekom et al., 1965; Letts et al., 2011; Giebel et al., 2019)

2.2.2 Characteristics of the different lithologies of the Phalaborwa complex and its Archaean wallrocks

2.2.2.1 The Archaean-Gneiss complex

Hanekom et al. (1965) describe the granitic rocks around the Phalaborwa complex as having a significant compositional and textural variation. Both typical granite-gneiss textures with modal banding and true granite textures without banding were observed. However, in the latter case, the official classification of granite-gneiss does not apply, and the rock should be called granite (Hanekom et al., 1965). These granites (with true granitic texture) commonly occur in the area, and they were described in the western part (Mashishimala) and crosscutting veins and dykelets around the complex. At least three different granite types were recognised (Hanekom et al., 1965 and references therein). The typical granite-gneiss rocks are prominent in the south and southwestern corners of the complex. The rock was described as medium- to coarse-grained, grey and yellowish-grey. The mineral composition includes feldspar, quartz and biotite. The gneiss was intruded by an almost mica-free granite with a close-to-pegmatitic texture. Granitic veins crosscut both rock types above and dykes with a different composition from the granitic rocks above.

The field relation of the different granite types and gneiss is the best exposed in the Selati Riverbed. Figure 2.2.3 shows the relationship between the different Phalaborwa granite types. The prominent rock type observed in the exposures was a pink granite (pinkish-grey), which formed narrow veins crosscutting the gneiss. The pegmatitic texture of the pink granite was observed locally, displaying large quartz and orthoclase crystals. The emplacement of the pink granite was followed by the intrusion of a narrow vein system with a darker colour and more basic composition. The rock was described as fine-grained, equigranular textured, containing orthoclase, green pyroxene and titanite with accessory apatite and magnetite. The next event was the intrusion of reddish, more acidic,6-cm wide veins with large quartz crystals and reduced mafic mineral content. The origin of the dark and reddish vein systems was linked to the intrusive syenite plugs of the area (Hanekom et al., 1965). The latest intrusion of the Archaean age is represented by approximately 0.3-m wide, basaltic or doleritic dykes, which

crosscut the previously described lithologies (Hanekom et al., 1965 and references therein).

Another granite type was observed around the main pyroxenite body. This leucocratic granite can be massive, unfoliated or can display biotite-defined foliation. Its modal mineralogy is dominated by quartz and feldspars of various compositions (microperthite, oligoclase, microcline) and texture and includes minor biotite and occasional muscovite. Where foliation occurs, it follows the local E-W tectonic fabric (Hanekom et al., 1965). Granite surrounding the Phalaborwa complex, the “Palabora granite”, was formed after the previously described granite types and belongs to the later stage of the Archaean Complex (Hanekom et al., 1965).

Alkali metasomatism (fenitisation) of the granitic rocks was described at their contact with the clinopyroxenite and syenite intrusions. Pegmatitic veins with a greenish colour mark the affected granite and feldspathic clinopyroxenite area. Along the northeastern boundary of the clinopyroxenite body, the gneiss is brecciated and mylonitised and the crosscutting fractures. Hanekom et al. (1965) described joints filled with diopside and sodium-amphibole. The altered gneiss can contain aegirine-augite and sodium-amphibole along its foliation planes at other places. Feldspar-rich zones also developed at the clinopyroxenite and granite-gneiss contacts. The dominant constituent of the fenite is feldspar, but it occasionally can contain scattered clinopyroxene crystals or apatite lumps. The texture of the fenite varies from fine- to coarse-grained (Hanekom et al., 1965).

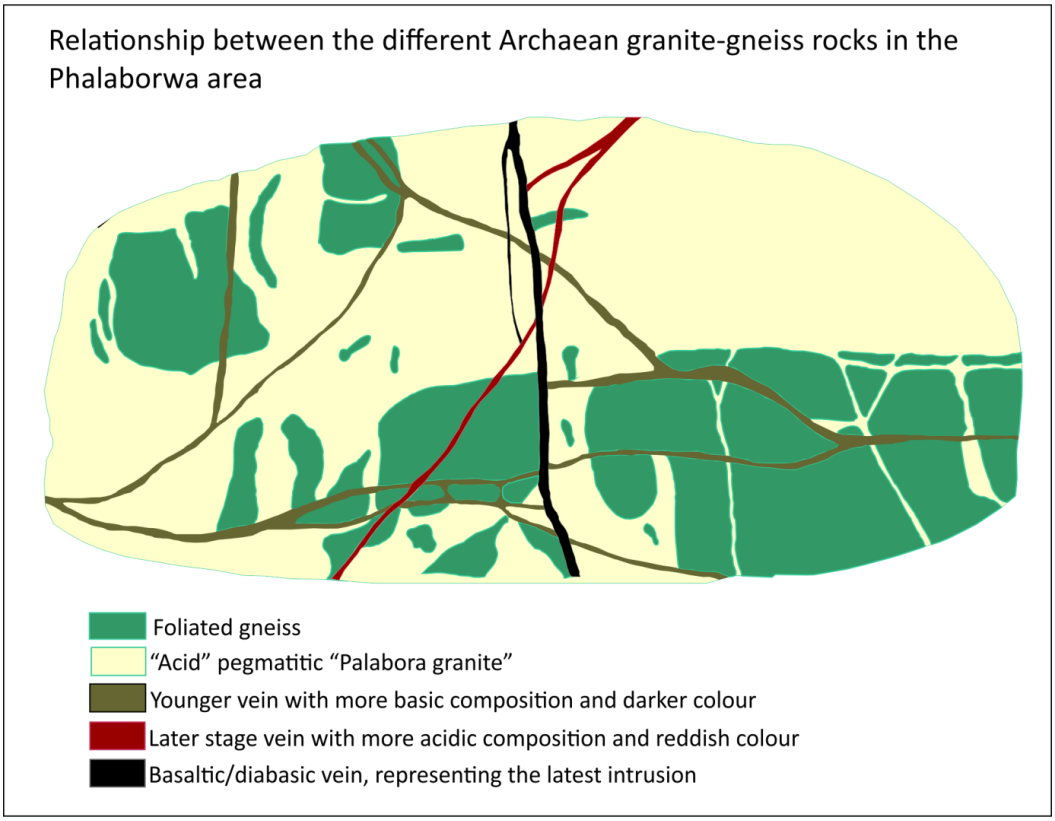

Figure 2.2.3. Relationship between the gneiss and different types of granitic rocks of the Phalaborwa area (after Hanekom et al., 1965)

2.2.2.2 The characteristics of the main clinopyroxenite body

The clinopyroxenite is the most abundant rock of the igneous complex and forms an extensive, kidney-shaped body around the carbonatite-phoscorite intrusion of Loolekop, with a surface area of ~9.67 km2. The maximum length of the body reaches 6.44 km, while the maximum is 3.22 km in the northern part and 2.33 km in the southern part. The Loolekop intrusion separates the clinopyroxenite body into a northern and a southern part, the former covering two-thirds of the entire body.

As Hanekom et al. (1965) describe, the clinopyroxenite contact towards the granite-gneiss is often covered. However, where it is visible, it appears to be sharp and mainly composed of feldspathic clinopyroxenite. In the areas where feldspathic clinopyroxenite is missing, the clinopyroxenite – granite gneiss contact is marked by clinopyroxenite dykes. Based on texture and modal

composition, three main clinopyroxenite types were separated: massive clinopyroxenite, micaceous clinopyroxenite and feldspathic clinopyroxenite.

As mentioned, the feldspathic clinopyroxenite occurs at the contacts towards the granite gneiss. The massive and micaceous clinopyroxenite makes up the bulk of the body. All three clinopyroxenite types can show significant modal variations spatially. There is a general inconsistency in naming the rocks of the Phalaborwa complex, which probably comes from the incredibly widespread modal variations and textures of the rocks. Based on field observations that showed that the two types of clinopyroxenites occur in either equal amounts or with the excess of the micaceous component, Hanekom et al. (1965) suggested that the main clinopyroxenite body that surrounds Loolekop should be referred to as “pyroxenite-glimmerite”; however, this name was not used in subsequent publications. Later, the name micaceous clinopyroxenite glimmerite was introduced for these units. The geological map provided by Hanekom et al. (1965) is not entirely consistent with the lithological descriptions provided in the text either. The geological map indicates micaceous pyroxenite only as the main pyroxenite body and does not mention massive pyroxenite. It also indicates a glimmerite body, which was not described in the text separately. The term glimmerite-pyroxenite does not appear on the geological map.

The massive clinopyroxenite consists of closely intergrown diopside crystals with occasional phlogopite and disseminated apatite. It was described as an equigranular, compact, light to dark green rock composed primarily of diopside with an average grain size between 1 and 4 mm. Under the microscope, the crystals are euhedral or subhedral, colourless or light green. Apatite is almost always present at concentrations between 8 and 10 vol%. Its colour is pale bluish-green, white or, less often, pinkish. The texture changes between coarse-grained and sugary. Mica in massive clinopyroxenite is a minor constituent and not always present (Hanekom et al., 1965).

The micaceous clinopyroxenite has a strong association with the massive type. The clinopyroxene in this rock is also diopside, and similarly to the massive clinopyroxenite, apatite is a common constituent. Microcline occurs locally. Apatite occurs as “segregations” or veins parallel to the mica-defined fabric. The micas are black to golden brown. The presence of vermiculite and phlogopite provides the micaceous character to this rock. The micaceous clinopyroxenite

occurs as stringers and schlieren in the massive clinopyroxenite and can be highly variable modally, reaching levels where the rock should be referred to as glimmerite or glimmerite-clinopyroxenite. The micaceous stringers display schistosity, which is caused by the parallel orientation of the mica flakes. The parallelism coincides with the contact between the massive and micaceous clinopyroxenites. The micaceous component also forms bodies with pegmatitic texture locally. The micaceous component and glimmerite are composed of biotite-vermiculite of various modal compositions.

The spatial relationship of the two clinopyroxenite types is complex. Irregular isolated or near-vertical vein-like bodies of massive clinopyroxenite occur inside the micaceous type. Hanekom et al. (1965) observed the bending of micaceous clinopyroxenite around the massive clinopyroxenite fragments and suggested that these represent flow structures. Hanekom et al. (1965) suggested that at places where the joints and fractures of the massive clinopyroxenite have narrow spacing, the micaceous component can completely overprint the former, while in the case of broader joint and fracture spacings, the massive clinopyroxenite is still observable.

Both the micaceous and massive clinopyroxenites are associated with apatite mineralisation. As Hanekom et al. (1965) describe, in the massive clinopyroxenite, the apatite occurs as disseminated grains, but it can also form clusters where clinopyroxenite recrystallisation took place. In places, the massive clinopyroxenite can be completely apatite-free. In the micaceous clinopyroxenite, apatite can also be disseminated but more often forms segregations with either irregular or vein-like outlines. Three main joint systems were recognised in the clinopyroxenite with east, northeast and northwest strike directions. Lenticular apatite bodies are associated with the east-trending joint system. Similar apatite mineralisation was also observed in the northwest and northeast systems (Hanekom et al. 1965 and references therein). A narrow apatite-vermiculite zone with the northwesterly strike was associated with joints in the fine-grained massive clinopyroxenite. Further apatite and vermiculite zones in association with joints were observed, and Hanekom et al. (1965) drew the general conclusion that the joint systems of the clinopyroxenite body had particular strikes and were associated with apatite and vermiculite

mineralisation. Phlogopite-vermiculite mineralisation forming parallel, northeast and northwest-trending zones was also observed.

Both micaceous and massive clinopyroxenites are crosscut by approximately 15 cm wide microcline veins. Other rocks that traverse both clinopyroxenite types are syenite and carbonate veins and dykelets. The carbonate veins are most common close to the Loolekop carbonatite, radiating outwards from the intrusion into the clinopyroxenite, but carbonate veins were also observed at a greater distance from the intrusion (Hanekom et al., 1965).

The contact between the main clinopyroxenite body and the surrounding granite and syenite is marked by developing a feldspathic clinopyroxenite rim with a maximum width of ~61 meters. The feldspathic clinopyroxenite has a wide modal variation, and the proportion of the feldspar increases from the clinopyroxenite contact towards the syenite contact. The feldspar is predominantly pink microcline (Hanekom et al., 1965), opposite to the inner parts of the main clinopyroxenite body, where the dominant feldspar (where it is present) is orthoclase. In places, large microcline crystals can include euhedral clinopyroxene crystals and form a poikiloblastic texture. The composition of clinopyroxene varies between diopside and aegirine-augite. Another texture of the feldspathic clinopyroxenite is characterised by large diopside crystals with interstitial-skeletal microcline and apatite, which can be interstitial or idiomorphic and poikilitic. The texture of the feldspathic clinopyroxenite is very variable, sometimes showing schlieren. Where it is in contact with quartz-syenite and granite, the feldspathic clinopyroxenite also contains quartz. It was also reported that the feldspathisation is less prominent when the rock is in contact with granite instead of syenite.

Three smaller clinopyroxenite bodies, referred to as "satellite pyroxenite", also occur in the vicinity of Phalaborwa alongside the main clinopyroxenite body; they fall outside of the mapped area shown in Figure 2.2.2. Two of these smaller bodies consist of feldspathic clinopyroxenite. They are located at Kitcheners Kop, approximately 3 km from Phalaborwa in a west-northwest direction and at Molotho Hill, located in the south-eastern part of the area. The third satellite body resembles the massive clinopyroxenite and is situated east of Cleveland Hill. The largest and most important of the satellite bodies is the one at Kitcheners Kop, as the feldspathic clinopyroxenite hosts primary copper sulphide

mineralisation, which is exploited in the Guide copper mine. The other satellite feldspathic clinopyroxenite body is similar to the latter described one but lacks copper-sulphide mineralisation.

2.2.2.3 Characteristics of the pegmatoid clinopyroxenite bodies

As Hanekom et al. (1965) describe, three pegmatoid bodies of the complex formed inside the main clinopyroxenite body and are named the Northern Pegmatoid body, Southern Pegmatoid body and Loolekop pegmatoid. The Northern and Southern Pegmatoids were formed in the approximate centre of the northern and southern parts of the main clinopyroxenite body. At the same time, the Loolekop pegmatoid is situated at the centre of the complex. The pegmatoid bodies are not compositionally homogenous, but based on their mineralogy, two main types can be recognised, namely the Inner-zone and the Outer–zone pegmatoids. The Inner-zone pegmatoid occurs only in the core of the Northern Pegmatoid body and consists of serpentine (from olivine alteration), vermiculite, and phlogopite with or without apatite. The main constituents of the Outer-zone pegmatoid are diopside, apatite, vermiculite, phlogopite and serpentine. This type occurs in all three pegmatoid bodies, forming a contact rim around the Northern Pegmatoid body and Loolekop towards the micaceous/massive clinopyroxenite contact. The Southern Pegmatoid body is built up entirely by the Outer-zone type pegmatoid rock.

The Northern Pegmatoid body contains an Inner-zone pegmatoid core, surrounded by the Outer-zone pegmatoid. The transition is marked by large, pegmatitic diopside crystals that increase in proportion towards the contact. At the contact towards the Inner-zone pegmatoid, the rock is more vermiculite- and serpentine-rich, and diopside occurs in clusters. Apatite is generally more abundant in the Outer-zone, but areas without apatite also occur. Younger carbonatite and dolerite dykes crosscut the pegmatoid body, and the carbonatite dykes show signs of copper-sulphide mineralisation.

The Southern Pegmatoid consists of an Outer-zone pegmatoid, similar to the one described in the Northern Pegmatoid, apart from irregular serpentinite lenses at the centre and the higher apatite content of this body. Diopside is abundant and forms large, pegmatitic crystals at the centre. Exposures of the

rock show the linear nature of vermiculite-phlogopite, serpentine and diopside bodies with an east-west strike in the southern and western part of the area and a northwest-north strike in the eastern and northern areas. The diopside in these bands has a different habit than the main clinopyroxenite body, displaying lighter green-coloured pegmatitic crystals, which are often cleaved and twinned. The crystal size of this diopside can reach 25-30 cm in diameter and 60-76 cm in length. Apatite has two prominent appearances. It can occur as disseminated grains forming concentrations locally or near-vertical veins of variable width. Large, hexagonal apatite crystals up to ~15 cm are observed in wider veins. The pegmatoid body is crosscut by transgressive carbonatite, dolerite dyke, and syenite veins.

At Loolekop, the Outer-zone pegmatoid and pegmatitic phoscorite occur. Large diopside crystals, abundant veins of large phlogopite-vermiculite crystals and vein-like bodies of apatite characterise the Outer-zone pegmatoid. In places, the mica content exceeds that of diopside. The contact between the Outer-zone pegmatoid and the phoscorite is mainly gradational, according to Hanekom et al.'s (1965) observations. The disappearance of magnetite and increase of phlogopite and diopside contents towards the Outer-zone pegmatoid marks the transition. In some cases, the Outer-zone pegmatoid follows the ring-like structure of the phoscorite body (Hanekom et al., 1965).

Hanekom et al. (1965) note that the sizeable pegmatitic diopside crystals in the pegmatitic bodies have a different appearance and composition than the diopside of the massive and micaceous clinopyroxenites. The colour is a lighter green or pale yellowish-green, and they have lower iron and aluminium content than the diopside of the massive and micaceous clinopyroxenites.

2.2.2.4 The Loolekop phoscorite-carbonatite body

The ring-type phoscorite-carbonatite body of Loolekop intruded into the centre of the main clinopyroxenite body. Two carbonatites occur: banded carbonatite, which can be subdivided into older and younger types, and transgressive carbonatite. The banded carbonatite has a close spatial association with the phoscorite body, forming an annular structure, while the bulk of transgressive carbonatite is situated in the core of the Loolekop. At the edges of the main body,

smaller transgressive carbonatite sills and dykes follow the structure of the banded carbonatite and the phoscorite. Overall, the Loolekop carbonatite appears as an elliptically shaped body on the surface, elongated in an east-west direction with a size of ~670 m by ~366 m. The transgressive carbonatite core has a surface exposure of 600 m in length and 120 m in width. Based on gravity data, the depth of the intrusion reaches at least 5 km (Eriksson, 1982), and drillholes reach a depth of 2 km (Giebel et al., 2017). Carbonatite veins that crosscut the transgressive carbonatite were also described (Hankeom et al., 1965 and references therein) and were interpreted as products of the final stage of the carbonatite magmatism.

Hanekom et al. (1965) also noted another carbonatite outcrop ~600 m west of the Guide copper mine. However, the contacts of the exposure are covered, and it was not possible to determine whether this carbonatite body is an entirely independent, plug-like intrusion or dyke related to the Loolekop carbonatite body.

2.2.2.4.1 The characteristics of the phoscorite

The phoscorite is weathered to an approximate depth of 60 meters, and above this depth, its constituent olivine is almost entirely replaced by serpentine. Two types of serpentine were observed: a yellow-brown, limonitic type and a purple-brown type, which occurs in isolated bands and is less common. Vermiculite also occurs in the phoscorite in two types: golden-brown and black vermiculite, also referred to as hydrobiotite by Hanekom et al. (1965). They can occur as disseminated flakes or, more commonly, as pegmatitic bodies or crosscutting vermiculite-phlogopite veins. The average modal composition of weathered phoscorite is presented in Hanekom et al. (1965): 25 vol% apatite, 35 vol% magnetite, 18 vol% carbonate and 22 vol% serpentine, vermiculite and other secondary minerals.

The unaltered part of the phoscorite (below ~60 m) consists primarily of olivine, magnetite and apatite. The modal composition is strongly variable, with olivine sometimes forming small dunite bodies. Milani et al. (2017a) observed that in their extensive sample set, the most primitive phoscorite sample consisted of large, euhedral partially serpentinised olivine, abundant magnetite, a minor amount of fluorapatite, nests of calcite and scarce interstitial phlogopite.

Phlogopite was the modally dominant phase in the most evolved phoscorite samples presented in the same work.

Phlogopite was described as large tabular red-brown crystals defining slight foliation but without signs of strong deformation fabrics (Milani et al., 2017a, b). Interstitial phlogopite was also reported (Milani et al., 2017b). Near phlogopite, Giebel et al. (2019) observed the presence of tetraferriphlogopite both in the phoscorite and the carbonatites. The minerals are characterised by light red-orange to brown pleochroic colours and inverse pleochroism, which is caused by tetrahedral Fe^{3+} - Al substitution (requires $^{IV}Fe^{3+}$ of >0.25 apfu with ^{IV}Al < 0.75 apfu at ~3 ^{IV}Si). Inverse pleochroism and its cause were also reported by Eriksson (1989), who still classified this mineral as phlogopite. Olivine was described as large, euhedral and partially serpentinised crystals by Milani et al. (2017a). Fluorapatite forms large, anhedral crystals, intergrown with phlogopite and irregular magnetite patches, and can also be interstitial (Milani et al., 2017a).

Magnetite in phoscorite was described as intergrowths with phlogopite, large anhedral crystal aggregates, or late-stage magnetite veins (Milani et al., 2017 a, b). Rudashevsky et al. (2004) reported magnetite rims around sulphides. The same work described ilmenite to be the most abundant in the phoscorite magnetite, where it forms intergrowths, discreet euhedral crystals, trellis and sandwich patterns that are parallel to {111} plane, or lamellae that swelled into fine grains. It also occurs as anhedral crystals containing magnetite as anhedral inclusions. Late-stage magnetite veinlets can crosscut ilmenite. Carbonate is randomly distributed in the rock and occurs in large, course-grained, irregular lenses or interstitial blebs (Hanekom et al., 1965; Milani et al., 2017 a, b).

Sulphide phases in the phoscorite include bornite, chalcopyrite, pyrrhotite and pyrite. Sulphides can be crosscut by late-stage magnetite veinlets (Milani et al., 2017a). In one sample, Milani et al. (2017a) reported bornite, which was replaced by chalcopyrite, pyrite, chalcocite and valleriite. Eriksson (1989) described bornite and chalcocite as the primary sulphides in the phoscorite.

Hanekom et al. (1965) observed that the contact between the phoscorite and the banded carbonatite is usually gradational, but sharp contacts also occur. In the phoscorite, parallel layers of magnetite and bands of pure olivine with the same orientation are characteristic and similar to the texture of the banded

carbonatite. Alternating bands of phoscorite and carbonatite occur close to the banded carbonatite contact and are parallel to the primary banding of the latter. Crosscutting veins of the younger transgressive carbonatite intersect the structure.

2.2.2.4.2 The characteristics of the banded carbonatite

The banded carbonatite can be further subdivided based on the emplacement order to an older and a younger component, both with different textural characteristics.

The older banded carbonatite is described as medium-coarse-grained granular rock. The major constituents include Mg-bearing calcite and magnetite, while accessory phases are apatite and silicate minerals. Hanekom et al. (1965) noted that the older banded carbonatite contains economic copper mineralisation, where the main phase is bornite. Later, Verwoerd (1967) noted that the bornite-rich portions of the transgressive carbonatite could be found at its contact with the banded carbonatite. This contradiction might result from the fact that the older banded carbonatite and the transgressive carbonatite are two very similar rocks; the only real difference is the presence of extensive sulphide-mineralisation in the latter. Hanekom et al. (1965) also note thorianite and baddeleyite as economic mineral ores of the older banded carbonatite. Milani et al. (2017 a, b) describe the sulphide phases as interstitial patches of chalcopyrite exsolved into bornite and chalcocite. The chalcopyrite, cubanite, pyrrhotite and accessory pyrite form anhedral crystals associated with magnetite or interstitial phases, forming patches and veinlets.

Continuous, parallel, and nearly vertical magnetite bands characterise the older banded carbonatite. The magnetite can form clots or separate crystals. The minor constituents also can follow the parallelism, and Hanekom et al. (1965) note that this is especially true for chondrodite. The orientation of the streaks and bands is parallel to the outline of the pipe, creating a concentric elliptical pattern and conforming to the phoscorite banding (Hanekom et al., 1965; Milani et al., 2017a).

The younger banded carbonatite intruded as dykes and veins and is a subordinate phase of carbonatite intrusion. Hanekom et al. (1965) noted that

these more minor dykes do not extend to great lengths, but they can be prominent at places and crosscut both the older banded carbonatite and the pegmatoid bodies. It was also noted that the boundary between the two types of banded carbonatite is not always clear. The younger banded carbonatite is characterised by the fine banding of mainly magnetite and silicates. The bands contain sulphides and apatite, which are also aligned with the bands. The magnetite is much finer-grained than in the older banded carbonatite and is mostly anhedral.

The carbonate is mainly calcite with minor dolomite, which often forms exsolution texture in the calcite. The appearance of the exsolution texture is very similar to myrmekitic texture occurring in felspathic rocks, although the formation method and minerals are different. The dolomite in the calcite was described as rod-shaped, sigmoidal or rounded (Dawson and Hinton, 2003).

Apatite is abundant in the banded carbonatite and was described as either large “bladed” or small rounded crystals with small inclusions of calcite and dolomite in both (Dawson and Hinton, 2003). Milani et al. (2017b) describe apatite as fluorapatite, which forms euhedral individual crystals with a size rarely exceeding 0.5 mm in their analysed sample.

The silicate phases include chondrodite and olivine and minor phlogopite and tetraferriphlogopite (Hanekom et al., 1965; Milani et al., 2017 a. b; Giebel et al., 2019). In agreement with Hanekom et al. (1965), the phlogopite is described as a minor phase which can be disseminated (Milani et al., 2017a). However, phlogopite was abundant in another banded carbonatite sample (Milani et al., 2017b), showing that the distribution is inconsistent throughout the rock. Tetraferriphlogopite was noted to be associated with magnetite veins with or without Fe-Cu sulphide phases and showed parallel orientation with the veins (Giebel et al., 2019). Milani et al. (2017a, b) did not report chondrodite, only olivine in their banded carbonatite samples. According to the description, the olivine can be abundant and forms polygonal euhedral to subhedral crystals that

can be serpentinised. Eriksson (1989) observed that olivine was replaced by monazite, phlogopite and clinohumite in the banded carbonatite.

2.2.2.4.3 The characteristics of the transgressive carbonatite

The transgressive carbonatite formed the core of the Loolekop and was the last to intrude. This lithology is the principal host of the economic copper sulphide mineralisation of the deposit. According to Hanekom et al. (1965), the transgressive carbonatite was emplaced along an existing fracture system, which ultimately controlled the distribution and shape of the body. The body structure and the discordant contacts between the transgressive carbonatite and the other lithologies indicate its intrusive nature. Smaller veins and dykes radiate from the main transgressive carbonatite body and crosscut all other lithologies. Milani et al. (2017a) observed a sharp transition between the banded and transgressive carbonatite marked by a cumulate magnetite layer together with “rare sulphides”, large fluorapatite and calcite crystals and minor phlogopite.

The rock is coarse to fine-grained, the finer-grained, sugary textures being more common in the narrower dykes and veins. The main carbonate phase is calcite, and other major constituents include magnetite, silicates (clinopyroxene, olivine, chondrodite, phlogopite) fluorapatite and copper sulphides. The calcite is reported as magnesian-calcite, and exsolution textures with dolomite were often observed (e.g., Hanekom et al., 1965; Verwoerd, 1967; Dawson and Hinton, 2003; Milani et al., 2017 a). Magnetite has a high abundance in the transgressive carbonatite; according to Hanekom et al. (1965), it gives approximately 25 vol% of all carbonatite rocks of Loolekop. It can form local clots and lenses and display large, euhedral-subhedral crystals. It commonly contains several inclusions of spinel, apatite, calcite, baddeleyite, olivine and chondrodite. It is very often replaced by valleriite.

Milani et al. (2017a) differentiated three magnetite types. Type I magnetite is primary, euhedral-subhedral, forms aggregates or cumulus layers, often surrounded by sulphides and is the most abundant type. Type II magnetite is anhedral and disseminated and common in all lithologies. It occurs as interstitial isolated grains or interconnected networks. In the banded carbonatites, it can form layers and is often in close association with sulphides. Milani et al. (2017a)

also note that this type is usually unaltered and, although rarely, can have a valleriite reaction rim around it. Similarly to type II, it has a distinct relation with the copper sulphide mineralisation, which they observed as an interstitial phase that post-dates the magnetite. Type III magnetite is minor compared to the other types but is common in carbonatite. It forms isolated medium-small size grains, micro veinlets radially developing from magnetite nuclei or parallel swarms of veins filling out microfractures. This type either post-dates sulphides or is associated with the final stage of their formation.

Apatite occurs as grey to greenish-grey crystals with euhedral-prismatic habit but also can form irregular, granular aggregates. The crystals are often bent or twisted and can contain inclusions such as calcite, chondrodite magnetite, thorianite and spinel (Hanekom et al., 1965). Milani et al. (2017b) report apatites as large crystals forming aggregates, and based on composition, they are fluorapatites. Giebel et al. (2019) suggested that most of the apatites are orthomagmatic or, in a lesser amount, are of a later stage. Based on EPMA (electron-probe microanalysis) results, the same study observed that the orthomagmatic apatites are low in REE, Si, Sr and Na. In contrast, the late apatites have higher REE content.

Mica minerals include mainly phlogopite, while the more Fe-rich members of the biotite series are subordinate to phlogopite. Tetraferriphlogopite was reported by Giebel et al. (2019). The mica crystals are often strained or bent, but Giebel et al. (2019) noted that phlogopites of the transgressive carbonatite tend to form large, euhedral crystals. Phlogopite replacement by sulphide minerals was also reported (Hanekom et al., 1965), and Giebel et al. (2019) noted that tetraferriphlogopite in both transgressive and bended carbonatite is associated with veins of magnetite with or without Cu-Fe sulphides, showing parallel orientation with the veins. Less commonly, tetraferriphlogopite is associated with monazite, britholite and apatite-monazite dissolution textures (Giebel et al., 2019). Ba-rich phlogopites with kinoshitalite-rich composition and Al-enrichment were observed exclusively in the transgressive carbonatite (Giebel et al., 2019)

Further silicate minerals include olivine and chondrodite. Olivine was described as fine-grained aggregates cemented by calcite, and it was noted that the individual crystals show polygonal outlines (Hanekom et al., 1965) and commonly have a fresh appearance, although serpentinised crystals also occur

(Hanekom et al., 1965; Milani et al., 2017a, b). Chondrodite was described as anhedral-subhedral crystals or crystal aggregates with reddish-brown or greyish-green colour (Hanekom et al., 1965). Milani et al. (2017 a, b) did not report the presence of chondrodite in any of the transgressive carbonatite samples. Minor constituents include baddeleyite and spinel, while fluorite and thorianite are accessories. Reported secondary phases of the carbonatites include valleriite, serpentine and magnesite.

The detailed mineralogical and textural description of the minor and accessory REE-phases was given by Giebel et al. (2017) and suggested a multi-stage formation. The study proposed that during orthomagmatic stages, fergusonite, REE-Ti-betafite and REE-F carbonates were formed, followed by monazite and britholite crystallisation at the late magmatic stages. The low REE content in apatite and its absence in olivine make the introduction of an REE-rich fluid necessary in the system. This was further supported by a later study by Giebel et al. (2019), showing that although the apatite did not have significant compositional variations in the phoscorite and carbonatites, there were some outstanding exceptions in the transgressive carbonatite that showed enrichment in REE. These exceptional apatites were found in transgressive carbonatite samples with a clear sign of alteration by late-magmatic fluids. The post-magmatic redistribution of the REE caused the formation of cordylite, ancylite, and further REE-F carbonates (bästnasite, parisite, synchysite) and anzaite. Cordylite is strongly associated with strontianite and baryte, and it was suggested that the three phases replace a precursor REE-Ca-Sr phase or phases that could not be identified but assumed to be carbocernaite or burbankite. Giebel et al. (2017) observed that monazite, in association with sulphides, could alter to late-stage apatite accompanied by valleriite formation and sometimes thorite formation.

The most abundant sulphide phase of the Phalaborwa complex is chalcopyrite, followed by bornite. Hanekom et al. (1965) described chalcopyrite as massive irregular patches and “schlieren” with no visible crystal outlines and veinlets. Chalcopyrite was described as replacing non-sulphides along the plane of weakness and grain boundaries. Cubanite and pentlandite were described in chalcopyrite as residual grains, but contemporaneous formation and exsolution origin were also observed in the case of the latter. Sphalerite was observed with

star-shaped skeletal crystals or anhedral blebs. Minor millerite and secondary covellite were also observed in chalcopyrite (Hanekom et al., 1965). Chalcocite group minerals in the Loolekop include chalcocite, djurleite, digenite and anilite, with notable variability in composition (Rudashevsky et al., 2004). Hanekom et al. (1965) described pyrrhotite as irregular, granular aggregates commonly associated with residual granular pentlandite. Rudashevsky et al. (2004) reported the presence of troilite and hexagonal pyrrhotite.

Minor linnaeite was observed along the chalcopyrite margins, while bravoite was described as a secondary phase associated with pentlandite (Hanekom et al. (1965). Rudashevsky et al. (2004) also report the presence of cobalt pentlandite and cobalt-rich pentlandite. Further minor and accessory sulphide phases include marcasite, covellite, tetrahedrite, violarite, galena, millerite, parkerite, wittichenite, shadlunite-(Pb), betekhtinite, tin and native bismuth. (Hanekom et al., 1965, Rudashevsky et al., 2004).

Rudashevsky et al. (2004) described Au and Ag-containing noble metal minerals as accessories, forming individual grains, aggregates and intergrowths with other ore minerals (Table 2.2.1). Intergrowths were described between tetra-auricupride and electrum, kustelite and electrum, kustellite and native gold. Characteristic intergrowths of Au and Ag phases with other minerals are reported as tetra-auricupride and electrum with bornite, cobalt pentlandite and digenite; kustelite intergrowth with chalcopyrite, bornite and native bismuth; native silver with cobalt pentlandite, chalcopyrite and bornite. Three other associations of native silver are with bornite, parkerite, native bismuth and galena, with bornite and digenite, and finally, with magnetite rims around chalcocite-bornite aggregates where they occur as inclusions in the magnetite. Stromeyerite forms intergrowth with chalcocite-group minerals (Rudashevsky et al., 2004).

Table 2.2.1. Noble metal minerals described by Rudashevsky et al. (2004) in concentrates from Loolekop carbonatites.

Mineral	Formula based on analysis
Tetra-auricupride	$Au_{1.00}Cu_{1.00}$
Tetra-auricupride	$Au_{0.99}Cu_{1.01}$
Electrum	$(Au_{0.78}Cu_{0.09})_{\Sigma 0.87}Ag_{1.13}$
Electrum	$Au_{0.93}Ag_{1.07}$
Electrum	$Au_{1.00}Ag_{1.00}$
Kustelite	$Ag_{3.21}Au_{0.79}$
Kustelite	$Ag_{3.07}Au_{0.93}$
Kustelite	$Ag_{2.82}Au_{1.18}$
Au_3Ag	$Au_{2.79}Ag_{1.21}$
Silver+kustelite?	$(Ag_{0.83}Au_{0.17})_{\Sigma 1.00}$
Silver+kustelite?	$(Ag_{0.91}Au_{0.09})_{\Sigma 1.00}$
Silver+kustelite?	$(Ag_{0.88}Au_{0.12})_{\Sigma 1.00}$
Silver	$Ag_{1.00}$
Silver	$Ag_{1.00}$
Jalpaite	$(Ag_{2.55}Fe_{0.43})_{\Sigma 2.98}Cu_{1.05}S_{1.98}$
Stromeyerite	$Ag_{0.94}Cu_{1.06}S_{1.00}$
Stromeyerite	$Ag_{0.96}Cu_{1.07}S_{0.97}$
Stromeyerite	$Ag_{0.99}Cu_{1.03}S_{0.98}$
Argentopentlandite	$Ag_{1.05}(Fe_{5.62}Ni_{2.52})_{\Sigma 8.14}S_{7.91}$
Hessite	$Ag_{2.00}Te_{1.00}$

The presence of platinum group minerals (PGM) in the Phalaborwa carbonatites was reported in early studies. However, the most extensive description was provided by Rudashevsky et al. (2004) (Table 2.2.2). The study used a mixed sulphide-rich sample from the banded and transgressive carbonatites and another concentrate produced by flotation. The PGMs were described as primarily monomineralic, euhedral to anhedral grains between 19 and 77 μm with an average grain size of 34 μm. They were also described as inclusions in noble metal minerals (Rudashevsky et al., 2004). Most recently Le Bras et al. (2021) investigated the Loolekop Cu-sulphide mineralization and presented trace element data, including PGE. The analysis of the Cu-sulphides show low-levels of PGE present; this will be in discussed in Chapter 6.

Table 2.2.2. Platinum group minerals described by Rudashevsky et al., (2004) in concentrates from the Loolekop carbonatites.

Mineral	Formula based on analysis
Sperrylite	$Pt_{1.00}As_{2.00}$
Cabriite I.	$Pd_{1.99}Cu_{1.03}Sn_{0.98}$
Cabriite II.	$Pd_{1.99}Cu_{0.96}(Sn_{0.85}Sb_{0.20})_{\Sigma 1.05}$
Cabriite III.	$(Pd_{1.86}Pt_{0.21})_{\Sigma 2.07}Cu_{0.93}Sn_{1.00}$
Cabriite IV.	$Pd_{1.97}Cu_{1.01}(Sn_{0.96}Sb_{0.06})_{\Sigma 1.02}$
Taimyrite	$(Pd_{2.18}Cu_{0.73}Pt_{0.12})_{\Sigma 3.03}(Sn_{0.94}Pb_{0.03})_{\Sigma 0.97}$
Atokite	$(Pd_{2.84}Cu_{0.15}Pt_{0.09})_{\Sigma 3.0.8}(Sn_{0.81}Bi_{0.06}Pb_{0.05})_{\Sigma 0.92}$
Majakite	$Pd_{1.03}Ni_{0.99}As_{0.98}$
Arsenopalladinite	$(Pd_{7.90}Pt_{0.11}Cu_{0.11})_{\Sigma 8.12}(As_{1.05}Sn_{0.99}Bi_{0.32}Sb_{0.26}Pb_{0.26})_{\Sigma 2.88}$
Mertieite II	$(Pd_{7.48}Cu_{0.37})_{\Sigma 7.85}(Sb_{3.02}Sn_{0.13})_{\Sigma 3.15}$
Froodite	$Pd_{0.97}Bi_{2.03}$
$Pd_{11}As_2(Pb,Hg)_2$	$Pd_{10.95}As_{2.10}(Pb_{1.16}Hg_{0.79})_{\Sigma 1.95}$

The thin oxidation zone of the Loolekop contains hypogene mineralisation composed of malachite, chrysocolla, azurite, cuprite, and native copper (Hanekom et al., 1965 and references). More recently, a new carbonatite type, referred to as transitional carbonatite, has been differentiated (e.g., Milani et al., 2017 a, b). It was described as abundant in fluorapatite, which forms large elongated euhedral crystal aggregates in calcite and magnetite groundmass, but also can form anhedral, stubby grains. The magnetite is mostly interstitial but forms a 10 cm thick cumulitic band (Milani et al., 2017a).

2.2.2.5 Syenite characteristics

There are several syenite intrusions around the main body of the Phalaborwa complex, and their occurrence extends to a large area. The field and mineralogical descriptions of this section rely solely on Hanekom et al. (1965). The syenite bodies around Phalaborwa form conchoidal, plug-like bodies, often elongated in an east-west direction and one, near Spitskop, was noted to have ring-dyke structure. The field observation of these syenite bodies suggested that they are independent intrusions, not only the outcrops of a continuous body in depth. The syenite contacts with other rocks are brecciated. This stage of

magmatism also includes the emplacement of peralkaline granite, which preceded the syenite intrusion (Hanekom et al., 1965).

The peralkaline granite has a variable modal composition, the general constituents being Na-amphibole and Na-pyroxene, microcline or anorthoclase and orthoclase, quartz accessory biotite and sometimes calcite, which replaces the other minerals. The texture also varies between equigranular, trachytic, granophyric and porphyritic.

The syenite also displays great textural variety. Hanekom et al. (1965) differentiated several types that can grade into each other.

Syenite pegmatite with pegmatitic texture and an average >3cm grain size occurs widely in the area, mainly near the contacts of gneiss and main syenite intrusions. The syenite pegmatites can be independent or, in one case, crosscut another syenite body. The rock is composed of large (>25 cm) microcline, prismatic aegirine-augite (>10 cm), titanite (<5 cm) and minor quartz. In some cases, near the clinopyroxenite body, it is almost monomineralic.

The occurrence of coarse- and medium-grained syenite is also widespread. The colour ranges between light grey, pinkish grey, dark grey and almost black. The rock is usually equigranular but sometimes can be slightly porphyritic. The feldspar is prominently microcline, but orthoclase is also common. Both feldspars have characteristic submicroscopic inclusions of small red flakes, probably biotite and needle-like light-green minerals. Plagioclase is a minor constituent and also contains inclusions. The mafic components are aegirine-augite, commonly altered to amphibole and secondary Fe-Ti oxides. It also can be zoned with augite core and aegirine mantle. Arfvedsonite is also a common constituent. Accessory phases include apatite, titanite, zircon and magnetite.

Fine-grained, porphyritic and trachytic syenites are less extensive than the previous types, usually forming small irregular bodies, dykes and veins that crosscut other syenites. Porphyritic syenite can grade into fine-grained syenite. The fine-grained syenite was described as a compact, pinkish rock with microcline, microcline-perthite and orthoclase as main phases. Aegirine-augite and arfvedsonite, formed by pyroxene alteration, are also common. The occasional synneusis texture of the syenite is caused by the dark minerals forming aggregates or clusters. In the porphyritic syenite, the feldspars and clinopyroxenes are embedded into a fine-grained groundmass with a similar composition and sometimes display flow texture around the phenocrysts.

2.2.2.6. Dolerite characteristics

Extensive dolerite intrusion formed several dykes with a consistent northeast strike in the area, crosscutting all of the lithologies of the Phalaborwa complex. Basson et al. (2017) separate two episodes of intrusion. During the first episode was the emplacement of northeast-trending dykes, which pre-dates the syenite intrusions. The dykes display contact-strained margins with amphibole formation and sinistral shearing. The second episode involved the emplacement of the larger volume, more prominent dolerite dykes. Wu et al. (2011) determined the age of the dykes as 2035 ± 35 Ma based on Pb/U and Rb/Sr isotopic compositions, while Yuhara et al. (2005) showed 2062 ± 35 Ma formation age. Wu et al. (2011) suggested that the relatively significant age differences gained by isotope studies were possibly due to Sr and Nd contamination of the dykes during their intrusion through the main complex. Today, it is generally accepted that the mafic dykes are coeval with the main intrusive bodies of the complex.

The dykes have a variable thickness between a couple of centimetres and ~90 m and also have very variable lengths that can reach several kilometres. Hanekom et al. (1965) note that the dolerite can completely disappear from the surface due to its higher susceptibility to erosion. The contacts with the other lithologies are reported to be sharp with commonly developed chill-zones, but apparently, the dolerite intrusion did not cause alteration of the other rocks, except in the syenite where, at the contacts, the feldspars developed a pink colouration.

2.2.3. The structure of the complex

The effects of tectonic processes were recognised in the earliest field studies (e.g., Hanekom et al., 1965 and references; Verwoerd, 1967), but the most recent and detailed study on the tectonic structure of the complex is provided by Basson et al. (2017).

The carbonatite body is affected by later-stage shearing. According to the observations (Hanekom et al., 1965 and refs), the focal point of these shear zones is located in the centre of the transgressive carbonatite and follows the pre-existing fracture system. The shear zones contain individual parallel shears and random fine fractures as well. Post-carbonatite fracturing took place along the transgressive carbonatite and younger banded carbonatite veins. The small

displacement of the dolerite dykes that crosscuts the carbonatite provides evidence for shearing rejuvenation. Harmer (2000) suggested that the crosscutting relationship between the phoscorite-banded carbonatite and the transgressive carbonatite may indicate a change in the stress regime.

The post-carbonatite fractures displaced the carbonatite veins but only by a few inches. The direction of the fracture system is N 30^{o} W and N 40^{o} E. Along these fractures, deposition of secondary minerals is typical. The secondary minerals include calcite, serpentine, magnesite, brucite and occasional pyrite (Hanekom et al., 1965).

Basson et al. (2017) conducted an extensive structural study and 3D modelling on the Phalaborwa Complex. Some of the images of the study are presented here without significant modification (Fig.2.2.4). Basson et al. (2017) put the main structural directions of the complex into the context of the regionally dominant trends and related them to major tectonic events during the Kaapvaal craton evolution. The structural trends created during the tectonic events are rejuvenated later and can be detected in the Phalaborwa complex (Basson et al., 2017). It was noted that the most relevant regional trends in the case of Phalaborwa are the north, northeast and east. The tectonic events and their effect on Phalaborwa are summarised in Table 2.2.3.

Basson et al. (2017) separated at least five significant structures in the complex, namely: Mica Fault Zone (MFZ), Tree Fault Zone (TFZ), South West Fault Zone (SWFZ), North-Nort West Structural Orientations (NNWSO) and Central Fault Zone (CFZ). (Fig.2.2.4). Minor structures include the Second Fault and the Ramp Fault. As the authors describe, these structures are defined by ductile shear zones with brittle or brittle-ductile reactivation or overprint. As in earlier studies (Hanekom et al., 1965 and references), the presence of filling minerals in the shear and fault zones, including calcite, chlorite, talc, serpentine, valleriite and copper sulphides, was described here as well. It was noted that slickensides, pervasive alteration, loss of cohesion and abundant fractures commonly accompany the presence of these minerals.

Table 2.2.3. The relationship between the local structural lines of Phalaborwa and the regional tectonic lines, and their relation to the main events of tectonic evolution of the Kaapvaal craton (from Basson et al., 2017).

Trend	Phalaborwa Structures	Related Regional Structures	Related Tectonic Events
NNW and NNE	- Mica Fault Zone - N-NW structural orientation - Main axis of the complex	Colesburg Lineament, Kalahari Line, Great Dyke+fractures, Lebombo-Explora Rift and Monocline + fracture zones	
NE	- SW fault Zone - Tree Fault Zone	Features related to Gondwana break-up: parallel to sections of coastline (Somalia and	Break-up of Gondwana
	- Jointing in the banded NE carbonatite - Paleoproterozoic dykes	Kenya), Agulhas –Falklands Fracture Zone, accretional margin, dykes and faults in northern Zimbabwe craton, Orange River dyke swarm, long axis of Ventersdorp Basin	
E to ESE	- Central Fault Zone - EW trend of the banded carbonatite - Post-Transgressive carbonatite- mineralised veins	Trend of the Limpopo Belt and most of the northern part of the Kaapvaal craton, long axis of the Transvaal Basin and Bushveld Complex, Soutpansberg Lineament, Thabazimbi-Murchison Lineament, Pietersburg-Giyani Lineament, Barberton Lineament, Tuli-Sabi Rift and related faults and dyke swarms, Eastern parts of the Natal Belt, Zambezi Belt, Zambezi Rift and Cape Fold Belt	Collision of Kalahari and Zimbabwe cratons; near-field forces due to the intrusion of the Bushveld Complex

The oldest fault within the complex is the Mica Fault Zone, which appears to be restricted to the micaceous and feldspathic clinopyroxenites, the fenite and the glimmerite. It pre-dates the transgressive carbonatite. However, its relationship with the phoscorite and the banded carbonatite is unclear. The MFZ has an approximate N-S strike with a steep, east dip, and its formation is interpreted as the result of “extensive fault gouge and a significant zone of contact strain” due to brittle deformation. The N-S direction of the fault zone is parallel to the N-S trend of the longest axes of the complex, also with the eastern margin of the Kaapvaal craton and the Lebombo Lineament.

The relatively poorly defined Tree Fault Zone has W-SW directions with a dip that changes or inflects across the carbonatite body. The fault zone is parallel to the South-West Fault Zone and offset by the Central Fault Zone and the Second Fault. The South-West Fault Zone showed an ENE-WSW trend associated with chloritic alteration in the southwestern area of the open pit. The dip directions inflict in the carbonatite body and change from NW to SE from the west towards the eastern parts of the pit. Basson et al. (2017) note that the fault zone forms an anastomosing fault network based on the pit mapping. The NNW-trending structural orientation/set (NNWSO) includes at least three faults and pervasive

jointing orientations. A steep west dip is typical in the group, except for the Glimmerite Fault, with an east dip. Apart from the banded and transgressive carbonatites, the singular joints and joint sets in all lithologies have a predominant NNW direction. The narrow Central Fault Zone has a WNW-ESE strike with a sub-vertical dip and is characterised by stockwork texture with at least one infill phase. Infliction in the carbonatite body dips south on the eastern margin and north on the western margin. The Second and Ramp Faults are parallel to the Central Fault Zone.

Basson et al. (2017) observed that the jointing in the banded carbonatite has a predominant east-northeast trend with a less prominent north-south trend. The north-east trend is characteristic in the Kaapvaal craton being the direction of accretionary craton margin, fault and dyke systems of the eastern Kaapvaal craton and northern Zimbabwe craton, the Ventersdorp Basin and several greenstone belts. The work also notes that the process that could have created the E-W compressional regime of the area at the time of the formation of the Phalaborwa complex is the eastward-directed stress caused by the emplacement of the Burgersfort Bulge of the Bushveld Complex. Basson et al. (2017) observed that the jointing in the banded carbonatite has a predominant E-NE trend with a less prominent N-S trend.

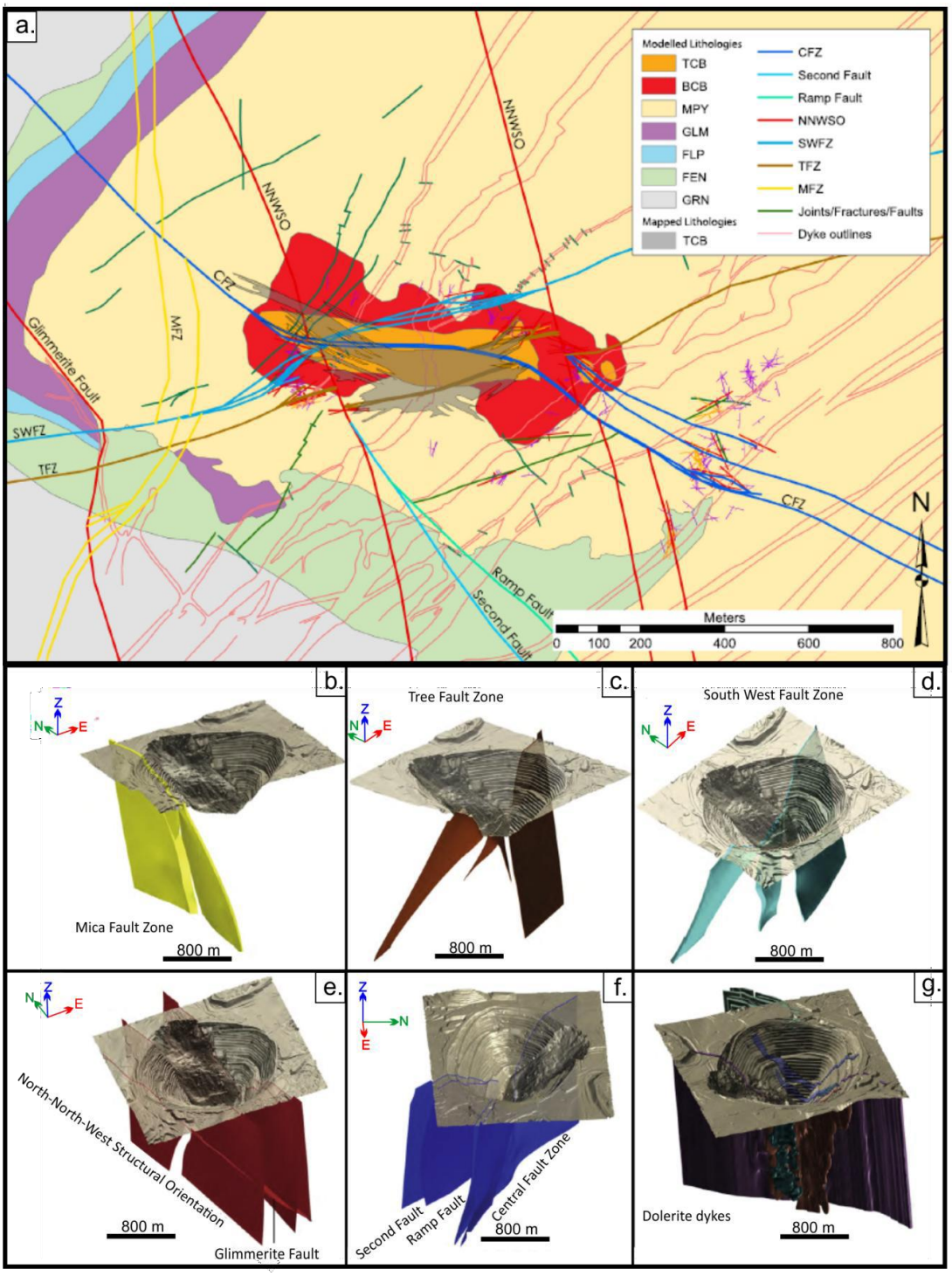

Figure 2.2.4. Structural lines of the Phalaborwa Igneous complex (From Besson et al., 2017).

2.2.4 The isotope profile of the Phalaborwa complex: Age and origin

Several isotopic studies were carried out on the different rock types and minerals of Phalaborwa to determine the age of the deposit. Wu et al. (2011) provided the emplacement date of the main lithologies of the complex. Although all of the previous isotope studies yielded similar ages, Wu et al. (2011) was the first study

which separately investigated the emplacement age and source of each one of the different lithologies of the Phalaborwa complex.

Wu et al. (2011) used separated baddeleyite and zircon crystals for U-Pb analysis. Zircon U- Pb analysis was conducted in the clinopyroxenite, phoscorite and transgressive carbonatite. The analysis of zircon in the clinopyroxenite yielded a $^{207}Pb/^{206}Pb$ age of 2050±13 Ma. Zircon from the phoscorite had $^{207}Pb/^{206}Pb$ age of 2047±27 Ma. Zircon from the transgressive carbonatite had a $^{207}Pb/^{206}Pb$ weighted age of 2053±14 Ma. Zircons of the Spitskop syenite showed $^{207}Pb/^{206}Pb$ age of 2060±17 Ma. Baddeleyite from clinopyroxenite phoscorite, banded carbonatite and transgressive carbonatite was used for U-Pb age determination to establish whether the different lithologies show different ages. All the samples showed similar ages ranging from 2057±3 Ma to 2062±2 Ma, giving a weighted average of 2060±2 Ma. In conclusion, Wu et al. (2011) stated that the different lithologies of Phalaborwa emplaced simultaneously. The mafic dykes crosscutting all complex lithologies showed a $^{206}Pb/^{238}U$ age of 2035±35 Ma determined from apatite.

Wu et al. (2011) used calcite and apatite for Sr-Nd-Hf isotope analysis. Eriksson (1989) presented Rb-Sr data from the clinopyroxenites and carbonatites. Both studies found a wide $^{87}Sr/^{86}Sr$ variation, with transgressive carbonatite showing the widest range (Wu et al., 2011).

The results of Eriksson (1989) showed the different isotopic composition of co-existing phases, and the author noted that the differences are outside the limits of experimental uncertainty. Especially notable is the high initial $^{87}Sr:^{86}Sr$ ratio of the clinopyroxene xenocryst. Processes considered as possible causes of the different ratios were either secondary (hydrothermal fluids or groundwater) or contamination by another magma (Eriksson, 1989 and references). Based on further experimental studies, Eriksson (1989) concluded that the secondary process could have caused the more minor differences between the initial $^{87}Sr:^{86}Sr$ ratios (≤0.0003) but not the more significant differences (≥0.002). Furthermore, the measured high Sr concentrations would require an unlikely level of crustal contamination and slower magma ascent than that is characteristic of carbonatite magmas (Eriksson, 1989). Based on these conclusions, Eriksson (1989) proposed that the differences in the initial $^{87}Sr:^{86}Sr$ ratios are primary and the result of the mixing of at least two different carbonatite magmas; one with an initial $^{87}Sr:^{86}Sr$ ratio ≤0.7039 and another with ≥0.710.

Similarly to Eriksson (1989), Wu et al. (2011) also gained very different $^{87}Sr/^{86}Sr$ ratios for the clinopyroxenite, phoscorite and carbonatite. There is an agreement between the two studies that the possible reasons for these differences include the different mantle sources of the different rock types, post-crystallisation processes that affected the isotopic composition of the individual rock types and contamination. However, due to the extremely high Sr content, the latter would have little effect on the initial Sr isotopic composition of the carbonatite.
Wu et al. (2011) carried out the Nd isotope study on apatite. The study noted that the Nd isotopic composition of the carbonatites show a wider range than in the clinopyroxenite and phoscorite. The Hf isotopic profile of the different lithologies was investigated by Wu et al. (2011) using zircon and baddeleyite. Wu et al. (2011) concluded that based on the Sr-Nd-Hf isotopic profile, the primary carbonatite magma of Phalaborwa falls into the enriched part of the oceanic island basalts (OIB). The syenite and granite isotopic profiles significantly differ from the main complex's, suggesting different mantle sources or formation processes.

The Sr-Nd isotope composition showed that relative to bulk Earth, the source region of the Phalaborwa magmas was enriched in LIL elements and represents a metasomatised mantle. Compared to other carbonatites, however, Phalaborwa shows uniquely high initial $^{87}Sr:^{86}Sr$ ratios and uniquely low $^{143}Nd:^{144}Nd$ compared to the bulk Earth values 2050 Ma ago. The variation in Nd and Sr data also can be explained by the mixing of magmas from two chemically distinct mantle sources (Eriksson, 1989; Yuhara et al., 2005; Wu et al., 2011)
Harmer (2000) especially emphasised that Phalaborwa's Sr and Nd isotopic composition is highly anomalous compared to other carbonatites. However, he favoured the involvement of crustal material to explain the anomalously high Sr in opposition to Eriksson (1989) and Wu et al. (2011). Harmer (2000) notes that the only other carbonatite with a similar isotopic signature is the Ihouhaouene complex in Algeria, which has a similar age (~2.0 Ga) to Phalaborwa.
Harmer (2000) objects to the possibility that the carbonatite evolved in a closed system from the same magma as the pyroxenite and highlights the isotopic results of the two rock types (Eriksson, 1989) as evidence. The work of Eriksson (1989) suggests a complex evolution with multiple magmas involved. Unlike the values of the previous isotope systems, the U-Pb isotope study carried out on

carbonatite samples indicates a homogeneous source and crustal contamination) (Eriksson, 1989).

The magma mixing model was supported by the oxygen and carbon stable isotope composition of the Phalaborwa carbonatites and clinopyroxenites investigated by Eriksson (1989). The carbonatites showed $\delta^{18}O$ of +7.7 - +8.6‰ and δ^{13} of 5.1 - 3.6‰. Clinopyroxenes from the clinopyroxenite showed $\delta^{18}O$ of +7.26 - +7.53‰, which were then used to calculate whole-rock $\delta^{18}O$ composition with values of +7.5 - +7.7. Eriksson (1989) suggested that Phalaborwa's high $\delta^{18}O$ end-member magmas are similar to subcontinental mantle compositions. Crustal contamination was closed out by Eriksson (1989) in this case, too, based on the lack of a significant amount of carbonate phase in the Archaean granites could have caused the high $\delta^{13}C$ upon assimilation. Furthermore, Eriksson (1989) notes that previous data on crustal contaminated alkaline magmas showed a variation of $\delta^{18}O$ near unchanged ^{87}Sr:^{86}Sr ratios, but in Phalaborwa, both vary. Eriksson (1989) concluded that the two end-members could be separated based on $\delta^{18}O$ values, an enriched and an extremely enriched end-member. The former is more enriched than many oceanic and tholeiitic basalt types, while the latter is slightly more enriched than some potassium-rich magmas (Eriksson, 1989).

Harmer (2000) suggests that the circulating fenitising fluids at the final stage of carbonate solidification had a significant role in concentrating metals and causing the isotopic disequilibrium between the different phases.

Based on the isotopic evidence, the magmatic rocks emplaced simultaneously during the same event. Wu et al. (2011) showed that the pegmatitic clinopyroxenite emplaced at 2060± 4 Ma, the phoscorite at 2062±2 Ma, the banded carbonatite at 2060±2 Ma and the transgressive carbonatite at 2060±1 Ma. The syenite plugs and mafic dykes outside the main complex yielded a formation age of 2068±17 and 2062±53 Ma, respectively. The results indicated that the formation of the large amount and highly variable magmatic rocks of Loolekop is coeval. The mafic dykes intruded later but are not significantly younger than the main complex. The isotope composition also indicates a multi-stage process with most possibly multiple mantle sources.

Most recently, Bolhar et al. (2020) conducted an S-isotope investigation on the sulphide minerals in transgressive and banded carbonatite and phoscorite. They found that the S-isotope values vary widely, but the primary sulphides carry mantle signatures. They suggested that the S isotope profile reflects sulphur from

an astenospheric mantle plume component, metasomatised by fluids and melts from a subducting slab.

2.3 Previously proposed petrogenetic models of Phalaborwa based on field, mineralogical and geochemical studies

The very early stages of the Phalaborwa research are summarised in Hanekom et al. (1965). The magmatic origin of the complex was first suggested by Brandt (1948), who recognised the intrusive nature of the carbonatite. The proposed petrogenetic model assumed the differentiation of a basic magma to produce a pyroxenite fraction, a carbonate fraction and a silica–sulfide fraction. Although the physical and geochemical constraints of the suggested model were not elaborated in the source material (Hanekom et al., 1965), it is clear that even the earliest work considered the genetic relationship between all of the intrusive lithologies to be complex.

Bouwer (1957) established his model using the results of the first diamond drillings and underground exploration of the complex. Bouwer (1957) placed the syenite as the first stage of intrusions based on its spatial relationship with the clinopyroxenite. Bouwer (1957) argued that the syenite occurrence only in the peripheral areas of the clinopyroxenite shows its earlier emplacement. As discussed, Wu et al. (2011) showed that the syenite was emplaced simultaneously with the other intrusive rocks. Bouwer (1957) also discussed the possibility that the feldspathic clinopyroxenite (called shonkinite in the work) was formed due to the chemical interaction of the two rocks (Hanekom et al., 1965).

Lombaard et al. (1964) suggested that the relationship between the phoscorite and the older carbonatites is more like a replacement than an intrusive one. This suggestion was based on the contact of the two rock types, which display indefinite, gradational and “interdigitated” nature (Verwoerd, 1967). Verwoerd (1967) explained the same phenomenon with the possible simultaneous emplacement and ascent of immiscible silicate and carbonate liquids and brought Koster van Groos and Wyllie (1963) as a supporting experimental study which showed silicate-carbonate liquid immiscibility above 750 ^{o}C at 1kbar pressure.

As the earliest magmatic evolution models of the Phalaborwa complex above show, the studies came across the same problems of many other genetic models of phoscorite-carbonatite deposits, namely whether they were formed by

fractionation or immiscibility. Alongside this ongoing debate, the strong association with silicate rocks and sulphide mineralisation further complicates the problem. The “next generation” of studies including Aldous (1980; 1986) and Eriksson (1982; 1989), used geochemical links between the ubiquitous mineral phases of Loolekop, isotope compositions of the different lithologies and fluid inclusion analyses in order to investigate the evolutionary path between the different rock types and to establish a genetic model.

The nature of the clinopyroxenites was investigated by Eriksson (1982; 1989). Based on the extensive mineralogical and geochemical results, the studies suggested that the formation of Phalaborwa clinopyroxenites involved flow differentiation and gravity separation. These rocks are cumulate, and the whole rock major element composition does not reflect a liquid composition. The cumulate origin is supported by the textural characteristics and the significant changes in major element composition over very short distances. The feldspathic and massive clinopyroxenites showed consistently high Mg-numbers 82-89 and 76-89, respectively, and the micaceous and pegmatitic clinopyroxenites showed the highest values of 90. Eriksson (1989) suggested that multiple fresh magma surges could have caused the spatial variation of the Mg-numbers. The crosscutting relationship between the rock types further supported the previous statement. Eriksson (1989) proposed that the parental magma has a peralkaline, ultrabasic composition with extremely high K: Na ratios. The combination of high Mg-numbers and low Zr contents together with low Cr suggests that Phalaborwa's silicate magmas had a small level of differentiation but primarily were undifferentiated. Eriksson (1989) also proposed that the carbonatites, clinopyroxenites and phoscorites cannot be the product only of magmatic differentiation due to their different isotopic composition and also objects formation via liquid immiscibility. Eriksson (1989) suggested the co-genesis of the phoscorite and carbonatite and proposed that the early formation and accumulation of apatite, magnetite, phlogopite and olivine from a silicate-rich carbonatite magma (silicocarbonatite) could have produced the phoscorite.

Further support for co-genesis is the similar olivine Mg-numbers and low Ni contents in both phoscorite and carbonatite, together with the low Cr content of the clinopyroxenes. Eriksson (1989) suggests that the syenite chemistry (high K/Na, low Al, enriched REE and Light REEs (LREEs: La, Ce, Pr, Nd) indicates a similar source to the main complex but a greater degree of differentiation and that

these rocks were not derived directly from the main complex but may have been derived from different mantle levels by higher degrees of partial melting. The phlogopite is the result of magmatic crystallisation, and the clinopyroxenes are cumulates.

Milani et al.'s (2017b) main focus was the REE profile of the carbonate, phosphate and, to a lesser extent, silicate phases. LA-ICPMS (Laser Ablation Inductively Coupled Plasma Mass Spectrometry) study was carried out on fluorapatite, calcite, and dolomite of the carbonatites and phoscorite with additional phlogopite and olivine analysis in the banded carbonatite and phoscorite. The study separated an earlier and later stage phoscorite based on the olivine composition of the analysed samples, where a forsterite-rich sample represented the former, and a phlogopite-rich phoscorite represented the latter. No fluorapatite composition differences were detected between the forsterite-rich, early phoscorite, the later-stage phoscorite and the carbonatite rocks.

Based on the LREE characteristics of the fluorapatite and calcite analysed in the phoscorite and the carbonatite rocks of Phalaborwa, Milani et al. (2017b) suggested a common evolutionary path between the two rocks. Milani et al. (2017a) note that the magmatic magnetites of the phoscorite and the carbonatites are geochemically indistinguishable, further confirming the co-genetic origin of these rocks, which are the fractionation products of a shared parental magma as suggested by several earlier works.

Milani et al. (2017b) note one phoscorite sample where dolomite is the only carbonate and occurs as an interstitial phase. This dolomite shows higher REE contents than many of the calcites of the sample set. This characteristic was singled out in the study, as earlier works (e.g., Dawson and Hinton, 2003) showed that dolomite is depleted in REE when co-existing or segregating from calcite. Milani et al. (2017b) concluded that this sample (B66) could not be linked petrogenetically to the other analysed phoscorite samples. The study interpreted the anomalous data from the phoscorite sample B66 to represent a magma batch with a different composition.

Milani et al. (2017b) modelled the crystallisation process following the La and Ce changes along the path and found that fractional crystallisation is the most appropriate to describe the changes. Milani et al. (2017b) also found discrepancies with the fractional crystallisation model:

I. One of these inconsistencies is that with the lowest Ce and La content, the

youngest transgressive carbonatite shows the most primitive composition. The authors suggest the fractionation model only applies to carbonatites with low fluorapatite content. It was also stated that the proposed model does not account for wall rock assimilation and fractionation at a crustal level.

II; The study found that the similar LREE levels of fluorapatite and calcite in the phoscorite and the carbonatites are not consistent with the previously published results that showed that the apatite/melt distribution coefficient for REEs is lower in carbonate systems than in silicate systems.

Another considered explanation of the data by Milani et al. (2017b) is that there is no genetic link between the primary carbonatite and silicate melts. The overlapping LREE levels represent different melt compositions. The third explanation of the LREE results includes simple mixing of carbonatite magmas, which is, despite the lack of mixing textures in the rocks, consistent with the radiogenic isotope profile of the rocks given by Eriksson (1989) and Wu et al. (2011). Milani et al. (2017b) suggest that based on the mixing model, the transgressive carbonatite can represent a less-enriched end-member, which would explain the more primitive trace element profile of this rock.

Based on the identical mica compositions, Giebel et al. (2019) suggested that the banded carbonatite and the phoscorite may have a shared parental magma. According to the same work, formation from a common parental magma is further supported by the fact that the two rocks are only modally different; otherwise, they have identical mineral compositions. Mica compositions from the transgressive carbonatite and the clinopyroxenites are entirely different. Giebel et al. (2019) suggested that based on the mineralogy, mineral chemistry and field relations, the banded carbonatite and phoscorite are formed as the result of immiscibility rather than fractional crystallisation, while the transgressive carbonatite is a relatively evolved magma with different evolution. The study suggests that although the clinopyroxenites are coeval, they are not genetically related to the phoscorites and the carbonatites.

The primary magma composition was considered to be peralkaline and ultrabasic, with an extremely high K/Na ratio (Eriksson, 1989). Eriksson suggested a very low Al and Nb parental magma. Later, this was also supported by Giebel et al. (2017), who noted that fergusonite is the most important Nb phase, and its low abundance indicates that the carbonatite is depleted in Nb. Giebel et al. (2019) also suggested low Al parental magma based on phlogopite

geochemistry. Trace element studies suggested that the parental melts of the carbonatites and phoscorites were extremely enriched in Sr.

The late and post-magmatic fluids affected the deposit, altering the mineralogy and chemistry. The nature of these fluids still needs to be well established, but based on the mineralogy, at least two post-magmatic fluids, one with elevated REE-rich fluid, were considered (Giebel et al., 2019). Based on the presence of hydrothermal magnetites, Milani et al. (2017a) suggested that the elements which are not affected by alteration processes but show low levels in the hydrothermal magnetites of Phalaborwa (Zr, Hf, Ta, Nb) were initially depleted in the hydrothermal fluids.

2.4 Conditions of the magmatic processes: Temperature and oxidation state

Russel et al. (1954) suggested the high-temperature formation of the carbonatite based on the presence of dolomite exsolution and high Sr and Ba content in calcite. The use of the dolomite exsolution texture in calcite as a geothermometer was developed by Goldsmith and Heard (1961). It was recognised that the complete segregation of pure calcite and dolomite from Mg-rich calcite takes place during cooling or recrystallisation processes. Verwoerd (1965) argued that some of the dolomite of the transgressive carbonatite was in equilibrium with the magnesian calcite and formed independent crystals at the start of the crystallisation. This suggestion assumed that the transgressive carbonatite, which has higher magnesium content, has a lower formation temperature than the banded carbonatite. The estimated formation temperature of the banded carbonatite was 676 ^{o}C (Verwoerd, 1965).

Dawson and Hinton (2003) also showed that the Mg in calcite is a thermometer (developed by Goldsmith and Newton, 1969), suggesting a formation temperature of 524 ^{o}C for the banded carbonatite. The same study also presented the oxygen and carbon isotope composition of the calcite and dolomite of the banded carbonatite (from the unpublished dataset of S.M.F. Sheppard and J.B. Dawson). The analysis gave an isotopic composition of δ^{13}C -4.75‰ and δ^{18}O 8.37‰ for calcite and δ^{13}C -4.22‰ and δ^{18}O 8.35‰ for dolomite. Dawson and Hinton (2003) suggested that the results fall into the primary carbonatite field of the isotopic systems with minimal interaction with meteoric water.

The thermo-oxybarometer Milani et al. (2017a) used was based on the temperature-dependent element exchange between magnetite and ilmenite. The measurements resulted in a decreasing trend from 590 ^{o}C to 400 ^{o}C and Δlog fO_2 = 21 to 35, with most of the samples falling between Δlog fO_2 = 21 and 27. The study notes that the re-equilibration temperature results agree with Aldous (1980), measuring 400–500 ^{o}C on magnetite-ilmenite pairs. Milani et al. (2017a) concluded that the re-equilibration of Fe-Ti oxides of Phalaborwa begins early on during the cooling of the deposit, close to the carbonatite solidus.

Giebel et al. (2019) used Fe^{2+} and Fe^{3+} phlogopite geochemistry to investigate the oxygen fugacity conditions of the Phalaborwa magmas during crystallisation. The study stated that the used buffer limits were originally prepared for biotites in silicate rocks; therefore, the results must be interpreted with caution. Giebel et al. (2019) suggest that the geochemical evolution of the tetraferriphlogopite illustrates the increasing fO_2 of the late magmatic fluid, showing a constant Fe^{2+}/Mg ratio near increasing Fe^{3+}. The study notes that the earlier work of Milani et al. (2017b) observed positive Eu anomalies in the phlogopite (tetraferriphlogopite), which is a sign of reducing conditions. Giebel et al. (2019) interpreted that the tetraferriphlogopite was modified by reducing post-magmatic fluid, which is in disagreement with Dawson and Hinton (2003) who suggested only a minor interaction with meteoric water.

Chapter 3: Sampling and analytical methods and sample description

The chapter aims to present the sample set of the research and the analytical methods that were used to describe and analyse the rocks and minerals. The non-sulphide phases were described using optical microscopy and semi-quantitative scanning electron microscopy, while the sulphide phases were analysed using electron-probe microanalysis and laser ablation inductively coupled plasma mass spectrometry. The results are presented in Chapters 4-6.

3.1 The origin of the sample set

The samples for analytical studies were selected from a set that included sixty samples from four different collections. Samples of collection KM2012 were collected by Dr Kathryn Moore at Phalaborwa in 2012. Clinopyroxenites, glimmerites and pegmatites were collected from the Loolekop open pit (KM2012 Coll.). The banded and transgressive carbonatite samples were provided by the chief geologist of the mine and were collected underground. The sample set DK2014 was collected by the author in 2014 (DK2014 Coll.). The transgressive carbonatite samples were collected in situ from 1200 m underground, while clinopyroxenite and phoscorite samples were received from the chief geologist and were derived from tailings. Further samples were received as a courtesy of the Camborne School of Mines and the University of Witwatersrand, who gave permission to use their Phalaborwa collection (CSM Phal Coll. And Wits. Coll). These collections represent the typical Phalaborwa lithologies, including transgressive and banded carbonatites, clinopyroxenites, pegmatites and phoscorites. The list of the complete sample set is presented in Table 3.1.1.

Table 3.1.1. The list of the samples used in the study.

Sample ID.	Rock type	Sample origin	The major character of the sample
Pa2	Transgressive carbonatite	CSM Phal.Coll.	Coarse-grained calcite carbonatite with large magnetite crystal aggregates and minor chalcopyrite patches.
Pa2.4	Transgressive carbonatite	CSM Phal.Coll.	Coarse-grained calcite carbonate with extensive chalcopyrite patch and smaller veinlets.
Pa15	Transgressive carbonatite	CSM Phal.Coll.	Coarse-grained calcite carbonatite with extensive chalcopyrite-cubanite patches and veins.

Table 3.1.1. Continuation.

Sample ID.	Rock type	Sample origin	The major character of the sample
Pa25	Sulphide-rich sample from the transgressive carbonatite	CSM Phal.Coll.	Massive chalcopyrite-block samples with minor patches of carbonate(calcite>>dolomite).
PaX	Transgressive carbonatite	CSM Phal.Coll.	Coarse-grained calcite carbonatite with minor sub- and anhedral magnetite and chalcopyrite veinlets and patches.
Pa23	Sulphide-rich sample from the transgressive carbonatite	CSM Phal.Coll.	Coarse-grained calcite carbonatite with abundant chalcopyrite veinlets and patches. Bornite and valleriite occur at the contacts.
Pa6	Younger banded carbonatite	CSM Phal.Coll.	Calcite carbonatite with regular mafic bands composed of magnetite and sulphide grains.
Pa6.2	Younger banded carbonatite	CSM Phal.Coll.	Calcite carbonatite with regular mafic bands composed of magnetite and sulphide grains.
Pa3.3	Phoscorite	CSM Phal.Coll.	Coarse-grained phoscorite with rounded and serpentinised olivine, apatite, subhedral magnetite and lesser amount of interstitial carbonate.
Pa3	Phoscorite	CSM Phal.Coll.	
Pa4	Clinopyroxenite	CSM Phal.Coll.	Clinopyroxenite sample with dominant diopside and minor apatite, trace phlogopite and (interstitial) calcite.
Po5-u1	Sulphide-rich sample from the transgressive carbonatite	KM2012 Coll.	Coarse-grained calcite carbonatite with magnetite and massive bornite.
Po5-u2	Sulphide-rich sample from the transgressive carbonatite	KM2012 Coll.	Massive chalcopyrite-block sample with minor patches of calcite and subordinate dolomite at sulphide contacts.
Po5-u3	Younger banded carbonatite	KM2012 Coll.	Calcite carbonatite with regular mafic bands composed of magnetite and sulphide grains.
Po5-05	Clinopyroxenite	KM2012 Coll.	Coarse-grained green diopside with minor phlogopite.
Po5-01	Pegmatite (phlogopite-apatite)	KM2012 Coll.	Coarse-grained glimmerite with abundant apatite and minor interstitial calcite.
Po5-02	Glimmerite (olivine- bearing) with carbonate band	KM2012 Coll.	Coarse-grained phlogopite-rich rock with olivine and with a crosscutting calcite vein.
Po5-03	Glimmerite (diopside-bearing) with carbonate band	KM2012 Coll.	Coarse-grained phlogopite-rich rock with diopside and with a crosscutting calcite vein.
PTC1	Sulphide-rich sample from the transgressive carbonatite	DK2014 Coll.	Coarse-grained calcite carbonatite (subordinate dolomite) with sub-anhedral magnetite crystals and aggregates and with irregular sulphide patches (primarily bornite+chalcopyrite).
PTC2		DK2014 Coll.	
PTC3		DK2014 Coll.	
PTC4		DK2014 Coll.	
PTZ1	Sulphide-rich sample from the transgressive carbonatite	DK2014 Coll.	Coarse-grained calcite carbonatite (subordinate dolomite) with sub-anhedral magnetite and chalcopyrite-bornite lattice, forming extensive patches and veinlets.
PTZ2		DK2014 Coll.	

Table 3.1.1. Continuation

Sample ID.	Rock type	Sample origin	The major character of the sample
PW4	Clinopyroxenite	DK2014 Coll.	Clinopyroxenite sample with dominant diopside, tabular dark bronze phlogopite and lesser amount of apatite.
GC1610	Transgressive carbonatite	Wits. Coll.	Coarse-grained calcite carbonatite (subordinate dolomite) with minor anhedral, coarse magnetite. Sulphides (chalcopyrite+pyrrhotite) form a series of globules and veinlets. The sulphide-carbonate contacts are often light red due to valleriite.
C1611	Sulphide-rich sample from the transgressive carbonatite	Wits. Coll	Coarse-grained calcite carbonatite (subordinate dolomite) with chalcopyrite-bornite lattice texture, forming extensive patches and veinlets.
GC811A	Transgressive carbonatite	Wits. Coll	Coarse-grained calcite carbonatite (subordinate dolomite) with chalcopyrite patches and veins.
GC808	Transgressive carbonatite	Wits. Coll	
GC810	Transgressive carbonatite	Wits. Coll	
GC815	Transgressive carbonatite	Wits. Coll	Transgressive calcite carbonatite (subordinate dolomite) with very coarse-grained apatite, magnetite and olivine. Minor, small, anhedral Cu-Fe-S sulphide patches.
GC815b	Transgressive/banded carbonatite	Wits. Coll	Coarse-grained calcite carbonatite with dark bands of magnetite and silicates.
GC813/5	Carbonatite -phoscorite contact	Wits. Coll	Coarse-grained phoscorite with rounded and serpentinised olivine, apatite, sub-anhedral magnetite, carbonate, minor phlogopite and trace sulphide patches. The centre part of the sample contains bands of finer grained magnetite, sulphide and phlogopite, and crosscutting calcite vein.
PAL16	Phoscorite	Wits. Coll	Coarse-grained phoscorite with serpentinised olivine, subhedral, fractured magnetite, minor, interstitial calcite and dolomite and accessory chalcopyrite which forms elongated patches.
GC817	Phoscorite	Wits. Coll	Coarse-grained phoscorite with rounded and serpentinised olivine, apatite, subhedral magnetite that appear as individual crystals or aggregates and lesser amount of interstitial calcite and dolomite.
GC1187	Glimmerite	Wits. Coll	Coarse-grained glimmerite with abundant apatite and minor interstitial calcite.
BM18385	Clinopyroxenite with phlogopite bands	Wits. Coll	Clinopyroxenite with dominant diopside, lesser amount of apatite and minor interstitial calcite and dolomite (only visible under microscope). Abundant phlogopite forms regular bands throughout the sample.

Table 3.1.1. Continuation

Sample ID.	Rock type	Sample origin	The major character of the sample
GC826	Clinopyroxenite with phlogopite bands	Wits. Coll	Clinopyroxenite with dominant diopside, lesser amount of apatite and minor interstitial microcline (only visible under microscope). Abundant phlogopite forms regular bands throughout the sample.
BM15464 (box 3-2)	Clinopyroxenite with phlogopite	Wits. Coll	Clinopyroxenite sample with dominant diopside, lesser amount of apatite. Tabular, dark-bronze coloured phlogopite is abundant.
Box1-1	Clinopyroxenite	Wits. Coll	Clinopyroxenite with dominant diopside, lesser amount of apatite and phlogopite and minor interstitial calcite (only visible under microscope).
Box 3-1	Feldspathic clinopyroxenite	Wits. Coll	Feldspathic clinopyroxenite sample with dominant diopside, lesser amount of apatite and minor interstitial microcline. Tabular, dark bronze coloured phlogopite is abundant.

3.2 Analytical methods

The selected rock samples were prepared as 30 μm thick, thin sections, polished thin sections and 30 mm diameter polished blocks. The optical analysis was carried out with a Nikon Eclipse E600 Pol optical microscope. The photos of the thin sections were taken using a Nikon Digital Sight 5MP camera and processed by NIS Elements f 3.0 software. Following the optical analysis, the selected samples were carbon coated (25 nm), and their compositions were investigated using SEM (scanning electron microscopy), EPMA and LA-ICPMS.

The sample preparation, optical analysis, semi-quantitative SEM, and EPMA were carried out at the Camborne School of Mines (CSM) Analytical Laboratory, where sulphide and non-sulphide phases were analysed. LA-ICPMS on the sulphide phases was carried out at Cardiff University.

3.2.1 Electron microbeam techniques and methodology

Electron beam techniques used in the present study include scanning electron microscopy (SEM) and electron-probe microanalysis (EPMA). The following

section gives a short overview of the technique (after Reed, 2005), followed by the specifications of the analyses and instruments used in this study.

Electron beam techniques are based on X-ray generation by bombarding the specimen with electrons. During the process, an electron beam is focused on the specimen surface. Electron interaction with the atomic nuclei generates continuous X-ray spectra, and electron transitions between the different inner atomic energy levels produce characteristic X-rays specific to each element, making the techniques suitable for chemical analyses. The source of the electrons in the instrument is the electron gun, which accelerates the electrons while three electron lenses focus the electron beam onto the sample surface. Different detectors collect the electrons exiting the specimen, either low-energy secondary electrons (SE) or high-energy backscattered electrons (BSE). An image-display system creates BSE and SE images. An energy-sensitive detector collects BSE. The produced images show varying brightness depending on the mean atomic number of the various phases present in the specimen, thus displaying compositional variation.

Energy-dispersive spectrometry (EDS) or wavelength-dispersive spectrometry (WDS) are used for X-ray collection. EDS simultaneously records all X-rays of all energies, resulting in a plot of intensity versus photon energy. WDS uses Bragg reflection, generated by crystals of different interplanar spacings, to cover the required wavelength range. The WDS is set to measure only one wavelength at a time. The generated X-ray spectrum comprises X-ray lines characteristic of each element present. Quantitative data are acquired by comparing the peak intensities of characteristic X-rays emitted by unknown samples with those emitted by well-characterised standard materials.

SEMs use SE and BSE detectors for imaging purposes and additional EDS for element mapping and analyses. EPMA uses multiple WDS and can produce quantitative data with high accuracy and measure elements down to tens of ppm detection limit. A detailed discussion of the atom physics behind the method and the instrument description can be found in Reed (2005).

Semi-quantitative SEM analysis was conducted in the CSM Analytical Lab using a TESCAN VEGA3 GMU instrument. The instrument is fitted with a BSE, a SE detector, and an X-ray EDS. The analyses were carried out under high vacuum

(< 9 x 10-3 Pa2), using an accelerating voltage of 20.0 kV. The detectable element range of the instrument includes ^{6}C to ^{92}U, with a detection limit of approximately 1%. Carbon and carbon-coat signals in carbon coated samples can be separated by analysing a carbon-coated resin area and comparing it to the signal from the probable carbon in the sample. The presence of carbon is confirmed in the sample when the carbon peak from the probable carbon is higher than that of the carbon-coated resin. The EDS spectra were analysed by Aztec software.

EPMA was carried out at the CSM Analytical Lab using a JEOL JXA-8200 Superprobe. The state-of-the-art instrument provides spot-analysis and elemental maps of the analysed samples. The instrument contains one EDS and four WDS spectrometers (including two low count rate detectors for trace elements) a BSE and SE detector, and it is also fitted with an optical microscope. All four WDS use a crystal [(TAP, PET(H), LIF(H)] with different properties (interplanar spacings) to measure elements from boron to uranium.

A 10 μm spot was used for sulphide analyses, with an accelerating voltage of 15-20 kV and a charge of 15 nA. The instrument was calibrated for the selected elements expected to be present in the samples. For the calibration, the Astimec Scientific Limited (AST), Serial XL, MINM25-53 and AST, Serial JG, METM25-44 standard collections were used (Appendix). Different measurement durations were used depending on whether the specific element was a major or a minor constituent of the analysed phase. The calibration process included three points on each standard; standard deviations were below 1.2%. After the calibration, secondary standards, with elements in a proportion similar to those expected in the unknown samples, were used to determine whether the calibration was accurate. The data were compared to the known values of the standard, and the error was kept under 1%. In the case the accuracy was low, the element was recalibrated. The unknown measurements were carried out after the calibration without changing the settings.

The analytical totals were accepted between 98.45% and 102%. Measured elements in all sulphide phases (with the mean detection limits (dl)) included S (dl:0.05 wt%), Cu (dl: 0.13 wt%), Pb (dl: 0.13 wt%), Fe (dl: 0.09 wt%, Bi (dl: 0.13 wt%), Co (dl: 0.12 wt%), Ni (dl: 0.09 wt%) and Zn (dl: 0.15 wt%). The error ranges and mean errors of major elements of each mineral species are presented in

Table 3.2.1. Generally, elements below 1 wt.% show significant errors and are not presented here, nor are the data used in discriminatory diagrams in the thesis.

Table 3.2.1. Calculated error ranges and mean errors of the major element concentration from the Phalaborwa sulphides, determined with EPMA.

Mineral	Element considered in formuale	Range of percentage relative error (%)	Means of percentage relative error (%)
Chalcopyrite	Cu	0.79 – 1.30	1.04
	Fe	1.35 – 2.23	1.79
	S	1.07 – 1.81	1.45
Bornite	Cu	0.60 – 0.97	0.76
	Fe	2.12 – 3.63	2.89
	S	1.20 – 2.08	1.59
Cubanite	Cu	1.49 – 1.54	1.51
	Fe	1.86 – 1.89	1.87
	S	1.75 – 1.80	1.77
Cu-S phases	Cu	0.54 – 0.86	0.6
	S	1.26 – 2.14	1.49
Pyrrhotite	Fe	0.95 – 1.58	1.3
	S	1.05 – 1.80	1.51
Sphalerite	Zn	0.01 – 0.78	0.34
	Fe*	4.24 – 7.41	5.91
	S	1.08 – 1.80	1.47
Galena	Pb	1.12 – 1.14	1.13
	S	3.21 – 3.23	3.22
Millerite	Ni	0.07	0.07
	S	1.81	1.81
Cobalt-/Cobalt-rich pentlandite			
Type I	Co	0.01 – 0.94	0.79
	Ni	1.79 – 2.38	1.85
	Fe	1.64 – 2.79	1.95
	S	1.09 – 1.83	1.2
Type II.	Co	0.01 – 0.69	0.15
	Ni	2.72 – 5.87	4.79
	Fe	2.31 – 2.93	2.82
	S	1.09 – 1.87	1.71
Type III.	Co	0.01 – 1.23	0.68
	Ni	0.84 – 2.16	1.57
	Fe	1.38 – 2.54	1.89
	S	1.14 – 1.84	1.38
Siegenite	Co	0.86 – 0.88	0.87
	Ni	1.76 – 1.79	1.78
	Fe*	4.24 – 5.49	4.66
	S	0.99 – 1.03	1.01

The EPMA results were used to calculate the sulphide mineral formulae. The calculation process was as follows:

i; measured wt% of element 'a' divided by atomic weight% of element 'a' = Xa.

X is determined for each element.

ii; Summation of X of each element of the measurement point.

iii; Determining the number of elements in the ideal formulae of the analysed mineral = Z

iv; The number of element 'a' in the formulae: Za/ΣX*Xa

3.2.2 Laser ablation inductively coupled plasma mass spectrometry

Laser ablation (LA) paired with inductively coupled plasma mass spectrometry (ICPMS) is a widely used technique that provides spatially resolved measurement of elemental and isotopic composition of solid materials and fluid inclusions inside them (Sylvester and Jackson, 2016). The sample is placed in the gas-tight ablation cell, and a pulsed laser is directed on the surface.

The parameters of the laser beam include spot size (µm), frequency (Hz) and pulse energy (mJ/pulse). Fluence (J/cm^{-2}) is the energy of a laser pulse divided by the area it illuminates (asi-pl.com.au), and it is frequently used to characterise the laser and the measurement. The process of fluence calculation is as follows (from asi-pl.com.au): *"If the on-sample spot is a 50 µm round spot with an area of 7.854 x 10-9 m2, we compute: energy/area = 0.5 × 10^{-3} / 7.854 × 10^{-9} = 6.4 × 104. A more convenient way to write this is 6.4 J/cm2"*.

The ablation of the sample produces a stream of aerosol, which is combined with a carrier gas, usually He (flow rates are noted and given as L/min). The carrier gas transports the ablated material into an inductively coupled Ar plasma (ICP) for ionisation after vaporising the aerosol. The mass spectrometer separates the ions based on their mass-to-charge ratios, and the detector quantifies them. The ion-signal intensities are translated into element concentrations, isotopic ratios or ages. The element concentrations are compared to external standards (Sylvester and Jackson, 2016). For quantitative analysis, one element in the material needs

to be determined by EPMA. More information about the ICPMS instrumentation can be found in Gill (1997).

The present study used LA-ICPMS to determine the trace element composition of selected sulphide phases of the Phalaborwa carbonatite, phoscorite and silicate rocks. The measured isotopes included: ^{57}Fe, ^{59}Co, ^{60}Ni, ^{65}Cu, ^{66}Zn, ^{75}As, ^{77}Se, ^{99}Ru, ^{101}Ru, ^{103}Rh, ^{105}Pd, ^{108}Pd, ^{109}Ag, ^{111}Cd, ^{121}Sb, ^{125}Te, ^{185}Re, ^{189}Os, ^{193}Ir, ^{195}Pt, ^{197}Au, ^{206}Pb, ^{209}Bi.

Time-resolved analysis (TRA) by LA-ICPMS was performed on each selected sulphide phase at Cardiff University on a New Wave Research UP213 UV laser system attached to a Thermo X Series 2 ICP-MS. The calibration of the instrument and the data processing was carried out by Dr Iain McDonald.

Twelve polished blocks were selected, representing sulphide phases from the Phalaborwa transgressive carbonatite, banded carbonatite, phoscorite and glimmerite. The analysed sulphide phases included chalcopyrite, bornite, digenite, cobalt–pentlandite–siegenite, sphalerite and pyrrhotite. Each analysed sulphide underwent multiple line analyses to allow for data repeatability and homogeneity to be assessed. The line analyses involved the movement of the laser across a pre-determined course of a maximum length of ~150 µm, where data were obtained using TRA. Ablation was carried out using a 40 µm diameter spot size at a frequency of 10 Hz and fluence of 3.5 J/cm^{-2}. The ablation was performed under a He-loaded (flow rate: 0.7 L/min) laser cell. The resulting vapour was blended with Ar (flow rate: 0.65 L/min) before being transported to the ICP-MS. The acquisition times ranged from 60 to 100 seconds, with a gas blank measured for 20 seconds before the ablation. Thermo Plasmalab software was used for gas blank subtraction and internal standard corrections.

The instrument calibration was carried out using synthetic quenched Ni-Fe-S and galena standards, and the accuracy was checked by the analysis of the Mem Po724 and UQAC FeS standards as an unknown against the Cardiff quenched sulphide standards. A detailed summary of the standards used during this analysis can be found in McDonald (2005). For each sulphide sample were used as per the practice of the research laboratory. Detection limits for the LA-ICP-MS are based on three standard deviations (3σ) of the gas blank (Table 3.2.2). Where 3σ exceeded the measured isotope values, the results were discarded.

Table 3.2.2. Analysed trace elements and the specific isotopes measured by LA-ICPMS and their detection limits.

Element	Detection limit (ppm)
^{57}Fe	3
^{59}Co	3
^{60}Ni	50
^{65}Cu	50
^{66}Zn	9
^{75}As	1.5
^{77}Se	9
^{99}Ru*	0.07
^{101}Ru*	0.07
^{103}Rh*	0.1
^{105}Pd*	0.08
^{106}Pd*	0.07
^{108}Pd*	0.07
^{109}Ag	0.21
^{111}Cd	0.29
^{121}Sb	0.18
^{125}Te	0.2
^{185}Re	0.02
^{189}Os	0.02
^{193}Ir	0.02
^{195}Pt	0.02
^{197}Au	0.01
^{206}Pb	3.9
^{209}Bi	0.04

Note: Isotopes with "": The mean of the different isotopes were used in the study*

3.3 Sample description

3.3.1 Transgressive carbonatite

3.3.1.1 Macroscopic appearance of the rock

The transgressive carbonatite is coarse-grained, macroscopically characterised by the most abundant calcite, which hosts large magnetite crystals and irregular patches or strings of sulphides, mainly chalcopyrite and bornite (Fig. 3.3.1 a-f). Magnetite forms crystal aggregates or individual, primarily subhedral crystals that can reach cm-range (Fig. 3.3.1 a, c, d). Euhedral and anhedral crystals also occur. Macroscopically visible apatite is subhedral and mildly rounded with a pale green colour. It can be very abundant locally. Rounded olivine crystals and subhedral phlogopite also occur at the macroscopic scale. The dominant sulphide phase in Phalaborwa is chalcopyrite, but bornite can also be significant locally. Although the sulphide assemblage contains several other phases, the macroscopic appearance is characterised by chalcopyrite and bornite, sometimes cubanite covellite and digenite and in one case of the sample set, pyrrhotite (GC1610). Macroscopically, both chalcopyrite and bornite can obtain a massive appearance. However, it is more common in the case of chalcopyrite, which can look monomineralic to the naked eye (Fig. 3.3.1 g, h). Alongside the massive appearance, both phases can form anhedral patches connected by veinlets (Fig. 3.3.1 e, f). Chalcopyrite can also form a series of globules. The bornite can display a uniform dark purple colour when it is massive (Fig. 3.3.1 d) or the typical “peacock ore” colour range when it forms smaller patches. Covellite and digenite are associated with bornite; both form irregular patches or strings along the edges, displaying a strong blue colour (Fig. 3.3.1. b). Chalcopyrite and bornite also form a shredded texture in sample GC1611, where the net-like intergrowth texture of the two phases is visible in the hand specimen (Fig. 3.3.1 e). Pyrrhotite can also be observed in hand specimens, but it infrequently forms large enough patches to see. In sample GC1610, pyrrhotite occurs together with chalcopyrite. Although the intergrowth is relatively fine-grained in a hand specimen, the pyrrhotite can be recognised by its brass-pinkish colour (Fig. 3.3.1 f). Valleriite is a prominent alteration product, usually occurring at the contact of sulphide patches, non-sulphide minerals, and magnetite. It forms fine-grained, dark reddish-brown patches and strings (Fig.3.3.1 f). The modal proportion of the different phases varies from sample to sample.

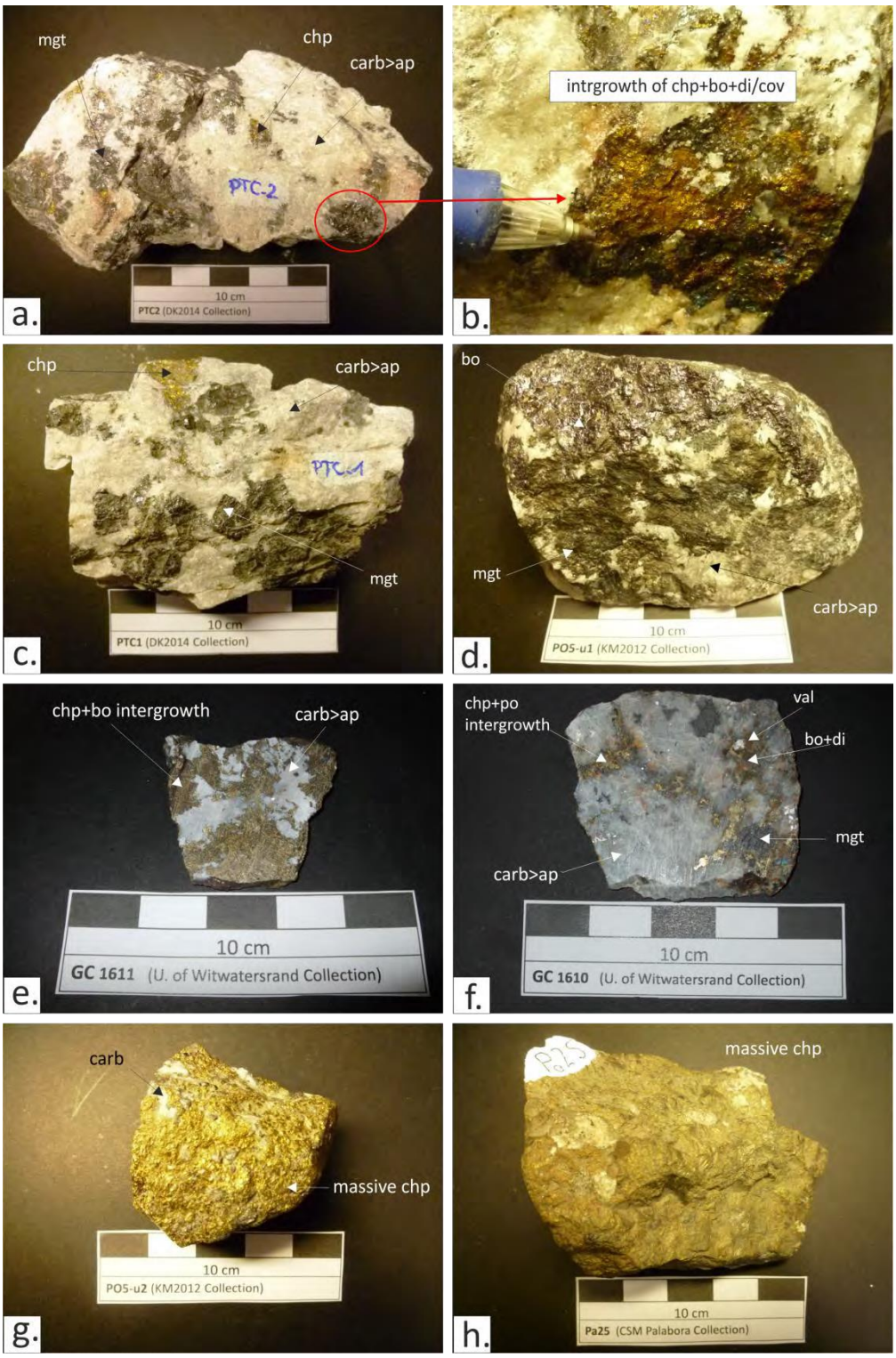

Figure 3.3.1. Photographs. a: Coarse magnetite crystals, chalcopyrite and bornite patches in transgressive carbonatite. b: The bornite is associated with digenite and covellite at the edges, and with abundant valleriite. c: Eu- to subhedral, coarse magnetite crystals in calcite and minor dolomite with sugary macrotexture. Chalcopyrite forms patches and strings. d: Bornite can form relatively extensive patches with a deep purple colour. Magnetite can form crystal aggregates, with extensive anhedral patch appearances. e: Grater/shredded intergrowth texture between chalcopyrite and bornite, where bornite form a network of lamellae along the structural planes of chalcopyrite. f: Pyrrhotite occurs with chalcopyrite and has a brassy-pink colour. Bornite with abundant digenite and valleriite occurs in patches. Valleriite is abundant and forms dark reddish-brown fine-grained patches that follow the edges of the sulphides. Apatite forms large, sub- to anhedral, pale-green crystals g, h: massive chalcopyrite with patches of carbonate. mgt: magnetite; chp: chalcopyrite, carb: carbonate; ap: apatite; bo: bornite; di: digenite; cov: covellite; po: pyrrhotite; val: valleriite

3.3.1.2 Micromineralogy

Magnetite is the major oxide phase, with two primary types occurring in the transgressive carbonatite sample set. Type 1a magnetites are ubiquitous across the sample set, represented by large sub- or euhedral crystals or crystal aggregates, forming cumulus phases (Fig.3.3.2 a). Type 1b magnetites have an interstitial appearance with an anhedral, space-filling shape between large eu- to subhedral cumulus apatite crystals (Fig.3.3.2 b). Both types can appear after strong resorption when found inside chalcopyrite or bornite. The crystals can be intensely fractured, broken up, and often replaced by valleriite and late-stage sulphides at the contacts towards sulphides or non-sulphide minerals. Large cavities inside the crystals are also common, especially in the more altered samples. Magnetite crystals enclosed inside chalcopyrite are altered and dissolved, showing a spongy texture, where the cavities are filled with valleriite and chalcocite (Fig.3.3.2 c). The fractures can form a network throughout the crystal and are filled with various phases, primarily valleriite. However, calcite, dolomite, haematite and secondary Cu-sulphide phases with mixed compositions are also common. Both magnetite types contain unmixed spinel, which forms euhedral, or less often, subhedral (Fig.3.3.2 d). The size of the spinel crystals varies between micron and mm scale. The type 1a and 1b magnetites are primary magmatic. The relationship between type I magnetite and sulphide minerals is interstitial, where the main sulphides (chalcopyrite and bornite) fill the space between the large magnetite crystals. The carbonate minerals (calcite and dolomite) are interstitial to the type 1a magnetite. Type 1b magnetites are interstitial to large euhedral apatite crystals. Secondary magnetite (type 2) postdating the primary sulphide phases occurs in transgressive carbonatite. It forms fine-grained anhedral crystal aggregates that can extend over the fracture system of the sulphide phases and also appears in fractures and rims of silicates (Fig.3.3.2 e-f).

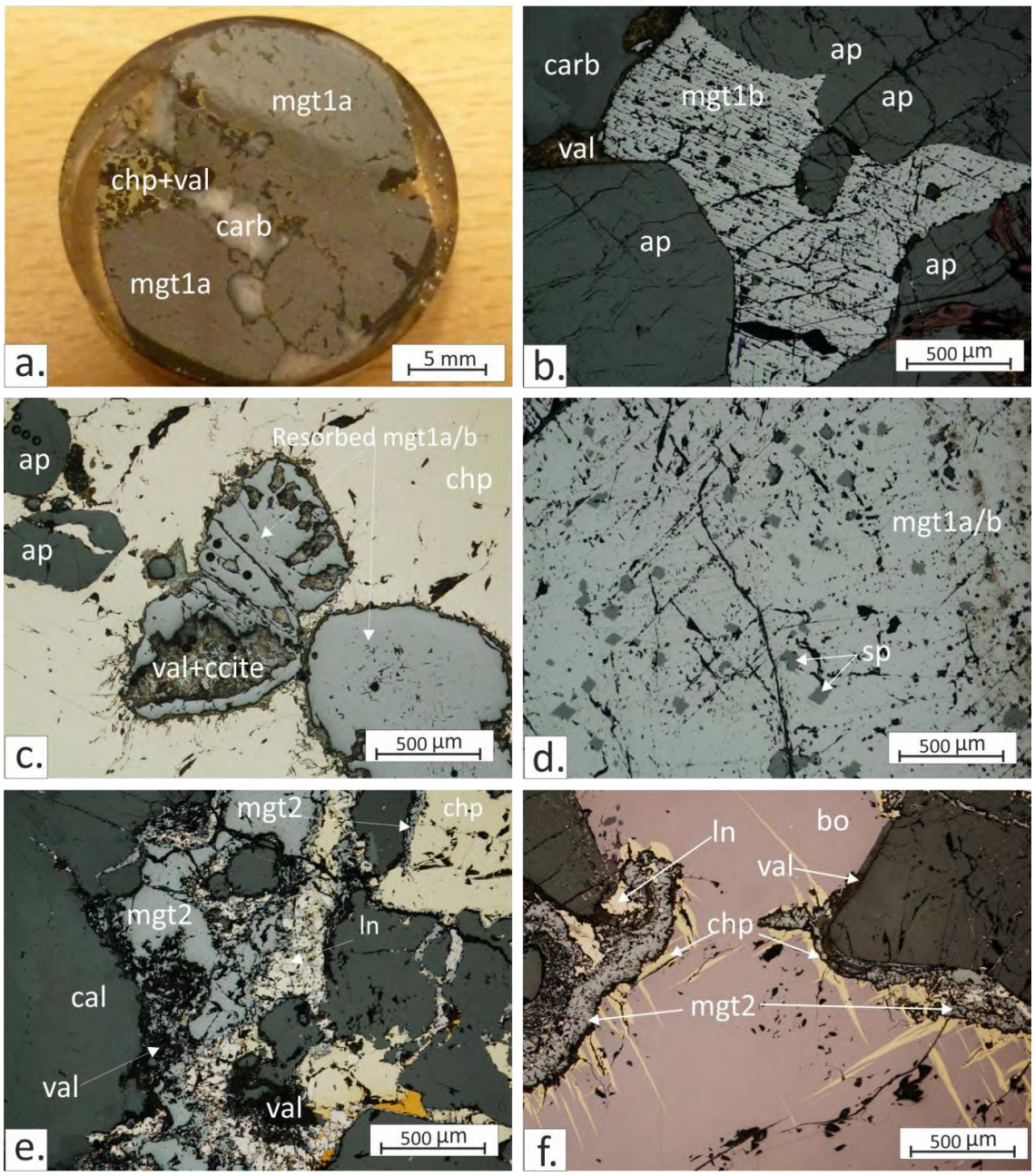

Figure 3.3.2. Reflected light photomicrographs. Magnetite textures in the transgressive carbonatite. a: Large subhedral cumulus magnetite (type1a), often fractured and cavities filled with primary secondary sulphide phases. b: (1N) type1b magnetite with anhedral, space-filling habit between cumulate apatite crystals. c: (1N), resorbed magnetite crystals inside chalcopyrite, displaying spongy texture where the cavities are filled with valleriite and secondary chalcocite. d: (1N) Exsolved spinel cubes in fractured, type 1 magnetite. e-f: (1N) Secondary magnetite (type2) forming anhedral, fine-grained aggregates at contact areas between sulphide and non-sulphide phases. 1N: under plain polarised light, mgt: magnetite, chp: chalcopyrite, val: valleriite, carb: carbonate, ap: apatite, ccite: chalcocite, sp: spinel, ln: linnaeite group minerals, bo: bornite

Large cumulus apatite reaches several mm in size, with an intensely fractured, subhedral appearance (Fig.3.3.2 b, Fig 3.3.3 a-d). The crystals can be replaced by sulphides, carbonates and magnetite along the fractures. Large apatite can be very abundant locally and form crystal aggregates with polygonal contacts. Very

small (<10 μm) REE-phases occur inside the crystals, in fractures and along the edges. Often, this apatite type shows irregular zonation that can only be seen on BSE images. Dolomite frequently appears in the contact areas towards other phases. Small euhedral apatite occurs as an inclusion inside magnetite and silicates. Apatite is associated with secondary monazite, which occurs as a fracture-filling phase in the large crystals (Fig.3.3.3 a) or as a rim around the small types. The sulphide and the carbonate phases are both interstitial to the apatite.

Calcite is the most abundant mineral of the rock, with a texture varying between euhedral-subhedral crystals with straight-polygonal contacts and anhedral crystals with irregular-loboid grain boundaries and crystal bulging (Fig.3.3.3 c, g). According to Chakhmouradian et al. (2016), this texture is granoblastic and indicates recrystallisation. In most cases, multiple twinning was observed in most of the crystals where broad twin lamellae are overprinted by fine lamellae (Fig.3.3.3 c, g); this is also consistent with a recrystallisation process Chakhmouradian et al. (2016). Dolomite and calcite form intergrowths in the transgressive carbonatite that can develop to a myrmekite-resembling (only in appearance) texture or remain as small irregular dolomite grains (Fig.3.3.3 h). Areas with small, equigranular and polygonal calcite crystals suggest a recrystallisation process in the transgressive carbonatite. Apart from the intergrowth with calcite, dolomite occurs at grain boundaries, sometimes forming a recrystallised rim around the other minerals phases (Fig.3.3.3 a, e, f). Areas with abrupt grain size and texture change suggest brecciation, supported by the abundant microfractures of the other major mineral phases. Both calcite and dolomite can be fracture-infill inside other crystals. The observed accessory phases associated with calcite and dolomite include Ba, Sr-Ba and REE-phases as very small inclusions (<10 μm), which are especially abundant along twin lamellae.

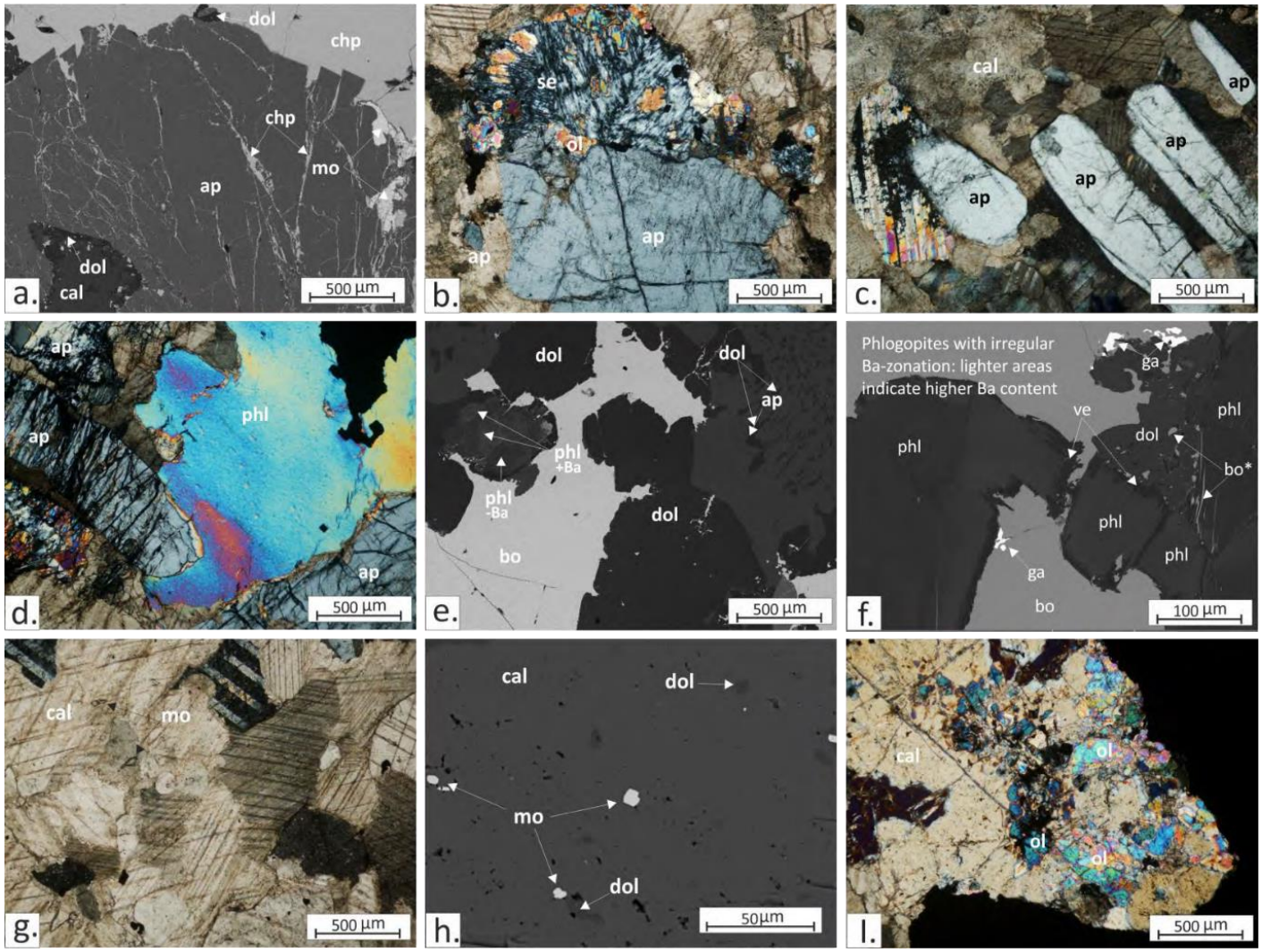

Figure 3.3.3. Transmitted light photomicrographs and BSE images. Various mineral-microtextures in transgressive carbonatite. **a**: (BSE) Large fractured cumulus apatite with chalcopyrite, carbonate and monazite infill. **b**: (xN) Large fractured cumulus apatite with strongly serpentinised olivine. **c**: (xN) Fractured, cumulus apatite. The calcite shows twin lamellae of various broadness and lamellae overprint. The crystal boundaries vary from irregular to polygonal. **d:** (xN) Large fractured cumulus apatite with interstitial phlogopite and dolomite **e**: (BSE) Interfingering bornite in contact with dolomite and phlogopite. Dolomite occurs at the contact areas and as an exsolution phase in calcite, unmixed from Mg-rich calcite. Phlogopite shows irregular Ba-zonation and vermiculitisation at the crystal edges. **f:** (BSE) Phlogopite with irregular Ba-zonation showing vermiculitisation at the edges in contact with bornite. Bornite infiltrates phlogopite along the cleavages and cavities. Dolomite and anhedral galena occur at bornite-non-sulphide contacts. **g**: (xN) Calcite crystals are primarily anhedral with irregular rounded contacts. In some cases, polygonal, adjusted contacts are still identifiable. Twin lamellae show various thicknesses with thinner lamellae overprint. Accessory monazite inclusions occur in calcite. **h**: (BSE) Calcite with minor dolomite grains and accessory subhedral monazite. **i**: (xN) Anhedral, resorbed olivine xenocrysts being replaced by carbonate and serpentine. **1N**: under plain polarised light, xN: under crossed polarised light, BSE: Backscattered electron image ap: apatite, mo: monazite, chp: chalcopyrite, dol: dolomite, ol: olivine, se: serpentine, cal: calcite, phl: phlogopite, phl +/-Ba: phlogopite with Ba-rich and poor zones. bo: bornite, ve: vermiculite, ga: galena

Silicate minerals observed in the transgressive carbonatite sample set include phlogopite, olivine and their alteration products of vermiculite and serpentine. Phlogopite is a ubiquitous minor constituent of the transgressive carbonatite. It forms euhedral to subhedral crystals, which can reach one mm in size and contain irregular zonation (detected on BSE image) with Ba-rich zones (Fig.3.3.3 d-f). Vermiculite alteration is common, occurring primarily at the edges of the crystals, and chalcopyrite and bornite can infiltrate along cleavages (Fig.3.3.3 f). Olivine occurs as resorbed and strongly fractured crystals of various sizes (Fig.3.3.3 b, g). The replacement of olivine by serpentine along the fractures is common and occurs in various stages throughout the samples. Serpentine can form relatively extensive fibrous patches as it replaces olivine. Silicate minerals are subordinate to carbonates, apatite, magnetite and sulphide phases.

The transgressive carbonatite contains several accessory phases associated with the magnetite and non-sulphide minerals. Usually, these are inclusions of very small size, and many of them were observed only during SEM analysis. Monazite is a very common phase in calcite, dolomite and apatite, where it can form sub- to anhedral crystals with a size of ~10 μm (Fig.3.3.3 a, g, h). Monazite can form rim around apatite. Baddeleyite also occurs in most of the samples; it is associated with dolomite and magnetite. Often, it appears together with thorite and can form intergrowths with other REE-Nb-phases (<5 μm). Baddeleyite forms subhedral crystals, which rarely reach 100 μm. Thorite forms mostly euhedral and subhedral crystals in the carbonate phase that can reach 100 μm. Another Th-bearing mineral was also observed; the Pb and U contents detected with EDS indicated that the mineral was probably thorianite (Th, U)O_2. It is less common than the other accessories described above, but in one sample (GC811A), its size reached 500 μm. Ubiquitous accessories are baryte and strontian baryte, observed in all samples as <20 μm inclusions in the non-sulphide minerals (except magnetite), especially in carbonates. Strontianite and celestine also occur in the same association but are less common. Fluorite was only observed in samples GC1611 and PB1, forming very small <10 μm crystals.

3.3.1.3 Textural relationship of the minerals and the order of crystallisation in the transgressive carbonatite

It was suggested that the crystallisation sequences of igneous rocks cannot be confidently established based on rock microtexture only, because magmas with complex compositions can crystallise over a wide range of temperatures, and crystals can form simultaneously until the solidus temperature is reached (Vernon, 2004). The textural characteristics of simultaneous crystallisation include irregular, interpenetrating crystal contacts and signs of subsolidus adjustments, such as polygonal contacts (Vernon, 2004). Polygonal contacts in carbonatites. These textural features are present in the transgressive carbonatite. Based on the extensive study of Chakhmouradian et al. (2016) on carbonate textures, the transgressive carbonatite displays signs of recrystallisation. This contrasts with Milani et al., (2017b) who suggested that the Phalaborwa carbonatites were not recrystallised extensively. Based on the appearance of type 1a magnetite, apatite and olivine are cumulus phases, while type 1b magnetite and phlogopite formed later. Dolomite at contact areas and secondary monazite around apatite crystals and fractures also represent a later magmatic stage. Among accessory phases, the eu- to subhedral thorite and baddeleyite are also part of the earlier magmatic assemblage. Type 2 magnetite postdates all the previously mentioned phases. Later-stage phases have resulted from alteration processes, including serpentine, vermiculite, and valleriite. Chalcopyrite fills the space between euhedral and subhedral non-sulphide minerals (magnetite, phlogopite). A similar texture in chalcopyrite was discussed by Roger (2009), who described it as a triangular-acute angle texture and interpreted it as a later-stage infiltration of chalcopyrite. Very small-scale chalcopyrite veinlets derived from the main chalcopyrite blotches which infiltrated the phlogopite crystals along their cleavages.

3.3.2 Banded carbonatite

3.3.2.1 Macroscopic appearance of the rock

The investigated sample set contains specimens that represent the younger banded carbonatite. The field relations of the younger and older banded carbonatite and the transgressive carbonatite are described in Chapter 2. The

appearance of the older banded carbonatite is very similar to the transgressive carbonatite apart from the lack of sulphide mineralisation (e.g., Hanekom et al., 1965). The younger banded carbonatite is characterised by the fine grain bands comprising mainly magnetite, but a minor amount of sulphides also occur. In sample Po5-03, the fine grain bands repeat every <0.5 cm (Fig.3.3.4 a), while in sample Pa6.2, the banding is less regular (Fig.3.3.4 b). Generally, the rock shows a much finer grain size compared to the transgressive carbonatite, both for the carbonates and the mafic minerals.

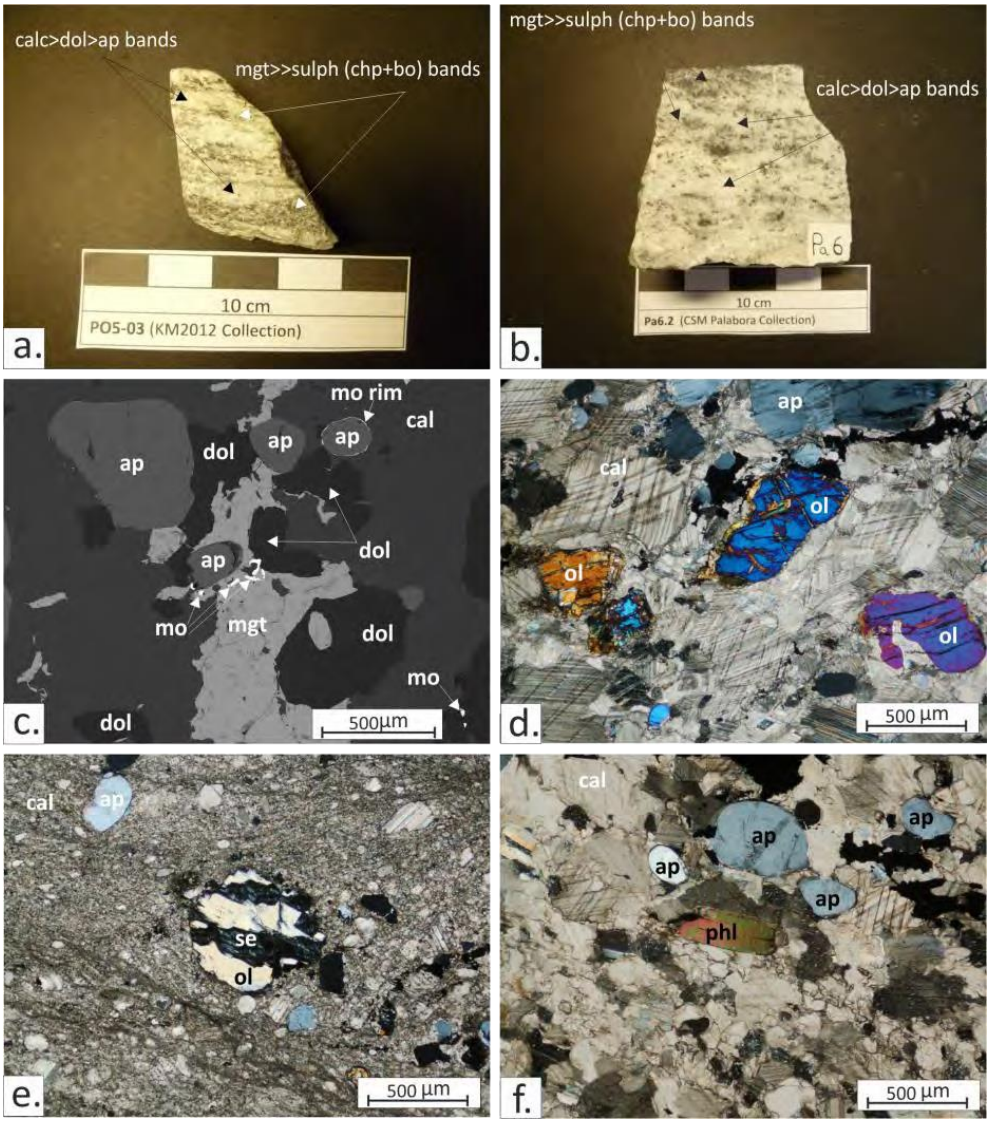

Figure 3.3.4. Photographs, transmitted light photomicrographs and BSE images. a-b: Banded carbonatite hand specimens displaying regular (a), and slightly less regular (b) dark, magnetite-sulphide bands in the coarse carbonatite. c: (BSE) Interstitial magnetite, with dolomite forming at the contacts with calcite and apatite. Subhedral and rounded apatite can have secondary monazite-rim formed around it. Anhedral monazite crystals also occur inside magnetite and calcite. d: (xN) Olivine xenocrysts showing re-equilibrated texture with phlogopite-rim developed around and in its fractures. Dolomite occurs around the olivine xenocrysts. Calcite forms large crystals with twin lamellae of various thickness and finer overprint, while apatite occurs in various sizes, with fractured crystals and undulouse extinction. e: (xN) Deformed/sheared banded carbonatite texture. The carbonate (calcite and dolomite) is disseminated, showing orientation and much finer grain size than the magmatic texture. The larger carbonate grains are elongated and oriented in the same direction. The olivine xenocryst with serpentine fracture infill displays

an almost perfectly rounded shape. f: (xN) Subhedral phlogopite and apatite in carbonate with interstitial chalcopyrite grains. Calcite is elongated with multiple twin lamellae overprints. Dolomite shows smaller grains with irregular contacts. 1N: under plain polarised light, xN: under crossed polarised light, BSE: Backscattered electron image, calc: calcite, dol: dolomite mgt: magnetite, chp: chalcopyrite, bo: bornite, ap: apatite, mo: monazite, ol: olivine, se: serpentine, phl: phlogopite

3.3.2.2 Micromineralogy

Under the microscope, the complexity of the banded carbonatite texture is more apparent, showing alternating bands of various textures and mineral proportions of several different minerals. The magnetite-containing bands usually contain more apatite, olivine and phlogopite phenocrysts and calcite crystals. The calcite crystals are anhedral with a general size of ~300-500 µm, twinned crystals with loboid boundaries and polygonal crystal mass with various twinning overprints (Fig.3.3.4 d, f). Between the larger calcite crystal types, very fine-grain carbonates also occur (~<100 µm) (Fig.3.3.4. d). The former bands are interrupted by calcite bands of smaller calcite crystal size (~<200 µm) with fewer silicate phases and apatite and usually lacking magnetite. The latter bands are usually associated with fractures along which the carbonate grain size is even finer (Fig.3.3.4 f).

As described above, the calcite and dolomite display diverse habits in the banded carbonatite (Fig.3.3.4 d-f). Similar to transgressive carbonatite, the abundance of dolomite is minor compared to calcite. Textures that suggest deformation and recrystallisation were observed in sample 6A. The latter textures include recrystallised calcite along fractures, showing very fine-grained crystals (Fig.3.3.4 e). Calcite can also form larger, elongated crystals in the non-deformed parts of the samples and display twinning with various thicknesses and thinner twin overprint (Fig.3.3.4 d, f). Between the large calcites, smaller but with a wide size range, polygonal crystals with various twining occur (Fig.3.3.4 d, f). Calcite is interstitial to apatite, olivine and phlogopite. Dolomite forms individual crystals (Fig. 3.3.4 c), and similar to the transgressive carbonatite, intergrowth with calcite also occurs. The size of the dolomite crystals is usually below 100 µm. Dolomite also occurs at carbonate and non–carbonate mineral contacts, forming finer-grained crystals with irregular contacts (Fig.3.3.4 c).

Magnetite forms anhedral, elongated and often disseminated crystals with irregular edges. The size of the crystals can reach one mm. It is often fractured

with carbonate infill (Fig.3.3.4 c). Magnetite is interstitial to apatite and calcite and often displays ilmenite exsolution lamellae.

Apatite in the non-deformed part of the banded carbonatite is mostly euhedral to subhedral, but anhedral crystals also occur (Fig.3.3.4 d, f). The size of the crystals can reach one mm, but crystals with ~500 μm size are the most common. The larger crystals are often more fractured (Fig.3.3.4 d). Inside these larger crystals, sub-grain formation occurs, displaying slightly undulatory extinction. In the deformed areas, apatite is primarily anhedral to subhedral, rounded and fractured with often prominent undulatory extinction.

Phlogopite is a minor constituent with primarily subhedral-anhedral and, less often, euhedral crystals, displaying various sizes up to one mm (Fig.3.3.4 f). Chloritic alteration is common. In the deformed part of sample 6A, the phlogopite crystals are bent. Phlogopite was also formed as a secondary phase along reequilibrated olivine xenocrysts (Fig.3.3.4 e).

Olivine appears large (~700 μm) sub- to anhedral, intensely fractured, and serpentinised crystals along the fractures and the rims. The textures of some of these olivine crystals suggest that they are re-equilibrated xenocrysts (Fig.3.3.4 d). The smaller type is approximately 200 μm in size and forms rounded or oval crystals and does not show prominent alteration. In the deformed part of sample 6A, the olivine shows a more developed serpentinic alteration (Fig.3.3.4 e).

The banded carbonatite contains minor amounts of sulphides in the form of anhedral patches that rarely reach one mm. The sulphide assemblage consists of chalcopyrite, bornite, digenite and covellite. These phases form intergrowths in most of the grains in sample 6B, but in sample 6A, the chalcopyrite is absent. Very minor sphalerite was also found in sample 6B as part of the sulphide assemblage. A very minor amount of galena was found in sample 6A in association with altered areas. The sulphide phases are interstitial to the other constituents of the rock. A minor valleriite reaction rim developed around some of the grains.

Accessory minerals of the banded carbonatite include monazite that can form rims around apatite or occurs as sub- to anhedral, <20 μm size, crystals in calcite and magnetite (Fig.3.3.4 c). It can also be abundant at sulphide-carbonate

contacts. Further accessory phases inside calcite include baddeleyite (~50 µm), baryte (<10 µm) and REE-carbonate (<10 µm).

Flow texture is present in the banded carbonatite, and internal deformation of crystals was also observed. Signes of flow within a melt include for example the alignment of elongated or tabular minerals which form foliated or lineated textures (e.g., Winter, 2014). Phlogopite and apatite crystals occasionally showed alignment in the banded carbonatite. The internal deformation is not prominent in the non-sheared sample, providing a good example of the differences between foliated textures created by magmatic flow and (in the present case) enhanced by deformation. Therefore, the textural progression of the younger banded carbonatite includes primary magmatic foliation due to the flowing of the magma subsolidus adjustment and is locally affected by ductile and possible brittle deformation, causing recrystallisation. Mineral alignment and banding are also can be caused by flow near magma chamber walls (Winter, 2014). Early crystallising phases were apatite, olivine, primary phlogopite and calcite with dolomite exsolution texture (exsolved from Mg-rich calcite as shown by Dawson and Hinton, 2003), followed by magnetite and primary sulphides and finally dolomite that occurs at contacts and monazite around apatite. Chlorite and serpentine are later-stage alteration products.

3.3.3 Phoscorite

3.3.3.1 Macroscopic appearance of the rock

The phoscorite samples of the sample set are coarse-grained rocks with magnetite, olivine, and apatite as major constituents (Fig.3.3.5). Magnetite forms the large, (mm<) eu- to anhedral crystals or crystal aggregates. Olivine (mm<) is strongly fractured with a subhedral or rounded habit that often shows extensive serpentinic alteration. Apatites (mm<) form eu- to subhedral or rounded crystals with pale green and greyish colours. Calcite and dolomite are minor phases occurring in patches between the large apatite, magnetite and olivine crystals. Similar to the banded carbonatite, the phoscorite also can show magnetite banding.

3.3.3.2 Micromineralogy

Similarly to the transgressive carbonatite, two types of primary magnetite were differentiated in the banded carbonatite based on appearance. Type1a magnetite forms large cumulus eu- to subhedral crystals (Fig 3.3.5 c, Fig 3.3.6 b). The crystals are strongly fractured. Type 1b magnetite is anhedral and interstitial between cumulus phases (Fig.3.3.6 a). The type 1 magnetites contain exsolved ilmenite lamellae and anhedral grains. Spinel is also common (Fig.3.3.6 b, c). Magnetite is often replaced by valleriite, which forms fine grain mass or variously developed crystal laths along the magnetite fractures and cavities. Type I magnetite has numerous inclusions, including phlogopite with Ba-zonation and serpentinic alteration, apatite, dolomite and baddeleyite. Secondary anhedral magnetite (type 2) is associated with altering silicate minerals. The crystals are usually subhedral and sometimes exceed 500 μm in size (Fig.3.3.6 c).

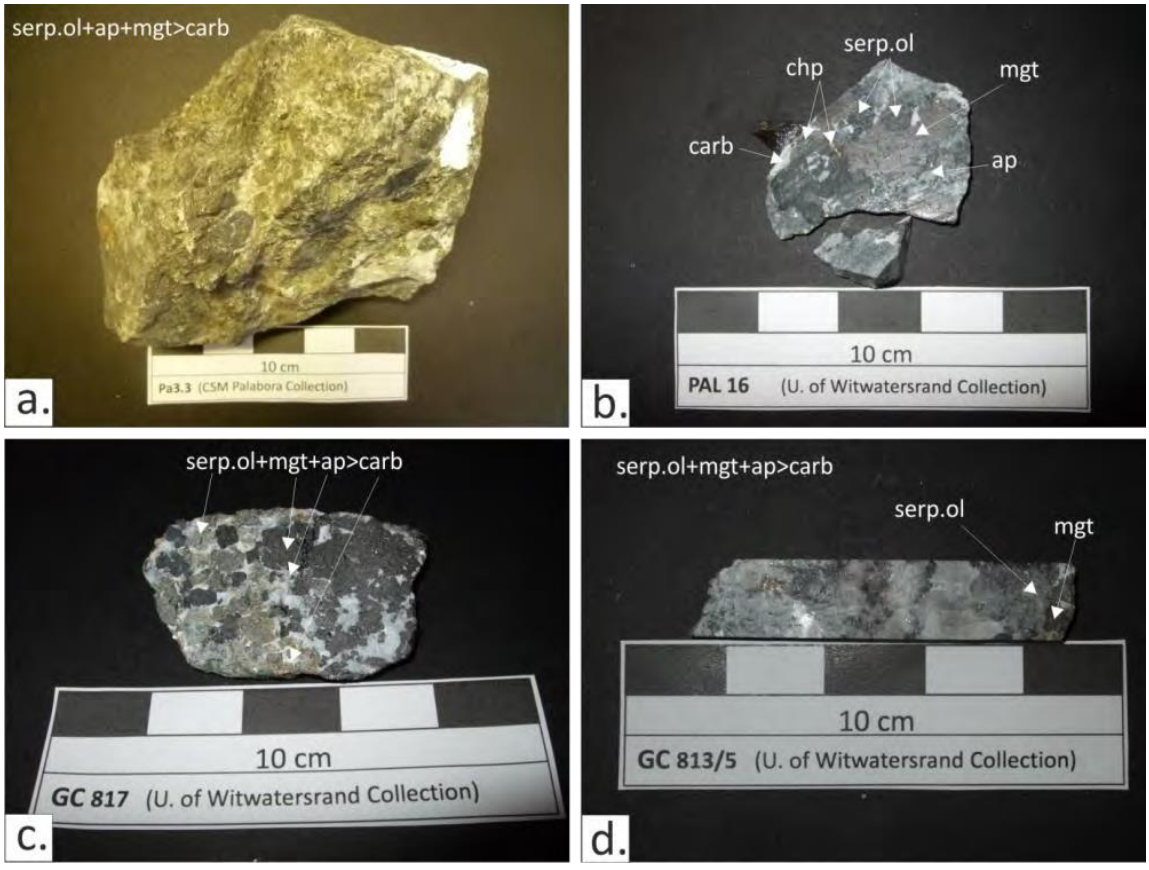

Figure 3.3.5. Photographs. Phoscorite hand specimens used in the study (a-d) The phoscorites are coarse-grained cumulate rocks where the main constituents include olivine, magnetite and apatite. The olivine is serpentinised to various degrees. Carbonate is minor interstitial phase. Serp ol: serpentinised olivine, mgt: magnetite, ap: apatite, carb: carbonate (calcite+dolomite)

The originally large (>500 μm) olivine crystals are broken up by strong fracturing and serpentinisation (Fig.3.3.6 a, c-f). Serpentinisation can be extensive,

completely consuming the olivine, leaving only the original outline (Fig.3.3.6 e). Calcite occurs inside the fractured crystals, which can suggest replacement. Apatite, phlogopite, and baddeleyite inclusions also occur. Eu- to subhedral pyrites are associated with serpentine-filled fractures. Magnetite can occur along contacts with other phases.

Apatite forms large (1 mm<) sub-to anhedral, intensely fractured crystals and often shows adjusted contacts with olivine (Fig.3.3.6 d). Recrystallisation and subgrain formation with undulatory extinction occur in larger crystals (Fig.3.3.6 e). Apatite also can be space-filling between the cumulus olivine. The fractures can be filled with secondary Fe-oxides, calcite, dolomite and very small Cu-Fe-sulphide inclusions. Dolomite, olivine and phlogopite also occur inside the crystals. Baddeleyite forms eu- to subhedral crystals, ~50 µm size inclusion inside the crystals. Subhedral apatite also occurs as inclusions in magnetite. Apatite also can form crystal aggregates with adjusted, polygonal grain boundaries. Valleriite can replace apatite along fractures.

Phlogopite is usually a minor constituent in the phoscorite samples. Primarily, it forms large (<cm) subhedral crystals (Fig.3.3.6 f). The crystals can be serpentinised, occasionally strongly resorbed. In sample Pa3.3, the phlogopite crystals can be strongly fractured and bent. Eu- to subhedral pyrite can be found in cleavages (<250 µm) and serpentinised areas. Phlogopite is associated with secondary magnetite (type 2) and contains relict olivine crystals (Fig.3.3.6. f). Small (~100 µm) phlogopite crystals in the carbonate and magnetite also occur with similar, irregular Ba-zonation and often serpentinic alteration. An elongated baddeleyite inclusion (<60 µm) in phlogopite was observed in sample Pa3.

Calcite is a minor interstitial phase forming subhedral-anhedral crystals (Fig.3.3.6 c, d, e). Calcite shows a wide range of sizes, crystal shapes and contacts and twinning with overwrites. Dolomite is always a minor carbonate phase, forming intergrowths with calcite (Fig. 3.3.6 c), individual crystals (< 100 µm) or associated with the contact areas of the carbonate phase and other minerals, in which case it can extend to one mm. It was also found as fracture fracture-filling phase in apatite.

Baddeleyite appears as eu- to subhedral, fractured crystals inside magnetite, less often at the junctions of the serpentine-filled olivine fractures. The size is usually

200x100 µm and below, but one crystal reaches 400x200 µm in the current sample set. In sample GC813_5, baddeleyite can form groups of loosely connected crystals with a usual size of ~200 µm with some up to 500 µm. These crystals are heterogeneous, with thorite inclusions (<10 µm). In the same sample, the usual inclusion type is baddeleyite, which also occurs inside magnetite and apatite. In sample Pa3.3, thorite (~ 20 µm) is associated with serpentine and secondary magnetite in olivine fractures. In the same sample, other accessory phases found in calcite include REE-carbonate (<10 µm) and baryte inclusions (<10 µm). Sphalerite (< 10 µm) was found inside magnetite along a phlogopite rim in one case. Celestite (< 10 µm) occurs in calcite. Zircon (<100 µm) was found in magnetite and apatite. Monazite was found in sample GC813_5 at the contacts of non-sulphides and sulphides and in apatite, forming rounded, subhedral (<150 µm) crystals.

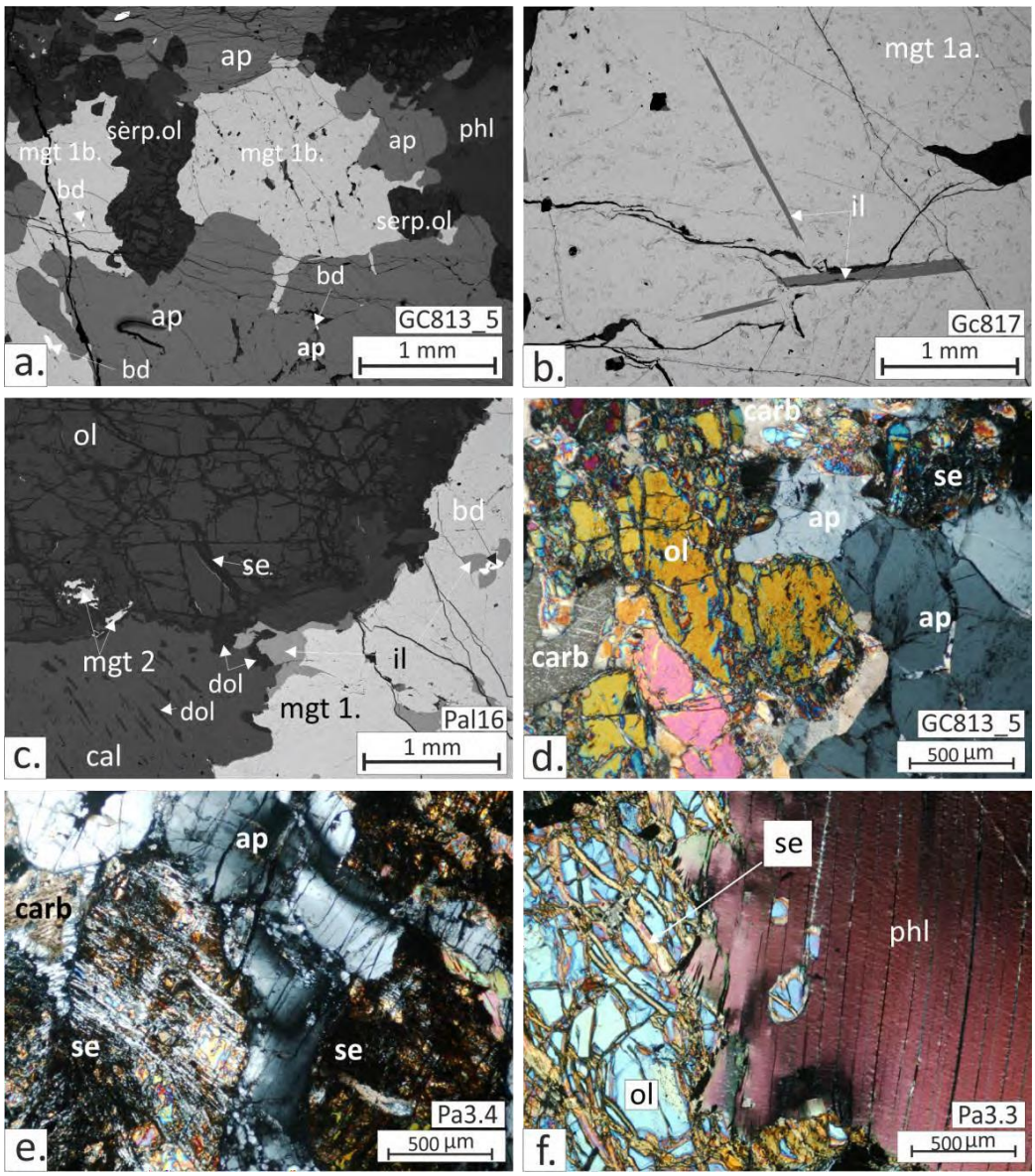

Figure 3.3.6. Transmitted light photomicrographs and BSE images. a: (BSE) Type 1b magnetite showing anhedral shape and interstitial nature between large, fractured cumulus apatite and resorbed, fractured and serpentinised olivine. Accessory monazite and baddeleyite occurs in apatite and magnetite. b: (BSE) Type 1. magnetite with ilmenite exsolution lamellae. c: (BSE) Strongly fractured and partly serpentinised olivine, with secondary type 2 magnetite, formed in fractures. Type 1 magnetite with exsolved ilmenite grains and accessory zircon. Interstitial calcite with exsolved, rod-shaped dolomite grains. Secondary dolomite occurs at the contact of the primary phases. d: (xN) Large fractured and partly serpentinised olivine crystals with large, fractured apatite with strong undulatory extinction. The two crystals show adjusted grain boundaries. Dolomite formed around and between the crystals. e: (xN) serpentine after cumulus olivine, fractured and partly re-crystallised apatite with undulatory extinction and interstitial carbonate. f: (xN) cumulus olivine with starting serpentinisation along the fractures, phlogopite with undulatory extinction. xN: under cross polarised light, BSE: backscattered electron image, phl: phlogopite, di: diopside, ap: apatite, ol: olivine, se: serpentine, cal: calcite, mgt: magnetite, il: ilmenite, mon: monazite, bd: baddeleyite.

3.3.4 Silicate rocks

The silicate rocks of Phalaborwa are very variable in terms of the rock texture and modal proportion (Fig.3.3.7 a-h). The main minerals observed with the naked eye in the Phalaborwa clinopyroxenites include diopside, apatite and phlogopite (Fig.3.3.7 a-e). The amount of phlogopite in clinopyroxenites differs widely from a couple of visible crystals to up to ~35 vol%. Phlogopite also can form relatively thin (5 mm) bands in the clinopyroxenite (Fig.3.3.7 c). Where apatite is visible, it forms angular or rounded crystals with a lighter shade of green than the surrounding diopside. Pegmatite, represented by sample Po5-01 (Fig. 3.3.7 f), comprises two minerals: eu- to subhedral, tabular apatite with crystal size of mm to cm scale and has green or pale green–white colour, and eu- to subhedral phlogopite that can reach larger than 10 cm in length. Rocks with phlogopite as the most abundant constituents are glimmerites (Fig.3.3.7 g-h). The rocks can contain either diopside or olivine as the second most abundant phase, in both cases with serpentinic alteration. In the diopside-rich glimmerites (Fig. 3.3.7 g), apatite and carbonate also occur, while both phases are minor constituents of the olivine-rich glimmerites (Fig.3.3.7 h). Magnetite occurs in the latter as a minor phase. Olivine and phlogopite have approximately the same modal proportions and show finer grain sizes, as represented in sample Po5-03. In the sample set, carbonate veins occur in the glimmerite rocks (Fig.3.3.7 g-h). Sample Box 3-1 represents feldspathic-clinopyroxenite (Fig.3.3.7 a); however, this is only apparent under a microscope as the interstitial microcline is a minor constituent.

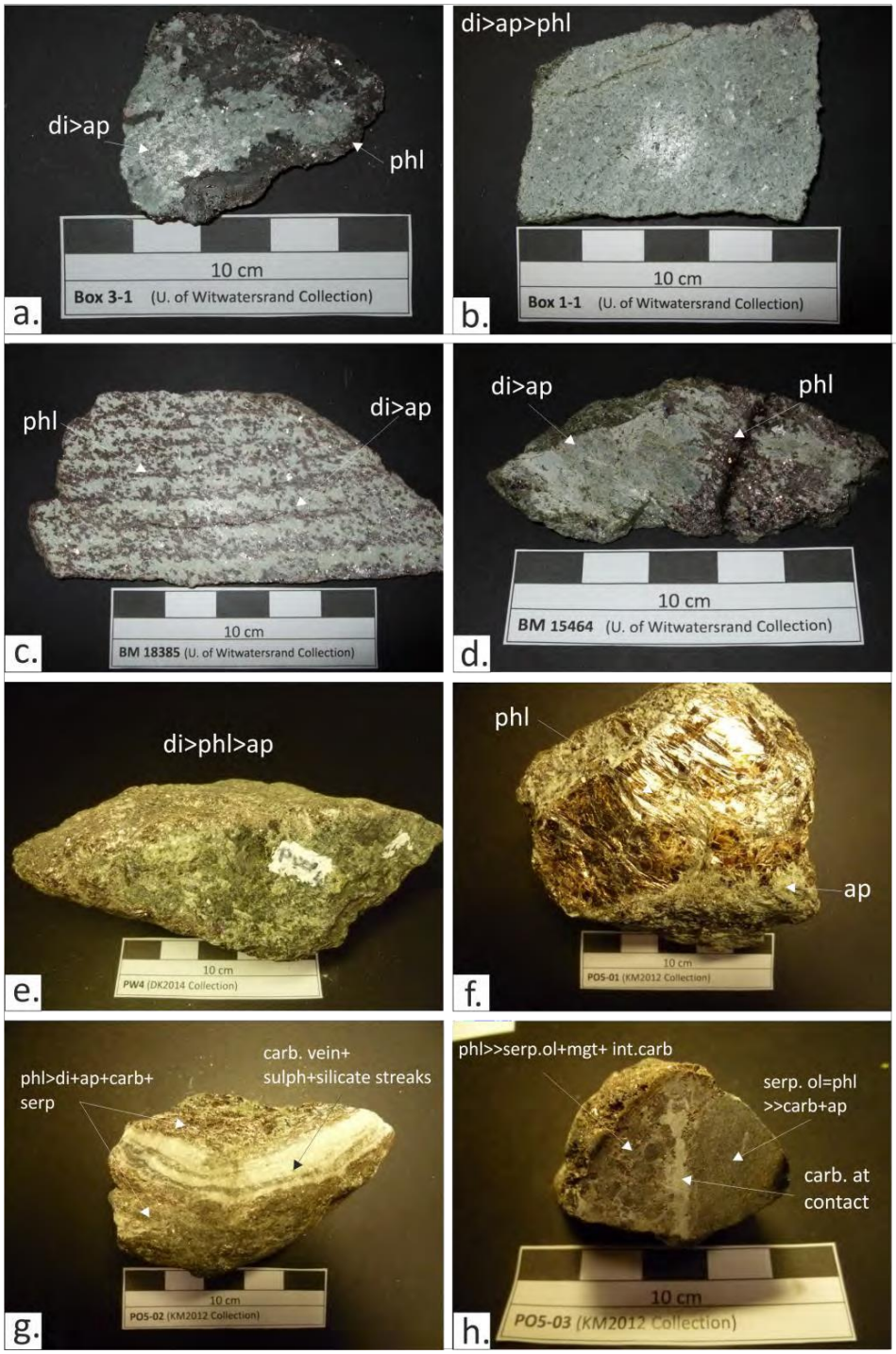

Figure 3.3.7. Photographs. Silicate rock hand specimens described in the study. a: Feldspathic clinopyroxenite cumulate containing diopside with lesser amount of apatite, phlogopite and interstitial microcline b-e: Clinopyroxenite (b) and micaceous clinopyroxenite (c-e) cumulates with diopside as the most abundant phase, followed by apatite and phlogopite. Phlogopite can form regular bands in the micaceous clinopyroxenites (c).f: Pegmatoid rock with large, pegmatitic phlogopite and apatite crystals. g: Glimmerite rock, where the phlogopite proportion exceeds partially serpentinised diopside. Apatite and calcite are major constituents. The rock is crosscut by a carbonate vein which contains dark-gray coloured streaks of sulphide, magnetite and silicate phases. h: The sample represents two olivine-rich rock types with abundant magnetite-ilmenite and interstitial calcite. In olivine–glimmerite The olivine is strongly serpentinised. In the other rock type, the olivine and phlogopite proportion is roughly the same. The olivine is serpentinised. The contact of the two rock types is marked by a carbonate vein di: diopside, phl: phlogopite, ap: apatite, carb: carbonate (calcite/dolomite), serp: serpentine, mgt: magnetite: int: interstitial, sulph: sulphide

3.3.4.1 Micromineralogy

3.3.4.1.1 Feldspathic clinopyroxenite

According to the description of Hanekom et al. (1965), the felspathoid-clinopyroxenite developed at the contact between the main clinopyroxenite body and the surrounding granite and syenite. It has a wide modal variation, with the proportion of the feldspar increasing from the clinopyroxenite contact towards the syenite contact. The sample contains only a minor amount of microcline, suggesting that it represents areas closer to the clinopyroxenite body than the syenite body.

Feldspathic-clinopyroxenite contains diopside as a cumulus phase with usually well-developed crystal habits (Fig.3.3.8 a, c, e). The crystals can also be rounded or have adjusted edges (Fig.3.3.8 d). The crystal size changes between ~100 µm and ~1 mm. Diopside often contains anhedral titanite (~20 µm), subhedral zircon (can reach 500 µm) and a subhedral Th-silicate phase (<20 µm). Cumulus apatite is eu- to subhedral, fractured, and shows recrystallisation at contact areas and adjusted edges (Fig.3.3.8 a-f). Inclusions found in apatite include REE-silicate (<10 µm) and baryte (< 10 µm). Phlogopite is represented by large (<mm), subhedral crystals (Fig.3.3.8 a, f). Tetraferriphlogopite forms smaller and thin (~500 x 100 µm) crystal laths with diverse orientations (Fig.3.3.8 b, f) and reverse pleochroism. Both can contain euhedral apatite (~300 µm) as inclusions. The interstitial microcline is a minor phase with well-developed, characteristic cross-hatched twinning (Fig.3.3.8 a, c, e). Accessory phases include baryte, which forms sub- to anhedral crystals of <50 µm size but rarely reach ~90 µm. Baryte is associated with clinopyroxene grain contacts and occurs as inclusions inside apatite. Titanite, zircon and thorite are all associated with clinopyroxene as described above.

The texture of the rock is coarse-granular, dominated by large, subhedral crystals, forming poikilitic textures. The irregular, interpenetrating crystal contacts suggest simultaneous crystallisation, but there are definite signs of subsolidus boundary adjustment. This is identifiable by the dihedral angles of the grain boundaries and indicates slow cooling (Vernon, 2004) and later-stage deformation. Solid-state adjustment occurs during cooling, when the neighbouring crystal boundaries mutually adjust to minimise local interfacial energies (Vernon, 2004). The subhedral grains developed good crystal faces

towards the interstitial places, while at the contact with other grains, they are more often irregular. These contacts can also show solid-state adjustment with polygonal boundaries. The later stage deformation process is represented by apatite and phlogopite recrystallisation, sub-grain formation, and deformation twinning of the interstitial microcline (Fig.3.3.8 a, b, f). Undulatory extinction is common in the large and smaller phlogopite crystals. The small phlogopite crystals are clearly in the deformation zones (as near recrystallised apatite contacts and bended phlogopite aggregates). They might be the product of the advanced stage recrystallisation of earlier large phlogopite crystals (Fig.3.3.8 b, f). Undulose extinction is the sign of dynamic recrystallisation during static recrystallisation.

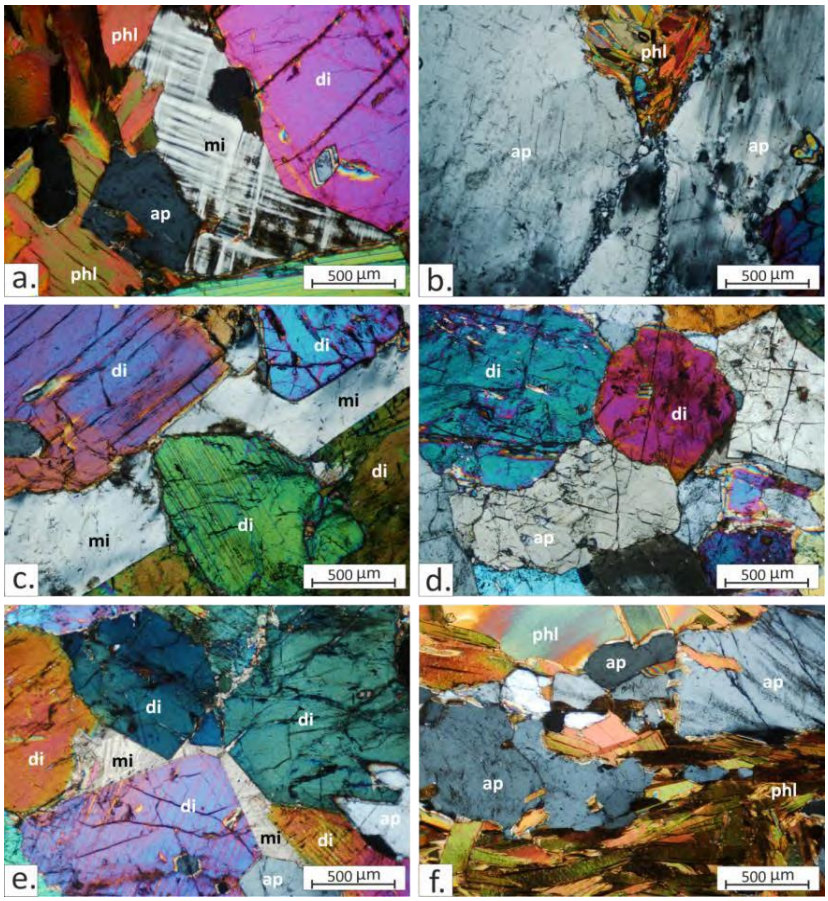

Figure 3.3.8. Transmitted light photomicrographs (xN). Sample Box3-1 representing feldspathoid rocks of Phalaborwa. The interstitial feldspar is microcline (a, c, e). The microcline can display its characteristic cross-hatched twinning (a). The diopside crystals are primarily subhedral with well-developed crystal faces and abundant twinning (a,c ,d, e). Both diopside and apatite can show near- polygonal, adjusted crystal edges (d). Large apatite crystals can display strong fracturing, irregular edges and undulatory extinction (b, d, f), and sub- grain formation and recrystallisation at the crystal contacts (b). Subhedral or close to euhedral apatite crystals also occur (a, e), often inside diopside (c, e). Phlogopite form subhedral, often bent laths of various sizes, crosscutting the cumulate phases and each other (a, b, f). xN: under cross polarised light, phl: phlogopite, di: diopside, ap: apatite, mi: microcline

3.3.4.1.2 Massive and micaceous clinopyroxenites

Phalaborwa clinopyroxenites have poikilitic texture where the dominant clinopyroxene is diopside, but minor augite also occurs. The crystals are primarily subhedral, less often anhedral, connecting with each other or other cumulus crystals with adjusted, polygonal or bulging edges (Fig.3.3.9 a-d). The crystals are often strongly fractured and twinned. The size of the crystals has a wide range, with a maximum of ~1mm x ~600 µm. The clinopyroxene also contains smaller (100-250 µm), eu- to subhedral apatite crystals and subhedral zircon (~50 µm). Undulose extinction and stronger twinning of diopside were observed in sample GC826.

The second most dominant phase is apatite, which forms sub-euhedral, rounded or tabular crystals (Fig. 3.3.9 b, d, e) or shapes adjusted with the surrounding cumulus phases, similar to the clinopyroxenes (Fig. 3.3.9 a-c, d). The size of the cumulus apatite crystals is similar to the clinopyroxenites, usually below 1 mm. It often forms crystal aggregates. The crystals also can be disseminated or form sub-grains with undulatory extinction (Fig.3.3.9 b). Small (100- 250 µm), eu- to subhedral apatite inclusions occur in cumulus clinopyroxene and phlogopite.

Phlogopite occurs as sub- to anhedral crystals with a wide size range (~ 100 µm – 0.5 cm) between cumulus clinopyroxenes and apatite (Fig.3.3.9 c). It can form crystal aggregates of bent laths that crystallised around apatite and clinopyroxene (Fig.3.3.9 b); this type formed later than the phlogopite described previously. It is usually fresh without significant signs of vermiculite or chloritic alteration, except for the slightly more altered phlogopites in sample PW4. In samples where phlogopite forms bands in the clinopyroxenite (Fig.3.3.7 c), the bands are associated with slightly coarser-grained clinopyroxenites. Tetraferriphlogopite with inverse pleochroism is much less abundant; it was observed in the massive clinopyroxenite sample (Pa4), forming a few large subhedral laths. In the same sample, phlogopite is smaller, anhedral and intercumulus between diopside crystals.

Minor minerals in clinopyroxenites include interstitial calcite, with various broad twin lamellae (Fig.3.3.9 c, e). Titanite (<10 µm) occurs at the edges of the diopside, inside the diopside crystals and along the cleavages (Bm18385, Box1-1, GC826). Furthermore, titanite occurs in secondary magnetite with abundant ilmenite lamellae (Fig.3.3.9 f). The secondary magnetite replaces diopside (Fig.3.3.9 f).

Accessory phases include baryte (<50 µm) as inclusions in apatite, calcite and phlogopite (Bm18385, Box1-1) (Fig.3.3.9 g). In sample Bm15464, baryte can reach 300 µm and form sub- to anhedral crystals between the cumulus clinopyroxenes, inside the crystals, and inside apatite. Anhedral galena (<20 µm) was found in fractures in diopside (Bm18385). Baddeleyite inclusions (<50 µm) with zircon heterogeneity and individual zircon inclusions occur (<25 µm) in apatite (Bm18385, PW4). Zircon can also form small subhedral, needle-like crystals at the phlogopite-apatite contact or as a rim around apatite inclusion inside phlogopite (Bm18385).

Accessory sulphides were observed in sample PW4; they occur as anhedral patches (<200 µm) of chalcopyrite, bornite, sphalerite and a Co-rich pentlandite assemblage. Monazite was found in apatite as very fine-grained inclusions (PW4).

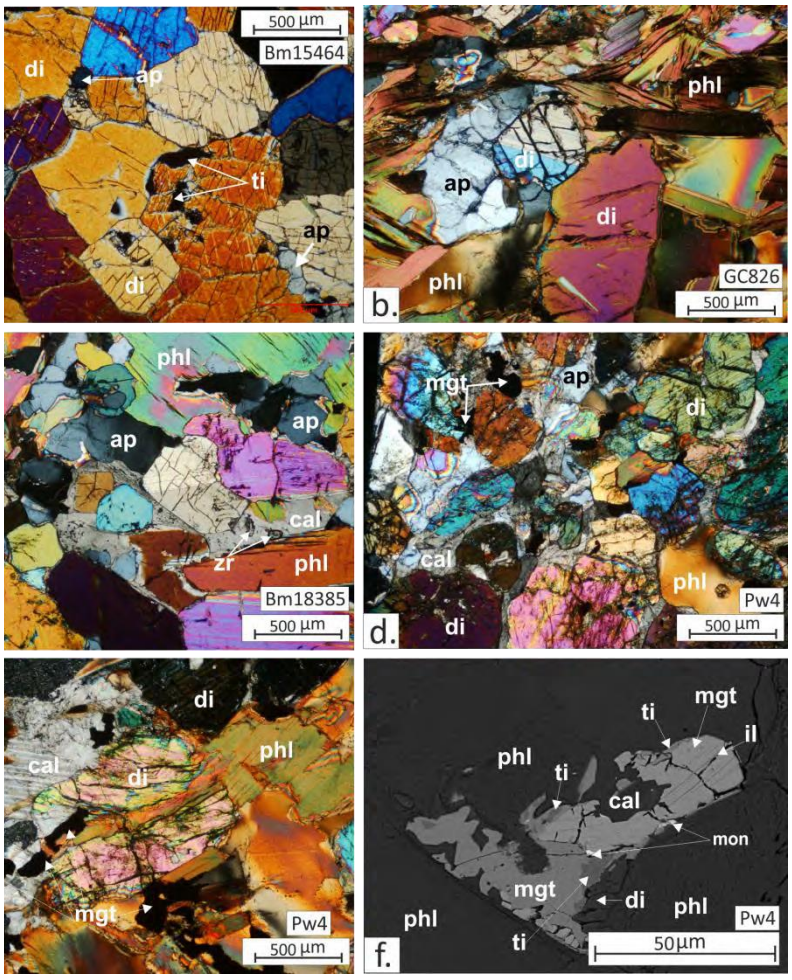

Figure 3.3.9. Transmitted light photomicrographs and BSE images. Microtexture of the clinopyroxenite/micaceous clinopyroxenite cumulate samples (a: Bm15464; b,e: GC826; c: Bm18385; f-h: PW4). a: (xN) Cumulus diopside crystals with polygonal-adjusted crystal edges. The diopsides are strongly twinned and fractured. Finer-grained cumulus apatite also occurs. b: (xN) Phlogopite-rich band in phlogopite-banded micaceous clinopyroxenite. Thin banded phlogopite laths form around cumulus apatite and diopside. c: (xN): Phlogopite-banded micaceous clinopyroxenite texture between phlogopite bands: Cumulus diopside and apatite with primarily subhedral shape. Large phlogopite crystal of this area show a different habit from the phlogopite laths forming bands, suggesting a more primary origin than the latter. Calcite is a minor interstitial phase. d: (xN) Cumulus diopside and apatite in micaceous clinopyroxenite with interstitial calcite. Secondary anhedral titanite (ti) and magnetite show association with diopside. e: (xN) Phlogopite replacing cumulus diopside. Secondary anhedral magnetite is associated with diopside and phlogopite. f: (BSE) Secondary anhedral magnetite, associated with diopside alteration.

3.3.4.1.3. Phlogopite-apatite pegmatite

The rock type is represented by samples GC1187 and Po5-01 (Wits. Collection – location unknown, KM Collection: in situ from open pit of the main intrusive unit). The rock type is characterised by large, cm-scale apatites and phlogopites with a modal proportion of ~30% and ~65%, respectively (Fig.3.3.10 a, c). Tetraferriphlogopite is minor, observed only in sample Po5-01, with the same habit as the large phlogopite crystals. The phlogopite crystals are eu- to subhedral, strongly fractured, and commonly contain magnetite-ilmenite patches (Fig.3.3.10 a-d). The apatite is subhedral, with a tabular appearance but with adjusted edges. It usually has polygonal contacts with phlogopite (Fig.3.3.10. a). The apatite is also intensely fractured. Undulatory extinction and sub-grain formation in apatite are widespread (Fig.3.3.10 c). Minor components of the pegmatite include interstitial calcite and ilmenite that can form individual crystals (<500 μm) and inclusions in phlogopite. The crystals are anhedral, fractured and can be found between the other constituents. Diopside was observed on one occasion, forming a large, twinned, anhedral crystal between the apatite and phlogopite crystals (Fig.3.3.10 b). It is replaced by calcite around and along the twin planes. Accessory phases include thorite (<25 μm) as inclusions in phlogopite and apatite. Sr-baryte/celestite forms anhedral fracture infill in apatite (Fig.3.3.10 d). Bornite inclusions (<20 μm) occur in phlogopite. Zircon was observed as sub- to anhedral, compositionally heterogeneous crystals that can reach 250 μm and are primarily associated with apatite.

3.3.4.1.4 Diopside-glimmerite

This rock type is represented by sample Po5-02. The apatite crystals are mostly subhedral, tabular and strongly fractured (Fig.3.3.11 b). However, the diopside is resorbed, serpentinised, and broken up into smaller, strongly fractured crystals (Fig.3.3.11 a). Partial replacement by secondary magnetite-ilmenite-titanite is common. The phlogopite replaces apatite and diopside, forming large (mm scale) laths that are often bent (Fig.3.3.11 a-b).

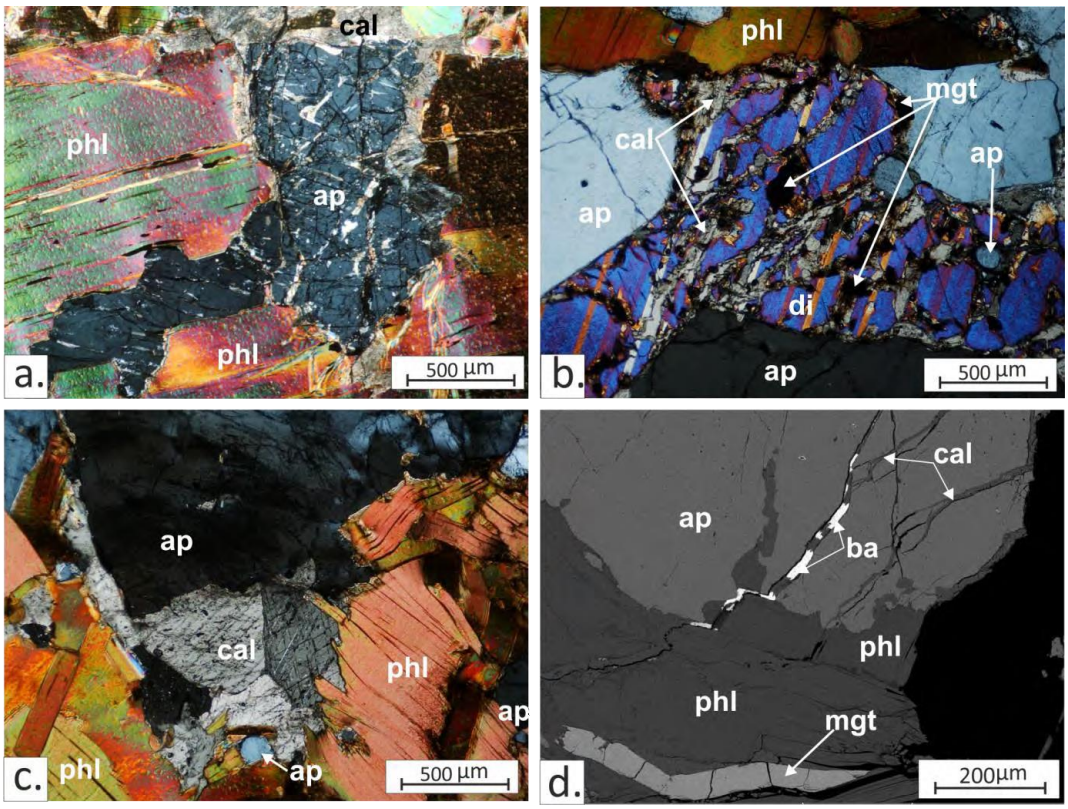

Figure 3.3.10. Transmitted light photomicrographs and BSE images. Texture of the pegmatite rocks (a-c: xN, d: BSE). Phlogopite is the most abundant mineral phase, with large crystals that are often bent or fractured and recrystallised (a, c). In the latter case, the new laths are much smaller and thinner (c). Apatite is the second most abundant phase; it forms large subhedral crystals that are strongly fractured with undulatory extinction (a). One relict diopside was observed forming large, anhedral crystals, filling out space between apatite and phlogopite crystals. The crystal is fractured and display strong twinning, with secondary magnetite, calcite and apatite inside the fractures and cavities (b). Calcite is an interstitial phase between and inside the fractures of the silicate and apatite crystals (a-d). Secondary magnetite occurs in association with diopside resorption, and inside phlogopite cleavages (a, b, d). Accessory baryte occurs in apatite fractures (d). xN: under cross polarised light, BSE: backscattered electron image, phl: phlogopite, di: diopside, ap: apatite, cal: calcite, mgt: magnetite, ba: baryte

Phlogopite is also associated with secondary magnetite and ilmenite that form small, anhedral patches and streaks inside the phlogopite crystals, along the cleavages, and at the edge of the laths. Calcite is more abundant in this rock type than in the clinopyroxenites, reaching around ~20 vol%. The phlogopite-rich part is in contact with a carbonate vein that contains apatite-rich and serpentinised-olivine-rich bands, magnetite and chalcopyrite-pyrrhotite streaks. The modal proportions of the rock would suggest that it is a silicocarbonatite; however, no rock with such composition was previously reported from Phalaborwa. The appearance of the minerals, the rock texture, and the knowledge of the general Phalaborwa lithologies suggest that the rock represents a later-stage cross-cutting vein.

3.3.4.1.5 Olivine glimmerite and phlogopite olivinite

Sample Po5-03 comprises two different lithologies separated by a carbonate vein. The sample was collected from the open pit of the main intrusive unit. In Fig.3.3.7 h, on the left-hand side, is serpentinised olivine-containing glimmerite. The phlogopite takes up ~80 vol% of the rock, forming eu- to subhedral crystals of 1-2 mm. Tetraferriphlogopite occurs with reverse pleochroism. Interstitial calcite is the second most abundant phase, taking up ~10 vol%. Olivine is a minor (~6 vol%) constituent; the anhedral, resorbed crystals are replaced mainly by serpentine. Apatite is also a minor component (~3 vol%), forming sub- to anhedral crystals of 0.5-1 mm size. Secondary magnetite (~2 vol%) is associated with phlogopite, where it forms anhedral crystals.

Phlogopite-olivinite is also represented in sample Po5-03, on the right-hand side of the sample shown in Fig. 3.3.7 h. It is generally finer-grained than the previously described rock. The amount of serpentinised olivine and phlogopite is very similar; the former is only slightly more abundant, ~40 vol% and 35 vol%, respectively. The olivine is very strongly altered, almost wholly consumed by serpentine. Phlogopites are sub- to anhedral, with various size crystals, usually below 1mm and associated with secondary anhedral magnetite with ilmenite exsolution (~3 vol%). Calcite is an interstitial phase of ~13 vol%, while apatite is a minor component of ~8 vol%. Accessory phases include small, resorbed, anhedral sulphide grains with complex chalcopyrite and bornite intergrowths associated with the serpentinised olivine. Baddeleyite is also present; it was observed in subhedral (~100 µm) zirconium-mineral, possibly zirconolite (based on semi-quantitative EDS, which showed a Zr- Ti-Ca-oxide phase). It also forms subhedral, rounded crystals in calcite (<50 µm).

Overall, the silicate rock samples have similar constituent minerals but show diverse modal proportions and rock textures. This was also established by several previous works introduced in chapter 1. The sample set reflects this diversity, and they can be placed into the different lithology types of the Phalaborwa complex due to the well-established field relations and descriptions by the previous authors, especially Hanekom et al. (1965).

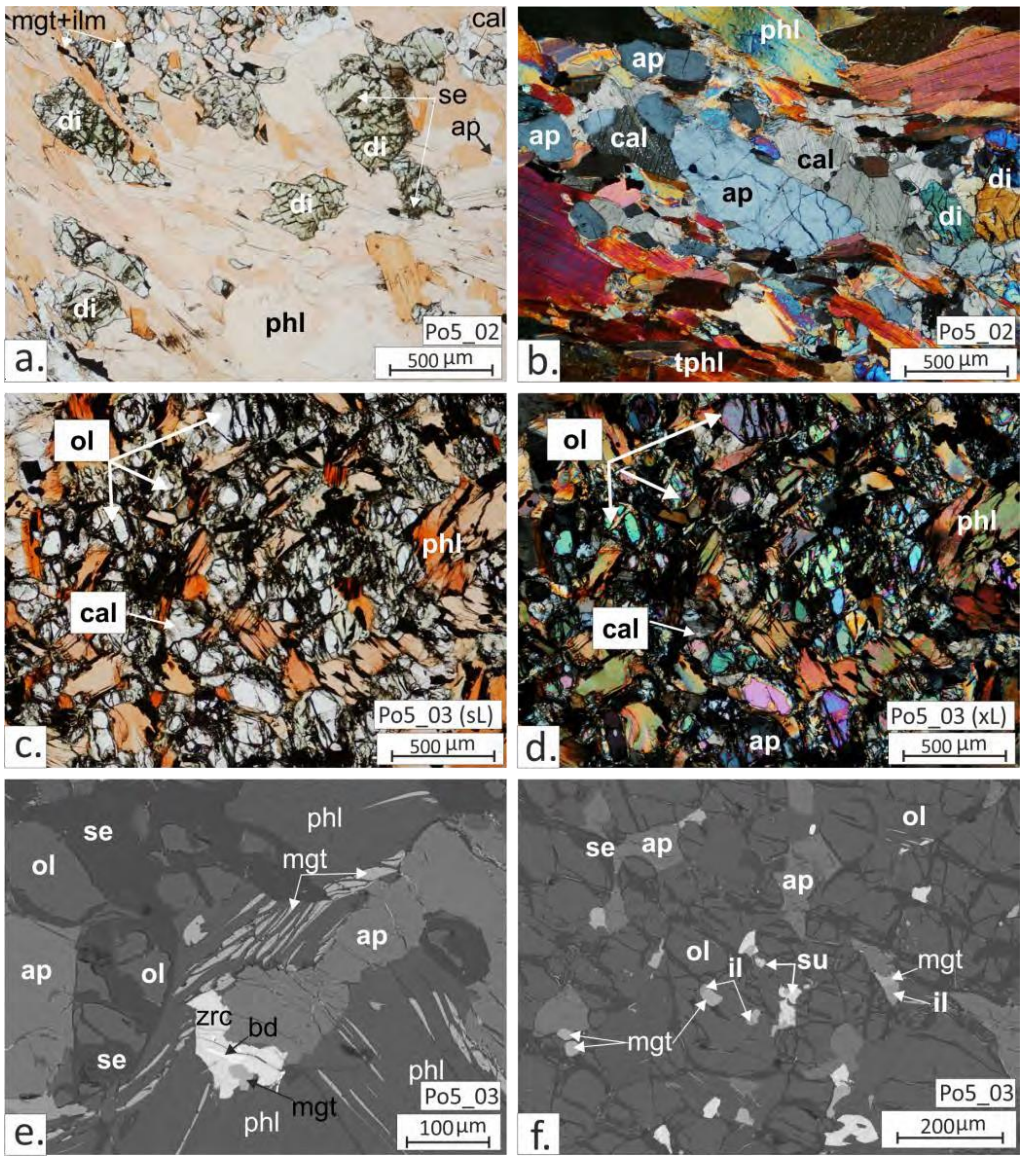

Figure 3.3.11. Transmitted light photomicrographs and BSE images. a (1N)-b (xN): Glimmerite and tetraferriphlogopite with partially serpentinised diopside, apatite and calcite. Diopside is anhedral and strongly fractured. Apatite is sub- to anhedral, also with strong fracturing and dissemination. Minor phases include interstitial calcite and secondary magnetite- ilmenite formed in diopside and phlogopite cleavages. Phlogopite is the most abundant phase, forming frequently bent, oriented laths and giving the rock an overall impression of orientation in the microtexture. The smaller, banded laths suggest recrystallisation. c (1N), d (xN), e (BSE): Olivine glimmerite with heavily serpentinised, fractured and disseminated olivine. Phlogopite laths are small sub- to anhedral and fractured with abundant secondary magnetite along the cleavages. Apatite is sub-anhedral, strongly fractured; magnetite can occur in the fractures (e). Subhedral accessory zircon with baddeleyite and magnetite inclusions is associated with apatite (e). f: (BSE): Phlogopite-rich olivinite: The major constituent is olivine which is partially serpentinised along the fractures but to a lesser extent then in the olivine glimmerite. Apatite is finer grained, filling space between the olivine crystals. Secondary anhedral magnetite-ilmenite grains formed in association with serpentine and phlogopite. Anhedral mixed (Cu-Fe) sulphide grains associated with the serpentinised olivine. 1N: under plain polarised light, xN: under cross polarised light, BSE: backscattered electron image, phl: phlogopite, di: diopside, ap: apatite, ol: olivine, se: serpentine, cal: calcite, mgt: magnetite, il: ilmenite, zrc: zircon, bd: baddeleyite

Chapter 4: Textural study of the Phalaborwa sulphides

4.1 The mineralogy and microtextures of the Phalaborwa sulphide assemblage

The macroscopic appearance of the rocks was described in Section 3.3. The present chapter will focus on the sulphide phases and their microtextures observed in the Phalaborwa lithologies (transgressive carbonatite, younger banded carbonatite, phoscorite, and silicate rocks) to establish the sulphide petrogenetic sequence and separate the phases of sulphide formation. Alongside describing the textural relationships of the sulphide phases, the chapter will discuss the reliability of such relationships and texture types in the formation interpretation.

Transgressive carbonatite lithologies are differentiated based on the sulphide assemblage they are representing and classed as *bornite-rich*, *chalcopyrite-rich, troilite-rich and chalcopyrite-bornite-replacement transgressive carbonatite*. Troilite and pyrrhotite are not distinguishable optically, and both were reported from Phalaborwa by previous works (e.g., Hanekom et al., 1965; Rudashevsky et al., 2004). The major element analysis (Chapter 5) showed that the Fe-S phases identified in these samples as “pyrrhotite” have compositions that range between ideal pyrrhotite and troilite, and are closer to the latter; therefore, they will be called troilite. Examples of these lithologies are shown in Figure 3.3.1, and the macroscopic appearance is described in Section 3.3.1.

4.1.1 Transgressive carbonatite

The sulphide assemblage of the investigated sample set comprises several phases with very diverse proportions throughout the sample set; in many cases, it can only be observed by optical microscopy or SEM.

Chalcopyrite displays a variable textural relationship with the non-sulphide minerals. Macroscopically, chalcopyrite appears as connected or unconnected veins, veinlets, patches and droplets. Under the microscope, it generally fills the space between euhedral to subhedral magnetite, silicate and carbonate-minerals; it occurs as interstitial blobs in the carbonate groundmass, or it follows magnetite grain boundaries and also penetrates non-sulphide crystals along cleavages and fractures. The appearance is massive-anhedral, often fractured,

especially at the rims where it is usually resorbed. At the contacts towards the magnetite and gangue minerals, a reaction rim with various thicknesses can often be observed. Massive chalcopyrite hosts several different sulphide phases, mainly cubanite, troilite, bornite, sphalerite and cobalt pentlandite.

Cubanite is the most common sulphide phase hosted by the chalcopyrite, forming abundant lamellae which can reach several mm in thickness (Fig. 4.1.1.a-d). Lamellae parallel to the faces of the chalcopyrite is a very typical cubanite appearance (Ramdohr, 1969) and it was observed in the present sample set as well. The lamellae can partially be replaced by magnetite/haematite and valleriite and are crosscut by troilite and sphalerite. Aldous (1980) notes that cubanite is especially abundant in the central part of the transgressive carbonatite. The work also notes the presence of minor mackinawite at the cubanite rims, but this was not observed in the present sample set.

Cobalt pentlandite is a common mineral in the transgressive carbonatite and occurs in most of the samples regardless of whether they are chalcopyrite or bornite rich; however, there is a difference between the habit of cobalt pentlandite within these two sulphide mineral hosts. Cobalt pentlandite typically forms subhedral to euhedral crystals, displaying well-formed crystal faces in chalcopyrite. The crystals are usually highly fractured. The fractures are often straight cracks and have very fine-grained secondary phases along them (Fig.4.1.1.e-h), including haematite, Fe-Ni and Co-Ni sulphides. The latter were too fine-grained for accurate analysis, but based on the paragenesis, most possibly belong to the linnaeite group. The maximum cobalt pentlandite grain size reaches 500 μm. Cobalt pentlandite can occur as single crystals in chalcopyrite groundmass; however, they often form clusters of several crystals with well-developed crystal forms. This appearance changes at more fractured and altered areas of the host chalcopyrite, usually at the edges where it is broken and replaced by other phases. The cobalt pentlandite forms crystal aggregates of anhedral (rarely subhedral) and rounded grains. Replacement by secondary magnetite and haematite along fractures and around the boundaries is a common feature (Fig.4.1.1.e-h; Fig. 4.1.2.a-e).

Troilite forms irregular stringers with elongated, wedge-like shapes and ragged edges (Fig. 4.1.1. a, b). Another type of appearance is troilite flames or spindles along fractures (Fig. 4.1.1.a). In this case, troilite forms elongated grains with a broader end penetrating the chalcopyrite. These grains form at both sides of the fracture, creating a feather-like appearance. Similarly shaped cobalt pentlandite grains may occur near the troilite in this texture, but they are much less common. Troilite stringers and spindles crosscut the cubanite lamellae and strongly stand out due to the significantly higher relief.

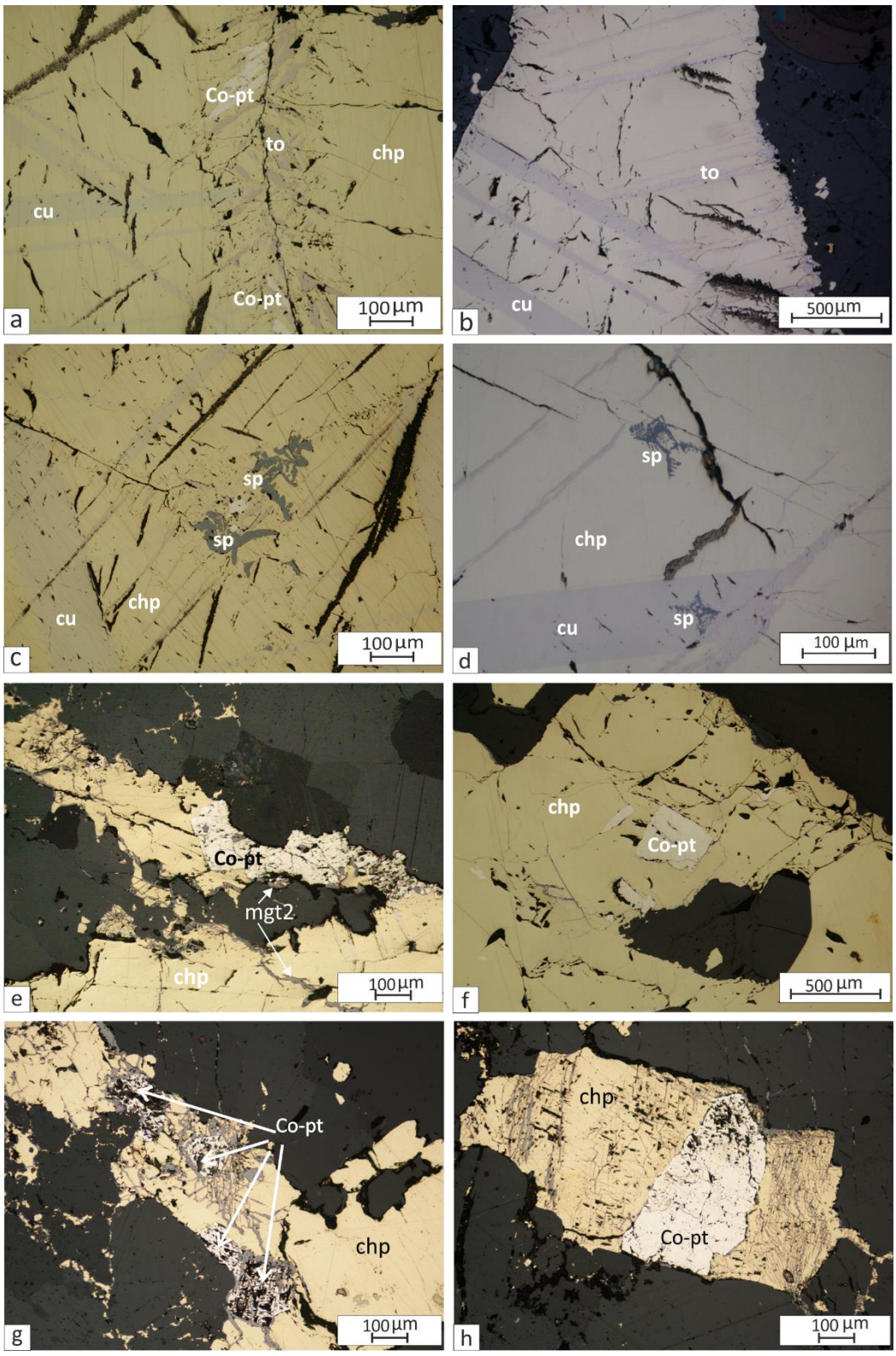

Figure 4.1.1. Reflected light photomicrographs; a: massive chalcopyrite with cubanite lamellae; troilite and cobalt pentlandite flames/spindles along fracture. b; Cubanite lamellae and troilite stringers in massive chalcopyrite. c; Cubanite lamellae and myrmekite-resembling sphalerite in massive chalcopyrite. d; cubanite lamellae and sphalerite stars in massive chalcopyrite. Chp: chalcopyrite; co-pt: cobalt-rich/cobalt pentlandite; cu: cubanite; to: troilite; sp: sphalerite Subhedral Co-pt in chp, often fractured and altered (a – d).

Troilite also can be a massive phase in the transgressive carbonatite when it forms extensive (>1 mm) patches with smooth contact towards the chalcopyrite (Fig. 4.1.2.a-d). These troilite grains are anhedral, often rounded. The grains crosscut the cubanite lamellae of the chalcopyrite host and contain several fractures and inclusions of Fe-oxides in the studied samples. Sub-anhedral cobalt pentlandite grains (<500 µm) commonly occur at the contact of the troilite grains and host chalcopyrite.

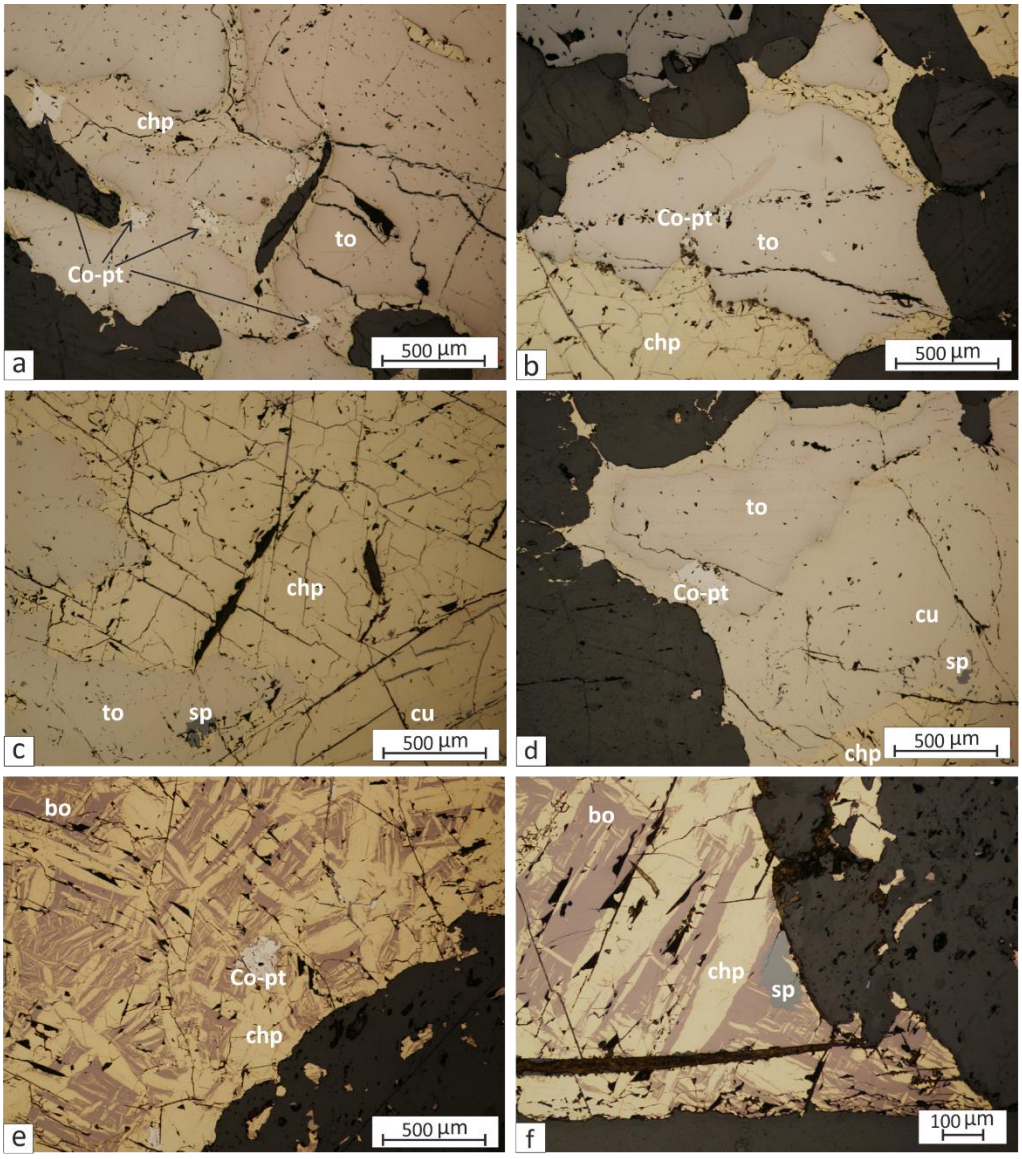

Figure 4.1.2. Reflected light photomicrographs; a-d: anhedral, rounded, extensive troilite grains in chalcopyrite. The massive chalcopyrite contains cubanite lamellae and anhedral sphalerite grains. Sub-anhedral co-pentlandite occurs at the contact of the troilite and chalcopyrite. E-f: shredded texture of bornite and chalcopyrite showing a replacement relationship between them. Anhedral sphalerite and sub-anhedral co-pentlandite commonly occur. Bo: bornite; chp: chalcopyrite; co-pt: cobalt-rich/cobalt pentlandite; cu: cubanite; to: troilite sp: sphalerite

Sphalerite in chalcopyrite appears in various forms. Sphalerite stars are common, often with a partially developed form that resembles myrmekite-resembling texture (Fig. 4.1.1.c; d). The grain size is very small, usually extending to less than 100 μm area, with the individual grains being even smaller (<20 μm). The second type of sphalerite occurs at the contacts of chalcopyrite and gangue minerals. It has a rounded or convex-shaped side towards the inner part of the chalcopyrite and a concave shape side towards the contact and sometimes follows the outline of the gangue mineral in contact (Fig.4.1.2.f.). This sphalerite type could have formed by grain migration and coalescence. The grains are isotropic and have abundant internal reflections of white-yellow-pink colour. Sphalerite can also be a fracture-filling phase in chalcopyrite, although it is rare.

Bornite in chalcopyrite occurs as flames, irregular patches or with myrmekite-resembling texture. A lattice of chalcopyrite and bornite is shown in Figure 4.1.2 (e-f), a texture which largely resembles that described by Ramdohr (1969) and is called shredded texture. The latter types either form a very fine, irregular network or an intergrowth of broader laths with chalcopyrite. This texture grades into massive bornite towards the phase boundaries. In one sample, bornite was observed to form irregular patches inside chalcopyrite.

Millerite was observed only on one occasion in the present transgressive carbonatite samples. The small (~10 μm) millerite crystal occurred in chalcopyrite with abundant bornite replacement and had an uneven, porous surface, suggesting secondary-replacement origin. Previous studies described millerite as a common minor constituent of the Phalaborwa sulphide assemblage. Aldous (1980) reported millerite in association with secondary magnetite and bornite patches and flames in chalcopyrite and suggested that the millerite itself is secondary, replacing pentlandite. Hanekom et al. (1965) reported millerite laths replacing chalcopyrite. The description and interpretation of Aldous (1980) are consistent with the present observations.

Accessory phases associated with massive chalcopyrite include a Pb-telluride phase with a white colour and very strong brightness (Fig.4.1.3.b,c). The phase was identified as altaite based on the optical properties and composition. It occurs as rounded grains of <10 μm. A small (<10 μm) anhedral Ag-telluride phase was observed on one occasion; Rudashevsky et al. (2004) also observed the phase,

and analysis showed hessite composition (Ag_2Te). Native Ag was also found in chalcopyrite (Fig.4.1.3.d).

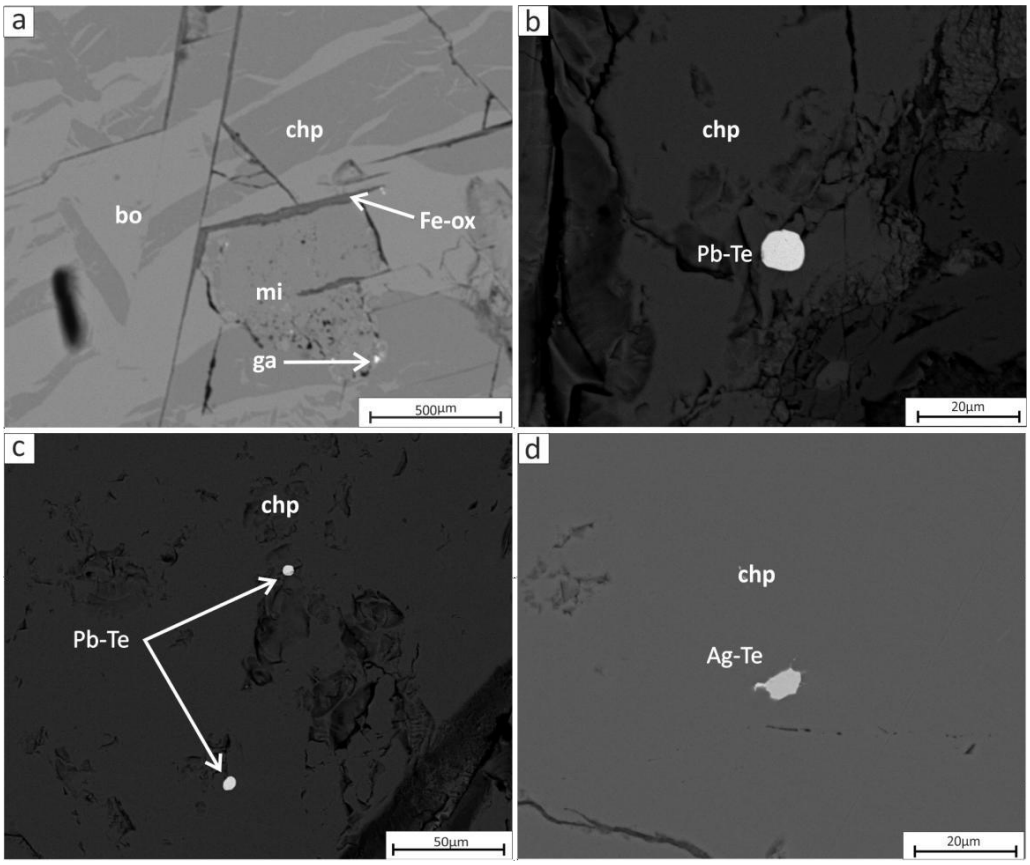

Figure 4.1.3. BSE images; a – d: Accessory phases in chalcopyrite. a: Secondary millerite with porous surface and Fe-oxide rim, inside chalcopyrite with bornite replacement; b-c: Round Pb-telluride (altaite) grains in massive chalcopyrite; d: Anhedral Ag-Te phase in chalcopyrite host. mi: millerite, bo: bornite, chp: chalcopyrite, ga: galena.

Bornite can either form intergrowths with chalcopyrite as described earlier or has an extensive-massive appearance (Fig.4.1.4). Samples with massive bornite usually do not contain a significant amount of chalcopyrite. However, it can usually occur at the edge of the massive bornite, forming spindles or flames penetrating the bornite inwards or associated with cobalt pentlandite grains (Fig.4.1.4 a-c).

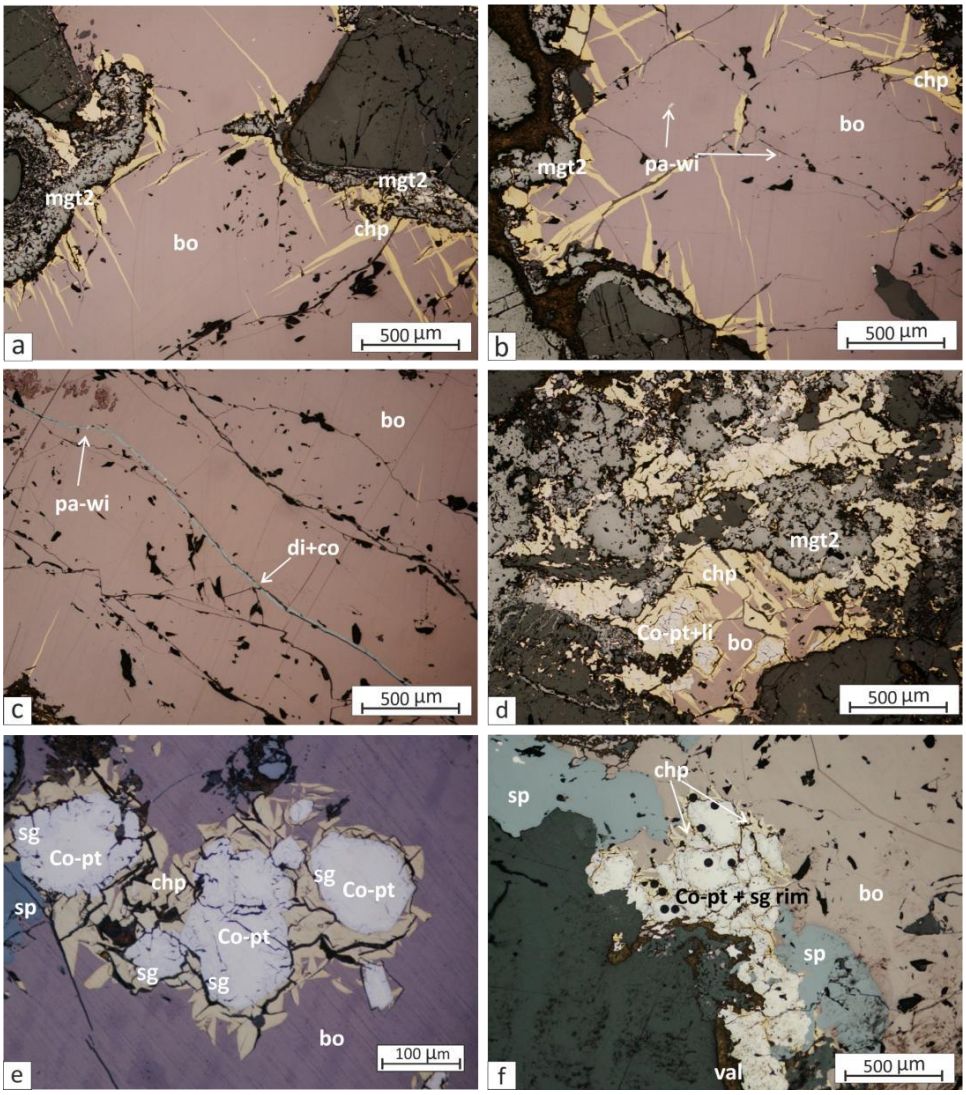

Figure 4.1.4. Reflected light photomicrographs; Massive bornite with chalcopyrite spindles at the edges (a – c). Secondary magnetite formed at the contacts of the sulphide assemblage (a – c). Cobalt pentlandite and linnaeite group minerals formed in close association with the secondary magnetite at the gangue contacts, possibly indicating an oxidation assemblage (b). The massive bornite contains Pb-Te inclusions and along the fractures digenite and covellite were formed (c – d). Anhedral, rounded cobalt pentlandite form aggregates in massive bornite. The grains have a rim of linnaeite group minerals and chalcopyrite towards the bornite (e – f). Sphalerite forms relatively large, anhedral grains at the edges of massive bornite (e); Anhedral cobalt pentlandite forms a rim around magnetite (f). Bo: bornite; chp: chalcopyrite; co: covellite*; co-pt: cobalt-rich/cobalt pentlandite; cu: cubanite; li: linnaeite group minerals; mgt: magnetite; sp: sphalerite, pa: parkerite; wi: wittichenite, di; digenite*, *: nonstoichiometric

Massive bornite is generally associated with a higher degree of alteration than in the chalcopyrite-rich samples; the mineral rims are resorbed and broken up with a higher abundance of secondary alteration products such as valleriite, haematite and silicate alteration products (Fig. 4.1.4. a-c). The valleriite in these samples can be especially well developed, showing bent and thin crystal laths with good cleavage (fig. 4.1.5. a-d). The massive bornite is usually associated with Cu-S

phases, including chalcocite, digenite and covellite (Fig.4.1.4.d; Fig.4.1.6. a-e). The digenite forms tabular lamellae with various thicknesses (Fig.4.1.5.a-e). The lamellar texture often occurs with myrmekite-resembling texture, forming intergrowths with bornite (Fig.4.1.5.a-c). In this form, the phase either has the same blue or a lighter colour, often close to white, indicating a possible compositional change towards chalcocite. Less often, myrmekite-resembling chalcocite also occurs in the bornite. Lamellar digenite can occur along fractures and often along contacts towards valleriite and non-sulphide minerals (Fig.4.1.5.d). The lamellar digenite sometimes contains thin covellite lamellae. Another form of covellite is a fine-grained mass of scale or feather-like crystals on the surface of lamellar digenite, in some cases almost wholly replacing it. (Fig.4.1.5.b). The subsequent major element analyses showed that these phases are nonstoichiometric; the stoichiometric name will be used for clarity with an additional '*'.

Cobalt pentlandite grains in massive bornite are rounded with a rim of linnaeite group minerals and surrounded by chalcopyrite spindles radiating outwards from the cobalt pentlandite grain boundaries into the bornite (Fig 4.1.7 e-g). The linnaeite rim has a heterogeneous, wrinkled surface with very fine lines cutting through it, and in some cases, it completely replaces the cobalt pentlandite. In contrast to the previously described form in the massive chalcopyrite, this type is not associated with Fe-oxides. Based on the chemical composition, the linnaeite-group mineral was identified as siegenite, although the optical properties (isotropic, grey, pale purple (violet) colour) could also suggest violarite.

Massive bornite characteristically contains large sphalerite grains, constantly occurring at the edge of the phase. This different appearance from the sphalerite of the massive chalcopyrite was also noted by Aldous (1980). The work also described bornite, chalcopyrite, bravoite and linnaeite inclusions in the large sphalerite grains, which were not observed in the present study.

Valleriite is a typical phase in transgressive carbonatite; however, it shows higher abundance when associated with massive bornite. Most commonly, it forms fine-grained or fibrous masses or sometimes more developed crystals, infills of fractures and voids in chalcopyrite and magnetite, or appears around the crystals as a rim. When well developed, the valleriite forms elongated laths with good cleavage. The valleriite has low hardness and is pleochroic with dark brown-

yellow colours and shows strong anisotropy. The association with phase contacts and cavities suggest a secondary origin of valleriite.

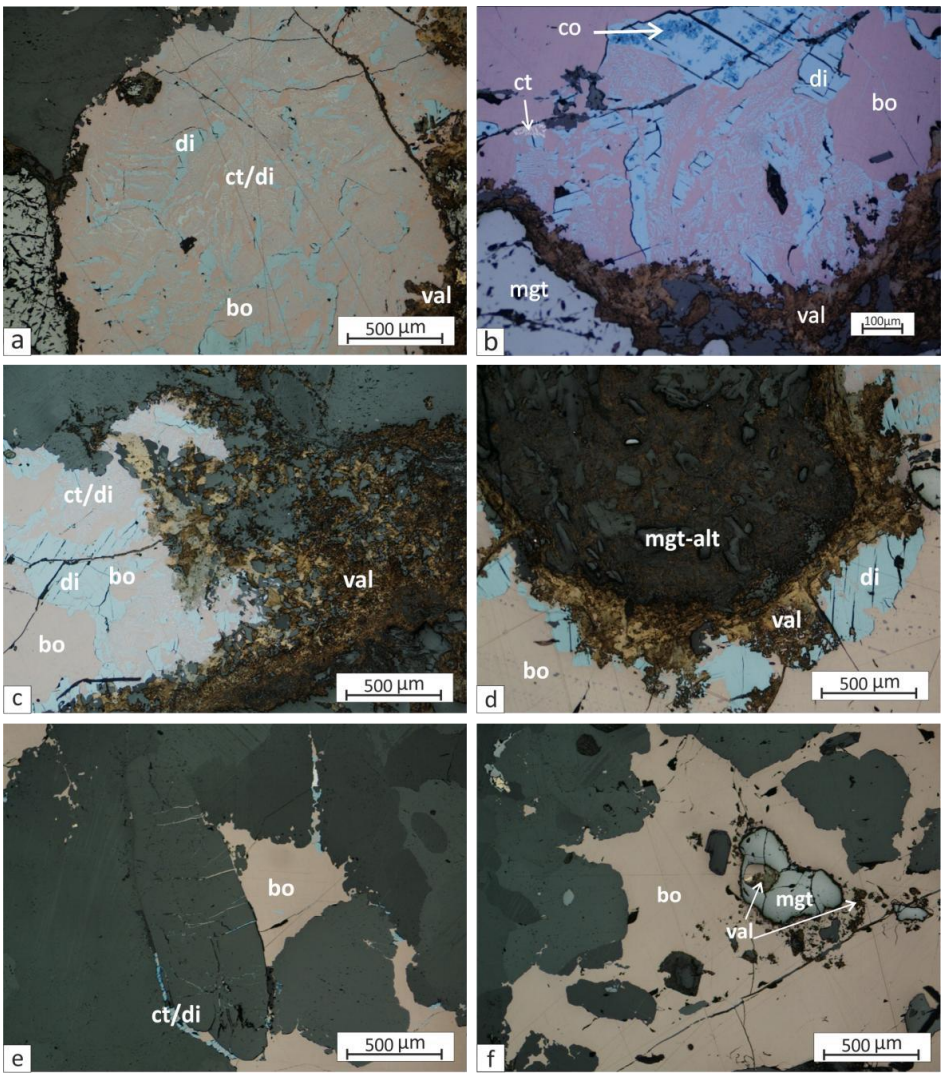

Figure 4.1.5. Reflected light photomicrographs; Massive bornite contains lamellar di (a – d) and myrmekite-resembling Cu-S* together with lighter coloured myrmekite-resembling mineral indicating a possible change of composition towards chalcocite* (a-c). White myrmekite-resembling chalcocite* occurs less often (b). Covellite often replaces lamellar digenite* and forms fine-grained, scale-like crystals (b). The Cu-S phases are very often associated with contacts, and fractures (b – e). Valleriite formed at magnetite and sulphide contact; it is variously developed and replacing the former (a –d; f). Bo: bornite; chp: chalcopyrite; co: covellite*; co-pt: cobalt-rich/cobalt pentlandite; cu: cubanite; di: digenite*; ct: chalcocite*, mgt: magnetite; mgt-alt: altered magnetite; sp: sphalerite, *: nonstoichiometric

Massive bornite is the primary host for accessory Bi-Ni phases. These form very small (<30 µm), rounded grains inside the bornite (Fig.4.1.6). The grains have sometimes developed a rim around them, where the rim has a lower reflectivity than the core. EDS spectra of the phases showed that the compositional difference between the core and the rim is the presence of Cu instead of Ni in the latter. The core–rim pair were identified as parkerite and wittichenite, respectively.

The grey colour and strong anisotropy observed in the rim phase indicate wittichenite.

In contrast, the high reflectivity, cream-white colour and strong anisotropy observed in the cores are characteristics of parkerite. Although the phase is small, it stands out due to its high reflectivity. The parkerite-wittichenite phase at Phalaborwa was first reported by Aldous (1980), and consistently, with the present study, it was described in association with massive bornite. Another accessory phase, which is associated with massive bornite, is galena. It forms small (20-50 µm) disseminated grains with sub-anhedral shape. It is the most abundant at the contact of bornite and valleriite, or non-sulphide minerals. Galena was also reported as a primary phase in chalcopyrite (e.g., Hanekom et al., 1965; Aldous, 1980).

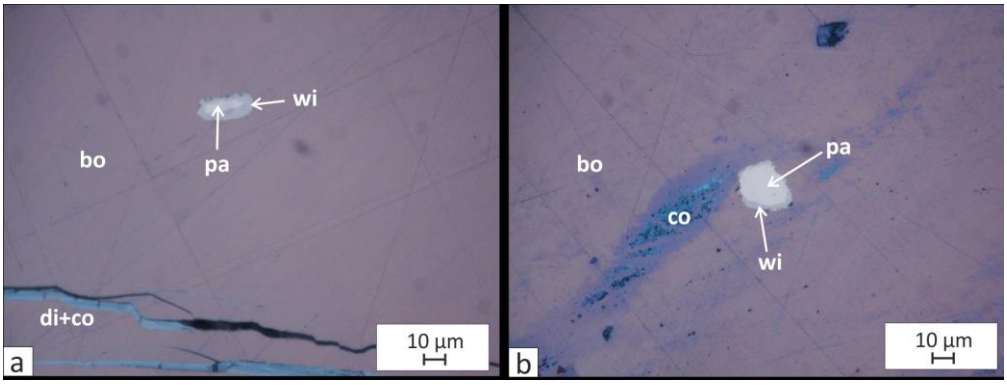

Figure 4.1.6. Reflected light photomicrographs; The massive bornite contains common accessory phases of zoned Bi-rich sulphide phase. The cream-white core of the phase is a Bi-Ni sulphide: parkerite, while the grey rim is a Bi-Cu sulphide phase: wittichenite. Bo: bornite; co: covellite*; di: digenite*; pa: parkerite; wi: wittichenite. *: nonstoichiometric.

4.1.2 Banded carbonatite

The younger banded carbonatite contains a minor amount of sulphides in the form of anhedral patches that rarely reaches 1 mm diameter (Fig.4.1.7). The sulphide patches are interstitial and closely associated with magnetite and sometimes very thin valleriite rim developed around them. The sulphide assemblage consists of chalcopyrite (70 vol %), bornite (25 vol %), digenite and covellite (5%). These phases form intergrowths in most grains, but bornite and chalcopyrite can also occur independently. Very minor sphalerite was also

observed, and also galena at altered areas. Digenite and covellite are very minor and associated with bornite, mostly occurring at the edge of bornite.

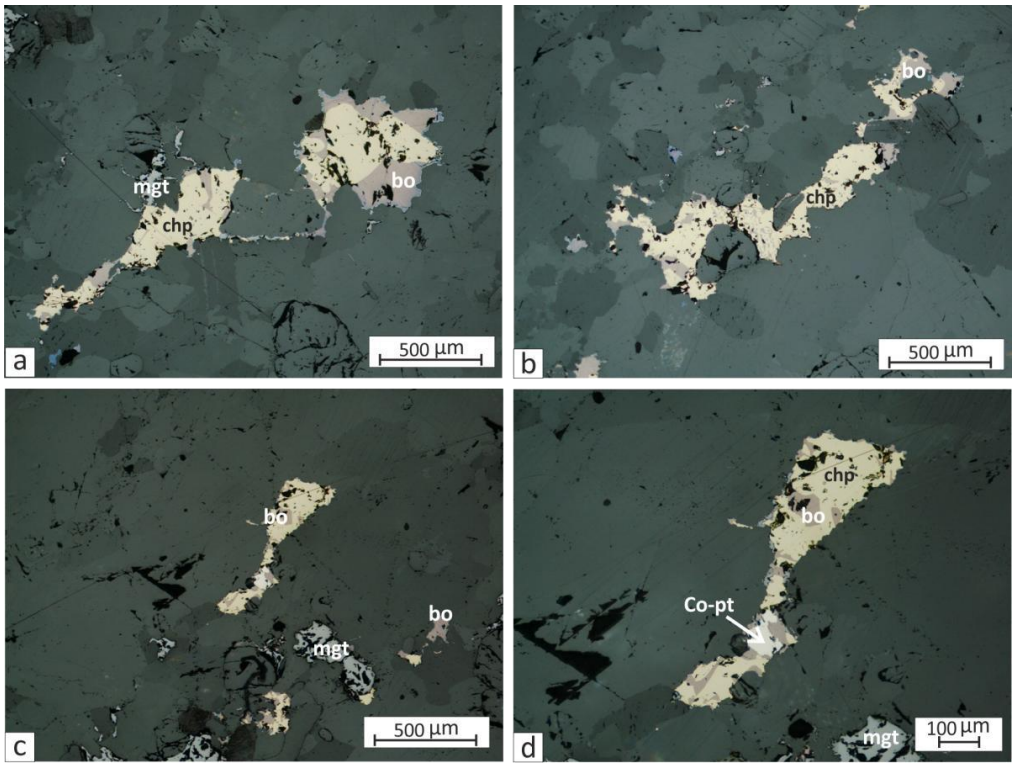

Figure 4.1.7. Reflected light photomicrographs; Disseminated, interstitial sulphide phases of bornite-chalcopyrite (a – d) with minor Co-pentlandite (d). Bo: bornite; chp: chalcopyrite; co-pt: cobalt-rich/cobalt pentlandite.

4.1.3 Disseminated sulphide grains in phoscorite and glimmerite

Phoscorite and olivine-glimmerite contain disseminated sulphide phases, mainly bornite and chalcopyrite. The appearance of the sulphides is similar only in the glimmerite, but the grains are sometimes more resorbed. The ratio of the two minerals varies from sample to sample and grain to grain. The sulphide grains can composed entirely of bornite or chalcopyrite or show the intergrowth of the two phases (Fig.4.1.8.a-f). The sulphide grains occur interstitially between the magnetite, olivine, phlogopite crystals, and occasional carbonates. The sulphide grains are strongly resorbed with irregular edges and often with magnetite rims (a feature which sets them apart from the disseminated sulphides of the banded carbonatite). The size of individual sulphide grains is generally below 1 mm. The

grains show complex chalcopyrite-bornite intergrowth textures with flames, lamellae, patches and shredded textures of both phases. Minor myrmekite-resembling chalcocite* and digenite-covellite* patches were also observed in bornite, where it occurs as a relatively extensive phase (Fig.4.1.8.c). Sub-anhedral cobalt pentlandite (<50 μm) is a minor but common constituent (Fig.4.1.8.d). Valleriite occurs in contact with non-sulphide minerals (Fig.4.1.8.c-d). The grains are more resorbed in contact with serpentine (Figure 4.1.8. f).

Table 4.1.1 shows summary of the textural and mineralogical observations.

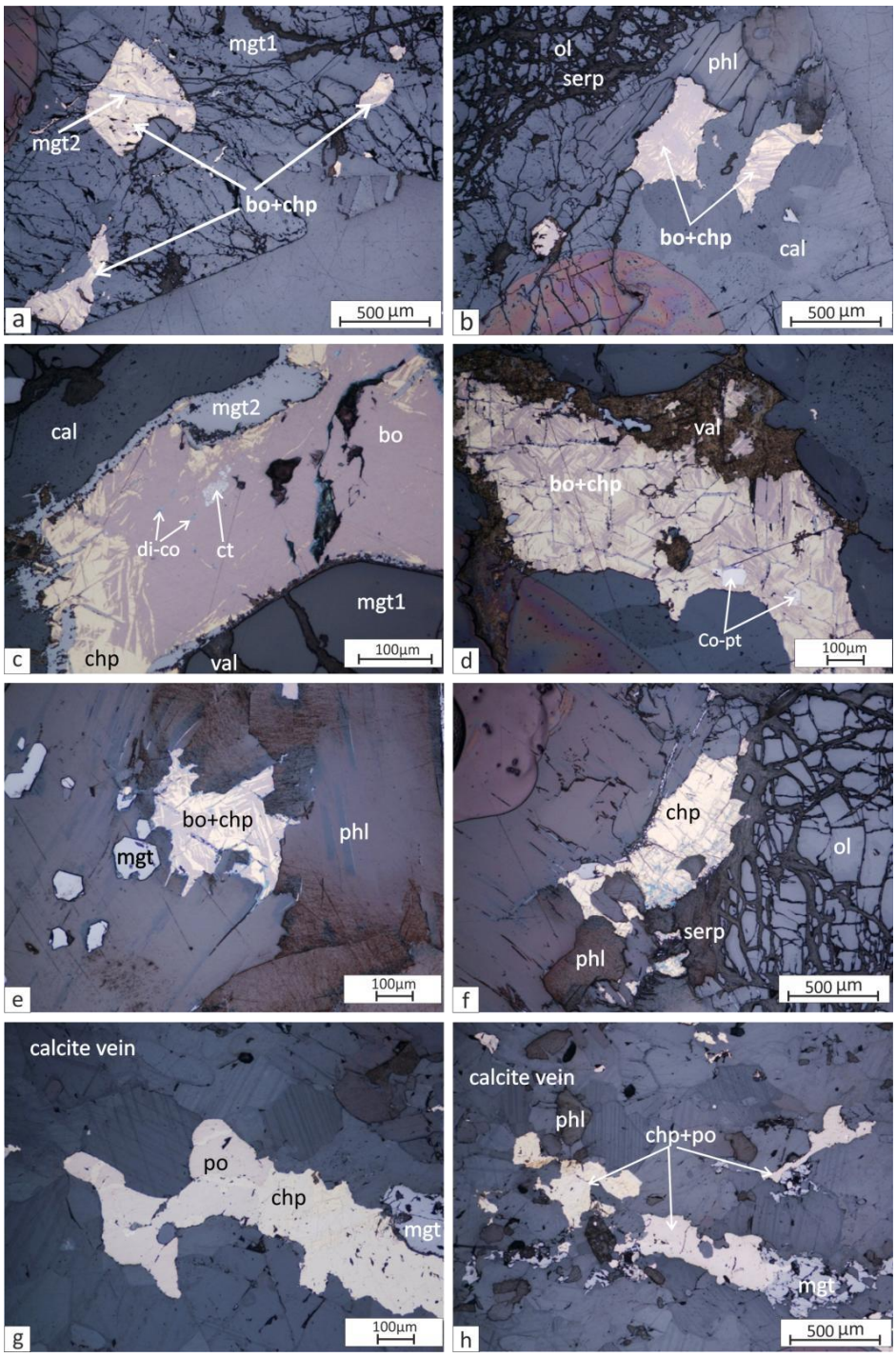

Figure 4.1.8. Reflected light photomicrographs; The main sulphide phases are chalcopyrite and bornite forming disseminated, resorbed, interstitial grains with complex texture in phoscorite (a – f). The sulphide grains are commonly associated with secondary magnetite (a; c). Where bornite is relatively extensive, it hosts myrmekite-resembling chalcocite* and digenite*+covellite* (c). Sub-anhedral Co-pentlandite is common (d). Valleriite is common and can be extensive at contacts (d). The sulphide phases of the calcite vein crosscutting glimmerite and phoscorite are less/unaltered and associated with coeval magnetite (g; h). The main phases are chalcopyrite and troilite, the latter forming rounded grains inside the former (g). Bo: bornite; cal: calcite; chp: chalcopyrite; co: covellite; co-pt: cobalt-rich/cobalt pentlandite; ct: chalcocite*; di: digenite*; mgt: magnetite; ol: olivine; phl: phlogopite; to: troilite; serp: serpentinite; val: valleriite. *nonstoichiometric

Table 4.1.1. Summary table of the observed sulphide textures in the different type of transgressive carbonatite samples, banded carbonatite, phoscorite and silicate rocks.

Type I.: Massive or stockwork sulphides of the economic transgressive carbonatite				
Type I/a.: Chalcopyrite-rich transgressive carbonatite samples				
General description: Samples with a sulphide assemblage composed primarily of chalcopyrite with massive, patchy or stockwork appearance. Cubanite, troilite and cobalt pentlandite and sphalerite are common constituents. Relative abundance (vol %) of chalcopyrite, cubanite and troilite varies from sample to sample with the general sequence: chalcopyrite > cubanite ≥ troilite > cobalt pentlandite > sphalerite where cobalt pentlandite and sphalerite are minor constituents (<10 vol %).				**Samples in the category**: Pa15; Pax, Pa23, Pa2, Pa2.4, Po5-U2, GC808, PTC1—4,
Primary sulphides	**Texture characteristics**	**Secondary sulphides and non-sulphides**	**Texture**	**Accessories (associated with sulphides)**
Chalcopyrite (60-80 vol %)	Massive, patches, stockwork	Bornite (≤5 vol %)	Irregular patches, myrmekite-resembling intergrowth, flames	Alltaite
Cubanite (≤30 vol %)	Lamellae or extensive rounded grains	Millerite	Subhedral with porous surface	Ag-telluride
Troilite (≤ 5 vol %)	Flames or stringers with elongated wedge-like shape and ragged edges	Valleriite (≤10 vol %)		Native-Bi
Cobalt pentlandite (≤7 vol %)	Subhedral grains	Magnetite, haematite		Native Ag
Sphalerite (<1 vol %)	Small rounded, anhedral grains, sphalerite stars			

Type I/b.: Chalcopyrite and troilite-rich transgressive carbonatite sample		**Type I/c.: Massive chalcopyrite with bornite replacement (transgressive carbonatite sample)**			
General description: The most abundant sulphide phase is chalcopyrite which is strongly fractured and contains extensive (>1 mm) trolite patches. Cubanite lamellae are also significant constituent. Sub-anhedral cobalt pentlandite occurs at troilite-chalcopyrite contact. Sphalerite forms small anhedral grains.		**General description:** The samples display shredded texture showing the massive chalcopyrite being replaced by bornite along crystal planes, resulting in a very characteristic net-like appearance. The ratio of chalcopyrite and bornite changes as the replacement progressing and can grade into massive bornite. The sample otherwise have the same characteristics as the chalcopyrite-rich samples without replacement.			
Samples: GC1610		**Samples:** GC1611, GC815A			
Mineralogy: Primary sulphides	**Texture characteristics**	**Primary sulphides**	**Texture characteristics**	**Secondary sulphides and non-sulphides**	**Texture**
Troilite (30 vol %).	Extensive rounded grains	Chalcopyrite (~50–60 vol %)	Massive with extensive bornite replacement	Bornite (~40–50 vol %)	Shredded texture: replacing chalcopyrite
Chalcopyrite (50 vol %)	Massive, strongly fractured	Sphalerite (< 1 vol %)	Small anhedral grains		

Table 4.1.1. Continuation.

Cubanite (~10 vol %).	Lamellae in chalcopyrite	Cobalt pentlandite (<1 vol %)	Small sub-anhedral grains		
Cobalt pentlandite (7 vol %)	Subhedral grains				
Sphalerite (~3 vol %)	Small anhedral grains				

Type I/d.: Bornite-rich transgressive carbonatite samples					
General description: The main sulphide phase in these samples is bornite with massive appearance or forming smaller patches. The samples show a more progressed alteration than the chalcopyrite-dominated samples which manifests in the more resorbed and broken-up sulphide edges, abundant valleriite and more resorbed magnetite crystals. Later stage and secondary sulphide phases and large-grained sphalerite are characteristic to the sample type.					Samples: Po5-u1, PTZ 1- 2, GC815, GC1811A,
Primary sulphides	**Texture characteristics**	**Secondary sulphides and non-sulphides**	**Texture**	**Accessories (associated with sulphides) Samples in the category**	
Cobalt pentlandite	Resorbed, rounded grains with siegenite rim around them	Bornite	Massive	Covellite*: Observed on digenite* lamellae, forming streaks or feather and scale-like crystals.	
Sphalerite	Anhedral grains, mostly at the edge of the massive bornite	Siegenite	Rim around cobalt pentlandite grains	Parkerite with wittichenite rim	
		Chalcopyrite	Wedges around siegenite rim and bornite, and at bornite-gangue contact	Galena: at resorbed bornite-gangue contact areas; Fine, disseminated grains	
		Digenite*; chalcocite*	Lamellar and myrmekite-resembling texture in massive bornite, can follow fractures		
		Valleriite	Anhedral mass at sulphide-non sulphide contacts and in fractures, can show well developed crystal laths.		
		Magnetite	Anhedral crystal aggregates at sulphide-gangue contacts		
		Dolomite	At sulphide-gangue and magnetite contact: mosaic texture; Myrmekite-resembling intergrowth with calcite		

Table 4.1.1. Continuation.

Type II.: Samples with disseminated sulphide grains in carbonatites, phoscorites and olivine-glimmerite				
Type II/a.: Disseminated sulphide grains in younger banded carbonatite				
General description: The elongated anhedral sulphide grains (≤700 μm) are composed mainly of chalcopyrite and bornite are primary interstitial phases in the carbonatite rock. The sulphides together with the more abundant magnetite form the characteristic banding of the rock.				**Samples in the category:** Pa6, Pa6.2,
Primary sulphides	**Texture characteristics**	**Secondary/exsolved sulphides and non-sulphides**	**Texture**	**Accessories (associated with sulphides)**
Chalcopyrite (70 vol %)	Intergrowth of the two phases	Bornite (25 vol %)		Sphalerite (<1 vol %)
+/- Bornite		Digenite* and covellite (2 vol %)	Occurs at the edge of bornite	Galena (<1 vol %)
Cobalt pentlandite (~1 vol %)	Subhedral grain	Valleriite (1 vol %)	Forms thin rims around sulphide grains	
Type II/b.: Disseminated sulphide grains in phoscorite and olivine glimmerite				
General description: anhedral interstitial sulphide grain s (<1mm), characterised by complex intergrowth of chalcopyrite and bornite. Myrmekite-resembling digenite-chalcocite* and digenite-covellite* patches also occur. The grains are often resorbed when in contact with valleriite and serpentine. Magnetite rim can develop around them, but it is not very common.				**Anhedral grains Samples in the category:** Pal16, GC813/5, GC817, Samples: Po5-03
Primary sulphides	Texture characteristics	Secondary/exsolved sulphides and non-sulphides	Texture	Accessories (associated with sulphides)
Chalcopyrite-borite	Intergrowth, bornite flames, lamellae in chalcopyrite	Chalcocite-digenite	Myrmekite-resembling intergrowth	
		Digenite-covellite*	Patches in bornite	
Cobalt pentlandite	(<50 μm) rounded grains in chalcopyrite-bornite	Valleriite	Replacing sulphides and non-sulphides	
		Magnetite	Rim around sulphide grains	
Type II/c.: Disseminated sulphide grains in carbonate vein crosscutting glimmerite				
General description: Elongated anhedral sulphide grains, composed mainly of chalcopyrite and trolite. The sulphides are interstitial to the non- sulphide phases.				Samples: Po5-02
Primary sulphides	**Texture characteristics**	**Secondary/exsolved sulphides and non-sulphides**	**Texture**	
Chalcopyrite (~60 vol %) Troilite (~40 vol %)	The interstitial sulphide grains are composed of the Intergrowth of the two phases.	Magnetite	Anhedral, often elongated grains at sulphide-gangue contacts	
Type II/d.: Disseminated sulphide grains in silicate rocks				

Table 4.1.1. Continuation**.**

General description: The sulphide grains display complex intergrowth of bornite, chalcopyrite and chalcocite and also contain small grains of cobalt pentlandite. Secondary magnetite is commonly associated with the sulphide grains, often forming rims around them. The grains are often resorbed, with valleriite rims. They occur interstitial between large magnetite and slightly serpentinised silicate (phlogopite and olivine) crystals.				**Samples in the category:** Po5-03
Primary sulphides		**Texture characteristics**	**Secondary sulphides and non-sulphides**	**Texture**
-		Interstitial between non-sulphide phenocrysts, strongly resorbed and replaced by later stage sulphides	Chalcopyrite-Bornite	Bornite replaces chalcopyrite, can form flames, patches and shredded texture which grades into optically pure bornite
	Cobalt pentlandite	Small (≤ 50 μm) sub-anhedral grains inside chalcopyrite	Digenite-covellite*, chalcocite*	Patches or myrmekite-resembling intergrowth inside bornite
			Valleriite	Forms rims around sulphide grains at contact areas
			Magnetite	Anhedral, forms rims around sulphide grains at contact areas

*: nonstoichiometric

4.2 Interpretation of the macro and microtextures of the sulphide assemblage

4.2.1 Formation processes and definitions of sulphide microtextures

The mineralogical and textural study found numerous sulphide phases in a complex relationship with each other or non-sulphide phases, often displaying different textures and degrees of later-stage alteration. Many of these characteristics are linked to lithologies or sample types (in the case of the transgressive carbonatite). Exsolution and replacement textures of the sulphide mineralisation in the transgressive carbonatite and the disseminated sulphides of the other lithologies suggest that the sulphides formed by multiple-stage processes and a range of temperatures, including later-stage fluids. However, pinpointing the classification of these texture types is sometimes challenging due to their ambiguity. Phases in solid solution may form typical exsolution intergrowth textures. At the same these textures can look similar to each other but they formed by different processes which can cause difficulties when establishing the paragenetic sequence. A straightforward exsolution sequence in a Cu-Fe-S system, with progressively decreasing Cu, can be reversed by the effect of Cu-rich fluids (e.g., Ramdohr, 1969). The ambiguous interpretation of the sulphide textures was discussed by several earlier works (Ramdohr, 1969), which cautions against drawing definite conclusions regarding sulphide paragenesis based solely on textural features. Numerous factors, including temperature, pressure, composition, purity, the grain size of the solid solution, the coefficient of diffusion, the stress distribution within the crystal and crystallographic orientations, control a phase's exsolution. The number of variables and their interdependence makes it extremely difficult to predict texture, and it is potentially impossible to treat them in a "quantitative manner" (Ramdohr, 1969). Although the textures that form during exsolution and replacement processes can look identical, they are fundamentally different regarding genetics and formation mechanism. These processes are defined in Ramdohr (1969) and presented in the following paragraphs.

Exsolution textures form when a homogenous solid solution becomes unstable due to changing physio-chemical conditions and separates into different phases. Exsolution textures can be formed when supersaturation is reached or freeze as

non-equilibrium mixtures (Ramdohr, 1969). In simple exsolution, the chemical composition and ratio of the end-products reflect the composition of the parent solid solution which they formed from, while complex exsolution causes stoichiometric changes, and the composition of the original solid solution cannot be reconstructed straightforwardly. This process is common in the case of anomalous solid solutions, where the high-temperature parent crystal does not have perfect stoichiometry. Ramdohr (1969) lists chalcopyrite-troilite solid solution in this category. Exsolution bodies separated at high temperatures are often solid solutions or complex nonstoichiometric phases. With decreasing temperature, they can exsolve into new phases by sub-exsolution and exsolution in multiple stages. Sub-exsolution processes result in the formation of mixed phases (Ramdohr, 1969). Another type of complex exsolutions occurs when, during the exsolution of a mineral, a second exsolution takes place simultaneously, forming another phase. Ramdohr (1969) suggests this formation process for chalcopyrite and wittichenite exsolution in bornite. Several factors, including slow cooling, anomalous mixture composition, inclusions and tectonic stress, promote the exsolution process. At the same time, the shape of the resulting phases is primarily determined by the crystal structure of the original crystal (Ramdohr, 1969).

Exsolution-like texture can also be formed during material addition or removal in systems where element mobility is high. However, Ramdohr (1969) notes that the textures formed during these processes are not true exsolutions (despite their close resemblance). In this category of processes, Ramdohr (1969) lists decomposition and re-mineralisation. The most relevant example is the decomposition of bornite, resulting in the formation of chalcopyrite and chalcocite. There can be a continuous transition between simple exsolutions, complex exsolutions, decomposition and complete re-mineralisation processes Ramdohr (1969).

Ramdohr (1969) describes replacement textures as highly variable. The classification of the replacement textures is somewhat arbitrary as transitions can always occur between the different types, and each structure can form via processes other than replacement. Thus, replacement and exsolution textures can be very similar in appearance, which makes interpretation difficult. In the case of lamellar texture, it helps to differentiate that replacement causes material

extension at the lamellae joints. In contrast, exsolution causes shortness in the material at the lamellae joints, and the lamellae pinch out at the intersections. However, Ramdohr (1969) notes that this was hardly ever observed in the case of lamellar chalcocite, a highly relevant texture in the Phalaborwa samples. As Ramdohr (1969) explains, reaction rims genetically belong to the replacements. Certain minerals which are stable at high temperatures may react with each other at a lower temperature or may be catalysed by an exchange reaction with residual solutions (particularly if these late solutions are no longer in equilibrium with the minerals). The rims often have two or more phases (Ramdohr, 1969)).

4.2.2 Exsolution phases in massive chalcopyrite

Chalcopyrite is the most abundant sulphide phase in Phalaborwa, and it hosts several other sulphide minerals. At higher temperatures (>250 ^{o}C), the chalcopyrite structure can accommodate excess FeS, ZnS, NiS, and CoS, but with cooling, these can form exsolution phases (Ramdohr, 1969). The most abundant phase hosted by chalcopyrite is cubanite. As Ramdohr (1969) describes, the hexagonal lamellar cubanite forms a four-dimensional octahedral net in the cubic chalcopyrite. Cubanite lamellae of various thicknesses were observed in the massive chalcopyrite samples, and according to Ramdohr (1969), chalcopyrite can exsolve cubanite at both high and low temperatures, with finer lamellae indicating low temperatures. Both fine (<10 µm) and board (~500 µm) cubanite lamellae were observed in transgressive carbonatite samples with the massive chalcopyrite. Therefore, this textural feature is not diagnostic and could indicate either boarding of the initially thin lamellae or cooling.

Another characteristic phase observed inside the chalcopyrite is myrmekite-resembling sphalerite, sometimes called skeletal sphalerite. Ramdohr (1969) described skeletal sphalerite crystals that looked ragged and similar to the myrmekite-resembling texture, interpreting these as exsolution products of the chalcopyrite. The description was similar to the myrmekite-resembling sphalerite found in the samples from this study. Sphalerite stars with similar formation processes were observed in massive chalcopyrite and lamellar cubanite – thus, this study interprets these as having exsolved from the chalcopyrite in Phalaborwa. According to Ramdohr (1969), the features described above

(cubanite lamellae, sphalerite exsolution stars) are characteristic of high-temperature chalcopyrite (min. 250 ^{o}C).

Three forms of the troilite were observed in the transgressive carbonatite: flames or feathers along fractures, elongated, irregular stringers or extensive large anhedral grains, all in massive chalcopyrite. Ramdohr (1969) suggests that $Fe_{1-0.8}S$ can form as the decomposition of cubanite lamellae. In the troilite-rich sample, the cubanite lamellae terminate at the troilite–chalcopyrite contact. Troilite exsolution probably follows the cubanite and sphalerite.

In summary, Phalaborwa massive chalcopyrite contains cubanite lamellae and skeletal sphalerite; both phases may indicate exsolution from high-temperature chalcopyrite, troilite postdates cubanite and sphalerite exsolution.

4.2.3 The relationship of chalcopyrite and bornite in the transgressive carbonatite

The relationship between chalcopyrite and bornite across the sample set is much less straightforward; there are numerous textures the two phases form together that can be interpreted as exsolution, decomposition, eutectic intergrowths or replacement processes. Additionally, with temperature and pH changes, the mineral sequence can reverse. In the case of exsolution, the order would be bornite exsolving chalcopyrite. The presence of later-stage bornite indicates additional Cu-enrichment in the system. In this case, Cu-rich fluids would interact with the sulphide assemblage, causing bornite formation that replaces the chalcopyrite. In the present sample set, the observed bornite-chalcopyrite textures are irregular bornite patches inside chalcopyrite, a network-like intergrowth (shredded texture) and massive bornite with chalcopyrite flames or spindles at the edges. The shredded texture is formed during replacement (Ramdohr, 1981), which implies that either bornite is replaced by chalcopyrite or the opposite. Hanekom et al. (1965) also observed crystallographic intergrowth texture between chalcopyrite and bornite, interpreting it as the result of unmixing. In the Phalaborwa samples from this study, it is more likely that the bornite is replacing the massive chalcopyrite, especially considering the more altered nature of the bornite-rich samples.

The interaction of chalcopyrite with hot Cu-bearing solutions can result in its replacement by bornite and chalcocite, while magnetite and haematite also form

during the process (Ramdohr, 1969). During supergene enrichment processes, Cu-rich solutions react with primary sulphides and create secondary phases richer in copper than the original minerals. Ramdohr (1969) states that the enrichment sequence is chalcopyrite → bornite → covellite → chalcocite. This sequence corresponds well with the phase relationships and textures observed in the bornite-rich transgressive carbonatite samples. Such fluids would also explain the generally altered nature of the massive bornite-containing samples, in contrast to unaltered chalcopyrite-rich samples. Ramdohr (1969) states that this reverse Cu-enrichment trend and replacement process occurs primarily in ascendant ore deposits. Apart from the shredded texture, another crystallographic texture, the Widmanstätten intergrowth of bornite and chalcopyrite was observed by Aldous (1980) and Rudashevsky et al. (2004) in Loolekop sulphides. The origin of the variable texture was demonstrated by the experimental study of Amcoff (1988), who showed that under reducing conditions, the direct replacement of chalcopyrite by bornite is controlled by the mineral structure can result in the formation of “exsolution textures” referred to as replacement-exsolution textures. In the case of bornite and chalcopyrite, the replacement exsolution textures manifested in the form of crystallographically oriented bornite plates in the chalcopyrite host (Amcoff, 1988). Durazo and Taylor (1982) suggested that Widmanstätten texture forms by rapid cooling below 475 ^{o}C. The authors also suggested that the version of this texture with broad chalcopyrite lamellae indicates exposure to high temperatures below the solidus, where nucleation and growth were promoted. Durazzo and Taylor (1982) emphasised that Widmanstätten texture can also form via replacement, and Zhao et al. (2014) have demonstrated this experimentally (revealing a sharp reaction front develops between chalcopyrite and bornite). This reaction is initially fast at the surface of the chalcopyrite, slowing as it progresses towards the core and with preferential replacement along twin planes in chalcopyrite. Zhao et al. (2014) demonstrated that bornite immediately precipitates as the chalcopyrite dissolves and is an interface-coupled dissolution-precipitation reaction.

Chalcopyrite flames and spindles occur at the rim of the massive bornite, penetrating inwards. According to Ramdohr (1969), the chalcopyrite exsolution in bornite forms thin lamellae, thicker spindle or lensoid shapes. They can result from spontaneous unmixing or mechanically induced in the early stages of weathering (Ramdohr, 1969). Chalcopyrite flames in bornite are thick, spindle-

shaped, warped grains that penetrate from the edge of the host towards the centre and are formed by the disintegration of bornite along fractures, grain boundaries, inclusions, fissures or zones of latent stress (Ramdohr, 1969). This description fits well with the chalcopyrite wedges found at the edge of the massive bornite and probably represents late-stage chalcopyrite formed from the weathering of the bornite.

Loolekop samples from this study demonstrate that bornite is a replacing phase. Every sample that contains massive bornite shows a higher level of alteration than the chalcopyrite-rich samples. In the massive bornite samples, the cobalt pentlandite grains have a violarite rim around them, sometimes being entirely consumed by it, and the occurrence of wittichenite-rimmed parkerite, specifically in the massive bornite suggests the involvement of secondary processes as well. Valleriite is always more abundant and more developed in association with massive bornite. These characteristics more readily suggest the replacement of chalcopyrite by bornite during a later stage event than the bornite being a primary phase.

In summary, the chalcopyrite-bornite textural relationships, accompanied by the progressive alteration of magnetite and gangue minerals and more extensive valleriite formation in bornite-rich samples, indicate that the bornite replaced the primary chalcopyrite. The replacement resulted from chalcopyrite interaction with Cu-rich fluids, which caused the formation of secondary, more Cu-enriched sulphide phases. Chalcopyrite flames and spindles in massive bornite represent secondary chalcopyrite formed by the decomposition of bornite along fractures and grain boundaries.

4.2.4 Relationship between the bornite and Cu-S phases

The various Cu_2S - $Cu_{2-x}S$ phases within the massive bornite display mostly lamellar and myrmekite-resembling textures. Based on optical properties, the lamellae were identified as digenite* while the myrmekite-resembling texture as chalcocite*. Latter chemical analysis (Chapter 5) showed that the phases are nonstoichiometric. Russel et al. (1954) showed via XRD studies that the latter texture is formed by hexagonal chalcocite (Aldous, 1980). Djurleite and anilite were also reported (Aldous, 1980; Rudashevsky et al., 2004). Ramdohr (1969)

stated that the myrmekite-resembling intergrowths can grade into lamellar intergrowth, but rounded terminations remain. In the Loolekop samples, the myrmekite-resembling textures were often closely associated with lamellar digenite*. The composition of the $Cu_{2-x}S$ phases can be diverse based on the formation temperature, which determines the phases' crystal structure, as presented, for example, in Fleet (2006). At 500 ºC, cubic high-digenite has the composition of Cu2S and is entirely identical with cubic chalcocite, while digenite ($Cu_{1.8}S$) exists only below 436 ºC, with hexagonal crystal structure (e.g., Will et al., 2002). Myrmekite-resembling intergrowths of chalcocite and bornite are very frequent. Although they can form in several ways including hydrothermal or collection crystallisation (grain enlargement over time due to PT-change or interaction with fluids or after exsolution and replacement). Ramdohr (1969) considered eutectic formation as the most common origin. He also suggests that this texture can form during simultaneous precipitation from mainly aqueous solutions at low temperatures. Rearrangement of exsolved chalcocite is also important. Ramdohr (1969) described that bornite myrmekite-resembling intergrowths can easily undergo collection crystallisation, destroying the previous lamellar texture. Amcoff and Nysten (1990) suggested that myrmekite-resembling chalcocite* in bornite host changing into unaffected, optically clean bornite is indicative of replacement origin. This latter feature was also observed in the Loolekop massive bornites.

Ramdohr (1969) noted that it is inevitable that in a pure Cu_2S-Cu_5FeS_4 system, no real eutectic occurs as the components are miscible even at a relatively low temperature that is far below the melting point. Several different hypogene or supergene processes can form the same texture. The replacement relationship between bornite and chalcocite can also occur during both hypogene and supergene processes. The differentiation between hypogene and supergene chalcocite is essential in order to establish the genetic relationships of the sulphide phases; however, the similarities in their appearances make this exercise difficult, if not impossible. Bornite can be replaced by hypogene digenite and lamellar or hypogene hexagonal chalcocite. The replacement occurs along specific crystallographic orientations, and usually, the new chalcocite penetrates bornite along {100} and less often {111}. The supergene replacement of bornite and chalcopyrite by chalcocite can result in textures resembling lamellar chalcocite. During this process, both hexagonal chalcocite and digenite can be

formed (Ramdohr, 1969). Myrmekite-resembling or graphic textures can occur as exsolutions, especially where the crystal structures of the components are very similar (it should be noted that different cut directions can provide different textural appearances). There are numerous transitions, and lamellar texture can form very similar textures due to collection crystallisation (Ramdohr, 1969). Therefore, the Cu-S phases of the massive bornite may represent both exsolution and replacement.

Covellite* was observed as small, scale-shaped crystals on digenite lamellae, a form which is common in the case of chalcocite lamellae. Chalcocite alteration can have multiple complex stages, and chalcocite that forms covellite with higher S content is an example of this (Ramdohr, 1969). Another form of covellite (also observed by Hanekom et al., 1965 and Aldous, 1980) is a fine-grained mass of scale or feather-like crystals on the surface of lamellar digenite, sometimes almost wholly replacing it. (Fig.4.1.5.b). Besides the secondary forms, Aldous (1980) also reports covellite as a rare, teardrop-shaped inclusion in chalcopyrite with primary origin. This form was not observed in the present sample set. Goh et al. (2006) showed that the oxidation products of chalcopyrite and bornite were primarily Fe-sulphides while Cu_2S oxidiation produced CuO (tenorite) which was not observed in the samples. These findings indicate that the covellite is not an oxidation product but perhaps replacement during sulfidation.

In summary, the lamellar digenite* and myrmekite-resembling chalcocite* in the massive bornite could represent both exsolution or replacement and both origins can occur. Covellite* is the product of digenite* alteration possibly by high H_2S fluids.

4.2.5 Parkerite-wittichenite in massive bornite

The abundance of parkerite is one of the characteristic features of the massive bornite. Several very small, anhedral-rounded parkerite grains were observed in the bornite host, without exception, accompanied by a wittichenite reaction rim. The wittichenite-rim formation indicates a progressive reaction during which the rim protected the parkerite core from complete alteration. The parkerite-wittichenite phase at Phalaborwa was first reported by Aldous (1980), and consistently with the present study, it was described in association with massive

bornite. Aldous (1980) suggested that the phase formed by replacing early Ni-Bi phases with bornite. It was shown by Amcoff and Nysten (1990) that Bi-rich sulphides react slower to alteration than Cu-Fe sulphide phases, allowing the development of the reaction rim around the former and protecting it from further alteration. Amcoff and Nysten (1990) investigated the wittichenite rim formation around native bismuth hosted in bornite and chalcocite. The samples were derived from the skarn (dolomitic) hosted Långban Fe-Mn oxide deposit (Sweden) with minor sulphide mineralisation. The authors suggested that the wittichenite rim formed due to component exchange between the ore minerals and an oxidising fluid during the supergene alteration of the copper ore. Ivaschenko (2021) reported parkerite and wittichenite from skarn ores of the Pitkäranta Mining District (Ladoga Karelia, Russia). The work described parkerite as a rare mineral that usually occurred in sulphide-nickel ores and formed intergrowths with native Ag, galena, and acanthite. The occurrence is rather different from Phalaborwa, but the established paragenetic sequence placed parkerite earlier than wittichenite. In contrast, wittichenite was very common and associated with several non-sulphide (fluorite, serpentine, magnetite) and sulphide minerals (chalcopyrite, bornite, sphalerite, löllingite). As mentioned before, the texture of the bornite-rich Loolekop samples highly suggests the operation of supergene processes, which is consistent with the model of Amcoff and Nysten (1990) regarding the wittichenite formation. Another similarity is that the wittichenite formed in the most Cu-rich milieu in both cases. However, there is an apparent difference between the two cases, as is the case in the Loolekop samples; the wittichenite was formed around parkerite and not native bismuth (as was observed in the Långban bornite). It was shown that wittichenite could form by unmixing in primary magmatic Cu-Fe-Bi-S and Cu-Bi-S systems (e.g., Sugaki et al., 1981) and was observed as such in natural ores (Ramdohr, 1969). It can also be a secondary phase, as suggested in the case of Långban. The Loolekop wittichenite also appears to be of secondary origin.

In the transgressive carbonatite, the parkerite is associated with the massive bornite; it was not observed in chalcopyrite samples. The observations are consistent with Rudashevsky et al. (2004), who also observed parkerite with wittichenite rim around parkerite and native bismuth, both in association with bornite. This would suggest a later stage enrichment or remobilisation of Bi and Ni, which formed parkerite in the replacing bornite phase, where the source of

the Ni could be pentlandite or cobalt pentlandite. The source of Bi could be native Bi, which was observed in both this and earlier works as an accessory phase in massive chalcopyrite.

In summary, parkerite characteristically occurs in massive bornite and is formed via the remobilisation of Ni and Bi from primary sulphides. The wittichenite rim developed in response to supergene alteration by an oxidising fluid.

4.2.6 Cobalt pentlandite in massive chalcopyrite and bornite

Cobalt pentlandite was observed mainly in two forms: euhedral to subhedral grains in massive chalcopyrite or as rounded grain aggregates with reaction rims around them in massive bornite. Additionally, it was found as subhedral to anhedral grains in disseminated sulphides and as flames along fractures in massive chalcopyrite.

Cobalt pentlandite and pentlandite are isostructural and form a complete solid solution (e.g., Petruk et al., 1969; Kitakaze and Sugaki, 2004). Riley (1977) recognised two different trends of Co substitution in pentlandite, where it replaces either Fe or Ni.

Ramdohr (1969) suggested a correlation between cobalt pentlandite crystal shape and its formation order with troilite. The work described that when the two phases are coeval, or the cobalt pentlandite is slightly earlier, it forms rounded grains with the indications of octahedral forms. This description fits the cobalt pentlandite grains observed in this study near large troilite grains. It might suggest that the two phases were formed simultaneously or that the cobalt pentlandite preceded the troilite. In contrast, Ramdohr (1969) suggests that cobalt pentlandite forms later than troilite, forming xenomorphic shapes. Although a couple of anhedral crystals were observed in the carbonatites, the previously described forms are more characteristic. Merkle and Gruenewalt (1986) discussed that although pentlandite often appears as flame-like exsolution inside troilite, cobalt pentlandite tends to form granular exsolution and euhedral grains. The reason for this is that Co increases the upper thermal stability of pentlandite, meaning the exsolution of cobalt pentlandite from the monosulphide solid solution (mss) starts at a higher temperature than pentlandite (e.g., Vaasjoki et al., 1974; Merkle and Gruenewalt, 1986). Higher temperatures allow for a higher diffusion

rate, which more readily forms granular grain shapes (Merkle and Gruenewalt, 1986).

4.2.7 Cobalt pentlandite and siegenite

In the massive bornite, the cobalt pentlandite crystals have variously developed secondary rims around them. This secondary phase belongs to the linnaeite group, and based on the Co-rich composition, it was identified as siegenite. Earlier works (e.g., Hanekom et al., 1965; Aldous, 1980; Rudashevsky et al., 2004) also reported the presence of violarite and bravoite. The Ni-rich linnaeite-group mineral, violarite, is a common alteration product of pentlandite (Misra and Fleet, 1974; Tenailleau et al., 2006; Xia et al., 2009) therefore, it is not unexpected that the Co-rich member of the group, siegenite, will form from the alteration of cobalt pentlandite. Petruk et al. (1969) found siegenite-cobalt pentlandite lamellar intergrowths with bravoite rim around the grains (Langis Mine, Ontario, Canada). This form was not observed in the present study, but Petruk et al. (1969) interpreted a replacement relationship between them, with the formation sequence of cobalt pentlandite, followed by siegenite, followed by bravoite. The sequence of deposition reflected a decrease in S-fugacity during the process. The alteration of the cobalt pentlandite causes it to be replaced by siegenite, which process can be extensive during early stages, especially along grain boundaries, fissures and cracks (Ramdohr, 1969). As Ramdohr (1969) describes, reaction rims genetically belong to the replacement texture and often consist of two or more phases.

Cobalt pentlandite is observed in both chalcopyrite- and bornite-rich samples but with a different appearance. The grains in the bornite are rounded with a prominent siegenite rim around them, or it can occur in strongly fractured and resorbed areas with secondary haematite. The cobalt pentlandite in the chalcopyrite forms mostly subhedral grains and is associated with thin secondary haematite veins. The relationship between pentlandite and violarite has been the subject of various studies (e.g., Misra and Fleet, 1974; Grguric, 2002; Tenailleau et al., 2006; Xia et al., 2009) as it is a potential economic mineral of the supergene alteration zones of massive and disseminated Ni-sulphide deposits. In these

deposits, violarite replaces primary Ni-sulphide minerals. Violarite can also form via hypogene processes, forming from pentlandite via exsolution.

Pentlandite replacement by violarite is a pseudomorphic replacement process during which the supergene violarite inherits the crystallographic form of the pentlandite. This process was investigated in detail, among others, by Misra and Fleet (1974), Tenailleau et al. (2006), and Xia et al. (2009). Although violarite was reported from Phalaborwa, in the present sample set, cobalt pentlandite and siegenite were observed, with textures similar to that described in the case of pentlandite and violarite replacement by the studies above. Replacement relationship between cobalt pentlandite and siegenite was also suggested by Petruk et al. (1969) as mentioned above.

Xia et al. (2009) simulated two conditions under which synthetic violarite formed from pentlandite: (i) pH between 1 and 6 and (ii) pH < 1. The two experiment conditions yielded contrasting violarite textures. In (i), violarite formation began at cracks and unreacted surfaces of the pentlandite crystals towards the core. The reaction front of the two phases was sharp, without a visible gap between the phase boundaries, indicating a very thin reaction zone. The new violarite inherited the shape, size and texture of the pentlandite. Fine cracks appeared perpendicularly to the reaction front in the violarite, but its surface was smooth. Significant differences exist between the form above and the appearance of the Loolekop violarite, which is either rim or only slightly follows the original shape of the cobalt pentlandite, and the surface is rough and wrinkled.

In contrast, the violarite formed in (ii) resulted in a texture resembling the Loolekop violarite. The texture was described as rough, and the external dimensions and texture of the pentlandite were not preserved. The violarite did not follow cracks but only appeared as an outer rim around the pentlandite core. In some cases, the pentlandite cores were wholly consumed, and the violarite formed coarse grains separated by micron-scale pores and cracks. Misra and Fleet (1974) showed that the rough and wrinkled surface of the violarite is caused by ~17% volume reduction due to the different structures of pentlandite and violarite.

In summary, siegenite is formed by the weathering of cobalt pentlandite, and based on earlier analogue experiments (Xia et al., 2009), the textures indicate that the process took place under low pH conditions (pH<1).

4.2.8 Disseminated sulphides

In the younger banded carbonatite, phoscorite, and the olivine glimmerite rock samples, disseminated sulphides (chalcopyrite, bornite, chalcocite*, digenite*) were observed. In the younger banded carbonatite, the phases formed a relatively simple intergrowth texture composed of chalcopyrite and bornite, possibly formed by a similar replacement process described in the transgressive carbonatite. The sulphide grains of the younger banded carbonatite do not show the level of alteration which was observed in the transgressive carbonatite. The sulphide grains follow the general banding of the rock, forming fine-grained interstitial (up to ~500 μm) patches and blobs between the carbonate crystals. These textural characteristics, and the lack of fracture and vein-filling sulphides in these rocks suggest that the sulphides are more likely to be of magmatic origin than the result of later-stage processes.

In contrast, disseminated sulphides observed in the phoscorite and olivine glimmerite samples have complex sulphide intergrowths, including chalcopyrite, bornite, chalcocite* and other Cu-S phases* (Table 4.1.1). The grains are broken up and resorbed at the edges, sometimes with a magnetite rim or valleriite at the contacts. The sulphide grains are primary but can be strongly resorbed and altered. Their appearance is different from the unaltered sulphides of the younger banded carbonatite. Calcite veins crosscutting phoscorite and silicate rocks also contain fresh sulphide grains of chalcopyrite and troilite and are associated with secondary magnetite.

4.2.9 The paragenetic sequence of the Loolekop sulphides

The earliest sulphide phases in the Phalaborwa complex are the disseminated interstitial sulphide grains observed in the banded carbonatite. The disseminated sulphide grains in phoscorite and olivine glimmerite are primary but can be strongly altered, especially in the latter rock type. Isotope and trace element

studies that run parallel to the present work also confirmed the magmatic origin of these sulphides (Bolhar et al., 2020; Le Bras et al., 2021). The economic sulphide mineralisation in the transgressive carbonatite postdates the primary disseminated magmatic sulphides. The sequence starts with the primary phases, which were in solid solution. The main phase is chalcopyrite, which hosts several unmixed minerals, including sphalerite, cubanite, troilite, cobalt pentlandite and galena. Their textural relationship indicated the relative formation time of sphalerite, cubanite and troilite. Cobalt pentlandite had a relatively long formation phase based on the relationship with chalcopyrite and troilite. Native Ag and native Bi were only observed in chalcopyrite in the present study. However, Rudashevsky et al. (2004) reported Ag, Bi (and Pb) minerals in association with chalcopyrite and bornite and suggested that they formed at the later stages of bornite and chalcopyrite formation. The sequence continues with the formation of replacement minerals with three different stages separated according to their textures. The main phase of the first replacement stage is bornite, followed by and slightly overlapping with digenite* and chalcocite*. Parkerite, millerite and siegenite formation potentially overlap with bornite, the latter extending much further. Wittichenite, galena, and chalcocite* fall in stage two of the replacement processes and their formation postdate that of the bornite. Stage three represents the latest replacement stage, including late-stage siegenite and covellite*. Valleriite and haematite formation extends all through the replacement stages.

The disseminated sulphides have a similar formation sequence with much fewer phases involved. The primary phases are chalcopyrite-bornite, troilite, sphalerite, and sometimes cobalt pentlandite. Bornite also can be a replacing phase, followed by other Cu-S phases*. Valleriite and haematite are also present here, and similarly to the previously described sequence, they belong to the replacement stages.

The SEM images of the Ag-Au minerals presented in Rudashevsky et al. (2004; Fig 11.7) reveal primarily anhedral crystal shapes, often entombed in bornite-digenite grains with or without chalcopyrite present. Although it is a small sample set and might not be fully representative, following the petrogenetic sequence of the present study, it is probable that the Ag-Au minerals are more readily associated with the later-stage sulphide assemblage. Rudashevsky et al. (2004) presented a different type of Au-Ag mineral associations based on their

intergrowth with sulphide phases; in each group, bornite was present. Rudashevsky et al. (2004) separated two noble-metal parageneses: an early, associated with cobalt pentlandite, chalcopyrite and bornite, and a later in association with millerite and chalcosine-group minerals.

The most abundant PGMs of Loolekop are Pd-arsenides and stannides, with the only Pt-bearing PGM species being a Pt-arsenide: sperrylite (Rudashevsky et al., 2004). In contrast to the Au-Ag phases, PGMs often have euhedral shapes (Rudashevsky et al., 2004). Due to the lack of textural context, it is not known where these euhedral PGMs originally sit in the sulphide phases or if they are consistently associated with the sulphides at all, although SEM images also presented by Rudashevsky et al. (2004) showed anhedral cabriite grain and a rounded sperrylite grain entombed in bornite-chalcopyrite grains.

It has to be mentioned that recent isotope (Bolhar et al., 2020) and trace element (Le Bras et al., 2021) studies reported primary magmatic bornite from the carbonatites; however, the present textural study interpreted the mineral as replacement based on the textural relationships with the associated phases. Primary bornite and its significance will be discussed in the following chapters.

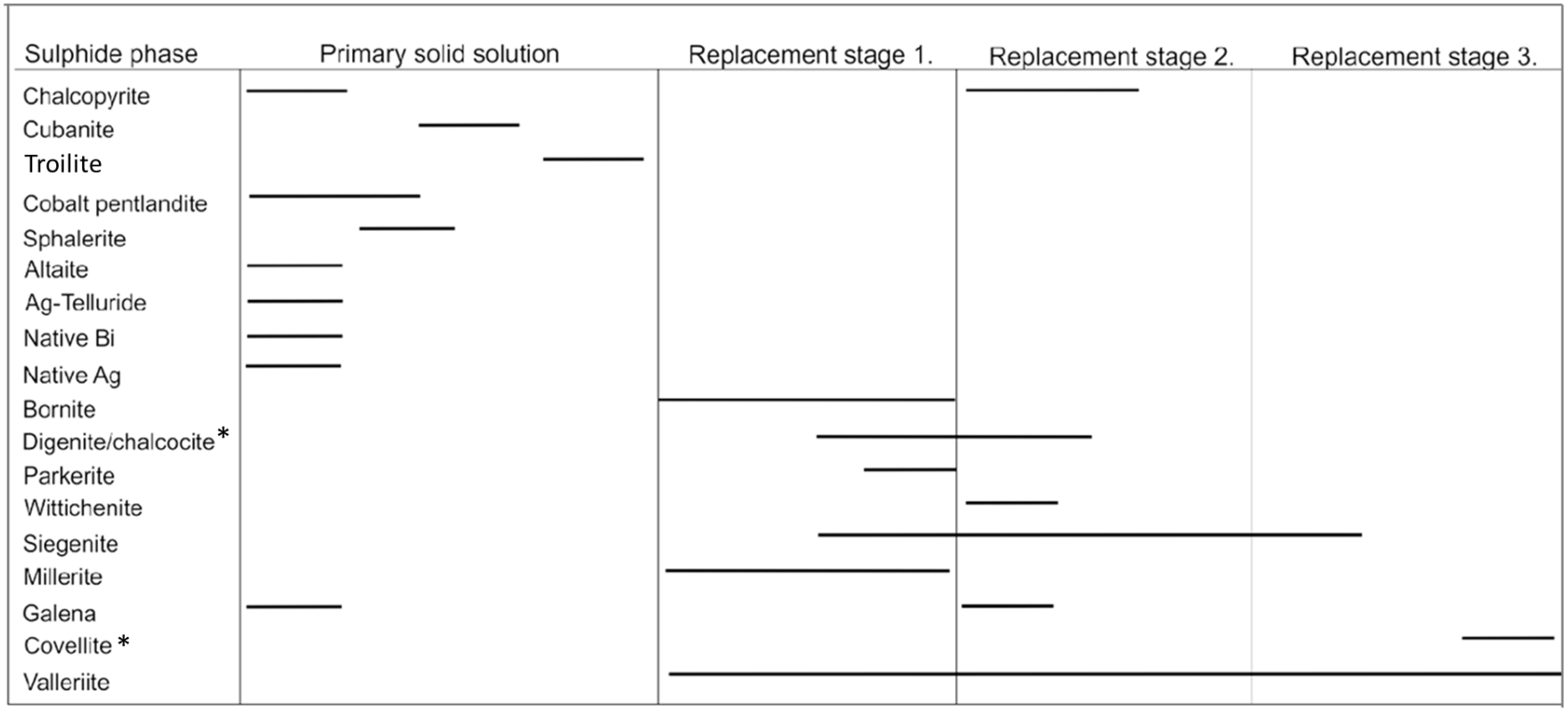

Figure 4.1.9. Sulphide paragenetic sequence in the transgressive carbonatite. Digenite/chalcocite and covellite are not stoichiometric (*).

4.3 Implication for the origin of the sulphide mineralisation based on the textural characteristics

In summary, the Phalaborwa sulphides formed during several stages. Unaltered disseminated interstitial sulphides are most likely magmatic. The economic sulphide mineralisation in the transgressive carbonatite showed a range of textures which could also suggest magmatic origin (individual interstitial sulphide blobs and patches). Other textures indicate later-stage sulphide emplacement: Very small-scale chalcopyrite veinlets derived from large chalcopyrite blotches which infiltrated the phlogopite crystals along their cleavages. Chalcopyrite can fill the space between euhedral-subhedral non-sulphide minerals (magnetite, phlogopite). Roger (2009) discussed a similar chalcopyrite texture and, described it as a triangular-acute angle texture and interpreted it as later stage infiltration of chalcopyrite. Ramdohr (1969) discussed the problem of textural interpretations, and he argued that it could be rather difficult to classify the sulphide assemblage that belongs to the high-temperature magmatic stage of the ore formation sequence. The sulphide phases in question can crystallise at very low temperatures. The interpretation of the Phalaborwa sulphide textures can range from magmatic to pneumatholytic and hydrothermal conditions.

Characteristics that suggest a complex, multi-stage sulphide emplacement at Phalaborwa include lithology-bound mineralisation, lack of extensive hydrothermal alteration of the host rock, sulphide presence in primary melt inclusions in phoscoritic olivine (Aldous, 1980) mixed S-isotope results (Mitchell and Krouse, 1975; Bolhar et al., 2020) and a series of sulphide textures that ranges from magmatic to later-stage hydrothermal, the latter being the most common.

Some sulphide phases had a magmatic origin, while sulphides in the transgressive carbonatite can have multiple origins and generations. In the former case, as Aldous (1980) suggested, the host of the sulphides would be an S-bearing magmatic fluid, separated from the transgressive carbonatite magma with probable country rock interaction, which provides Cu and crustal S. Bolhar et al. (2020) showed the presence of crustal Pb in the sulphides. Crustal contamination or mixing with geothermal fluids is common in epithermal or hydrothermal deposits. This would result in a mixed isotope signature in the sulphide phases. Giebel et al. (2019) suggested possible crustal contamination

for the transgressive carbonatite, bringing anomalous Al-(and Ba)-rich orthomagmatic phlogopite as probable evidence. The same work alongside Milani et al. (2017b) suggested that the transgressive carbonatite has a separate evolutionary path from the phoscorite and the banded carbonatite based on non-sulphide mineral chemistry. If the fluid/fluids responsible for the sulphide formation are part of the mentioned separate evolutionary path, it would explain why the sulphide mineralisation is bound to the transgressive carbonatite. The observations concur with Bolhar et al. (2020) and Le Bras et al. (2021), who recently showed that the S-isotope and trace element compositions of the Phalaborwa sulphides reflects magmatic origin, but crustal influence was also found.

Chapter 5: Sulphide geochemistry: Major and minor element compositions

Further investigation of sulphide phase characteristics in the Phalaborwa lithologies was carried out by determining the major element compositions. The results are presented in this chapter. The study aimed to discover potential differences in the compositions of sulphides belonging to the different textual types, associations or lithologies. The results and published sulphide phase diagrams help to further refine the sulphide petrogenetic sequence (Section 4.3) by indicating the potential temperature ranges of the compositions and the relationships. Box and whisker diagrams were used for exploratory data analysis. The diagrams visualise the major characteristics (minimum, maximum, mean, median, the first to the third and first interquartile range) of the compositional data of the main sulphide minerals in the different lithologies.

The study used EPMA to analyse the major element composition of the sulphides from the different lithologies. The list of the samples and their analysed sulphide phases are presented in Table 3.2.3. The setup of the EPMA was described in section 3.2.2, while the errors are presented in Table 3.2.1. The representative chemical compositions with the calculated mineral formulae and diagnostic chemical ratios are presented in this chapter. The complete list of EPMA results is presented in Appendix 1.

5.1 Cu-S, Cu-Fe-S and Fe-S mineral phases

The analysed Cu-S, Cu-Fe-S and Fe-S mineral phases include (optically identified) chalcopyrite, bornite, digenite, troilite, and cubanite, which formed complex intergrowths textures (Fig.4.1.10. a-f).

A Fe-Cu-S ternary diagram depicts the major element ratios (Fig. 5.1.a). The diagram also depicts additional sulphide major element data from Rudashevsky et al. (2004) for comparison, showing overlapping values with the present dataset. The major element compositions of sulphide minerals measured in the different lithologies overlap and have relatively consistent sulphur values. However, the total-metal ratios of each sulphide phase vary, leading to wider total metals/S ratios (Fig.5.1.b). Generally, the Cu-Fe-S and Cu-S phases of most of the present dataset

have lower mean metal/S ratios than the ideal values (Fig.5.1.b). The individual geochemistry of the minerals in each lithology will be discussed in separate sections. Figure 5.1.b gives an overview of the general range of the metal/S ratios of the Phalaborwa sulphides. In the case of bornite, the mean metal/ S value (1.45) is closest to x- bornite (1.48), a bornite composition which was observed at low temperatures by Yund and Kullerud (1966), but the values change in a wide range (1.43-1.46) with outliers (1.33, 1.37 and 1.51). The observed compositional variation is reconcilable with the abundant intergrowth and exsolution phases in bornite and may indicate later-stage processes (Section 4.2.3-4).

The means of total metal/S ratios of chalcopyrite (0.98) and cubanite (0.97) also fell below the ideal ratio of 1 but vary in a much narrower range than the bornite (0.95-1.01 and 0.96- 0.99). Lamellar digenite was the most suitable for analysis among the Cu-S phases as the other texture types (myrmekite-resembling, complex intergrowth: Figure 4.1.6. a-d) were too fine-grained. However, even the thick digenite lamellae were affected by late-stage alteration, including covellite formation on the lamellae or replacement by valleriite (Fig. 4.1.5.a-d). The chemical composition of the lamellar digenite reflected the effects listed above, producing nonstoichiometric results. It showed a wide range of metal/S ratios (1.64-1.96) that overlap with not only digenite (1.8) but several other Cu-S phases, including djurleite (~1.94) and anilite (1.75) (Fig.5.2.a). The Fe-S phase optically identified as pyrrhotite measured in phoscorite fell into the ideal range of metal/S ratio (0.8-1.0) (Fig.5.2.b) and was closer to troilite composition. The previously published pyrrhotite and troilite compositions from the transgressive carbonatite (Rudashevsky et al., 2004) overlapped with the analysis results of this study. Troilite is a discrete endmember of the compositional range of the analyses results; the present metal/S ratios are closer to this composition than to stoichiometric pyrrhotite ($Fe_{11}S_{12}$), but both are present in the samples.

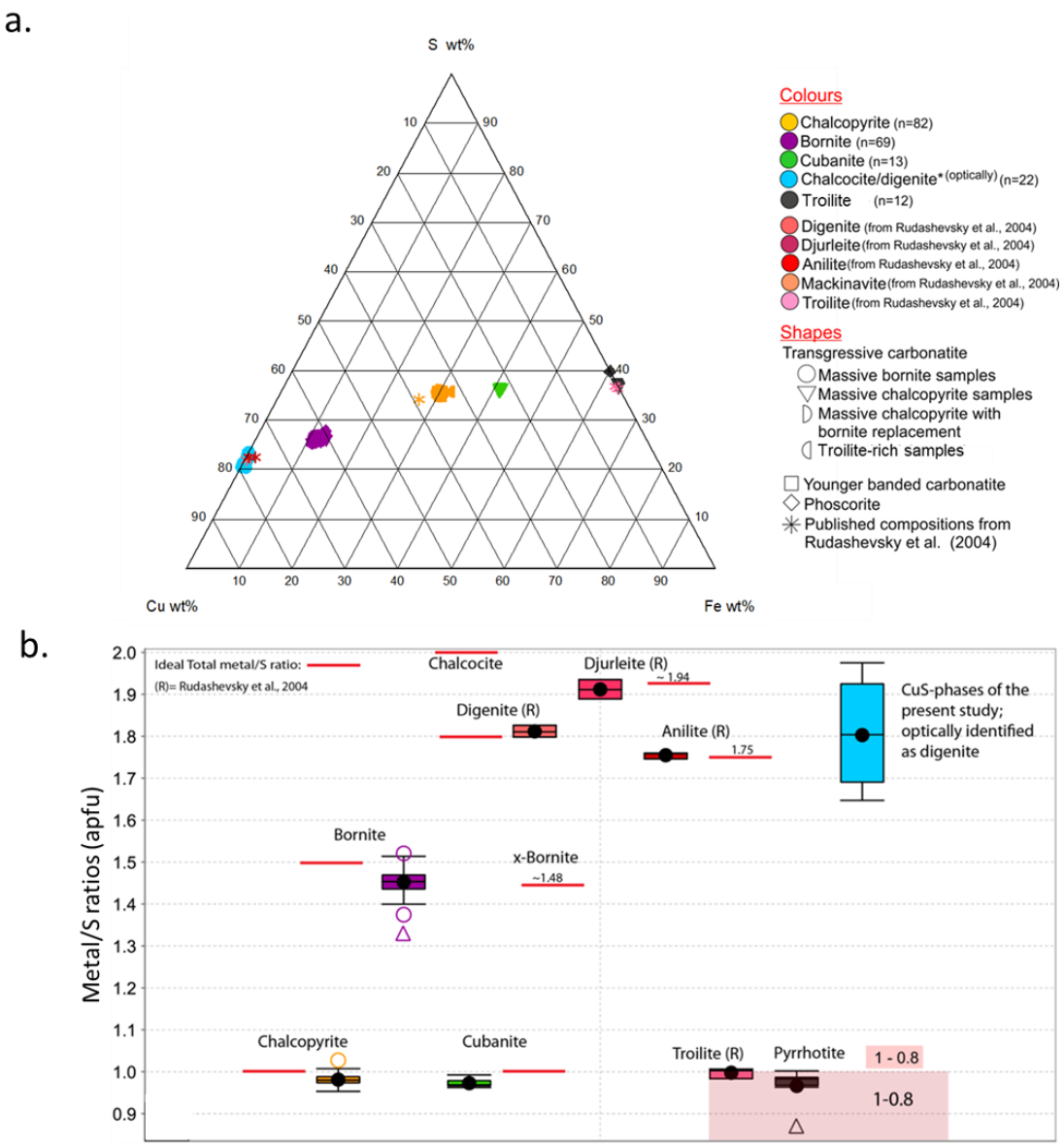

Figure.5.1. a; Ternary diagram showing the composition ranges of the different Cu-Fe-S phases. The stars depict published compositions of the same phases by Rudashevsky et al. (2012). The published compositions are mostly overlap with the present data, apart from one chalcopyrite datapoint which shows slightly higher Cu content. b: The diagram shows the range of the total metals/S ratios calculated in the analysed Phalaborwa sulphide phases from all lithologies, depicted with different coloured columns. The black circles indicate the mean values, while the empty circles and triangles show outliers. The red lines (and the red box for troilite) indicate the ideal total metals/S ratio of each phase and/or the ratios from Rudasehvsky et al., (2012) measured in Phalaborwa sulphides.

5.1.1 Chalcopyrite

Chalcopyrite was analysed in the different transgressive carbonatite types and banded carbonatite. The ideal metal/S ratio of chalcopyrite is 1, and the values measured in the sample set fall between 0.95 and 1.01 (Table 5.1) and thus are reasonable compared to the ideal ratio. Although Figure 5.3 shows differences

between the chalcopyrite metal/S ratios in different sample types and lithologies, these are not significant to be diagnostic.

Massive chalcopyrite showed metal/S ratios between 0.97 and 0.99. This textural type has a minimal variation of the element proportions with a Cu/Fe ratio between 0.97 and 1.01 (Table 5.2). The variation is mainly controlled by Cu and S. Most measurements showed metal deficiency. Massive chalcopyrite in samples with abundant bornite replacement showed metal/S values between 0.97 and 0.99. The Cu/Fe ratio varies from 0.97 to 0.99, showing that this chalcopyrite type is always slightly Fe-rich and Cu-deficient compared to the other chalcopyrite types. Chalcopyrite in troilite-rich samples showed a slightly lower range of metal/S ratios (Table 5.1) compared to the previous chalcopyrite types and also has the widest Cu/Fe ratio range (0.87 and 1.02). The low numbers indicate that the chalcopyrite can be relatively high in Fe compared to the other types. Chalcopyrite wedges and splinters in massive bornite have the highest Cu proportions (Cu/Fe: 0.96-1.04) in this type among the samples, although the difference is not significant.

The samples from separate lithologies also have different chalcopyrite textures. The chalcopyrite-rich and troilite-rich transgressive carbonatite samples have massive chalcopyrite texture; the bornite-rich transgressive carbonatite sample has chalcopyrite spindles and wedges, while the banded carbonatite and phoscorite have disseminated chalcopyrite. The results show that the major element geochemistry of the chalcopyrite is not characteristic of texture types or lithologies.

The difference in Cu/Fe ratios might reflect the excitation volume (caused by the beam during EPMA analysis) versus the other non-chalcopyrite phases within that volume. Considering that Cu-rich chalcopyrite occurs in bornite and Fe-rich chalcopyrite was associated with troilite, the feature above is very likely. The fact that these chemical changes vary with texture type but not lithology further supports this.

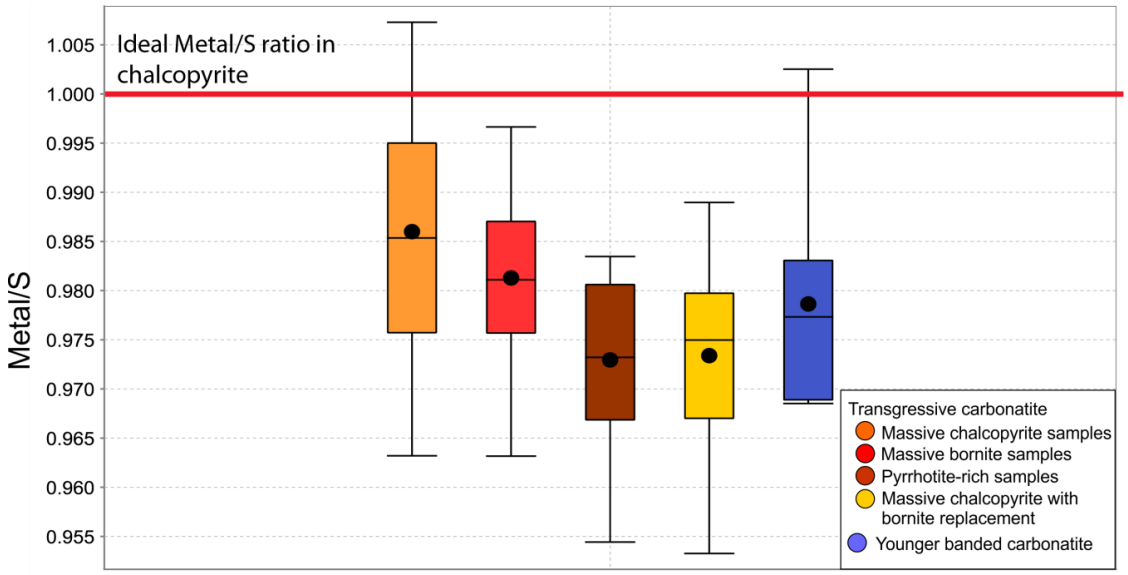

Figure. 5.3. Total metal/S ratios of the chalcopyrite in the various Phalaborwa lithologies. The ideal ratio is shown by the red line. The values of the box and whisker diagram are shown in the table below the diagram.

Table 5.1. Metal/S ratios of analysed chalcopyrite, depicted on the box-and-whisker diagrams above (Fig 5.3). The table shows the number of analysed chalcopyrite in each lithologies (n), the mean Metal/S ratios, the median of the lower half of the data set (Q1) and the median of the upper half of the dataset (Q3). The minimum (WMin) and maximum (WMax) values of the whiskers indicate the lowest and highest values of the dataset. Explanation of the statistics behind the Box and Whiskers diagrams is given in Chapter 3.

Chalcopyrite metal/S ratios						
	n	**Mean**	**WMin**	**WMax**	**Q1**	**Q3**
TRC Chp-rich	15	0.988	0.967	1.007	0.976	0.997
Trc Bo-rich	37	0.981	0.963	0.997	0.976	0.987
TRC.To-rich	10	0.973	0.954	0.984	0.967	0.981
TRC.Bo+Chp	12	0.973	0.953	0.989	0.967	0.980
BC	8	0.979	0.969	1.003	0.969	0.983

Abbreviations: TRC Chp-rich: transgressive carbonatite sample with massive chalcopyrite; TRC Bo-rich: transgressive carbonatite sample with massive bornite; TRC To-rich: trolite-rich transgressive carbonatite sample; TRC Bo+Chp: transgressive carbonatite where bornite replaces chalcopyrite forming shredded texture; BC: younger banded carbonatite.

Table 5.2. Representative chalcopyrite major element compositions (wt%) and calculated formulae in the different Phalaborwa lithologies, determined with EPMA. The calculated errors (ε) are presented with every element.

Chalcopyrite	Pb1_chp1	ε	GC1811A_A_9	ε	GC1611_B2_1 1	ε	PTC3_C7	ε	GC808_B3	ε	PA25_B1 2	ε	GC1610_C_4	ε	26B_A28	ε
S (wt%)	35.36	1.10	35.26	1.79	35.59	1.78	35.14	1.08	34.75	1.11	35.47	1.78	35.54	1.78	35.47	1.78
Cu (wt%)	34.47	0.83	34.37	1.25	33.79	1.25	33.61	0.82	33.65	0.79	32.98	1.25	33.61	1.25	34.06	1.24
Fe (wt%)	29.88	1.39	30.19	2.19	30.20	2.19	30.22	1.35	30.39	1.38	29.83	2.21	30.09	2.19	29.90	2.21
Error correted Total	99.71		99.82		99.84		99.04		98.89		98.38		99.35		99.56	
Lithology	TRC: Bo-rich		TRC: Bo-rich		TRC: Bo replacement in Chp		TRC: chp-rich		TRC: chp rich		TRC: chp rich with lots of cubanite		TRC: To-rich		BC	
Texture	at bo edges, around Co-ptl		rim/splinters in massive bo		chp-bo network ex/repl		chp with extensive bo		primary. Interstitial		massive (cub lamellae)		between Po patches		disseminated, with bornite and dig at edges	
Calculated formulae (Ideal formulae: CuFeS2)																
S	2.02		2.01		2.03		2.02		2.01		2.05		2.04		2.03	
Cu	0.99		0.99		0.97		0.98		0.98		0.96		0.97		0.98	
Fe	0.98		0.99		0.99		1.00		1.01		0.99		0.99		0.98	
Cu/Fe	1.01		1.00		0.97		0.98		1.00		0.98		0.98		0.97	
Total Metals	1.97		1.98		1.96		1.98		1.99		1.95		1.96		1.97	
Metal/S (Ideal: 1)	0.98		0.99		0.97		0.98		0.99		0.95		0.96		0.97	

Abbreviations: chp: chalcopyrite, bo: bornite, Co-ptl: cobalt pentlandite, cub: cubanite, To: troilite, dig: digenite, TRC: transgressive carbonatite, BC: banded carbonatite

5.1.2 Bornite

Bornite was analysed in chalcopyrite-rich, bornite-rich, chalcopyrite-bornite replacement transgressive carbonatite, banded carbonatite and phoscorite. The metal/S ratios show that bornite has a metal deficiency, with most values falling below the ideal ratio of 1.5. The changes in the metal content in the bornite are consistent with the previous study of Rudashevsky et al. (2004). The different lithologies/sample types also represent different bornite textures. The transgressive carbonatite samples with chalcopyrite-bornite replacement have shredded texture (Fig.4.1.3. a-d). The bornite-rich transgressive carbonatite samples have massive bornite, while in the chalcopyrite-rich samples, bornite occurs as irregular patches or fine, irregular lamellae. In phoscorite, bornite is part of the disseminated sulphide grains with complex Cu-S and Cu-Fe-S intergrowths. The major element compositions of the bornites with different textures (from different lithologies or sample types) mostly overlap, as shown in Figure 5.4. Most analysed bornites have S-rich and metal-deficient compositions; exceptions were found in a chalcopyrite-rich sample (GC808) and in massive bornite (Fig.5.3; Table 5.4). Bornite in sample GC808 showed higher Fe proportions (Table 5.4). The bornite analysis in this sample provided unreliable data as the mineral forms fine, irregular lamellae in massive chalcopyrite, which resulted in higher Fe values. The highest Cu/Fe ratios were observed in massive and replacement bornites (4.8-5.1 and 4.7-5.1, respectively). The bornite compositions in the banded carbonatite overlap with the transgressive carbonatite. Bornite of the disseminated sulphide grains in phlogopite-rich phoscorite showed an extensive compositional range (Fig.5.4; Table 5.3-4), but this is a common feature of this texture not only in the case of bornite but Cu-S phases as well.

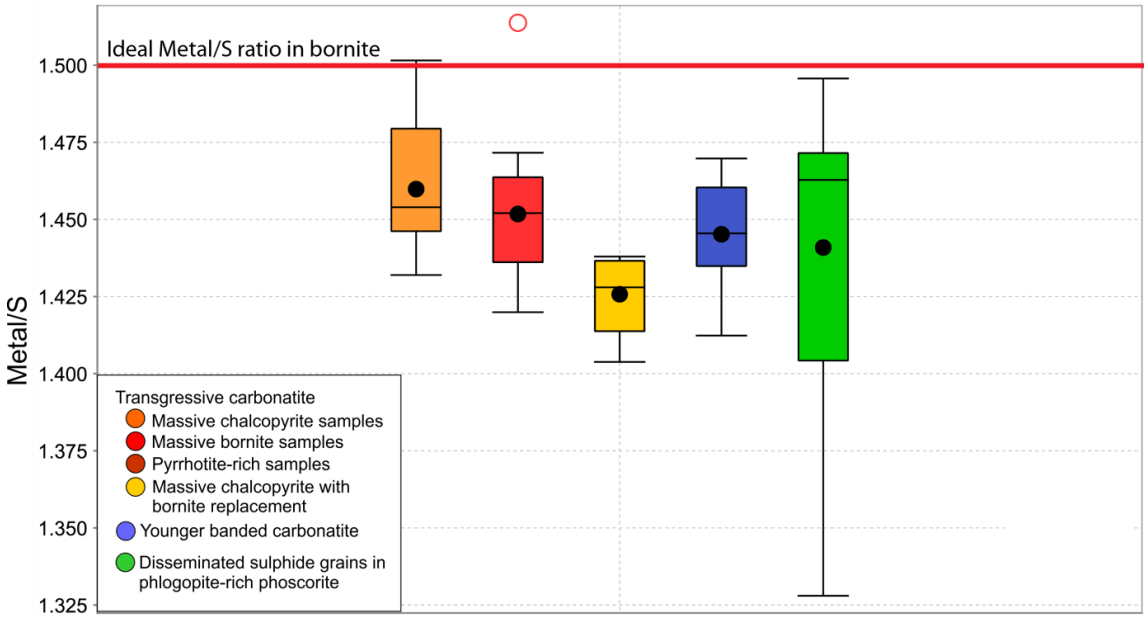

Figure. 5.4. Total metal/S ratios of bornite in the different Phalaborwa lithologies. The ideal ratio is shown by the red line. The values of the box and whisker diagram are shown in the table below the diagram.

Table 5.3. Metal/S ratios of analysed bornites, depicted on the box-and-whisker diagrams above (Fig 5.4). The table shows the number of analysed chalcopyrite in each lithologies (n), the mean Metal/S ratios, the median of the lower half of the data set (Q1) and the median of the upper half of the dataset (Q3). The minimum (WMin) and maximum (WMax) values of the whiskers indicate the lowest and highest values of the dataset. Explanation of the statistics behind the Box and Whiskers diagrams is given in Chapter 3.

Bornite **metal/S ratios**							
	n	**Mean**	**WMin**	**WMAx**	**Q1**	**Q3**	**outlier threshold**
TRC Chp-rich	21	1.460	1.432	1.502	1.446	1.479	
Trc Bo-rich	23	1.452	1.420	1.472	1.436	1.464	Upper: 1.505
TRC.Bo+Chp	5	1.426	1.404	1.438	1.414	1.437	
BC	8	1.445	1.412	1.470	1.435	1.460	
Phoscorite	12	1.441	1.328	1.496	1.404	1.472	

Abbreviations: TRC Chp-rich: transgressive carbonatite sample with massive chalcopyrite; TRC Bo-rich: transgressive carbonatite sample with massive bornite; TRC Bo+Chp: transgressive carbonatite where bornite replaces chalcopyrite forming shredded texture; BC: younger banded carbonatite

Table 5.4. Representative bornite major element compositions (wt%) and calculated formulae in the different Phalaborwa lithologies, determined with EPMA. The calculated errors (ε) are presented with every element.

Bornite	PTC3_B 8	ε	Pb1_Bo 4	ε	GC1811A_B_3	ε	Pa23_2	ε	GC808_B 5	ε	GC1611_ B2_9	ε	26B_A_2	ε	P03_phosc_F3_1	ε
S (wt%)	26.75	1.20	26.12	1.25	25.91	2.03	25.91	2.03	25.44	1.27	26.35	2.03	26.15	2.01	26.03	1.26
Cu (wt%)	61.85	0.62	62.38	0.63	62.68	0.96	60.93	0.96	61.46	0.61	62.36	0.94	62.46	0.94	61.26	0.61
Fe (wt%)	10.99	2.30	11.22	2.31	10.82	3.76	11.88	3.55	12.45	2.17	11.16	3.69	11.22	3.67	11.94	2.24
Error cor. Total	99.60		99.80		99.53		98.84		99.54		99.94		99.91		99.23	
Lithology	TRC chp-bo replacement		TRC bo rich		TRC bo-rich		TRC chp rich		TRC-chp rich		TRC chp-bo replacement		BC		Phoscorite	
Texture	extensive with Chp		massive with chp at edges		Cu-Fe-S intergrowths		Irregular exsolution lamellae In chp		Irregular exsolution in chp		Bo-Chp shredded texture		Cu-Fe-S phase intergrowths		Cu-Fe-S phase intergrowths	
	Calculated formulae (Ideal formulae: Cu5FeS4)															
S	4.16		4.08		4.06		4.08		4.00		4.10		4.08		4.08	
Cu	4.85		4.92		4.95		4.84		4.87		4.90		4.91		4.84	
Fe	0.98		1.01		0.97		1.07		1.12		1.00		1.00		1.07	
Cu/Fe	4.95		4.89		5.09		4.51		4.34		4.91		4.89		4.51	
Total Metals	5.83		5.93		5.92		5.91		5.99		5.90		5.91		5.91	
Metal/S (Ideal: 1.5)	1.40		1.45		1.47		1.45		1.50		1.44		1.45		1.45	

Abbreviations: chp: chalcopyrite, bo: bornite, TRC: transgressive carbonatite, BC: banded carbonatite

5.1.3 Cubanite

Cubanite occurs in massive chalcopyrite and troilite-chalcopyrite-rich samples, forming lamellae or more extensive patches (Fig.4.1.2). The ideal metal/S ratio of cubanite is 1. At the same time, the Phalaborwa analyses vary from 0.96 to 0.99, indicating slight metal deficiency (Fig.5.5, Table 5.5). The measured Cu/Fe ratios are also slightly below the ideal (0.5) in most analyses, reaching 0.49 (Table 5.5).

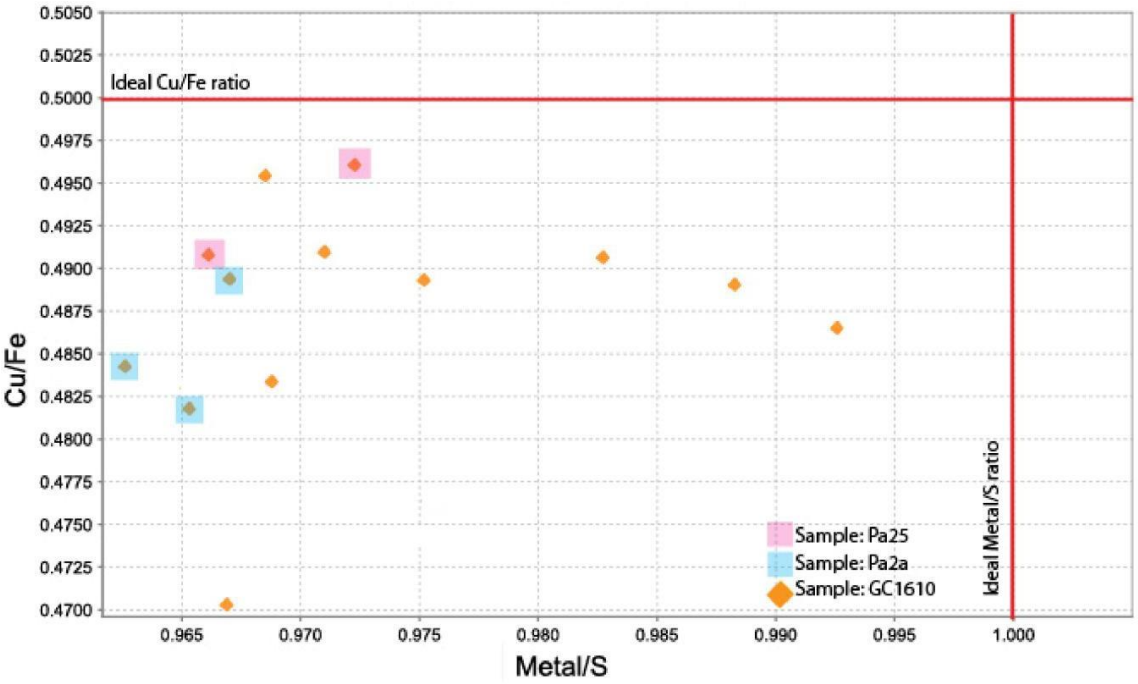

Figure 5.5. Relationship between Cu/Fe (at%) and Metal/S (at%) ratios of cubanite in chalcopyrite-rich (Pa25, Pa2a) and troilite-rich (GC1610) transgressive carbonatite samples where cubanite forms lamellae of various broadness.

Table 5.5. Representative cubanite major element compositions (wt%) and calculated formulae in the different Phalaborwa lithologies, determined with EPMA. The calculated errors (ε) are presented with every element.

Cubanite	Pa2a_10	ε	PA25_B8	ε	PA25_B7	ε	GC1610_B_4	ε	GC1610_C_2	ε
S (wt%)	36.12	1.75	35.86	1.76	35.81	1.77	35.83	1.77	35.55	1.78
Cu (wt%)	22.68	1.49	22.86	1.50	22.55	1.50	22.63	1.52	22.51	1.52
Fe (wt%)	40.73	1.87	40.50	1.88	40.38	1.88	40.51	1.88	40.43	1.88
Error cor. Total	99.58		99.26		98.76		99.07		98.59	
Lithology	TRC chp-rich		TRC chp-rich		TRC chp-rich		TRC To-rich		TRC To-rich	
Texture	Lamellae		Lamellae		Lamellae		Lamellae		Lamellae	
Calculated Formulae (Ideal Formulae: $CuFe2S_3$)										
S	3.05		3.04		3.05		3.04		3.04	
Cu	0.97		0.98		0.97		0.97		0.97	
Fe	1.98		1.97		1.98		1.98		1.98	
Cu/Fe	0.49		0.50		0.49		0.49		0.49	
Total Metals	2.95		2.95		2.95		2.95		2.95	
Metal/S (Ideal: 1)	0.97		0.97		0.97		0.97		0.97	

Abbreviations: chp: chalcopyrite, bo: bornite, to: troilite TRC: transgressive carbonatite

5.1.4 Cu-S phases

The lamellar Cu-S phases in the massive bornite of the transgressive carbonatite were optically identified as digenite, often with later-stage covellite or resorbed by secondary alteration (Fig.4.1.6). The ideal metal/S ratio of digenite is 1.8. The analysed lamellar phases fall below this value, showing ratios between 1.65 and 1.7 (Fig.5.6). These values are closer to the anilite metal/S ratios of 1.75. As mentioned before, the lamellae and, generally, the Cu-S phases are not homogeneous, which will affect the chemical compositions even near decisive optical properties. The disseminated grains of complex sulphide intergrowths show a wide range of metal/S ratios, ranging between anilite/digenite and djurleite/chalcocite values (Fig. 5.6, Table 5.7). The observed compositional range is reasonable considering the intergrowth textures observed (Fig.4.1.10). One data point from a banded carbonatite shows a composition close to anilite. The representative chemical compositions of the analysed Cu-S phases are presented in Table 5.7.

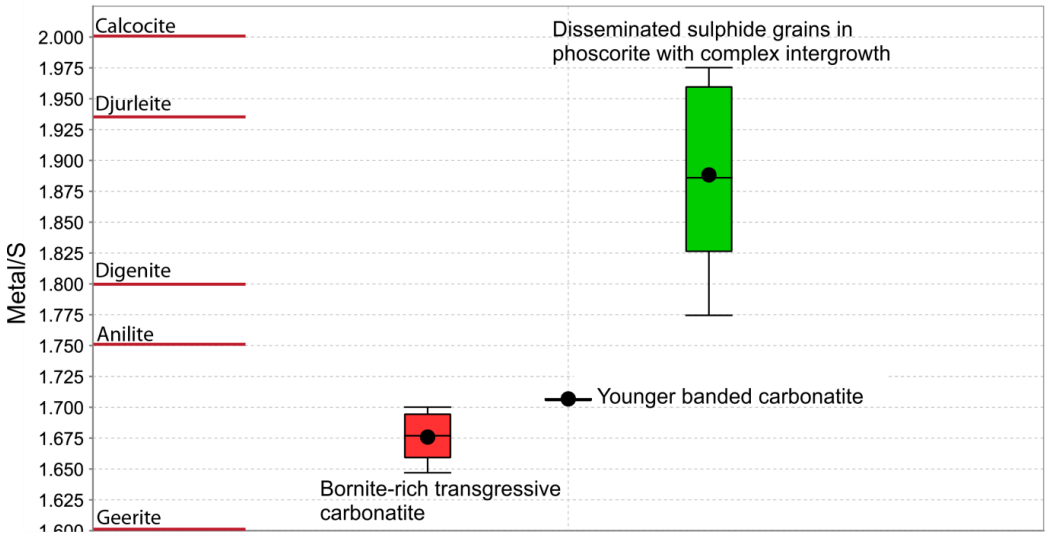

Figure. 5.6. Total metal/S ratios of the Cu-S minerals in the different Phalaborwa lithologies. The ideal ratio is shown by the red line. The values of the box and whisker diagram are shown in the table below the diagram.

Table 5.6. Metal/S ratios of analysed Cu-S minerals, depicted on the box-and-whisker diagrams above (Fig 5.6). The table shows the number of analysed chalcopyrite in each lithologies (n), the mean Metal/S ratios, the median of the lower half of the data set (Q1) and the median of the upper half of the dataset (Q3). The minimum (WMin) and maximum (WMax) values of the whiskers indicate the lowest and highest values of the dataset. Explanation of the statistics behind the Box and Whiskers diagrams is given in Chapter 3.

Cu-S phases: **metal/S ratios**						
	n	**Mean**	**WMin**	**WMAx**	**Q1**	**Q3**
TRC Bo-rich	8	1.676	1.647	1.700	1.659	1.694
BC	1	1.707	1.707	1.707	1.707	1.707
Phoscorite	13	1.888	1.775	1.975	1.826	1.960

Abbreviations: TRC Bo-rich: transgressive carbonatite sample with massive bornite; BC: younger banded carbonatite

Table 5.7. Major element compositions (wt%) of the Cu-S phases and calculated metal/S ratios in the different Phalaborwa lithologies, determined with EPMA. The calculated errors (ε) are presented with every element**.** Formulae was not calculated for the mixed phases.

CU-S	2Pb5_di4	ε	2Pb5_ di 5	ε	2PB3_C2_ 7	ε	2/GC813/5_A2b_ 1	ε	2/GC813/5_A 3	ε	GC815_D _4	ε	6A_SEMc_ 2	ε
S (wt%)	22.80	1.32	22.92	1.32	22.96	2.14	21.86	1.35	20.41	1.40	21.09	1.37	22.52	1.35
Cu (wt%)	76.80	0.58	76.92	0.58	75.63	0.86	76.98	0.55	78.23	0.54	77.51	0.54	75.91	0.55
Error cor. Total	99.60		99.84		98.59		98.84		98.64		98.60		98.43	
Lithology	TRC-Bo-rich		TRC-Bo-rich		TRC-Bo-rich		Phoscorite		Phoscorite		Phoscorite		BC	
Texture	Thick lamellae		Thick lamellae		Thick lamellae		Thick lamellae		Thinner irregular network in assemblage		Lamellae		Grain near Bo	
Metal/S	1.70		1.69		1.66		1.78		1.94		1.86		1.70	

Abbreviations: Bo: bornite, TRC: transgressive carbonatite, BC: banded carbonatite

5.1.5 Troilite

The major element composition of troilite was analysed in transgressive carbonatite samples where troilite forms large anhedral grains in chalcopyrite (in troilite-rich samples) or strings and flames in chalcopyrite-rich samples (Fig.4.1.2). The metal/S ratio of both textural types overlap; 0.98 in the massive chalcopyrite and 0.96-0.99 of the large grains in the troilite-rich sample (Fig.5.7, Table 5.8). The metal/S ratios fall between the ideal values of troilite (1) and hexagonal pyrrhotite (0.916) and are closer to the former (Fig.5.7). Rudashevsky et al. (2004) also reported the presence of troilite in the transgressive carbonatite. Representative chemical compositions are presented in Table 5.9.

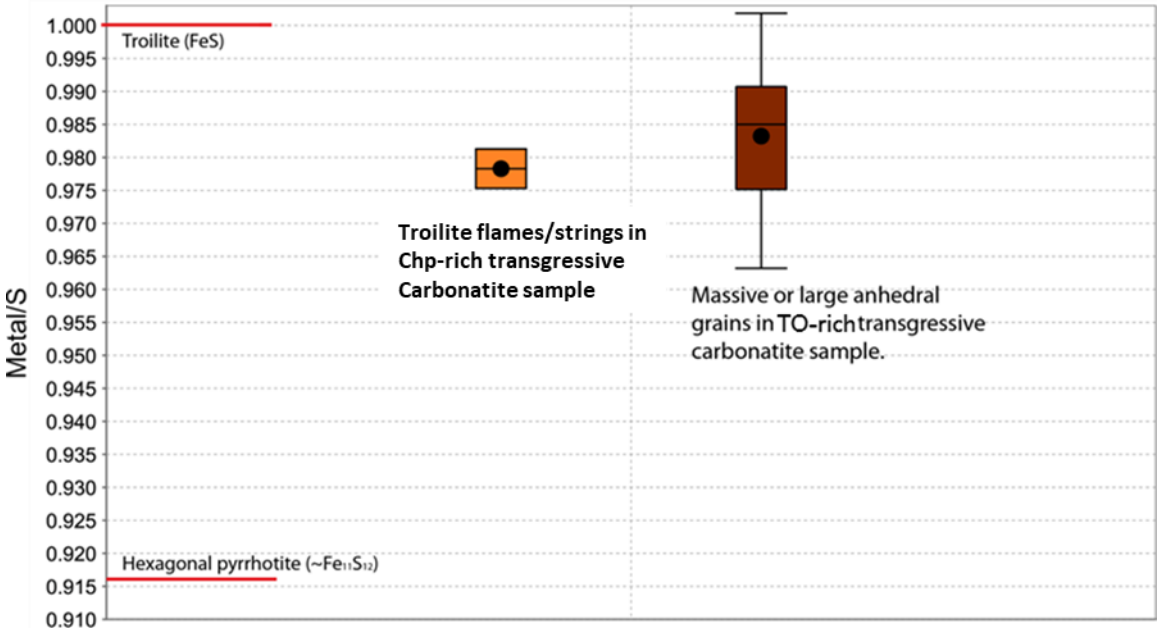

Figure. 5.7. Total metal/S ratios of the Cu-S phases in the different Phalaborwa lithologies. The ideal ratio is shown by the redline. The values of the box and whisker diagram are shown in the table below the diagram. Chp: chalcopyrite, TO: troilite

Table 5.8. Metal/S ratios of analysed troilite, depicted on the box-and-whisker diagrams above (Fig 5.7). The table shows the number of analysed chalcopyrite in each lithologies (n), the mean Metal/S ratios, the median of the lower half of the data set (Q1) and the median of the upper half of the dataset (Q3). The minimum (WMin) and maximum (WMax) values of the whiskers indicate the lowest and highest values of the dataset. Explanation of the statistics behind the Box and Whiskers diagrams is given in Chapter 3.

Troilite **metal/S ratios**						
	n	**Mean**	**WMin**	**WMAx**	**Q1**	**Q3**
TRC To-rich	10	0.983	1.647	1.002	0.975	0.991
TRC Chp-rich	2	0.978	0.975	0.981	0.975	0.981

Abbreviations: **TRC Chp-rich**: transgressive carbonatite sample with massive chalcopyrite; **TRC To-rich**: troilite-rich transgressive carbonatite sample.

Table 5.9. Representative troilite major element compositions (wt%) and calculated formulae in the different Phalaborwa lithologies, determined with EPMA. The calculated errors (ε) are presented with every element.

Troilite	PA25_E 4	ε	GC1610_A_1	ε	GC1610_A_2	ε	GC1610_semD_5	ε
S (wt%)	36.54	1.77	36.5	1.77	36.71	1.80	36.73	1.80
Fe (wt%)	62.31	1.48	62.56	1.51	62.93	1.50	63.87	1.48
Error cor. Total	99.00		99.14		99.76		100.68	
Lithology	TRC Chp-rich		TRC To-rich		TRC To-rich		TRC To-rich	
Texture	"flame"-shaped grain in massive chp		extensive anhedral patches in chp		extensive anhedral patches in chp		extensive anhedral patches in chp	
	Calculated Formulae (Ideal Formulae: FeS, Ideal Metal/S ratio: 1)							
S	1.01		1.01		1.02		1.02	
Fe	0.99		0.99		0.99		1.00	
Metal/S	0.98		0.98		0.97		0.98	

Abbreviations: Chp: chalcopyrite, To: troilite, TRC: transgressive carbonatite

5.1.6 Co-Ni-Fe Sulphides

The major element composition of cobalt pentlandite was analysed in chalcopyrite-rich, bornite-rich, troilite-rich and chalcopyrite-bornite replacement transgressive carbonatite samples. The disseminated sulphide grains of the phoscorite provided one data point with acceptable error. The results are depicted on Co+Ni- S -Fe and Fe-Ni-Co ternary diagrams (Fig.5.8.a-b). Figure 5.8.a shows that although the phases have similar S (at%) values, the (Co+Ni)/Fe ratios vary widely. The Fe-Ni-Co compositional space effectively separated three main cobalt pentlandite types (Fig.5.8.b). Type III has significantly lower Co-content than Type I and II cobalt pentlandites and is referred to as cobalt-rich pentlandite, it is further divided into two subtypes.

i. **Type I**. Cobalt pentlandite has metal/S ratios between 1.08 and 1.12 (Fig.5.8.c, Table 5.10) and relatively high Ni/Co ratios of 0.43-0.85. The Fe/Ni and Fe/Co ratios are between 0.57-1.32 and 0.41-1.10, respectively (Table 5.11). The phases occur in bornite-rich transgressive carbonatite samples. They are either associated with alteration zones and secondary Fe-oxides or form rounded grain aggregates with siegenite around them (Fig.4.1.5.d-f). In chalcopyrite-rich samples, cobalt-pentlandite appears as sub-anhedral grains

(Fig.4.11.e-f, h), which can be replaced by magnetite (Fig.4.1.1.g), spindles (Fig.4.1.1.a). Cobalt-pentlandite formed sub-anhedral grains in chalcopyrite-bornite replacement samples (Fig.4.1.3.c).

ii. **Type II**. Cobalt pentlandite has lower Ni/Co ratios (0.16 and 0.24) than TypeI. The metal/S ratios are between 1.08 and 1.11, overlapping Type I. Fe/Ni ratio ranges from 1.09 to 2.21 and Fe/Co ratios from 0.17 to 0.48. Type II appears in chalcopyrite-rich and chalcopyrite-bornite replacement transgressive carbonatite samples. However, its primary host is the troilite-rich transgressive carbonatite sample, forming primarily euhedral-subhedral grains at troilite and chalcopyrite contacts (Fig.4.1.2.a,d, f).

iii. **Type III**: cobalt-rich pentlandites: The group is represented by two data points, one from a bornite-rich transgressive carbonatite and the other from a disseminated sulphide grain in phoscorite. The two data points have similar Co content (13.04 wt% and 12.85 wt%), significantly lower than the previous types (Table 5.11). The two data points are set apart from each other and the other types by their Ni and Fe contents (Fig.5.8.b), showing the highest Ni content (30.60 wt%) and the highest Fe content (29.17 wt%) among the different groups (Table 5.11).

Mahalanobis distance with p=0.95 confidence interval (fitted with ioGAS software) was used to test the validity of the group separations (Fig.5.9). Mahalanobis distance visualises the distance (number of the given standard deviation) of a given data point from the mean of the distribution. The results showed that although there are outliers, especially on the Co: Ni variogram, these are still close to the respective group. Ni/Co ratios can be highly variable in cobalt pentlandite.

The ideal metal/S ratio of the pentlandite is 1.125. In the case of Type I and II. cobalt pentlandites, and one of the Type III cobalt-rich pentlandites, the metal/S ratios are below the ideal values. The other Type III cobalt-rich pentlandite analysis showed higher metal/S ratio (Fig.5.8.c, Table 5.10). A siegenite rim developed around the cobalt-pentlandite in the bornite-rich transgressive carbonatite (Fig.4.1.5 d-f). The Ni/Co ratio is similar to the Type I cobalt pentlandite, but the S and Fe content separates the two phases (Fig.5.8.a-b). Alongside the result of this study, a range of published cobalt-pentlandite,

pentlandite, bravoite, siegenite and violarite composition data (Berg, 1927; Vokes, 1956; Petruk et al., 1969; Harris and Nickel, 1972; Merkle and Gruenewaldt, 1986; Grguric, 2002; Rudashevsky et al., 2004; Kovalev et al., 2014; Sciortino et al., 2015; Cavender, 2015; Baidya et al., 2018) was also depicted on the ternary diagrams (Fig. 5.8). These earlier works were not entirely consistent about the definition of the different Co-Fe-Ni-Sulphide phases, and cobalt pentlandite, cobaltian pentlandite and cobalt-rich pentlandite names were used seemingly arbitrarily. Since there is a textural overlap between compositional types I and II in the present dataset, it was decided that type III, with a different texture and lowest Co contents, will be called cobalt-rich pentlandite. As Fig.5.8.a-b shows, in some cases, published pentlandite compositions overlapped with published and present Phalaborwa cobalt-rich pentlandite compositions. The siegenite compositions of the present study are close to previously published siegenites (Fig.5.8.a-b).

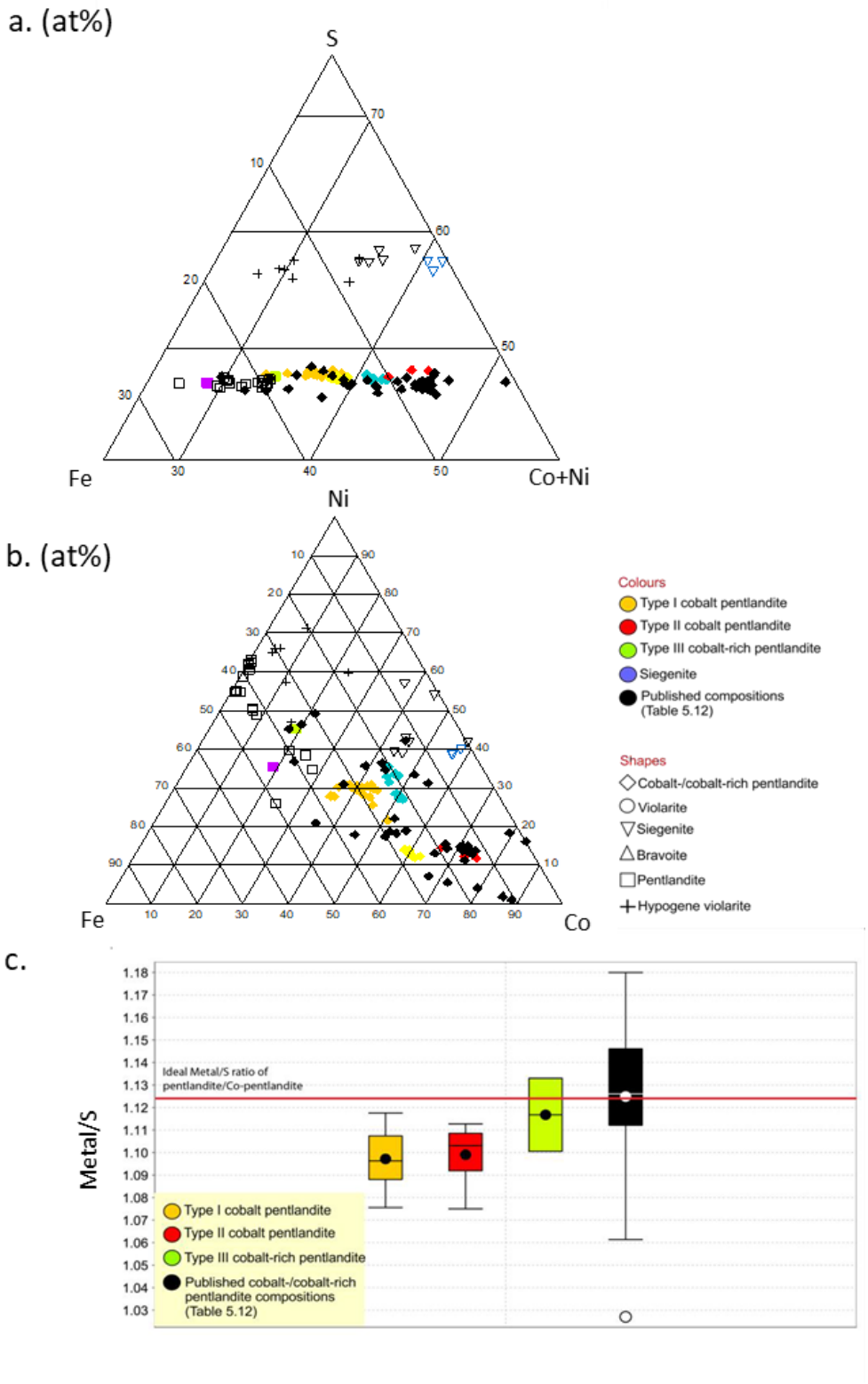

Figure. 5.8. a, b. Ternary diagrams show the major element ratios of the analysed Co- and Co-rich pentlandites, and the different types that were separated based on these ratios. C; Total metal/S ratios of the different type of Co and Co-rich pentlandite in the different Phalaborwa lithologies, compared with the total metal/S data from published literature (Bert, 1927; Vokes, 1956; Petruk et al., 1969; Harris and Nickel, 1972; Merkle and Gruenewaldt, 1986; Rudashevsky et al., 2004; Grguric, 2002; Sciortino et al. 2015; Cavender, 2015; Kovalev et al., 2014; Baidya et al., 2018). The ideal ratio is shown by the red line. The values of the box and whisker diagram are shown in the table below the diagram.

Table 5.10. Metal/S ratios of analysed cobalt-/cobalt-rich pentlandite types, depicted on the box-and-whisker diagrams above (Fig 5.8.b). The table shows the number of analysed chalcopyrite in each lithologies (n), the mean Metal/S ratios, the median of the lower half of the data set (Q1) and the median of the upper half of the dataset (Q3). The minimum (WMin) and maximum (WMax) values of the whiskers indicate the lowest and highest values of the dataset. Explanation of the statistics behind the Box and Whiskers diagrams is given in Chapter 3.

Cobalt/cobalt-rich pentlandite: **metal/S ratios**						
	n	**Mean**	**WMin**	**WMAx**	**Q1**	**Q3**
Type I.	37	1.097	1.076	1.118	1.088	1.107
Type II.	10	1.099	1.075	1.113	1.092	1.109
Type III.	2	1.117	1.101	1.133	1.101	1.133
Siegenite	3	0.761	0.749	0.772	0.749	0.771

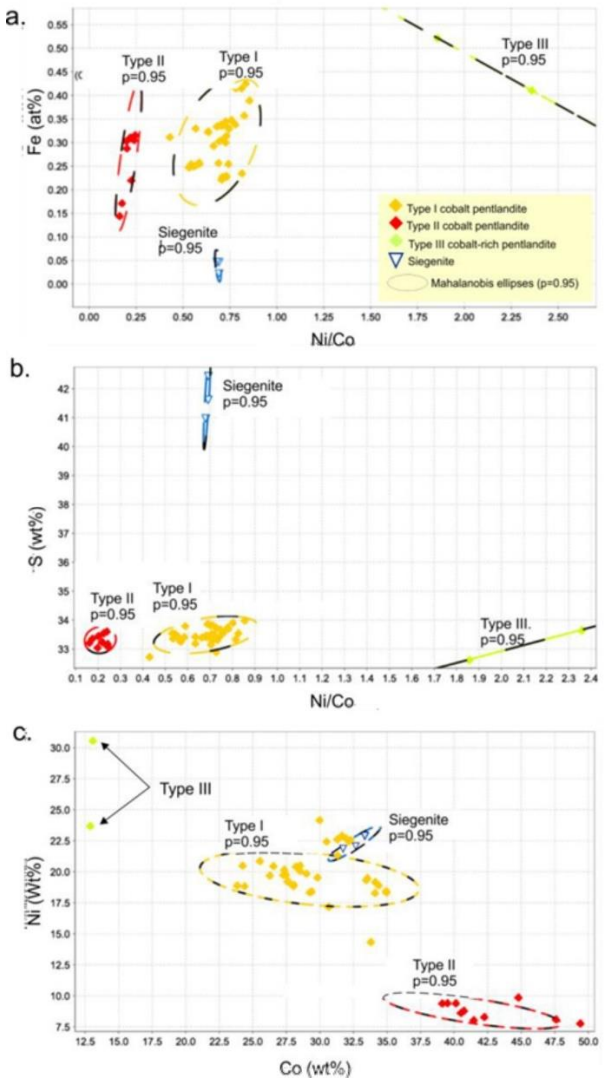

Figure 5.9. The diagram shows the Ni/Co vs F (a), Ni/Co vs S (b) and Ni vs Co (c) ratios (wt%) of the different cobalt and cobalt-rich pentlandite types and siegenite identified in the present study. The ellipses represent Mahalanobis distance (p=0.95) fitted with ioGas software with p=0.95 method (fitted with ioGAS software) was used to test the validity of the group separation

Table 5.11. Representative cobalt pentlandite and cobalt-rich pentlandite major element compositions (wt%) and calculated formulae in the different Phalaborwa lithologies, determined with EPMA. The calculated errors (ε) are presented with every element.

	Type I /Cobalt- and cobalt-rich pentlandite/													
	PTC3_C1	**ε**	**GC1611_B_5**	**ε**	**2/GC813/5_A2b_9**	**ε**	**Pa2a_4**	**ε**	**Pb2_ptl1**	**ε**	**Pb1_ptl9**	**ε**	**Pb1_ptl14**	**ε**
S (wt%)	33.76	1.10	33.30	1.83	32.74	1.15	33.71	1.80	33.54	1.13	33.51	1.1	33.44	1.14
Fe (wt%	18.94	1.71	18.48	2.79	17.46	1.76	23.25	2.47	14.25	2.01	12.75	2.1	14.27	2.00
Co (wt%)	26.50	0.94	30.61	0.01	33.76	0.81	24.34	0.02	34.06	0.86	31.89	0.9	30.46	0.90
Ni (wt%)	20.49	1.80	17.21	2.38	14.37	2.16	18.87	1.87	18.33	1.94	22.74	1.8	22.41	1.77
Ni/Co	0.77		0.56		0.43		0.78		0.54		0.71		0.74	
Fe/Co	0.71		0.60		0.52		0.96		0.42		0.40		0.47	
Fe/Ni	0.92		1.07		1.22		1.23		0.87		0.56		0.64	
Error cor. Total	99.69		99.70		98.57		100.24		100.19		100.89		100.58	
Lithology	TRC chp-bo replacement		TRC chp-bo replacement		Phoscorite		TRC chp rich		TRC chp-rich		TRC bo-rich		TRC bo-rich	
Texture	Late stage around mgt, alteration contacts		Inside chp -bo with shredded texture		In disseminated sulphide grain with complex Cu-Fe-S intergrowths		Eu-and subhedral grains in chp		An-subhedral in chp, near mgt		Core in siegenite rim		Core in siegenite	
	Calculated Formulae (Ideal formulae: $(Fe,Ni,Co)_9S_8$; Ideal Metal/S ratio: 1.125)													
S	8.17		8.08		8.07		8.11		8.11		8.06		8.07	
Fe	2.63		2.58		2.47		3.21		1.98		1.76		1.98	
Co	3.49		4.04		4.53		3.19		4.48		4.18		4.00	
Ni	2.71		2.28		1.93		2.48		2.42		2.99		2.95	
Total Metals	8.83		8.90		8.93		8.88		8.88		8.93		8.93	
Metal/S	1.08		1.10		1.11		1.10		1.10		1.11		1.11	

Abbreviations: bo: bornite, chp-: chalcopyrite, TRC: transgressive carbonatite

Table 5.11. Continuation: Representative cobalt pentlandite and cobalt-rich pentlandite major element compositions (wt%) and calculated formulae in the different Phalaborwa lithologies, determined with EPMA. The calculated errors (ε) are presented with every element.

	Type II /Cobalt pentlandite/						Type III /Cobalt-rich pentlandite/				Siegenite*			
	Pa15_A1	**ε**	**GC1610_A_7**	**ε**	**GC1611_B_3**	**ε**	**GC1811A_B_10**	**ε**	**2/GC813/5_A1**	**ε**	**Pb1_ptl1**	**ε**	**Pb1_ptl13**	**ε**
S (wt%)	33.37	1.09	33.26	1.86	33.56	1.85	33.66	1.84	32.63	1.14	41.63	1.01	42.45	0.99
Fe (wt%	9.62	2.31	17.39	2.83	12.34	3.34	22.98	2.54	29.17	1.38	2.63	4.27	1.28	5.49
Co (wt%)	47.55	0.70	40.46	0.01	44.75	0.01	13.04	0.01	12.85	1.23	31.75	0.88	33.34	0.86
Ni (wt%)	8.13	2.72	8.66	5.47	9.90	5.05	30.60	0.84	23.73	1.72	21.83	1.78	22.93	1.76
Ni/Co	0.17		0.21		0.22		2.35		1.85		0.69		0.69	
Fe/Co	0.20		0.43		0.28		1.76		2.27		0.08		0.04	
Fe/Ni	1.18		2.01		1.25		0.75		1.23		0.12		0.06	
Error cor. Total	98.68		99.80		100.66		100.37		98.52		95.21*		98.71 *	
Lithology	TRC chp-rich		TRC po-rich		TRC chp-bo repl		TRC bo-rich		Phoscorite		TRC bo-rich		TRC bo-rich	
Texture	Eu-and subhedral grains in chp		Anhedral at chp-po around contact		An-subhedral inside chp –bo with shredded texture		An-subhedral grain		In disseminated sulphide grain with complex Cu-Fe-S intergrowth		Siegenite-rim around co-ptl		Siegenite-rim co-ptl	
	Calculated Formulae (Ideal formulae: $(Fe,Ni,Co)_9S_8$; Ideal Metal/S ratio: 1.125)										Calculated formulae (Ideal formulae: $NiCo_2S_4$; Ideal Metal/S ratio: 0.75)			
S	8.19		8.07		8.10		8.09		7.97		3.97		4.00	
Fe	1.36		2.42		1.71		3.17		4.09		0.14		0.07	
Co	6.35		5.34		5.88		1.71		1.71		1.65		1.71	
Ni	1.09		1.15		1.31		4.02		3.17		1.14		1.18	
Total Metals	8.80		8.91		8.89		8.90		8.97		2.93		2.96	
Metal/S	1.08		1.10		1.10		1.10		1.13		0.74		0.74	

Abbreviations: bo: bornite, chp-: chalcopyrite, to: troilite, co-ptl: cobalt pentlandite, TRC: transgressive carbonatite

5.1.7 Sphalerite

Sphalerite was analysed in chalcopyrite-rich transgressive carbonatite, where it forms sphalerite stars and small grains (Fig.4.1.1. c, d), and in bornite-rich transgressive carbonatite, where it forms large anhedral grains (Fig.4.1.5.f). The small-grained sphalerites of the chalcopyrite-rich transgressive carbonatite provided Fe wt% data with significant error, as indicated in Table 5.13. The cause of the erroneous data is most possibly the small grain size and interference with the host chalcopyrite. The ideal sphalerite metal/S ratio is 1, and in both sample types, the ratios fall well below this (Fig.5.10). The sphalerite of the chalcopyrite-rich samples shows the lowest ratios of 0.93-0.95 while in the massive bornite, it is 0.95-0.97 (Table 5.13).

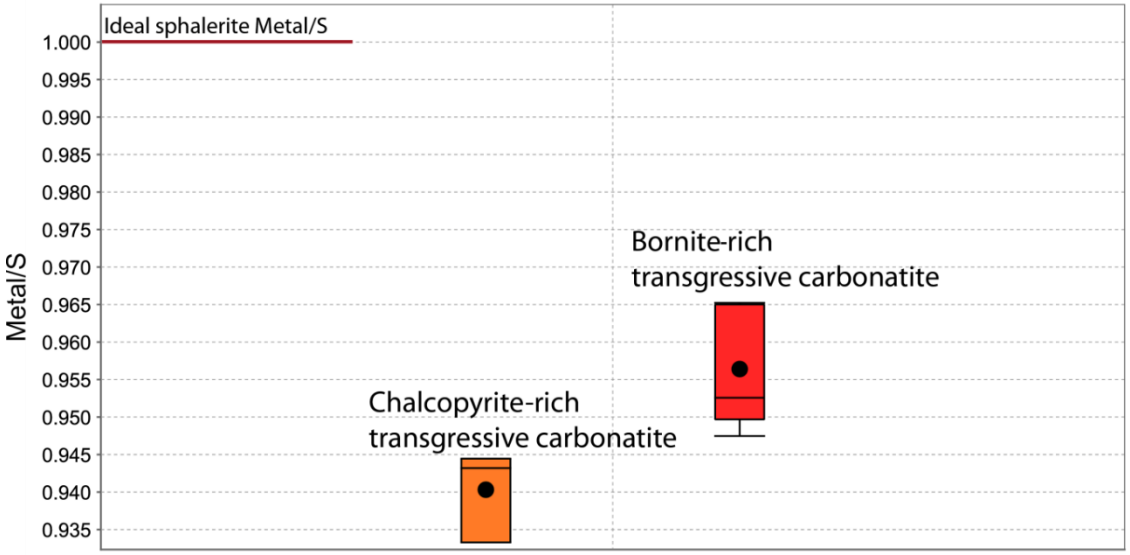

Figure 5.10. Total metal/S ratios of sphalerite in the different Phalaborwa lithologies. The ideal ratio is shown by the red line. The values of the box and whisker diagram are shown in the table below the diagram.

Table 5.12. Metal/S ratios of analysed sphalerite, depicted on the box-and-whisker diagrams above (Fig. 5.10.). The table shows the number of analysed chalcopyrite in each lithologies (n), the mean Metal/S ratios, the median of the lower half of the data set (Q1) and the median of the upper half of the dataset (Q3). The minimum (WMin) and maximum (WMax) values of the whiskers indicate the lowest and highest values of the dataset.

Sphalerite metal/S ratios						
	n	Mean	WMin	WMAx	Q1	Q3
TRC Chp-rich	3	0.940	0.933	0.944	0.933	0.944
TRC Bo-rich	5	0.956	0.947	0.965	0.950	0.965

Abbreviations: TRC Chp-rich: transgressive carbonatite sample with massive chalcopyrite; TRC Bo-rich: transgressive carbonatite sample with massive bornite

Table 5.13. Representative sphalerite major element compositions (wt%) and calculated formulae in the different Phalaborwa lithologies, determined with EPMA. The calculated errors (ε) are presented with every element.

Sphalerite	Pb2_sphl 1	3σ	Pb1_sphl 1	3σ	PA25_B1	3σ	GC1610_B _6	3σ
S (wt%)	34.09	1.09	33.87	1.08	33.98	1.75	33.93	1.79
Zn (wt%)	65.55	0.78	65.73	0.76	58.44	0.01	58.66	0.01
Fe (wt%)					6.95*	4.46	7.01 *	4.46
Error cor. Total	99.69		99.61		92.53 *		92.94 *	
Lithology	TRC chp-rich		TRC bo-rich		TRC chp-rich		TRC to-rich	
Texture	large anhedral grain		large anhedral grain		Myrmekitic/star sphalerite in massive chp		Small anhedral grain in massive chp-exsolution ~ 100 µm	
Calculated Formulae (Ideal Formulae: ZnS, Ideal Metal/S ratio: 1)								
S	1.03		1.02		1.02		1.02	
Zn	0.97		0.98		0.86		0.86	
Fe	0.01		0.01		0.12		0.12	
Total Metals	0.98		0.99		0.98		0.98	
Metal/S	0.95		0.97		0.96		0.96	

Abbreviations: bo: bornite, chp-: chalcopyrite, to: troilite, TRC: transgressive carbonatite (* data presented with high percentage error, not used in further calculations or on diagrams).

5.2. Discussion

5.2.1 Phase relations and formation temperatures based on the present study

5.2.1.1. Cu-Fe-S system

The primary sulphide phases of Phalaborwa belong to the Cu-Fe-S system. The phase relations of the system have been widely investigated (e.g., Sugaki et al., 1975; Grguric et al., 1998; Fleet, 2006). Experimental studies regarding the Cu-Fe-S, binary FeS – CuS, and the Fe- Co-Ni-S systems are discussed in Fleet (2006) and Bowles et al. (2011) and are compared in the following sections in order to contextualise the observations of this study. It is not the purpose of the present study to review the entirety of these experimental works, only to use the established temperature-dependent phase relations regarding the Phalaborwa sulphide evolution.

The highest temperatures ever suggested for the Phalaborwa sulphides was 700 °C for pyrrhotite by Mitchell and Krouse (1975), who suggested a magmatic origin for the pyrrhotite. Fe-S phase of the troilite-pyrrhotite series occur in the banded carbonatite primary magmatic sulphides and crosscutting carbonatite veins, as observed in this study. The banded carbonatite magma temperature was estimated at 675 °C (Verwoerd, 1967) and 524 °C (Dawson and Hinton, 2003). Based on magnetite-ilmenite thermo-oxy barometry, Milani et al. (2017a) determined re-equilibration temperatures between 590 °C and 400 °C, which agreed with the earlier results of Aldous (1980), who measured 400-500 °C on Phalaborwa magnetite-ilmenite pairs. In the Cu-Fe-S system, intermediate solid solution (iss) with sphalerite structure crystallises at 960 °C, extending into cubanite composition at 700 °C. When the system cools to 600 °C, the dominant phases include three solid solutions of high digenite-high bornite on the Cu-rich side and pyrrhotite in the Fe-rich part of the system with an iss field in between (Fleet, 2006). Chalcopyrite solid solution appears at 557 °C. This is the fitting upper-temperature range for the primary (magmatic where present) sulphides of the Phalaborwa carbonatites, considering the carbonatite magma formation temperature. Cu-Fe sulphide phase relations at 600 °C are depicted in Fig 5.11.a. with the relevant Phalaborwa sulphide compositions (chalcopyrite, bornite, cubanite, troilite) plotted. The Phalaborwa sulphide compositions partly overlap with the respective stoichiometric sulphide compositions indicated on the phase diagrams determined for 600 °C (Fig.5.11.a).

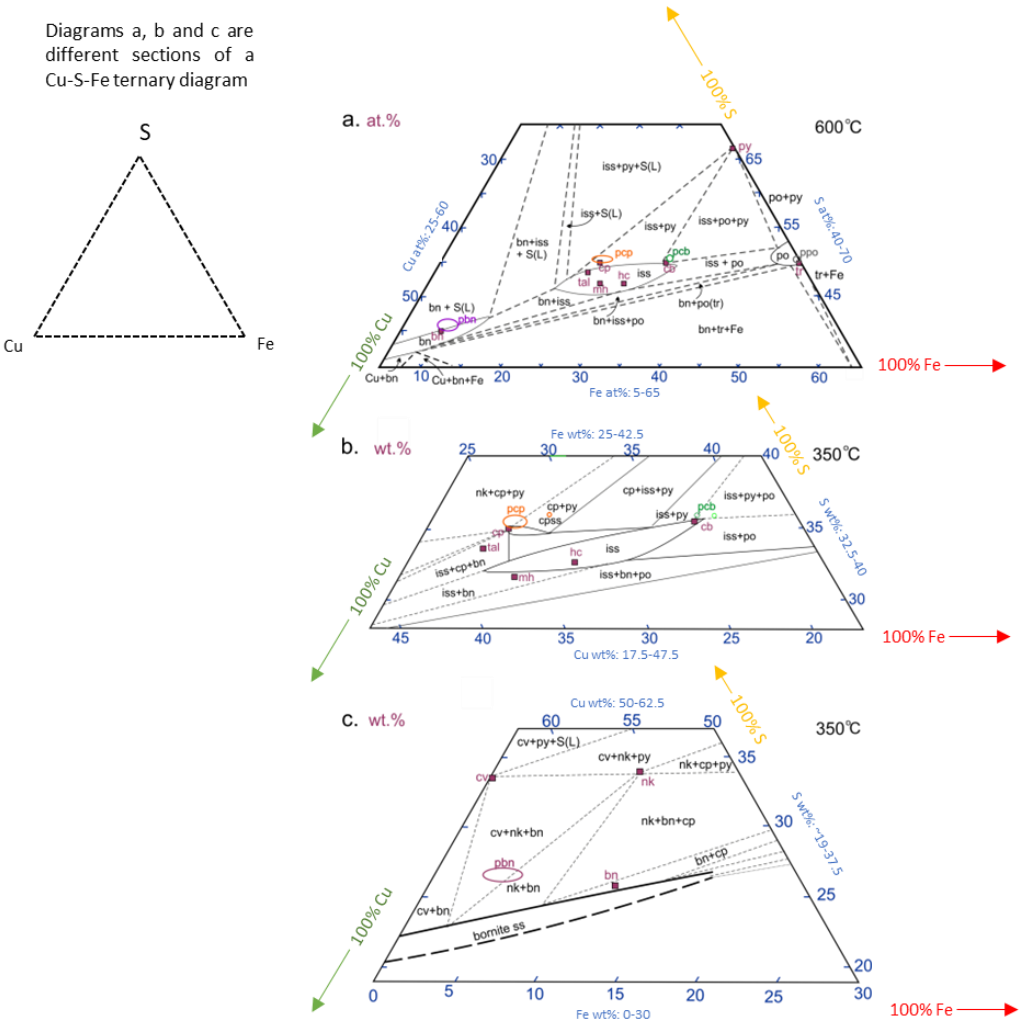

Figure 5.11. Phase relations in Cu-Fe-S system at 600 °C (a) and at 350°C where b: Fe-rich side and c: Cu-rich side. The Phalaborwa sulphide compositions that were plotted on the phasediagrams include chalcopyrite (pcp), cubanite (pcb), troilite (ppo) and bornite (pbn). Squares depict stoichiometric compositions. Abbreviations of the diagrams: iss: intermediate solid solution, cp: chalcopyrite, po: pyrrhotite, to: troilite, py: pyrite, bn: bornite, cv: covellite, nk: nukundamite, tal:talnakhite, mh: mooihekite, hc: haycockite, ss: solid solution: S: sulphur, L: liquid. After Bowles et al., 2011 who reworked a: after Cabri, 1973 and b-c: after Sugaki et al., 1975)

The Phalaborwa troilite plots are very close to the ideal troilite composition, as expected from the results presented in Fig.5.7. The Phalaborwa cubanites are also close to the stoichiometric cubanite of the phase diagram. Chalcopyrite and bornite have a wider compositional range that reaches into the more S-rich phase fields.

Experiments at low temperatures of 300-350 °C under hydrothermal conditions were carried out by Sugaki et al. (1975). They showed that the iss separates into tetragonal chalcopyrite and a less extensive iss field at low temperatures. The tie line change from iss-pyrite to chalcopyrite-pyrrhotite occurs at 328 +/- 5 °C. This may suggest that equilibrium textures between chalcopyrite and pyrrhotite can

indicate that the system cooled to at least 328 °C. This is the most relevant in the troilite-rich transgressive carbonatite samples (Fig.4.1.2) and the carbonate vein in glimmerite (Fig.4.1.10). These samples may represent low-temperature sulphide assemblages. Especially notable is the troilite-rich sample (GC1610), which also contains Type II. (low-Ni) cobalt-pentlandite grains formed at the contact of troilite/pyrrhotite and chalcopyrite. The experimental studies summarised above show that chalcopyrite is stable up to 557 °C. Chalcopyrite and pyrrhotite equilibrium textures indicate that the temperature cooled to at least 328 +/- 5 °C, but chalcopyrite-pyrrhotite-cubanite equilibrium textures were observed down to 300 °C (Sugaki et al., 1975).

In lower temperature systems, the Phalaborwa bornites did not overlap with the stoichiometric bornite composition but between the covellite+nukundamite+bornite and nukundamite+bornite field, suggesting a possible mixed composition. The bornite composition also overlapped with the previously described X-bornite composition (Fig.5.2.a). The experiments (<400 °C) of Yund and Kullerud (1966) suggested that X-bornite forms directly from low-temperature solutions with high S-activity or by reactions of such solutions with tetragonal bornite, and it is an indicator of a low-temperature process with aqueous solutions. Due to the wide compositional variation of the analysed bornites, the values on a phase diagram may lead to incorrect conclusions. The observed bornite textures in this study included lamellae in massive chalcopyrite and shredded texture. The former suggests unmixing while the latter replacement (Section 4.2.3).

5.2.1.2 Cu-S system

The present study identified (optically) digenite and chalcocite, but the chemical compositions vary in a wide range (Fig.5.2). Djurleite, anilite, chalcocite and yarrowite were commonly found at Phalaborwa (e.g., Rudashevsky et al., 2004), and fall into the low-temperature region of the Cu-S phase diagram (Fig.5.12). Anilite marks the lowest temperature with a stability field extending to a maximum of 76 °C. Cu-S phases, which might indicate higher temperatures but overlap with low-temperature ones, include covellite (Tmax= 503 °C) and high-digenite (Tmax= 1105 °C). Digenite is only stable above 76 °C; anilite, djurleite and low-

temperature chalcocite are stable below this. Lamellar digenite (optically digenite, but mixed composition probably due to further alteration) occurs in massive bornite at Phalaborwa. Grguric et al. (1998) showed that bornite and digenite form a complete solid solution above ~ 300 ºC. However, most economically significant deposits containing bornite and digenite were formed by hydrothermal processes between the temperatures of 150-300 ºC. This temperature range fits Phalaborwa as well. Both phases commonly occur in many deposits, from high-temperature magmatic deposits to ores precipitated from meteoric waters at near-ambient temperatures.

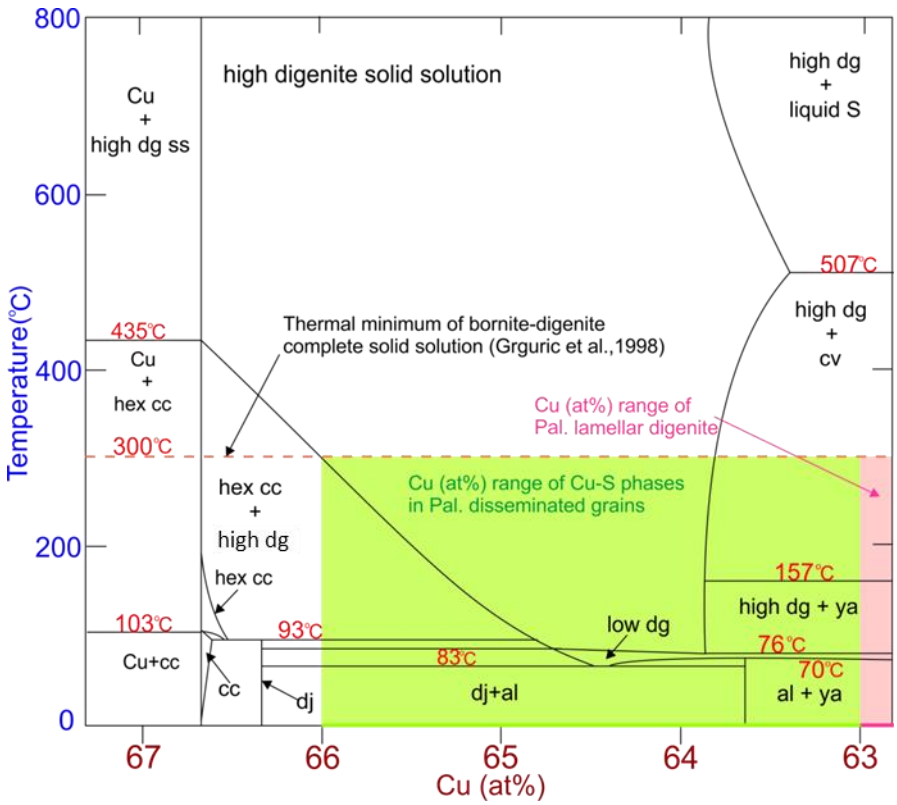

Figure 5.12. Partial temperature-composition phase diagram for binary Cu-S system centred on the field of high digenite solid solution. The diagram depicts the Cu-S phase stability fields as the function of temperature and Cu proportion (at%) (from Fleet, 2006) The Cu (at%) proportion range of the Phalaborwa (Pal) lamellar digenite and Cu-S phases in disseminated grains are shown in the shaded areas. The dashed red line indicates the thermal minimum if the bornite-digenite complete solid solution (Grguric et al., 199 8). Abbreviations: dg: digenite, ss: solid solution, hex: hexagonal, S: sulphur, cc: chalcocite, cv: covellite, dj: djurleite, ya: yarrowite, al: allinite.

5.2.1.3 Co-Ni-S system

Cobalt pentlandite in the Phalaborwa massive (primary) chalcopyrite has primarily (eu)- subhedral crystals with well-formed crystal faces, suggesting an

early formation (Fig.4.1.1.e- h). Some of these grains were resorbed, suggesting disequilibrium decomposition of a residual grain (Fig.4.1.1.g). Pentlandite was observed in other studies (Hanekom et al., 1965; Rudashevsky et al., 2004) and was interpreted as a primary phase. The presence of abundant cobalt pentlandite is characteristic of assemblages where the amount of chalcopyrite considerably exceeds that of the conventional pentlandite-pyrrhotite and pyrrhotite assemblages (Vaasjoki et al., 1974). This latter observation is especially relevant in the case of Phalaborwa.

Based on the phase relations presented by Craig and Kullerud (1969), pentlandite forms at 610 ^{o}C. At 575 ^{o}C, the formation of a tie line between chalcopyrite and pentlandite, marking the temperature range of their stable coexistence. Later, Kitakaze et al. (2016) established three ways pentlandite can form: The first process takes place between 615 ^{o}C and 584 ^{o}C, and it is a transition from the high-form pentlandite, crystallised directly from the sulphide liquid via a series of eutectic and peritectic reactions. The second process is formation via exsolution from S-rich, high-form pentlandite solid solution during decreasing temperatures between 625 ^{o}C and 503 ^{o}C, and finally, pentlandite formation via exsolution from the metal-rich part of the mss below 625 ^{o}C. In contrast, Peregoedova and Ohnenstetter (2002) found that direct crystallisation of pentlandite from Cu-bearing sulphide melt is considered unlikely as pentlandite was not stable in the high-temperature assemblage of their experiments and suggested that in Cu-containing sulphide associations with pentlandite appear at subsolidus temperatures lower than 760 ^{o}C.

Complete solid solution between pentlandite and cobalt pentlandite in the system Fe-Ni-Co- S occurs below 610 ^{o}C between the end member compositions of $Fe_{4.5}Ni_{4.5}S_8$ and Co_9S_8 (e.g., Kitakaze and Sugaki, 2004). Kaneda et al. (1986) also observed that in natural occurrences, the Co content of pentlandite varies from zero to nearly Co_9S_8 composition. Complete solid solution was observed between compositions $(Fe, Ni)_{9\pm x}S_8$ and $Co_{9\pm x}S_8$ in the 600-300 ^{o}C temperature range. The study presumed that pentlandite solid solution decomposes at 200 ^{o}C into two fields towards $(Fe, Ni)_9S_8$ and Co_9S_8 members.

The studies above showed the presence of a solid solution between pentlandite and cobalt pentlandite and that the presence of Co extends the stability field of pentlandite. However, considering the Phalaborwa assemblage, this will not

significantly affect our estimation of its formation temperature. Based on its appearance, cobalt pentlandite is a primary phase in the primary chalcopyrite, but their petrogenetic relationship is a question. Although a complete solid solution between haezelwoodite and iss in the system Fe-Ni-Cu-S at 760 ^{o}C was shown, pentlandite is unlikely to crystallise from a Cu-bearing liquid directly (Peregoedova and Ohnenstetter, 2002). The chalcopyrite crystallised from the iss while pentlandite is the product of the mss. Many of the eu- and subhedral cobalt pentlandite grains in the massive chalcopyrite show signs of variously progressed alteration. Since the chalcopyrite and the surrounding gangue minerals do not show signs of alteration, the grains may display the result of re-equilibration. Hanekom et al. (1965) also noted the presence of pentlandite as residual grains. If the cobalt pentlandite is not in equilibrium with the host chalcopyrite, then that would suggest an earlier formation of the phase. In samples where this type of cobalt pentlandite was present, cubanite lamellae or pyrrhotite were not found.

On the other hand, in samples where the two latter were present, cobalt pentlandite had different appearances. The former samples may represent a higher temperature state of the system. The cobalt-pentlandite would indicate a maximum temperature around 600 ^{o}C and, in the state of re-equilibration with chalcopyrite, exsolving from the iss between around 550 ^{o}C and 590 ^{o}C. The samples with exsolved chalcopyrite, cubanite-lamellae and pyrrhotite grains can represent the slightly cooled stage of the system. Pyrrhotite can also occur at high temperatures. Hanekom et al. (1965) estimated the Phalaborwa sulphide formation temperature at around 600 ^{o}C. The pyrrhotite low-temperature coexistence with chalcopyrite under hydrothermal conditions was marked at 328 +/- 5 ^{o}C.

5.2.1.4 Cu-Fe-Zn system

The evolution of the Cu-Fe-Zn-S system is also relevant in the case of Phalaborwa, as sphalerite is a prevalent phase in the primary chalcopyrite, its texture suggesting exsolution origin and thus that Zn is present in the primary solid solution. Sphalerite stars, also observed in the Phalaborwa samples, were formed via exsolution from Zn-bearing iss (Sugaki et al., 1987). Although the Cu-Fe-S system was described in the previous section, the study of Lusk and Calder (2004) suggests that under 550 ^{o}C, sphalerite has little effect on the phase

relations of the Cu-Fe-S and Fe-S systems. The experiments showed that chalcopyrite in a Cu-Fe-S system has mainly constant compositions between 453 and 251 ºC. However, at the same temperature in a Cu-Fe-Zn-S system, chalcopyrite shows small but systematic compositional changes by decreasing Zn concentration upon cooling. The Zn concentration is decreasing mainly due to the Cu substitution, which increases during cooling (Lusk and Calder, 2004). The solubility of Zn in chalcopyrite was found to be up to 1.1 wt% between 250 and 535 ºC, decreasing with decreasing S-fugacity (Lusk and Calder, 2004). The massive chalcopyrite of the transgressive carbonatite showed the highest Zn (in solid solution), which was 559 ppm (0.056 wt%). Bornite is generally more depleted in Zn, with the massive bornite containing Zn in solid solution up to only 19 ppm.

Phase relations in the Cu-Fe-Bi-S system are relevant to Phalaborwa, as both previous and present studies found Bi-containing phases, including native bismuth, parkerite and wittichenite. Experiments carried out under hydrothermal conditions (300 ºC) produced stable assemblages, including chalcopyrite-wittichenite, bornite-wittichenite and chalcopyrite-bornite-wittichenite (Sugaki et al.,1981). None of these assemblages was observed at the higher temperature (420 ºC) experiments. Sugaki et al. (1981) suggested that sulphur fugacity might have a significant effect on the behaviour of Bi. Native Bi did not appear in any of the assemblages; however, earlier experimental works carried out at similar temperatures but at lower S fugacity reported the presence of native Bi in every assemblage, suggesting that high S fugacity is unsuitable for native Bi formation (Sugaki et al., 1981). Both the present and all previous studies on Phalaborwa reported the presence of native Bi. Oen and Kieft (1976) reported Ag-bearing wittichenite-chalcopyrite-bornite intergrowths in the sulphide mineralisation of the Mangulado pegmatite (Portugal). They describe wittichenite as veinlets and blebs that often create a rim around various inclusions, including, for example, native Bi and Ag sulphides and tellurides. This appearance also occurs in the Phalaborwa sulphides. According to Oen and Kieft (1976), wittichenite and chalcopyrite segregate from bornite solid solution. After further recrystallisation and accumulation, wittichenite forms veins, blebs and the rim texture mentioned above, and chalcopyrite also segregates into larger blebs, veinlets and rims around the earlier wittichenite. A similar appearance of chalcopyrite was also observed in the massive bornite samples of Phalaborwa, further supporting the

conclusion of the present study that chalcopyrite formed in different stages. In the Mangaludo bornite, 0.2 wt% Bi and 0.2 wt% Ag were detected, while the Ag content of wittichenite changed between 0.2 and 1.1 wt%. Oen and Kieft (1976) concluded that the intergrowths formed by unmixing high-temperature Ag and Bi-bearing bornite solid solution cooling below the melting point of native Bi, which is 271 ºC. The temperature range fits well with the Phalaborwa low-T Cu-S assemblages. Furthermore, the observation of Sugaki et al. (1981) that high S-fugacity is unsuitable for native Bi concurs with decreasing S-fugacity regarding the large sphalerite grain-massive bornite association and the features indicate a progressive decrease in temperature and S-fugacity.

5.3. Summary and conclusions

Based on the phase relations of the sulphide mineralisation, the upper range of the Phalaborwa sulphide mineralisation falls between 700 ºC and 557 ºC. The upper boundary marks cubanite and pyrrhotite separation from the iss and the lower the appearance of chalcopyrite and primary sphalerite unmixed from it. Pentlandite may form at a slightly higher temperature (<760 ºC), but a complete solid solution between pentlandite and cobalt-pentlanite occurs below 610 ºC (Peregoedova and Ohnenstetter, 2002; Kitakaze and Sugaki, 2004). Bornite+iss and bornite + S(liquid) are also present in this temperature range. Although the bornite in transgressive carbonatite was identified as a chalcopyrite-replacement phase, the presence of primary bornite cannot be ruled out. Chalcopyrite-bornite sulphide grains in the banded carbonatite have a different habit from the mineralisation in the transgressive carbonatite and likely indicate a magmatic assemblage. This concurs with Bolhar et al. (2020), who showed that most of their banded carbonatite bornite samples produced δ^{34}S-isotope compositions in the Mantle range. Accessory parkerite forms above 400 ºC (Fleet, 2006 and references therein). A digenite-bornite solid solution exists above 300 ºC. Therefore, the unmixed phases indicate temperatures below this (Fleet, 2006). At Phalaborwa, two possible bornite-digenite generations can occur depending on the presence of magmatic and replacement bornite. White chalcocite was observed in the transgressive carbonatite massive bornite forming myrmekite-resembling texture. Although the temperature range of hexagonal chalcocite is 435-93 ºC, the maximum temperature for the Phalaborwa phases is ~300 ºC,

given the exsolution from bornite. The bornite-wittichenite assemblage was stable under 300 ºC, while native Ag and Bi were stable under ~271 ºC (Oen and Kieft, 1976). This is also the maximum temperature found when the maximum Cu (at%) content was plotted on the Cu-S phase diagram (Figure 5.12). The covellite stability thermal minimum is ~157 ºC. The very low-temperature Phalaborwa phases include yarrowite (157-0 ºC), chalcocite (93-0 ºC), djurleite (83-0 ºC) and anilite (70-0 ºC). These low-temperature phases were reported by Rudashevsky et al. (2004), and apart from high-temperature hexagonal chalcocite and low-temperature orthorhombic chalcocite, the compositions were identified in the mixed Cu-S phases of this study. The revisited sulphide petrogenetic sequence, including the temperature changes, is presented in Figure 5.1.3.

The upper-temperature range of the sulphide formation coincides with the estimated carbonatite magma formation temperature of 675 ºC. As described in Section 4.4, certain sulphide textures may indicate that the mineralisation or a part of it was emplaced in the still plastic carbonatite magma, and the similar temperatures of the two systems may promote this. However, later stage, magmatic-hydrothermal or hydrothermal phases are also present, considering the bornite replacement in chalcopyrite and the general more altered state of these samples compared to the chalcopyrite-rich transgressive carbonatites. The conclusion of the textural studies of the banded carbonatite sulphides was that these sulphides are magmatic. The high-temperature range described above applies to these sulphides as well. Bolhar et al. (2020) showed that the $\delta^{34}S$-isotope compositions in the transgressive carbonatite sulphides vary widely, covering mantle and atmospheric values. In contrast, the S-isotope compositions in banded carbonatite showed mostly mantle origin and differed from the transgressive carbonatite. The previous S-isotope and the present textural and phase relation studies support each other. The revisited petrogenetic sequence is presented in Fig. 5.13. Trace element studies of the Phalaborwa sulphides will be presented in Chapter 6 to characterise the system further.

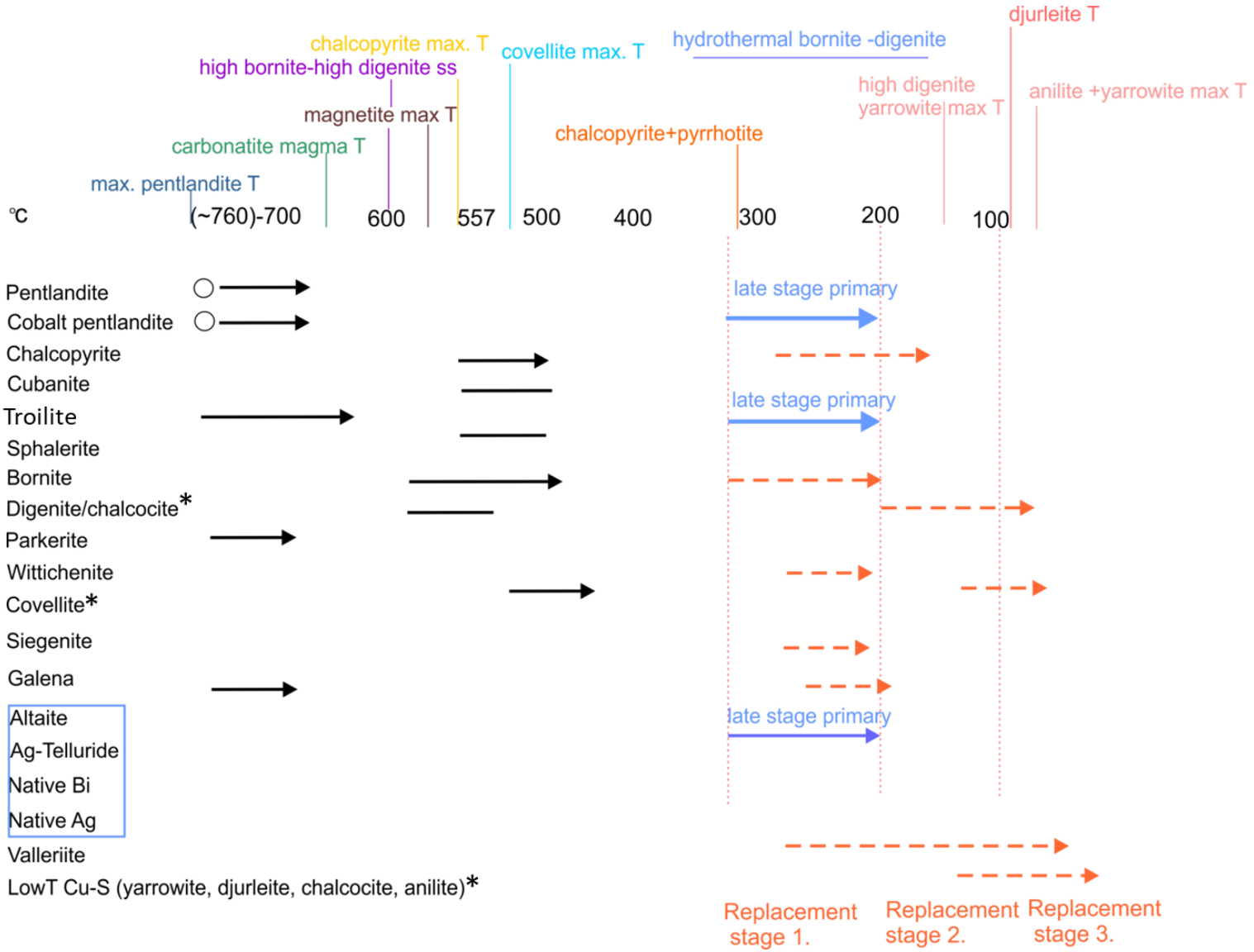

Figure 5.13. Revisited paragenetic sequence of the Phalaborwa sulphides including the temperature ranges discussed in this chapter. Black arrows: primary sulphides in the carbonatites and phoscorite. Red dashed arrows: replacement phases. Blue arrows: primary low-T phases. Blue frame: accessory phases. *: Nonstoichiometric phases

Chapter 6: Trace elements characteristics of the Phalaborwa sulphides

6.1 Introduction

The present study investigated the PGE (Os, Ir, Ru, Rh, Pt, Pd), Ag, Au, metalloid (As, Se, Sb, Te), Cd and Bi characteristics of sulphides from transgressive and banded carbonatites, phoscorite, late-stage carbonate vein in diopside glimmerite and from olivine glimmerite of the Phalaborwa complex. PGM from the banded and transgressive carbonatite were previously investigated by e.g., Rudashevsky et al. (2004) (Section 2.2.2.5). The study was designed to detect and analyse PGM and noble metals, and used heavy mineral concentrates prepared with density separation. The results from the lithologies were not presented separately. More recently Bolhar et al. (2020) presented S isotope and Le Bras et al. (2021) presented Cu-sulphide trace element and results from Phalaborwa.

The present study aimed to identify differences between the lithologies and link potential characteristic trace element signatures to lithologies and to different stages of sulphide formation and to identify potential secondary PGM remobilisation by analysing the sulphide assemblages (Cu-S, Cu-Fe-S, Fe-S, Ni-Co-S, Zn-S) in the different Phalaborwa lithologies. This required the samples to remain intact and the analyses to be carried out in situ. For this purpose, LA-ICPMS line analysis was used instead of spot-analysis. The line analysis was designed to find PGM in the sulphide phases alongside of giving information about the trace element composition of the sulphide assemblages of the different lithologies. The majority of these microinclusions were not identified during the SEM studies due to their small size. Due to the nature of the analysis, microinclusions and occasionally contacts between two sulphide phases were analysed which is reflected in the results. Analyses of “clear” sulphide phases resulted in stoichiometric (stoich) compositional data, while “mixed analyses” although were carried out on optically clear areas, produced nonstoichiometric compositions (nonstoich). The clear and mixed analyses were separated from each other, clearly indicated where a phase is stoichiometric or not. Where the line analysis produced data not suitable to distinguish a sulphide mineral but a sulphide assemblage, the phrases Mixed Cu>Fe (Cu-rich Cu-Fe sulphide), Mixed Fe>Cu (Fe-rich Fe-Cu sulphide) and lamellar Cu-S were used.

The sulphide trace element characteristics of the different lithologies were studied by using the sulphide assemblages of each lithologies where the assemblage includes both stoichiometric sulphides and nonstoichiometric sulphide phases (boundary and microinclusion trace element data).

The chapter will review the PGE behaviour during magmatic, hydrothermal and supergene processes in Sections 6.1.1-6.1.2.

The present study also investigates the S/Se ratios and its relation to PGE in the Phalaborwa sulphide phases. The S/Se ratio by itself and combined with the total PGE and Pt+Pd and ^{33}S isotope signatures of the sulphide phases is a well-established tool in the investigation of their origin and the later processes they were subjected to. The method was described in detail in Queffurus and Barnes (2015) and Smith et al. (2016) and will be briefly summarised in Section 6.1.3. The selected mantle rocks for comparison sampled SCLM of various types and ages, belonging to different cratons. S/Se ratios of primitive mantle calculated by O'Neill (1991), McDonough and Sun (1995) and Palme and O'Neill (2003). To represent the Proterozoic mantle composition before the large-scale mantle metasomatism event during the Mesozoic, mantle rocks of Proterozoic age were used. S/Se ratio of whole rock mantle peridotites of the Muscox Layered Intrusion (chromium-rich to feldspathic compositions) were presented by Mackie et al. (2009) and were used in the present work. The age of these samples are Meso-Proterozoic (~1.27 Ga). S/Se ratios of whole rock Proterozoic pyroxenite from the Merensky Reef (Kaapvaal Craton) were presented by Hutchinson et al. (2015). S/Se ratios of Proterozoic Kimberlites from the Dharwar Craton were presented by Paton et al. (2009). Sulphide S/Se ratios of eclogite xenoliths sampled by the Cretaceous Roberts Victor Kimberlite in the Kaapvaal craton (Hughes et al., 2021). Peridotite xenolith of Quaternary age from the Central Asian Foldbelt by Wang and Becker (2013). The information listed above including the S/Se ratios of the different mantle-derived samples are listed in Table 6.1.

Table 6.1. The list of the published mantle S/Se ratio ranges used in the study.

Lithology	Location	Age	Sample	S/Se ppm	Source
Kimberlite	Dharwar Craton	Proterozoic	Whole rock	400-6000	Paton et al. (2009)
Cr-rich peridotite	Muskox Layered Intrusion	Proterozoic	Whole rock	5000-7350	Mackie et al. (2009)
Peridotite	Muskox Layered Intrusion	Proterozoic	Whole rock	666-1500	Mackie et al. (2009)
Feldsphatic peridotite	Muskox Layered Intrusion	Proterozoic	Whole rock	2166-11143	Mackie et al. (2009)
Pyroxenite	Kaapvaal, Platreef	Proterozoic	Whole rock	1103-1694	Hutchinson et al. (2015)
Eclogite	Kaapvaal Roberts Victor kimberlite	Cretaceous	Sulphides mms	4394-13678	Hughes et al. (2021)
Peridotite xenolith	Central Asian Foldbelt	Quaternary	Whole rock	479-4065	Wang and Becker (2013)
Primitive mantle 1				2535	Palme and O'Neill(2003).
Primitive mantle 2				3066	McDonough and Sun (1995)
Average mantle domain				2850-4350	Eckstrand and Hulbert (1987)

6.1.1 Review of PGE and metalloid behaviour in magmatic systems

PGE occur either as solid solution in the base metal sulphides or as distinct phases as metals, alloys or particles formed with other metals (e.g., Bi), chalcogenes (S, Se, Te) and semimetals (As, Sb). At high temperature (>1200 ^{o}C) PGE has a selective chemical preference, where IPGE+Rh tend to form metal-metal, metal-S and metal-AsS complexes while Pt and Pd form semi-metal complexes (Helmy and Bragagni, 2017). A common pattern of PGE distribution between PGM and BMS was observed by multiple studies (e.g., Holwell and McDonald, 2010; Prichard et al., 2013) which showed that Os, Ir, Ru and Rh concentrate in pentlandite and pyrrhotite, Pd in pentlandite while Pt and Au tend to form discrete minerals instead of partitioning into BMS.

The general process of PGE partitioning between the mss and sulphide liquid and its further behaviour during early magmatic processes is well established. As Holwell and McDonald (2010) summarise, at 1000 ^{o}C the IPGE+Rh partitions into mss while Pt, Pd and Au together with semi-metals go into the Cu-rich residual liquid, formed after mss crystallisation, and upon cooling crystallises iss around 900 ^{o}C. Platinum, Pd and Au are incompatible in iss and concentrates in an immiscible semi-metal rich melt, which remains liquid after the iss crystallised. If the system has a high Pd level at this point, it can partition

into mss. At low temperature of 650-200 ^{o}C, the mss recrystallises into pentlandite and pyrrhotite, with IPGE (most commonly Rh and Pd) in their solid solution. The iss also recrystallises to chalcopyrite with no PGE in solid solution. Ballhaus and Ulmer (1995) also showed that PGE dissolved in mss at high temperature would eventually be exsolved to form discrete phases upon cooling as the mss recrystallises to $Fe_{1-x}S$ and pentlandite. Based on these results the work concluded that the association between base metal sulphides and PGM is a low- temperature phenomenon, for example, even as low as 400 ^{o}C $Fe_{1-x}S$ would accept up to 2200 ppm Pd in solid solution. It was suggested that all the PGE content of the base metal sulphides would be released by the time the closure temperature is reached (Ballhaus and Ulmer, 1995). At low temperature, the semimetal-rich liquid crystallises resulting in the formation of discrete PGMs around the margins of sulphide blebs and in small veinlets emplaced in the surrounding silicates (Holwell and McDonald, 2010).

Experiments carried out at high temperature (<1000 ^{o}C) showed that PGE behaviour could be further influenced by the base metal proportions in the system, temperature and sulphur fugacity or by the presence of other trace elements (e.g., Stone and Fleet, 1991; Fleet et al., 1993; Peregoedova and Ohnenstetter, 2002). Peregoedova and Ohnenstetter (2002) found that in liquid sulphide systems near-constant S content, the formation of the different PGM phases is controlled by the starting proportions of the base metals (Cu, Fe, Ni), and in particular Pt forms distinct phases as the Ni and Cu increases. Fleet and Stone (1991) showed that the affinity of Pd changes based on its base metal association while Fleet at al. (1993) found that the presence of As, Te and Bi might cause the Pd and Pt to divert in affinity, where Pt follow the elements above while Pd remains in the sulphide liquid. The fS_2 dependence of Pt and Pd partitioning was observed by Fleet at al. (1993) while that of Rh by Ballhaus et al. (2001) and Peregoedova and Ohnenstetter (2002). Ballhaus et al. (2001) found that although experimental studies show that PGEs are sensitive to the fractionation processes, the experimental results do not correlate well with the naturally observed PGE signatures of Sudbury, where sulphide fractionation was observed. The work suggested that because of the subsolidus PGE redistribution, it is not possible to match experimental PGE distribution data to PGE ore ratios.

Several studies showed the profound effect of semi-metal presence on the PGE partitioning (e.g., Holwell et al., 2015; Helmy et al., 2013a; Helmy et al., 2013b; Helmy and Bragagni, 2017). Platinum and palladium form complexes with Se, Te, As, Sb and Bi. Arsenides form complexes, especially with Pt (e.g., Helmy et al., 2013 a, b). Sperrylite ($PtAs_2$) was also observed at Phalaborwa. Pt-arsenide complex solubility is considerably less than Pt metals, hydroxide and bisulfide complexes. Selenides and tellurides are formed with HSe^-, SeO_3^{2-}, HTe^-, and TeO_3^{2-} ligands. HSe^-, HTe^- might be important but SeO_3^{2-} and TeO_3^{2-} are unlikely to play an important role in Pt and Pd transport. The presence of tellurides and selenides decrease the solubility of Pt-and Pd- chloride and hydroxide complexes by several orders of magnitude and together with As, generally decrease Pt and Pd mobility. Based on the poor solubility of As, Sb, Te, Bi and Sn in mss, Helmy et al. (2013a) suggested that instead of exsolving from the mss together with PGE, semi-metals and Bi become enriched in the late- stage sulphide melt together with PGE. When phase saturation is reached, they precipitate as arsenides, antimonides, tellurides, bismutotellurides and stannides. PGE-ligand associations at high temperature in magmatic sulphides form stable clusters and molecules well before the respective PGE minerals become stable (Helmy et al., 2013a; b). The presence of these nanoparticles can provide a flat TRA curve suggesting a solid solution phase as it was observed in the case of As by Helmy et al. (2013b) and Holwell et al. (2015) suggested the same in the case of Te. Partitioning of Se, As, Sb, Te and Bi between mss and sulphide liquid was investigated by Helmy at al. (2010) at 960 ^oC. They found that all of the elements are variably incompatible in mss, with Se partitioning into the sulphide systems in anion form, Sb, Te, and Bi occur either as cations or neutral metallic phases, while As can be present as either. As it was mentioned above in regard of PGE behaviour, during sulphide evolution the Te, Bi, As and Sb generally fractionate into immiscible telluride, bismuthide, arsenide and antimonide melts upon cooling and crystallisation of the sulphide liquid, scavenging noble metals in the process more effectively than the sulphide melt (e.g., Holwell et al., 2015). The metalloids in the magmas can derive from the assimilation of crustal rocks (e.g., Hutchinson and Kinnaird, 2005).

6.1.2 Review of PGE-transport and enrichment by secondary processes

Apart from magmatic processes PGM remobilisation and formation by hydrothermal fluids is also important as it was recognised in the largest PGE ore deposits including Sudbury and Bushveld. The volatility of PGE was investigated by Wood (1987) between temperatures 527-1327 ^{o}C. The study found that only Pd is significantly volatile as metal while PGE oxides are extremely volatile at atmospheric oxygen fugacity. The only PGE with significant volatility at magmatic conditions (fO_2, T> ~1127 ^{o}C) are Os and Ru. Pd and Ru are more volatile as chlorides than as oxides and vapour transport of more volatile PGE as chlorides can play a significant role in mafic magmatic complexes. However, Wood (1987) notes that under the conditions where PGE are the most volatile, Fe, Ni and Cu are significantly more so, suggesting that chloride transport alone is not sufficient enough to create PGE and Cu enrichment over Ni and Fe. Platinum and Pd behaviour in hydrothermal solutions between 25-300 ^{o}C was described by Mountain and Wood (1988). The soft acid character of Pt^{2+} and Pd^{2+} causes them to form complexes preferentially with soft ligands, a character that is also true in the case of Au, Ag, Hg and Cu. The most likely ligands are OH^-, HS^- and Cl^-. Complexes formed with hard anions such as CO_3^{2-}, HCO_3^-, SO_4^{2-}, PO_4^{3-} and F^- have low stability and have no significant role in PGE transport. At 25 ^{o}C and 300 ^{o}C, chloride complexes can transport Pt and Pd in an acidic, oxidising environment. Hydroxide complexes may play a role in transporting in near neutral to basic solutions near intermediate fO_2 values, even when the chloride concentration is high in the solution. Bisulfide and mixed bisulfide-hydroxide complexes can be important at 300 ^{o}C and near high fS_2 conditions. Mountain and Wood (1988) also observed that between 25 and 250 ^{o}C, the solubility of bisulfides increase with increasing temperature while at the same time, the solubility of chloride and hydroxide complexes decrease. At higher temperatures; however, between 280 ^{o}C and 350 ^{o}C, the behaviour of the complexes reverses.

Mountain and Wood (1988) discussed that if Pt and Pd were transported as bisulfides, then the deposition of PGM happened due to a temperature drop or pressure drop, the latter would lead to boiling. Addition of Fe to the ore-bearing fluids also may promote PGM deposition, by the formation of Fe-sulphides and consequently lowering S concentration of the fluid. As a result, bisulfide

complexes destabilise, and Pd and Pt (with other metals) would precipitate. The additional Fe would derive from Fe-bearing oxides and silicates of the wall rock. If Pt and Pd were transported as hydroxide complexes, then deposition can be triggered by pH decrease and reduction of fO_2.

The fluids that remobilised PGE and base metal sulphides in Sudbury were highly saline (>16% NaCl) with a temperature between 60-135 ^{o}C (Marshall et al., 1999), and it was suggested that chlorides were the most likely transporting ligands (Farrow and Watkinson, 1992; Marshall et al., 1999). PGE and sulphide remobilisation due to serpentinisation was observed by Hutchinson and Kinnaird (2005) and Pritchard et al. (2013) in the case of Platreef and the Jinchuan intrusion in Northwest China, respectively. In these cases, the sulphide together with the PGM were hosted in silicate crystals and were re-mobilised and recrystallised during or after the serpentinisation. Sulphide and PGE remobilisation in a non-magmatic environment was also observed and attributed to fluids of metamorphic and groundwater origin, causing serpentinisation in the host rock. Examples include the fracture-filling PGE+Au mineralisation in podiform chromite and dunitic host rocks of the Coclac Serpentine Belt (Eastern Australia) and where primary silicates oxides or sulphides are PGM-free (Franklin et al., 1992). In the Flin Flon Greenstone Belt (Manitoba, Canada) the hydrothermal, PGE-rich Ni-Cu sulphide mineralisation was originated from metamorphosed basic and ultrabasic volcanic rocks or hidden Ni-Cu magmatic sulphides (Bursztyn and Olivo, 2010).

6.1.3 The significance of S/Se ratios in sulphide phases.

S/Se ratio is a good indicator of mantle origin with the mantle ratios falling between 2850 and 4350 (Eckstrand and Hulbert, 1987). The average mantle values determined as 3333 (McDonough and Sun, 1995), 3300 (Hattori et al., 2002) and 3150 (Lorand et al., 2003). The present study will use the S/Se ratio range defined by Eckstrand and Hulbert (1987) as an average mantle domain in the comparison diagrams. In the case of magmatic rocks, the S/Se ratios are close to mantle values, indicating the mantle origin of S (Queffurus and Barnes, 2015). S/Se ratios higher than mantle values were interpreted as the result of contamination by S of crustal origin, while low S/Se values indicate S-loss. S/Se ratios can be affected by: a: preferential retention of Se during partial melting

(Hattori et al., 2002); b: Refertilisation of mantle lithosphere by metal-rich sulphide melts (Lorand and Alard, 2010); c: Changes in the Si/Sulphide ratio, i.e. R-factor (Thériault and Barnes, 1998); d: Early segregation of sulphide liquid (Barnes et al., 2009); e: Partial desulphurisation caused by an S-undersaturated fluid (Godel and Barnes, 2008).

Pt+Pd vs S/Se is used to distinguish between the various Ni-Cu-PGE ore types. Within each Ni-Cu deposit, there can be a wide range in S/Se ratios and Pt+Pd corresponding to the different types of ore textures and compositions (Queffurus and Barnes, 2015). In general, massive sulphides tend to have higher S/Se ratios and lower Pt+Pd than disseminated sulphides (Queffurus and Barnes, 2015). The statement above does not apply to every single massive sulphide deposit as in some of them the composition ranges between Fe-rich and Cu-rich type, both having relatively low S/Se ratios and high Pt+Pd) (Queffurus and Barnes, 2015).

The use of the S/Se ratio described above relies on the knowledge that Se tends to be rather stable (immobile) in base metal sulphides. However, Prichard et al. (2013) found that Se, in fact, can be remobilised from base metals by low pH, oxidising fluids. The sign of this process is the presence of Se-PGE phases which are frequently associated with carbonates.

The applicability of experimental PGE+Au partitioning features to natural systems was discussed by Fleet at al. (1993). They suggested that the general characteristics of PGE and Au partitioning in magmatic sulphide systems which were determined via experiments can be achieved by any other high-temperature ore-forming processes and is not restricted only to fractionation of the sulphide magma. Furthermore, the PGE behaviour observed in natural komatiite massive sulphides and associated disseminated sulphides (observed by Naldrett, 1989) did not fully coincide with the experimental results in the study and the cause of this might lies in the bulk composition of disseminated sulphides which is inconsistent with a sulphide fractionation origin. Hutchinson and Kinnaird (2005) reported a poor correlation between base metal sulphides and PGE contents, meaning that high Cu+Ni content does not necessarily imply high PGE content, but it can occur. It was suggested that the addition of metalloids and later stage metasomatism and serpentinisation redistributed PGE in the system.

6.2 Results of the LA-ICPMS analysis

As described before, the line analysis produced stoichiometric and nonstoichiometric composition results. An example of separation of the separation of these phases is shown in Figure 6. 2.1, which illustrates the Cu/Fe ratio changes in the analysed Cu-Fe sulphides. The line analysis often included microinclusions of which the most common are listed in Table 6.2.1. Figures 6.2.1-3 display time resolved analysis (TRA) diagrams of representative Phalaborwa sulphide phases. The TRA diagrams show counts-per-second (cps) values of the measured elements through the line analysis time (70-100 seconds). The different phases can be separated based on the relative cps values of the major elements (^{35}S, ^{57}Fe, ^{59}Co, ^{60}Ni, ^{65}Cu, ^{66}Zn, ^{68}Zn, ^{206}Pb). The LA-ICPMS analysis results are listed in Table 6.2.2, including the major and trace elements, and the calculated formulae of the stoichiometric results.

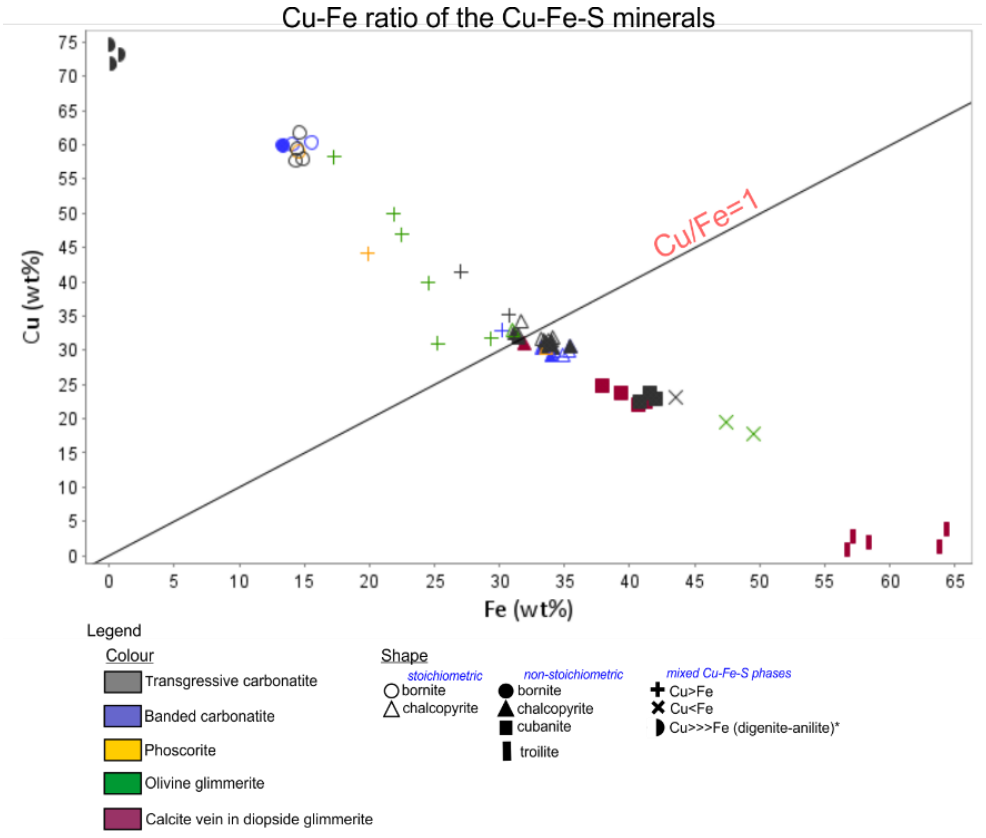

Figure 6.2.1. The diagram shows the Cu/Fe ratios of the stoichiometric and nonstoichiometric Cu-Fe-S phases. The Cu/Fe=1 line indicates the area where ideal chalcopyrite composition lies. The analysed phases were separated based on the calculated formulae. The mixed phases fall between known compositions and were separated by the relative Cu/Fe ratios.

Table 6.2.1. Microinclusions and particles observed in the TRA diagrams based on element cps peaks in the line analyses.

Lithology:	**Transgressive carbonatite: Chalcopyrite-rich**		**Transgressive carbonatite: Bornite-rich**			**Transgressive carbonatite: Bornite-chalcopyrite replacement**		**Banded Carbonatite**			**Phoscorite**	
Mineral host	Chp	Cub	Bo	Dig*	Co-ptl	Bo	Co-ptl	Chp	Bo	Co-ptl	Mixed Cu-Fe-S	Co-ptl
Microinclusions												
AgAuPd							x					
AuAg											x	
IrRuTe											x	
PbTe	x											
PbTeBi	x											
PbBi									x			
Native Bi	x		x		x	x	x		x		x	
Sphalerite										x	x	x
Sphalerite-Cd	x	x	x	x							x	
Galena	x		x					x		x		
Co-Ni	x	x	x					x			x	
Ni-Ag	x											
AgSnBi								x				
GeBiAs(Se)								x				
PbNiBi(Te,Sn)			x			x						
AgTe			x									
PtIr											x	
AuPd											x	
AgAuPd							x					
SnPd											x	
BiSn											x	

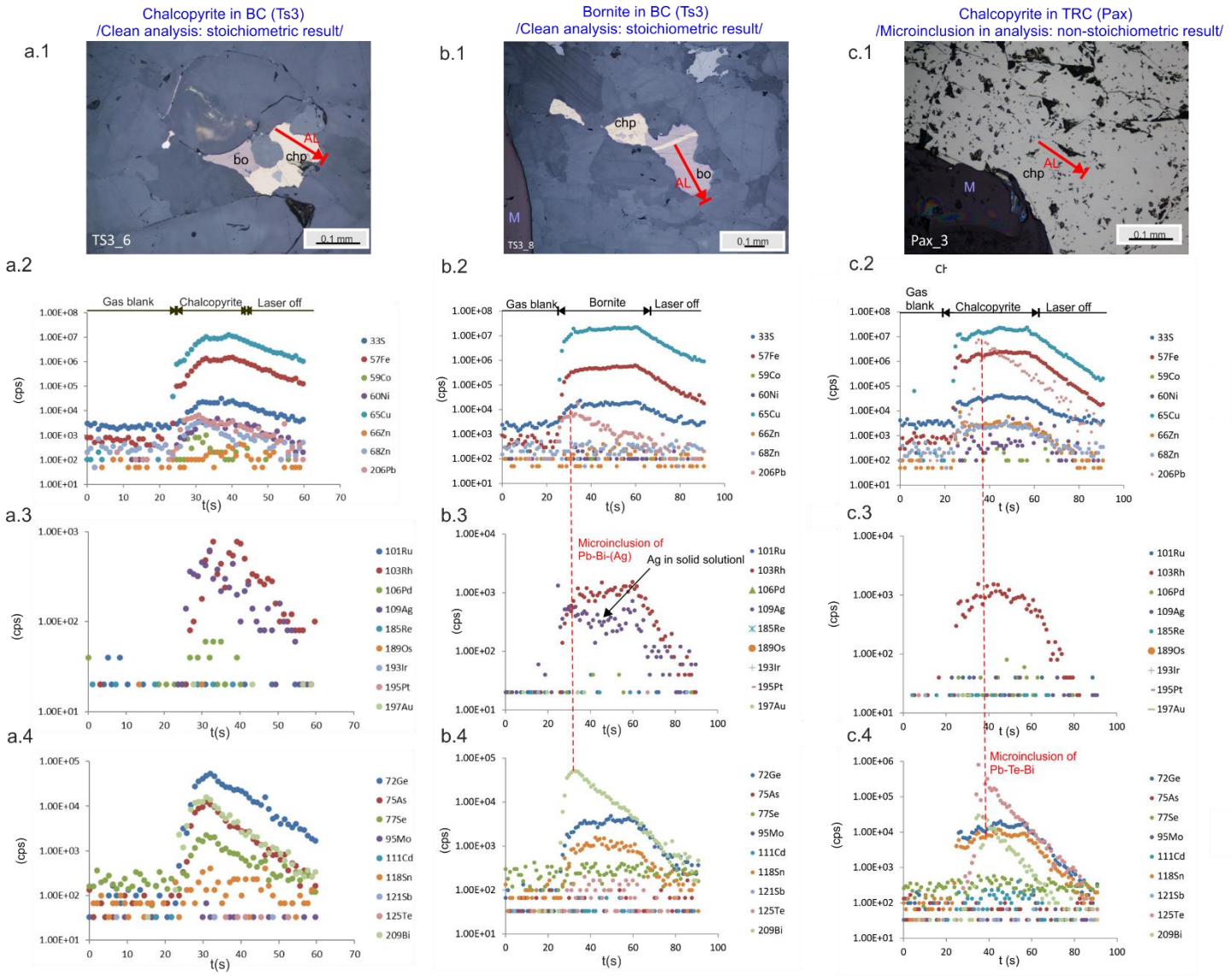

Figure 6.2.2. The edited micro-photographs (a.1, b.1, c.1) of the sulphide grains show the analysis lines (AL) that produced the TRA diagrams for each individual lines. a.: Chalcopyrite in banded carbonatite; a.2-4: TRA diagrams show clean analysis without significant contamination. b: Bornite in banded carbonatite. The TRA diagrams (b.2-4) indicate the presence of trace microinclusion (Pb-Bi-(Ag)); the analysis still produced stoichiometric composition. c: Chalcopyrite in Chalcopyrite-rich TRC. The analysis produced nonstoichiometric composition due to the presence of microinclusion (Pb-Te-Bi). bo: bornite; chp: chalcopyrite, M: marker; BC: banded carbonatite, TRC: transgressive carbonatite.

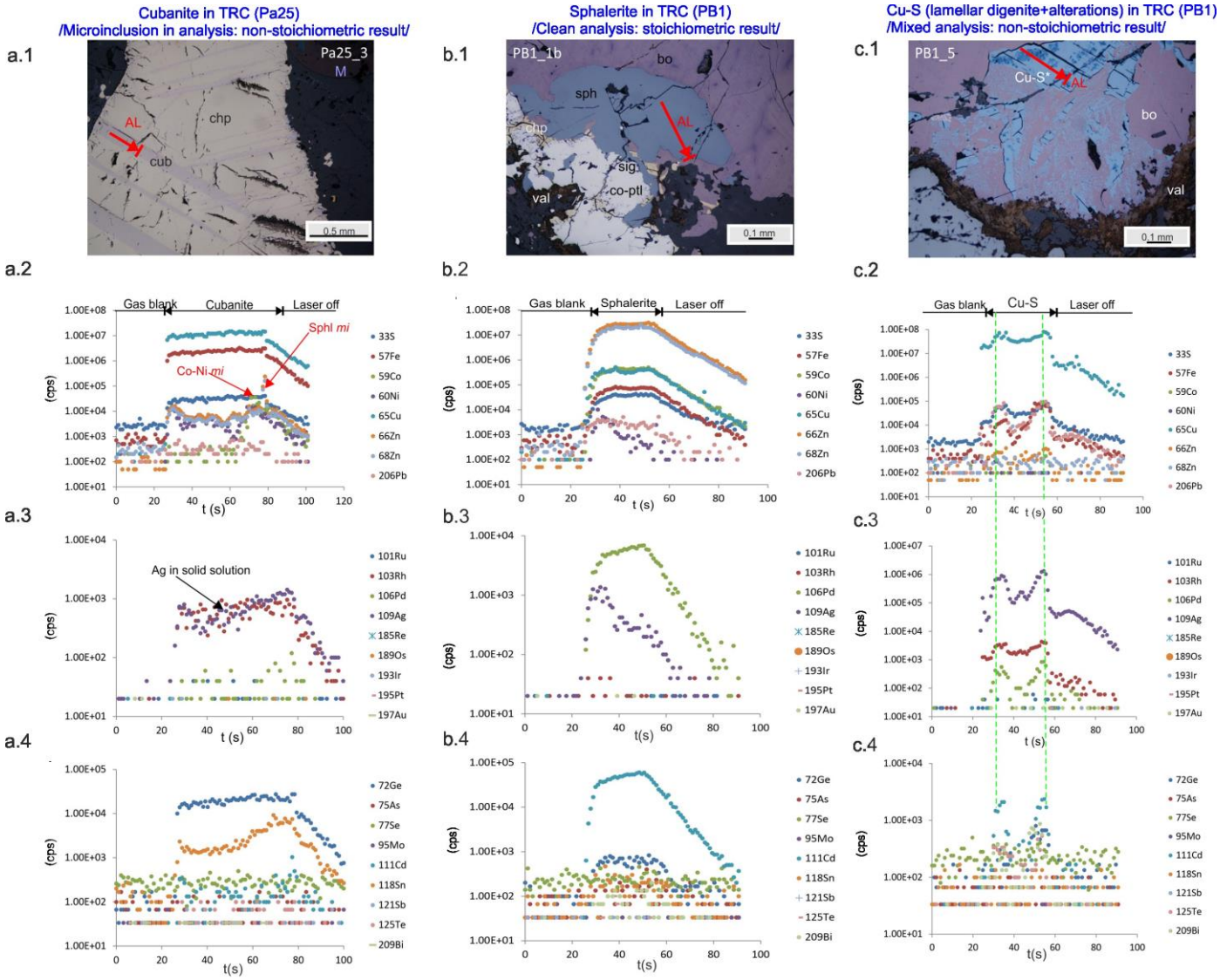

Figure 6.2.3. The edited micro-photographs (a.1, b.1, c.1) of the sulphide grains show the analysis lines (AL) that produced the TRA diagrams for each individual lines. a: Cubanite lamellae in chalcopyrite-rich TRC. The TRA diagrams (a.2-a.4) indicate the presence of Co-Ni microinclusion, The analysis produced nonstoichiometric composition. and ag in solid solution. b: Sphalerite grain in massive bornite (Bornite-rich TRC). The TRA diagrams (b.2-4) indicate a clean analysis without contamination; the analysis produced a stoichiometric composition. Cadmium is present in solid solution. c: lamellar digenite* and alteration products. The nonstoichiometric compositions resulted from the alteration process that affected the phase. The edges of the lamellae showed high Ag levels (c.3). bo: bornite; chp: chalcopyrite, cub: cubanite; sph: sphalerite; Cu-S* mixed Cu-S phases; val: valleriite; co-ptl: cobalt pentlandite; sig: siegenite; sphl: sphalerite; *mi*: microinclusion; M: marker, TRC:transgressive carbonatite.

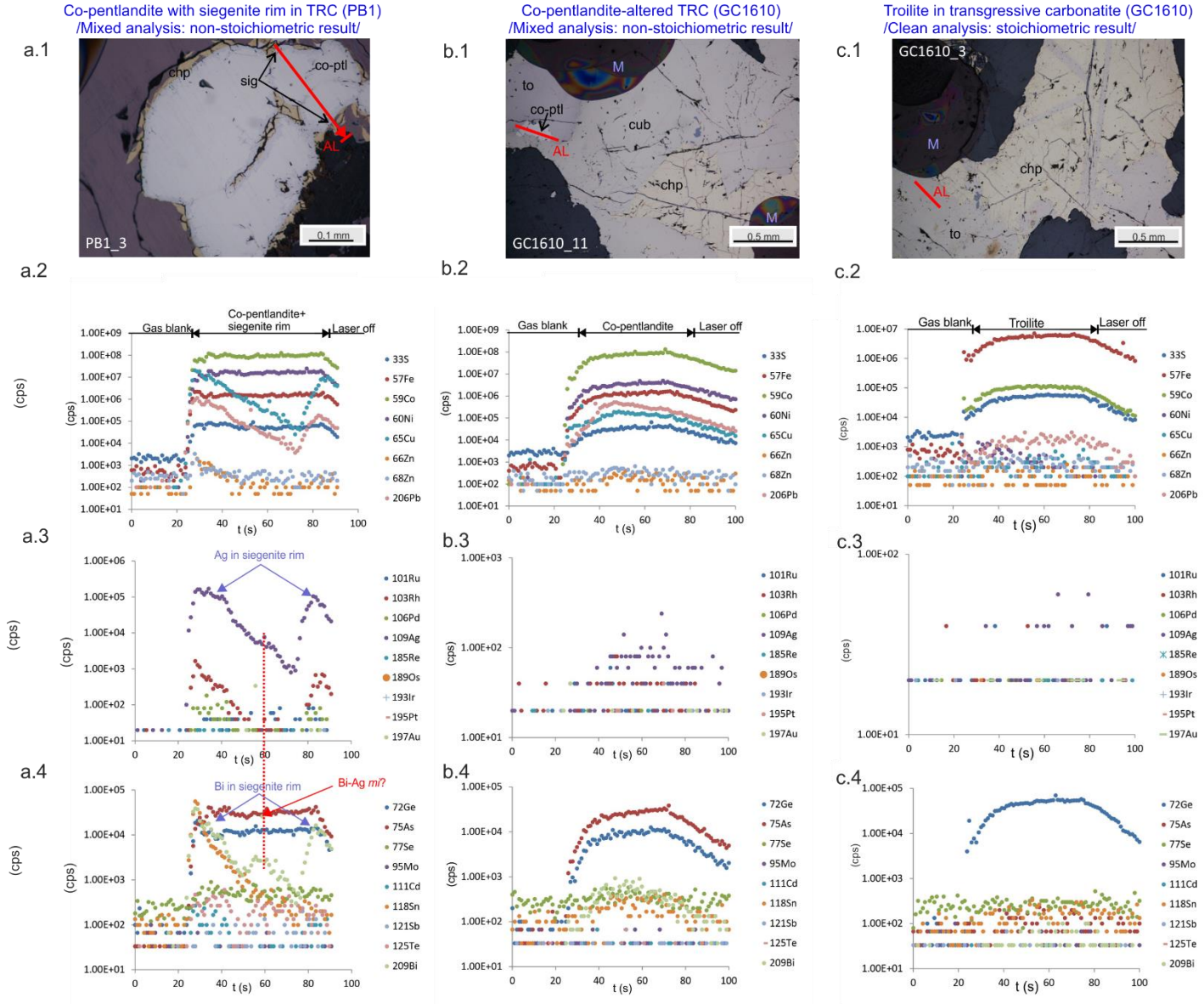

Figure 6.2.4. The edited micro-photographs (a.1, b.1, c.1) of the sulphide grains show the analysis lines (AL) that produced the TRA diagrams for each individual lines. a: Cobalt pentlandite with siegenite rim around it (a.1). The analysis produced nonstoichiometric composition due to the AL including two phases and the chalcopyrite contact. The TRA diagrams (a.2-4) show the changes in the composition from the centre towards the edges and at one point in the centre where the AL crossed a siegenite patch. The results show that siegenite is more enriched in Ag, Bi and Pb then the cobalt pentlandite. b: Cobalt pentlandite in troilite-rich TRC gave nonstoichiometric result. As occurred in solid solution (b.4), but generally the phase was depleted in trace elements. Troilite in troilite-rich TRC gave stoichiometric compositions, based on the TRA diagrams (c.2-4) it is depleted in trace elements. bo: bornite; chp: chalcopyrite, cub: cubanite; co-ptl: cobalt pentlandite; sig: siegenite; to: troilite; M: marker, TRC: transgressive carbonatite.

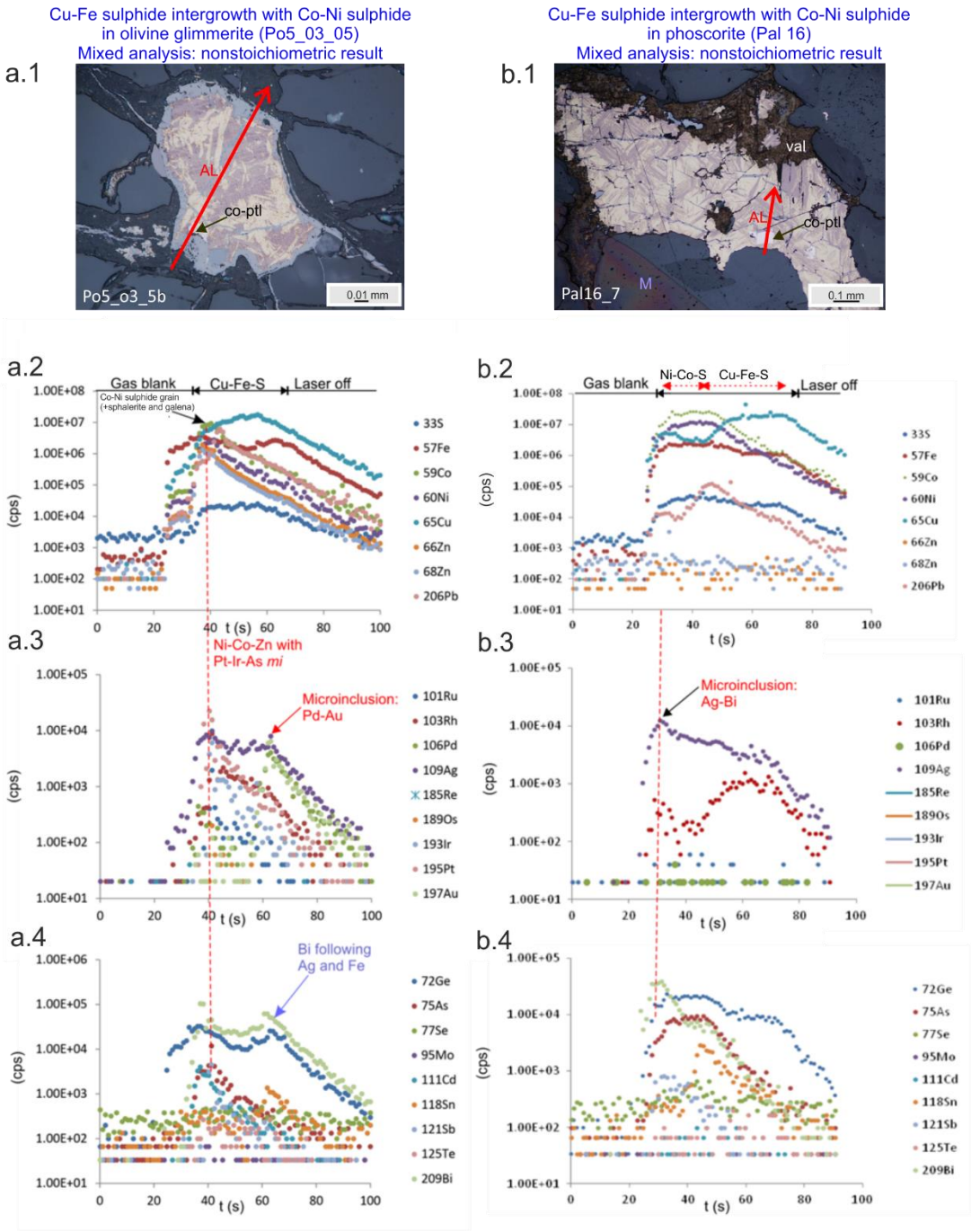

Figure 6.2.5. The edited micro-photographs (a.1, b.1) of the sulphide grains show the analysis lines (AL) that produced the TRA diagrams for each individual lines. a: Sulphide grain in olivine glimmerite with complex intergrowth of Cu-Fe-S phases. The analysis of the mixed phases gave nonstoichiometric results as expected. The TRA diagrams (a.2-4) showed the presence of PGE at the edges of the grain. The PGE formed microinclusions with As (Pt, Ir) or Au (Pd). The former was associated with Co-Ni sulphide grain. b: Sulphide grain in phoscorite with complex Cu-Fe-S phases and Co-Ni sulphide grain. The grain is strongly resorbed at the edges. The analysis produced nonstoichiometric composition as the AL included different phases. Ag-Bi microinclusion occurred in the Co-Ni sulphide grain.: co-ptl: Co-Ni sulphide grain; val: valleriite M: marker, *mi:* microinclusion.

Table 6.2.2. LA-ICPMS analysis results of the Phalaborwa sulphides. Calculated formulae were presented for stoichiometric compositions.

Lithology	Transgressive carbonatite /Stoichiometric results/										
TRC Type	Chp+Bo	Chp+Bo	Chp+Bo	Bo-rich	Bo-rich	Bo-rich	Bo-rich	Chp-rich	Chp-rich	Chp-rich	To-rich
Mineral	Bo	Chp	Chp	Bo	Bo	Bo	Chp	Chp	Chp	Chp	Chp
Analysis ID	GC1611_2_bo	Gc1611_1_cp	GC1611_4_bo(ni) Cp?	pb1_5_bo	Pb1_5_bo2	Gc811A_Bo(ni Bi)2	GC811A_7_cp	PAx_4_cp	PAx_6_cp	PAx_5_cp	GC1610_4_cp
S wt% stc.	25.60	35.00	35.00	25.60	25.60	25.60	35.00	35.00	35.00	35.00	35.00
^{57}Fe wt%	14.87	33.75	34.06	14.61	14.45	14.37	33.21	31.66	31.46	33.47	35.41
^{59}Co wt%	bd.	0.00	bd.	bd.	bd.	bd.	0.00	bd.	bd.	bd.	0.00
^{61}Ni wt%	bd.	bd.	bd.	bd.	bd.	bd.	bd.	bd.	bd.	bd.	0.01
^{65}Cu wt%	57.95	31.52	32.09	61.71	59.44	57.66	31.69	34.25	32.44	31.48	30.72
^{66}Zn wt%	bd.	bd.	bd.	bd.	bd.	bd.	bd.	0.01	0.01	0.01	0.00
^{206}Pb wt%	0.00	0.00	0.01	0.00	bd.	bd.	0.00	bd.	0.00	0.03	bd.
^{209}Bi wt%	0.00	0.00	0.00	0.00	0.00	0.00	0.00	bd.	0.00	0.00	bd.
Calculated formulae											
S	4.04	1.99	1.98	3.93	4.01	4.07	2.00	1.99	2.02	2.00	1.98
Fe	1.35	1.10	1.11	1.29	1.30	1.31	1.09	1.03	1.04	1.10	1.15
Co	0.00	0.00	0.00	0.00	0.00	0.00	0.00	0.00	0.00	0.00	0.00
Ni	0.00	0.00	0.00	0.00	0.00	0.00	0.00	0.00	0.00	0.00	0.00
Cu	4.61	0.91	0.92	4.78	4.69	4.62	0.91	0.98	0.94	0.91	0.88
Zn	0.00	0.00	0.00	0.00	0.00	0.00	0.00	0.00	0.00	0.00	0.00
Pb	0.00	0.00	0.00	0.00	0.00	0.00	0.00	0.00	0.00	0.00	0.00
Bi	0.00	0.00	0.00	0.00	0.00	0.00	0.00	0.00	0.00	0.00	0.00
Total Metals	1.18	1.10	1.11	1.23	1.19	1.16	1.09	1.11	1.07	1.10	1.12
Metal/S	1.48	1.01	1.02	1.54	1.50	1.46	1.00	1.01	0.98	1.00	1.02
^{59}Co ppm	bd.	6.59	bd.	bd.	bd.	bd.	0.00	bd.	bd.	bd.	17.71
^{66}Zn ppm	bd.	bd.	bd.	bd.	bd.	bd.	bd.	84.01	95.56	110.98	18.00
^{75}As ppm	bd.	bd.	bd.	bd.	bd.	bd.	bd.	bd.	bd.	bd.	bd.
^{77}Se ppm	15.76	19.64	31.80	14.75	17.09	38.87	bd.	22.55	29.15	27.96	bd.
Ru* ppm	bd.	bd.	bd.	bd.	bd.	0.13	bd.	bd.	bd.	bd.	0.13
^{103}Rh ppm	bd.	bd.	bd.	bd.	bd.	bd.	bd.	bd.	bd.	bd.	bd.
Pd* ppm	bd.	bd.	bd.	bd.	bd.	bd.	bd.	bd.	bd.	bd.	bd.
^{109}Ag ppm	13.41	5.95	9.76	153.89	62.26	42.60	38.25	bd.	bd.	bd.	0.43
^{111}Cd ppm	0.70	bd.	0.71	1.47	1.28	0.86	bd.	4.29	3.96	6.01	0.43
^{121}Sb ppm	bd.	bd.	bd.	bd.	bd.	bd.	bd.	bd.	0.40	bd.	bd.
^{125}Te ppm	19.96	18.13	38.65	10.16	7.57	30.52	43.90	2.55	25.96	609.91	0.66
^{185}Re ppm	bd.	bd.	bd.	bd.	bd.	bd.	bd.	bd.	bd.	bd.	bd.
^{189}Os ppm	bd.	bd.	bd.	bd.	bd.	bd.	bd.	bd.	bd.	bd.	bd.
^{193}Ir ppm	bd.	bd.	bd.	bd.	bd.	bd.	bd.	bd.	bd.	bd.	bd.
^{195}Pt ppm	bd.	bd.	bd.	bd.	bd.	bd.	bd.	bd.	bd.	bd.	bd.
^{197}Au ppm	bd.	bd.	bd.	bd.	bd.	bd.	bd.	bd.	bd.	bd.	bd.
^{206}Pb ppm	33.07	9.27	51.00	5.32	bd.	bd.	10.91	bd.	26.89	294.12	bd.
^{209}Bi ppm	6.09	0.33	1.47	1.35	7.82	1.55	0.14	bd.	0.06	1.03	bd.
S/Se	16246	17819	11007	17358	14984	6586	bd.	15521	12006	12516	bd.
Pt+Pd	bd.	bd.	bd.	bd.	bd.	bd.	bd.	bd.	bd.	bd.	bd.

*TRC: transgressive carbonatite; Chp+Bo: Chalcopyrite-bornite replacement, Chp: chalcopyrite, Bo: bornite, To: troilite, Co-Ni S: Co-Ni sulphides, stc: stoichiometric; * mean values of ^{99}Ru+^{101}Ru; ^{105}Pd+^{106}Pd+^{108}Pd; "bd": below detection.*

Table 6.2.2. Continuation

Lithology	Transgressive carbonatite /nonstoichiometric results/												
TRC Type	Chp+Bo	Chp+Bo	Chp+Bo	Chp+Bo	Chp+Bo	Bo-rich	Bo-rich	Bo-rich	Bo-rich	Bo-rich	Bo-rich	Bo-rich	Bo-rich
Mineral	Chp	Chp	Sphl	Co-Ni S	Co-Ni S	Chp	Co-Ni S	Co-Ni S	Co-Ni S	Co-Ni S	Co-Ni S	Dig/An	Dig/An
Analysis ID	GC1611_2_cp	GC1611_3_cp	GC1611_2_sp	Gc1611_1_pt	GC1611_3_pt	Pb1_c_boCp	PB1_2_ptl(Bomix_	Pb1_1_ptl(bomix_	Pb1_1c_Ptl(bomix)	GC811A_4a_ptl Co rich	Pb1_3_ptl	Pb1_4_cct	Pb1_4_cct
S wt% stc.	35.00	35.00	33.10	33.80	33.80	30.00	30.00	30.00	30.00	33.50	33.80	25.00	25.00
^{57}Fe wt%	34.08	33.94	3.78	12.91	12.91	27.01	10.23	13.92	15.04	15.04	14.15	0.17	0.94
^{59}Co wt%	0.01	0.00	0.06	36.92	41.35	0.06	25.38	24.36	22.87	6.43	24.23	bd.	bd.
^{61}Ni wt%	0.02	0.01	bd.	14.32	11.37	0.11	24.02	22.70	21.01	26.34	24.22	bd.	bd.
^{65}Cu wt%	30.51	31.54	5.16	0.53	1.08	41.40	8.32	3.17	7.64	14.58	1.99	74.55	73.20
^{66}Zn wt%	0.00	bd.	55.26	bd.	bd.	0.00	bd.	1.61	0.00	bd.	0.00	bd.	0.00
^{206}Pb wt%	0.00	0.03	0.00	0.04	0.01	0.00	0.09	0.06	0.05	0.08	0.03	bd.	0.00
^{209}Bi wt%	0.00	0.00	0.01	0.01	0.01	0.00	0.00	0.00	0.00	0.00	0.00	0.00	0.00
^{59}Co ppm	114.56	31.18	593.36	369159.62	413532.23	599.90	253806.91	243643.35	228706.13	64324.43	242285.24	bd.	bd.
^{66}Zn ppm	47.33	bd.	552583.54	bd.	bd.	13.66	bd.	16052.70	13.92	bd.	1.67	bd.	11.21
^{75}As ppm	bd.	bd.	bd.	987.05	1104.11	1.90	691.68	656.02	614.04	208.17	650.46	bd.	bd.
^{77}Se ppm	bd.	19.51	14.86	71.60	48.56	bd.	63.05	61.41	68.16	48.70	59.07	bd.	14.50
Ru* ppm	bd.	0.10	bd.	bd.	bd.	bd.	bd.	bd.	bd.	bd.	bd.	bd.	bd.
^{103}Rh ppm	bd.	bd.	bd.	bd.	bd.	bd.	bd.	bd.	bd.	bd.	bd.	bd.	bd.
Pd* ppm	bd.	bd.	bd.	0.26	2.21	0.12	bd.	bd.	0.19	0.18	bd.	bd.	bd.
^{109}Ag ppm	6.14	33.66	13.95	289.78	2790.86	188.92	384.99	231.00	193.25	282.01	115.87	619.50	335.97
^{111}Cd ppm	bd.	0.61	1302.67	0.95	bd.	2.14	1.91	422.80	0.80	1.45	0.75	bd.	bd.
^{121}Sb ppm	bd.	bd.	bd.	bd.	bd.	bd.	0.37	bd.	0.51	bd.	0.24	bd.	bd.
^{125}Te ppm	15.39	19.61	22.46	23.24	14.84	5.94	27.85	9.54	16.37	50.00	10.01	10.97	7.46
^{185}Re ppm	bd.	bd.	bd.	bd.	bd.	bd.	bd.	bd.	bd.	bd.	bd.	bd.	bd.
^{189}Os ppm	bd.	bd.	bd.	bd.	bd.	bd.	bd.	bd.	bd.	bd.	bd.	bd.	bd.
^{193}Ir ppm	bd.	bd.	bd.	bd.	bd.	bd.	bd.	bd.	bd.	bd.	bd.	bd.	bd.
^{195}Pt ppm	bd.	bd.	bd.	bd.	bd.	bd.	bd.	bd.	bd.	bd.	bd.	bd.	bd.
^{197}Au ppm	bd.	0.04	0.15	4.36	9.72	0.02	bd.	bd.	bd.	bd.	0.02	bd.	bd.
^{206}Pb ppm	33.94	315.77	27.08	431.64	76.86	23.99	858.31	634.40	455.84	823.10	269.13	bd.	16.06
^{209}Bi ppm	0.77	1.80	108.53	69.85	70.14	1.57	19.07	2.76	41.53	5.39	4.30	0.24	0.54
S/Se	bd.	17944	22281	4720	6960	bd.	4758	4885	4401	6879	5723	bd.	17236
Pt+Pd	bd.	bd.	bd.	0.26	2.21	0.12	bd.	bd.	0.19	0.18	bd.	bd.	bd.

*TRC: transgressive carbonatite; Chp+Bo: Chalcopyrite-bornite replacement, Chp: chalcopyrite, Bo: bornite, Dig/An: altered lamellar Cu-S, Sphl: sphalerite, Co-Ni S: Co-Ni sulphides; stc: stoichiometric; * mean values of ^{99}Ru+^{101}Ru; ^{105}Pd+^{106}Pd+^{108}Pd; "bd": below detection.*

Table 6.2.2. Continuation

Main lithology	Transgressive carbonatite /nonstoichiometric results/											
Lithology	Bo-rich	Bo-rich	Bo-rich	Chp-rich	Chp-rich	Chp-rich	Chp-rich	Chp-rich	Chp-rich	To-rich	To-rich	To-rich
Mineral	Dig/An	Sphl	Sphl	Chp	Chp	Chp	Chp	Chp	Chp	Chp	Co-Ni S	To
Analysis ID	Pb1_5_cct	Pb1_1_sp	Pb1_1sp2	Pa25-1 Cp1	Pa25-9_cp	PAx_1_cp	PAx_2_cp	PAx_3_cp	Pa25-3_cp	GC1610_3_cp	GC1610_4_x Co-rich	GC1610_2_po
S wt% stc.	25.00	33.10	33.10	35.00	35.00	35.00	35.00	35.00	35.00	35.00	35.00	38.00
^{57}Fe wt%	0.33	0.82	1.03	31.11	33.69	31.37	30.70	33.49	33.75	43.59	34.46	60.89
^{59}Co wt%	bd.	0.14	0.17	0.03	0.00	bd.	0.01	bd.	bd.	bd.	25.61	0.04
^{61}Ni wt%	bd.	bd.	bd.	0.07	0.11	bd.	0.20	bd.	bd.	bd.	4.63	bd.
^{65}Cu wt%	71.77	0.39	0.58	32.64	30.61	32.08	35.09	31.19	30.89	23.10	0.12	bd.
^{66}Zn wt%	0.00	63.40	66.69	0.01	0.02	0.06	0.01	0.01	0.02	0.05	bd.	bd.
^{206}Pb wt%	0.01	0.00	0.00	0.00	bd.	0.01	0.00	0.57	bd.	bd.	0.00	bd.
^{209}Bi wt%	0.00	bd.	0.00	bd.	bd.	0.00	bd.	0.00	bd.	bd.	0.00	bd.
^{59}Co ppm	bd.	1384.15	1655.79	261.33	10.48	bd.	119.71	bd.	bd.	bd.	256096.18	373.52
^{66}Zn ppm	10.48	634046.68	666948.97	97.07	158.85	559.43	129.44	94.37	199.84	512.11	bd.	bd.
^{75}As ppm	bd.	3.56	2.68	bd.	bd.	bd.	bd.	bd.	bd.	bd.	730.35	1.64
^{77}Se ppm	17.60	20.47	12.69	bd.	29.79	28.01	24.72	36.84	bd.	bd.	25.66	bd.
Ru* ppm	bd.	bd.	bd.	bd.	0.14	bd.	bd.	0.11	bd.	0.11	bd.	bd.
^{103}Rh ppm	bd.	bd.	bd.	bd.	bd.	bd.	bd.	bd.	bd.	bd.	bd.	bd.
Pd* ppm	bd.	bd.	bd.	bd.	bd.	bd.	bd.	bd.	bd.	bd.	bd.	bd.
^{109}Ag ppm	2223.93	4.69	2.03	bd.	1.06	bd.	3.73	bd.	bd.	bd.	1.47	bd.
^{111}Cd ppm	23.86	3413.82	1653.12	0.91	1.16	9.21	5.90	5.66	1.35	5.56	bd.	bd.
^{121}Sb ppm	bd.	bd.	bd.	bd.	bd.	bd.	bd.	bd.	bd.	bd.	bd.	bd.
^{125}Te ppm	15.76	0.26	0.89	2.28	2.40	137.92	5.87	7542.75	1.98	2.58	bd.	0.19
^{185}Re ppm	bd.	bd.	bd.	bd.	bd.	bd.	bd.	bd.	bd.	bd.	bd.	bd.
^{189}Os ppm	bd.	bd.	bd.	bd.	bd.	bd.	bd.	bd.	bd.	bd.	bd.	bd.
^{193}Ir ppm	bd.	bd.	bd.	bd.	bd.	bd.	bd.	bd.	bd.	bd.	bd.	bd.
^{195}Pt ppm	bd.	bd.	bd.	bd.	bd.	bd.	bd.	bd.	bd.	bd.	bd.	bd.
^{197}Au ppm	bd.	bd.	bd.	bd.	bd.	bd.	bd.	bd.	bd.	bd.	bd.	bd.
^{206}Pb ppm	91.41	10.67	8.79	34.78	bd.	60.64	5.89	5674.83	bd.	bd.	18.69	bd.
^{209}Bi ppm	0.34	bd.	0.11	bd.	bd.	0.17	bd.	10.30	bd.	bd.	0.73	bd.
S/Se	14204	16172	26089	bd.	11750	12498	14158	9501	bd.	bd.	13641	bd.
Pt+Pd	bd.	bd.	bd.	bd.	bd.	bd.	bd.	bd.	bd.	bd.	bd.	bd.

*TRC: transgressive carbonatite, Chp: chalcopyrite, To: troilite, Co-Ni S: Co-Ni sulphide; stc: stoichiometric; * mean values of ^{99}Ru+^{101}Ru; ^{105}Pd+^{106}Pd+^{108}Pd; "bd": below detection.*

Table 6.2.2. Continuation

Lithology	Transgressive carbonatite /nonstoichiometric results/										
TRC Type	To-rich	To-rich	Chp-rich	Chp-rich	Chp-rich	Chp-rich	To-rich	To-rich	To-rich	To-rich	To-rich
Mineral	Co-Ni S	Co-Ni S	Chp	Chp	Chp	Chp	Chp	Co-Ni S	To	Co-Ni S	Co-Ni S
Analysis ID	GC1610_4_ ptl Co rich	GC1610_11_ptl Co rich	PAx_1_cp	PAx_2_cp	PAx_3_cp	Pa25-3_cp	GC1610_3_cp	GC1610_4_x Co-rich	GC1610_2_po	GC1610_4_ptl Co rich	GC1610_11_ptl Co rich
S wt% stc.	33.50	33.50	35.00	35.00	35.00	35.00	35.00	35.00	38.00	33.50	33.50
^{57}Fe wt%	26.79	20.71	31.37	30.70	33.49	33.75	43.59	34.46	60.89	26.79	20.71
^{59}Co wt%	34.06	35.98	bd.	0.01	bd.	bd.	bd.	25.61	0.04	34.06	35.98
^{61}Ni wt%	7.61	8.97	bd.	0.20	bd.	bd.	bd.	4.63	bd.	7.61	8.97
^{65}Cu wt%	0.05	0.27	32.08	35.09	31.19	30.89	23.10	0.12	bd.	0.05	0.27
^{66}Zn wt%	bd.	bd.	0.06	0.01	0.01	0.02	0.05	bd.	bd.	bd.	bd.
^{206}Pb wt%	0.00	0.13	0.01	0.00	0.57	bd.	bd.	0.00	bd.	0.00	0.13
^{209}Bi wt%	0.00	0.00	0.00	bd.	0.00	bd.	bd.	0.00	bd.	0.00	0.00
^{59}Co ppm	340564.81	359830.37	bd.	119.71	bd.	bd.	bd.	256096.18	373.52	340564.81	359830.37
^{66}Zn ppm	bd.	bd.	559.43	129.44	94.37	199.84	512.11	bd.	bd.	bd.	bd.
^{75}As ppm	1005.65	1021.25	bd.	bd.	bd.	bd.	bd.	730.35	1.64	1005.65	1021.25
^{77}Se ppm	33.56	38.07	28.01	24.72	36.84	bd.	bd.	25.66	bd.	33.56	38.07
Ru* ppm	bd.	bd.	bd.	bd.	0.11	bd.	0.11	bd.	bd.	bd.	bd.
^{103}Rh ppm	bd.	bd.	bd.	bd.	bd.	bd.	bd.	bd.	bd.	bd.	bd.
Pd* ppm	bd.	bd.	bd.	bd.	bd.	bd.	bd.	bd.	bd.	bd.	bd.
^{109}Ag ppm	bd.	0.41	bd.	3.73	bd.	bd.	bd.	1.47	bd.	bd.	0.41
^{111}Cd ppm	bd.	bd.	9.21	5.90	5.66	1.35	5.56	bd.	bd.	bd.	bd.
^{121}Sb ppm	bd.	bd.	bd.	bd.	bd.	bd.	bd.	bd.	bd.	bd.	bd.
^{125}Te ppm	bd.	0.40	137.92	5.87	7542.75	1.98	2.58	bd.	0.19	bd.	0.40
^{185}Re ppm	bd.	bd.	bd.	bd.	bd.	bd.	bd.	bd.	bd.	bd.	bd.
^{189}Os ppm	bd.	bd.	bd.	bd.	bd.	bd.	bd.	bd.	bd.	bd.	bd.
^{193}Ir ppm	bd.	bd.	bd.	bd.	bd.	bd.	bd.	bd.	bd.	bd.	bd.
^{195}Pt ppm	bd.	bd.	bd.	bd.	bd.	bd.	bd.	bd.	bd.	bd.	bd.
^{197}Au ppm	bd.	bd.	bd.	bd.	bd.	bd.	bd.	bd.	bd.	bd.	bd.
^{206}Pb ppm	38.58	1287.98	60.64	5.89	5674.83	bd.	bd.	18.69	bd.	38.58	1287.98
^{209}Bi ppm	0.18	0.91	0.17	bd.	10.30	bd.	bd.	0.73	bd.	0.18	0.91
S/Se	9983	8801	12497.67	14158.18	9501.06	bd.	bd.	13640.52	bd.	9983.02	8800.55
Pt+Pd	bd.	bd.	bd.	bd.	bd.	bd.	bd.	bd.	bd.	bd.	bd.

TRC: transgressive carbonatite, Chp: chalcopyrite, To: troilite, Co-Ni S: Co-Ni sulphide; *stc: stoichiometric; * mean values of ^{99}Ru +^{101}Ru; ^{105}Pd+^{106}Pd+^{108}Pd; "bd": below detection.*

Table 6.2.2. Continuation

Lithology	**Banded carbonatite**											
	Stoichiometric results							Nonstoichiometric results				
Mineral	Bo	Bo	Bo	Chp	Chp	Chp	Chp	Chp	Chp	Chp	Chp	Co-Ni S
Analysis ID	TS3_3_bo	TS3_8_bo	6B_3_bo	TS3_6_cp	6B_3_cp	6B_5_cp2	6B_5_cp3	6B_5_cp	TS3_4_cp	TS3_1_cp	6B_6_cp	6B_4_pt
S wt% stc.	25.60	25.60	25.60	35.00	35.00	35.00	35.00	35.00	35.00	35.00	35.00	33.80
^{57}Fe wt%	13.34	14.08	15.54	35.39	34.90	35.28	34.18	33.92	30.19	24.83	33.24	13.19
^{59}Co wt%	bd.	bd.	bd.	bd.	bd.	bd.	0.01	bd.	0.01	0.01	0.01	16.54
^{61}Ni wt%	bd.	bd.	bd.	0.01	bd.	bd.	bd.	0.02	0.15	bd.	0.66	23.31
^{65}Cu wt%	59.88	60.05	60.36	30.73	29.37	30.06	30.03	29.32	32.91	41.57	30.44	12.18
^{66}Zn wt%	bd.	bd.	bd.	0.00	bd.	bd.	bd.	0.01	0.01	0.00	bd.	bd.
^{206}Pb wt%	0.16	0.00	bd.	0.00	0.00	0.00	0.00	0.00	0.00	0.00	0.00	0.00
^{209}Bi wt%	0.00	0.01	0.01	0.00	0.00	0.00	0.00	0.00	0.00	bd.	0.00	0.00
Calculated Formulae												
S	4.03	4.00	3.94	1.98	2.00	1.99	2.01					
Fe	1.21	1.26	1.37	1.15	1.15	1.15	1.12					
Co	0.00	0.00	0.00	0.00	0.00	0.00	0.00					
Ni	0.00	0.00	0.00	0.00	0.00	0.00	0.00					
Cu	4.76	4.74	4.69	0.88	0.85	0.86	0.87					
Zn	0.00	0.00	0.00	0.00	0.00	0.00	0.00					
Pb	0.00	0.00	0.00	0.00	0.00	0.00	0.00					
Bi	0.00	0.00	0.00	0.00	0.00	0.00	0.00					
Total Metal	1.98	2.00	2.03	2.02	2.00	2.01	1.99					
Metal/S	1.48	1.50	1.54	1.02	1.00	1.01	0.99					
^{59}Co ppm	bd.	bd.	bd.	bd.	bd.	bd.	76.70	bd.	57.20	74.17	78.67	165427.77
^{66}Zn ppm	bd.	bd.	bd.	10.57	bd.	bd.	bd.	88.10	57.59	23.67	bd.	bd.
^{75}As ppm	bd.	bd.	bd.	275.80	bd.	bd.	bd.	bd.	47.49	bd.	bd.	468.30
^{77}Se ppm	20.88	40.67	55.35	61.16	24.51	bd.	21.57	21.80	102.02	37.16	bd.	49.24
Ru* ppm	bd.	bd.	bd.	bd.	0.16	bd.	bd.	bd.	bd.	bd.	bd.	bd.
^{103}Rh ppm	bd.	bd.	bd.	bd.	bd.	bd.	bd.	bd.	bd.	bd.	bd.	bd.
Pd* ppm	bd.	bd.	bd.	bd.	bd.	bd.	bd.	bd.	bd.	bd.	bd.	bd.
^{109}Ag ppm	5.08	4.23	59.12	3.27	2.19	1.21	4.40	4.95	7.90	1.01	45.41	33.14
^{111}Cd ppm	52.95	1.44	1.03	bd.	bd.	bd.	bd.	1.89	1.29	2.20	1.46	43.02
^{121}Sb ppm	bd.	bd.	bd.	bd.	bd.	bd.	bd.	bd.	bd.	bd.	bd.	0.53
^{125}Te ppm	11.45	15.68	41.01	1.25	1.40	0.33	3.31	0.54	8.84	15.93	9.41	10.67
^{185}Re ppm	bd.	bd.	bd.	bd.	bd.	bd.	bd.	bd.	bd.	bd.	bd.	bd.
^{189}Os ppm	bd.	bd.	bd.	bd.	bd.	bd.	bd.	bd.	bd.	bd.	bd.	bd.
^{193}Ir ppm	bd.	bd.	bd.	bd.	bd.	bd.	bd.	bd.	bd.	bd.	bd.	bd.
^{195}Pt ppm	bd.	bd.	bd.	bd.	bd.	bd.	bd.	bd.	bd.	bd.	bd.	bd.
^{197}Au ppm	bd.	bd.	0.03	bd.	bd.	bd.	bd.	0.04	bd.	bd.	0.02	0.03
^{206}Pb ppm	1630.69	20.26	bd.	20.21	7.27	6.54	11.33	11.91	18.19	48.11	30.35	41.97
^{209}Bi ppm	0.22	65.85	57.19	17.82	0.60	0.14	0.64	0.28	17.27	bd.	0.88	1.10
S/Se	12260	6294	4625	5722	14279	bd.	16223	16056	3431	9418	bd.	6864
Pt+Pd	bd.	bd.	bd.	bd.	bd.	bd.	bd.	bd.	bd.	bd.	bd.	bd.

*Bo: bornite, Chp: chalcopyrite, Co-Ni S: Co-Ni sulphides; stc: stoichiometric; * mean values of ^{99}Ru+^{101}Ru; ^{105}Pd+^{106}Pd+^{108}Pd; "bd": below detection.*

Table 6.2.2. Continuation

Lithology	Phoscorite					Calcite vein in diopside glimmerite									
	Stoichiometric		Nonstoichiometric			Nonstoichiometric									
Mineral	Bo	Chp	Cu>Fe S	Co-Ni S	Co-Ni S	Chp	Cub	Cub	Cub	Cub	To	To	To	To	To
Analysis ID	Pal16_8_bo	Pal16_3_cp	Pal16_4	Pal16_6_bo(pt)	Pal16_7_bo(pt)	po5_02_5_cp	Po5_02_6-cp	po5_02_6_cp2	Po5_02_4_cp	Po5_02_3	Po5_02_1b	Po5_02_5_bo (Po?)	Po5_02_5_bo1(Po?)	Po5_02_6_bo (Po?)	Po5_02_4_bo (Po?)
S wt% stc.	25.60	35.00	35.00	25.60	25.60	35.00	35.00	35.00	35.00	35.00	35.00	38.00	38.00	38.00	38.00
^{57}Fe wt%	14.58	33.51	19.87	24.53	27.00	31.84	37.85	39.32	40.67	41.23	57.20	56.70	58.34	64.33	63.85
^{59}Co wt%	bd.	0.00	0.00	4.37	4.76	0.00	0.01	0.00	0.00	0.26	0.01	0.01	0.05	0.10	0.36
^{61}Ni wt%	bd.	bd.	bd.	11.51	4.22	0.21	0.08	0.04	0.04	0.37	bd.	0.03	0.05	0.08	0.34
^{65}Cu wt%	58.97	30.47	44.14	25.96	29.80	31.21	24.79	23.80	22.05	22.48	2.91	0.98	2.04	3.83	1.37
^{66}Zn wt%	0.00	bd.	bd.	bd.	0.00	0.03	0.59	0.10	0.34	0.02	bd.	bd.	bd.	0.00	0.00
^{206}Pb wt%	0.03	0.00	0.02	0.01	0.03	bd.	0.00	0.00	0.00	0.00	bd.	bd.	0.00	0.00	0.00
^{209}Bi wt%	0.00	bd.	0.00	0.00	0.00	0.00	0.00	0.00	0.00	0.00	0.00	0.00	0.00	0.00	0.00
Calculated Formulae															
S	4.02	2.01													
Fe	1.31	1.11													
Co	0.00	0.00													
Ni	0.00	0.00													
Cu	4.67	0.88													
Zn	0.00	0.00													
Pb	0.00	0.00													
Bi	0.00	0.00													
Total Metals	1.49	0.99													
Metal/S	1.49	0.99													
^{59}Co ppm	bd.	9.05	9.07	43743.05	47612.80	34.55	69.17	25.69	15.02	2614.53	56.38	92.13	483.96	1015.61	3613.73
^{66}Zn ppm	10.59	bd.	bd.	bd.	17.78	276.17	5936.91	1047.83	3371.35	173.72	bd.	bd.	bd.	33.93	33.97
^{75}As ppm	2.81	bd.	bd.	124.49	133.40	bd.	bd.	bd.	bd.	5.32	bd.	bd.	bd.	2.17	9.91
^{77}Se ppm	52.69	17.17	24.52	36.49	15.67	12.63	10.30	bd.	16.15	9.69	bd.	bd.	16.16	12.93	bd.
Ru* ppm	bd.	bd.	bd.	bd.	bd.	bd.	bd.	bd.	bd.	bd.	bd.	bd.	bd.	bd.	bd.
^{103}Rh ppm	bd.	bd.	bd.	bd.	bd.	bd.	bd.	bd.	bd.	bd.	bd.	bd.	bd.	bd.	bd.
Pd* ppm	2.38	bd.	bd.	bd.	bd.	bd.	bd.	bd.	bd.	bd.	bd.	bd.	bd.	bd.	bd.
^{109}Ag ppm	207.78	1.86	19.71	28.00	6.68	3.48	16.50	10.04	4.57	0.71	22.34	0.82	0.75	6.78	1.39
^{111}Cd ppm	1.84	0.39	0.86	1.16	1.12	0.71	32.01	6.18	17.65	0.82	bd.	bd.	bd.	bd.	bd.
^{121}Sb ppm	bd.	bd.	bd.	1.51	bd.	bd.	bd.	bd.	bd.	bd.	bd.	bd.	bd.	bd.	bd.
^{125}Te ppm	21.43	8.88	11.31	6.71	5.37	1.52	1.60	2.82	1.55	1.00	bd.	bd.	bd.	bd.	bd.
^{185}Re ppm	bd.	bd.	bd.	bd.	bd.	bd.	bd.	bd.	bd.	bd.	bd.	bd.	bd.	bd.	bd.
^{189}Os ppm	0.04	bd.	bd.	bd.	bd.	bd.	bd.	bd.	bd.	bd.	bd.	bd.	bd.	bd.	bd.
^{193}Ir ppm	0.20	bd.	bd.	bd.	bd.	bd.	bd.	bd.	bd.	bd.	bd.	bd.	bd.	bd.	bd.
^{195}Pt ppm	0.44	bd.	bd.	bd.	bd.	bd.	bd.	bd.	bd.	bd.	bd.	bd.	bd.	bd.	bd.
^{197}Au ppm	0.32	bd.	bd.	bd.	bd.	0.02	0.07	0.05	0.03	bd.	bd.	bd.	bd.	bd.	bd.
^{206}Pb ppm	291.33	4.37	179.43	123.26	325.40	bd.	6.41	7.87	9.78	9.29	bd.	bd.	14.69	9.64	18.76
^{209}Bi ppm	0.07	bd.	0.04	7.89	0.22	0.39	0.45	1.18	1.54	1.93	0.20	0.33	0.66	2.29	0.53
S/Se	4858	20383	14272	7016	16339	27711	33993	bd.	21672	36107	bd.	bd.	23517	29387	bd.
Pt+Pd	2.81	bd.	bd.	bd.	bd.	bd.	bd.	bd.	bd.	bd.	bd.	bd.	bd.	bd.	bd.

*Bo: bornite, Chp: chalcopyrite, Co-Ni S: Co-Ni sulphides, Cub: cubanite, To: troilite, Cu>Fe S: mixed Cu-Fe sulphide analysis; stc: stoichiometric; * mean values of ^{99}Ru+^{101}Ru; ^{105}Pd+^{106}Pd+^{108}Pd; "bd": below detection.*

Table 6.2.2. Continuation

Lithology	Olivine glimmerite										
	Stoichiometric	Nonstoichiometric									
Mineral	Chalcopyrite	Bornite	Cu<Fe S	Cu>Fe S	Cu>Fe S	Cu<Fe S	Cu>Fe S	Cu<Fe S	Cu>Fe S	Cu>Fe S	Co-Ni S
Analysis ID	Po5_o3_3_cp	Po5_o3_1_bo	Po5_o3_5b_bo(mix)	Po5_o3_5d_bo(mix)	Po5_o3_6b_bo(mix)	Po5_o3_6c_bo(mix)	Po5_o3_6d_bo(mix)	Po5_o3_5c_chp	Po5_o3_4b_cp(mix)	Po5_o3_4_cp(mix)	Po5_o3_7_ptl
S wt% stc.	35.00	25.60	30.00	30.00	30.00	30.00	30.00	35.00	35.00	35.00	33.50
^{57}Fe wt%	30.99	17.28	36.34	29.37	22.50	49.48	21.89	47.44	25.26	24.53	20.37
^{59}Co wt%	0.00	0.01	0.72	0.02	0.00	0.01	0.01	0.02	0.13	0.01	2.91
^{61}Ni wt%	bd.	0.14	1.31	0.05	0.01	0.02	0.02	0.04	0.57	0.03	21.21
^{65}Cu wt%	33.13	58.23	30.56	31.69	46.86	17.68	49.93	19.58	30.99	39.84	19.63
^{66}Zn wt%	bd.	0.01	0.77	0.01	0.06	0.01	0.02	0.03	0.01	0.01	0.03
^{206}Pb wt%	0.01	0.01	0.81	1.79	0.13	0.04	0.06	0.05	0.01	0.01	0.12
^{209}Bi wt%	0.01	0.00	0.01	0.00	0.00	0.00	0.00	0.00	0.00	0.00	0.00
Calculated Formulae											
S	2.01										
Fe	1.02										
Co	0.00										
Ni	0.00										
Cu	0.96										
Zn	0.00										
Pb	0.00										
Bi	0.00										
Total Metals	0.99										
Metal/S	0.99										
^{59}Co ppm	16.16	137.30	7178.79	159.53	19.18	130.88	50.42	155.99	1285.35	51.11	29145.39
^{66}Zn ppm	bd.	83.76	7665.48	72.71	648.98	114.11	211.70	252.66	124.21	109.25	308.40
^{75}As ppm	bd.	bd.	47.41	2.62	bd.	bd.	bd.	bd.	3.80	2.00	95.88
^{77}Se ppm	64.44	55.51	63.65	46.60	70.73	49.98	28.32	24.57	81.18	89.78	113.63
Ru* ppm	0.10	0.15	2.39	bd.	bd.	bd.	bd.	bd.	bd.	bd.	bd.
^{103}Rh ppm	bd.	bd.	1.62	bd.	bd.	bd.	bd.	bd.	bd.	bd.	bd.
Pd* ppm	0.15	bd.	1.93	bd.	bd.	bd.	bd.	bd.	bd.	bd.	0.95
^{109}Ag ppm	107.04	61.71	40.87	43.51	294.48	8.57	55.15	17.81	45.92	27.46	215.26
^{111}Cd ppm	1.43	0.94	15.95	3.33	bd.	1.08	2.68	bd.	1.20	0.58	21.82
^{121}Sb ppm	bd.	bd.	2.76	0.20	bd.	bd.	bd.	bd.	bd.	bd.	1.24
^{125}Te ppm	42.62	18.82	16.06	11.66	8.89	7.03	10.95	12.13	8.55	6.70	19.81
^{185}Re ppm	bd.	bd.	bd.	bd.	bd.	bd.	bd.	bd.	bd.	bd.	bd.
^{189}Os ppm	bd.	bd.	0.17	bd.	bd.	bd.	bd.	bd.	bd.	bd.	bd.
^{193}Ir ppm	bd.	bd.	1.85	bd.	bd.	bd.	bd.	bd.	bd.	bd.	bd.
^{195}Pt ppm	bd.	bd.	17.17	bd.	bd.	bd.	bd.	bd.	bd.	bd.	bd.
^{197}Au ppm	bd.	0.05	1.29	0.06	0.11	0.22	0.17	0.04	0.09	0.02	0.57
^{206}Pb ppm	142.65	111.62	8112.13	17933.45	1250.70	392.24	593.78	477.18	56.64	71.30	1226.94
^{209}Bi ppm	99.29	0.41	57.71	47.17	0.23	34.08	34.37	10.37	30.79	1.03	5.83
S/Se	5432	4612	4713	6437	4242	6002	10594	14247	4312	3898	2948
Pt+Pd	0.15	bd.	19.10	bd.	bd.	bd.	bd.	bd.	bd.	bd.	0.95

*Bo: bornite, Chp: chalcopyrite, Co-Ni S: Co-Ni sulphides, Cub: cubanite, To: troilite, Cu>/<Fe S: mixed Cu-Fe sulphide analysis; stc: stoichiometric; * mean values of ^{99}Ru+^{101}Ru; ^{105}Pd+^{106}Pd+^{108}Pd; "bd": below detection.*

6.2.1 Stoichiometric sulphide minerals

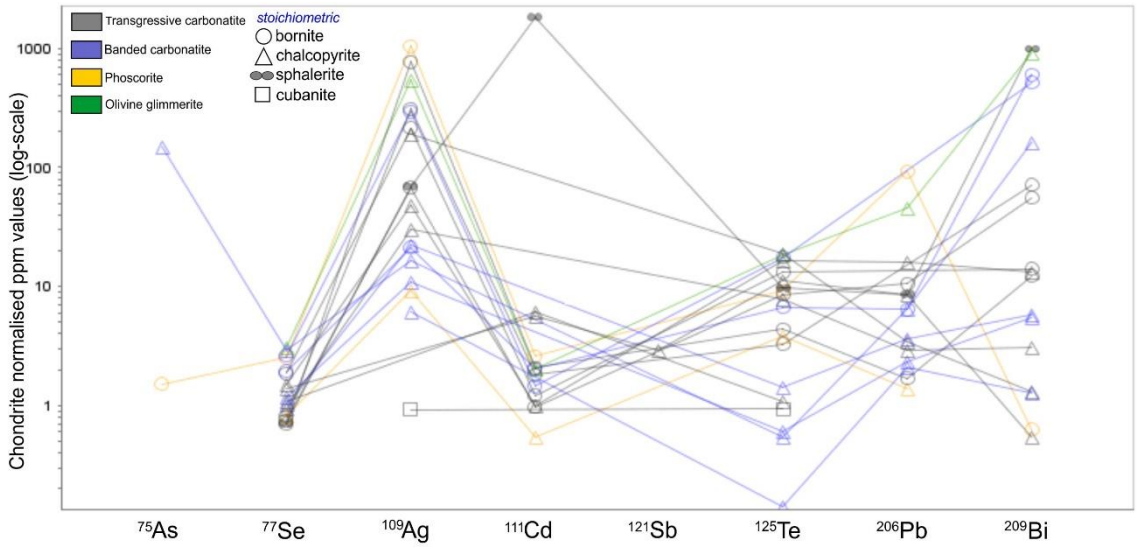

Figure 6.2.6. The diagrams show the trace element compositions of the stoichiometric sulphide phases from the studies Phalaborwa lithologies. Stoichiometric chalcopyrites were found in the transgressive and banded carbonatites, phoscorite and in the olivine glimmerite. Stoichiometric bornite was analysed in the transgressive and banded carbonatites and in the phoscorite, while sphalerite was found in the transgressive carbonatite. The trace elements are presented as chondrite normalised values (Anders and Grevesse, 1989) on a log-scale.

The trace element compositions of stoichiometric chalcopyrite, bornite, sphalerite and cubanite are shown in Table 6.2.2 and depicted in Figure 6.2.6. Analyses of the other sulphide phases provided mixed signals due to the nature of the method described in Section 6.1. The stoichiometric mineral compositions were the results of line analyses in “clean” sulphide grains where the line did not include mineral contacts or microinclusions (Fig. 6.2.2. a, b; 6.2.3. b; 6.2.4. c). The general comparison of chalcopyrite and bornite showed that trace elements in solid solution in both phases include Ag, Cd, Te, Bi and Pb. Selenium was present in solid solution in low quantities in both phases. Ag, Bi and Pb concentrations showed a wide range in both bornite (transgressive carbonatite: Ag: 30-769 ppm; Bi: 13-71 ppm, Pb: 1.69-10.5 ppm; banded carbonatite: Ag: 21-296 ppm, Bi: 519-598 ppm, Pb: 6 ppm) and chalcopyrite (transgressive carbonatite: Ag: 30-191 ppm; Bi: 0.5-13 ppm, Pb: 2.9-16 ppm; banded carbonatite: Ag: 6-191 ppm, Bi: 1.3-162 ppm, Pb: 2.1-6.4 ppm), while Cd and Te showed a wide range in chalcopyrite (transgressive carbonatite: 1.1-19 ppm; banded carbonatite: 0.14-1.42 ppm) relative to bornite (transgressive carbonatite: 3.3-13 ppm; banded carbonatite: 6.7-17.6 ppm). Tellurium levels in the banded carbonatite

chalcopyrite were lower than in the transgressive carbonatite; this pattern was not observed in the case of bornite. The bornite composition seemed more uniform in both carbonatite types and generally overlapped.

One pure chalcopyrite analysis in olivine glimmerite showed higher levels of all many of the measured elements than the carbonatites. However, chalcopyrite in phoscorite showed lower levels apart from telluride (Fig.6.2.2). One pure sphalerite analysis in transgressive carbonatite showed the highest Cd levels and lowest Se levels among all the pure sulphide phases (Fig.6.2.6).

In summary, bornite in the carbonatites had a more uniform composition with fewer outlier values than chalcopyrite and generally showed a higher Ag level. The chalcopyrite compositions differed in the transgressive and banded carbonatites, showing higher Te and Cd levels in the former. Tellurium also showed a positive correlation with Pb in the transgressive carbonatite chalcopyrite. The single analysis for phoscorite and olivine glimmerite chalcopyrite showed that the former is lower in Se, Cd and Pb (Fig.6.2.6). At the same time, the latter is higher in Ag, Te, Pb and Bi than the chalcopyrite in the carbonatites. Sphalerite is the primary host for Cd.

6.2.2 Trace element composition of the sulphide assemblages of the Phalaborwa lithologies

6.2.2.1 Trace element composition of the transgressive carbonatite sulphide assemblage

The stoichiometric chalcopyrite and bornite analyses (Fig.6.2.7a) showed that the massive bornite showed the highest Ag levels (43-154 ppm) among the phases. The other elements generally overlapped, apart from Cd, which showed the highest level in the chalcopyrite of the chalcopyrite-rich samples (4.2 ppm). All of the phases were depleted in As. When the nonstoichiometric bornite and chalcopyrite analyses were included (Fig.6.2.7b), the presence of microinclusions, especially in chalcopyrite, created a more diverse pattern caused mainly by microinclusions. Abundant PbTe(+/-Bi) microinclusions, especially in chalcopyrite of the chalcopyrite-rich samples, are well identified in the diagrams (Fig.6.2.7b).

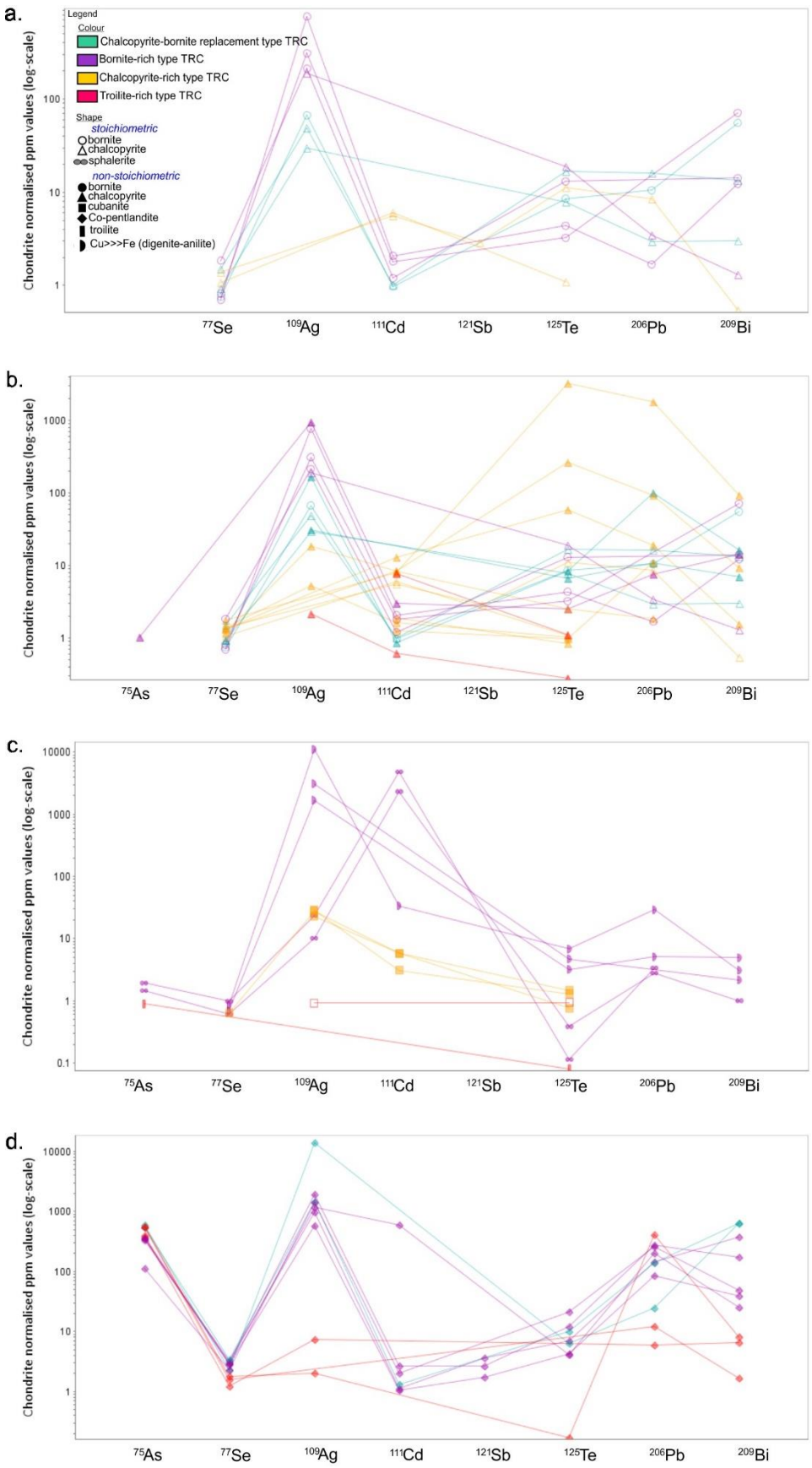

Figure 6.2.7. Sulphide trace element composition of the different transgressive carbonatite (TRC) types including bornite-rich, chalcopyrite-rich, chalcopyrite-bornite replacement and troilite-rich types. a: stoichiometric bornite and chalcopyrite; b: Stoichiometric and nonstoichiometric bornite and chalcopyrite together; d: Stoichimetric and nonstoichiometric cubanite, nonstoichiometric lamellar digenite-anilite; troilite d: nonstoichiometric Co-Ni sulphides. The trace elements are presented as chondrite normalised values (Anders and Grevesse, 1989) on a log-scale.

Lamellar Cu-S phases of the massive bornite samples showed the highest Ag levels (336-2224 ppm) among all lithologies, while sphalerite was the primary host of Cd (1303-3414 ppm). (Fig.6.2.7.c). A positive correlation was observed between Ag and Pb in both stoichiometric and nonstoichiometric sphalerite.

Co-Ni sulphides (cobalt pentlandites, cobalt-rich pentlandites and siegenite where the analysis included the edge of the pentlandite grain: Fig.6.2.4.a) showed the highest As levels in the massive bornite (208-692 ppm) and the bornite-(987-1104 ppm) replacement samples (Fig.6.2.7.d). The high As was often accompanied by high Ag levels but they were much higher in the bornite replacement samples. The trace element composition of these Co-Ni sulphides was very similar to each other. The high As levels in these phases were associated with Sb, which usually reach low levels (0.12-0.5 ppm). Positive correlations were observed between Sb, Bi and Se (Fig.6.2.8.a-b). The sulphide phases of the troilite-rich samples show lower trace element levels than those of the other lithologies (Fig.6.2.8.b-d). Selenium was present in most of the phases in solid solution; the range was relatively narrow compared to the other elements (13-72 ppm), where Ni-Co sulphides reached the highest level (Fig.6.2.7.d).

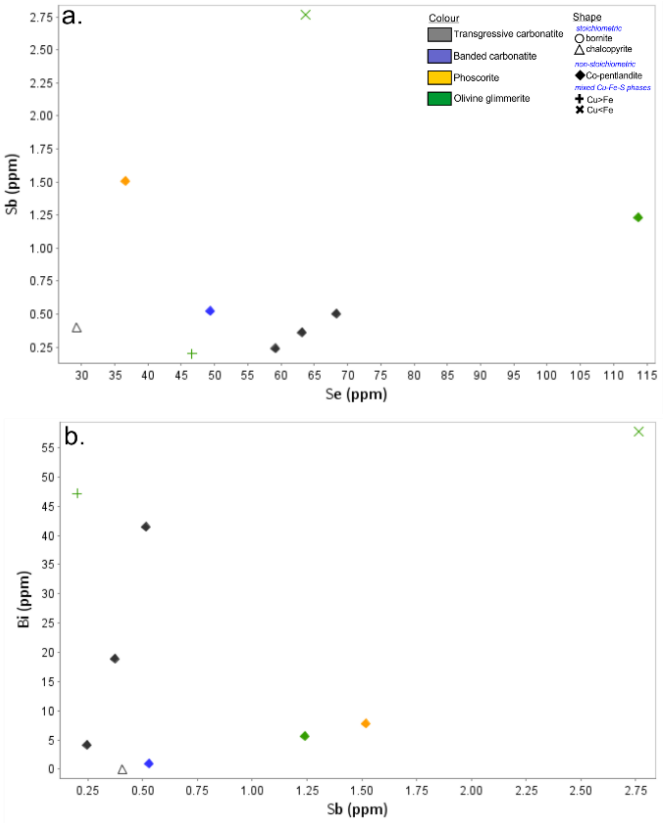

Figure 6.2.8. Ni-Co sulphides in the transgressive carbonatite showed positive correlation between Se and Sb (a) and Bi and Sb. The phases that showed the correlation were found in the bornite-rich transgressive carbonatite.

The trace element characteristics of the different Phalaborwa lithologies are compared in Figures 6.2.9-10. The transgressive carbonatite was also included for comparison, and it showed a more diverse pattern than the other lithologies (Fig.6.2.9.a).

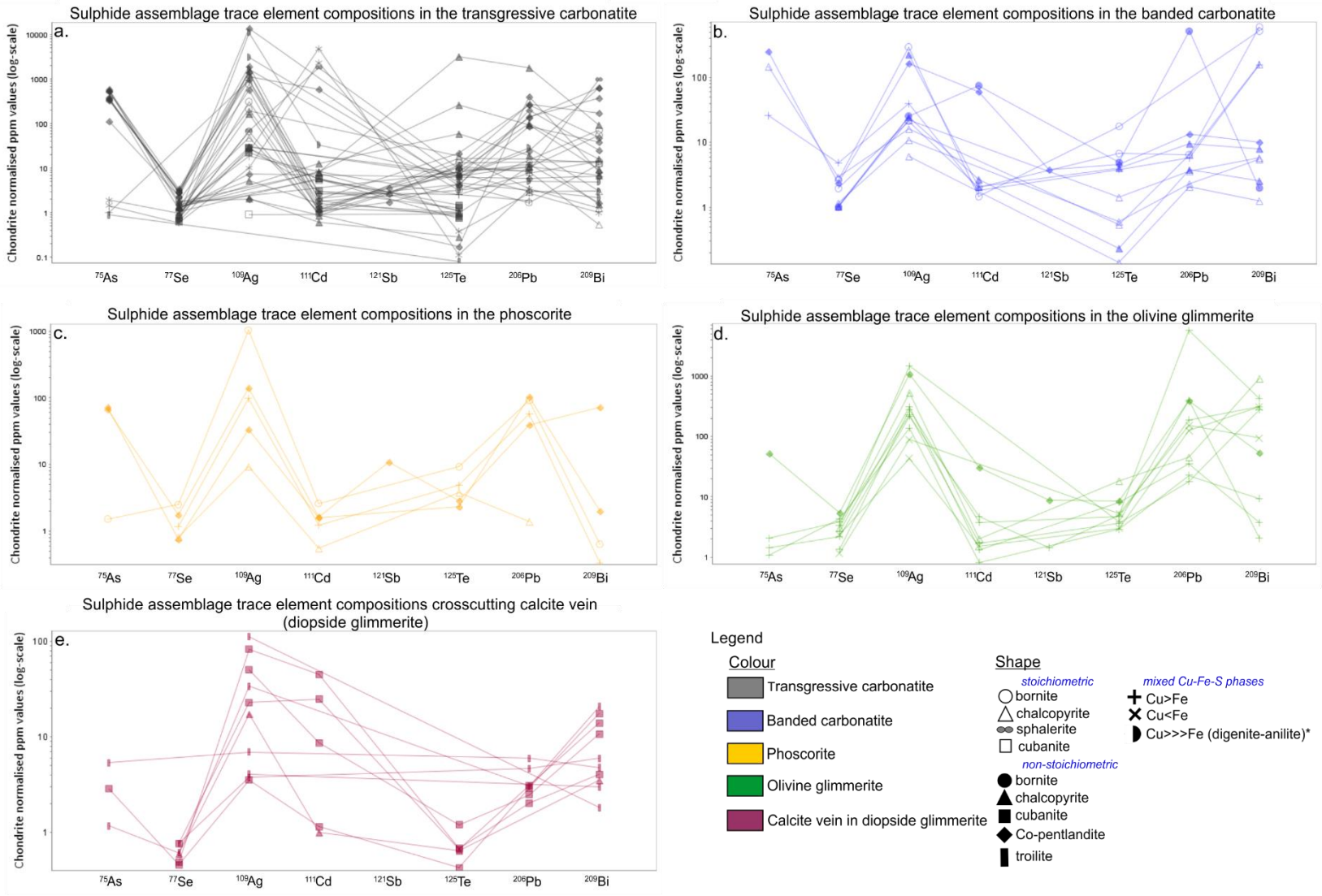

Figure 6.2.9. Trace element profile of the sulphide assemblages in the transgressive carbonatite (a), banded carbonatite (b), phoscorite (c), olivine glimmerite (d) and in the crosscutting calcite vein in diopside glimmerite (e). The trace elements are presented as chondrite normalised (Anders and Grevesse, 1989) values on a log-scale.

.

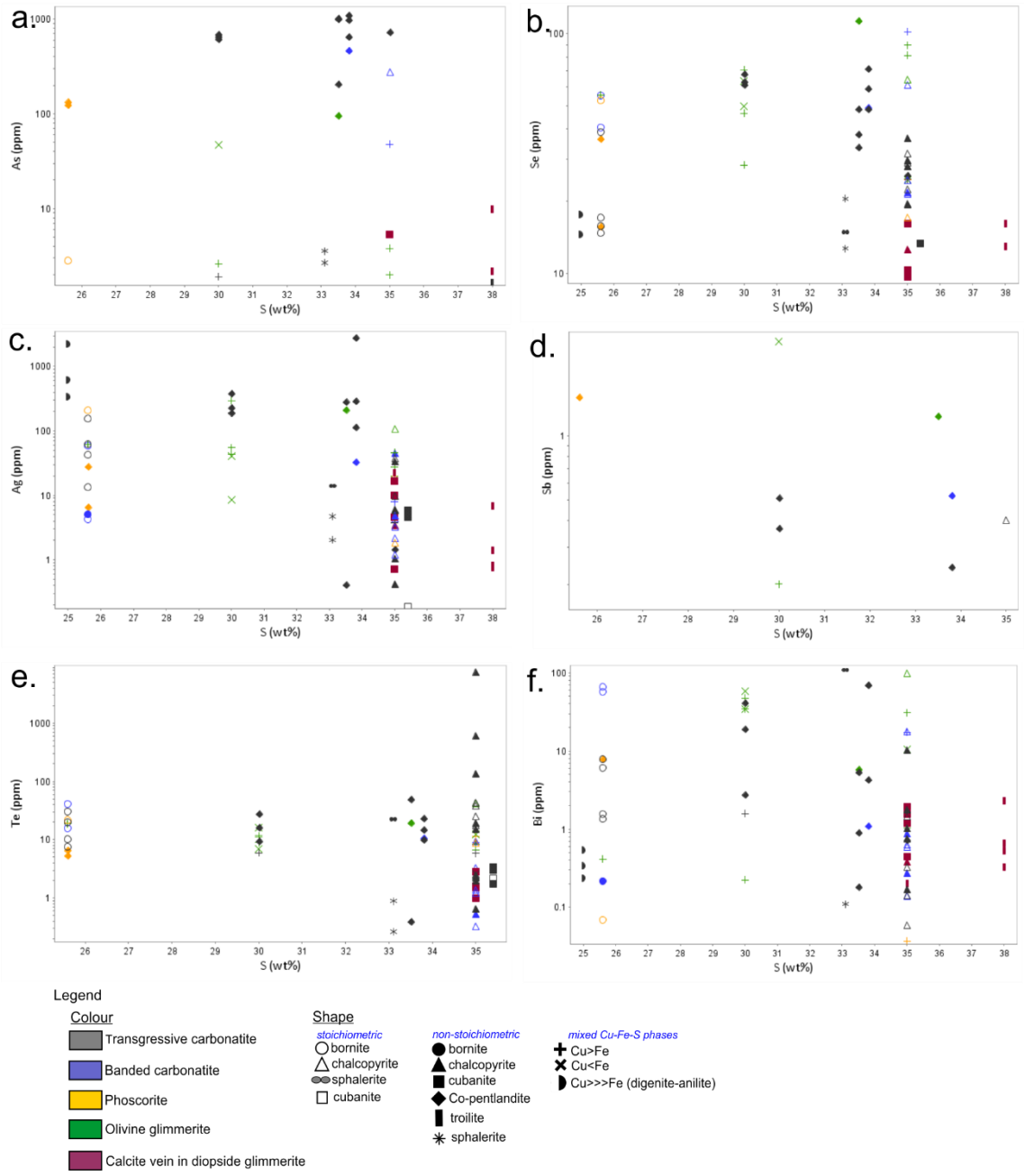

Figure 6.2.10. The diagrams show the relative abundance of the selected trace elements of the different sulphide phases in the Phalaborwa lithologies. The trace element values are not chondrite normalised in this case and they are depicted on a log-scale against the S (wt%). This way the different sulphide phases are clearly separated.

6.2.2.2 Trace element composition of the banded carbonatite sulphide assemblage

The sulphide assemblage of the banded carbonatite showed two main trends. One trend was characterised by higher Cd, Te, Pb and Bi levels and came from chalcopyrite, bornite and cobalt pentlandite (stoich. and nonstoich.) (Fig.6.2.10)

analyses. Bornite and Co-Ni sulphide line analyses showed higher Ag (4.2-59 ppm), Te (11.5-41 ppm) and Bi (0.2-66 ppm) levels in the former than in cobalt pentlandite (Fig.6.2.10.c, e, f), but high Ag-Cd-Sb microinclusion occurred in the latter (Fig.6.2.9.b). Cadmium was below detection in the second trend, and the Te, Pb and Bi were also lower than in the first trend and were observed only in chalcopyrite (Fig.6.2.9.b). Selenium changed between 0.99 and 4.9 ppm.

6.2.2.3 Trace element composition of the phoscorite sulphide assemblage

The sulphide assemblage analysis of the phoscorite showed a smaller microinclusion presence than in the transgressive carbonatite, although the sample number was small. The sulphide grains were often resorbed and altered, as shown in Figure 6.2.5.b. The trace element patterns and comparison with the other lithologies are shown in Figures 6.2.9-10. The element ranges generally overlapped with those of the transgressive carbonatite but were more confined, and the maximum values were also lower. The widest range was shown by Ag (1.85-208 ppm). The trace element compositions of the analysed samples were similar to each other.

Similarly to transgressive carbonatite, Co-Ni sulphide line analysis showed the highest As levels (124-133 ppm) (Fig.6.2.9.c, Fig.6.2.10.a). One analysis showed relatively high As and Bi in the presence of Sb, which is probably a microinclusion (Fig.6.2.9.c). Further microinclusion observed on the TRA diagram included an Ag-Bi phase, which was observed in Co-Ni sulphide (Fig.6.2.5.b). The low Bi levels were notable (especially in bornite) in the assemblage compared to the transgressive carbonatite. Se, Te and Cd levels overlapped with those of transgressive carbonatite, but Te showed a much narrower range (5.4-21.4 ppm) (Fig.6.2.10.b, e).

6.2.2.4 Trace element composition of the glimmerite sulphide assemblage

The sulphide grains in the glimmerite were usually resorbed with variously developed alteration rims around them (Fig.6.2.5.a). The general trace element profile of the olivine glimmerite was similar to the other lithologies; the exceptions included Pb and Sb (Fig.6.2.9.d, Fig.6.2.10). The sulphide assemblage in olivine glimmerite was relatively high in Pb (56.6-1250 ppm + far outlier: 4627 ppm) compared to the other lithologies. The highest Sb level was also measured in

these samples (0.2-2.76 ppm) (Fig.6.2.10.d). Chalcopyrite lines were consistently low in As, while Co-Ni sulphide lines were relatively high. As-Cd-Sb microinclusions occur in Co-Ni sulphide line analysis, and PGM with As was observed at the edge of the sulphide grain (Fig.6.2.5.a). Selenium showed the most widespread values in this lithology (25-114 ppm), with four out of ten analyses being below detection (Fig.6.2.9.d).

The sulphide assemblage analysed in crosscutting calcite vein in diopside glimmerite (composed of nonstoich cubanite, troilite and chalcopyrite) had the lowest Se levels compared to the other lithologies (10-16 ppm) (Fig.6.2.9.e; Fig.6.2.10.b). Compared to the other lithologies, the low Te and Pb levels were a common characteristic of the banded carbonatite (Fig.6.2.10.b,e). Antimony was not detected. The Ag levels showed a wide range and overlapped in cubanite (0.7-16.5 ppm) and troilite (0.8-22 ppm). The former showed a positive correlation between Cd and Zn and Ag and Au (Fig.6.2.11.a-b) and contained Te in contrast to the troilite.

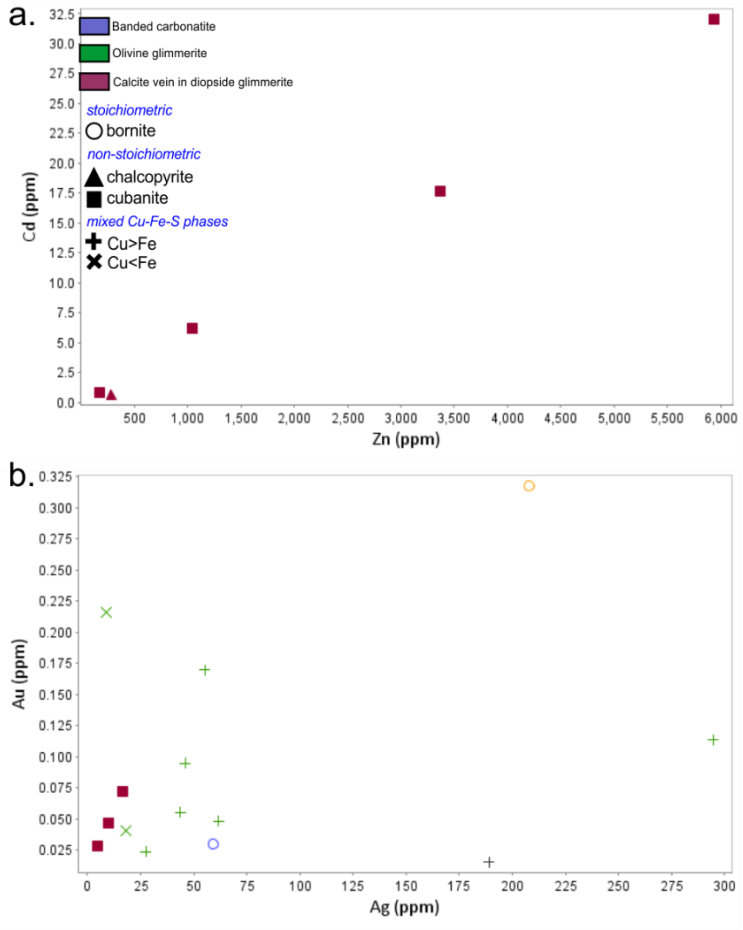

Figure 6.2.11. The nonstoichiometric cubanite found in the calcite vein crosscutting the diopside glimmerite showed positive correlation between Zn and Cd (a) and Ag and Au (b).

6.2.2.5 PGE in the Phalaborwa sulphide assemblages

The analysed sulphide phases did not show common PGE occurrence, and only a few PGM were found (Fig.6.2.12). PGMs were found in the disseminated sulphides of phoscorite and olivine glimmerite, both in the presence of Au (6.2.12.a). The most common IPGE and PPGE were Ru and Pd, respectively. Pd-Au microinclusions were found in transgressive carbonatite and olivine glimmerite Ni-Co-sulphides and Cu-rich Cu-Fe sulphides of the former. Very low Ru levels were found in chalcopyrite (0.1-0.15) and cubanite (0.1 ppm) (stoich and nonstoich) in the carbonatites and olivine glimmerite (chalcopyrite: 0.1 ppm, mixed Cu-Fe sulphides: 0.15-2.4 ppm) as a solid solution phase. IPGE was concentrated in Cu-Fe-S phases, while PPGE was associated with Ni-Co sulphide phases (Fig.6.2.12.b).

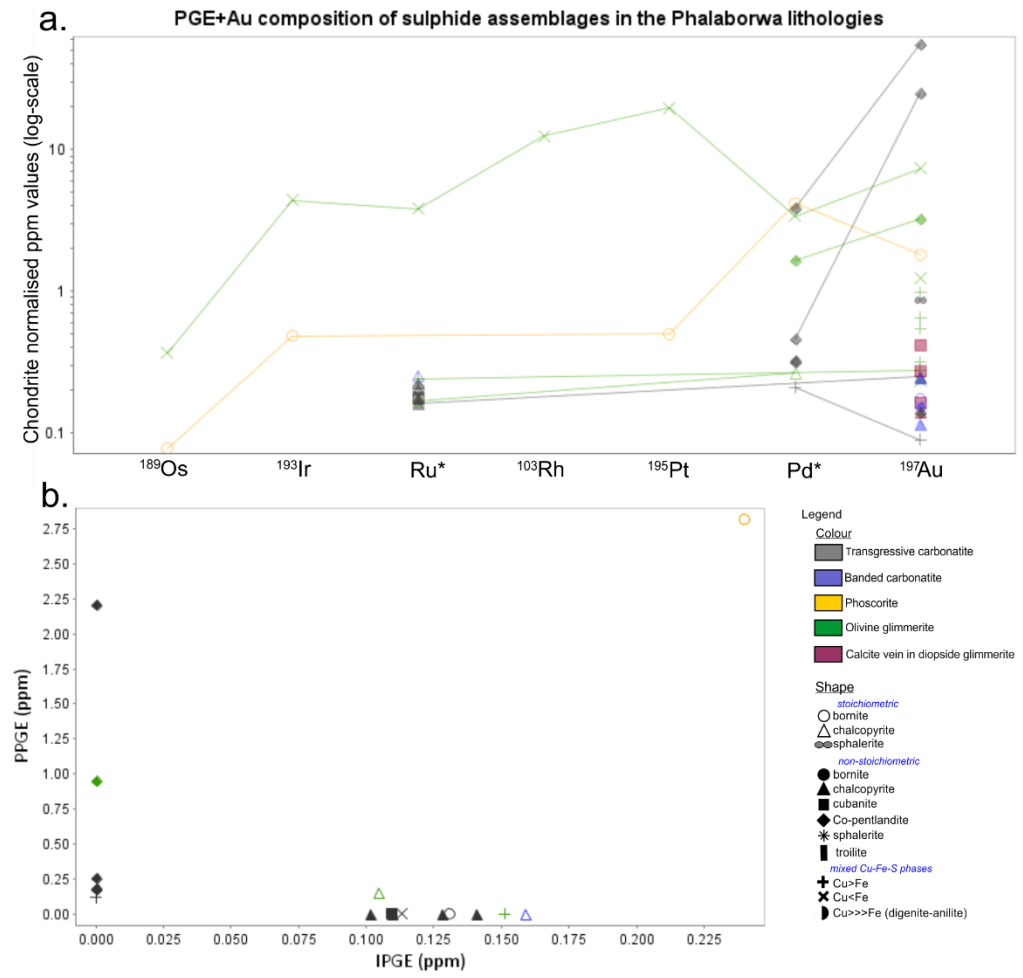

Figure 6.2.12. The analysed Phalaborwa sulphides were depleted in PGE. PGM and Au were found in the disseminated sulphides of phoscorite and olivine glimmerite (a). The IPGE and PPGE groups were represented by Ru and Pd, respectively. The PPGE were more readily associated with Co-Ni sulphides, while IPGE with Cu-Fe sulphides (b). In diagram a, the trace elements are presented as chondrite normalised values (Anders and Grevesse, 1989) on a log-scale. "*": mean values of $^{99}Ru+^{101}Ru$; $^{105}Pd+^{106}Pd+^{108}Pd$.

6.3 Discussion

6.3.1 The interpretation of As, Te, Se and Bi characteristics in the Phalaborwa sulphides.

In sulphide minerals, Se generally occurs between tens of ppm up to around 250 ppm in some cases, with the highest recorded values in magmatic sulphides found in the Platinova Reef, between 400 and 1200 ppm (Holwell et al., 2015). Selenium partitions into solid sulphide phases, and as Holwell et al. (2015) observed in the case of Platinova Reef, it generally shows consistent concentrations in the sulphides of the same samples. Se occurred from below detection limit up to 114 ppm in the Phalaborwa sulphides, with the maximum measured in a disseminated Ni-Co sulphide in olivine glimmerite. Selenium in the carbonatites was generally below 70 ppm. Le Bras et al. (2021) found that Se showed a 3-16 ppm variation between different sulphide types and that the variation was small within samples but could be significant between different samples. This characteristic was also observed in the transgressive carbonatite Cu-Fe sulphides in the present study, the most significant difference being 2 ppm in bornite and 6-12 in chalcopyrite. In the banded carbonatite, the Se variation in bornite was 14 ppm. However, the (nonstoich.) Ni-Ci sulphides showed a much wider variation, the largest being 23 ppm. Selenium is the least compatible in the mss among the trace elements, and its partition coefficient ($DSe_{mss/melt}$: 0.65±0.05) does not change with fS_2. Selenium replaces S^{2-} in the mss with divalent anions of Se^{2-} regardless of fS_2. Discrete Se phases are rare in magmatic sulphide deposits as Se is not significantly enriched compared to S during mss fractionation (Helmy et al., 2010). The present study did not observe discrete Se phases, and they were not reported by other studies (e.g., Rudashevsky et al., 2004; Le Bras et al., 2021).

Selenium rarely occurs in PGM, and when it does, it is frequently associated with secondary minerals, suggesting the Se can be remobilised (Prichard et al., 2013). The textural observations in Chapter 4 suggested that the sulphide grains in the glimmerites were affected by secondary processes that caused the resorption of the grains and remobilisation of elements; the high Se levels found in these phases could have resulted from these processes.

Arsenic was not a particularly abundant trace element in the Cu-Fe sulphides (apart from one outlier in the banded carbonatite with 276 ppm). The sample

number is small, but the variation is not substantial where As occurred. The present study found the highest As levels (1104 ppm) in Ni-Co sulphides of transgressive carbonatite. Arsenic was also part of As-Pt microinclusions in the olivine glimmerite disseminated sulphides. Eu-subhedral sperrylite (PtAs2) was reported by Rudashevsky et al. (2004) from the carbonatites. Further As-containing PGM found by Rudashevsky et al. (2004) included arsenopalladinite ($Pd_8(As,Sb)_3$), anhedral majakite (PdNiAs) and an undefined phase with the composition of $Pd_{11}As_2(Pb,Hg)_2$. The study found that the early eu- and subhedral arsenic-bearing PGM were Pt-dominant. At the same time, the anhedral, possibly secondary As-phases, were Pd-dominant (consistent with the higher mobility of Pd). In the present study As was more likely to occur together with Pd than Pt.

Helmy et al. (2010) showed that As has the most extensive range of partition coefficients, which changed with fS_2 (At the lowest fS_2 $DAs_{mss/melt}$: 0.4 while at the highest fS_2 it is 0.01). During changes in fS_2, As goes through a significant oxidation state change where the anion state is the main form. In a relatively reduced sulphide melt, As may partition into mss or form discrete phases. Helmy et al. (2010) observed that the As can become particularly enriched in oxidised sulphide melt. In the most oxidised experimental runs, it partitioned into the vapour phase, suggesting the importance of As cations in hydrothermal processes as As^{n+} can be enriched in derivative sulphide melts and eventually partition into hydrothermal fluids. The experiments showed that as much as the oxidation state, the metal content of the sulphide melt was also an important controlling factor of As behaviour. When Pt was dominant in the melt, As formed euhedral sperrylite, which crystallised before the mss, preventing the enrichment in the later sulphide melts. However, with dominant Pd present, As was exsolved from the sulphide melt as droplets of immiscible Pd-rich arsenide melt (Helmy et al., 2010). The Phalaborwa arsenides described by Rudashevsky et al. (2004) may represent the shift in composition from an early Pt-rich system (euhedral sperrylite) towards Pd-enrichment. The different PGE-arsenide mineral forms observed by Rudashevsky et al. (2004) may represent a multistage formation of arsenides, where the euhedral sperrylite formed before mss crystallisation, while anhedral, secondary Pd-arsenides formed during a later stage and remobilisation. This is also consistent with the higher mobility of the Pd compared to Pt (Helmy et al., 2010). Differences in As levels between Ni-Co and Cu sulphides in the transgressive carbonatite and the changing habit of the As-PPGE

minerals can suggest a shift towards more oxidised conditions in the magmatic-hydrothermal system.

The three least compatible trace elements in mss are Sb, Te and Bi; these strongly partition into the derivative sulphide melts (Helmy et al., 2010). In the Phalaborwa sulphides, Sb is rare, while Bi and Te are common. The low solubility of these elements in mss prohibits the formation of discrete antimonide, telluride or bismuthide phases in magmatic sulphides by solid-state exsolution from mss. Helmy et al. (2010) suggested that discrete Sb-Te-Bi-PGE phases derive from droplets of immiscible melts enriched in Sb-Te-Bi, and they were exsolved from late-stage fractionated sulphide melt (Helmy et al., 2010).

Antimony was the least common and lowest level metalloid analysed in the Phalaborwa sulphides; the highest level was 3 ppm in olivine glimmerite, but it occurred the most frequently in Ni-Co sulphides (0.2-1.5ppm) in all lithologies. Additionally, it was observed in chalcopyrite (0.4 ppm) in the transgressive carbonatite. The TRA diagrams indicated that it formed microinclusions with Cd, Te, Pb(±Bi, Ag). Helmy et al. (2010) suggest that this occurrence probably represents immiscible melts from the late-stage sulphide liquid. Antimony is highly incompatible with mss regardless of fS_2 of the system, with $D_{mss/melt}$: ~0.003. Considering the findings of the study above, the low abundance of Sb in the Phalaborwa sulphides could indicate that the sulphides represent an earlier rather than a later-stage sulphide liquid or that the general Sb depletion of the system.

Tellurium commonly formed Pb-Te (±) Bi microinclusions in the Phalaborwa sulphides. It must be mentioned that a microinclusion with very high (~7500 ppm) Te, identified as altaite in the optical studies, occurred only in one sample. Apart from this sample, the Te levels were relatively similar in bornite (transgressive carbonatite: 8-31 ppm; banded carbonatite: 16-41 ppm) and chalcopyrite in the transgressive carbonatite (3-44 ppm). The chalcopyrite in the banded carbonatite showed lower levels (0.3-3 ppm). The nonstoichiometric sulphides showed a wide range of Te levels in all lithologies, including microinclusions. Tellurium is highly incompatible in mss ($DTe_{mss/melt}$: ~0.02); it is insoluble and present as a cation or metallic phase. With the changes in the metal/S ratio of the mss, the partition coefficient shows a weak trend, and Te becomes slightly more compatible with stoichiometric mss than with oxidised mss (Helmy et al., 2010). Holwell et al. (2015) found low levels of Te in the solid solution of Cu-sulphides of the Platinova

Reef with the range of 50-100 ppm, noticeably lower than the Phalaborwa sulphides. The previous work also found Te in PGM and concluded that the distribution is generally inconsistent. In magmatic sulphides, Te usually reaches only a few ppm (Holwell et al., 2015). In the Phalaborwa sulphides, Te was between 0.26 and 137.92 ppm and was ubiquitously present except in troilite, suggesting that the samples may represent multiple stages of sulphide evolution. Similarly to the findings of Holwell et al. (2015), the distribution is very inconsistent.

Bismuth in the Phalaborwa sulphides is ubiquitous, ranging from below detection up to ~100 ppm and occurs as parkerite and wittichenite in bornite. The stoichiometric bornite in transgressive carbonatite contained up to 7.8 ppm Bi, while the banded carbonatite bornite had 57-66 pm. Chalcopyrite showed more uniform Bi levels in the two carbonatites (transgressive carbonatite: 0.06-0.63 ppm, banded carbonatite: 18 ppm), while in the olivine glimmerite reached a higher level (99 ppm). Bismuth is also highly incompatible with the maximum partition coefficient with the mss of ~ 0.002 (Helmy et al., 2010). In the Platinova Reef sulphides, Bi occurred up to 20 ppm, with less than 1 ppm in most, and high values were attributed to microinclusions (Holwell et al., 2015). Phases with high Bi content may indicate later-stage processes, a characteristic that Le Bras et al. (2021) also observed. The study found that valleriite was generally more enriched in Bi than the magmatic sulphides and suggested enrichment by crustal-contaminated fluids containing Pb and As. This is consistent with the presence of wittichenite, which was formed from earlier parkerite in the transgressive carbonatite massive bornite.

The Ag in the Phalaborwa sulphides behaves similarly to Bi and Te; additionally, there is an association with Te in altered bornite samples. Chalcopyrite is considered a good host for Ag, but the distribution is controlled by the proportion of coexisting galena and sphalerite (Cook et al., 2011). Cook et al. (2011) observed clear discrimination between bornite and chalcocite based on Bi and Ag content, where Ag partitioned into the chalcocite/digenite while Bi concentrated in the bornite. However, the Ag was retained in bornite when no coexisting Cu-S phase was present. Similar feature was observed in the Phalaborwa sulphides, where Ag was higher in the lamellar Cu-S phase than in the bornite, while the opposite was true for Bi.

The metalloid signatures of the analysed Phalaborwa sulphides were shaped by the evolution of the system from early magmatic and hydrothermal and later-stage alteration processes. Tellurium enrichment may indicate a lower temperature hydrothermal emplacement of some chalcopyrite, indicating multi-generation of magmatic-hydrothermal sulphide emplacement. The As behaviour (this and previous studies) seems to correspond with fS_2 and fO_2 changes as the system becomes more oxidised, as shown by the secondary phases, which were also more enriched in Bi.

6.3.2 PGE characteristics of the Phalaborwa sulphides

The trace element analysis of the present sample set showed a higher PGE and PGM presence in the disseminated sulphides of the phoscorite and silicate rocks compared to the carbonatites. Overall, the results indicate a PGE depletion in the Phalaborwa lithologies. Rudashevsky et al. (2004) found PGE composition of bulk sulphide concentrate (by Rudashevsky et al., 2004) showed 0.23 ppm Pt, 0.40 ppm Pd and 2.0 ppm Au. Le Bras et al. (2021) also found low-level PGE in the Cu-sulphide phases (average values: Pd: 0.091, Pt: 0.012, Os: 0.015, Ir: 0.003). In comparison, the sulphide fraction of the Merensky Reef ores contains 279 ppm Pt, 120 ppm Pd and 22 ppm Au (Ballhaus and Ulmer, 1995).

Consistently with Rudashevsky et al. (2004) and Le Bras et al. (2021), the present study showed that the Pd-group (PPGE) is the dominant PGE group in the Phalaborwa sulphides. PPGE includes Rh, Pt and Pd with the common occurrence of Au and was often associated with Cu, Fe and Ni sulphides. Although the dataset was small, a preferential distribution of IPGE and PPGE was observed, where IPGE was primarily found in Cu-sulphides and PPGE in the Ni-Co sulphides. This distribution pattern was not observed by previous studies, which did not include Ni-Co sulphides.

In relation to the base metal deposits, it was shown that PPGE and IPGE fractionate between the mss and iss, leading to PPGE-enriched Cu-sulphides and IPGE-enriched Fe-rich mss (Holwell and McDonald, 2010). Based on these findings, Le Bras et al. (2021) interpreted their finding as PPGE and sulphide phase exsolution from a Cu-rich iss, which was fractionated from mss during ascent. In

the present study, Ni-Co sulphides that showed PPGE were found in transgressive carbonatite with bornite replacement; these phases were interpreted as early magmatic phases representing the mss.

The present study found that the Ni-Co sulphides were the main hosts of Pd over Cu-Fe sulphides. Peregoedova and Ohnenstetter (2002) showed that in the system Cu-Fe-Ni-S, Pd is distributed mainly between the sulphide solid solutions at 760 ^{o}C. At this temperature, the heazlewoodite-iss (Hz-iss) phase coexisted with mss. Hz-iss showed an intermediate compositional range from heazlewoodite $(Ni, Fe)_{3\pm x}$ and intermediate $Cu_{1\pm x}Fe_{1\pm y}S_2$ solid solutions. The primary Pd collector was the (Hz-iss) quaternary solid solution, and partitioning into the base metal sulphide solutions was very low. The Pd content of the Hz-iss increased with increasing Ni and Cu. According to the study, Pd entered the Hz-iss structure at 760 ^{o}C. The exsolved phases with Pd content included pentlandite, a lamellar Pd-Cu-Fe-Ni sulphide complex, and Pd(Cu, Fe) alloy. Palladium also partitioned into the mss during the experiments and showed an equal distribution between mss and Hz-iss, and the bornite solid solution can also potentially host Pd (Peregoedova and Ohnenstetter, 2002). Fleet and Stone (1991) and Fleet et al. (1991) found that Pd partitioned into the sulphide liquid at low fS_2 while at the same time, Pt preferred to form alloys, as mentioned previously. Based on the PGE patterns, the Ni-Co sulphides of the present study interpreted as primary (based on textures and phase relations – Chapters 4 and 5), probably represent either the mss or the Hz-iss that exsolved, in this case, cobalt pentlandite with Pd relatively enriched compared to the Cu-Fe sulphides. The Pt-Pd distribution feature suggests a low or decreasing fS_2 environment for the Phalaborwa sulphides.

Alongside Pd, the Ni-Co sulphides also showed high As (100-1000 ppm) content. Helmy et al. (2010) showed that the Cu-rich sulphide liquid with added native S, Bi, Te, and As produced segregations enriched with these elements upon quenching, scavenging Pt preferentially over Pd into these segregations. The spatial distribution of Pt closely overlapped with As-rich areas. As mentioned before in relation to As behaviour, in the Pt-dominant system, As forms euhedral sperrylite, crystallised before the mss, while with Pd dominance, the arsenic forms immiscible Pd-rich arsenide melt (Helmy et al., 2010). The different PGE-arsenide mineral forms observed by Rudashevsky et al. (2004) may represent a multistage formation of arsenides, where the euhedral sperrylite formed before mss crystallisation, while

anhedral, secondary Pd-arsenides formed during a later stage.

The TRA diagrams show that Pd, As, and Bi reached higher cps when the line analyses reached the siegenite rim of the cobalt pentlandite. Le Bras et al. (2021) observed higher Pd levels in the transgressive carbonatite valleriite compared to the primary magmatic sulphides and metalloid enrichment. PGE and metalloid enrichment in the secondary sulphides point towards the remobilisation of these elements by hydrothermal fluids with crustal contribution, as the metalloids can be of crustal origin (Hutchinson and Kinnaird, 2005). Le Bras et al. (2021) also considered external metalloid influence.

The disseminated sulphide grains were formed between large cumulus olivine or phlogopite, often at areas with strong serpentinitic alteration and valleriite formation (Fig. 4.1.10 a-f). The sulphides are magmatic; however, they are often subjected to extensive resorption during the serpentinisation of the host rock. The disseminated sulphide grains in the olivine glimmerite showed the presence of PGM, usually at the edges of the grains. The remobilisation of sulphides and PGE were observed in multiple significant massive sulphide deposits, including the Platreef in the Bushveld complex (e.g., Hutchinson and Kinnaird, 2005). Hutchinson and Kinnaird (2005) observed a weak correlation between the base metal and PGE contents. PGMs were found within secondary silicates, around orthopyroxenes or along sulphide margins and only very rarely within sulphides as inclusions. The disseminated sulphides of the study often showed PGE content at the margins. Petrographic evidence suggested that PGMs were originally associated with large composite sulphides in the unaltered silicates but were remobilised (alongside sulphides) and recrystallised during or soon after serpentinisation. Metalloids that influenced PGE behaviour (S, As, Te, Bi, Sb) were derived from metasedimentary rocks and were introduced to the system after the emplacement of Platreef (Hutchinson and Kinnaird, 2005). Another example of remobilised PGE associated with Ni-Cu sulphide deposit is Jinchuan intrusion in Northwest China, where Pd-PGM and Au-bearing PGM are present in serpentinised rocks (Prichard et al., 2013).

In the case of Phalaborwa, two serpentinisation stages were differentiated by Giebel et al. (2017). During the first late-magmatic process, secondary apatite, chondrite, and phlogopite chloritisation occurred due to interaction with aqueous-carbonic fluids. The second stage occurred after the main sulphide mineralisation

emplacement and caused valleritisation, galena, barite, celestite, late-stage, apatite, thorianite and thorite formation. The aqueous fluid had H^+, CO_3^{2-} and F^- content. Further post-magmatic fluids with OH^-, HF and CO_3^{2} were also described by Giebel et al. (2017). Interaction with these fluids might cause PGE redistribution in the Phalaborwa sulphides. As Mountain and Wood (1988) described, PGE (Pt^{2+}, Pd^{2+}) form ligands preferentially with soft ligands such as OH^-, HS^-, and Cl^-, while complexes formed with hard anions (CO_3^{2-}, HCO_3^{1-}, SO_4^{2-}, PO_3^{1-} and F) are not stable. Hydroxide complexes can transport PGE near neutral to basic solutions near intermediate fO_2 values. More petrographical evidence is required to show late-stage PGE remobilisation, but the serpentinisation processes and the estimated fluid compositions presented by Giebel et al. (2017) were suitable to transport PGE, which re-deposited with the secondary sulphide phases observed in the phoscorite and silicate samples of the present study. Other agents that could have played a part in the PGE remobilisation were bisulfide and mixed bisulfide-hydroxide complexes. Mountain and Wood (1988) suggested that these complexes can be important in PGE transport at 300 ^oC and near high fS_2 conditions. Le Bras et al. (2021) also suggested later-stage desulfurisation affecting the sulphide trace element distribution.

6.3.3 S/Se ratios of the Phalaborwa sulphides

S/Se ratios of the Phalaborwa sulphides were compared to S/Se ratios of mantle-derived samples (Fig.6.3.1). The selected mantle rocks sampled SCLM of various types and ages (Table 6.3.2), belonging to different cratons. The main focus was to compare the S/Se ratios of the present sample set to other Kaapvaal samples that represent the Kaapvall mantle. The selected published S/Se ratios and their source were described in Section 6.1.3. The few phases containing both Pt+Pd and Se above the detection limit were plotted in the S/Se vs Pt+Pd diagram (Fig. 6.3.2). As it was described in Section 6.1.3, The S/Se ratios can be affected by various syn- and post-magmatic processes, and S/Se ratios with the combination of in-situ S-isotope analysis is a more robust indicator of the sulphide origin (e.g., Smith et al., 2016). Although the present study did not carry out S-isotope analysis, the magmatic origin of the Phalaborwa sulphides was shown (Mitchell and Krouse, 1975; Bolhar et al., 2020; Le Bras et al., 2021). Using S/Se ratios of sulphides from the different sulphide generations and different lithologies and comparing them to

S/Se ratios of different mantle-derived samples may provide additional information and future study directions regarding the Phalaborwa sulphides and the characteristics of the Phalaborwa SCLM.

The S/Se ratios of the Phalaborwa sulphides were compared to the average mantle and to several different mantle types from different cratons (Fig.6.3.1). Using the average or primitive mantle domain compositions only can be misleading as carbonatites are derived from an enriched, metasomatised mantle potentially leading to different S/Se ratios than the primitive or average mantle even without post-magmatic effects. Figure 6.3.1 shows that the S/Se ratios of the different mantle-derived samples changed based on the SCLM they sampled and the host-rock types. Samples of the Dharwar craton kimberlite and the Central Asian Foldbelt peridotite showed the broadest S/Se ranges. The majority of the values fell below the average mantle but also exceeded it. The endmembers of the Muscox samples included peridotites, with lower than the average mantle S/Se ratios, and felspathic peridotites which overlapped or exceeded the average mantle values. The different peridotite types represented different level of crustal contamination due to wall rock assimilation (Mackie et al., 2009).

The Kaapvaal pyroxenite S/Se values overlapped with that of the average mantle; while the Kaapvaal eclogitic pyrite-dominated base metal sulphides (BMS) showed a similarly wide S/Se range as the Phalaborwa lithologies. Although these BMS were derived from the Cretaceous Roberts Victor eclogites, Hughes et al., (2021) concluded that the BMS budget originated from ancient subduction processes during the formation of the Colesberg Magmatic Lineament (~2.9 Ga) and the Kaapvaal cratonisation processes. Although the Roberts Victor eclogites underwent multiple stages of metasomatism (e.g., Huang et al., 2014), Hughes et al. (2021) concluded that the trace element composition of the BSE reflected that of the protolith, and that the predominance of pyrite resulted directly from subduction and eclogitisation rather than subsequent SCLM metasomatism or supergene alteration. It was suggested that the high S/Se ratios (relative to the average/primitive mantle values) of the eclogitic BMS possibly resulted from the increased S abundance in the BMS as the modal sulphide content decreased during eclogitisation (Hughes et al., 2021). The following sections will compare the S/Se ratios of Phalaborwa lithologies and the mantle xenoliths described above.

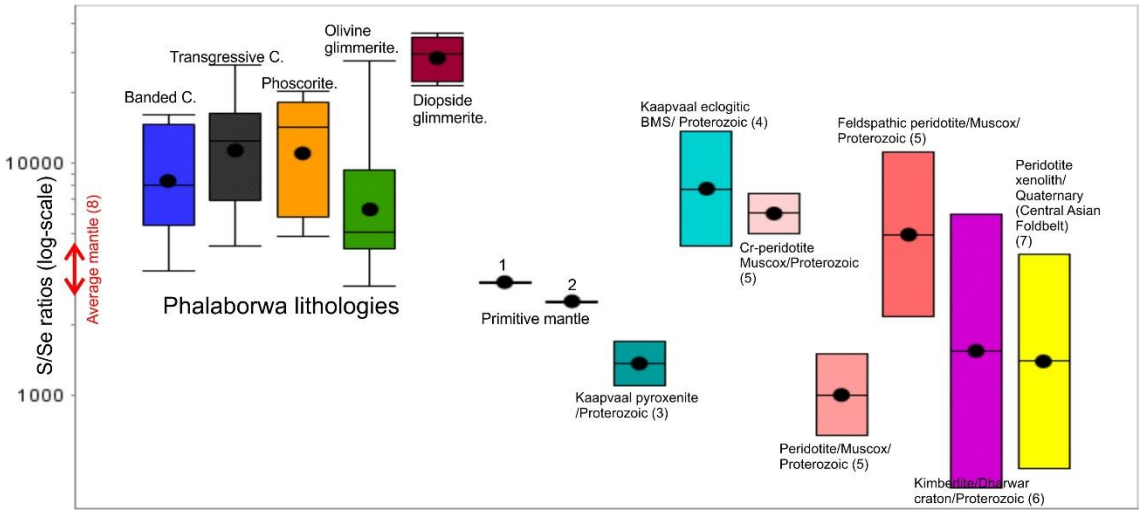

Figure 6.3.1. The S/Se ratios (log scale) of the Phalaborwa sulphide assemblages depicted together with S/Se ratios of different mantle-derived samples that represent different mantle sources. The average S/Se mantle ratios are indicated on the axis of the diagram. (1) Palme and O'Neill (2003); (2) McDonough and Sun (1995); (3) Hutchinson et al. (2015); (4) Hughes et al. (2021); (5) Mackie et al. (2009); (6) Paton et al. (2009); (7) Wang and Becker (2013); (8) Eckstrand and Hulbert (1987).

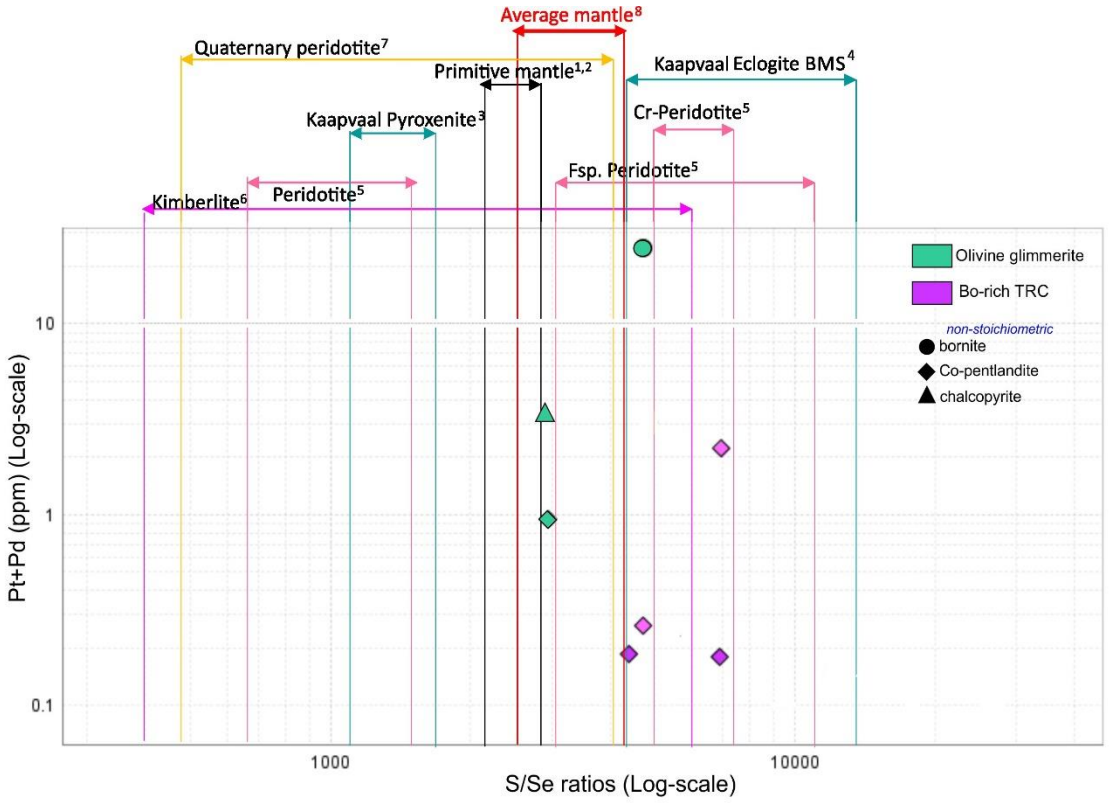

Figure 6.3.2. The Phalaborwa sulphides were depicted on a S/Se vs Pt+Pd diagram. The S/Se ratio ranges of the different mantle-derived samples, primitive mantle and the average mantle S/Se are also indicated. The diagram shows that the majority of the sulphides fall into the S-rich side of the diagram when compared to the average mantle range, which indicate crustal S-enrichment. The other mantle-derived samples may represent different mantle sources. (1) Palme and O'Neill (2003); (2) McDonough and Sun (1995); (3) Hutchinson et al. (2015); (4) Hughes et al. (2021); (5) Mackie et al. (2009); (6) Paton et al. (2009); (7) Wang and Becker (2013); (8) Eckstrand and Hulbert (1987).

6.3.3.1 Transgressive carbonatite

The stoichiometric chalcopyrite and bornite S/Se ratios (Fig.6.3.3) showed that bornite varied in a broader range than chalcopyrite. The bornite S/Se ratios in the transgressive carbonatite changed between 14984 and 17358. One bornite measurement showed a ratio of 6585, which is close to average mantle values. Bolhar et al. (2020) found that some of the bornites from the transgressive carbonatite showed mantle S isotope composition and regarded bornite as a primary magmatic phase that preceded chalcopyrite formation. Chalcopyrite in bornite-replacement samples (11007-17818) varied in a wider range than massive chalcopyrite (12006-15521). The results indicated that the stoichiometric sulphides of the transgressive carbonatite had overlapping S/Se ratios, which showed higher than average unmetasomatised mantle values but overlapped with sulphide S/Se ratios from a Kaapvaal eclogitic BMS. Including the nonstoichiometric bornites and chalcopyrites did not change the outcome (Fig.6.3.3). As described in the previous section, the Kaapvaal eclogitic BMS presented here (Hughes et al., 2021) were derived from an eclogoitised Proterozoic oceanic crust. Two chalcopyrite analyses in massive bornite and troilite-rich transgressive carbonatite show Se below detection.

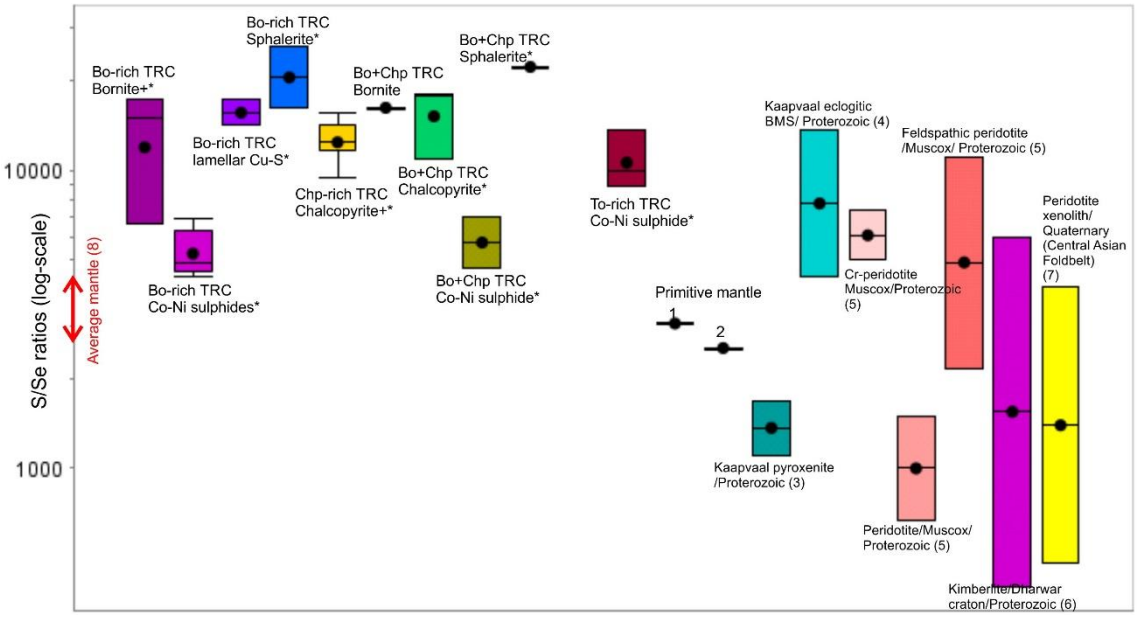

Figure 6.3.3. The sulphide S/Se ratios (log scale) of the different transgressive carbonatite types depicted together with S/Se ratios of different mantle-derived samples that represent different mantle sources. The average S/Se mantle ratios are indicated on the axis of the diagram. (1) Palme and O'Neill (2003); (2) McDonough and Sun (1995); (3) Hutchinson et al. (2015); (4) Hughes et al. (2021); (5) Mackie et al. (2009); (6) Paton et al. (2009); (7) Wang and Becker (2013); (8) Eckstrand and Hulbert (1987). *: nonstoichiometric analyses were included, which did not change the interpretations.

Ni-Co sulphides in the massive bornite and replacement transgressive carbonatite had similar S/Se ratios (4401-6879) and (4720-6960), respectively. These values were much lower than those of the Cu-Fe sulphides (except one bornite analysis). However, S/Se ratios in the troilite-rich transgressive carbonatite (8800-13641) overlapped with the Cu-sulphides of the other transgressive carbonatite types. S/Se ratios of Ni-Co sulphides in bornite replacement transgressive carbonatite showed that these phases fell closest to the average mantle values. Additionally, PPGE showed a preference for these phases over the Cu-sulphides. As discussed previously, the cobalt pentlandites of the transgressive carbonatite were interpreted based on their texture and general phase relation and trace element composition as an early, high-temperature magmatic phase that was crystallised either from the mss or the Hz-iss, with possible later-stage alteration that introduced crustal metalloids. The low S/Se ratios could also indicate that the phases were affected by desulphurisation proposed by Le Bras et al. (2021), and suffered S-loss, leading to high Se/S ratios. However, the trace element results in this study showed that the analysed Ni-Co sulphides were relatively enriched in Se compared to the Cu-sulphides. The Pt+Pd vs S/Se profile also shows that the cobalt pentlandite data points from the massive bornite (transgressive carbonatite) fell into the mantle domain (Fig.6.3.2). In the case of massive bornite, the cobalt pentlandite was subjected to alteration where a siegenite rim developed around it; this could have affected the S/Se ratios by adding S by S-rich fluids or removing Se by oxidising fluids.

Based on the textural studies in Chapter 4, the sulphide assemblage of the troilite-rich transgressive carbonatite was characterised as a primary, high-temperature sulphide assemblage. The trace element analysis; however, showed a significantly depleted nature and the S/Se ratios are much higher than the mantle values. Therefore, the previous conclusions need reconsideration. The sample did not show any significant alteration that would indicate a late-stage hydrothermal effect either. A possible explanation can be that the used hand specimen sampled a late-stage, hydrothermal phase of the sulphide mineralisation where trace element-depleted sulphides formed, although enrichment in mobile metalloids such as As would still be expected. Low-temperature experiments under hydrothermal conditions showed that chalcopyrite-pyrrhotite assemblage appeared at 328 ^{o}C (Sugaki et al., 1975). The formation of the depleted cobalt pentlandite fits with the temperature above. Complete solid solution between Co and Ni+Fe end members

was observed between 600-300 ºC, and the decomposition of the solid solution was observed under 200 ºC (Kaneda et al., 1986).

The highest S/Se ratios were found in the sphalerites (16171-26088) of the massive bornite. The large anhedral sphalerites in these samples were interpreted as part of the primary sulphide assemblage and may have coarsened during collection crystallisation. The high S/Se can indicate a crustal S addition. Le Bras et al. (2021) suggested that the Zn content of the Cu sulphides was derived from assimilated crustal material before the exchange between the melt and the sulphide liquid was interrupted.

6.3.3.2 Banded carbonatite

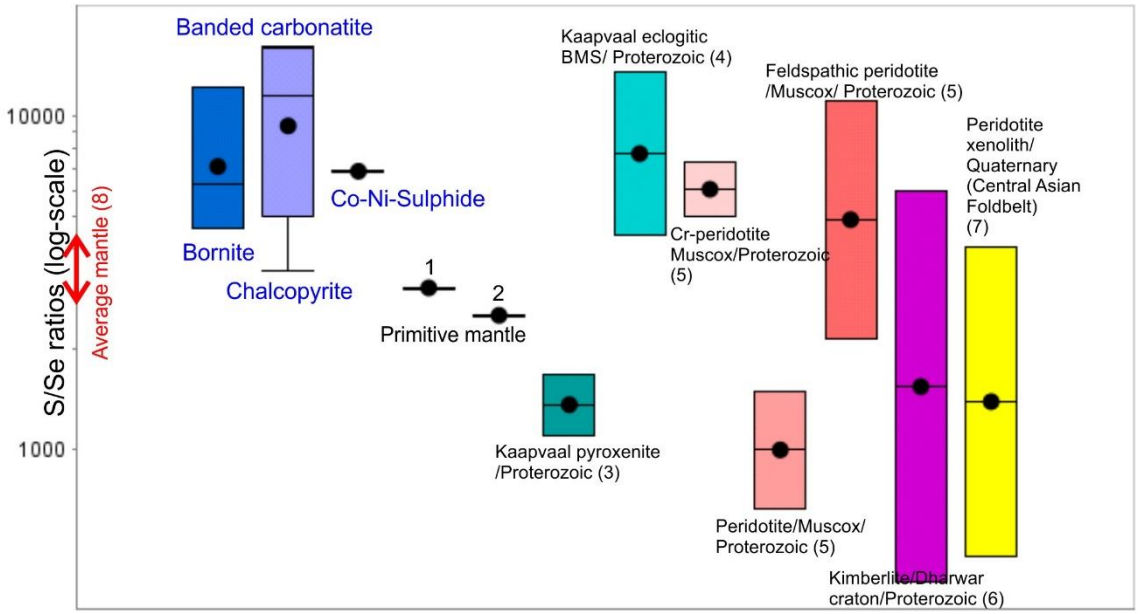

Figure 6.3.4. The S/Se ratios (log scale) of the banded carbonatite stoichiometric and nonstoichiometric sulphides depicted together with S/Se ratios of different mantle-derived samples that represent different mantle sources. The average S/Se mantle ratios are indicated on the axis of the diagram. (1) Palme and O'Neill (2003); (2) McDonough and Sun (1995); (3) Hutchinson et al. (2015); (4) Hughes et al. (2021); (5) Mackie et al. (2009); (6) Paton et al. (2009); (7) Wang and Becker (2013); (8) Eckstrand and Hulbert (1987).

Stoichiometric bornite and chalcopyrite of the banded carbonatite showed S/Se ratios of 4625-12220 and 3431-16223, respectively (Fig.6.3.4). The banded carbonatite nonstoichiometric chalcopyrite showed a wide range (5432-27711). These ratios were lower, or in the case of chalcopyrite, lower and overlapping with the transgressive carbonatite. The banded carbonatite sulphide S/Se ratios were closer

to the average mantle values. Both the textural study of this work (Chapter 4) and previous studies based on isotopes (Bolhar et al., 2020) and trace elements (Le Bras et al., 2021) suggested a magmatic origin for these sulphides with mantle signature, which agrees with the present results.

6.3.3.3 Phoscorite

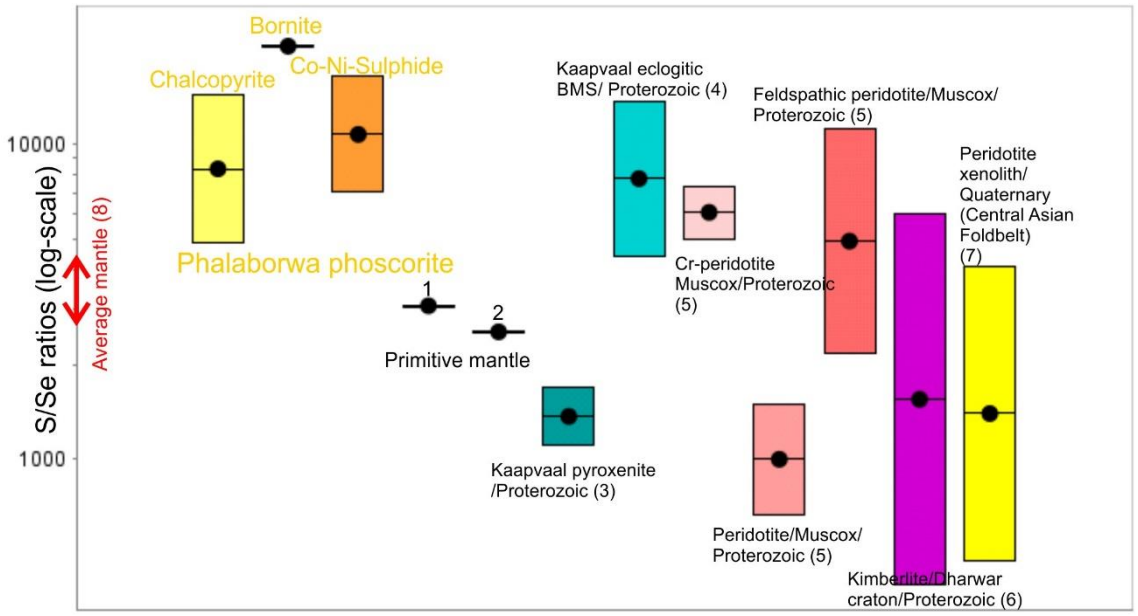

Figure 6.3.5. The (stoichiometric and nonstoichiometric) S/Se ratios (log scale) of the phoscorite sulphides depicted together with S/Se ratios of different mantle-derived samples that represent different mantle sources. The average S/Se mantle ratios are indicated on the axis of the diagram. (1) Palme and O'Neill (2003); (2) McDonough and Sun (1995); (3) Hutchinson et al. (2015); (4) Hughes et al. (2021); (5) Mackie et al. (2009); (6) Paton et al. (2009); (7) Wang and Becker (2013); (8) Eckstrand and Hulbert (1987).

The single stoichiometric bornite analysis in phoscorite provided a S/Se ratio of 4859. The stoichiometric chalcopyrite changed between 3893 and 4312 (Fig.6.3.5). These ratios overlapped with the banded carbonatite results and were close to the average mantle values. The nonstoichiometric bornites and chalcopyrite reached 14272 and 20383, respectively, while Ni-Co sulphides had a range of 7016-16339. Similarly to banded carbonatite, the phoscorite sulphides were interpreted as magmatic based on texture and earlier studies also suggested mantle origin (Bolhar et al., 2020; Le Bras et al., 2021); S/Se ratios of the stoichiometric sulphides concur with the previous interpretations.

6.3.3.4 Disseminated sulphides in glimmerite

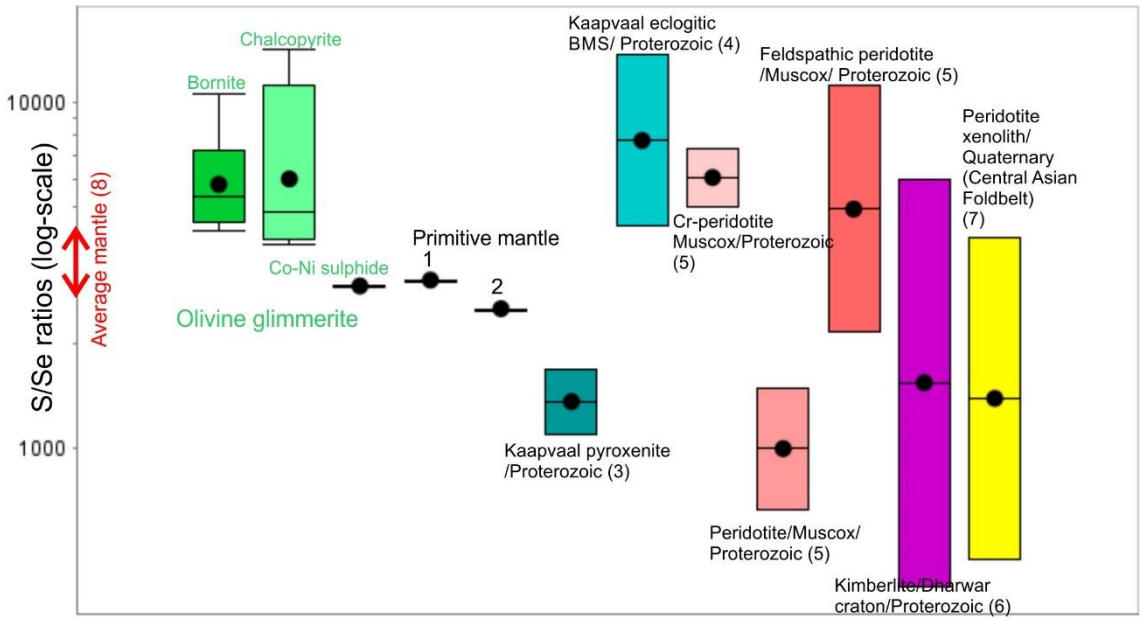

Figure 6.3.6. The (stoichiometric and nonstoichiometric) S/Se ratios (log scale) of the olivine glimmerite sulphides depicted together with S/Se ratios of different mantle-derived samples that represent different mantle sources. The average S/Se mantle ratios are indicated on the axis of the diagram. (1) Palme and O'Neill (2003); (2) McDonough and Sun (1995); (3) Hutchinson et al. (2015); (4) Hughes et al. (2021); (5) Mackie et al. (2009); (6) Paton et al. (2009); (7) Wang and Becker (2013); (8) Eckstrand and Hulbert (1987).

The S/Se ratios (Fig.6.3.6) of the mixed Cu-Fe sulphides of the olivine glimmerite were relatively low compared to the other lithologies. The single stoichiometric bornite had a S/Se ratio of 4612, and nonstoichiometric bornite fell between 10594 and 42242; these values overlap with the carbonatites. The relatively high Se content in these samples may indicate that S-loss did not entirely cause the low S/Se ratio. This is an important observation because of the altered nature of the sulphide grains. These sulphide grains contain PGE, which was probably remobilised from primary assemblages during later-stage processes, as discussed previously. Prichard et al. (2013) showed the mobility of Se in low pH, oxidising fluids. The high Se content in these sulphides could result from remobilisation during the serpentinisation processes described earlier. The primary origin of some of the sulphides that showed mantle values is also possible. Le Bras et al. (2021) interpreted sulphides from the clinopyroxenes as primary. The nonstoichiometric chalcopyrite and Ni-Co sulphide Pt+Pd vs S/Se ratios fell into the mantle domain (Fig.6.3.2).

The crosscutting calcite vein sulphide assemblage had S/Se ranges of 23517-29387 and 21672-39107 for nonstoichiometric troilite and cubanite, respectively, and 27711 for chalcopyrite (Fig.6.3.7). These are the highest S/Se ratios measured in the sample set, falling well above the mantle values, indicating a late-stage origin with crustal influence for these sulphides.

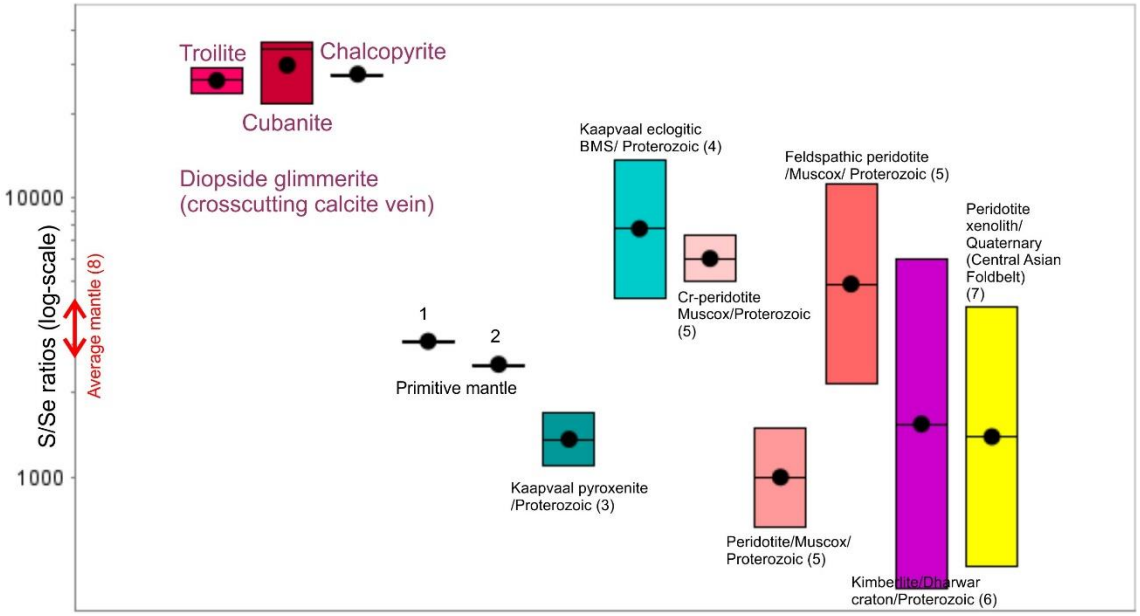

Figure 6.3.7. The (nonstoichiometric) sulphide S/Se ratios (log scale) of the calcite vein in the diopside glimmerite depicted together with S/Se ratios of different mantle-derived samples that represent different mantle sources. The average S/Se mantle ratios are indicated on the axis of the diagram. (1) Palme and O'Neill (2003); (2) McDonough and Sun (1995); (3) Hutchinson et al. (2015); (4) Hughes et al. (2021); (5) Mackie et al. (2009); (6) Paton et al. (2009); (7) Wang and Becker (2013); (8) Eckstrand and Hulbert (1987).

6.3.3.5 Summary of the S/Se studies

In summary, the box and whisker diagram showed that the Phalaborwa values of this study plotted relatively close to each other, apart from the sulphides from the crosscutting calcite vein, which was also the farthest from the mantle values, by showing high S/Se ratios. The rest of the Phalaborwa sulphide values overlapped with each other, the carbonatites and phoscorite especially close, while the olivine glimmerite showed a wider range of S/Se ratios. When compared to the pyroxenite and eclogitic sulphides from the Kaapvaal Craton, the Phalaborwa sulphides overlapped with the latter, while the pyroxenite showed lower S/Se ratios with a narrower overall range. The mantle-derived pyroxenite represents a relatively depleted mantle compared to both the carbonatitic and eclogitic mantle and is seemingly featured in their low S/Se ratios. However, the S/Se range of

sulphides from the Kaapvaal eclogite overlapped with some of the Phalaborwa sulphide S/Se ratios. Both carbonatites and eclogites represent a different mantle source composition than the primitive mantle, and the similarities in the sulphide S/Se ratios in the two rock types may reflect this. Similarity in the S/Se ratios is not enough evidence by itself to imply eclogite presence in the Phalaborwa SCLM, but it shows that the depleted and enriched mantle types can be differentiated with S/Se ratios; however, the potential post-magmatic processes must be considered. The Investigation of the potential Phalaborwa mantle sources is presented in Chapter 7, where the possibility of an eclogite component is discussed.

The majority of the analysed Phalaborwa sulphides showed higher S/Se ratios than the average mantle range. High S/Se ratios in sulphide phases were attributed to contamination from crustal S. This is expected in the case of the Phalaborwa sulphides as the presence of crustal S (Bolhar et al., 2020; Le Bras et al., 2021) and the crustal contamination based on orthomagmatic mineral compositions in the transgressive carbonatite (Giebel et al., 2019) were confirmed. The textural studies and previous works (e.g., Kavecsanszki et al., 2013; Giebel et al., 2019; Le Bras et al., 2021) indicated that the presence of both primary magmatic and secondary sulphide phases where crustal influence was suggested.

6.3.4 Summary and conclusions

The Phalaborwa sulphides were analysed with LA-ICPMS to determine their PGE, Au, Ag, metalloid (As, Se, Sb, Te, Cd) and Bi content. The analysed lithologies included the different transgressive carbonatite types, banded carbonatite, phoscorite, olivine glimmerite and sulphides from a late-stage calcite vein, crosscutting diopside glimmerite.

The results showed that the sulphides are generally depleted in PGE. Where they occurred, IPGE were associated with Cu-sulphides and PPGE with Ni-Co sulphides. Ni-Co sulphides of the present study were interpreted as primary (based on textures and phase relations – Chapters 4 and 5), representing either the mss or the Hz-iss that exsolved cobalt-pentlandite with Pd relatively enriched compared to the Cu-Fe sulphides. Le Bras et al., (2021) interpreted the low Co content of the Cu-sulphides as crustal addition; the origin of the pentlandites and

cobalt-pentlandites were not discussed. The Pt-Pd and arsenic distribution (after the PGE-arsenides described by Rudashevsky et al., 2014) feature suggest a low or decreasing fS_2 environment for the Phalaborwa sulphides over time. During later-stage alterations, secondary sulphides became enriched in metalloids (As, Bi). The remobilisation of PGE was also proposed based on PGE occurrence in serpentinised glimmerite and phoscorite sulphides. PGM was found at the margins of the disseminated and resorbed grains, a similar form to what was described by Hutchinson and Kinnaird (2005). The strongly altered and resorbed sulphide grains were affected by the fluids (neutral-basic, intermediate fO_2) that caused serpentinisation of the silicates and sulphide, and possibly PGE and metalloid remobilisation. Fluid compositions that caused serpentinisation described by Giebel et al. (2017); these fluids would be suitable for PGM transport.

The S/Se ratios and S/Se vs Pt+Pd profiles showed the presence of multiple sulphide generations in the Phalaborwa carbonatite and phoscorite rocks, which coincides with the petrographical and geochemical results of this and previous studies. Bornites and chalcopyrites showed S/Se ratios close to average mantle values and higher than average mantle values as well. Most of the Ni-Co sulphides had mantle S/Se ratios; these results may support the magmatic origin for these phases. The high S/Se values can be explained by later-stage alteration of the sulphides that also involved crustal influence. This is supported by petrographical observations and other trace element and isotope studies (Bolhar et al., 2020; Le Bras et al., 2021). Cubanite and troilite S/Se ratios and depleted nature (troilite-rich transgressive carbonatite) also suggest the presence of a later-stage hydrothermal sulphide assemblage. Similarly to the carbonatites and phoscorites, the glimmerite sulphides also showed S/Se ratios that covered mantle and crustal domains, indicating magmatic origin with later-stage alterations. In contrast, sulphides of the glimmerite-crosscutting calcite vein showed significantly higher S/Se ratios than all of the other lithologies, and they were depleted in all trace elements. These sulphides most possibly represent late-stage remobilised sulphides or precipitated at a low-temperature hydrothermal stage.

The Kaapvaal eclogitic BMS S/Se ratios showed the best match with the Phalaborwa sulphides, indicating that the enriched mantle types can be

differentiated from the primitive or average mantle types after establishing the potential post-magmatic processes that can alter the S/Se ratios.

Chapter 7: Mantle melting models: Investigation of the Phalaborwa mantle source and the evolution of the magmatic system

7.1 Introduction

The study aims to understand the Phalaborwa mantle composition and processes which led to the formation of this unique deposit. Its economic importance granted decades-long study (petrography, fluid inclusion study, bulk and mineral chemistry, isotopic characteristics) by various researchers (e.g., Aldous, 1980; Eriksson, 1989; Wu et al., 2011; Milani et al., 2017 a, b; Giebel et al., 2019) but the reason for this uniqueness is still not fully understood. One of the methods that has yet to be sufficiently utilised is numerical and chemical modelling. Milani et al. (2017b) modelled fractional crystallisation between phoscorite and carbonatites, but the results were inconclusive. Although all previous studies agree on a heterogeneous metasomatic mantle source, the nature of this mantle has not yet been fully specified (Eriksson, 1989; Wu et al., 2011; Milani et al., 2017b; Bolhar et al., 2020).

Previous authors used mineral occurrence and chemistry to infer that the primary magma(s) was/were peralkaline and ultrabasic with extremely high K/Na ratio, high Sr and Mg numbers, very low Al, Nb and Cr content (e.g., Eriksson, 1989; Giebel et al., 2017). Chemical characteristics are inherited and amplified from primary magmas by fractionation. Milani et al. (2017b) and Giebel et al. (2017) showed that multiple processes obscure the nature of the primary magma. Starting with the nature of the metasomatised mantle gives a clearer picture of what a primary magma may have looked like. Evidence for the characteristics of the mantle also comes from xenoliths that sampled the underlying Kaapvaal craton. Metasomatised mantle is heterogeneous in composition. Phlogopite wehrlite xenoliths from the Bulfontein locality (described by Grégoire et al., 2002) sampled the Kaapvaal mantle prior to the Mesozoic overprinting and may represent the nature of the Proterozoic mantle at the time of Phalaborwa intrusion. Eclogite has also been sampled from the Kaapvaal craton; for example, a xenolithic bimineralic (garnet + clinopyroxene) eclogite occurs in the Robert Victor kimberlite (Huang et al., 2014). There is a genetic association between carbonatite and kimberlite (e.g., Gudfinnsson and Presnal, 2005). The mantle

samples from kimberlite pipes in Kimberley also include MARID (Mica-Amphibole-Rutile-Ilmenite-Diopside) xenolith (Grégoire et al., 2002). By using different mantle xenolith types as a starting point, the present study will systematically model the effect of heterogeneity in variably veined metasomatised mantle sources on primary melt composition.

Several lithological groups (silicate rocks, carbonatites, phoscorites) suggest either that the Phalaborwa complex formed from multiple magma batches or a single continuously evolving magma. Clinopyroxenite cumulates, which vary in type, composition and Mg-numbers, provide evidence for the former (e.g., Eriksson, 1989). The evidence for a shared magma differentiation process is found in the relationship between diopside pegmatoids, phoscorite and banded carbonatite, which all crosscut the clinopyroxenites. Hanekom et al. (1965) described the contact between the diopside-bearing pegmatoids and the phoscorite as gradational and the modal composition of phoscorite as strongly variable with olivine sometimes forming small monomineralic bodies. Milani et al. (2017a; 2017b) modelled fractional and equilibrium crystallisation and geothermobarometry using carbonatite samples and concluded that a common magma source exists for the carbonatite and phoscorite suites. The present research compares the model and observed geochemical characteristics to consider whether one or more primary magmas should be invoked to explain the range of lithologies at Phalaborwa.

Minerals that are major constituents of the Phalaborwa lithologies include clinopyroxene, forsterite, phlogopite, calcite and dolomite. Phase equilibria relevant to magmatic systems producing corresponding mineral assemblages are shown in Figure 7.1.1. $KAlSiO_4$-Mg_2SiO_4- SiO_2 phase relations at 2.8 GPa under either H_2O-saturated or CO_2-saturated conditions (Gupta and Green, 1988; Gupta, 2015) demonstrated the presence of water for phlogopite crystallisation but a strongly water-undersaturated system to drive magmas towards the silica-undersaturated thermal minima. In the system SiO_2-CaO-MgO-CO_2, the main changes of the vapour-saturated liquidus surface with decreasing pressure from 2.8 GPa (Gupta, 2015) to 1 GPa (Lee and Wyllie, 2000) include the shrinking of the calcite liquidus field with the expansion of the forsterite liquidus field, and the replacement of the magnesite field by periclase (Fig. 5.1.1 e). Wendlandt and Eggler (1980 a; b) in the water-saturated forsterite-kalsilite-quartz experimental

system (17-30 kbar/ 900-1300 ºC) showed that the phlogopite liquid field expands with increasing pressure. The analogue simple system phase diagrams collectively provide a framework for describing the mantle source region for Phalaborwa.

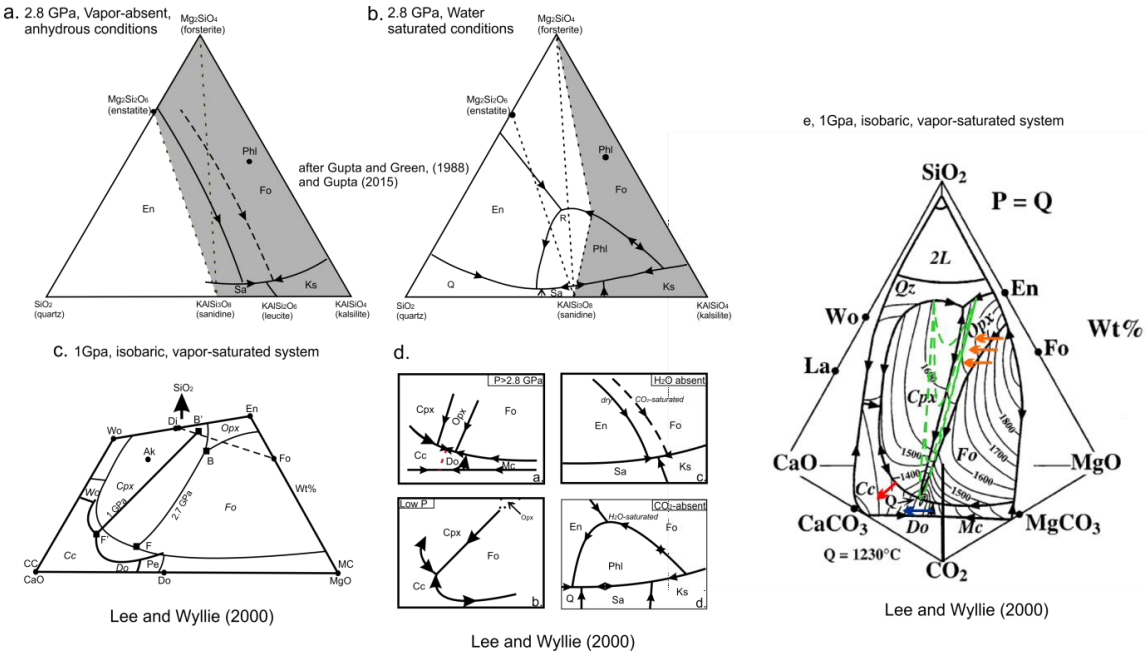

Figure 7.1.1. The figure shows the phase diagrams that were considered for the Phalaborwa system, where phlogopite, diopside calcite, dolomite and olivine needs to be considered. The phase diagrams were used to estimate the phase relations in a Phalaborwa-like system. The result of this estimation is a strictly theoretical phase diagram depicted on Figure 7.1.2. The phase diagrams are from: Gupta (2015) (**a-b**) and Lee and Wyllie (2000) (**c-e**). Figure e shows the the estimated position of the phlogopite solidus with decreasing pressure (green line). At the same time the forsterite field expanses for the expense of the orthopyroxene. (En: enstatite, Phl: phlogopite; Fo forsterite; Sa: sanidine; Ks: kalsilite; Q/*Qz* quartz; Cc calcite; Do dolomite; Pe: periclase; Mc: magnesite; Ak: akermanite; Cpx: clinopyroxene; Di: diopside; Opx: orthopyroxene; Wo: wollastonite; La: larnite; *2L*: two liquid field; *With italics: liquid field equivalents*).

No single experimental investigation satisfactorily describes the hybrid volatile (H_2O + CO_2 + F)-bearing systems that would be most relevant to Phalaborwa. Gupta and Green (1988) showed that the fluorine-rich phlogopite has a much higher thermal stability (1490-1500 ºC) than the OH-rich phlogopite (<1200 ºC), such that fluorine should be considered. Moreover, Gupta (2015) shows that the volatiles H_2O and CO_2 have an opposing effect to each other as they lower phlogopite thermal stability. Eggler (1989) determined phase relations in the peridotite-H_2O-CO_2 system near vapour-saturated and carbonatitic-vapour-absent solidi, but carbonatitic-vapour-saturated solidus was not presented. Gupta (2015) demonstrated that H_2O has an essential role in stabilising phlogopite at

liquidus temperatures, and it moves the liquid composition in equilibrium with harzburgite towards olivine and pyroxene-normative compositions. Additionally, the presence of CO_2 drives liquid compositions from harzburgitic to strongly silica-undersaturated compositions. The mantle's variable CO_2: H_2O ratio can significantly change phlogopite stability. Figure 7.2.1 shows a sketch that depicts the possible end-member scenario where the phlogopite stability field expands to the undersaturated thermal minimum Q for an unknown depth and water content. The arbitrary conditions cannot be fixed or compared quantitatively to experimental results but demonstrate that the SiO_2–CaO–MgO–CO_2 projection is helpful for the consideration of model results.

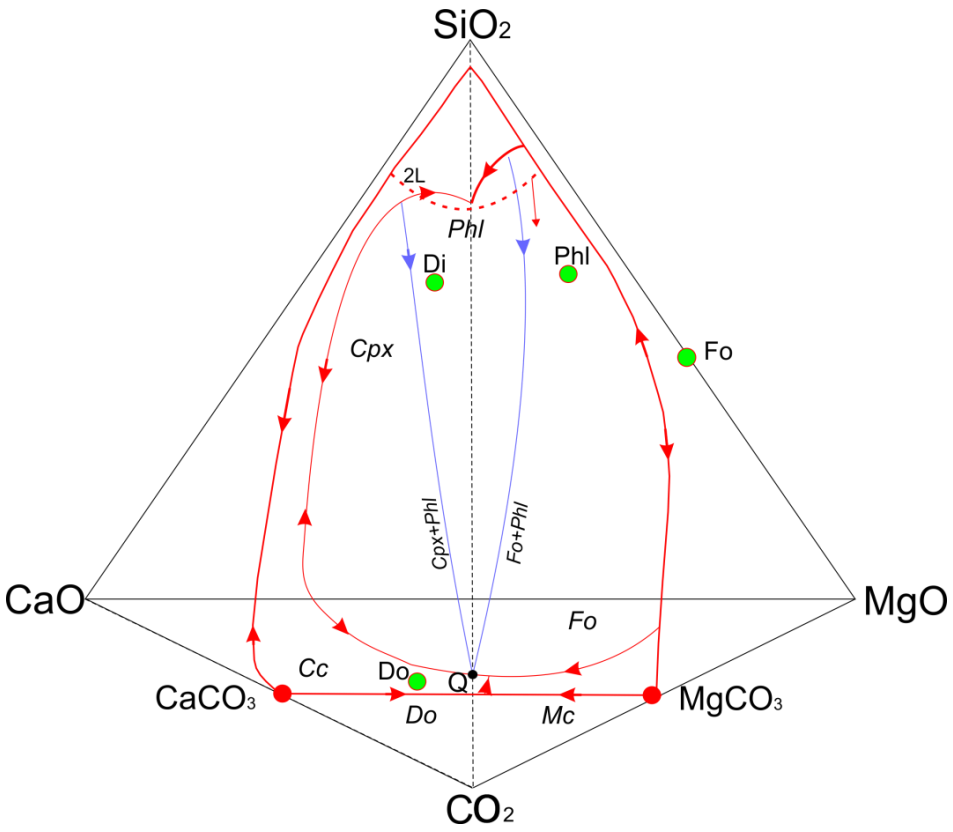

Figure 7.1.2. Sketch of a quaternary phase diagram estimated after Gupta and Green (1988) and Lee and Wyllie (2000) at an arbitrary pressure and H_2O/CO_2 ratio.

7.2 Methodology of the mantle melting modelling

7.2.1 Starting compositions

The present study uses starting compositions determined based on reported natural phlogopite wehrlite, MARID and eclogite xenoliths compositions from the Kaapvaal craton (Grégoire et al., 2002; Bell et al., 2005; Huang et al., 2014; Spandler et al., 2017). Glimmerite vein material (phlogopite+apatite+carbonate) was used as a metasomatic vein composition (Grégoire et al., 2002).

(i) Phlogopite wehrlite: The used modal composition was based on a xenolith (sample BD2321) from Bultfontain locality described by Grégoire et al. (2002). The composition includes 70 vol% olivine, 20.5 vol% clinopyroxene, 1 vol% spinel and 1.5 vol% phlogopite.

(ii) Eclogite: Primitive eclogite compositions of 50 vol% garnet with 50 vol% clinopyroxene and 30% garnet and 70% clinopyroxene described unmetasomatised eclogite mantle component. A second eclogite composition was modelled on a xenolith from the Robert Victor kimberlite (Huang et al., 2014), which has variable proportions of metasomatic garnet, rutile, phlogopite and sulphides.

(iii) MARID: Three starting compositions were MARID xenoliths from the Kimberley area (Grégoire et al., 2002). MARID 1 had 73% modal phlogopite, 24.7% amphibole and 2.3% rutile. Clinopyroxene was added as an accessory phase in a few models (1 vol% was assumed, and the modal composition was re-normalised. MARID 2 had 87.5% phlogopite, 9.7% amphibole and 2.8% ilmenite. MARID 3 had 21% phlogopite, 44.5% clinopyroxene, 31% amphibole and 3.5% ilmenite.

(iv) Metasomatic vein material: The modal composition of a natural calcite-apatite glimmerite xenolith from the Kimberley area (Grégoire et al., 2002) is 89.1 vol% phlogopite, 7.8 vol% ilmenite, 1.55 vol% apatite and 1.55 vol% carbonate.

Metasomatic vein material was added to the mantle compositions in different proportions (5 vol%-20 vol%), effectively creating new model starting compositions representing several variously metasomatised mantle compositions. The calculation method is presented below in Section 7.2.2.1.

7.2.2 Calculations methods for major element modelling

7.2.2.1 Starting composition calculations

The change of the major element composition during mantle melting was determined via a multi-stage calculation process and the results were depicted on SCM+CO_2 (**SiO_2** (+TiO_2+ Al_2O_3)–**CaO**(+Na_2O+K_2O+Ce_2O_3+La_2O_3)–**MgO**(+FeO+MnO+Cr_2O_3)–**CO_2** (+P_2O_5)) pseudo-quaternary phase diagrams. Three natural mantle source compositions were used; they were described in the previous section. Metasomatic vein material was added to the mantle compositions in different proportions, effectively creating new model starting compositions representing variously metasomatised mantle compositions. The calculation method of the new model compositions is described below, with an example calculation presented in Table 7.2.1.

ax+bx+cy=Z
ax/Z*100=A
bx/Z*100=B
cy/Z*100=C

Where:
a,b: vol% of mineral a and b in original host mantle rock c: vol% of mineral c in metasomatic vein
x: proportion of mantle rock in the new model composition
y: proportion of metasomatic vein in the new model composition
A, B, C: mineral vol% of new model metasomatised mantle composition.

Table 7.2.1. Example of the starting model composition calculation. The model starting composition was calculated from the summation and re-normalisation a host rock and added vein material.

Original composition	Rock type	Ol	Cpx	Phl	Spin	Ilm	Carb	Ap	Proportion in model starting composition
Host	Phlogopite wehrlite	77	20.50	1.50	1.00				0.95
Vein (5%)	Calcite-apatite glimmerite			89.10		7.80	1.55	1.55	0.05
Calculation of model starting composition	Phlogopite wehrlite	73.15	19.48	1.43	0.95				95
	Calcite-apatite glimmerite			4.46		0.39	0.08	0.08	5
New model rock composition:		**73.15**	**19.48**	**5.88**	**0.95**	**0.39**	**0.08**	**0.08**	100

7.2.2.2 Calculation process of the chemical composition

The chemical compositions needed to be calculated to plot the model compositions in a quaternary phase diagram. For this purpose, the published chemical composition of the constituting minerals was used (Grégoire et al., 2002; Soltys et al., 2016; Giuliani et al., 2017). The mineral compositions were recalculated according to the appropriate element substitutions in the system SiO_2(+TiO_2+Al_2O_3)–CaO(+Na_2O+K_2O+Ce_2O_3+La_2O_3)–MgO(+FeO+MnO+Cr_2O_3) –CO_2 (+P_2O_5). An example for this calculation is shown in Table 7.2.2.

Table 7.2.2. Mineral chemical composition calculation for depiction in quaternary phase diagrams for both starting and melt fraction compositions. The model compositions were created by using mineral modal percentages. For rock/melt chemical composition, the chemical composition of each constituting mineral needs to be used (Step1). The mineral chemical compositions were taken from published literature. The chemical components needed to be simplified for SCM-CO2 system, therefore substitutions for SiO_2, MgO and CaO were calculated as shown in Step 2. The new SiO_2 (S) C (CaO) and M (MgO) normalised composition is shown in Step3.

Step 1	Clinopyroxene				
	Published composition (wt%)				
	SiO_2	55.44			
	TiO_2	0.23			
	Al_2O_3	0.49			
	Cr_2O_3	2.7			
	FeO	2.75			
	MnO	0.11			
	MgO	16.29			
	CaO	20.83			
	Na_2O	2.02			
	K_2O	0.03			
	Total	100.89			
Step 2	Recalculation process	**A**: #mol = (wt% / mol weight)	**B**	**A/B**	**Σ (A/B)**
	TiO_2 → SiO_2	TiO_2 #mol	mol weight of SiO_2	TiO_2 to SiO_2	ΣSiO_2 substitution
		0.003	60.08	0.17	0.46
	Al_2O_3 → SiO_2	Al_2O_3 #mol	mol weight of SiO_2	Al_2O_3 to SiO_2	
		0.005	60.08	0.29	
	Cr_2O_3 → MgO	Cr_2O_3 #mol	mol weight of MgO	Cr_2O_3 to MgO	ΣMgO substitution
		0.02	40.30	0.72	2.32
	FeO → MgO	FeO #mol	mol weight of MgO	FeO to MgO	
		0.04	40.30	1.54	
	MnO →MgO	MnO #mol	mol weight of MgO	MnO to MgO	
		0.002	40.30	0.06	
	K_2O → CaO	K_2O #mol	mol weight of CaO	K_2O to CaO	ΣCaO-substitution
		0.0003	56.08	0.02	1.85
	Na_2O → CaO	Na_2O #mol	mol weight of CaO	Na_2O to CaO	
		0.03	56.08	1.83	
Step 3	Recalculated mineral composition				
	SiO_2	55.90			
	MgO	18.61			
	CaO	22.68			

7.2.2.3 Calculation process of the individual melt fraction compositions

The progressive melting of the new metasomatised mantle compositions was modelled from 1% melting to 51% melting, using melt portions equivalent to 1-5% melting. The calculation starts with 1% melting of the first mineral phase (usually carbonate) and the calculation of the chemical composition of this melt portion. The first melt fraction is indicated as F1 (F1=0.01). The second melt fractions indicate an additional 5% or, in the case of a few MARID starting compositions, 4% melting of the selected mineral phases. Therefore, F2 is equivalent to 6% (F2=0.06) or, for some of the MARID, 5% (F2=0.05) melting, as indicated in Tables 7.3.1-3, presented in Section 7.3.1. The following melt fractions, F3-F11, always include 5% (0.05) melt increments. After each melt extraction, the composition of the residual melt was recalculated to 100 before the next melt portion was extracted, as shown in Table 7.2.3.

Table 7.2.3. Recalculation method of the starting composition of the residual melt after increment extraction.

	Carbonate	Apatite	Phlogopite	Clinopyroxene	Amphibole	Ilmenite	
X: Starting modal composition	2.38	2.38	83.33	0.00	9.24	2.67	100.000
First melting stage with 1% melting: F1=0.01							
Y : Extracted melt portion (increment)	0.01						0.010
Z: Melt composition after extracted melt portion: Z=X-Y	2.37	2.38	83.33	0.00	9.24	2.67	99.990
Re-normalised residual melt composition:	**0.024**	**0.024**	**0.833**	**0.000**	**0.092**	**0.027**	1.000

The chemical compositions of the melt fractions (F1-F11) were depicted on the pseudo-quaternary phase diagram, marking the composition of the melt produced by 1%-51% melting of the starting model composition. The calculation process is shown in Table 7.2.4. Every extracted melt portion is added to the previous portions, and the chemical compositions are re-calculated each time, showing how the composition changes with larger melt fractions (Table 7.2.4).

Table 7.2.4. Calculation process of the chemical composition of the individual melt fractions (F). The example shows the composition of a melt fraction produced by 50% melting. The recalculated mineral compositions (B) were calculated with the method shown in Table 7.2.2.

	Proportion of the mineral phases melting in each increment							
	Dolomite	Apatite	Phlogopite	Clinopyroxene	Amphibole	Ilmenite	Σ	
F1=0.01	0.01							
F2=-0.05	0.024	0.016						
F3=0.10		0.008	0.042					
F4=0.15			0.05					
F5=0.20			0.05					
F6=0.25			0.04		0.01			
F7=0.30			0.03		0.02			
F8=0.35			0.025		0.024	0.001		
F9=0.40			0.025		0.024	0.001		
F10=0.45			0.025		0.024	0.001		
F11=0.50			0.025		0.024	0.001		
Σ	0.034	0.024	0.312		0.126	0.004	0.5	
Normalised to 100% A	**0.068**	**0.048**	**0.624**	**0.000**	**0.252**	**0.008**	**1.000**	
	Recalculated mineral compositions **B**							
SiO_2 (wt%)	0.00	0.02	49.323		56.262	40.208		
MgO (wt%)	0.21	0.00	28.545		24.350	38.431		
CaO (wt%)	0.33	0.55	6.157		12.264	0.060		
CO_2 (wt%)	0.49	0.37						
Mineral compositions calculated for phase diagrams **(A*B)**							Σ	**Normalised Σ at F11**
SiO_2 (wt%)	0.00	0.00	30.78	0.00	14.18	0.32	45.28	**59.12**
MgO (wt%)	0.01	0.00	17.81	0.00	6.14	0.31	24.27	**31.69**
CaO (wt%)	0.02	0.03	3.84	0.00	3.09	0.00	6.98	**9.12**
CO_2 (wt%)	0.03	0.02	0.00	0.00	0.00	0.00	0.05	**0.07**
							76.58	100.00

The major element compositional evolution of the melt fractions of the different starting compositions was depicted on a SCM+CO_2 pseudo-quaternary phase diagrams. The quaternary space was determined by the 100 wt% of the following chemical constituents:

SiO_2 (+TiO_2+Al_2O_3)

CaO (+Na_2O+K_2O+Ce_2O_3+La_2O_3)

MgO (+FeO+MnO+Cr_2O_3)

CO_2 (+P_2O_5)

The phase diagrams were designed with the CSpace software, which allows the depiction of data points determined by four variants in a quaternary space. In the present case each point represents a chemical composition (of a melt fraction, starting mantle composition, mineral composition, and rock composition) with calculated SiO_2 ($+TiO_2+Al_2O_3$) – CaO ($+Na_2O+K_2O+Ce_2O_3+La_2O3$) – MgO ($+FeO+MnO+Cr_2O_3$) – CO_2 ($+P_2O_5$) values that must add up to 100%.

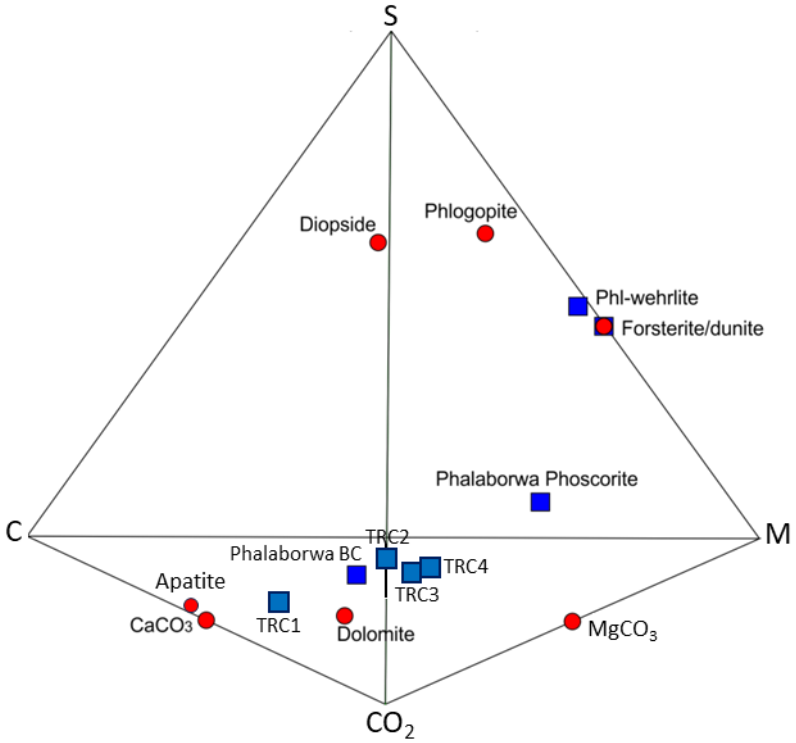

Figure 7.2.1. The structure of the quaternary diagram in which the results of the major element calculations were depicted. The Quaternary diagrams were constructed by using CSpace software. BC: average banded carbonatite (Hanekom et al., 1965), Phalaborwa average phoscorite (Hanekom et al., 1965); TRC: transgressive carbonatite: different composition types displayed (Milani et al., 2017). The chemical compositions were recalculated for the system SCM+CO_2 where S: SiO_2 ($+TiO_2+Al_2O_3$), C: CaO ($+Na_2O+K_2O+Ce_2O_3+La_2O_3$), M: MgO ($+FeO+MnO+Cr_2O_3$) and CO_2: CO_2 ($+P_2O_5$).

Table 7.2.5.a. Starting modal and trace element compositions used in phlogopite wehrlite and eclogite mantle melting models. The compositions were calculated from published compositions of phlogopite wehrlite xenolith, apatite-calcite glimmerite (Grégoire et al., 2002) and eclogite (Huang et al., 2014).

Phlogopite Wehrlite & Eclogite													
(vol%)	**PW1,2,3**	**PW4**	**PW5**	**PW6,7,8**	**PW 9,10,11**	**E1**	**E2**	**E3**	**E10**	**E12**	**E13**	**E14**	**E15**
Added vein%	0%	5%	10%	20%	50%						5%	10%	20%
Phlogopite	1.5	5.88	10.26	19.02	44.55					10	4.46	8.91	17.82
Clinopyroxene	20.5	19.48	18.45	16.4	10.25	50	70	70	55	39.5	47.5	45	39.2
Olivine	77	73.15	69.3	61.6	38.5								
Garnet						50	30	28	44.5	40	47.5	45	40
Spinel	1	0.95	0.9	0.8	0.5								
Ilmenite	0	0.39	0.78	1.56	3.9						0.39	0.78	1.56
Rutile								2	0.5	0.5			0.8
Dolomite	0	0.08	0.16	0.31	0.78						0.08	0.16	0.31
Apatite	0	0.08	0.16	0.31	0.78						0.08	0.16	0.31
(ppm)													
Y	1.8	1.89	1.97	2.14	2.65	11.24	9.38	8.86	10.37	10.88	10.85	10.47	9.66
Nb	4.7	42.02	79.33	153.96	377.85	0.06	0.03	284.09	71.08	72.85	37.61	75.16	263.87
Ba	38	50.6	63.2	88.4	164	0.48	1.19	1.19	0.52	272.78	14.95	29.43	58.37
Sr	130	142.25	154.5	179	252.5	155.78	1.84	1.82	171.3	133.33	166.74	177.7	197.14
Ce	10	13.4	16.8	23.6	44	5.67	3.62	3.61	6.22	4.5	9.29	12.9	20.05
K	1411	4872.8	8334.6	15258.2	36029	0.07	0.13	0.13	0.08	0.06	3532.42	7064.76	14129.45
Gd	1.1	1.31	1.51	1.92	3.15	1.26	1.09	1.06	1.26	1.13	1.46	1.65	2.04
Ti	540	1367.3	2194.6	3849.2	8813	3300	990.28	20724.28	8223	8607	3989.3	4678.6	13951.6
Zr	44	44.5	45	46	49	43.25	29.24	84.22	57.51	52.26	43.79	44.33	67.17

Table 7.2.5.b. Starting modal and trace element compositions used MARID mantle melting models. The compositions were calculated from published MARID compositions and apatite-calcite glimmerite (Grégoire et al., 2002).

MARID											
(Vol%)	**AJE262**	**AJE262+ 5%**	**AJE262+ 10%**	**AJE288**	**AJE288+ 5%**	**AJE288+ 10%**	**AJE288+ 20%**	**AJE281_ a,b**	**AJE281_ 5%**	**AJE281_ 10%**	**AJE281_ 20%**
Added vein%		5%	10%		5%	10%	20%		5%	10%	20%
Phlogopite	73	74.3	75.083	87	87.52	87.6	87.77	21	46.73	48.96	53.42
Clinopyroxene	–	0	0	0	0	0	0	44.5	19.95	18.9	16.8
Amphibole	24.7	22.95	21.737	9.7	9.26	8.77	7.79	31	29.45	27.9	24.8
Rutile	2.3	2.2	2.083	0	0	0	0		0	0	0
Ilmenite	–	0.39	0.785	2.8	3.06	3.31	3.82	3.5	3.72	3.93	4.36
Calcite+Apatite	–	0.08	0.156		0.08	0.16	0.31		0.08	0.155	0.31
Accessories (Cpx2)		0.08	0.156		0.08	0.16	0.31		0.08	0.155	0.31
(ppm)											
Y	0.97	1.1	1.22	1.4	1.51	1.61	1.82	1.2	1.32	1.43	1.66
Nb	23	59.4	95.8	89	122.1	155.2	221.4	78	111.65	145.3	212.6
Ba	378	373.6	369.2	3328	3176.1	3024.2	2720.4	245	247.25	249.5	254
Sr	225	232.5	240	217	224.9	232.8	248.6	479	473.8	468.6	458.2
Ce	18	21	24	28	30.5	33	38	8.8	12.26	15.72	22.64
K	87400	86562.35	85724.7	94700	93497.35	92294.7	89889.4	59700	60247.35	60794.7	61889.4
Gd	0.72	0.94	1.17	0.6	0.83	1.06	1.52	0.65	0.88	1.11	1.56
Ti	31800	31064.3	30328.6	22100	21849.3	21598.6	21097.2	23600	23274.3	22948.6	22297.2
Zr	37	37.85	38.7	88	86.3	84.6	81.2	36	36.9	37.8	39.6

7.2.3 Trace element modelling

7.2.3.1 Partition coefficients

The relationship between the partition coefficient, melt and mineral is expressed as:

$$K_d = C_S/C_l \; Or \; K_d = C_l/C_o$$

Where:

K_d: Partition coefficient
C_S: Trace element concentration in solid C_L: Trace element concentration in liquid
C_l: Trace element concentration in forming liquid.
C_o: Trace element concentration in forming liquid.

The used partition coefficients (K_d) were strongly the subject of availability. A wide range of trace elements were modelled in several different minerals in three different systems. K_ds were not available for every single scenario; in these cases, a substitution was made and the potential difference in the outcome were considered. An example is shown in Figure 7.2.1, where the diagram depicts the differences in the used dolomite and calcite K_ds. Another example in the MARID models, where the xenolith composition includes calcite and not dolomite; however, calcite Kd were not available. Using dolomite K_ds gave the best approximation of the modelled system. The list of the Kds used in the modelling is listed in Table 7.2.6-8.

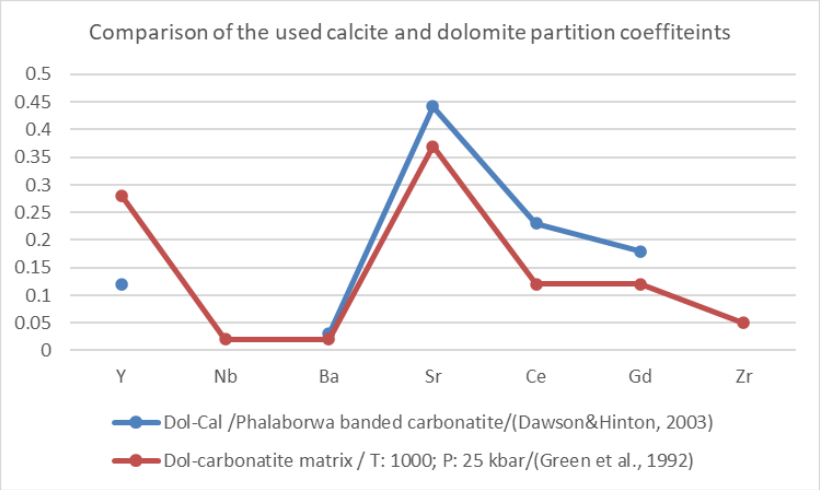

Figure 7.2.2. Comparison of the different partition coefficients (K_ds) determined under different conditions and used for calcite and dolomite in this study.

Table 7.2.6. Partition coefficients used in the phlogopite wehrlite models.

Phlogopite Wehrlite								
	Phlogopite	Clinopyroxene 10%H_2O/5%H_2O	Clinopyroxene II.	Olivine 10% H_2O/5%H_2O	Spinel	Ilmenite	Carbonate (dol/calc)	Apatite
Y	0.0215	0.53/0.51	-	0.003/0.008	0.0006	0.084	0.12	0.37
Nb	0.075	0.0035/0.005	0.004	0.00007/same	0.00065	2	0.02*2	0.004
Ba	1.03	0.0011/0.0001	0.003	0.0001/same	-	0.00034	0.03	0.025
Sr	0.038	0.102/0.113	0.304	0.00002/0.001	4E-06	0.004*2	0.442	0.652
Ce	0.00002	0.083/0.12	0.2	0.0001/0.001	0.0006*1	0.000054	0.23	0.49
Gd	0.0072	0.51/0.56	-	0.001/0.004	0.0006*1	0.0034	0.18	0.39
Ti	0.87	0.28/0.46	0.49	0.011/0.015	0.15*1	0.0067	-	-
Zr	0.012	0.11/0.2	0.098	0.001/0.002	0.00108	0.02*2	0.05 *2	0.03
Ref.	Schmidt et al. (1999)	Adam and Green, (2006)	Schmidt et al. (1999)	Adam and Green, (2006)	Johnston and Schwab, (2004), *1 Kelemen et al., (1993)	Zack and Brumm, (1998)	Dawson and Hinton, (2003); *2Green et al. (1992)	Klemme and Dalpé, (2003)
P	15 kbar	2 GPa/1GPa	15 kbar	2GPa/1GPa	Upper Mantle conditions	17 kbar	Phalaborwa Banded carbonatite (Crustal P), *2 25 kbar	1 GPa
T (□C)	1140	1100/1075	1140	1100/1075	Upper Mantle conditions	930	Phalaborwa Banded Carb. (<900), *2 1000	1250
System	Lamproite (crystal/matrix)	Hydrous nepheline basanite (crystal/mat rix)	Lamproite (crystal/matrix)	Hydrous nepheline basanite (crystal/matrix)	Peridotite (crystal/ matrix)	Garnet-Pyroxenite (crystal/ matrix)	Carbonatite (dolomite/calcite) *2 dolomite/ carb. matrix)	Carbonatite apatite/carb. matrix)

Table 7.2.7. Partition coefficients used in the eclogite models.

Eclogite							
	Phlogopite	Clinopyroxene	Garnet	Rutile	Ilmenite	Carbonate (dolomite)	Apatite
Y	0.0003 *1	0.58	2.9	0.01	0.18	0.12	0.37
Nb	0.047	0.021	0.008	83.4	13.3	0.02*1	0.004
Ba	3.04	0.0019	0.00004	0.01	0.007	0.03	0.025
Sr	0.14	0.08	0.005	0.15	0.004	0.442	0.652
Ce	0.00006	0.064	0.0034	0.25	0.013	0.23	0.49
Gd	0.0003 *1	0.44	0.59	0.04	0.14	0.18	0.39
Ti	0.71	0.36	0.21	-	-	-	-
Zr	0.008	0.093	0.4	5.95	0.02	0.05 *1	0.03
Reference	Adam and Green, (2006)	Klemme et al. (2002)		Pilet et al (2011) and references therein.		Dawson and Hinton, (2003) *2 Green et al., (1992)	Klemme and Dalpé, (2003)
P	2.5 Gpa	3 GPa		Mantle conditions		Phalaborwa Banded Carb. (crustal P) *2 25 kbar	1 GPa
T (ºC)	1100	1400		Mantle conditions		Phalaborwa Banded Carb. (<900), *2 1000	1250
system	Hydrous nepheline basanite (10% H_2O)	Eclogite (mineral/melt)		Eclogite (mineral/melt)		Carbonatite (Dolomite/Calcite) *2(dolomite/carbonate matrix)	Carbonatite (Ap/carbonate matrix)

Table 7.2.8. Partition coefficients used in the MARID models.

MARID							
	Phlogopite	Clinopyroxene	Amphibole	Rutile	Ilmenite	Carbonate (dolomite)	Apatite
HREE (Lu)/(Y)	0.0215	0.43	0.126	0.01	0.18	0.28	0.42
Nb	0.301378	0.0077	0.144	83.4	13.3	0.02	0.004
Ba	0.204	0.00068	0.00887	0.01	0.007	0.02	0.025
Sr	0.065	0.13	0.151	0.15	0.004	0.37	2.4
Ce	0.0001716	0.0858	0.043	0.25	0.013	0.12	0.49
MREE (Gd)	0.0072	0.48	0.153	0.04	0.14	0.12	0.39
Zr	0.00372	0.12	0.012	5.95	0.02	0.05	0.008
Reference	Fitzpayne et al. (2018)	Pilet et al., 2011	Fitzpayne et al. (2018)	Pilet et al., 2011	Pilet et al., 2011	Green et al. (1992)	Klemme and Dalpé, (2003)
P	Mantle conditions	Mantle conditions	Mantle conditions	Mantle conditions	Mantle conditions	25 kbar	1 GPa
T (ºC)	Mantle conditions	Mantle conditions	Mantle conditions	Mantle conditions	Mantle conditions	1000	1250
System	MARID	Eclogite	MARID	Eclogite	Eclogite	Carbonatite (dolomite/ carb. matrix	Carbonatite (apatite/ carb. matrix)

7.2.3.2 Trace element modelling calculations

The low viscosity and high mobility of carbonatite magmas requires that modelling is framed around fractional melting with accumulation in a mixed magma chamber (after O'Hara and Matthews, 1981). The Proportional Partition Coefficients (P) demonstrates how the fraction of each mineral contributes to the melt, and thereby influences trace element concentration. P is the average individual partition coefficients weighted according to the proportions in which the minerals enter the melt.

$$P=P_{mineral1}*K_{dmineral1}+ P_{mineral2}*K_{dmineral2}+...+ P_{mineral\ n}*K_{dmineral\ n}$$

Where:

$P_{mineral}$: the fraction of the mineral contributing to the melt at the

melting stage. And the partitioning equation becomes:

$$C_l/C_0 = 1/F\ [1- (1- PF/D_0)^{(1/P)}]$$

Where:

C_l: Trace element concentration in the forming melt C_0: Trace element concentration of the source rock D_0: bulk distribution coefficient: $D_0 = \Sigma\ W_A + WD_{iA}$

Where

W_A: weight fraction of mineral A

D_{iA}: Distribution coefficient of the element in mineral A

F: The weight fraction of the melt (melt/(melt+rock)

P: Proportional partition coefficient

(After O'Hara and Matthews, 1981 and Rollinson and Pease, 2021)

7.3 Results

The results of the major element modelling are presented in section 7.3.1. The melting models resulted in a series of melt fractions which were derived from different starting compositions. The modal mineral percentages and the chemical composition (SCM-CO_2 system) of the starting compositions and the derivative melt fractions are presented in Table 7.3.1 (Phlogopite wehrlite starting compositions; model codes: PW_M, where "$_M$" refers to "major element"), Table 7.3.2 (Eclogite starting composition; model codes E_M, where "$_M$" refers to "major element") and Table 7.3.3 (MARID starting composition; model codes: M_M, where "$_M$" refers to "major element". The chemical and modal mineral percentage calculations of the starting compositions and the melt fractions were discussed in Section 7.2.2.

Melt fraction compositions are depicted in Figure 7.3.1, which shows all three mantle source systems together for easier comparison. The phase diagrams show only the diagnostically significant melt fraction compositions, as including all would make the figures too crowded for interpretation. Phase diagrams with all of the modelled melt fraction compositions are presented in Appendix 3.

The results of the trace element modelling are presented in Section 7.3.2. Three diagram pairs (C_0/C_l vs F and C_l vs F) were used for every selected trace element to show their behaviour during the melting of the phlogopite wehrlite, eclogite and MARID mantle sources.

7.3.1 Major element compositions of primary mantle melts

Nineteen composition variations of the veined phlogopite wehrlite were modelled, and four compositions with their derivative melt fractions are presented here in the quaternary diagram described in section 7.2.4. (Fig.7.3.1. a). The compositions of the different melt fractions are listed in Table 7.3.1.a. The results from these four compositions bracketed the rest of the results and represented the end members of the tested compositions. The starting compositions of end member models PW_M4, 7, 9 and 10 are presented in Table 7.3.1. The first melt fractions produced by 1% melting always had dolomite composition; in the case of PW_M10, this was up to 5% melting due to the high dolomite content (20 vol%). In the models with high dolomite (PW_M10) and dolomite + apatite (PW_M9), the

compositions gradually shifted towards S and M component (silica and MgO) enrichment. This transition occurred earlier in models with lower (5%) apatite+dolomite content, i.e., in the lightly veined mantle (≤5%, and they produce fewer melt fractions with intermediate (CO_2(+P_2O_5) and S) compositions. In model mantle compositions with low olivine content and did not take part in the melting (e.g., PW_M4), the melt fraction compositions could not reach the forsterite field even at 50% melting. In the present starting compositions, the lowest olivine modal proportion, when the forsterite field was still reached, was 70% when apatite was present. Without apatite, with 60% olivine in the starting composition, the forsterite field was reached in model PWM8.

In summary, in the phlogopite wehrlite melting, the two most important factors controlling melt fraction compositions were the olivine/clinopyroxene ratios and apatite presence. The presence and melting of apatite push the compositions towards the C corner. A wider range of compositions occurred in the carbonate-rich melt fractions when apatite was present.

Table 7.3.1. Modal mineral percentages and chemical compositions (wt%) of the veined phlogopite wehrlite starting compositions (PW_M4, 7 ,9, 10) and melt fractions between 1% (F1) and 51% (F11) melting. See Notes below table.

Veined-phlogopite wehrlite model compositions (PW_M)											
		Dolomite	**Apatite**	**Phlogopite**	**Clinopyroxene**	**Olivine**	**Cpx/Ol**	**S**	**M**	**C**	**CO_2**
		Modal mineral % of the starting compositions and percentages of individual minerals melting in each increment between F1 and F11						**Starting chemical compositions** and recalculated chemical composition of each melt fraction (wt%)			
Starting comp.:	**PW_M4**	**2.5**	**2.5**	**15**	**40**	**40**	**1**	**48.44**	**36.27**	**12.98**	**2.3**
F1=0.01		1						0	20.2	32.37	47.43
F2=0.06		1.5	2.5	1				9.4	13.91	39.36	37.33
F3=0.11				5				30.37	21.9	26.01	21.72
F4=0.16				5				38.97	25.18	20.53	15.32
F5=0.21				5				43.65	26.97	17.55	11.83
F6=0.26				1	4			46.57	25.87	18.16	9.4
F7=0.31					5			48.48	24.7	19.06	7.76
F8=0.36					5			49.82	23.87	19.7	6.61
F9=0.41					5			50.82	23.26	20.17	5.75
F10=0.46					5			51.58	22.79	20.53	5.1
F11=0.51					5			52.19	22.42	20.82	4.57
Starting comp.:	**PW_M 7**	**5**		**5**	**10**	**80**	**0.1**	**41.81**	**51.09**	**4.51**	**2.59**
F1=0.01		1						0	20.2	32.37	47.43
F2=0.06		4		1				8.25	21.98	28.91	40.86
F3=0.11				4.3	0.7			29.4	25.64	21.06	23.9
F4=0.16					5			38.44	23.56	21.78	16.22
F5=0.21					5			43.07	22.49	22.16	12.28
F6=0.26					0.8	4.2		43.31	28.13	18.64	9.92
F7=0.31						5		43.04	32.97	15.65	8.34
F8=0.36						5		42.86	36.48	13.49	7.17
F9=0.41						5		42.71	39.13	11.86	6.3

Table 7.3.1. Continuation

F10=0.46						5		42.6	41.2	10.57	5.63
F11=0.51						5		42.51	42.87	9.54	5.08
Starting comp.:	**PW_M 9**	**10**	**10**	**5**	**5**	**70**	**0.1**	**34.78**	**45.26**	**10.87**	**9.1**
F1=0.01		1						0	20.2	32.37	47.43
F2=0.06		5						0	20.2	32.37	47.43
F3=0.11		4.3	0.7					0.12	19.04	33.88	46.96
F4=0.16			5					0.69	13.52	41.05	44.74
F5=0.21			5					1	10.51	44.96	43.53
F6=0.26			0.8	4.2				9.2	13.35	40.12	37.33
F7=0.31				1.8	3.2			16.8	14.95	36.72	31.53
F8=0.36					3.2	1.8		21.7	17.47	33.69	27.14
F9=0.41						5		24.11	22.39	29.64	23.86
F10=0.46						5		26	26.25	26.45	21.3
F11=0.51						5		27.52	29.36	23.88	19.24
Starting comp.:	**PW_M 10**	**20**		**5**	**5**	**70**	**0.1**	**34.27**	**47**	**8.5**	**10.23**
F1=0.01		1						0	20.2	32.37	47.43
F2=0.06		5						0	20.2	32.37	47.43
F3=0.11		5						0	20.2	32.37	47.43
F4=0.16		5						0	20.2	32.37	47.43
F5=0.21		5						0	20.2	32.37	47.43
F6=0.26		1		4				7.6	21.84	29.19	41.37
F7=0.31				2.3	2.7			15.12	22.31	27.32	35.25
F8=0.36					4	1		20.48	22.92	26.16	30.44
F9=0.41						5		22.97	27.08	23.08	26.87
F10=0.46						5		24.94	30.37	20.66	24.03
F11=0.51						5		26.54	33.03	18.69	21.74

Notes: 1; The chemical compositions were recalculated for the system SCM+CO_2 where S: SiO_2 (+TiO_2+Al_2O_3), C: CaO (+Na_2O+K_2O +Ce_2O_3+ La_2O_3), M: MgO (+FeO+MnO+Cr_2O_3) and CO_2: CO_2 (+P_2O_5). 2; The compositions of the melt fractions were re-normalised for the next calculation; therefore, the summed percentages of the individual constituting minerals do not match with the starting composition.

The early melt fractions of the veined eclogite mantle (Fig 7.3.1b, Table 7.3.1.b) show dolomite composition and gradual shift towards the C-corner of the quaternary diagrams indicating CaO-enrichment as the melting continues, followed by the transition towards the S corner SiO_2-rich compositions). The presence of apatite at the expense of dolomite pushes the melts towards the C corner; this is best shown in E_M9, where the lack of apatite produced melts with higher M/C ratios than any of the other models with apatite present. In contrast to the phlogopite wehrlite, the larger melt fractions stay on the C component-rich field while progressing towards diopside composition. The melting of garnet pushes the composition towards higher M/C component ratios, while rutile melting increases S component/ $CO_2(+P_2O_5)$ ratios (due to TiO_2 addition to the melt). Similarly to phlogopite wehrlite, the melting of poorly veined eclogite mantle produces fewer intermediate (with respect to S component and $CO_2(+P_2O_5)$ ratios) melt compositions.

Table 7.3.2. Modal mineral percentages and chemical compositions (wt%) of the veined eclogite starting compositions (E_M4, 5, 9, 15, 16) and melt fractions between 1% (F1) and 51% (F11) melting.

Veined Eclogite model compositions (E_M) (for major element modelling)											
		Dolomite	**Apatite**	**Garnet**	**Diopside**	**Rutile**	**Phlogopite**	**S**	**M**	**C**	**CO_2**
		Modal mineral % of the starting compositions and percentages of individual minerals melting in each increment between F1 and F11						**Starting chemical compositions** and recalculated chemical composition of each melt fraction (wt%)			
Starting comp.:	**E_M4**	**2.4**	**2.4**	**26.7**	**66.7**	**1.9**		**60.09**	**19.62**	**17.97**	**2.32**
F1=0.01		1							20.20	32.37	47.43
F2=0.06		1.4	2.5			1.1		19.28	8.56	36.67	35.48
F3=0.11					4.1	0.9		41.73	10.80	27.65	19.82
F4=0.16					5			48.20	12.64	25.36	13.80
F5=0.21					5			51.66	13.62	24.13	10.59
F6=0.26					5			53.81	14.23	23.36	8.60
F7=0.31					5			55.28	14.65	22.84	7.23
F8=0.36				0.5	4.5			56.35	15.10	22.30	6.25
F9=0.41				0.5	4.5			57.17	15.45	21.89	5.49
F10=0.46				1	4			57.82	15.83	21.43	4.92
F11=0.51				1	4			58.34	16.15	21.06	4.45
Starting comp.:	**E_M5**	**4.5**	**4.5**	**25.5**	**63.6**	**1.8**		**57.11**	**19.17**	**19.32**	**4.4**
F1=0.01		1							20.20	32.37	47.43
F2=0.06		3.6	1.4					0.45	15.87	38.00	45.68
F3=0.11			4			1		10.15	9.00	41.55	39.30
F4=0.16					4	1		28.51	10.29	33.77	27.43
F5=0.21					5			36.44	11.80	30.63	21.13
F6=0.26					5			41.41	12.74	28.66	17.19
F7=0.31					5			44.81	13.39	27.31	14.49
F8=0.36				0.5	4.5			47.29	14.01	26.17	12.53
F9=0.41				0.5	4.5			49.17	14.48	25.30	11.05

Table 7.3.2. Continuation

F10=0.46				1	4			50.66	14.97	24.49	9.88
F11=0.51				1	4			51.86	15.36	23.83	8.95
Starting comp.:	**E_M6**	**8.3**	**8.3**	**23.3**	**58.3**	**1.7**		**51.96**	**18.4**	**21.65**	**8**
F1=0.01		1							20.20	32.37	47.43
F2=0.06		5							20.20	32.37	47.43
F3=0.11		2.6	2.4					0.42	16.15	37.63	45.80
F4=0.16			5					0.91	11.44	43.75	43.90
F5=0.21			2.8			2.2		11.56	8.83	40.93	38.68
F6=0.26					5			20.99	10.30	37.11	31.60
F7=0.31					5			27.50	11.32	34.47	26.71
F8=0.36				0.5	4.5			32.24	12.20	32.40	23.16
F9=0.41				0.5	4.5			35.87	12.88	30.81	20.44
F10=0.46				1	4			38.72	13.53	29.43	18.32
F11=0.51				1	4			41.03	14.05	28.32	16.60
Starting comp.:	**E_M9**	**16.7**		**23.3**	**58.3**	**1.7**		**51.38**	**20.14**	**19.49**	**9**
F1=0.01		1							20.20	32.37	47.43
F2=0.06		5							20.20	32.37	47.43
F3=0.11		5							20.20	32.37	47.43
F4=0.16		5							20.20	32.37	47.43
F5=0.21		2			1	2		12.00	18.18	28.84	40.98
F6=0.26					5			21.05	17.95	27.28	33.72
F7=0.31					5			27.38	17.78	26.20	28.64
F8=0.36				0.5	4.5			32.02	17.81	25.24	24.93
F9=0.41				0.5	4.5			35.60	17.83	24.51	22.06
F10=0.46				1	4			38.43	17.96	23.80	19.81
F11=0.51				1	4			40.73	18.07	23.22	17.98

Table 7.3.2. Continuation

Starting comp.:	E_M15	5	5	31.5	36	4.5	18	55.27	20.34	19.42	4.97
F1=0.01		1							20.20	32.37	47.43
F2=0.06		4	1					0.32	17.12	36.37	46.19
F3=0.11			4.3				0.7	4.54	10.96	43.73	40.77
F4=0.16							5	20.89	13.49	37.43	28.19
F5=0.21							5	29.53	14.82	34.11	21.54
F6=0.26							5	34.87	15.65	32.05	17.43
F7=0.31							5	38.50	16.21	30.65	14.64
F8=0.36					2.1	0.9	2	42.49	15.99	28.88	12.64
F9=0.41					5			44.90	16.09	27.85	11.16
F10=0.46					5			46.80	16.17	27.04	9.99
F11=0.51				1	4			48.33	16.45	26.16	9.06
Starting comp.:	**E_M16**	**10**	**10**	**28**	**32**	**4**	**16**	**48.51**	**19.14**	**22.57**	**9.78**
F1=0.01		1							20.20	32.37	47.43
F2=0.06		5							20.20	32.37	47.43
F3=0.11		4.7	0.7					0.12	19.08	33.83	46.97
F4=0.16			5					0.67	13.68	40.85	44.80
F5=0.21			5					0.98	10.70	44.72	43.60
F6=0.26			0.9				4.1	9.66	11.65	41.89	36.80
F7=0.31							5	17.18	12.83	38.97	31.02
F8=0.36							5	22.66	13.69	36.85	26.81
F9=0.41							5	26.82	14.34	35.23	23.60
F10=0.46					1		4	31.05	14.44	33.44	21.07
F11=0.51				1	4			37.10	13.34	30.55	19.01

Notes: 1; The chemical compositions were recalculated for the system SCM+CO_2 where S: SiO_2 (+TiO_2+Al_2O_3), C: CaO (+Na_2O+K_2O +Ce_2O_3+ La_2O_3), M: MgO (+FeO+MnO+Cr_2O_3) and CO_2: CO_2 (+P_2O_5). 2; The compositions of the melt fractions were re-normalised for the next calculation; therefore, the summed percentages of the individual constituting minerals do not match with the starting compositions.

The first MARID melt fractions (Fig 7.3.1c, Table 7.3.1.c) always have a dolomite composition as expected. The C component and CO_2(+P_2O_5)-rich melt fractions extend to F3 or F4 with higher added vein proportion. The commencement of phlogopite melting shifts the melt fractions towards the S corner (SiO_2-rich compositions), and only model M_M7 with 20 vol% added vein material produces a melt fraction with intermediate composition (F5). The compositions progress towards more S component-rich, overlapping compositions, which are all close to phlogopite composition. Amphibole melting pushes the melt fractions very slightly towards the C corner due to the addition of CaO to the melt. As the melting progresses, the compositions shift away from the M corner, indicating a decrease in the mafic chemical components. The most significant difference between the MARID and the eclogite and phlogopite wehrlite mantle compositions is that the former did not produce intermediate melts with (approximate) silicocarbonatite or CaO-rich silicate compositions (apart from M_M7).

Table 7.3.3. Modal mineral percentage and chemical compositions (wt%) of the veined MARID starting compositions (M_M1-6 and AJE288) and melt fractions between 1% (F1) and 50% or 51% (F11) melting.

MARID (Sample AJE281 model compositions)											
		Carbonate	Apatite	Phlogopite	Clinopyroxene	Amphibole	Ilmenite	S	M	C	CO_2
		Modal mineral % of the starting compositions and percentages of individual minerals melting in each increment between F1 and F11						Starting chemical compositions and recalculated chemical composition of each melt fraction (wt%)			
AJE281		**0.00**	**0.00**	**44.50**	**21.00**	**31.00**	**3.50**	**45.03**	**45.20**	**9.77**	**0.00**
F1=0.01				0.01				59.59	33.10	7.31	0.00
F2=0.05				0.04				59.59	33.10	7.31	0.00
F3=0.10				0.04		0.01		56.23	36.20	7.57	0.00
F4=0.15				0.035		0.01	0.005	54.98	37.58	7.44	0.00
F5=0.20				0.03		0.015	0.005	53.65	38.91	7.44	0.00
F6=0.25				0.025	0.005	0.015	0.005	52.25	40.08	7.67	0.00
F7=0.30				0.025	0.005	0.015	0.005	51.37	40.82	7.81	0.00
F8=0.35				0.025	0.005	0.015	0.005	50.75	41.34	7.91	0.00
F9=0.40				0.025	0.005	0.019	0.001	50.13	41.82	8.05	0.00
F10=0.45				0.025	0.006	0.019		49.61	42.19	8.20	0.00
F11=0.50				0.025	0.006	0.019		49.20	42.48	8.32	0.00
AJE281_5%	**M_M1**	**0.08**	**0.08**	**46.73**	**19.95**	**29.45**	**3.72**	**45.47**	**44.76**	**9.71**	**0.06**
F1=0.01		0.01							20.20	32.37	47.43
F2=0.05		0.001	0.001	0.038				59.36	33.05	7.41	0.18
F3=0.10				0.045		0.005		57.54	34.89	7.50	0.07
F4=0.15				0.045		0.005		57.06	35.37	7.52	0.05
F5=0.20				0.04		0.005	0.005	56.65	35.95	7.37	0.03
F6=0.25				0.035		0.01	0.005	55.75	36.89	7.33	0.03
F7=0.30				0.03	0.005	0.01	0.005	54.58	37.88	7.52	0.02
F8=0.35				0.025	0.005	0.015	0.005	53.37	38.93	7.68	0.02
F9=0.40				0.025	0.005	0.015	0.005	52.51	39.69	7.79	0.01
F10=0.45				0.025	0.005	0.015	0.005	51.86	40.25	7.88	0.01

Table 7.3.3. Continuation

F11=0.50				0.025	0.005	0.015	0.005	51.36	40.69	7.94	0.01
AJE281_10%	**M_M2**	**0.16**	**0.16**	**48.96**	**18.90**	**27.90**	**3.93**	**45.92**	**44.31**	**9.65**	**0.12**
F1=0.01		0.01							20.20	32.37	47.43
F2=0.05		0.001	0.001	0.038				59.36	33.05	7.41	0.18
F3=0.10			0.001	0.045		0.004		57.89	34.55	7.48	0.08
F4=0.15				0.045		0.005		57.27	35.17	7.51	0.05
F5=0.20				0.04		0.005	0.005	56.80	35.80	7.36	0.04
F6=0.25				0.035		0.01	0.005	55.86	36.78	7.33	0.03
F7=0.30				0.03	0.005	0.01	0.005	54.67	37.80	7.51	0.02
F8=0.35				0.025	0.005	0.015	0.005	53.44	38.87	7.67	0.02
F9=0.40				0.025	0.005	0.015	0.005	52.56	39.64	7.78	0.02
F10=0.45				0.025	0.005	0.015	0.005	51.90	40.21	7.88	0.01
F11=0.50				0.025	0.005	0.015	0.005	51.40	40.65	7.94	0.01
AJE281_20%	**M_M3**	**0.31**	**0.31**	**53.42**	**16.80**	**24.80**	**4.36**	**46.86**	**43.38**	**9.52**	**0.24**
F1=0.01		0.01							20.20	32.37	47.43
F2=0.05		0.003	0.003	0.034				59.26	33.01	7.48	0.25
F3=0.10				0.045	0	**0.005**		57.41	34.96	7.53	0.10
F4=0.15				0.045	0	0.005		56.97	35.43	7.54	0.06
F5=0.20				0.04	0	0.005	0.005	56.57	36.00	7.38	0.05
F6=0.25				0.035	0	0.01	0.005	55.68	36.94	7.34	0.04
F7=0.30				0.03	0.005	0.01	0.005	54.51	37.93	7.53	0.03
F8=0.35				0.025	0.005	0.015	0.005	53.30	38.99	7.69	0.02
F9=0.40				0.025	0.005	0.015	0.005	52.44	39.74	7.80	0.02
F10=0.45				0.025	0.005	0.015	0.005	51.79	40.30	7.89	0.02
F11=0.50				0.025	0.005	0.015	0.005	51.30	40.74	7.94	0.02
AJE281_5%CarbAp	**M_M4**	**2.38**	**2.38**	**42.38**	**20.00**	**29.52**	**3.33**	**43.23**	**43.79**	**11.20**	**1.78**
F1=0.01		0.01							20.20	32.37	47.43
F2=0.05		0.02	0.02					0.62	14.21	40.15	45.02

Table 7.3.3. Continuation

F3=0.10			0.01	0.04				58.62	32.76	7.89	0.73
F4=0.15				0.05	0.00	0.01		57.28	34.69	7.71	0.32
F5=0.20				0.04	0.00	0.01	0.01	56.65	35.71	7.44	0.20
F6=0.25				0.04	0.00	0.01	0.01	55.54	36.94	7.37	0.15
F7=0.30				0.03	0.01	0.01	0.01	54.20	38.10	7.59	0.11
F8=0.35				0.03	0.01	0.02	0.01	52.87	39.28	7.76	0.09
F9=0.40				0.03	0.01	0.02	0.01	51.98	40.07	7.87	0.08
F10=0.45				0.03	0.01	0.02	0.01	51.34	40.64	7.95	0.07
F11=0.50				0.03	0.01	0.02	0.01	50.85	41.07	8.02	0.06
AJE281_10%CarbAp	**M_M5**	**4.55**	**4.55**	**40.45**	**19.09**	**28.18**	**3.18**	**41.57**	**42.49**	**12.51**	**3.42**
F1=0.01		0.01							20.20	32.37	47.43
F2=0.05		0.04							20.20	32.37	47.43
F3=0.10		0.006	0.044					0.86	11.88	43.18	44.08
F4=0.15			0.004	0.046				58.07	32.54	8.25	1.14
F5=0.20				0.04	0	0.005	0.005	56.73	35.18	7.56	0.53
F6=0.25				0.035	0	0.01	0.005	55.24	36.98	7.43	0.35
F7=0.30				0.03	0.005	0.01	0.005	53.69	38.38	7.68	0.25
F8=0.35				0.025	0.005	0.015	0.005	52.25	39.70	7.86	0.19
F9=0.40				0.025	0.005	0.015	0.005	51.35	40.52	7.97	0.16
F10=0.45				0.025	0.005	0.015	0.005	50.73	41.09	8.05	0.13
F11=0.50				0.025	0.005	0.015	0.005	50.28	41.51	8.10	0.11
AJE281_20%CarbAp	**M_M6**	**8.33**	**8.33**	**37.08**	**17.50**	**25.83**	**2.92**	**38.62**	**40.18**	**14.86**	**6.35**
F1=0.01		0.01							20.20	32.37	47.43
F2=0.05		0.04							20.20	32.37	47.43
F3=0.10		0.045	0.005					0.09	19.29	33.56	47.06
F4=0.15			0.05					0.71	13.31	41.33	44.65
F5=0.20			0.038	0.012				50.52	29.65	13.08	6.75

Table 7.3.3. Continuation

F6=0.25				0.035	0	0.01	0.005	52.18	38.07	8.39	1.36
F7=0.30				0.03	0.005	0.01	0.005	51.02	39.90	8.35	0.73
F8=0.35				0.025	0.005	0.015	0.005	49.82	41.29	8.39	0.50
F9=0.40				0.025	0.005	0.015	0.005	49.22	42.00	8.41	0.37
F10=0.45				0.025	0.005	0.015	0.005	48.85	42.43	8.42	0.30
F11=0.50				0.025	0.005	0.015	0.005	48.61	42.72	8.42	0.25
AJE281_10%carb	**M_M7**	**9.09**	**0.00**	**40.45**	**19.09**	**28.18**	**3.18**	**41.36**	**43.16**	**11.61**	**3.87**
F1=0.01		0.01							20.20	32.37	47.43
F2=0.05		0.04							20.20	32.37	47.43
F3=0.10		0.05							20.20	32.37	47.43
F4=0.15		0.003	0	0.047				58.04	32.77	7.96	1.23
F5=0.20				0.04	0	0.005	0.005	56.73	35.26	7.43	0.58
F6=0.25				0.035	0	0.01	0.005	55.25	37.02	7.35	0.38
F7=0.30				0.03	0.005	0.01	0.005	53.70	38.41	7.62	0.27
F8=0.35				0.025	0.005	0.015	0.005	52.27	39.71	7.81	0.21
F9=0.40				0.025	0.005	0.015	0.005	51.37	40.53	7.93	0.17
F10=0.45				0.025	0.005	0.015	0.005	50.75	41.10	8.01	0.14
F11=0.50				0.025	0.005	0.015	0.005	50.29	41.51	8.07	0.13

Notes: 1; The chemical compositions were recalculated for the system SCM+CO_2 where S: SiO_2 (+TiO_2+Al_2O_3), C: CaO (+Na_2O+K_2O +Ce_2O_3+ La_2O_3), M: MgO (+FeO+MnO+Cr_2O_3) and CO_2: CO_2 (+P_2O_5). 2; The compositions of the melt fractions were re-normalised for the next calculation; therefore, the summed proportions of the individual constituting minerals do not match with the starting compositions.

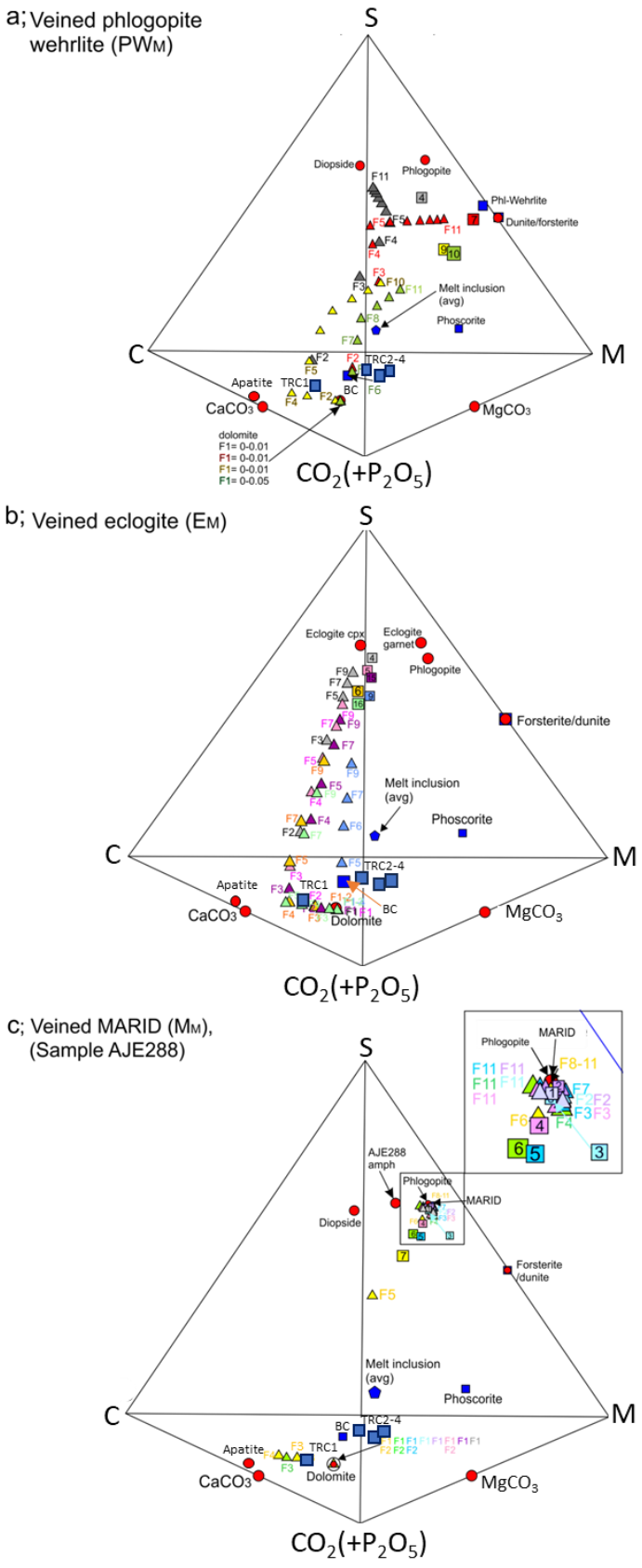

Figure 7.3.1. Primary magma composition, as a function of increasing melt fraction (F) from three different metasomatic mantle source regions. Squares denote (+model number) denote veined mantle starting compositions: (a) Veined phlogopite wehrlite source; (b) Veined eclogite model; (c) MARID. Triangle denote melt composition for fraction F, where colour of symbols tie starting compositions to melt fractions. Melt fractions ranged from 1% (F1) up to 50% (F11). The reference compositions for rocks and minerals are: Phalaborwa phoscorite and average banded carbonatite (BC) compositions (Hanekom et al. 1965); Examples for transgressive carbonatite compositions (TRC1-4) (Milani et al. 2027a); average composition of phoscoritic melt inclusions hosted in olivine (n=15; after Aldous, 1980); Phlogopite-Wehrlite (Gregoire et al. 2002); mineral compositions (Huang et al., 2014), where dunite = olivine. Compositions are listed in Table 7.3.1.a-c. The chemical compositions were recalculated for the system SCM+CO_2 where S: SiO_2 ($+TiO_2+Al_2O_3$), C: CaO ($+Na_2O+K_2O+Ce_2O_3+La_2O_3$), M: MgO ($+FeO+MnO+Cr_2O_3$) and CO_2: CO_2 ($+P_2O_5$) (See Appendix 5 for the full list of modal and major element compositions).

The same melt fractions of the different rock compositions are compared in figures 7.3.2-7.3.4: Melt fractions F4 and F7 represent 16% melting and 31% melting, respectively (and 15% and 30% melting for two MARID compositions M_M2 and M_M3).

Phlogopite wehrlite F4 fractions are separated into three groups based on S component/CO_2(+P_2O_5) ratios. The S component-rich melt fractions derive from mantle compositions between PW_M1 and PW_M7. The vein proportion in these rocks was 5% (2.5%-2.5% apatite and dolomite and 5% dolomite in composition PW_M7). This group has a divide based on the C/M component ratio. More M component-rich melts were derived from rocks with higher olivine proportions (overall higher levels of mafic components such as MgO, FeO, MnO and Cr_2O_3). The intermediate F7 fraction from composition 8 with an intermediate S component/CO_2 ratio. Mantle composition 8 does not contain apatite but 10% dolomite, placing the melt fraction to a relatively CO_2(+P_2O_5) and M component-rich (due to MgO from dolomite) part of the diagram. The third group were derived from compositions 9 to 19 with low S component/CO_2(+P_2O_5) ratios. Compositions (PW_M10, 12, 13, 16, 17, 19) with high (20% or 15%) dolomite have a dolomite composition upon melting to these proportions. Compositions where the vein also included apatite (PW_M9, 11, 15, 18) shift towards the C corner (due to CaO addition from apatite).

F7 fractions of the phlogopite wehrlite fractions separated into the same groups (based on S component/CO_2(+P_2O_5) ratios), although less clearly than on the diagrams illustrating the F4 models. F8 is also closer to the S component-rich group than the F4 fractions. As expected, the compositions with high vein proportions became richer in the S component in the higher melt fraction but still relatively CO_2-rich. The CO_2 (+P_2O_5) content in the latter group falls between 24.1 wt% and 35.7 wt%.

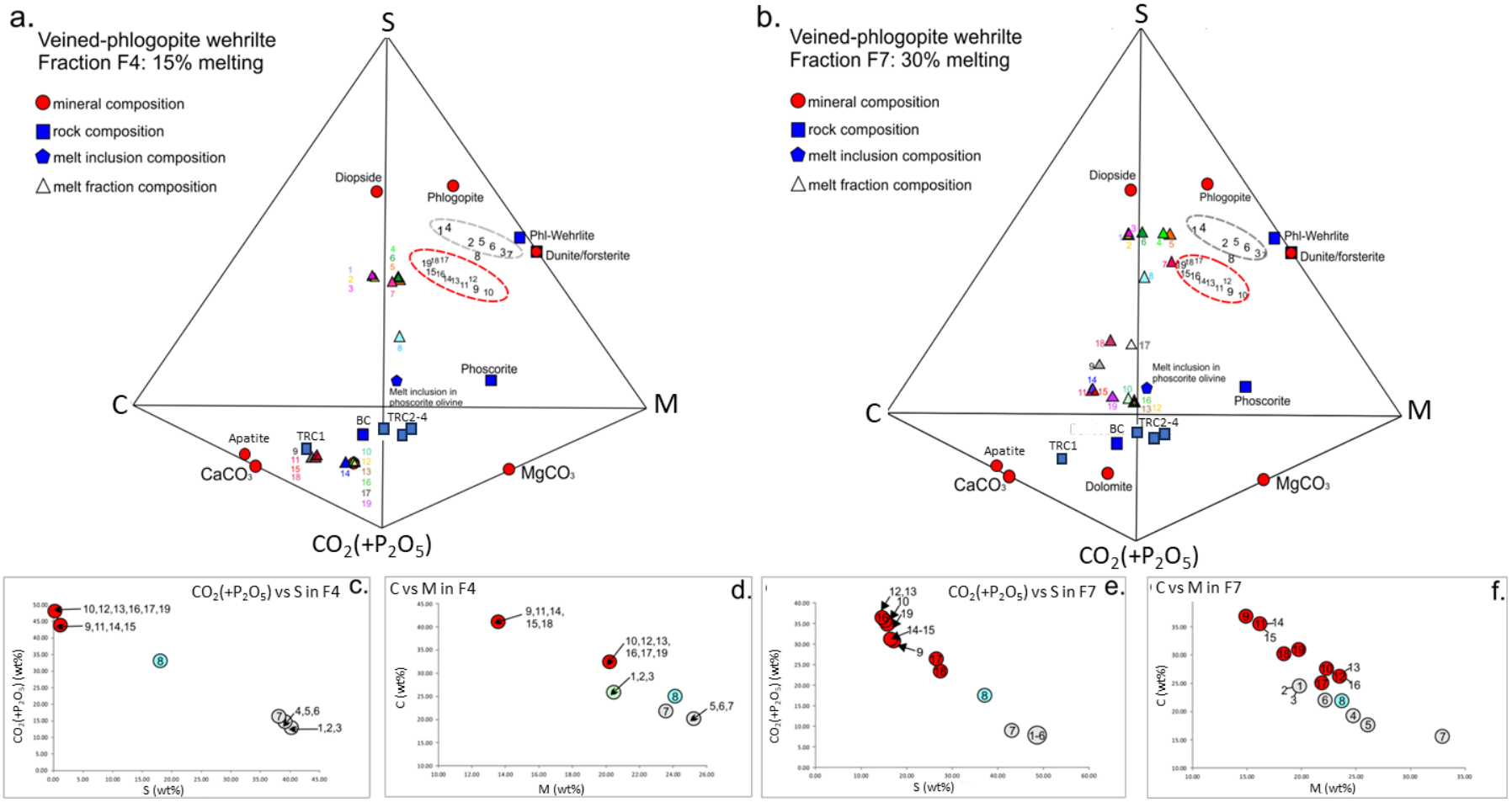

Figure 7.3.2. Composition differences between the melt fractions produced by a: 15% (F4) melting and b: 30% melting (F7) of the veined phlogopite wehrlite. The diagrams include nineteen different composition models. The grey and red dashed-circled numbers denote veined phlogopite wehrlite starting compositions. Triangles denote melt composition for fraction F4 (a.) and F7 (b.) representing 15 and 30% melting, respectively. The colour of triangles tie starting compositions to melt fractions. The variograms c-f contrast the S/CO_2 and C/M ratios of melt fraction F4 (c, d) and F7 (e, f) (See Appendix 3 for the full list of modal and major element compositions).TRC1-4: transgressive carbonatite compositions (Milani et al., 2017a), BC: average banded carbonatite composition (Hanekom et al., 1965), Phosocorite: average Phalaborwa phoscorite composition (Hanekom et al., 1965), Melt inclusion composition from Aldous (1970). The chemical compositions were recalculated for the system $SCM+CO_2$ where S: SiO_2 ($+TiO_2+Al_2O_3$), C: CaO ($+Na_2O+K_2O+Ce_2O_3+La_2O_3$), M: MgO ($+FeO+MnO+Cr_2O_3$) and CO_2: CO_2 ($+P_2O_5$)

The F4 fractions of the six eclogite compositions are similarly separated into three groups based on metasomatic vein proportions, following similar patterns to phlogopite wehrlite. The F7 fractions show similar patterns but with higher S component/CO_2(+P_2O_5) ratios. The melting of garnet pushes the composition towards higher MgO/CaO ratios, while, as expected, rutile melting increases S component/CO_2(+P_2O_5) ratios due to TiO_2 melting, as described before.

Similarly to eclogite and phlogopite wehrlite models, chemical ratios in MARID melt fractions F4 and F7 were compared. The F4 melt fraction of composition M_M7 is separated from the others by its high CO_2(+P_2O_5) /S component and C/M component ratios. Melt fraction F7 of M_M7 still separates from the rest of the compositions (high CO_2(+P_2O_5) /S ratios and much higher M and C levels than in the rest). C/M component ratios change in compositions M_M1-6 based on the melted phlogopite and amphibole proportion. MARID melt evolution significantly differs from eclogite and phlogopite wehrlite in the lack of intermediate melt fraction compositions and the shift towards more M component-rich compositions when clinopyroxene melts.

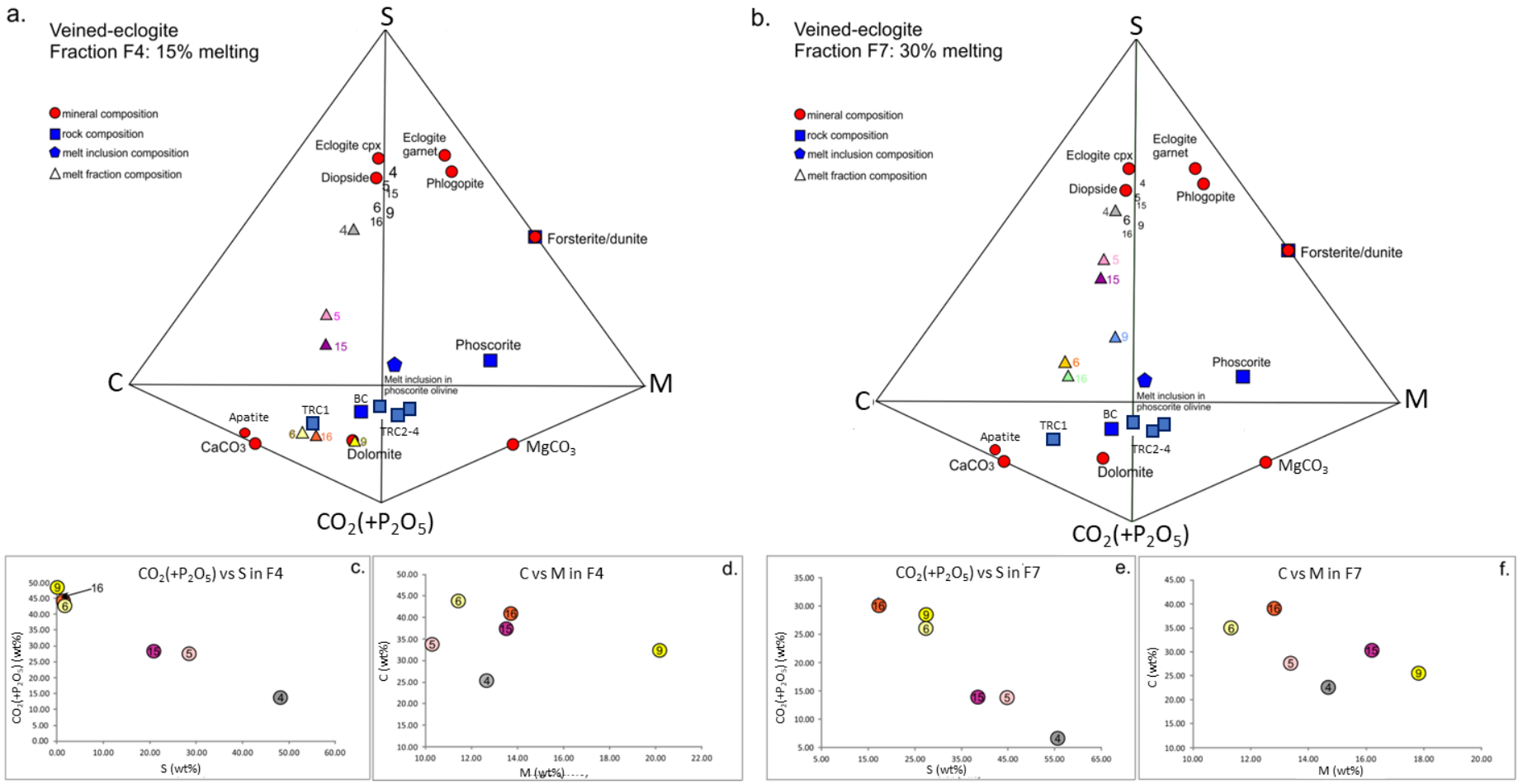

Figure 7.3.3. Composition differences between the melt fractions produced by a: 15% (F4) melting and b: 30% melting (F7) of the veined eclogite. The black numbers denote starting compositions. The triangles denote melt composition for fraction F4 and F7, where colour of the triangles tie starting compositions to melt fractions. The variograms c-f contrast the S/CO_2 and C/M ratios of melt fraction F4 (c, d) and F7 (e, f) (See Appendix 3 for the full list of modal and major element compositions). TRC1-4: transgressive carbonatite compositions (Milani et al., 2017a), BC: average banded carbonatite composition (Hanekom et al., 1965). Phoscorite: average Phalaborwa phoscorite composition (Hanekom et al., 1965), Melt inclusion composition from Aldous (1970). The chemical compositions were recalculated for the system SCM+CO_2 where S: SiO_2 (+TiO_2+Al_2O_3), C: CaO (+Na_2O+K_2O +Ce_2O_3+ La_2O_3), M: MgO (+FeO+MnO+Cr_2O_3) and CO_2: CO_2 (+P_2O_5)

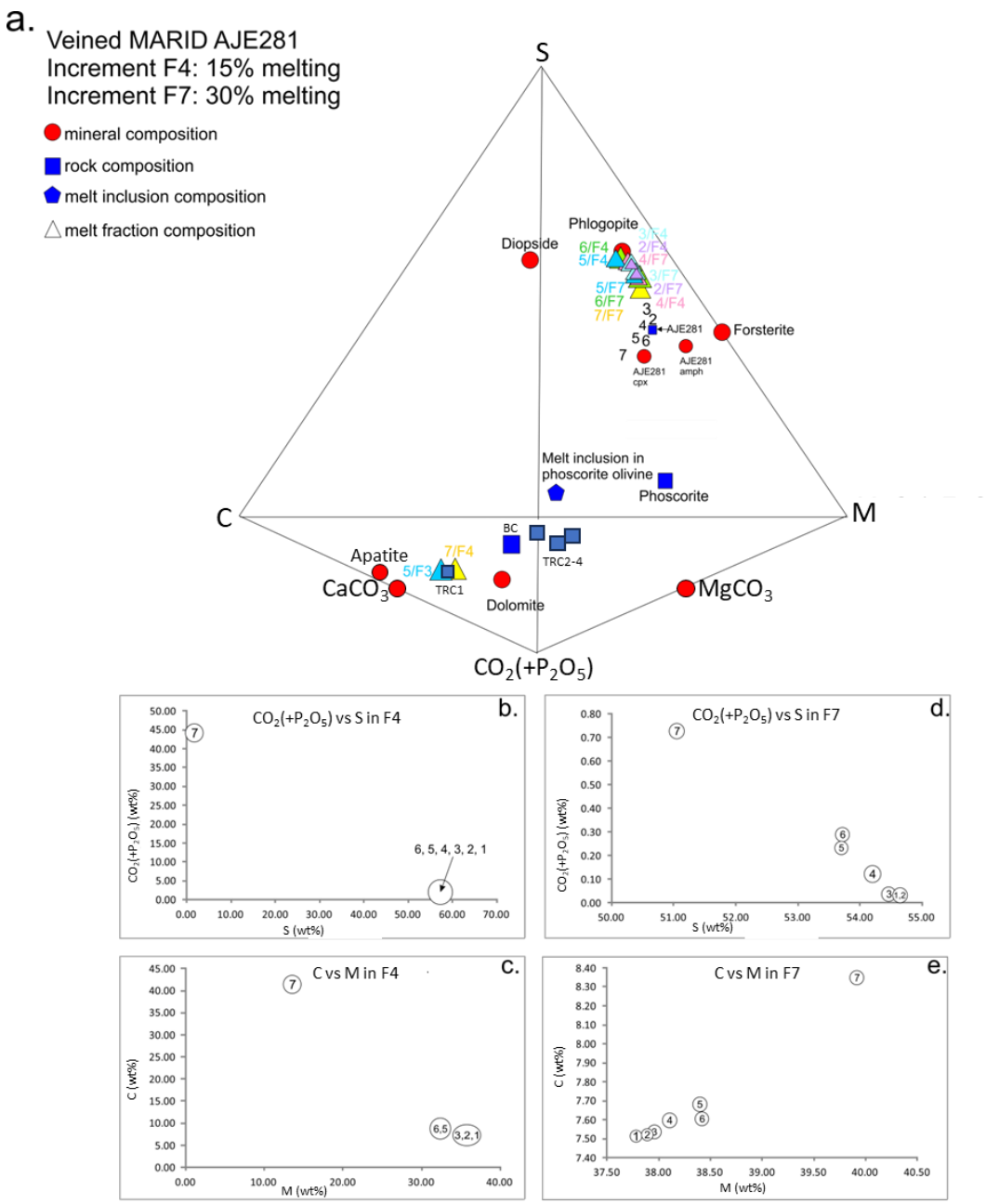

Figure 7.3.4. Composition differences between the melt fractions produced by a: 15% (F4) melting and b: 30% melting (F7) of the veined MARID. The original composition of AJE281 is shown by a blue square. The black numbers denote the veined starting compositions. The triangles denote melt composition for fraction F4 and F7, where the colour of the triangles tie starting compositions to melt fractions. The variograms (b-e) contrast the S/CO_2 and C/M ratios of melt fraction F4 (b, c) and F7 (d, e). TRC1-4: transgressive carbonatite compositions (Milani et al., 2017a), BC: average banded carbonatite composition (Hanekom et al., 1965), Phoscorite: average Phalaborwa phoscorite composition (Hanekom et al., 1965); Melt inclusion composition from Aldous (1970). (See Appendix 3 for the full list of modal and major element compositions). The chemical compositions were recalculated for the system SCM+CO_2 where S: SiO_2 (+TiO_2+Al_2O_3), C: CaO (+Na_2O+K_2O +Ce_2O_3+ La_2O_3), M: MgO (+FeO+MnO+Cr_2O_3) and CO_2: CO_2 (+P_2O_5).

7.3.2 Trace element behaviour during the melting of compositional end members of metasomatised mantle

7.3.2.1 Cerium (representing Light REEs: La, Ce, Pr, Nd, Pm)

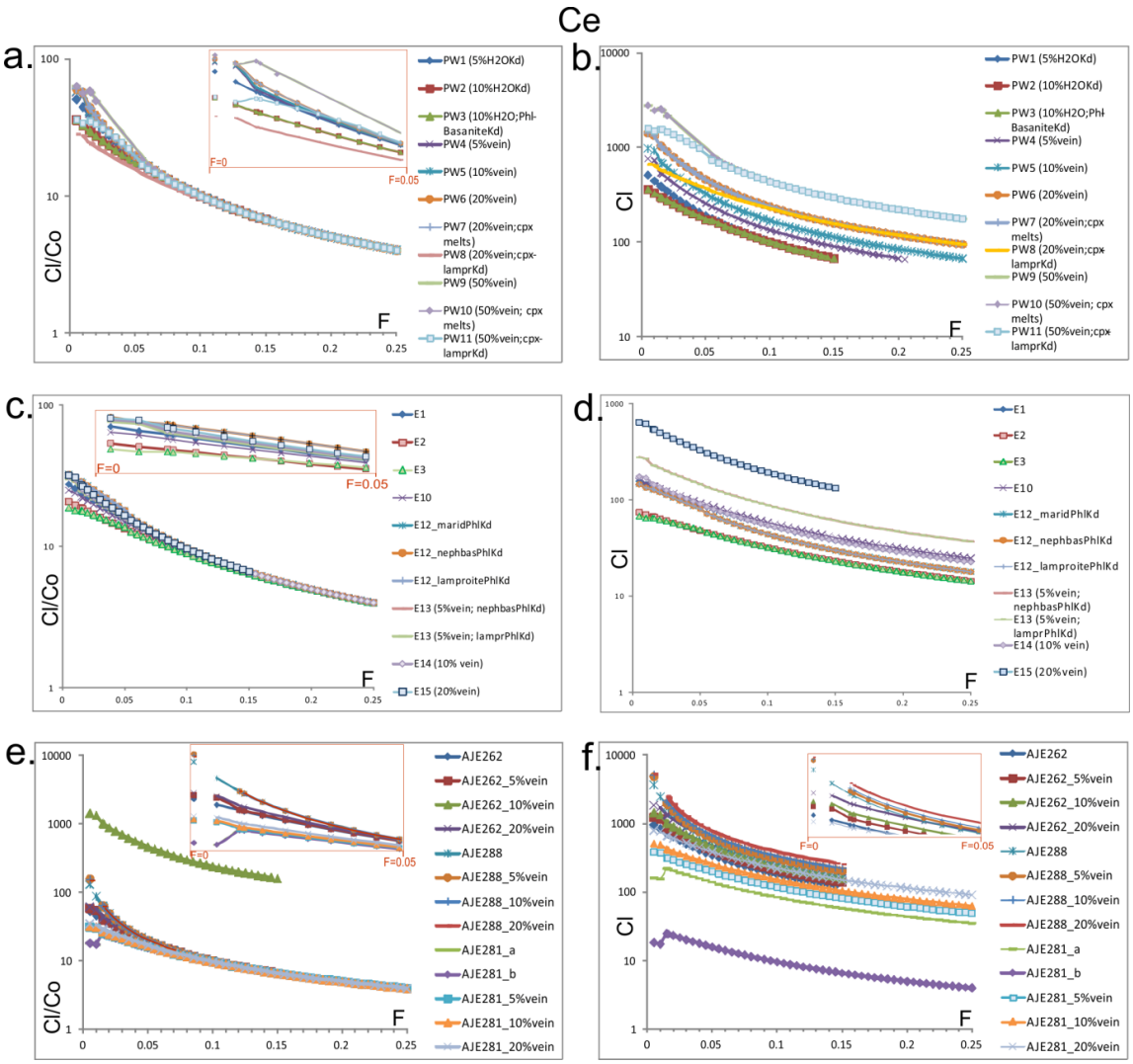

Figure 7.3.5. Ce partitioning behaviour (Cl/Co) and calculated liquid concentrations (Cl) during the melting of phlogopite wehrlite (a, b), eclogite (c, d) and MARID (e, f) mantles. The respective Cl/Co ratios and Cl are depicted against melt fractions (F) up to 25% melting. The legends show the included non-veined and veined model names.

In phlogopite wehrlite models (Fig. 7.3.5 a-b), the Ce C_l/C_o curves have a generally declining pattern. Where a large added vein proportion is present, the earlier melting stages produced increasing curves as carbonate apatite (±phlogopite) melted. The initial C_l/C_o ratios are very similar to each other and the highest in the first melt fractions. Using lamproite K_d for clinopyroxene (Table 7.2.2) lowered the C_l/C_o ratios and the calculated Ce concentrations in the melt. Using K_d determined near 5%H_2O produced higher C_l/C_o ratios and higher

concentrations than the 10% H_2O. Generally, the calculated Ce concentrations decrease with decreasing added vein proportions.

The melting of eclogite compositions (Fig. 7.3.5.c) produced gently declining and overlapping C_l/C_o curves. Adding metasomatic veins to the compositions resulted in slightly steeper curves during the melting of the vein material. The ratios slightly decrease with decreasing vein proportions. In the non-veined compositions, the higher garnet and phlogopite proportions indicate increasing metasomatism (Huang et al., 2014), which is reflected in the present results and models. Models E10, E12 and E1 produced higher C_l/C_o ratios than the other non-veined models. The models above have higher garnet and phlogopite proportions. The Ce concentrations increased with increasing vein proportions. In models where nepheline basanite, lamproite or MARID K_d were used for phlogopite, the C_l/C_o ratios did not show significant differences in value or curve shapes. At the same time, the Ce liquid concentration increased when lamproite K_d was used.

Apart from one example (AJE262_10%), the C_l/C_o ratios of the MARID models (Fig. 7.3.5.e) separate from each other based on the model group (AJE262, AJE288 and AJE281) they belong to and not based on their added vein proportion. The highest C_l/C_o ratios were observed in models AJE288 and the lowest in AJE281. The former composition has the highest (87.5 vol%) while the latter has the lowest (44.5 vol%) phlogopite content. Starting composition AJE262 falls between the two other models, with phlogopite content of 73 vol%. The relatively high amphibole content in AJE262 and AJE 281 (24.7 vol% and 31 vol%) compared to AJE288 (9.7 vol%) does not make up for their low phlogopite content. The Ce concentration levels follow the C_l/C_o trends, and the concentration increases with added vein proportions. The melting of clinopyroxene in model AJE281_b) lowers the Ce concentrations in the melt.

7.3.2.2 Gadolinium (representing Medium REEs: Sm, Eu, Gd)

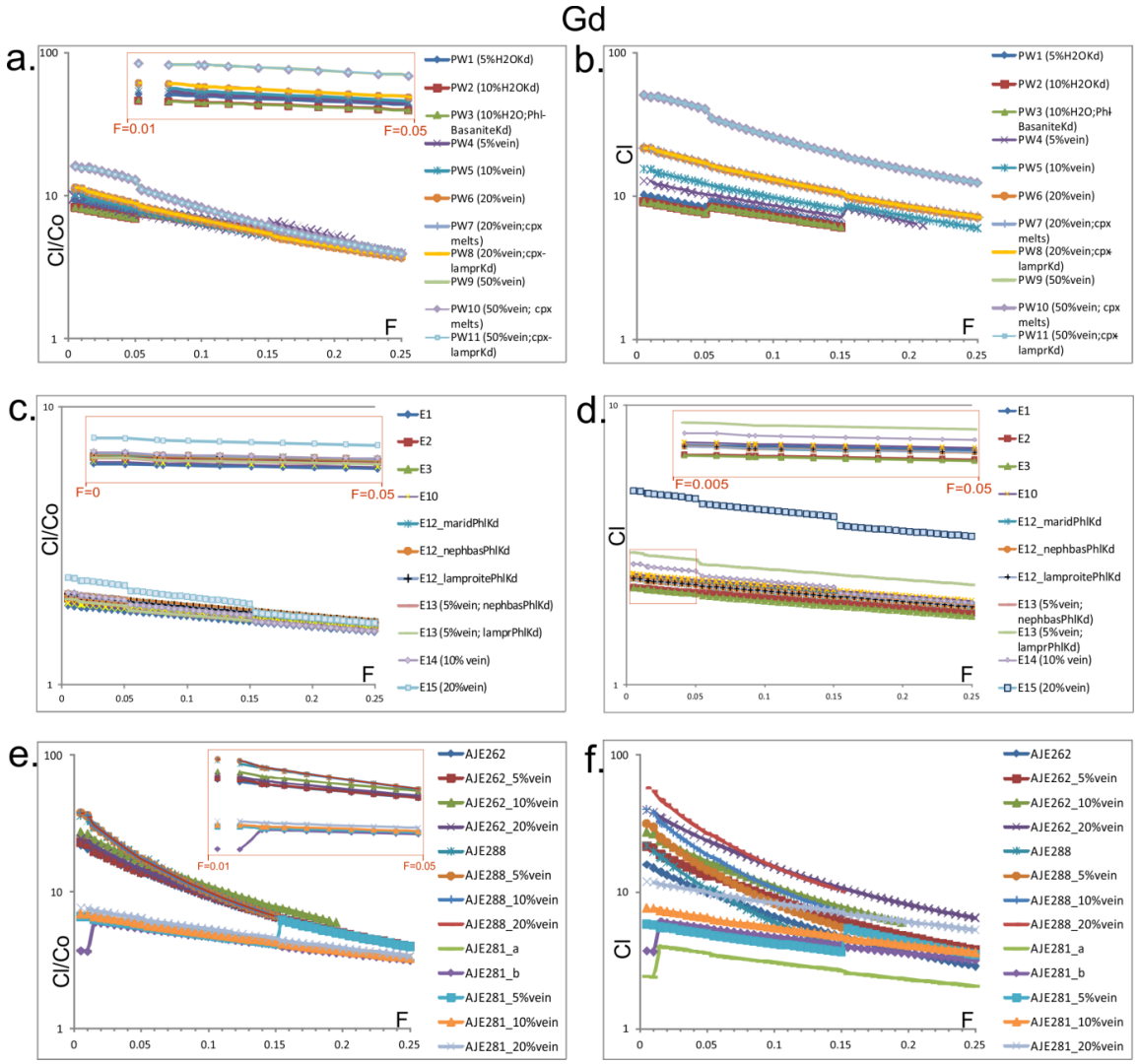

Figure 7.3.6. Gd partitioning behaviour (Cl/Co) and calculated liquid concentrations (Cl) during the melting of phlogopite wehrlite (a, b), eclogite (c, d) and MARID (e ,f) mantles. The respective Cl/Co ratios and Cl are depicted against melt fractions (F) up to 25% melting. The legends show the included non-veined and veined model names.

In the phlogopite wehrlite models (Fig.7.3.6 a-b), Gd showed decreasing C_l/C_o curves. However, a positive ratio jump occurred when clinopyroxene started to melt (Pw1-5) due to its relatively high Gd K_d value (0.51). The highest C_l/C_o ratios and concentration levels were observed in the 50%-vein models, gradually declining as the added vein proportion decreased. Using K_d determined at 5% H_2O produced slightly higher values than the 10%H_2O model.

Eclogite melting (Fig.7.3.6 c-d) produced nearly flat Gd C_l/C_o curves with similar ratios. The highest C_l/C_o ratio occurred in the 20% vein model (E15), while the lowest was in E1. C_l/C_o ratios increased with increasing added vein proportions. The Gd concentrations are also the highest in the veined models. Models with

high garnet and phlogopite proportions showed slightly higher Gd concentrations than the non-veined models. Using lamproite K_d for phlogopite increased liquid Gd concentrations compared to MARID or nepheline basanite K_ds.

In MARID models (Fig.7.3.6 e-f), the highest Gd C_l/C_o ratios were found in the AJE288 models, which also show the steepest declining curves. AJE262 models initially showed slightly lower ratios and flatter curves; however, after 1% melting, the AJE262_10% vein model shows the highest C_l/C_o ratios. The AJE288 models produced significantly lower C_l/C_o ratios and flatter curves than the other models. AJE288 compositions have the lowest phlogopite content and are the only models with clinopyroxene. The initial C_l/C_o ratios decrease with decreasing added vein proportion. In the 5% vein models, the beginning of amphibole and ilmenite melting causes increased C_l/C_o ratios due to their relatively high K_d values (0.153 and 0.14, respectively). The lowest C_l/C_o ratios were found in the non-veined AJE281 models, where, after phlogopite melting, the ratios increase during the latter melting stages. The Gd concentrations roughly follow the pattern of the C_l/C_o ratios. However, the individual models of each model group are more separated from each other and can overlap with the non-veined models. Especially in models of AJE288 and AJE262, the individual models tend to group together by their vein proportions.

7.3.2.3 Yttrium (representing Heavy REEs: Sc, Y, Tb, Dy, Ho, Er, Tm, Yb, Lu)

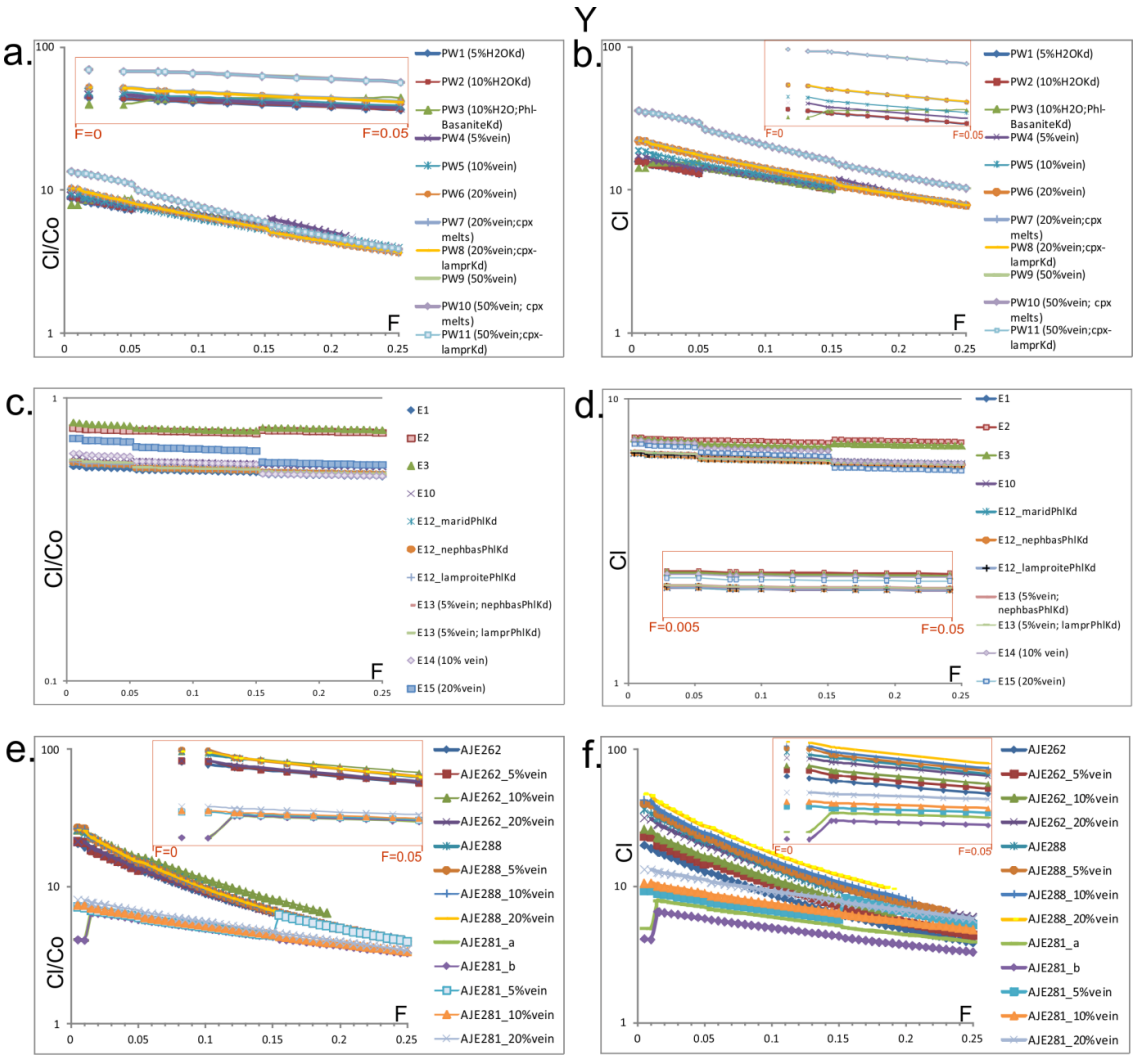

Figure 7.3.7. Y partitioning behaviour (Cl/Co) and calculated liquid concentrations (Cl) during the melting of phlogopite wehrlite (a, b), eclogite (c, d) and MARID (e ,f) mantles. The respective Cl/Co ratios and Cl are depicted against melt fractions (F) up to 25% melting. The legends show the included non-veined and veined model names.

In phlogopite wehrlite models (Fig.7.3.7 a-b), the Y C_l/C_o curves are mostly declining in shape, and the ratios are similar in all modelled compositions. The highest C_l/C_o ratio was observed in models with 50% added vein proportion (PW9-11). The ratio decreases with decreasing vein proportion. When clinopyroxene takes part in the later stage melting, the C_l/C_o ratio increases (PW4-5) at the beginning of the new melting stage, but the gently declining pattern remains. The using K_d s determined at different H_2O levels did not affect the C_l/C_o ratios; however, using basanite K_d instead of lamproite caused a slight decrease in the initial ratios. The calculated Y concentrations follow the curve patterns and orders described above, indicating that the initial Y concentration in the melt increases with increasing melt proportions.

Eclogite melting (Fig.7.3.7 c-d) produced almost flat C_l/C_o curves. The highest C_l/C_o ratios were observed in the non-veined models E2 and E3. The ratios of the other non-veined model, E1 (10% H_2O K_d) were among the lowest. The next highest C_l/C_o ratios were observed in the 20% vein model (E15), followed by the 10% vein model (E14). The 5% vein models (E13) roughly overlap with the high-phlogopite models (E12) and E1. The calculated Y concentrations follow the order of the C_l/C_o ratios; the highest Cl values were found in models E2 and E3, followed by the veined models with decreasing vein proportion, model E1, and the high-phlogopite models (E12). Changing phlogopite K_d s between lamproite, MARID, or nepheline basanite systems did not affect Y behaviour.

The three MARID (Fig.7.3.7 e-f) composition groups are separated into three groups of generally declining C_l/C_o curves, where AJE262 and AJE288 have very similar ratios and curve shapes. In contrast, AJE281 has lower ratios and flatter curve shapes. The two former models are extremely phlogopite-rich (73 vol% and 78.5 vol%, respectively). At low vein proportion (5%), model AJE281 showed a significant positive jump in the last melting stage (T: 0.15- 0.25) caused by the elevated amphibole and ilmenite ratio in the melt fraction. At higher vein proportions where clinopyroxene takes part in the melting, the curve remains declining without a change. The concentration curves follow the C_l/C_o curve patterns and orders. The highest concentrations were calculated in the AJE288 models, followed by AJE262 and AJE281. Inside the individual groups, the concentrations decreased with decreasing vein proportions.

In summary of the REE behaviour, Cerium (representing LREE) showed the strongest incompatibility among the modelled elements. The highest incompatibility was shown in MARID models, followed by phlogopite wehrlite models and the lowest incompatibility in eclogite models. Consequently, the highest Ce concentrations were observed in MARID and phlogopite wehrlite melts and lowest in eclogite melts. Gadolinium (representing MREE) fell between Ce and Y regarding incompatibility in the different source compositions. The MARID models showed the highest incompatibility, followed (and partially overlap) by the phlogopite wehrlite models. Gadolinium behaved the most compatibly in eclogite sources. The highest calculated Gd concentrations were observed in melts of MARID AJE262 and AJE288 compositions, closely followed by phlogopite wehrlite, while eclogite melts had the lowest concentrations. As

expected, Yttrium (representing HREE) showed the lowest incompatibility among the modelled REE. The highest compatibility was observed in MARID models, followed by phlogopite wehrlite models, while Y behaved the most compatibly in eclogite models. The Y showed the same relative concentrations in the different melts as Gd.

In phlogopite wehrlite melts, Ce reached the highest concentrations, especially in the veined models, followed by Gd and Y. Ce also reached the highest concentrations in eclogite melts, followed by Y, while Gd showed the lowest levels. In MARID melts, Ce showed marginally higher concentrations than Gd and Y, which showed similar levels.

7.3.2.4 Niobium

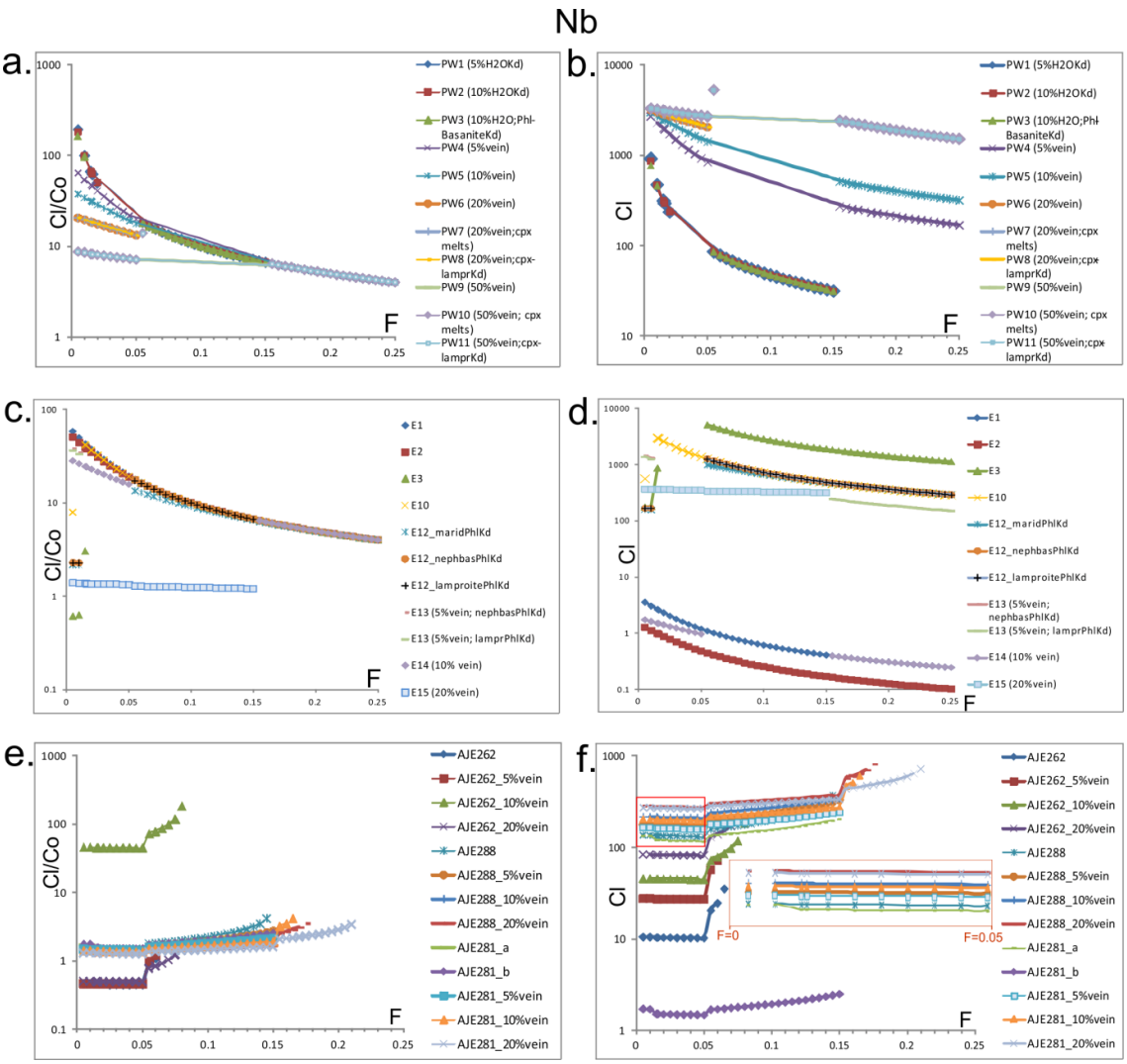

Figure 7.3.8. Nb partitioning behaviour (Cl/Co) and calculated liquid concentrations (Cl) during the melting of phlogopite wehrlite (a, b), eclogite (c, d) and MARID (e, f) mantles. The respective Cl/Co ratios and Cl are depicted against melt fractions (F) up to 25% melting. The legends show the included non-veined and veined model names.

In the phlogopite wehrlite (Fig.7.3.8 a-b) melting models, Nb reaches the highest C_l/C_o ratios in the un-veined models, and the initial ratio gradually decreases as the added vein proportion increases in the starting composition. The curve shape of the un-veined models is declining, with a relatively steep slope at the early melting stages and gradually flattening as the melting progresses. The veined models have a flatter curve shape with a gently declining pattern, displaying a positive jump as ilmenite melts due to its high K_d value (2.0). The concentration (Cl) curves display the same pattern as the C_l/C_o curves; however, the relative order of the individual models is the reverse of the latter. The highest calculated Nb concentrations were observed in the early melts of 50%-vein models and decreased with decreasing vein proportions.

In the eclogite melting models (Fig.7.3.8 c-d) where ilmenite and rutile were present (E13, E12, E10, E3), the Nb C_l/C_o ratios displayed a significant positive jump as the phases started to melt, regardless of in which melting stage this took place. Models E1 and E2 have the highest initial C_l/C_o ratios, followed by the veined models with decreasing ratios as the added vein proportion increases. The calculated Nb concentrations show the highest Nb levels in the metasomatised starting compositions but do not follow the order of the added vein proportions. Compositions with high rutile, ilmenite proportions can produce more Nb-enriched melts than melting of the veined compositions, indicating that these phases have a more significant effect on Nb concentrations than the proportion of metasomatic veins. C_l/C_o ratios overlapped when lamproite, MARID or nepheline basanite K_d were used for phlogopite, showing that these changes did not influence Nb behaviour.

The lowest C_l/C_o ratios in the MARID models were displayed by models AJE262, while models AJE288 and AJE 281 showed higher and roughly overlapping ratios and curves. The curves show a decreasing pattern up to 5% melting, followed by a positive jump and increasing pattern as ilmenite and rutile melt. Both phases have high K_d values, 13.3 and 83.4, respectively. Model AJE262-10% vein, showed anomalously high C_l/C_o ratios with the same curve shape as the other models. The concentration curves have similar shapes and relative order and show increasing Nb concentration with added vein proportions (Fig.7.3.8 e-f).

In summary, Nb showed the strongest incompatibility in phlogopite wehrlite models followed (and overlap) by eclogite models, including E1, E2, E10, E13 and E14. The highest compatibility was shown in MARID models. The highest calculated concentrations were found in the veined phlogopite wehrlite models, followed by eclogite models E3 and E10, where the melting degree exceeded 1%. Non-veined phlogopite wehrlite, then 20% veined eclogite followed, while MARID and eclogite models E1 and E2 showed the lowest concentrations.

7.3.2.5 Zirconium

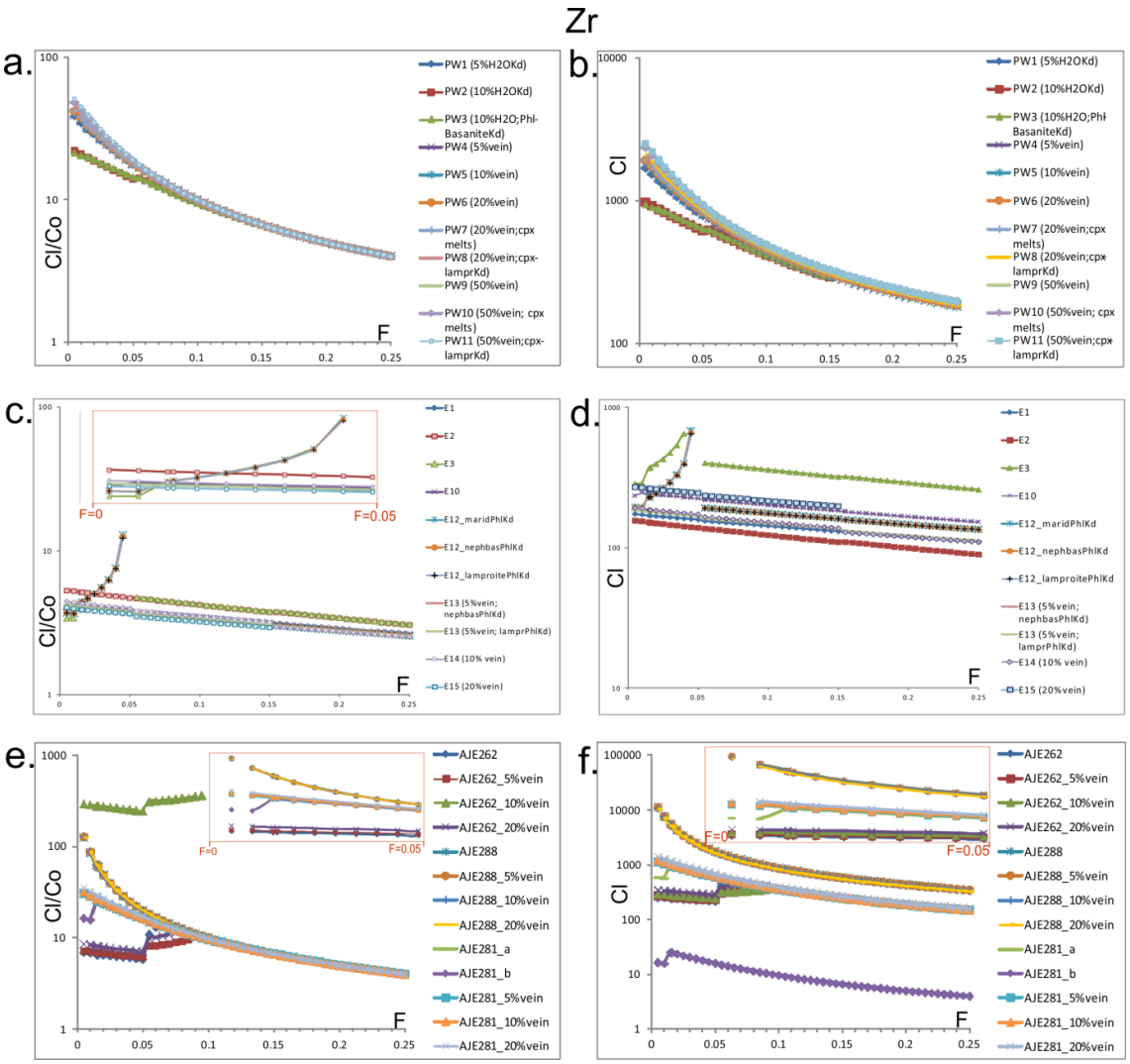

Figure 7.3.9. Zr partitioning behaviour (Cl/Co) and calculated liquid concentrations (Cl) during the melting of phlogopite wehrlite (a, b), eclogite (c, d) and MARID (e, f) mantles. The respective Cl/Co ratios and Cl are depicted against melt fractions (F) up to 25% melting. The legends show the included non-veined and veined model names.

In phlogopite wehrlite models (Fig.7.3.9 a-b), the C_l/C_o curves show a declining pattern where the non-veined model curves (PW2, PW3) are flatter and have lower, overlapping C_l/C_o ratios. The veined models and PW1 C_l/C_o ratios are very

similar to each other, with a slight decrease as the vein proportions decrease. Using lamproite K_d for clinopyroxene resulted in higher values. Similarly, using K_ds determined near 5% H_2O produced higher C_l/C_o ratios than K_ds at 10%H_2O. The calculated concentrations and the curve shapes follow the Cl/Co curves and orders.

In the eclogite models (Fig.7.3.9 c-d), in which only phlogopite melted in the first melting stages, the C_l/C_o curves showed increasing patterns, followed by decreasing patterns in the latter melting stages, similarly to the other models. The highest C_l/C_o ratios were observed in models E12 and E3, which reached the highest levels as the phlogopite melting progressed. The initial C_l/C_o ratios at 1% melting were highest in models E1 and E2, followed by the veined models and the phlogopite-rich models. The highest Zr concentrations were observed in models E3 and E15; the former composition has high (2 wt%) rutile content, while the latter has high (20 vol%) added vein proportion. The lowest concentrations were found in models E1 and E2. Reaching 5% melting, the highest Zr concentrations were in the phlogopite and rutile-rich models (E12, E3). Using phlogopite K_ds determined in different magmatic systems did not cause differences in Zr behaviour in any perceptible ways in the models.

In MARID models (Fig.7.3.9 e-f), the highest C_l/C_o ratios were found in model “AJE262_10% vein”. The curve showed a declining pattern during apatite, carbonate and phlogopite melting up to 5%. In the next melting stage, when ilmenite and rutile melted, the ratios increased with an increasing curve shape. The rest of the AJE262 models displayed the same patterns but with the lowest C_l/C_o ratios among all the models. The AJE288 models showed the second highest C_l/C_o ratios, with relatively steeply declining curves during the early melting stages, while AJE281 models produced flatter curves and slightly lower C_l/C_o ratios. The C_l/C_o ratios are generally decreasing with decreasing added vein proportions. The Zr concentration curve shapes and the relative order of the reached levels follow the C_l/C_o ratios with two exceptions. The C_l curve of model “AJE262_10% vein” overlaps with the other AJE262 models, while AJE 281_b shows lower concentrations than the other AJE281 models. Controlling factors are the general compositions. In summary, Zr showed the strongest incompatibility in MARID models AJE288 and the strongest compatibility in

MARID models AJE262. Relatively high incompatibility was also observed in phlogopite wehrlite.

7.3.2.6 Titanium

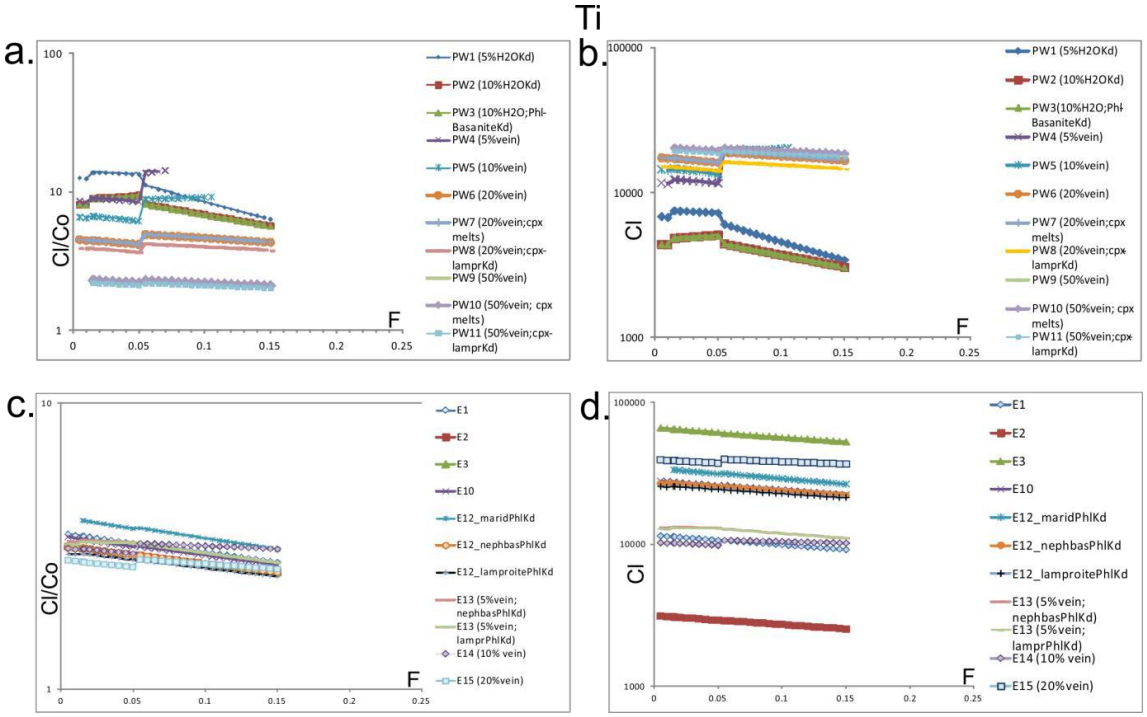

Figure 7.3.10. Ti partitioning behaviour (Cl/Co) and calculated liquid concentrations (Cl) during the melting of phlogopite wehrlite (a, b), eclogite (c, d) and MARID (e ,f) mantles. The respective Cl/Co ratios and Cl are depicted against melt fractions (F) up to 25% melting. The legends show the included non-veined and veined model names.

There were no available Ti K_d data for apatite; therefore, the C_l/C_o curves of the veined phlogopite wehrlite models (Fig.7.3.10 a-b) are controlled by phlogopite in the early stages. In these models, the C_l/C_o curves show a decreasing trend up to 5% melting followed by a positive jump when ilmenite spinel (±clinopyroxene) starts to melt alongside the phlogopite. Among all the constructing minerals, phlogopite has the highest Ti K_d (0.87), but clinopyroxene (0.28) and spinel (0.15) also have a considerable effect on Ti behaviour. The melting of the non-veined models produced curves with different patterns. In the case of PW2 and PW3, there is an increasing trend up to 5% melting, followed by a declining trend. Without additional vein material, phlogopite melts earlier, and spinel and clinopyroxene melt in earlier melting stages. Using K_ds determined at 10%H_2O increased the initial C_l/C_o ratios and changed the curve shape from increasing to decreasing in the early melting stages. The C_l/C_o ratios decrease with increasing

added vein proportions. The C_l/C_o ratios of the 5% and 10% vein models (PW4, PW5) overtake the non-vein models in the later melting stages. The calculated Ti concentrations are the highest in the veined models and decrease with decreasing vein proportion. Melts of the lightly veined compositions that formed later can be more enriched in Ti than melts of the highly veined models.

Eclogite melting (Fig.7.3.10 c-d) produced almost flat curves, indicating the compatibility of Ti in these compositions. The highest Ti concentrations were reached in models with high rutile (E3, E10, E12, E15) and relatively high phlogopite content (E15) contents. Using MARID K_ds for phlogopite increased the C_l/C_o ratios and calculated C_l compared to the nepheline basanite and lamproite systems, while the latter two showed overlapping values.

7.3.2.7 Strontium

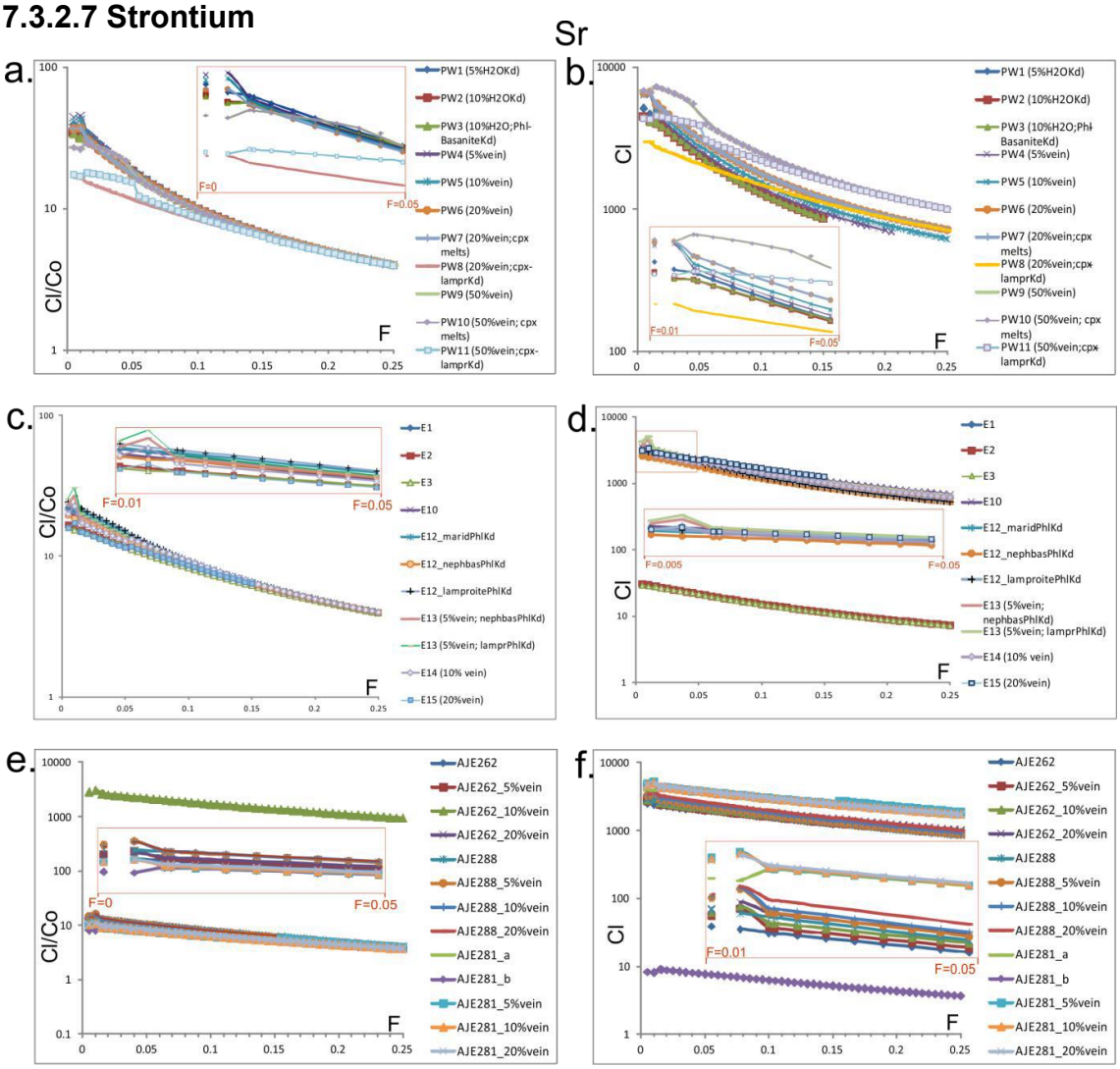

Figure 7.3.11. Sr partitioning behaviour (Cl/Co) and calculated liquid concentrations (Cl) during the melting of phlogopite wehrlite (a, b), eclogite (c, d) and MARID (e ,f) mantles. The respective Cl/Co ratios and Cl are depicted against melt fractions (F) up to 25% melting. The legends show the included non-veined and veined model names..

The phlogopite wehrlite melting (Fig.7.3.11 a-b) models produced declining Sr C_l/C_o curves. Models with 50% vein proportion (PW9-11) had an increasing pattern in the first melting stage up to 1% melting, where apatite and carbonate melted, followed by the general declining but flatter shape during the second melting stage (up to 5% melting) when phlogopite melted. The curves followed the declining pattern of the other models in the latter melting stages. The highest C_l/C_o ratios were found in the models with 5% vein followed by 10% and 20% veins, non-veined models and finally the 50% vein models. When lamproite K_d was used for clinopyroxene, the C_l/C_o ratios were significantly lower, and the higher vein proportions had high ratios. The calculated Sr concentrations were decreasing with decreasing vein proportions.

The melting of eclogite (Fig.7.3.11 c-d) produced almost flat C_l/C_o curves with very similar ratios. In the veined models, the curve had an increasing pattern in the first melting stage (up to 1% melting) while apatite, carbonate and phlogopite melted, followed by a decreasing pattern. In the non-veined models, the curve was continuously decreasing. The initial C_l/C_o ratios decreased with increasing vein proportions in the veined models. Non-veined models with high garnet and phlogopite content (E1, E12) also had relatively high C_l/C_o ratios. The calculated Sr concentrations followed the patterns described above. Using lamproite K_d for phlogopite slightly increased the C_l/C_o ratios and C_l values.

MARID models (Fig.7.3.11 e-f) produced nearly flat C_l/C_o curves. The ratios and curves overlap. Although the three starting compositions differ slightly, the different vein proportions inside a group overlap. AJE288 models have the highest, while AJE281 models have the lowest C_l/C_o ratios. C_l/C_o ratios in model "AJE262-10% vein" are outstandingly high compared to the other models. The calculated Sr concentrations have a reverse order compared to the C_l/C_o ratios. The highest concentrations were found in model AJE281, except AJE281_b, which has the lowest concentrations. The second most enriched melts were produced from the AJE288 compositions, followed by the AJE262 models.

7.3.2.8 Barium

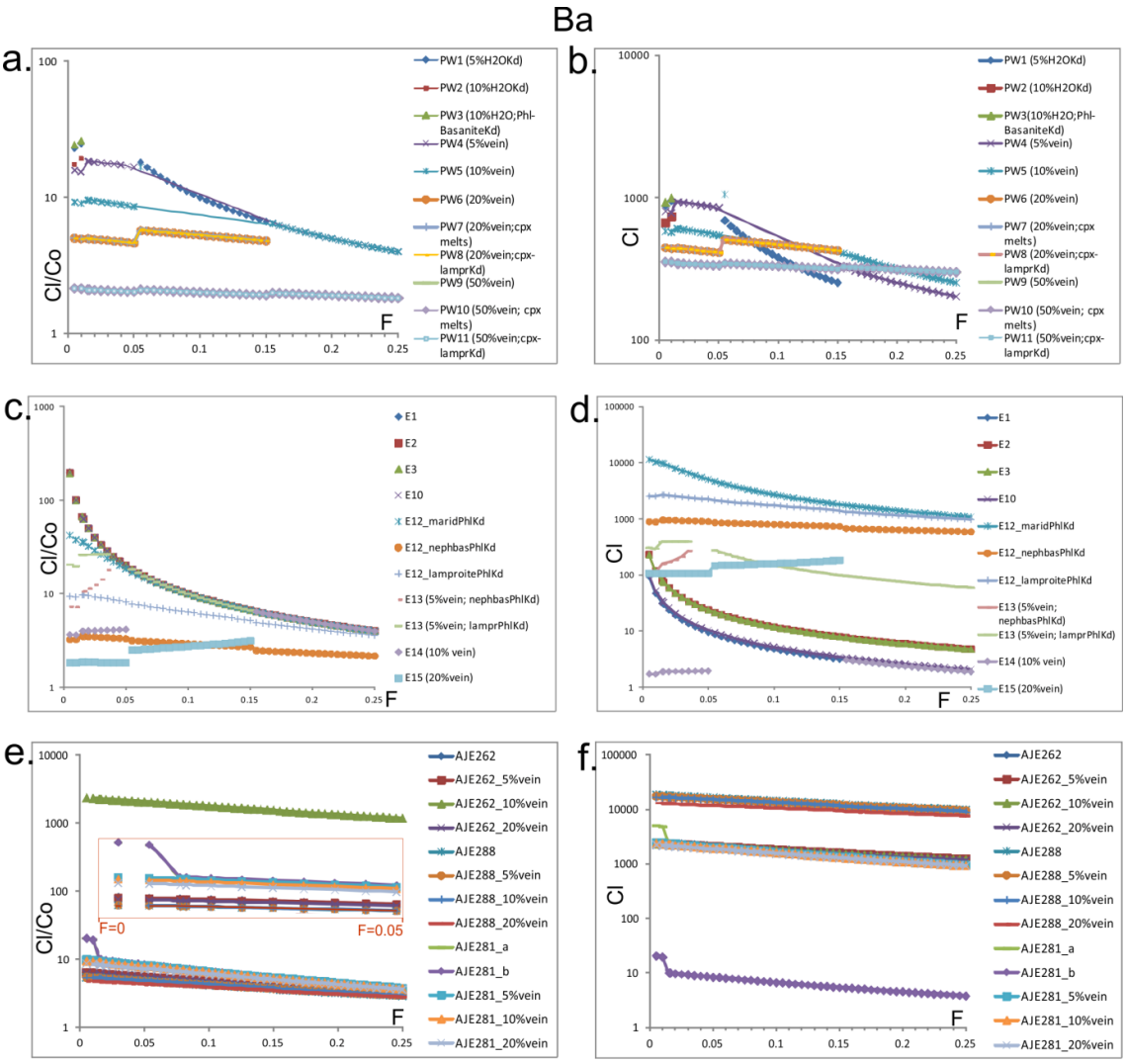

Figure 7.3.12. Ba partitioning behaviour (Cl/Co) and calculated liquid concentrations (Cl) during the melting of phlogopite wehrlite (a, b), eclogite (c, d) and MARID (e ,f) mantles. The respective Cl/Co ratios and Cl are depicted against melt fractions (F) up to 25% melting. The legends show the included non-veined and veined model names.

In the non-veined phlogopite wehrlite models (PW2, PW3), Ba melts out in the first stage during phlogopite melting (Fig.7.3.12 a-b). These models also showed the highest initial C_l/C_o ratios alongside PW1. In the latter model, basanite K_d (2.9) was used for phlogopite instead of lamproite (4.1). The C_l/C_o ratios decrease with increasing vein proportion. Ba behaves more compatibly in metasomatised sources. The highest Ba concentrations were found in non-veined (PW1, PW3) and lightly veined (PW4) models. As the vein proportion increased, the Ba concentration in the early melts decreased; however, the models with higher vein proportions became Ba-enriched relative to the non-veined and lightly veined models at the later stages of the melting.

The melting of non-veined eclogite compositions (E1-3, E10) produced decreasing and overlapping C_l/C_o curves with steeper patterns at the early melting stages (Fig.7.3.12 c-d). These models also had the highest C_l/C_o ratios. Barium behaved the most incompatibly during the early melting. The phlogopite-rich models showed almost flat curves, indicating that Ba was compatible in these compositions. Eclogite with 5% veins showed a slightly decreasing pattern in the first melting stage, then a relatively sharply increasing pattern, while phlogopite melted up to 5% melting, followed by a declining pattern in the later stages. The other veined models showed higher C_l/C_o ratios in the latter melting stages but lower initial C_l/C_o ratios with increasing vein proportions. The highest Ba concentrations were calculated in the phlogopite-rich models (E12) and using MARID K_ds for phlogopite further increased the concentrations. The non-veined models showed high initial concentrations but depleted rapidly as the melting progressed. In contrast, liquids of the 5% and 20% vein models remained relatively enriched up to 25% and 15% melting, respectively. Model E14 with 10% vein showed low concentrations compared to the models above. Barium showed the most significant sensitivity to phlogopite K_d changes compared to the other trace elements. When MARID K_ds were used, the C_l/C_o ratios and C_l were higher than in lamproite models, and nepheline basanite showed even lower ratios and C_l concentrations.

The melting of MARID compositions (Fig.7.3.12 e-f) resulted in gently declining C_l/C_o curves with similar ratios; the exception is the "AJE262_10%vein" model with high C_l/C_o ratios. Apart from the latter case, models AJE281 have the highest C_l/C_o ratios, followed by AJE262 and AJE288 models. In the AJE281 models, there is a slight decrease in Cl/Co ratios with increasing vein proportion, but in the other two groups, the ratios overlapped, regardless of vein proportion. The highest Ba concentrations were calculated in the AJE288 group, followed by AJE262 and AJE281 models with overlapping values. The lowest concentrations were calculated in AJE288_b, where clinopyroxene melts in the late stages.

In summary of the LILE behaviour in the present models, Sr behaved the most incompatibly in the phlogopite wehrlite and eclogite models and most compatibly in the MARID models.

The highest concentrations were calculated in the early phlogopite wehrlite melts, followed by the early eclogite melts, but the lowest concentrations were also

observed in the latter. Barium behaved the most incompatibly in eclogite models, while the most compatible behaviour was observed in MARID and phlogopite wehrlite models. The highest calculated Ba concentrations were found in the early eclogite melts, followed by MARID melts where the veined compositions overlap with the veined phlogopite wehrlite models.

7.3.3 Comparison of the trace element characteristics in the different mantle compositions

The comparison of the trace element profiles of the small melt fractions (Table 7.3.4) showed that a MARID mantle with the starting composition of phlogopite, amphibole and ilmenite (AJE288) ubiquitously produced the most REE and Zr-enriched melts, while the same trace elements were the lowest in eclogitic melts. Niobium showed the highest levels in the phlogopite wehrlite melts, regardless of metasomatic vein proportions and lowest in the rutile-free MARID (AJE281 a) melts. Among the non-veined mantle compositions, eclogite showed the highest Ba C_l/C_o ratios, while the calculated liquid concentrations were highest in the eclogite model with MARID phlogopite K_ds (E12marid-Kd-Phl) and phlogopite-rich MARID mantle (AJE288). In the case of the veined mantles, the calculated concentrations were always the highest in the phlogopite-rich MARID and lowest in the veined eclogite mantles. Strontium generally showed the highest levels in phlogopite wehrlite melts, and the clinopyroxene-containing MARID (AJE281) melts. However, it showed the lowest C_l/C_o ratios in the veined versions of the latter. Similarly to Ba, the high initial Sr levels in MARID AJE281 (AJE281: 479 ppm, AJE288: 217 ppm, AJE262: 225 ppm) caused higher enrichment in the early melts compared to sources with lower initial concentration but higher Sr incompatibility. The Sr concentration was also affected by the vein proportion changes. The lowest Sr concentrations in the non-veined mantle were shown in the clinopyroxene-containing MARID, where the clinopyroxene took part in the melting (AJE281b). In veined mantles, overlapping low Sr levels were found in clinopyroxene-free MARIDs (AJE262, AJE 288) eclogite and phlogopite wehrlite where lamproite K_d was used for clinopyroxene (PW8), Sr being more compatible in the latter source.

Table 7.3.4. The table shows the mantle types in which the trace elements reached highest and lowest C_l/C_o and Cl levels near increasing metasomatic vein proportions (MARID8: samples AJE288, MARID1: sample AJE281, MARID2: sample AJE262).

	Ce	
	C_l/C_o	C_l
Non-veined	MARID8 >...> E, MARID1	MARID8 >...> MARID1b, E
5% vein	MARID8 >...> E, MARID1	MARID8 >...> E
10% vein	MARID8 >...> E	MARID8 >...> E
20% vein	MARID8 >...> E	MARID8 >...> E
	Gd	
	C_l/C_o	C_l
Non-veined	MARID8 >..> E	MARID8 >...> E
5% vein	MARID8 >...> E	MARID8 >...> E
10% vein	MARID8 >...> E	MARID8 >...> E
20% vein	MARID8 >...> E	MARID8 >...> E
	Y	
	C_l/C_o	C_l
Non-veined	MARID8 >...> E	MARID8 >...> E
5% vein	MARID8 >...> E	MARID8 >...> E
10% vein	MARID8 >...> E	MARID8 >...> E
20% vein	MARID8 >...> E	MARID8 >...> E
	Nb	
	C_l/C_o	C_l
Non-veined	PW1,2 >...> MARID2	PW/E >...>E2
5% vein	PW4, E >...>MARID2	PW>...>MARID2
10% vein	PW5/MARID2>...>MARID8,1	PW >...>MARID2
20% vein	PW>...>MARID2	PW>...>MARID2
	Zr	
	C_l/C_o	C_l
Non-veined	MARID8 >..> E	MARID8 >..> E
5% vein	MARID8 >...> E	MARID8 >...> E
10% vein	MARID8 >...> E	MARID8 >...> E
20% vein	MARID8 >...> E	MARID8 >...> E
	Ba	
	C_l/C_o	C_l
Non-veined	E >...> E12	MARID8 >..>E, MARID1
5% vein	PW4 >...> MARID2,8	MARID8 >...> E
10% vein	MARID2 >...> E	MARID8 >...> E
20% vein	MARID1 >...> E	MARID8 >...> E
	Sr	
	C_l/C_o	C_l
Non-veined	PW1,2 >...> MARID8,2	PW, MARID1a >...> MARID1b,E
5% vein	PW >...> MARID1	PW, MARID1 >...>MARID2
10% vein	PW4, MARID2 >...>MARID1,8	PW, MARID1 >...>MARID2
20% vein	PW7 >...>MARID1	PW7, MARID1 >...>PW8, E

7.4 Discussion

7.4.1 Assessment of the limitation of the trace element models

The trace element modelling results showed the factors that significantly influence the behaviour of multiple trace elements. PW2 (5% H_2O) and PW1(10% H_2O) of the (not-veined) phlogopite wehrlite sources used two separate sets of K_d data for clinopyroxene and olivine, determined at 5% and 10% H_2O content (Adam and Green, 2006) respectively. Model PW2 (5% H_2O) produced higher C_l/C_o ratios than model PW1(10%H2O). The latter occurred because, in the lower H_2O system, the elements (Ce, Gd, Sr, Ti) show stronger partitioning in clinopyroxene and olivine (Table 7.2.2).

As mentioned earlier, the model input parameters included K_d values determined in various magmatic systems according to data availability. The magmatic systems used to determine the K_d inputs into phlogopite wehrlite melting models were nepheline basanite (for olivine, spinel and clinopyroxene), lamproite (for phlogopite), peridotite (ilmenite) and carbonatite (carbonate, apatite) (Table 7.2.6-8). Zirconium C_l/C_o ratios increased, and Ce, Nb, Ti, and Sr C_l/C_o ratios decreased. In contrast, Y and Gd C_l/C_o ratios were unaffected by using clinopyroxene K_d from a lamproite or from a nepheline basanite system (Table 7.4.1).

Similar changes were tested in the case of phlogopite during eclogite melting. Trace element behaviour in the non-veined eclogite was not particularly sensitive to K_d changes between lamproite and basanite systems. In contrast, using lamproite instead of nepheline basanite K_ds in the metasomatised (veined) eclogite source increased the C_l/C_o ratios for Ba and Sr, decreased for Nb, Ti and Zr and did not change for REE.

These changes were even more significant when MARID K_ds were used, as it was tested in the case of the non-veined eclogite source. In the latter case, not only did the initial C_l/C_o ratios change, but the curve shapes of the Ba and Sr models as well (Fig.7.3.12.c-d; Fig.7.3.11.c-d). The latter observation is especially notable as it shows how the input parameters, in this case, K_d, can alter the interpretation of specific trace element behaviour. Similarly to the previous case, the differences were most prominent in the early small melt

fractions, and the more metasomatised sources were more affected by these changes.

The examples above indicate how the chosen K_d input data influenced the results. No appropriate K_d data is available for all magmatic systems or conditions, and the potential effects of K_d substitutions on the results must be assessed.

Table 7.4.1. Differences between trace element C_l/C_o ratios when using nepheline basanite and lamproite K_ds for clinopyroxene (in phlogopite wehrlite models) and phlogopite (in eclogite and MARID models). In the case of eclogite, the MARID K_d results are presented for comparison, but ratios were not calculated between lamproite K_d, basanite K_d and the former.

Cl/Co at F=0.005	Y (ppm)	Nb (ppm)	Ba (ppm)	Sr (ppm)	Ce (ppm)	Gd (ppm)	Ti (ppm)	Zr (ppm)
Changing used K_d for Clinopyroxene in phlogopite wehrlite models (K_ds were determined in basanite and lamproite)								
PW50%basanite Kd	13.5	8.74	2.17	27.03	63.08	16.07	-	47.9
PW50%lamproite Kd	13.5	8.73	2.16	17.34	36	16.07	-	50.87
Ratio	**1**	**1**	**1**	**1.6**	**1.8**	**1**	**-**	**0.9**
PW20%basanite Kd	10.31	20.56	5.03	36.81	59.93	11.29	4.51	41.83
PW20%lamproite Kd	10.31	20.52	5.03	16.58	27.91	11.29	3.9	45.57
Ratio	**1**	**1**	**1**	**2.2**	**2.1**	**1**	**1.2**	**0.9**
Changing used K_d for Phlogopite in eclogite models (K_ds determined in basanite, lamproite and MARID)								
E12basanite Kd	0.59	2.29	3.26	19.47	32.46	2.12	3.12	3.71
E12lamproite Kd	0.59	2.28	9.43	24.28	32.46	2.12	2.97	3.7
Ratio	**1**	**1.01**	**0.33**	**0.8**	**1**	**1**	**1.05**	**1.001**
E13basanite Kd	0.6	38.18	7.28	22.89	29.89	2.04	3.28	4.219
E13lamproite Kd	0.6	36.47	20.5	25.54	29.89	2.04	3.21	4.216
Ratio	**1**	**1.05**	**0.36**	**0.9**	**1**	**1**	**1.02**	**1.001**
E12 MARID Kd	0.594	2.17	42.074	22.79	32.45	2.12		3.71

7.4.2 Relationship between variation in metasomatised mantle source region and primary magma characteristics

The major element composition of the primary veined phlogopite wehrlite melt progresses from early carbonatitic towards compositions with high M and S components and with intermediate compositions in between. Large fraction melts of the phlogopite wehrlite models reach the highest M content and plot closest to phoscorite but never reach the exact composition. The compositional transition

between CO_2 (+P_2O_5)-rich and S component-rich melts was more rapid in the case of the lightly veined mantle (≤5% vein) than in the non-veined mantle.

Changing the apatite proportion in melting models led to some important observations. The presence and melting of apatite pushed the melt fraction compositions towards the C corner by CaO enrichment. Furthermore, a wider range of compositions occurred in the CO_2 (+P_2O_5)-rich melt fractions when apatite was present. In phlogopite wehrlite models, the higher vein ratios moderately increased C_l/C_o ratios for REE and Zr. In the case of Nb, Ba, Sr and Ti, the C_l/C_o ratios decreased with increasing vein proportions, and the curves gradually flattened. The latter elements were more compatible in more metasomatised phlogopite wehrlite, while REE and Zr were less compatible.

The eclogitic mantle melt evolution shows a gradual enrichment in the S component from carbonatitic compositions in the early melts. Melts derived from eclogite also showed the highest general C component content, including the models with higher phlogopite content (E_M15, E_M16). The melt fraction compositions plotted on the pseudo-quaternary diagram (Fig. 7.3.1b) showed an evolution path between carbonatitic and silicate melts. The melting of garnet pushed the composition towards higher M/C component ratios. As Huang et al. (2014) observed in a natural eclogite xenolith sample, stealth metasomatism (an increasing proportion of certain minerals that are present as primary phases as well) is manifested in the increasing proportion of garnet and clinopyroxene in the sample. Phases whose appearance contributed to modal metasomatism (a new phase is introduced due to metasomatism) included phlogopite, ilmenite and rutile. In the present study, models E1 and E12 showed the effects of the two metasomatism types described above, which manifested in higher C_l/C_o ratios for Ce, Zr, Sr and Ti, lower ratios for Y and while Nb, Ba, Gd did not change. The early non-veined eclogite melt fractions showed higher Ba content than the veined eclogite melts. Niobium behaviour was strongly influenced by the presence and melting of ilmenite and rutile due to its strong partitioning into these minerals. The highest Nb levels were reached when the phases completely melted. In the lack of rutile and ilmenite, Nb behaved incompatibly in the non-veined eclogite mantle and relatively compatibly in the strongly veined eclogite mantle (20% metasomatic vein). Niobium levels in eclogite mantle-derived melts varied based on metasomatism level and the presence of minor minerals in the

starting composition. Zirconium was also strongly influenced by rutile presence. Without rutile in the source, Zr behaved only slightly incompatibly in metasomatised and unmetasomatised eclogite mantle melts, not indicating a particularly strong enrichment in the early small melt fractions. Cerium behaved incompatibly, and its enrichment in eclogite melts depended on the Ce levels in the source and increased with increasing metasomatism. With their close to flat C_l/C_o curve shapes in all models, MREE (Gd) and HREE (Y) showed less incompatible behaviour, increasing C_l/C_o ratios with increasing vein proportion. Exceptions included non-veined models with the highest clinopyroxene/garnet proportions (E2, E3), showing the highest Y C_l/C_o ratios and indicating increasing compatibility in more garnet-rich sources.

In the case of the MARID mantle, the earliest C component and CO_2 (+P_2O_5)-rich melt fractions transitioned into high M and S component melts, as the commencement of phlogopite melting immediately shifted the melt fractions to S component-rich compositions by adding SiO_2 to the system. Amphibole and clinopyroxene melting can push the composition towards M component enrichment (very slightly), but generally, the melt evolution progressed towards high S/M component ratios and the compositions clustered around phlogopite. MARID melt evolution significantly differed from eclogite and phlogopite wehrlite in the lack of intermediate melt fraction compositions and shifted towards more M and S component-rich compositions. The only exception was model 7, with high (20%) added apatite-carbonate vein material, showing one melt fraction (F5) with a more intermediate composition (SiO_2: 38.02 wt%; CO_2: 15.38 wt%). Early metasomatised MARID melts showed relatively high C_l/C_o ratios for REE, whereas models with clinopyroxene content (AJE281) had the lowest ratios and flattest curves, showing higher compatibility. Zirconium showed the highest incompatibility in the MARID mantle with the highest phlogopite and lowest amphibole content (AJE288). Niobium (apart from AJE262+10% vein) was also enriched in the MARID melts with very low C_l/C_o ratios. LILE also showed lower incompatibility in MARID melts with low C_l/C_o ratios (apart from AJE262+10% vein) and slightly declining curves. Changes in added vein proportion did not significantly affect the trace element compatibility; most of the curves overlap. When compared to the other models, the MARID model with rutile content (AJE262) showed outstandingly high C_l/C_o ratios (near normal C_l curves) for Ce, LILE, Nb and Zr when 10% metasomatic vein was added to the composition.

The major element modelling reconstructed the evolution of primary melt composition from carbonatite to silicocarbonatite and silicate magmas. The compositions of the resulting magmas included melts with C and S component-rich composition (from eclogite and phlogopite wehrlite source regions), M and S component-rich compositions (from phlogopite wehrlite) and magmas plotting around phlogopite composition (from MARID mantle). The models of primary melting of any mantle composition did not generate a phoscorite magma at any time. This result agrees with recent studies suggesting a fractional crystallisation (Milani et al., 2017a, b) and liquid immiscibility (Giebel et al., 2019) relationship between the banded carbonatite and the phoscorite. Moore (2012) showed that a primary silicocarbonatite parent can produce calciocarbonatite composition via forsteritic olivine crystallisation which increases Ca/(Ca+Mg) ratio of the evolving melt. The phoscorite is an extreme example of the reason why the direct comparison of primary model melt compositions with rocks of the Phalaborwa complex is still studied. The distinct trace element characteristics in Phalaborwa lithologies may provide a window to examine the nature of metasomatised mantle when compared with model melts for variable mantle source lithology and proportion of veining.

7.4.3 Implications of the modelling for the rock relations in the Phalaborwa complex

7.4.3.1 Implications of the major element modelling results to the genetic relationships between the Phalaborwa lithologies

The following sections will draw together key messages from the modelling as they relate to the Phalaborwa complex. The Phalaborwa lithologies and representative samples were described in Chapters 2 and 3.

The major element models showed a partial fit with the clinopyroxenite and banded carbonatite genetic relationship, an adequate result in case of comparing primary to non-primary magmas, and concurs with Wu et al. (2011), who showed the contemporaneous emplacement of the silicate and carbonatite suits in the Phalaborwa complex. Banded carbonatite composition was reached in PW_M10 (F6) and PW_M7 (F4), both lack apatite in their starting compositions (Fig.7.3.1.a). The apatite-bearing melt fractions of PW_M9 (F5) and PW_M4 (F2) have similar S

/CO_2 component ratios but higher C component levels than the banded carbonatite composition. Similarly to phlogopite wehrlite, eclogite melt with no apatite content (E_M9) plots closest to banded carbonatite while starting compositions with apatite produce melts with higher C/M component ratios (Fig.7.3.1.b). Apatite-free compositions are not likely candidates for Phalaborwa parental melts, given that apatite is ubiquitous in the lithologies. This suggests that the apatite-bearing starting compositions used in the modelling would need an additional mafic (MgO or FeO) phase, most likely amphibole which was not part of the natural starting compositions used in this study. MARID mantle produced melts with lower S and M component ratios than the banded carbonatite (Fig. 7.3.1.c). It must be considered that the banded carbonatite is a calcite carbonatite, but the model used dolomite, which pushed the composition towards the M-corner. Using pure $CaCO_3$ would shift the compositions towards the C-corner, closer to calcite and apatite composition, which would be reached in earlier melting stages. However, as mentioned above, additional mafic material in the starting composition would be desirable even with using dolomite instead of calcite. Dolomite melting instead of calcite would affect the early melt compositions, but it may give a better approximation for the late-stage melt composition than using only calcite.

Only lightly veined phlogopite wehrlite mantle composition (PW_M4) produced silicate melts (Fig.7.3.1.a). Veined eclogite mantle melt fraction compositions progressed towards the plotted diopside composition. Although Wu et al. (2011) showed that the rocks were emplaced in a narrow time interval (simultaneously in geological timescale), clinopyroxenites were the first to intrude among the lithologies. Isotopic and mineralogical evidence suggested that the formation of the silicate and carbonatite rocks cannot be explained by crystal fractionation or liquid immiscibility (Eriksson, 1989). However, other chemical and mineralogical data suggest similarities in crystallisation and parental magma characteristics of the silicate and carbonatite rocks (Eriksson, 1989). Magmatic clinopyroxenes in all lithologies are extremely low in Al (<0.5 wt%), Cr and Ti (Eriksson,1989). Carbonatitic and phoscoritic magnetites are Cr-poor (e.g., Eriksson, 1989; Milani et al., 2017a). Furthermore, Al-poor tetraferriphlogopite was found in unaltered phoscoritic olivine-hosted melt inclusions by Aldous (1980), who carried out the only melt inclusion study on the Phalaborwa rocks.

Aldous (1980) described the melt inclusions as rounded or irregular, multisolid inclusions with consistent composition throughout the sample set, where the daughter minerals displayed primary and pseudo-secondary crystal habits. The typical melt inclusions (Fig.7.4.1.a) had an estimated carbonate content of 40-60 vol% (calcite, dolomite, or mixed), with unidentified dark phases (P, Fe, S), low-Ti magnetite (3-5 vol%) and Cu-Ni sulphide (0.2-1 vol%) (Aldous, 1980).

Plotting the normalised, average melt inclusion composition on the quaternary diagrams (Fig.7.3.1.a-c) of this study shows that the melt would be more CO_2 (+P_2O_5) and CaO(+Na_2O+K_2O)-rich, very slightly more SiO_2 (+TiO_2+Al_2O_3)-rich and less MgO (+FeO+MnO+Cr_2O^3)-enriched than the average phoscorite composition. The melt inclusion does not have a phoscorite composition; however, it matches the silicocarbonatite melt fraction composition produced by veined phlogopite wehrlite melting (Fig.7.3.1.a). Model PW_M10, F8-melt fraction has the model composition closest to the average melt inclusion composition, and PW_M9 is the second closest. Both models' starting compositions have high olivine content (70 vol%) with 5-5 vol% phlogopite and clinopyroxene. The difference between the starting compositions is the presence of apatite in PW_M9 (10 vol%), while in PW_M10, there is only dolomite (20 vol%). As discussed in section 5.4.1, apatite pushes the compositions towards C component-enrichment, in this case, further away from the melt inclusion composition. Compositions PW_M4 and PW_M7 produced carbonatite magmas and silicate magmas; however, they could not produce intermediate compositions due to the rapid transition to SiO_2-rich compositions. In these models, the composition represented large melt fractions (F7: 26% melting; F8: 31% melting). The latter occurred as the feature of the modelling, as it used uniform increment sizes, and the large vein proportion of models PW_M10 and PW_M9 and E_M9 melted longer. This also means that if the mantle source is highly metasomatised, larger-scale melting is needed to produce carbonatite-silicocarbonatite-silicate associations, while in a less metasomatised mantle, intermediate compositions are not reached.

In the veined eclogite models model E_M9, the F7 melt fraction has the most similar composition to the melt inclusion due to the generally higher M component levels (Fig.7.3.1.b). This starting composition also has the highest dolomite proportion (16.7 vol%) without apatite, which is present in all other models. The MARID

model did not produce intermediate melt fraction composition as the melts became SiO_2-rich too rapidly (e.g., 9 wt% SiO_2 to 30 wt% SiO_2 between 5 and 10% melting) (Fig.7.3.1 c)

Aldous (1980) suggested that the multisolid inclusions were derived from a high temperature (>800-900^oC) melt, trapped in the growing olivine crystals. The melts represent either the earliest carbonatite melt or an immiscible melt coexisting with the silicate melt which produced the olivine (Aldous,1980). The presence of highly low-Al tetraferriphlogopite in the phoscoritic olivine melt inclusion suggests that the trapped melt was inherently Al-poor. Aldous (1980) reported the mean chemical composition of the daughter tetraferriphlogopite of the melt inclusions. In comparison to the orthomagmatic phlogopite chemistry (Giebel et al., 2019) from the phoscorite and carbonatites, the daughter tetraferriphlogopite displays lower #Mg and significantly lowerAl_2O_3 (wt%) levels (Fig. 7.4.1b).

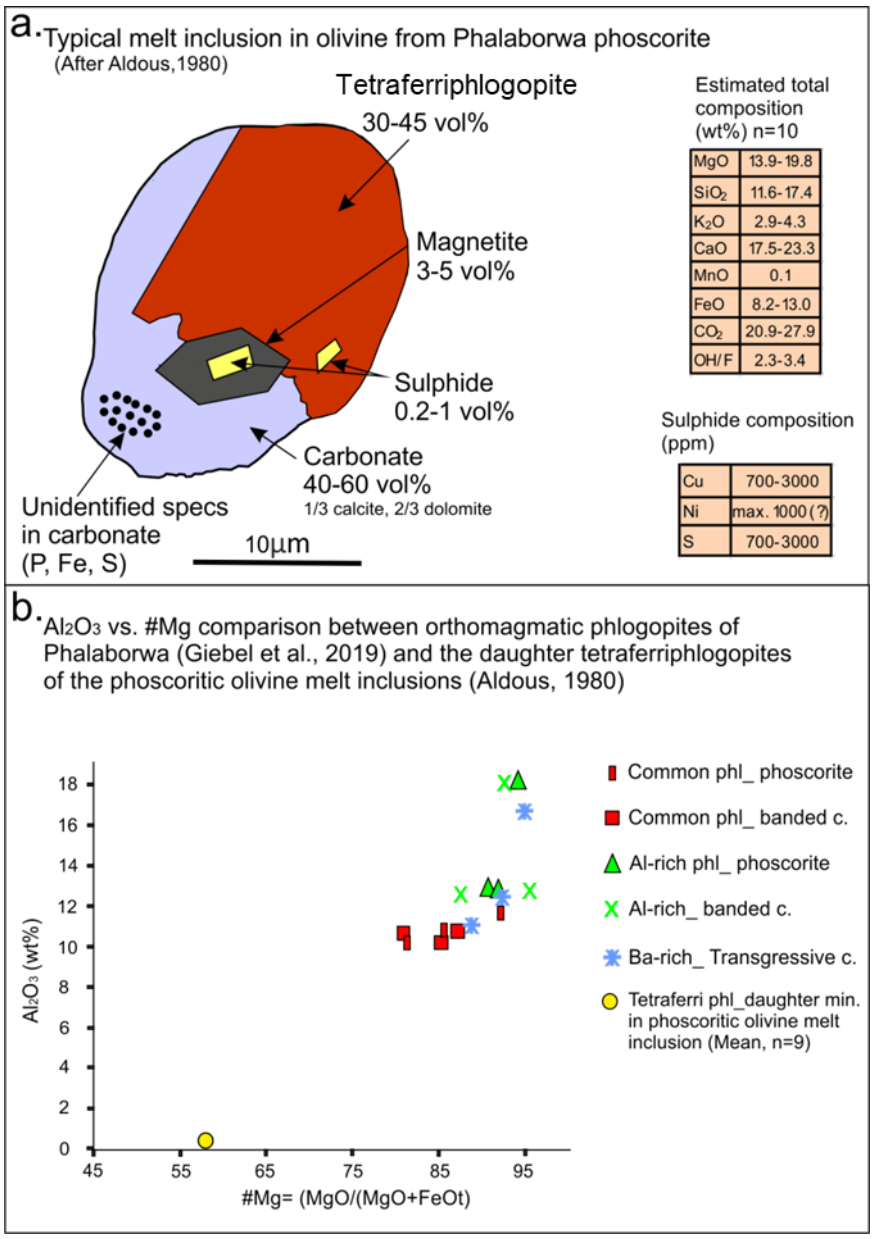

Figure 7.4.1. a: Sketch and estimated modal and chemical composition of the typical melt inclusion in phoscoritic olivine. b; comparison between the daughter tetraferriphlogopite mineral chemistry (Aldous, 1980) and the magmatic phlogopite chemistry (Giebel et al., 2019).

Al-enrichment compared to the common phlogopite was attributed to interaction with the more Al-enriched transgressive carbonatite magma, which might have gained excess Al via crustal contamination (Giebel et al., 2019). The mean #Mg of the daughter tetraferriphlogopite was also significantly lower than that of the magmatic phlogopites (Fig.5.4.1b), indicating decreasing Fe activity in the evolving magmas due to magnetite crystallisation. High-Fe daughter tetraferriphlogopite and daughter magnetite are in textural equilibrium, indicating a melt with high iron content. The estimated average FeO content of the whole melt inclusion was 8.2-13.0 wt% (Aldous, 1980).

7.4.4 Potential Phalaborwa parental magmas based on published and modelled major, minor and trace element characteristics

Earlier studies agreed that the Phalaborwa parental magma was Al, Nb, and Zr-poor with extremely high Sr-levels and K: Na ratios (e.g., Aldous, 1980; Eriksson, 1989; Giebel et al., 2019) and that the mixing of different (at least two) carbonatite magmas shaped the isotopic characteristics of the complex (Eriksson, 1989; Wu et al., 2011). The transgressive carbonatite overall showed higher Al, Fe and Ba levels and a more primitive REE signature than the banded carbonatite and the phoscorite; considering that it was the last to emplace, it was suggested that it is the product of a different magma evolution (Giebel et al., 2019).

Phlogopite melting would result in K-enrichment of the melt fractions. High Na content would require Na-bearing constituents in the mantle source. These could be Na-pyroxenes (e.g., jadeite) and Na-Ca amphiboles. Jadeite is an important constituent in subducted crusts of continental origin and can exist up to 500 km depth contributing to the mantle metasomatism and the enrichment of EMI and EMII mantle domains (e.g., Tutti et al., 2000; Hao et al., 2020). The natural xenolith's composition suggests that the main Na-bearing phase is potassirichterite, primarily occurring in MARID as a major constituent (e.g., Grégoire et al., 2002; Fitzpayne et al., 2018). Potassirichterite melting, in addition to phlogopite melting, has the potential to produce melts with high K: Na ratios.

All of the modelled mantle sources have the potential to reach very high Sr concentrations in the early, small melt fractions.

Compared to the other models, the phlogopite wehrlite melts were characteristically enriched in Sr, Nb and Zr. This partially fits with the "Phalaborwa system" due to the high Sr content; however, the high Nb and Zr levels do not. The two latter elements are controlled by ilmenite proportion in the starting compositions, which was primarily contributed by the added metasomatic glimmerite veins. This would mean that the Phalaborwa source had lower ilmenite in its composition than the used model starting composition had. Furthermore, the phlogopite wehrlite starting compositions can potentially yield K- rich melts while also producing a series of intermediate compositions between $C+CO_2(+P_2O_5)$ component-rich and C+S component-rich melts. This starting composition reached the highest mafic component levels; as mentioned earlier

the parental melt probably had a higher mafic content than the modelled compositions.

Eclogite starting compositions have the potential to yield highly Ba-enriched early melts based on the C_l/C_o curve shapes. They also showed the lowest REE and Zr levels near variable Sr and Nb levels. The high Ba content was a characteristic of the transgressive carbonatite. If this feature is a signifier of a different parental magma, then the eclogite model compositions should be considered. S isotope characteristics of magmatic sulphides of Phalaborwa suggested the influence of a subducted slab on the parental magma composition (Bolhar et al., 2020). The low REE levels of these models fit well with the transgressive carbonatite, as its REE profile is more primitive than the phoscorite or the banded carbonatite (Milani et al., 2017b). The eclogite starting compositions were not close to phlogopite composition depicted on the pseudoquaternary phasediagram. A more Al-rich parental magma was also proposed for the transgressive carbonatite. In the used starting mantle compositions, garnet is the prominent Al source (22.49 wt% Al_2O_3), followed by phlogopite (11.75 wt% Al_2O_3) and clinopyroxene (0.5-6.6 wt% Al_2O_3). Giebel et al. (2019) suggested that contamination from country rock also manifests in the high Al content of evolved transgressive carbonatite micas (usually, Al would decrease due to early mica crystallisation). The eclogite models produced large melt fractions poorest in the M component.

MARID source would yield characteristic Nb-poor and Zr enriched melts. Although the calculated LILE (light ion lithophile elements: Sr, Ba) concentrations are high, they behave compatibly in MARID melts. The low Nb matches the Phalaborwa system well, but the high Zr is not. MARID models also yielded K-rich large melt fractions without many intermediate compositions between CO_2(+P_2O_5) and S component-rich melts.

7.5 Summary and conclusions

The study aimed to understand the Phalaborwa mantle composition and processes that formed the deposit. End-member mantle compositions were used based on natural Kaapvaal xenoliths (phlogopite wehrlite, eclogite, MARID). The xenolith compositions were enriched with added carbonate-apatite-glimmerite xenolith composition (also reported from the Kaapvaal craton by Grégoire et al.,

2002) to model the metasomatised, veined mantle. The results of the major element modelling showed direct evolutionary paths between carbonatite and silicate magmas. The transition between CO_2(+P_2O_5)-rich and S component-rich melt compositions can be abrupt, but higher vein proportion in eclogite and phlogopite wehrlite will result in melt fractions with silicocarbonatite compositions. MARID melt did not produce silicocarbonatite melts as the melts became S component-rich without producing intermediate compositions (e.g., 0 wt%. SiO_2 to >50wt% SiO_2 between 1% and 15% melting).

Few intermediate/silicocarbonatite melt compositions were close to melt inclusion found in phoscoritic olivine (Fig.7.3.1). The melt inclusion had a silicocarbonatite composition and was interpreted as an immiscible pre-phoscorite melt trapped in the olivine (Aldous, 1980). None of the models could reconstruct evolutionary pathways by fractional crystallisation between carbonatite and phoscorite or silicate and phoscorite. This is consistent with both the cumulate nature and the suggested immiscibility origin (e.g., Aldous, 1980; Giebel et al., 2019) of the phoscorite. Calciocarbonatite magma can form from a silicocarbonatite parent by forsterite crystallisation (Moore; 2012). The trace element models showed that the MARID mantle generally produced the most enriched melts, while the eclogite mantle had the least enriched melts. Exceptions included Ba, Sr, and Nb, in which case, eclogite and phlogopite wehrlite produced the more enriched melts. Nb content can be the function of rutile (and, to a lesser extent, ilmenite) content in the melt. High Sr is a characteristic of the Phalaborwa rocks, while high Ba is characteristic of the transgressive carbonatite. Furthermore, only phlogopite wehrlite and eclogite melting produced silicocarbonatite melts. Among the chosen mantle starting compositions, eclogite and phlogopite wehrlite are the most likely candidates when considering a Phalaborwa source region.

Chapter 8: Synthesis and Conclusions

The Phalaborwa complex has been the subject of geological research since the 1930s. Until recently, the remaining questions included the origin and emplacement of the sulphide mineralisation, the genetic relationships between the different lithologies, the nature of the mantle source and the parental magma of the deposit. By addressing the gaps in the knowledge of the deposit, the presented research aimed to separate the crustal and mantle components in the formation processes.

8.1 The nature of the mantle source and magmatic differentiation processes in the Phalaborwa complex; implication to the carbonatite mantle sources, magma differentiation processes, rock associations and modelling techniques

The mantle source was investigated by modelling the major and trace element composition evolution during the melting of selected mantle sources (Chapter 7). It is generally accepted that carbonatites are derived from a metasomatised mantle. In the present modelling exercise, foregoing the primary metasomatism of the primitive mantle, the selected mantle (phlogopite wehrlites, eclogite MARID) starting compositions (Section 7.2.1) modelled phlogopite-rich, carbonated mantle. The selection of the starting composition took place after investigating the Kaapvaal craton in order to provide the closest match to a Phalaborwa mantle as possible. For this reason, natural mantle xenolith compositions from the Kaapvaal craton were used. Both the major element composition and the trace element behaviour were modelled during melting. The major element results were depicted on pseudoquaternary phase diagrams. The results showed that both trace and major element melt compositions could be characteristic of the different mantle sources, and it is possible to bracket a magmatic body with known major-trace element characteristics within possible mantle sources. In the case of certain trace elements (in this case, Zr and Nb), the presence of minor minerals (in this case, rutile) and their melting will determine their enrichment in the melt, regardless of the metasomatic vein content of the mantle (Section 7.4.2). The melt fraction (F) plays a significant role

in determining the melt composition characteristics and the type of silicate rocks forming in association with the carbonatite.

The modelling exercise found that Phalaborwa's most fitting end-member mantle compositions are phlogopite wehrlite and eclogite. The mixing of multiple mantle sources in the case of the Phalaborwa complex was proposed by previous studies (e.g., Eriksson, 1989; Wu et al., 2011). The overall isotope profile gained from these studies suggested mixing between enriched and depleted mantle sources. Furthermore, Bolhar et al. (2020) suggested that the S isotope profile is derived from an astenospheric mantle plume component, metasomatised by fluids and melts from a subducting slab. These studies indicate the complexity of the Phalaborwa source region. Wehrlites are established mantle sources of carbonatites. Previous studies showed that initial metasomatism of mantle peridotites by CO_2-rich melts produces wehrlites, and their formation makes it possible for carbonatite magmas to enter the crust without reacting and equilibrating with primitive mantle compositions (e.g., Harmer and Gittins, 1998; Lee and Wyllie, 2000). Phlogopite is a ubiquitous constituent of the Phalaborwa lithologies, and it can be abundant not only in clinopyroxenites but phoscorites as well, and therefore it was an important constituent in the model mantle compositions of this study. Giebel et al. (2019) also assumed the presence of phlogopite-rich metasomatised regions (metasomes) in the Phalaborwa source region. Additionally, the present study indicated that the S/Se ratios of the Phalaborwa sulphides are closest to eclogitic sulphide values (Section 6.3.3). Although the similarities in the sulphide S/Se ratios are not sufficient evidence to imply eclogite presence in the Phalaborwa SCLM, it may suggest the presence of an enriched mantle component.

Considering the findings of the study, the notion of "metasomatised mantle" as a carbonatite magma source seems unsatisfactory as the type of mantle source of a particular deposit can be approximated. It was shown that regardless of the mantle type, the small melt fractions (e.g., F=0.01) of metasomatised, carbonated mantle (added phlogopite-apatite-calcite veins) would be dolomitic and K-rich (where phlogopite melts) (Fig.7.3.1). This is in line with previous experimental works, e.g., Gudfinnsson and Presnall (2005) showed that at 0.15 wt% CO_2 content in the mantle, carbonate melts form by less than 0.5% melting. Larger melt fraction compositions will differ based on the starting compositions, which

might be reflected in the rock associations of the carbonatite deposit. Eclogite and phlogopite wehrlite large melt fractions (F> 0.25) cluster around diopside composition with CO_2 content" while MARID large melt fractions (F> 0.15) cluster around melt composition close to phlogopite (Fig.7.3.1).

Our models showed that the transitions between S and CO_2 (P_2O_5)-rich melts are rapid (e.g.,~9 wt% S to ~30% S between 5 and 10% melting) in the case of the lightly veined mantle (5%). Higher vein proportions in the starting melting material will produce a broader range of intermediate compositions between silica and carbonate-rich met compositions (Fig.7.3.1). Experimental studies in the CaO – MgO_2 – SiO_2 – CO_2 system concur with these results. Melting experiments at 3GPa showed abrupt change from 10 wt% to 30 wt% SiO_2 between 1475°C and ~1525°C in a simple CMSC system (Moore and Wood, 1998). The effect of additional alkalis showed that the compositional complexity of a Na_2O–CaO–MgO–Al_2O_3– SiO_2–CO_2 system would result in a less rapid transition from carbonate to silicate melt composition as sodium increases silica solubility in the carbonate melts resulting in several intermediate compositions, including silicocarbonatites (Moore, 2012).

The present models indicate that the compositional window where silicocarbonatite melt forms can be narrow, which may consequently mean that these intermediate melts would not crystallise, but only the carbonatite or, in the case of a larger degree of melting, silicate rocks. Furthermore, cumulate formation could prevent the crystallisation of rocks with silicocarbonatite (or close to the defined composition) as the settling silicate crystals would separate from or squeeze out the carbonate liquid before crystallisation. The model of density stratified silicocarbonatite magma chamber and the compositional evolution of such magmas were recently introduced by Moore et al. (2022). The Phalaborwa clinopyroxenite lithologies (introduced in Sections 2.2.2.2-3) and the representative samples (described in Section 3.3.4) do not represent the primary magma compositions but result from multiple stages of magma differentiation.

It was suggested that carbonatites and associated ultramafic pyroxenites are not genetically related (Harmer, 2000). An estimated ~10% of the known carbonatites are associated with ultramafic (UM) (olivine-pyroxene UM rocks+glimmerite+amphibolites, olivine-pyroxene UM rocks+syenite, pyroxenite+syenite) rocks (Woolley and Kjarsgaard, 2008), showing that this is

not an uncommon association. The models presented in Section 7.3.1 showed compositional pathways that link carbonatite and silicate melts (Fig.7.3.1). Clinopyroxenites can form as cumulates from a silicocarbonatite parent. The present study suggests that in the case of a highly veined mantle (20%), a large degree of melting is needed to produce silicate magma (>20%). This large degree of melting would not retain carbonatite metasomatism and metasomes in the SCLM due to the high heat flow.

The models of this study were unable to reconstruct a direct compositional path between the Phalaborwa carbonatites and phoscorite compositions (Fig.7.3.1). Some of the transgressive carbonatite showed higher mafic component ratio due to the significant magnetite content. The Phalaborwa phoscorites are cumulate rocks; their composition does not represent a melt composition; therefore, the result was expected. The liquid immiscibility relationship between the phoscorite and the banded carbonatite was suggested by Giebel et al. (2019), while fractionation by Milani et al. (2017b).

Melt inclusions from phoscoritic olivines were described by Aldous (1980), who suggested that they represent immiscible pre-phoscoritic melt. The estimated mean compositions of these melt inclusions were close to the melt fractions derived from the melting of veined eclogite and phlogopite wehrlite.

The transgressive carbonatite is considered to have a different parental melt or evolutionary path from the banded carbonatite as it showed a more primitive (depleted) REE profile (Milani et al., 2017b) and orthomagmatic phlogopite composition (high Ba and Al) suggesting crustal influence (Giebel et al., 2019). Eriksson (1989) also suggested at least two different carbonatite parental magmas based on isotopic evidence.

8.2 The characteristics of the Loolekop sulphide mineralisation

Petrography and phase relation interpretations (Chapters 4-5) together with results from earlier studies (e.g., Aldous, 1980; Kavecsanszki et al., 2013) and studies that were carried out parallel to this study (Bolhar et al., 2020; Bras et al., 2021) showed that the Phalaborwa lithologies contain multiple generations of sulphides. The present trace element results agree with the earlier conclusions. The research aimed to investigate the nature of the sulphide mineralisation and

its relationship with the magmatic rocks, establish a thermal history of the mineralisation, and identify crustal, magmatic and mantle characteristics in its trace element compositions. The tools of this research were comprehensive petrographic and major and trace element geochemical studies (Chapters 4-6). The results showed that the sulphide mineralisation formed during a broad thermal interval. The chalcopyrite mineralisation has an upper-temperature limit of ~554 ºC, but residual grains of pentlandite, and cobalt pentlandite may suggest higher temperature, as pentlandite has a maximum formation temperature of ~700 ºC. The subsequent trace element studies (Chapter 6) showed that the Ni-Co sulphides of the present study probably represent either the mss or the Hz-iss that exsolved cobalt-pentlandite with Pd relatively enriched compared to the Cu-Fe sulphides. Late-stage sulphide phases formed at low temperatures (<100) (Fig.5.13). The disseminated sulphide grains and patches of the banded carbonatite and phoscorite had magmatic trace element signatures (Chapter 6; Bolhar et al., 2020; Le Bras et al., 2021). The temperature of the Phalaborwa carbonatite was determined as ~600 ºC. Further consideration of higher temperatures for the carbonatite magma would be worthwhile due to the presence of orthomagmatic phlogopite. Phlogopite, in coexistence with carbonate, has a wide stability field (e.g., Eggler, 1989). However, the CO_2/H_2O ratio and F presence can significantly affect it (Gupta, 2015), which should be established in the magmatic system in question.

The early mineralisation was crystallised from the carbonatite and subjected to later-stage overprint by Cu-rich fluids. Textures that demonstrate this process include shredded bornite texture (Fig.4.1.2) and the progressive alteration of other sulphides and non-sulphides in these samples (Fig.4.1.4-5). Bolhar et al. (2020) suggested that the bornite formation predated the chalcopyrite in their samples. The bornite also showed S-isotope composition closer to mantle values. Le Bras et al. (2021) also suggested magmatic bornite presence and later-stage desulphurisation of the sulphides based on trace element signatures. The petrogenetic sequence of the present study was established primarily based on the mineral textures observed and supported by the study of the published phase relations determined by experimental studies. Experimental studies discussed in Section 5.2.1.1 indicated that high-bornite – high-digenite solid solution is present at higher temperatures than stoichiometric chalcopyrite and that bornite solid solution has a very wide stability field which extends well beyond stoichiometric

compositions (e.g., Fleet, 2006). It is possible that at certain areas of the deposit, bornite (and its exsolved phases like digenite and chalcocite) is a more primary phase than chalcopyrite. An excellent example of mineralisation heterogeneity is the troilite-rich transgressive carbonatite sample discussed in this study, which showed a generally depleted nature compared to the other transgressive carbonatite sample types. Another massive chalcopyrite contained abundant Pb-Te inclusions (Fig.4.1.3). Although Pb-Te occurred as microinclusions in the other samples and phases, no other sample showed the size and abundance seen in this sample. Tellurides usually concentrate in late-stage sulphide liquids (Pritchard et al., 2013). Ramdohr (1969) suggested that tellurides belong to the low-temperature, pneumatholic phases of hydrothermal mineralisation. The chalcopyrite samples above may represent different stages of the sulphide mineralisation from chalcopyrite samples that may represent higher temperature phases (with exsolved sphalerite stars, pentlandite flames, troilite stringers). The Loolekop pipe is mined for sulphide from the surface to ~2 km depth. The heterogeneity of the mineralisation is not surprising, and sampling these may lead to different interpretations. However, the interpretations do not need to be mutually exclusive. The Pt-Pd and arsenic distribution feature suggests a low or decreasing fS_2 environment for the Phalaborwa sulphides over time. Secondary sulphides became enriched in metalloids (As, Bi) during later-stage alterations (in agreement with Le Bras et al., 2021). The remobilisation of PGE was also proposed based on PGE enrichment in serpentinised glimmerite and phoscorite sulphides. The fluid compositions that caused serpentinisation in the Phalaborwa lithologies (Giebel et al., 2017) were suitable for PGM transport. Further petrographic evidence is needed to confirm PGE remobilisation.

Most of the sulphides were depleted in PGE and had high S/Se ratios. Based on the general interpretation of the S/Se ratio technique, values higher than the mantle range indicate contamination from crustal S (Queffurus and Barnes, 2015) (Fig.6.3.1-7). Crustal influence in the sulphide formation was also suggested by Le Bras et al. (2021) and the present results (Chapter 6). Further evidence provided by Giebel et al. (2019) based on orthomagmatic phlogopite mineral chemistry, which showed that the assimilation of crustal material by the carbonatite magma may influence the chemical composition of the orthomagmatic constituents of the transgressive carbonatite magma, causing high Al and Ba content in phlogopites (Section 7.4.3.1). The chemical composition

of early orthomagmatic biotites from the silicocarbonatite dykes of the Chagatai complex showed similar high Ba and Al/(Al+Si) ratios. The isotopic composition of these silicocarbonatites indicated mixing between depleted mantle and crustal end-members (Moore et al., 2009).

Consequently, crustal characteristics in the geochemistry of the sulphide mineralisation at Phalaborwa are not unexpected and may not indicate a strictly late-stage hydrothermal origin. The S/Se ratios of the sulphides were most similar to the eclogitic sulphides of the Kaapvaal craton. As previously mentioned, this does not directly suggest an eclogitic component in the Phalaborwa SCLM but rather a possibly more enriched mantle component compared to the average mantle composition. Recently, Bolhar et al. (2020) published the S and Pb isotope compositions of the Phalaborwa sulphides and suggested an origin from an astenospheric mantle plume source modified by fluids released from a subducting slab.

8.3 Implications to carbonatite-LIP connections and proterozoic carbonatite formation

Plume involvement in carbonatite formation and the relationship with Large Igneous Provinces (LIPs) was described in Section 1.3.3. The relationship between the Bushveld complex and Phalaborwa was suggested by Wu et al. (2011) based on similar age and isotopic characteristics. Wu et al. (2011) proposed that the magmatism of the two complexes was triggered by the same plume event, where the Phalaborwa magmas were generated by partial melting of the enriched SCLM by the peripheral fringes of the mantle plume. Plume involvement in the magma generation was also favoured by Giebel et al. (2019) and Bolhar et al. (2020).

Bolhar et al. (2020) showed different S and Pb isotope characteristics of the Phalaborwa and the Bushveld sulphides. The work argued that although the zircon Hf systematics (Wu et al., 2011) showed similarities, the difference between the sulphur and lead isotope characteristics rules out a common mantle source for the Bushveld and Phalaborwa sulphides. It is well established that the Phalaborwa magmas were derived from a metasomatised heterogeneous mantle with multiple components that caused diverse isotopic characteristics within the complex (e.g., Eriksson, 1989; Wu et al., 2011). Furthermore, the S isotopic

profile was shaped by the presence of a subducted slab in the mantle (Bolhar et al., 2020), which could be a local feature of the Phalaborwa SCLM. Mixing of multiple mantle sources and local characteristics of the underlying mantle may influence the isotopic compositions. The sulphur that created the Phalaborwa sulphide mineralisation might be derived from a different mantle region than the Bushveld sulphides, and the melting occurred during the same plume activity. Recently Wang et al. (2018) researched and summarised the different mantle sulphide melt reservoirs and fractionation in the mantle in different tectonic environments.

Woolley and Bailey (2012) showed that approximately two-thirds of the known and dated carbonatites are of Phanerozoic age, which indicates a frequency increase in carbonatite formation through time. However, at least 88% of the carbonatites are located on Precambrian cratons, and repeated episodes of carbonatite magmatism, separated sometimes by hundreds of millions of years, formed the carbonatite provinces (Woolley and Bailey, 2012). Smith et al. (2016) suggested a probable connection between the enrichment of the large REE-hosting carbonatite deposits and their Proterozoic age, which may reflect the formation of highly enriched Proterozoic mantle domains. Mantle overturn models and their implications for SCLM and crust evolution were introduced by Davies (1995) and Griffin et al. (2004), and they were used by Kavecsanszki et al. (2016 conference abstract) together with experimental results from Gudfinnsson and Presnall (2005) to investigate the potential changes in carbonatite magmatism through time. The temperature of the carbonate-mica-peridotite solidus (Gudfinnsson and Presnall, 2005) was significantly lower than the mantle geotherm during episodic intervals of large thermal events in the Proterozoic mantle. Underplating by voluminous magmas would either enrich metasomes in established SCLM or destroy metasomes by large fraction melting in new SCLM with higher heat flow. Between the thermal peaks, the carbonate-mica-peridotite solidus largely coincided with the geotherm at $P > 4$ GPa, implying that the formation of small-fraction, volatile-rich metasomatising melts was common and widespread. Magmas with compositions between carbonatite and kimberlite would generate extensive metasomes in the Proterozoic SCLM that acted as reservoirs for post-Proterozoic magmatic events or transported critical metals such as REE to the crust, where they were further concentrated in carbonatite by

fractionation from silicocarbonatite parental magmas. Figure 8.1 summarises the formation processes discussed in the thesis.

8.4 Further studies

The study of Smith et al. (2016) included only REE, but a similar exercise involving different commodities, such as Cu in the case of Phalaborwa, could provide further knowledge about the enrichment history of the mantle. Secondary processes are crucial in concentrating ore; however, locally enriched mantle source also plays a role in the formation of the deposits, and it is possible to separate mantle, magmatic and crustal influences.

The proximity (5km) of the Guide copper mine, where copper mineralisation is emplaced in a satellite body of the Phalaborwa complex consisting of feldspathoid clinopyroxenite (Hanekom et al., 1965; Aldous 1980, 1986) should be considered. The Cu-sulphides show a replacement relationship with the feldspathoid clinopyroxenite and are formed from residual magmatic hydrothermal fluid (Aldous, 1986). Fluid inclusion studies of the clinopyroxenes revealed that the primary aqueous, highly potassic and copper-bearing inclusions represent melts parental to the clinopyroxenes (Aldous, 1986). Primary melt inclusions in the Phalaborwa phoscorites were also copper-rich (Aldous, 1980) (Figure 8). Copper sulphides are present in the wider Phalaborwa area as constituents of the magmatic system and possibly due to magmatic assimilation of the crustal material. Determination of the isotope characteristics of the Guide feldspathoid clinopyroxenites and copper sulphides would help to refine the origin of the mineralisation further, and the results would most likely show a mixing of magmatic and crustal signatures, or after Bolhar et al. (2020) findings, subducted astenospheric S.

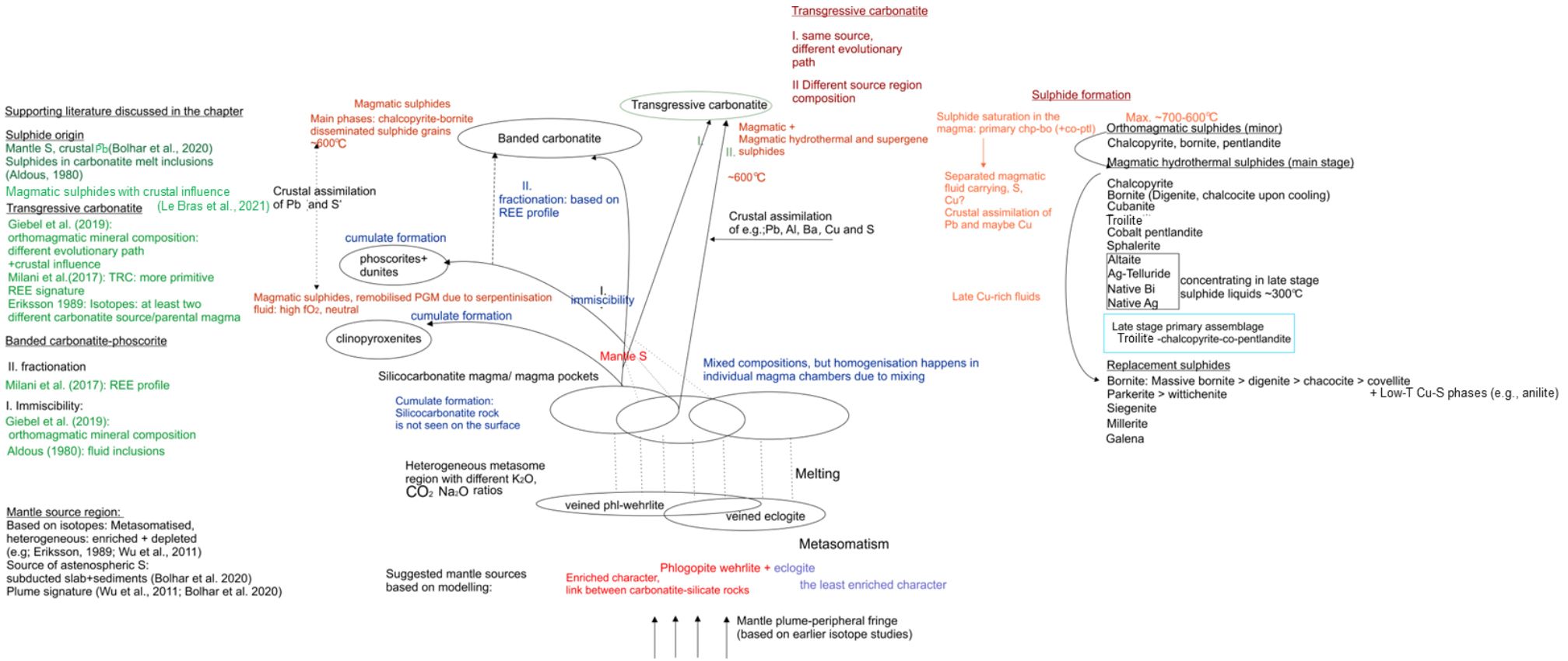

Figure 8.1. Summary image of the formation processes discussed in the thesis. The most referenced literature is listed on the right. The simplified sulphide paragenetic sequence is presented on the left.

8.5 Conclusions

The study addressed gaps in our knowledge regarding the Phalaborwa complex, focusing on the sulphide mineralisation, the nature of the mantle source and the genetic relationship between the different lithologies of the complex.

The textural study combined with EPMA analysis of the sulphide phases showed that the sulphides formed through various processes, including magmatic, hydrothermal and supergene. Disseminated sulphides of the banded carbonatite and phoscorite represent magmatic stages, and textures in the transgressive carbonatite suggest emplacement during magmatic-hydrothermal stages. Primary cobalt pentlandites probably represent either the mss or the Hz-iss that exsolved cobalt pentlandite with Pd relatively enriched compared to the Cu-Fe sulphides. Alongside magmatic bornite, interaction with Cu-rich fluids also caused bornite formation, and subsequent alterations led to valleriite formation and alteration of the non-sulphide phases. The trace element compositions and earlier studies suggested the crustal influence. Sulphides representing lower temperature ranges were formed during the cooling of the deposit and decomposition of the earlier sulphide phases. The in-situ trace element (LA-ICPMS) studies showed that the sulphides are generally depleted in noble metals and metalloids and tend to form microinclusions rather than being in a solid solution. The Pt-Pd and arsenic distribution suggested a low or decreasing $fS2$ environment during the sulphide evolution. PGE presence in serpentinised glimmerite and phoscorite sulphides suggested PGE remobilisation from primary sulphides by serpentinising fluids described by Giebel et al. (2017), but further study is needed for confirmation. The S/Se profile of the Phalaborwa sulphides showed mixed magmatic and non-magmatic signatures, which were similar to eclogitic sulphides from the Kaapvaal craton; this concurs with recent S isotope results by Bolhar et al. (2020). Although the sulphide S/Se ratios were similar to those of the eclogitic BSE, this does not prove an eclogitic mantle source but that the S/Se ratios can separate different mantle types.

The mantle melting models of veined phlogopite wehrlite and eclogite reconstructed direct evolutionary pathways between carbonatite and silicate rocks with intermediate compositions, including silicocarbonatites. The melts of the MARID mantle became S component-rich too rapidly to produce silicocarbonatite compositions. None of the models reconstructed evolutionary

pathways between carbonate and phoscorite, confirming that it does not represent a magma composition. We interpret that cumulate formation and/or immiscibility play a significant role in carbonatite and phoscorite formation (respectively) from a primary silicocarbonatite parent. Due to magma chamber processes, rocks with silicocarbonatite compositions might not be preserved and can be examined on the surface; however, this study suggests that genetic relationships between carbonatites and associated clinopyroxenite cumulates should not be dismissed. The trace element models best matched phlogopite wehrlite and eclogitic sources. The modelling exercise also showed that it is possible to approximate mantle compositions more precisely than the “metasomatised heterogeneous mantle” usually used for carbonatites.

The Phalaborwa lithologies do not represent the primary magma compositions but result from multiple stages of magma differentiation. Cumulate formation and liquid immiscibility from a primary silicocarbonatite parental magma played a major role in the carbonatite and phoscorite formation, respectively. Contamination from crustal material and multiple stages of hydrothermal and serpentinisation processes further altered the primary characteristics (modal, textural, geochemical).

References

Adam, J., and Green, T. (2006) Trace element partitioning between mica- and amphibole- bearing garnet lherzolite and hydrous basanitic melt: 1. Experimental results and the investigation of controls on partitioning behaviour. Contributions to Mineralogy and Petrology, 152(1), 1–17. http://doi.org/10.1007/s00410-006-0085-4

Aldous, R. T. H. (1980) Ore genesis in copper bearing carbonatites; A geochemical, mineralogical and fluid inclusion study: Unpub. Ph.D. thesis, Imperial College, 365 p.

Aldous, R. T. H. (1986) Copper-rich fluid inclusions in pyroxenes from the Guide copper mine, a satellite intrusion of the Palabora igneous complex, South Africa. Economic Geology, 81(1), 143–155. http://doi.org/10.2113/gsecongeo.81.1.143

Amcoff, O. (1988) Experimental replacement of chalcopyrite by bornite: Textural and chemical changes during a solid-state process. Mineralium Deposita, 23(4), 286–292. http://doi.org/10.1007/BF00206409

Amcoff, Ö., Nysten, P. (1990) Mechanism of formation of wittichenite rims around native bismuth in chalcocite and bornite from Långban, Sweden. Geologiska Föreningen i Stockholm Förhandlingar, 112(1), 45–50. http://doi.org/10.1080/11035899009453158

Armstrong, R. A., Compston, W., de Wit, M. J., Williams, I. S. (1990) The stratigraphy of the 3.5-3.2 Ga Barberton Greenstone Belt revisited: a single zircon ion microprobe study. Earth and Planetary Science Letters, 101(1), 90–106. https://doi.org/10.1016/0012-821X(90)90127-J

Anders, E., Grevesse, N. (1989) Abundances of the elements: Meteoritic and solar. Geochimica et Cosmochimica Acta, 53, 197-214.

Baidya, A. S., Sen, A., Pal, D. C. (2018) Textures and compositions of cobalt pentlandite and cobaltian mackinawite from the Madan-Kudan copper deposit, Khetri Copper Belt, Rajasthan, India. Journal of Earth System Science, 127(4), 1–15. http://doi.org/10.1007/s12040-018-0954-z

Bailey, D. K. (1964) Crustal warping - a possible tectonic control of alkaline magmatism. Journal of Geophysical Research 69(6).

Bailey, D.K. (1983) The chemical and thermal evolution of rifts. Tectonophysics, 94, 585-597.

Bailey, D.K. (1993) Carbonatite magmas. Journal of the Geological Society, London 150, 637- 651.

Bailey, D.K. (1992) Episodic alkaline igneous activity across Africa: implications for the causes of continental break-up. Geological Society,

London, Special Publications 6891-98.

Ballhaus, C., Ulmer, P. (1995) Platinum-group elements in the Merensky Reef: II. Experimental solubilities of platinum and palladium in $Fe_{1-x}S$ from 950 to 450°C under controlled fS_2 and fH_2. Geochimica et Cosmochimica Acta, 59(23), 4881–4888. http://doi.org/10.1016/0016-7037(95)00355-X

Ballhaus, C., Tredoux, M., Späth, A. (2001) Phase relations in the Fe-Ni-Cu-PGE-S system at magmatic temperature and application to massive sulphide ores of the Sudbury igneous complex. Journal of Petrology, 42(10), 1911–1926. http://doi.org/10.1093/petrology/42.10.1911

Barnes, S. J., Savard, D., Bédard, L. P., Maier, W. D. (2009) Selenium and sulfur concentrations in the Bushveld Complex of South Africa and implications for formation of the platinum-group element deposits. Mineralium Deposita, 44(6), 647–663. http://doi.org/10.1007/s00126-009-0237-3

Basson, I., Lourens, P., Paetzold, H. D., Thomas, S., Brazier, R., Molabe, P. (2017) Structural analysis and 3D modelling of major mineralizing structures at the Phalaborwa copper deposit. Ore Geology Reviews, 83(December), 30–42. https://doi.org/10.1016/j.oregeorev.2016.12.002

Bell, K. (2001) Carbonatites: Relationship to mantle plume activity. *In*: Ernst, R.E., Buchan K.L. (eds.) (2001) Mantle Plumes: Their Identification Through Time. Geological Society of America, Special Paper 352.

Bell, K., Tilton, G.R. (2001) Nd, Pb and strontium isotopic compositions of East African carbonatites: Evidence for mantle mixing and plume inhomogeneity. Journal of Petrology, 42(10), 1927-1945.

Bell, K., Rukhlov, A.S. (2004) Carbonatites from the Kola Alkaline Province; origin, evolution and source characteristics. 433-468. *In:* Wall, F., Zaitsev, A. N. (eds.) (2004) Phoscorites and Carbonatites from Mantle to Mine: the key example of the Kola alkaline province. The Mineralogical Society Series, 10. ISBN 0 903056 22 4. https://doi.org/10.1180/MSS.10.13

Bell, D. R., Grégoire, M., Grove, T. L., Chatterjee, N., Carlson, R. W., Buseck, P. R. (2005) Silica and volatile-element metasomatism of Archean mantle: A xenolith-scale example from the Kaapvaal Craton. Contributions to Mineralogy and Petrology, 150(3), 251–267. http://doi.org/10.1007/s00410-005-0673-8

Berg, G. (1927) Zonal distribution of deposits in Central Europe. Economic Geology 22(2), 113-132.

Bolhar, R., Whitehouse, M. J., Milani, L., Magalhães, N., Golding, S. D., Bybee, G., Le Bras, L., Bekker, A. (2020) Atmospheric S and lithospheric Pb in sulphides from the 2.06 Ga Phalaborwa phoscorite-carbonatite Complex, South Africa. Earth and Planetary Science Letters, 530. https://doi.org/10.1016/j.epsl.2019.115939

Bouwer, R. F. (1965) The Palabora copper deposits: Rep. geol. Unit Atom.

Energy Bd. S. Afr., G. 78. (unpl). *In:* Hanekom H. J., van Staden C.M.V.H., Smith P.J., Pike D.R. (1965) The Geology of the Phalaborwa Igneous Complex. Geological Survey of South Africa, Memoirs, 54.

Bowles, J. F. W., Howie, R. A., Vaughan, D. J., Zussman, J. (2011) Non-Silicates: Oxides, Hydroxides and Sulphides. Rock-Forming Minerals, Volume 5A, Second Edition. The Geological Society, London. ISBN 978-1-86-239-315-8, ISSN 2041-6296

Brandt, J. W. (1948) Die geologie van 'n gebied in Noordoos Transvaal met spesiale verwysing na die verspreiding en petrografie van die rotssoorte van die Palaborwastollings- kompleks. D.Sc. thesis, Unversity of Stellenbsoch, unpublished.

Brooker, R. A., Kjarsgaard, B. A. (2011) Silicate-carbonate liquid immiscibility and phase relations in the system SiO_2-Na_2O-Al_2O_3-CaO-CO_2 at 1-2 GPa with applications to carbonatite genesis. Journal of Petrology, 52(7-8), 1281–1305. http://doi.org/10.1093/petrology/egq081

Bursztyn, E. N., Ribeiro Olivo, G. (2010) PGE-rich Ni-Cu sulfide mineralization in the Flin Flon greenstone belt, Manitoba, Canada: Implications for hydrothermal remobilization of platinum group elements in basic-ultrabasic sequences. Economic Geology, 105(8), 1469–1490. http://doi.org/10.2113/econgeo.105.8.1469

Cabri, L. J. (1973) New data on phase relations in the CuFe-S system. Economic Geology 68, 443-454.

Carlson, R.W., Boyd, F.R., Shirey, S.B., Janney, P.E., Grove, T.L., Bowring, S.A., Schmitz, M. D., Dann, C., Bell, D.R., Gurney, J.J., Richardson, S.H., Tredoux, M., Menzies, A.H., Pearson, D.G., Hart, R.J., Wilson, A.H., Moser, D.J. (2000) Continental growth, preservation, and modification in Southern Africa. GSA Today, 10(2), 1-7.

Cavender, B. D. (2015) Atypical MVT, Zn-Cu-rich mineralisation in the lower portion of the Bonneterre Dolomite, Viburnum Trend, Southeastern Missouri, U.S.A. MSc Thesis, University of Missouri-Columbia.

Chakhmouradian, A. R., Reguir, E. P., Zaitsev, A. N. (2016) Calcite and dolomite in intrusive carbonatites. I. Textural variations. Mineralogy and Petrology, 110(2–3), 333–360. https://doi.org/10.1007/s00710-015-0390-6

Chen, H. (2013) External sulphur in IOCG mineralization: Implications on definition and classification of the IOCG clan. Ore Geology Reviews, 51, 74–78. http://doi.org/10.1016/j.oregeorev.2012.12.002

Compston, W., Kröner, A. (1988) Multiple zircon growth within early Archaean tonalitic gneiss from the Ancient Gneiss Complex, Swaziland. Earth and Planetary Science Letters, 87(1–2), 13–28. https://doi.org/10.1016/0012-821X(88)90061-1

Cook, N. J., Ciobanu, C. L., Danyushevsky, L. V., Gilbert, S. (2011) Minor and

trace elements in bornite and associated Cu-(Fe)-sulfides: A LA-ICP-MS study bornite mineral chemistry. Geochimica et Cosmochimica Acta, 75(21), 6473–6496. http://doi.org/10.1016/j.gca.2011.08.021

Cordiero, P. F. O., Brod, J. A., Dantas, E. L., Barbosa, E. S. R. (2010) Mineral chemistry, isotope geochemistry and petrogenesis of niobium-rich rocks from the Catalão I carbonatite-phoscorite complex, Central Brazil. Lithos, 118(3-4), 223-237. https://doi.org/10.1016/j.lithos.2010.04.007

Craig, J., Kullerud, G. (1969) Phase relations in the Cu-Fe-Ni-S system and their application to magmatic ore deposits. Economic Geology Monograph, 344–358. https://doi.org/10.5382/Mono.04.25

Dalton, J. A., Wood, B. J. (1993) The compositions of primary carbonate melts and their evolution through wallrock reaction in the mantle. Earth and Planetary Science Letters, 119(4), 511–525. http://doi.org/10.1016/0012-821X(93)90059-I

Dalton, L. A., Presnall, D. C. (1998) The continuum of primary carbonatitic–kimberlitic melt compositions in equilibrium with lherzolite: Data from the system CaO–MgO–Al_2O_3–SiO_2–CO_2 at 6 GPa. Journal of Petrology, 39(11-12), 1953-1964. https://doi.org/10.1093/petroj/39.11-12.1953

Dawson, J. B., Hinton, R. W. (2003) Trace-element content and partitioning in calcite, dolomite and apatite in carbonatite, Phalaborwa, South Africa. Mineralogical Magazine, 67(5), 921–930. https://doi.org/10.1180/0026461036750151

De Ronde, C. E. J., De Wit, M. J. (1994) Tectonic history of the Barberton greenstone belt, South Africa: 490 million years of Archean crustal evolution. Tectonics, 13(4), 983– 1005. https://doi.org/10.1029/94TC00353

De Wit, M. J., De Ronde, C. E. J., Tredoux, M., Roering, C., Hart, R. J., Armstrong, R. A., Hart, R. A. (1992) Formation of an Archaean continent. Nature, 357(6379), 553–562. https://doi.org/10.1038/357553a0

De Wit M.J., Tinker J. (2004) Crustal structures across the Kaapvaal Craton from deep-seismic reflection data, South African Journal of Geology, 107, 185-206. https://doi.org/10.2113/107.1-2.185

Donnelly, C. L., Griffin, W. L., O'Reilly, S. Y., Pearson, N. J., Shee, S. R. (2011). The kimberlites and related rocks of the Kuruman Kimberlite Province, Kaapvaal Craton, South Africa. Contributions to Mineralogy and Petrology, 161(3), 351–371. https://doi.org/10.1007/s00410-010-0536-9

Downes, H., Balaganskaya E., Beard, A., Liferovich, R., Demaiffe, D. (2005): Petrogenetic processes in the ultramafic, alkaline and carbonatitic magmatism in the Kola Alkaline Province: A review. Lithos, 85, 48–75.

Dunworth, E. A., Bell, K. (1998) Melilitolites: A new scheme of classification. The Canadian Mineralogist, 36(3), 895-903.

Dunworth, E. A., Bell, K. (2001) The Turiy Massif, Kola Peninsula, Russia: Isotopic and geochemical evidence for multi-source evolution. Journal of Petrology, 42(2), 377-405. https://doi.org/10.1093/petrology/42.2.377

Dunworth, E. A., Bell, K. (2003) The Turiy Massif, Kola Peninsula, Russia: mineral chemistry of an ultramafic-alkaline-carbonatite intrusion. Mineralogical Magazine, 63(3), 423-451. https://doi.org/10.1180/0026461036730109

Durazzo, A., Taylor, L. A. (1982) Experimental exsolution textures in the system bornite-chalcopyrite: Genetic implications concerning natural ores. Mineralium Deposita, 17(1), 79–97. http://doi.org/10.1007/BF00206377

Eckstrand, O. R., Hulbert, L. J. (1987) Selenium and the source of sulphur in magmatic nickel and platinum deposits: Geological Association Canada-Mineralogical Association Canada, Program with Abstracts, 12, 40.

Eggler, D. H. (1989) Carbonatites, primary melts, and mantle dynamics. *In*: Bell K. (1989) Carbonatites: Genesis and Evolution. Unwin Hyman, London, 221-254.

Eglington, B. M., Armstrong, R. A. (2004) The Kaapvaal Craton and adjacent orogens, southern Africa: A geochronological database and overview of the geological development of the craton. South African Journal of Geology, 107(1–2), 13–32. https://doi.org/10.2113/107.1-2.13

Eriksson, S. C. (1982) Aspects of the Petrochemistry of the Phalaborwa Complex Northeastern Transvaal, South Africa. PhD Thesis, University of the Witwatersrand, Johannesburg, South Africa.

Eriksson S. C. (1989) Phalaborwa: a saga of magmatism, metasomatism and miscibility. *In:* Bell K. (1989) Carbonatites: Genesis and Evolution. Unwin Hyman, London, 221-254.

Ernst, R. E., Bell, K. (2010) Large igneous provinces (LIPs) and carbonatites. Mineralogy and Petrology, 98(1-2), 55–76. http://doi.org/10.1007/s00710-009-0074-1

Fitzpayne, A., Giuliani, A., Hergt, J., Phillips, D., Janney, P. (2018) New geochemical constraints on the origins of MARID and PIC rocks: Implications for mantle metasomatism and mantle-derived potassic magmatism. Lithos, 318-319, 478–493. http://doi.org/10.1016/j.lithos.2018.08.036

Fleet, M. E., Stone, W. E. (1991) Partitioning of platinum-group elements in the Fe-Ni-S system and their fractionation in nature. Geochimica et Cosmochimica Acta, 55(1), 245–253. http://doi.org/10.1016/0016-7037(91)90415-2

Fleet, M. E., Chryssoulis, S. L., Stone, W. E., Weisener, C. G. (1993) Partitioning of platinum-group elements and Au in the Fe-Ni-Cu-S system: experiments on the fractional crystallization of sulfide melt. Contributions to Mineralogy and Petrology, 115(1), 36–44.

http://doi.org/10.1007/BF00712976

Fleet, M. E. (2006) Phase equilibria at high temperatures. Reviews in Mineralogy and Geochemistry, 61(July), 365–419. http://doi.org/10.2138/rmg.2006.61.7

Franklin, B. J., Marshall, B., Graham I. T., McAndrew, J. (1992) Remobilization of PGE in podiform chromitite in the Coolac Serpentinite Belt, Southeastern Australia. Australian Journal of Earth Sciences. Proceedings of the Sixth International Platinum Symposium, 39(3), 365-371. doi/abs/10.1080/08120099208728030

Freestone, I. C., Hamilton. D. L. (1980) The role of liquid immiscibility in the genesis of carbonatites – an experimental study. Contributions to Mineralogy and Petrology 73, 105-117. https://doi.org/10.1007/BF00371385

Giebel, R. J., Gauert, C. D. K., Marks, M. A. W., Costin, G., Markl, G. (2017) Multi-Stage formation of REE minerals in the Palabora Carbonatite Complex, South Africa. American Mineralogist. 102(6), 1218–1233. https://doi.org/10.2138/am-2017-6004

Giebel, R. J., Marks, M. A. W., Gauert, C. D. K., Markl, G. (2019) A model for the formation of carbonatite-phoscorite assemblages based on the compositional variations of mica and apatite from the Palabora Carbonatite Complex, South Africa. Lithos, 324-325, 89–104. http://doi.org/10.1016/j.lithos.2018.10.030

Gill, R. (1997) Modern Analytical Geochemistry. An Introduction to Quantitative Chemical Analysis Techniques for Earth, Environmental and Materials Scientists. Taylor & Francis Group. pp. 171-187. ISBN 978-0-582-0-9944-9 (pbk)

Gittins, J. (1989) The origin and evolution of carbonatite magmas. *In*: Bell K. (1989) Carbonatites: Genesis and Evolution. Unwin Hyman, London, 580-599.

Giuliani, A., Soltys, A., Phillips, D., Kamenetsky, V. S., Maas, R., Goemann, K., Woodhead, J. D., Drysdale, R. N., Griffin, W. L. (2017) The final stages of kimberlite petrogenesis: Petrography, mineral chemistry, melt inclusions and Sr-C-O isotope geochemistry of the Bultfontein kimberlite (Kimberley, South Africa), Chemical Geology, 455, 342-356. https://doi.org/10.1016/j.chemgeo.2016.10.011

Godel, B., Barnes, S. J. (2008) Platinum-group elements in sulfide minerals and the whole rocks of the J-M Reef (Stillwater Complex): Implication for the formation of the reef. Chemical Geology, 248(3-4), 272–294. http://doi.org/10.1016/j.chemgeo.2007.05.006

Goh, S. W., Buckley, A. N., Lamb, R. N., Rosenberg, R. A., Moran, D. (2006) The oxidation states of copper and iron in mineral sulfides, and the oxides formed on initial exposure of chalcopyrite and bornite to air. Geochimica et Cosmochimica Acta, 70(9), 2210-2228.

https://doi.org/10.1016/j.gca.2006.02.007

Goldsmith, J., R., Heard, H., C. (1961) Subsolidus phase relations in the system $CaCO_3$-$MgCO_3$. The Journal of Geology, 69(1).

Goldsmith, J. R., Newton, R. C. (1969) P–T–X relations in the system CaCO,-MgCO, at high temperatures and pressures. American Journal of Science, 267, 160-190.

Graham, S., Lambert, D., Shee, S. (2004) The petrogenesis of carbonatite, melnoite and kimberlite from the Eastern Goldfields Province, Yilgarn Craton. Lithos, 76(1-4), 519–533. http://doi.org/10.1016/j.lithos.2004.03.031

Green, T. H., Adam, J., Siel, S. H. (1992) Trace element partitioning between silicate minerals and carbonatite at 25 kbar and application to mantle metasomatism. Mineralogy and Petrology, 46(3), 179–184. http://doi.org/10.1007/BF01164645

Grégoire, M., Bell, D., Le Roex, A. (2002) Trace element geochemistry of phlogopite-rich mafic mantle xenoliths: their classification and their relationship to phlogopite-bearing peridotites and kimberlites revisited. Contributions to Mineralogy and Petrology, 142(5), 603–625. http://doi.org/10.1007/s00410-001-0315-8

Grguric, B. A., Putnis, A., Harrison, R. J. (1998) An investigation of the phase transitions in bornite (Cu_5FeS_4) using neutron diffraction and differential scanning calorimetry. American Mineralogist, 83(11-12), 1231–1239. http://doi.org/10.2138/am-1998-11-1211

Grguric, B. A. (2002) Hypogene violarite of exsolution origin from Mount Keith, Western Australia: field evidence for a stable pentlandite–violarite tie line. Mineralogical Magazine, 66(2), 313–326. http://doi.org/10.1180/0026461026620032

Griffin, W. L., Graham, S., O'Reilly, S. Y., Pearson, N. J. (2004) Lithosphere evolution beneath the Kaapvaal Craton: Re-Os systematics of sulfides in mantle-derived peridotites. Chemical Geology, 208(1–4), 89–118. https://doi.org/10.1016/j.chemgeo.2004.04.007

Groves, D. I., Vielreicher, N. M. (2001) The Phalabowra (Palabora) carbonatite-hosted magnetite-copper sulfide deposit, South Africa: An end-member of the iron-oxide copper-gold-rare earth element deposit group? Mineralium Deposita, 36(2), 189–194. http://doi.org/10.1007/s001260050298

Gudfinnsson, G.H., Presnall, D.C. (2005) Continuous gradations among primary carbonatitic, kimberlitic, melilititic, basaltic, picritic, and komatiitic melts in equilibrium with garnet lherzolite at 3–8 GPa. Journal of Petrology, 46(8), 1645–1659. https://doi.org/10.1093/petrology/egi029

Gupta, A. K., Green, D. H. (1988) The liquidus surface of the system forsterite

- kalsilite - quartz at 28 kb under dry conditions, in presence of H_2O, and of CO_2. Mineralogy and Petrology, 39(3-4), 163–174. http://doi.org/10.1007/BF01163032

Gupta A.K. (2015) P-T stability of phlogopite, K-richterite and phengite, as a source of potassium in the mantle. *In*: Gupta, A. K. (2015) Origin of Potassium-rich Silica-deficient Igneous Rocks. Springer Geology. Springer, New Delhi 351-379 https://doi.org/10.1007/978-81- 322-2083-1_12

Guzmics, T., Mitchell, R.H., Szabo, Cs., Berkesi, M., Milke, R., Ratter, K. (2012) Liquid immiscibility between silicate, carbonate and sulfide melts in melt inclusions hosted in co-precipitated minerals from Kerimasi volcano (Tanzania): evolution of carbonated nephelinitic magma. Contributions to Mineralogy and Petrology (2012) 164, 101–122. https://doi.org/10.1007/s00410-012-0728-6

Farrow, C. E. G., Watkinson, D. H. (1992) Alteration and the role of fluids in Ni, Cu and platinum-group element deposition, Sudbury Igneous Complex contact, Onaping-Levack area, Ontario. Mineralogy and Petrology 46, 67–83. https://doi.org/10.1007/BF01160703

Hanekom, H. J., Van Staden, C. M. V. H., Smith, P.J., Pike, D. R. (1965) The Geology of the Phalaborwa Igneous Complex. Geological Survey of South Africa, Memoirs, 54.

Hao, M., Zhang, J. S., Pierotti, C. E., Zhou, W. Y., Zhang, D., Dera, P. (2020) The seismically fastest chemical heterogeneity in the Earth's deep upper mantle-implications from the single-crystal thermoelastic properties of jadeite. Earth and Planetary Science Letters, 543, 116345. https://doi.org/10.1016/j.epsl.2020.116345

Harmer, R. E., Gittins, J. (1998) The case for primary, mantle-derived carbonatite magma. Journal of Petrology, 39(11–12), 1895–1903. https://doi.org/10.1093/petroj/39.11-12.1895

Harmer, R. E. (2000) Mineralisation of the Phalaborwa Complex and the carbonatite connection in iron-oxide-Cu-Au-U-REE deposits; *In* Porter, T. M. (2000) Hydrothermal Iron Oxide Copper-Gold & Related Deposits: A Global Perspective, PGC Publishing, Adelaide, 1, 331-340.

Harris, D. C., Nickel, E. H. (1972) Pentlandite compositions and associations in some mineral deposits. The Canadian Mineralogist, 11(4), 861-878.

Hattori, K. H., Arai, S., Clarke, D. B. (2002) Selenium, tellurium, arsenic and antimony contents of primary mantle sulfides. Canadian Mineralogist, 40(2), 637–650. http://doi.org/10.2113/gscanmin.40.2.637

Helmy, H. M., Ballhaus, C., Wohlgemuth-Ueberwasser, C., Fonseca, R. O. C., Laurenz, V. (2010). Partitioning of Se, As, Sb, Te and Bi between monosulfide solid solution and sulfide melt - Application to magmatic sulfide deposits. Geochimica et Cosmochimica Acta, 74(21), 6174–6179.

http://doi.org/10.1016/j.gca.2010.08.009

Helmy, H. M., Ballhaus, C., Fonseca, R. O. C., Nagel, T. J. (2013a) Fractionation of platinum, palladium, nickel, and copper in sulfide-arsenide systems at magmatic temperature. Contributions to Mineralogy and Petrology, 166(6), 1725–1737. http://doi.org/10.1007/s00410-013-0951-9

Helmy, H. M., Ballhaus, C., Fonseca, R. O. C., Wirth, R., Nagel, T., Tredoux, M. (2013b) Noble metal nanoclusters and nanoparticles precede mineral formation in magmatic sulphide melts. Nature Communications, 4, 1–7. http://doi.org/10.1038/ncomms3405

Helmy, H. M., Bragagni, A. (2017) Platinum-group elements fractionation by selective complexing, the Os, Ir, Ru, Rh-arsenide-sulfide systems above 1020 °C. Geochimica et Cosmochimica Acta, 216, 169–183. http://doi.org/10.1016/j.gca.2017.01.040

Holwell, D. A., McDonald, I. (2010) A review of the behaviour of platinum group elements within natural magmatic sulfide ore systems. Platinum Metals Review, 54(1), 26–36. http://doi.org/10.1595/147106709X480913

Holwell, D. A., Keays, R. R., McDonald, I., Williams, M. R. (2015) Extreme enrichment of Se, Te, PGE and Au in Cu sulfide microdroplets: evidence from LA-ICP-MS analysis of sulfides in the Skaergaard Intrusion, East Greenland. Contributions to Mineralogy and Petrology, 170(5-6), 1–26. http://doi.org/10.1007/s00410-015-1203-y

Huang, J. X., Griffin, W. L., Gréau, Y., Pearson, N. J., O'Reilly, S. Y., Cliff, J., Martin, L. (2014) Unmasking xenolithic eclogites: Progressive metasomatism of a key Roberts Victor sample. Chemical Geology, 364, 56–65. http://doi.org/10.1016/j.chemgeo.2013.11.025

Hughes, H.S., Compton-Jones, C., McDonald, I., Kiseeva, E.S., Kamenetsky, V.S., Rollinson, G., Coggon, J.A., Kinnaird, J.A. and Bybee, G.M. (2021) Base metal sulphide geochemistry of southern African mantle eclogites (Roberts Victor): Implications for cratonic mafic magmatism and metallogenesis. Lithos, 382, 105918.

Hutchinson, D., Kinnaird, J. A. (2005) Complex multistage genesis for the Ni-Cu-PGE mineralisation in the southern region of the Platreef, Bushveld Complex, South Africa. Transactions of the Institutions of Mining and Metallurgy, Section B: Applied Earth Science, 114(4), 208-224. http://doi.org/10.1179/037174505X82125

Hutchinson D, Foster J, Prichard H, Gilbert S. (2015) Concentration of particulate platinum-group minerals during magma emplacement; a case study from the Merensky Reef, Bushveld Complex. Journal of Petrology. 56(1), 113-59. https://doi.org/10.1093/petrology/egu073

Ionov, D.A., O'Reilly, S.Y., Genshaft, Y.S., Kopylova, M.G. (1996) Carbonatite-bearing mantle peridotite xenoliths from Spitzbergen: phase relationships,

mineral compositions, and trace-element residence. Contributions to Mineralogy and Petrology (1996) 125: 375- 392. https://doi.org/10.1007/s004100050229

Ivaschenko, V. I. (2021) Rare-Metal (In, Bi, Te, Se, Be) Mineralization of Skarn Ores in the Pitkäranta Mining District, Ladoga Karelia, Russia. Minerals, 11, 124. https://doi.org/10.3390/min11020124

Johnston, A. D., Schwab, B. E. (2004) Constraints on clinopyroxene/melt partitioning of REE, Rb, Sr, Ti, Cr, Zr, and Nb during mantle melting: First insights from direct peridotite melting experiments at 1.0 GPa. Geochimica et Cosmochimica Acta, 68(23), 4949– 4962. https://doi.org/10.1016/j.gca.2004.06.009

Kaneda, H., Takenouchi, S., Shoji, T. (1986) Stability of pentlandite in the Fe-Ni-Co-S system. Mineralium Deposita, 21(3), 169–180. http://doi.org/10.1007/BF00199797

Kavecsanszki, D., Moore, K.R., Wall, F., Rollinson, G.K., Lusty, P.A.J. (2013) Magma mingling between sulphide-rich and carbonatite magmas to form a multi-commodity metal deposit: reconstruction using QEMSCAN® analysis. Proceedings of the 12th Biennial SGA Meeting, 12–15 Aug. 2013, Uppsala, Sweden, Vol.3, pp. 1024-1027.

Kavecsanszki, D., Moore, K. R., Wall, F. (2016) Large thermal events in the proterozoic mantle and carbonatite formation. Goldschmidt Conference Abstract, 1451, Yokohama, Japan 2016.

Kelemen, P. B., Shimizu, N., Dunn, T. (1993) Relative depletion of niobium in some arc magmas and the continental crust: partitioning of K, Nb, La and Ce during melt/rock reaction in the upper mantle. Earth and Planetary Science Letters, 120(3–4), 111–134. https://doi.org/10.1016/0012-821X(93)90234-Z

Keshav, S., Gudfinnsson, G. H. (2013) Silicate liquid-carbonatite liquid transition along the melting curve of model, vapor-saturated peridotite in the system CaO-MgO-Al_2O_3-SiO_2-CO_2 from 1.1 to 2 GPa. Journal of Geophysical Research: Solid Earth, 118(7), 3341–3353. http://doi.org/10.1002/jgrb.50249

Kharlamov, Y. S., Kudryavtseva, G. P., Garanin, V. K., Korennova, N. G., Moskalyuk, A. A., Sandomirskaya, S. M., Shugurova, N. A. (1981) Origin of carbonatites of the Kovdor deposit. International Geology Reviews 23, 865–880.

Kitakaze, A., Sugaki, A. (2004) The phase relations between $Fe_{4.5}Ni_{4.5}S_8$ and Co_9S_8 in the system Fe-Ni-Co-S at temperatures from 400°C to 1100°C. Canadian Mineralogist, 42(1), 17–42. http://doi.org/10.2113/gscanmin.42.1.17

Kitakaze, A., Machida, T., Komatsu, R. (2016) Phase relations in the Fe-Ni-S system from 875 to 650 °C. Canadian Mineralogist, 54(5), 1175–1186. http://doi.org/10.3749/canmin.1500087

Kjarsgaard, B. A., Hamilton, D. L, (1989) The genesis of carbonatites by immiscibility. *In*: Bell, K. (ed.) (1989) Carbonatites: Genesis and Evolution, Unwin Hyman, London, pp. 388-404.

Kjarsgaard, B. A. (1998) Phase relations of a carbonated high-CaO nephelinite at 0.2 and 0.5 GPa. Journal of Petrology, Vol. 39 (11-12), 2061-2075. https://doi.org/10.1093/petroj/39.11-12.2061

Klemme, S., Blundy, J. D., Wood, B. J. (2002) Experimental constraints on major and trace element partitioning during partial melting of eclogite. Geochimica et Cosmochimica Acta, 66(17), 3109–3123. http://doi.org/10.1016/S0016-7037(02)00859-

Klemme, S., Dalpé, C. (2003) Trace-element partitioning between apatite and carbonatite melt. American Mineralogist, 88(4), 639–646. http://doi.org/10.2138/am-2003-0417

Kogarko, L. N., Handerson, C. M. B., Phacheco, H. (1995) Primary Ca-rich carbonatite magma and carbonate-silicate-sulphide liquid immiscibility in the upper mantle. Contributions to Mineralogy and Petrology, 121, 267-274. https://doi.org/10.1007/BF02688242

Kogarko, L. N., Lahaye, Y., Brey, G. P. (2010) Plume-related mantle source of super-large rare metal deposits from the Lovozero and Khibina massifs on the Kola Peninsula, Eastern part of Baltic Shield: Sr, Nd and Hf isotope systematics. Mineralogy and Petrology, 98(1-2), 197–208. http://doi.org/10.1007/s00710-009-0066-1

Korobienkov, A.N., Mitrofanov, F.P., Gehör, S., Laajoki, K., Pavlov, V.P., Mamontov, V.P. (1998) Geology and copper sulphide mineralization of the Smalagorskii Ring Igneous Complex, Kola Peninsula, NW Russia. Journal of Petrology 39 (11-12), 2033-2041. https://doi.org/10.1093/petroj/39.11-12.2033

Koster van Groos, A. F., Wyllie, P. J. (1963) Experimental data bearing on the role of liquid immiscibility in the genesis of carbonatites. Nature, 199, 801-802. https://doi.org/10.1038/199801a0

Kovalev, S. G., Puchkov, V. N., Kovalev, S. S. (2014) First findings of siegenite ($CoNi_2S_4$) in picritic and picrodoleritic complexes of the Southern Urals. Doklady Earth Sciences, 457(1), 796–802. https://doi.org/10.1134/S1028334X1407023X

Kramm, U., Kogarko, L. N. (1994) Nd and Sr isotope signatures of the Khibina and Lovozero agpaitic centres, Kola Alkaline province, Russia. Lithos, 32(3-4), 225–242. http://doi.org/10.1016/0024-4937(94)90041-8

Krasnova, N. I., Petrov, T. G., Balaganskaya, E. G. Moutte, J., Garcia, D., Hermie, B. (2002) Systematisation of the rocks' composition using the RHA language (exemplified on the deep-seated alkaline-ultrabasic and phoscorite-carbonatite complexes). 276-293 *In:* Vladykin, N. V. (2002)

Deep-Seated Magmatism, Magmatic Sources and the Problem of Plumes.

Krasnova, N. I., Petrov, T. G., Balaganskaya, E. G., Garcia, D., Moutte, J., Zaitsev, A. N., Wall, F. (2004) Introduction to phoscorites: occurrence, composition, nomenclature and petrogenesis. *In:* Wall, F., Zaitsev, A. N. (eds.) (2004) Phoscorites and Carbonatites from Mantle to Mine: the key example of the Kola alkaline province. The Mineralogical Society Series, 10. ISBN 0 903056 22 4. https://doi.org/10.1180/MSS.10.02

Kröner, A., Hegner, E., Wendt, J. I., Byerly, G. R. (1996) The oldest part of the Barberton granitoid-greenstone terrain, South Africa: Evidence for crust formation between 3.5 and 3.7 Ga. Precambrian Research, 78(1-3), 105–124. https://doi.org/10.1016/0301-9268(95)00072-0

Le Bas, M. J., (1989) Diversification of carbonatites. *In*: Bell, K. (ed.) (1989) Carbonatites: Genesis and Evolution, Unwin Hyman, London, pp. 428-447.

Le Bas M. J. (1981) Carbonatite magmas. Mineralogical Magazine, 44(334), 133-140. https://doi.org/10.1180/minmag.1981.044.334.02

Le Bras, L. Y., Bolhar, R., Bybee, G. M. (2021) Platinum-group and trace elements in Cu-sulfides from the Loolekop pipe, Phalaborwa: implications for ore-forming processes. Miner Deposita, 56, 161–177. https://doi.org/10.1007/s00126-020-01005-4

Lee, W.J., Wyllie, P. J. (1998) Petrogenesis of carbonatite magmas from mantle to crust, constrained by the system CaO-(MgO+FeO*)-(Na_2O+K_2O)-(SiO_2+Al_2O_3+TiO_2)-CO_2. Journal of Petrology 39(3), 495-517. https://doi.org/10.1093/petroj/39.3.495

Lee, W. J., Wyllie, P. J. (2000) The system CaO-MgO-SiO_2-CO_2 at 1 GPa, metasomatic wehrlites, and primary carbonatite magmas. Contributions to Mineralogy and Petrology, 138(3), 214–228. http://doi.org/10.1007/s004100050558

Lee, M. J., Garcia, D., Moutte, J., Williams, C. T., Wall, F. (2004) Carbonatites and phoscorites from the Sokli Complex, Finland. 129-158. *In* Wall, F., Zaitsev, A. N. eds. (2004) Phoscorites and carbonatites from mantle to mine: the key example of the Kola alkaline province. The Mineralogical Society Series, 10. ISBN 0 903056 22 4 https://doi.org/10.1180/MSS.10.05

Le Maitre, R. W. (1982) Numerical Petrology: Statistical interpretation of geochemical data. Elsevier, ISBN: 0-444-422098-3

Le Maitre, R. W. (2002) Igneous Rocks: A Classification and Glossary of Terms. Cambridge University Press. ISBN: 0 521 66215 X

Letts, S., Torsvik, T. H., Webb, S. J., Ashwal, L. D. (2011) New Paleoproterozoic palaeomagnetic data from the Kaapvaal Craton, South Africa. Geological Society, London, Special Publications 357, 9-26. https://doi.org/10.1144/SP357.2

Lombaard, A. F., Ward-Able, N. M, Bruce, R. W. (1964) The exploration and main geological features of the copper deposit in carbonatite at Loolekop, Palabora Complex. *In:* Hanekom, H. J., Van Staden C. M.V. H., Smith, P. J., Pike, D. R. (1965) The Geology of the Phalaborwa Igneous Complex. Geological Survey of South Africa, Memoirs, 54.

Lorand, J. P., Alard, O., Luguet, A., Keays, R. R. (2003) Sulfur and selenium systematics of the subcontinental lithospheric mantle: Inferences from the Massif Central xenolith suite (France). Geochimica et Cosmochimica Acta, 67(21), 4137–4151. http://doi.org/10.1016/S0016-7037(03)00305-3

Lorand, J. P., Alard, O. (2010) Determination of selenium and tellurium concentrations in Pyrenean peridotites (Ariege, France): New insight into S/Se/Te systematics of the upper in mantle samples. Chemical Geology, 278(1-2), 120–130. http://doi.org/10.1016/j.chemgeo.2010.09.007

Lowe, D.R. (1999) Geologic evolution of the Barberton Greenstone Belt and vicinity. *In*: Lowe, D.R., Byerly, G.R. (1999) Geological evolution of the Barberton Greenstone Belt, South Africa, Geological Society of America Special Paper, 329, 287-312. https://doi.org/10.1130/0-8137-2329-9.287

Lusk, J., Calder, B. O. E. (2004) The composition of sphalerite and associated sulfides in reactions of the Cu-Fe-Zn-S, Fe-Zn-S and Cu-Fe-S systems at 1 bar and temperatures between 250 and 535 °C. Chemical Geology, 203(3-4), 319–345. http://doi.org/10.1016/j.chemgeo.2003.10.011

Mackie, R. A., Scoates, J. S., Weis, D. (2009) Age and Nd–Hf isotopic constraints on the origin of marginal rocks from the Muskox layered intrusion (Nunavut, Canada) and implications for the evolution of the 1.27 Ga Mackenzie large igneous province, Precambrian Research,172(1-2), 46-66. https://doi.org/10.1016/j.precamres.2009.03.007.

Marshall, D., Watkinson, D., Farrow, C., Molnár, F., Fouillac, A. M. (1999) Multiple fluid generations in the Sudbury igneous complex: fluid inclusion, Ar, O, H, Rb and Sr evidence, Chemical Geology, 154(1-4), 1-19. https://doi.org/10.1016/S0009-2541(98)00122-3.

McCourt, S., Armstrong, R. A., Jelsma, H., Mapeo, R. B. M. (2013) New U–Pb SHRIMP ages from the Lubango region, SW Angola: insights into the Palaeoproterozoic evolution of the Angolan Shield, southern Congo Craton, African Journal of the Geological Society, 170(2), 353-363. https://doi.org/10.1144/jgs2012-059

McDonald, I. (2005) Development of sulphide standards for the in-situ analysis of platinum- group elements by laser ablation inductively coupled plasma-mass spectrometry (LA- ICP-MS). 10th International Platinum Symposium, Extended Abstracts, 468-471.

McDonough, W. F., Sun, S. S. (1995) The composition of the Earth. Chemical Geology, 120(3-4), 223–253. http://doi.org/10.1016/0009-2541(94)00140-4

McFall, K., McDonald, I., Tanner, D., Harmer, R. E. J. (2019). The mineralogy and mineral associations of platinum-group elements and precious metals in the Aurora Cu- Ni-Au-PGE deposit, Northern Limb, Bushveld Complex. Ore Geology Reviews, 106, 403–422. https://doi.org/10.1016/j.oregeorev.2019.02.008

Merkle, R. K., von Gruenewaldt, G. (1986) Compositional variation of Co-rich pentlandite; relation to the evolution of the upper zone of the western Bushveld Complex, South Africa. The Canadian Mineralogist. 24(3), 529-46.

Mikhailova, J.A., Kalashnikov, A.O., Sokharev, V.A., Pakhomovsky, Y.A., Konopleva, N.G., Yakovenchuk, V.N., Bazai, A.V., Goryainov, P.M. and Ivanyuk, G.Y. (2016) 3D mineralogical mapping of the Kovdor phoscorite–carbonatite complex (Russia). Mineralium Deposita, 51,131-149.

Mikhailova, J.A., Ivanyuk, G.Y., Kalashnikov, A.O., Pakhomovsky, Y.A., Bazai, A.V., Panikorovskii, T.L., Yakovenchuk, V.N., Konopleva, N.G. and Goryainov, P.M. (2018) Three-D Mineralogical Mapping of the Kovdor Phoscorite–Carbonatite Complex, NW Russia: I. Forsterite. Minerals, 8(6), 260.

Milani, L., Bolhar, R., Cawthorn, R. G., Frei, D. (2017a) In situ LA–ICP-MS and EPMA trace element characterization of Fe–Ti oxides from the phoscorite–carbonatite association at Phalaborwa, South Africa. Mineralium Deposita, 52(5), 747–768. https://doi.org/10.1007/s00126-016-0696-2

Milani, L., Bolhar, R., Frei, D., Harlov, D.E., Samuel, V.O. (2017b) Light rare earth element systematic as a tool for investigating the petrogenesis of phoscorite-carbonatite associations, as exemplified by the Phalaborwa Complex, South Africa. Mineral. Deposita, 52, 1105-1125. https://doi.org/10.1007/s00126-016-0708-2

Misra K. C; Fleet, M. E. (1974) Chemical composition and stability of violarite. Economic Geology, 69(3), 391-403. https://doi.org/10.2113/gsecongeo.69.3.391

Mitchell, R. H., Krouse, H. R. (1975) Sulphur isotope geochemistry of carbonatites. Geochimia et Cosmochimica Acta, 39(11), 1505-1513. https://doi.org/10.1016/0016-7037(75)90152-0

Mitchell, R. H. (2005) Carbonatites and carbonatites and carbonatites. The Canadian Mineralogist, 43(6), 2049-2068. https://doi.org/10.2113/gscanmin.43.6.2049

Moore, K. R., Wood, B. J. (1998) The transition from carbonate to silicate melts in the CaO-MgO-SiO_2-CO_2 system. Journal of Petrology, 39(11–12), 1943–1951. https://doi.org/10.1093/petroj/39.11-12.1943

Moore, K.R., Wall, F., Divaev, F.K., Savatenkov, V.M. (2009) Mingling of

carbonate and silicate magmas under turbulent flow conditions: Evidence from rock textures and mineral chemistry in sub-volcanic carbonatite dykes, Chagatai, Uzbekistan. Lithos, 110(1-4), 65-82. https://doi.org/10.1016/j.lithos.2008.11.013

Moore, K. R. (2012) Experimental study in the Na_2O–CaO–MgO–Al_2O_3 –SiO_2 –CO_2 system at 3 GPa: the effect of sodium on mantle melting to carbonate-rich liquids and implications for the petrogenesis of silicocarbonatites. Mineralogical Magazine, 76(2), 285–309. https://doi.org/10.1180/minmag.2012.076.2.04

Moore, K.R., Brady, A.E. and Costanzo, A., (2022) Crystal-liquid segregation in silicocarbonatite magma leads to the formation of calcite carbonatite. Journal of Petrology, 63(7), 1-14. https://doi.org/10.1093/petrology/egac056

Mountain, B. W., Wood, S. A. (1988) Chemical controls on the solubility, transport, and deposition of platinum and palladium in hydrothermal solutions: a thermodynamic approach. Economic Geology, 83(3), 492–510. http://doi.org/10.2113/gsecongeo.83.3.492

Naldrett, A. J. (1989) Magmatic sulfide deposits. Oxford Monographs on Geology and Geophysics, 14. New York: Calderon Press, 186 pp. *In* Fleet, M. E., Chryssoulis, S. L., Stone, W. E., Weisener, C. G. (1993) Partitioning of platinum-group elements and Au in the Fe-Ni-Cu-S system: experiments on the fractional crystallization of sulfide melt. Contributions to Mineralogy and Petrology, 115(1), 36–44. http://doi.org/10.1007/BF00712976

Nielsen, T. F. D. (1980) The petrology of a melilitolite, melteigite, carbonatite and syenite ring dike system, in the Gardiner complex, East Greenland. Lithos, 13(2), 181–197. http://doi.org/10.1016/0024-4937(80)90019-5

Oen, I. S., Kieft, C. (1976) Silver-bearing wittichenite–chalcopyrite–bornite intergrowths and associated minerals in the Mangualade pegmatite, Portugal. Canadian Mineralogist, 14, 185–193.

O'Hara, M. J., Mathews, R. E. (1981) Geochemical evolution in advancing, periodically replenished, periodically tapped, continuously fractionated magma chamber. Journal of the Geological Society, 138(3), 237-277. https://doi.org/10.1144/gsjgs.138.3.0237

O'Neill, H.S.C. (1991) The origin of the Moon and the early history of the Earth—A chemical model. Part 2: The Earth. Geochimica et Cosmochimica Acta, 55(4), 1159-1172.

Palme, H., O'Neill, H. S. C. (2003) Cosmochemical Estimates of Mantle Composition. 1-38. *In:* Carlson, R. W. (ed.) (2004) The Mantle and Core. Vol. 2 Treatise on Geochemistry. Elsevier-Pergamon, Oxford.

Paton, C., Hergt, J.M., Woodhead, J.D., Phillips, D., Shee, S.R. (2009) Identifying the asthenospheric component of kimberlite magmas from the Dharwar Craton, India. Lithos, 112, 296-310.

https://doi.org/10.1016/j.lithos.2009.03.019

Peregoedova, A., Ohnenstetter, M. (2002) Collectors of Pt, Pd and Rh in a S-poor Fe-Ni-Cu sulfide system at 760°C: Experimental data and application to ore deposits. Canadian Mineralogist, 40(2), 527–561. http://doi.org/10.2113/gscanmin.40.2.527

Petruk, W., Harris, D.C., Stewart, J.M. (1969) Langisite, a new mineral, and the rare minerals cobalt pentlandite, siegenite, parkerite and bravoite from the Langis Mine, Cobalt-Gowganda area, Ontario. The Canadian Mineralogist, 9(5), 597-616.

Pilet, S., Baker, M.B., Müntener, O., Stolper, E.M. (2011) Monte Carlo simulations of metasomatic enrichment in the lithosphere and implications for the source of alkaline basalts. Journal of Petrology, 52(7-8), 1415-1442. https://doi.org/10.1093/petrology/egr007

Prichard, H. M., Knight, R. D., Fisher, P. C., McDonald, I., Zhou, M. F., Wang, C. Y. (2013) Distribution of platinum-group elements in magmatic and altered ores in the Jinchuan intrusion, China: An example of selenium remobilization by postmagmatic fluids. Mineralium Deposita, 48(6), 767–786. http://doi.org/10.1007/s00126-013-0454-7

Queffurus, M., Barnes, S. J. (2015) A review of sulfur to selenium ratios in magmatic nickel-copper and platinum-group element deposits. Ore Geology Reviews, 69, 301–324. http://doi.org/10.1016/j.oregeorev.2015.02.019

Ramdohr, P. (1969) The Ore Minerals and Their Intergrowths. Pergamon, Oxford.

Ramdohr, P. (1981) The Ore Minerals and Their Intergrowths. Pergamon, Oxford (2nd edition)

Rass, I.T., Petrenko, D.B., Koval'chuk, E.V. and Yakushev, A.I. (2020) Phoscorites and carbonatites: Relations, possible petrogenetic processes, and parental magma, with reference to the Kovdor Massif, Kola Peninsula. Geochemistry International, 58, 753-778. https://doi.org/10.1134/S0016702920070095

Reed, S. J. B. (2005) Electron microprobe analysis and scanning electron microscopy in geology. Cambridge University Press, ISBN 10 0 521 84875 X

Richardson, S. H., Shirey, S. B., Harris, J. W. (2004) Episodic diamond genesis at Jwaneng, Botswana, and implications for Kaapvaal craton evolution. Lithos, 77(1-4), 143–154. https://doi.org/10.1016/j.lithos.2004.04.027

Riley, J. F. (1977) The pentlandite group $(Fe,Ni,Co)_9S_8$: New data and an appraisal of structure-composition relationships. Mineralogical Magazine, 41(319), 345–349. http://doi.org/10.1180/minmag.1977.041.319.05

Rollinson, H., Pease, V. (2021) Using Geochemical Data to Understand Geological Processes. Cambridge, UK; New York, NY: Cambridge University Press. ISBN 9781108777834 (epub)

Robertson, J. C., Barnes, S. J., Le Vaillant, M. (2015) Dynamics of magmatic sulphide droplets during transport in silicate melts and implications for magmatic sulphide ore formation. Journal of Petrology, 56(12), 2445–2472. https://doi.org/10.1093/petrology/egv078

Roger, T. (2009) Ore textures. Recognition and Interpretation. Springer, ISBN 978-3-642- 01782-7, DOI 10.1007/978-3-642-01783-4

Rudashevsky, N. S., Kretser, Yu. L, Rudashevsky, V. N., Sukharzhevskaya, E. S. (2004) A review and comparison of PGE, noble-metal and sulphide mineralization in phoscorites and carbonatites from Kovdor and Phalaborwa. 433-468. *In* Wall, F., Zatisev, A.N. (eds.) (2004) Phoscorites and Carbonatites from mantle to mine: the Key Example of the Kola Alkaline Province. The Mineralogical Society Series 10. https://doi.org/10.1180/MSS.10.11

Russel, H. D., Hiemstra, S. A., Groeneveld, D. (1954) The mineralogy and Petrology of the carbonatite at Loolekop, Eastern Transvaal. Trans. Geol. Soc. S. Afr., 57, pp. 197- 208. *In* Hanekom, H. J., Van Staden, C. M. V. H., Smith, P. J., Pike, D. R. (1965) The Geology of the Phalaborwa Igneous Complex. Geological Survey of South Africa, Memoirs, 54.

Schmidt, K. H., Bottazzi, P., Vannucci, R., Mengel, K. (1999) Trace element partitioning between phlogopite, clinopyroxene and leucite lamproite melt. Earth and Planetary Science Letters, 168(3-4), 287–299. http://doi.org/10.1016/S0012-821X(99)00056-4

Sciortino, M., Mungall, J. E., Muinonen, J. (2015) Generation of High-Ni sulfide and alloy phases during serpentinization of dunite in the Dumont sill, Quebec. Economic Geology, 110(3), 733–761. https://doi.org/10.2113/econgeo.110.3.733

Simonetti, A., Bell, K., Viladkar, S. G. (1995) Isotopic data from the Amba Dongar Carbonatite Complex, west-central India: Evidence for an enriched mantle source. Chemical Geology, 122(1-4), 185–198. http://doi.org/10.1016/0009-2541(95)00004-6

Smith, J. W., Holwell, D. A., McDonald, I., Boyce, A. J. (2016) The application of S isotopes and S/Se ratios in determining ore-forming processes of magmatic Ni-Cu-PGE sulfide deposits: A cautionary case study from the northern Bushveld Complex. Ore Geology Reviews, 73, Part 1, 148–174. http://doi.org/10.1016/j.oregeorev.2015.10.022

Smith, M. P., Moore, K., Kavecsánszki, D., Finch, A. A., Kynicky, J., Wall, F. (2016) From mantle to critical zone: A review of large and giant sized deposits of the rare earth elements. Geoscience Frontiers, 7(3), 315–334. http://doi.org/10.1016/j.gsf.2015.12.006

Solovova, I. P., Ryabchikov, I. D., Kogarko, L. N., Kononkova, N. N. (1998) Inclusions in minerals of the Palaborwa carbonatite complex, South Africa. Geochemistry International, 36(5), 377-388.

Solovova, I. P., Girnis, A. V., Kogarko, L. N., Kononkova, N. N., Rosatelli, G., Stoppa, F. (2005) Compositions of magmas and carbonate-silicate liquid immiscibility in the Mt. Vulture alkaline igneous complex, Italy. Lithos 85(1-4), 113-128. https://doi.org/10.1016/j.lithos.2005.03.022

Solovova, I. P., Girnis, A. V. (2012) Silicate-carbonate liquid immiscibility and crystallization of carbonate and K-rich basaltic magma: insights from melt and fluid inclusions. Mineralogical Magazine, 76(2), 411-439. https://doi.org/10.1180/minmag.2012.076.2.09

Soltys, A., Giuliani, A., Phillips, D., Kamenetsky, V.S., Maas, R., Woodhead, J. and Rodemann, T. (2016) In-situ assimilation of mantle minerals by kimberlitic magmas—direct evidence from a garnet wehrlite xenolith entrained in the Bultfontein kimberlite (Kimberley, South Africa). Lithos, 256, 82-196. https://doi.org/10.1016/j.lithos.2016.04.011

Spandler, C., Hammerli, J., Yaxley, G. M. (2017) An experimental study of trace element distribution during partial melting of mantle heterogeneities. Chemical Geology, 462, 74–87. http://doi.org/10.1016/j.chemgeo.2017.05.002

Stevenson, R., Upton, B. G. J., Steenfelt, A. (1997) Crust-mantle interaction in the evolution of the Ilímaussaq Complex, South Greenland: Nd isotopic studies. Lithos, 40(2–4), 189–202. http://doi.org/10.1016/S0024-4937(97)00025-X

Streckeisen, A. L. (1978) IUGS Subcommission on the Systematics of Igneous Rocks. Classification and nomenclature of volcanic rocks, lamprophyres, carbonatites and melilite rocks. Recommendations and suggestions. Neues Jahrbuch für Mineralogie, Abhandlungen, 141, 1–14.

Streckeisen, A. (1979) Classification and nomenclature of volcanic rocks, lamprophyres, carbonatites, and melilitic rocks: Recommendation and suggestion of the IUGS, Subcommission on the Systematic of Igneous Rocks. Geology, 4, 331-335.

Sugaki, A., Shima, H., Kitakaze, A., Harada, H. (1975) Isothermal phase relations in the system Cu-Fe-S under hydrothermal conditions at 350 °C and 300 °C. Economic Geology, 70(4), 806–823. http://doi.org/10.2113/gsecongeo.70.4.806

Sugaki, A., Kitakaze, A., Hayashi, K. (1981) Synthesis of minerals in the Cu-Fe-Bi-S system under hydrothermal condition and their phase relations. Bulletin de Mineralogie, 104(4), 484–495. http://doi.org/10.3406/bulmi.1981.7499

Sugaki, A., Kitakaze, A., Kojima, S. (1987) Bulk compositions of intimate intergrowths of chalcopyrite and sphalerite and their genetic implications. Mineral. Deposita 22, 26-32.

Sweeney, R. J., (1994) Carbonatite melt compositions in the Earth's mantle. Earth and Planetary Science Letters 128, 259-270. https://doi.org/10.1016/0012-821X(94)90149-X

Sylvester, P. J., Jackson, S. E. (2016) A brief history of laser ablation inductively coupled plasma mass spectrometry (LA-ICP-MS). Elements, 12(5), 307–310. https://doi.org/10.2113/gselements.12.5.307

Tenailleau, C., Pring, A., Etschmann, B., Brugger, J., Grguric, B., Putnis, A. (2006) Transformation of pentlandite to violarite under mild hydrothermal conditions. American Mineralogist, 91(4), 706–709. http://doi.org/10.2138/am.2006.2131

Thériault, R. D., Barnes, S. J. (1998) Compositional variations in Cu-Ni-PGE sulfides of the Dunka Road deposit, Duluth Complex, Minnesota: The importance of combined assimilation and magmatic processes. Canadian Mineralogist, 36(3), 869–886.

Tinker, J., De Wit, M. J., Grotzinger, J. P. (2002) Seismic stratigraphic constraints on Neoarchean - Paleoproterozoic evolution of the western margin of the Kaapvaal Craton, South Africa. South African Journal of Geology, 105(2), 107-134. https://doi.org/10.2113/105.2.107

Treiman, A. H., Schedl, A. (1983) Properties of carbonatite magma and processes in carbonatite magma chambers. The University of Chicago Press, 91(4), 437–447. http://www.jstor.org/stable/30064002

Tutti, F., Dubrovinsky, L. S. and Saxena, S. K. (2000) High pressure phase transformation of jadeite and stability of $NaAlSiO_4$ with calcium-ferrite type structure in the lower mantle conditions. Geophysical Research Letters, 27(14), 2025-2028. https://doi.org/10.1016/j.pepi.2007.02.004

Vaasjoki, O., Häkli, T. A., Tontti, M. (1974) The effect of cobalt on the thermal stability of pentlandite. Economic Geology. 69, 549-551.

Vartiainen, H. (1980) The petrography, mineralogy and petrochemistry of the Sokli carbonatite massif northern Finland. Bulletin of the Geological Survey of Finland, 313, 126.

Veksler, I.V., Petibon, C., Jenner, G.A., Dorfman, A.M. and Dingwell, D.B. (1998) Trace element partitioning in immiscible silicate–carbonate liquid systems: an initial experimental study using a centrifuge autoclave. Journal of Petrology, 39(11-12), 2095-2104. https://doi.org/10.1093/petroj/39.11-12.2095

Verhulst, A., Balaganskaya, E., Kirnarsky, Y. and Demaiffe, D. (2000) Petrological and geochemical (trace elements and Sr–Nd isotopes) characteristics of the Paleozoic Kovdor ultramafic, alkaline and carbonatite intrusion (Kola Peninsula, NW Russia). Lithos, 51(1-2), 1-25.

https://doi.org/10.1016/S0024-4937(99)00072-9

Vernon, R. H. (2004) A Practical Guide to Rock Microstructure. Cambridge University Press. ISBN 0 521 81448 X – ISBN 0 521 89133 7

Verwoerd, W. J. (1967) The Carbonatites of South Africa and Southwest Africa, Handbook 6, Department of Mines, Geological Survey, Republic of South Africa.

Vokes, F. M. (1967) Linnaeite from the Precambrian Raipas group of Finnmark, Norway - An investigation with the electron microprobe. Mineralium Deposita, 2(1), 11–25. https://doi.org/10.1007/BF00206818

Wallace, M.E., Green, D.H., (1988) An experimental determination of primary carbonatite magma composition. Nature 335, 343-346. https://doi.org/10.1038/335343a0

Wang, Z. and Becker, H. (2013) Ratios of S, Se and Te in the silicate Earth require a volatile-rich late veneer. Nature, 499(7458), 328-331.

Wang, Z., Becker, H., Liu, Y., Hoffmann, E., Chen, C., Zou, Z. and Li, Y. (2018) Constant Cu/Ag in upper mantle and oceanic crust: Implications for the role of cumulates during the formation of continental crust. Earth and Planetary Science Letters, 493, 25-35. https://doi.org/10.1016/j.epsl.2018.04.008

Watkinson, D. H., Wyllie, P. J. (1969) Phase equilibrium studies bearing on the limestone-assimilation-hypothesis. Geological Society of America Bulletin 80(8), 1565- 1576. https://doi.org/10.1130/0016-7606(1969)80[1565:PESBOT]2.0.CO;2

Watkinson, D.H., Wyllie, P. J. (1971) Experimental study of the join $NaAlSiO_4$-$CaCO_3$-H_2O and the genesis of alkalic rock-carbonatite complexes. Journal of Petrology 12, 357-378. https://doi.org/10.1093/petrology/12.2.357

Wendlandt, R. F., Eggler, D. H. (1980a) The origins of potassic magmas. 1. Melting relations in the systems $KAlSiO_4$-Mg_2SiO_4-SiO_2 and $KAlSiO_4$-MgO-SiO_2-CO_2 to 30 kilobars. American Journal of Science, 280(5), 385-420.

Wendlandt, R. F, Eggler, D. H.(1980b) Stability of phlogopite in natural spinel lherzolite and in the system $KAlSiO_4$-MgO-SiO_2-H_2O-CO_2 at high pressures and high temperatures. American Journal of Science, 280(5), 421-458.

Will, G., Hinze, E. and Abdelrahman, A.R.M. (2002) Crystal structure analysis and refinement of digenite, $Cu_{1.8}S$, in the temperature range 20 to 500 °C under controlled sulfur partial pressure. European Journal of Mineralogy, 14(3), 591-598.

Winter, J. D. (2014) Principles of Igneous and Metamorphic Petrology. Pearson Education Limited. ISBN 10: 1-292-02153-5 ISBN 13: 978-1-292-02153-9

Wilson, A. H., Carlson, R. W. (1989) A Sm Nd and Pb isotope study of Archaean greenstone belts in the southern Kaapvaal Craton, South Africa. Earth and Planetary Science Letters, 96(1–2), 89–105. https://doi.org/10.1016/0012-821X(89)90125-8

Wood, S. A. (1987) Thermodynamic calculations of the volatility of the platinum group elements (PGE): The PGE content of fluids at magmatic temperatures. Geochimica et Cosmochimica Acta, 51(11), 3041–3050. http://doi.org/10.1016/0016-7037(87)90377-2

Woolley, A. R., Kempe, D. R. C. (1989) Carbonatites; Nomenclature, average chemical compositions, and element distribution. *In*: Bell, K. (ed.) (1989) Carbonatites: Genesis and Evolution, Unwin Hyman, London, pp. 1-14.

Woolley AR (1989) The spatial and temporal distribution of carbonatites. *In*: Bell K (ed.) Carbonatites: Genesis and Evolution. Unwin Hyman Ltd, London,15-37.

Woolley. A. R., (2003) Igneous silicate rocks associated with carbonatites: Their diversity, relative abundances and implications for carbonatite genesis. Periodico di Mineralogia 72(1), 9-17.

Woolley, A., Kjarsgaard, B. A. (2008) Paragenetic types of carbonatite as indicated by the diversity and relative abundances of associated silicate rocks: Evidence from a global database. The Canadian Mineralogist 46(4), 741-752. https://doi.org/10.3749/canmin.46.4.741

Woolley, A. R., Bailey, D. K. (2012) The crucial role of lithospheric structure in the generation and release of carbonatites: geological evidence. Mineralogical Magazine,76(2), 259-270. https://doi.org/10.1180/minmag.2012.076.2.02

Wu, F. Y., Yang, Y. H., Li, Q. L., Mitchell, R. H., Dawson, J. B., Brandl, G., Yuhara, M. (2011) In-situ determination of U-Pb ages and Sr-Nd-Hf isotopic constraints on the petrogenesis of the Phalaborwa carbonatite Complex, South Africa. Lithos, 127(1-2), 309–322. http://doi.org/10.1016/j.lithos.2011.09.005

Wyllie, P. J. (1978) Mantle fluid compositions buffered in peridotite-CO_2-H_2O by carbonates, amphibole and phlogopite. The Journal of Geology, 86(6), 687-713. https://doi.org/10.1086/649737

Xia, F., Rugger, J., Chen, G., Ngothai, Y., O'Neill, B., Putnis, A., Pring, A. (2009) Mechanism and kinetics of pseudomorphic mineral replacement reactions: A case study of the replacement of pentlandite by violarite. Geochimica et Cosmochimica Acta, 73(7), 1945–1969. http://doi.org/10.1016/j.gca.2009.01.007

Yaxley, G. M., Green, D. H. (1996) Experimental reconstruction of sodic, dolomitic carbonatite melts from metasomatised lithosphere. Contributions to Mineralogy and Petrology (1996) 124: 359-369. https://doi.org/10.1007/s004100050196

Yegorov, L.S. (1993) Phoscorites of the Maymecha-Kotuy ijolite-carbonatite association. International Geology Review, 35(4), 346-358. https://doi.org/10.1080/00206819309465533

Yuhara, M., Hirahara, Y., Nishi, N., Kagami, H. (2005) Rb-Sr, Sm-Nd ages of the Phalaborwa Carbonatite Complex, South Africa. Polar Geoscience, 18, 101–113.

Yund, R. A., Kullerud, G. (1966). Thermal stability of assemblages in the Cu-Fe-S system. Journal of Petrology, 7(3), 454–488. http://doi.org/10.1093/petrology/7.3.454

Zhao, J., Brugger, J., Ngothai, Y., Pring, A. (2014) The replacement of chalcopyrite by bornite under hydrothermal conditions. American Mineralogist, 99(11-12), 2389–2397. http://doi.org/10.2138/am-2014-4825

Zack, T., Brumm, R. (1998) Ilmenite/liquid partition coefficients of 26 trace elements determined through ilmenite/clinopyroxene partitioning in garnet pyroxenites. International Kimberlite Conference: Extended Abstracts, 8, 986-988.

Zaitsev, A. and Bell, K. (1995) Sr and Nd isotope data of apatite, calcite and dolomite as indicators of source, and the relationships of phoscorites and carbonatites from the Kovdor massif, Kola peninsula, Russia. Contributions to Mineralogy and Petrology, 121, 324-335. https://doi.org/10.1007/BF02688247

Appendices

Appendix 1: The results of the EPMA analyses of the sulphide phases (wt%)

Trc: transgressive carbonatite, Bc: banded carbonatite, Phosc: phoscorite, bo: bornite, chp: chalcopyrite, sph:sphalerite, cub: cubanite

Table Chalcopyrite in Trc, Bc and Phosc.										
	Pb2_chp1	Pb2_chp2	Pb2_chp3	Pb2_chp4	Pb2_chp5	Pb1_chp1	Pb1_chp2	Pb1_chp3	Pb1_chp4	Pb1_chp5
S	35.38	35.36	35.58	35.45	35.76	35.36	35.01	35.29	35.19	35.27
Cu	33.33	34.37	33.86	34.18	34.10	34.47	33.47	33.88	34.37	34.15
Pb	0.26	0.00	0.27	0.00	0.26	0.20	0.00	0.15	0.17	0.21
Fe	30.23	30.19	30.48	30.31	30.61	29.88	30.46	29.82	29.89	30.06
Bi	0.00	0.00	0.00	0.00	0.00	0.00	0.00	0.00	0.00	0.00
Co	0.00	0.00	0.00	0.00	0.00	0.00	0.00	0.00	0.00	0.00
Ni	0.00	0.00	0.00	0.00	0.00	0.08	0.11	0.26	0.00	0.00
Zn	0.00	0.00	0.00	0.00	0.00	0.00	0.00	0.00	0.00	0.00
Total	99.20	99.98	100.19	100.03	100.73	99.99	99.08	99.45	99.65	99.71
Lithology	Trc-chp rich					Trc-bo rich				
Texture	massive					At bo edges, around Co-ptl				
	Calculated formulae (Ideal formula: $CuFeS_2$)									
S	1.10	1.10	1.11	1.11	1.12	1.10	1.09	1.10	1.10	1.10
Cu	0.52	0.54	0.53	0.54	0.54	0.54	0.53	0.53	0.54	0.54
Pb	0.00	0.00	0.00	0.00	0.00	0.00	0.00	0.00	0.00	0.00
Fe	0.54	0.54	0.55	0.54	0.55	0.54	0.55	0.53	0.54	0.54
Bi	0.00	0.00	0.00	0.00	0.00	0.00	0.00	0.00	0.00	0.00
Co	0.00	0.00	0.00	0.00	0.00	0.00	0.00	0.00	0.00	0.00
Ni	0.00	0.00	0.00	0.00	0.00	0.00	0.00	0.00	0.00	0.00
Zn	0.00	0.00	0.00	0.00	0.00	0.00	0.00	0.00	0.00	0.00
Total Metals	1.07	1.08	1.08	1.08	1.09	1.08	1.07	1.07	1.08	1.08
Metal/S	0.97	0.98	0.97	0.98	0.97	0.98	0.98	0.97	0.98	0.98

Chalcopyrite in Trc, Bc and Phosc.										
	Pb1_chp6	2Pb5_chp1	2Pb5_chp2	2Pb5_chp3	2Pb5_chp4	2Pb5_chp5	2Pb5_chp6	2Pb5_chp7	2Pb5_chp8	Pa2a_2
S	35.14	35.42	35.13	35.30	35.12	35.09	35.07	35.18	35.08	35.45
Cu	34.37	34.47	34.05	34.47	34.25	34.30	34.04	34.70	34.58	34.03
Pb	0.20	0.00	0.27	0.19	0.28	0.26	0.27	0.00	0.15	0.26
Fe	29.94	29.81	30.17	29.22	29.72	30.28	30.04	30.16	29.97	30.05
Bi	0.00	0.00	0.00	0.00	0.00	0.00	0.00	0.00	0.00	0.00
Co	0.00	0.00	0.00	0.00	0.00	0.00	0.00	0.00	0.00	0.00
Ni	0.00	0.00	0.00	0.00	0.00	0.00	0.00	0.00	0.00	0.00
Zn	0.00	0.00	0.00	0.00	0.00	0.00	0.00	0.00	0.00	0.11
Total	99.68	99.70	99.63	99.18	99.40	99.93	99.43	100.16	99.78	99.97
Lithology	Trc-bo rich									Trc-chp rich
Texture	At bo edges, around Co-ptl	at bo edges/fractures and inside								massive, between cubanite patches
	Calculated formulae (Ideal formula: $CuFeS_2$)									
S	1.10	1.10	1.10	1.10	1.10	1.09	1.09	1.10	1.09	1.11
Cu	0.54	0.54	0.54	0.54	0.54	0.54	0.54	0.55	0.54	0.54
Pb	0.00	0.00	0.00	0.00	0.00	0.00	0.00	0.00	0.00	0.00
Fe	0.54	0.53	0.54	0.52	0.53	0.54	0.54	0.54	0.54	0.54
Bi	0.00	0.00	0.00	0.00	0.00	0.00	0.00	0.00	0.00	0.00
Co	0.00	0.00	0.00	0.00	0.00	0.00	0.00	0.00	0.00	0.00
Ni	0.00	0.00	0.00	0.00	0.00	0.00	0.00	0.00	0.00	0.00
Zn	0.00	0.00	0.00	0.00	0.00	0.00	0.00	0.00	0.00	0.00
Total Metals	1.08	1.08	1.08	1.07	1.07	1.08	1.07	1.09	1.08	1.08
Metal/S	0.98	0.97	0.98	0.97	0.98	0.99	0.98	0.99	0.99	0.97

Chalcopyrite in Trc, Bc and Phosc										
	Pa2a_8	Pa2a_9	Pa23_1	Pa23_3	Pa23_4	Pa23_5	26B_A28	26B_A25	26B_A2_6	26B_A_12
S	35.02	35.96	34.56	35.07	35.34	34.92	35.47	35.11	35.56	35.72
Cu	34.14	34.57	34.56	34.18	33.87	34.15	34.06	34.09	34.00	34.60
Pb	0.00	0.00	0.26	0.30	0.18	0.00	0.00	0.13	0.19	0.00
Fe	30.50	30.39	29.97	29.12	30.21	29.32	29.90	29.95	29.96	29.86
Bi	0.00	0.00	0.23	0.16	0.14	0.00	0.00	0.00	0.00	0.13
Co	0.00	0.00	0.00	0.00	0.00	0.00	0.00	0.00	0.00	0.00
Ni	0.00	0.00	0.00	0.00	0.00	0.00	0.00	0.00	0.00	0.00
Zn	0.00	0.00	0.17	0.15	0.26	0.00	0.00	0.22	0.09	0.00
Total	99.78	101.15	99.75	98.97	100.02	98.49	99.56	99.59	99.93	100.44
Lithology	Trc-chp rich						Bc- disseminated			
Texture	massive, between cubanite patches		massive				disseminated, with bornite and dig at edges			
	Calculated formulae (Ideal formula: $CuFeS_2$)									
S	1.09	1.12	1.08	1.09	1.10	1.09	1.11	1.09	1.11	1.11
Cu	0.54	0.54	0.54	0.54	0.53	0.54	0.54	0.54	0.54	0.54
Pb	0.00	0.00	0.00	0.00	0.00	0.00	0.00	0.00	0.00	0.00
Fe	0.55	0.54	0.54	0.52	0.54	0.52	0.54	0.54	0.54	0.53
Bi	0.00	0.00	0.00	0.00	0.00	0.00	0.00	0.00	0.00	0.00
Co	0.00	0.00	0.00	0.00	0.00	0.00	0.00	0.00	0.00	0.00
Ni	0.00	0.00	0.00	0.00	0.00	0.00	0.00	0.00	0.00	0.00
Zn	0.00	0.00	0.00	0.00	0.00	0.00	0.00	0.00	0.00	0.00
Total Metals	1.08	1.09	1.09	1.06	1.08	1.06	1.07	1.08	1.07	1.08
Metal/S	0.99	0.97	1.01	0.97	0.98	0.98	0.97	0.98	0.97	0.97

Chalcopyrite in Trc, Bc and Phosc.										
	26B_A_11	26B_A_13	26B_A_14	26B_SE13	26B_SE1	PA25_B12	PA25_B13	PA15_A3_1	PA15_A3_2	PA15_D3
S	34.71	35.36	34.61	35.09	35.10	35.47	35.01	35.21	35.15	35.25
Cu	33.47	34.13	34.11	33.88	33.52	32.98	33.04	33.11	33.02	33.39
Pb	0.00	0.29	0.26	0.15	0.21	0.00	0.25	0.32	0.26	0.21
Fe	30.03	30.20	30.28	29.85	29.83	29.83	30.07	29.80	29.86	29.87
Bi	0.21	0.17	0.00	0.00	0.00	0.00	0.20	0.00	0.12	0.00
Co	0.00	0.00	0.00	0.00	0.00	0.00	0.00	0.00	0.00	0.00
Ni	0.00	0.00	0.00	0.18	0.12	0.00	0.00	0.00	0.00	0.00
Zn	0.00	0.16	0.11	0.00	0.18	0.14	0.11	0.22	0.11	0.10
Total	98.59	100.32	99.47	99.17	99.05	98.52	98.70	98.81	98.53	98.85
Lithology	Bc- disseminated					Trc- chp rich with lots of cubanite		Trc-chp rich		
Texture	disseminated, with bornite and dig at edges					massive (cub lam)			massive	
	Calculated formulae (Ideal formula: $CuFeS_2$)									
S	1.08	1.10	1.08	1.09	1.09	1.11	1.09	1.10	1.10	1.10
Cu	0.53	0.54	0.54	0.53	0.53	0.52	0.52	0.52	0.52	0.53
Pb	0.00	0.00	0.00	0.00	0.00	0.00	0.00	0.00	0.00	0.00
Fe	0.54	0.54	0.54	0.53	0.53	0.53	0.54	0.53	0.53	0.53
Bi	0.00	0.00	0.00	0.00	0.00	0.00	0.00	0.00	0.00	0.00
Co	0.00	0.00	0.00	0.00	0.00	0.00	0.00	0.00	0.00	0.00
Ni	0.00	0.00	0.00	0.00	0.00	0.00	0.00	0.00	0.00	0.00
Zn	0.00	0.00	0.00	0.00	0.00	0.00	0.00	0.00	0.00	0.00
Total Metals	1.07	1.08	1.08	1.07	1.07	1.06	1.06	1.06	1.06	1.06
Metal/S	0.98	0.98	1.00	0.98	0.98	0.95	0.97	0.97	0.97	0.97

Chalcopyrite in Trc, Bc and Phosc.										
	GC1610_B_1	GC1610_B_2	GC1610_B_3	GC1610_J3_1	GC1610_J3_2	GC1610_C_4	GC1610_C_5	GC1610_C_6	GC1610_A2_6	GC1610_A2_8
S	34.95	35.09	35.44	35.31	34.95	35.54	35.18	35.40	35.29	35.55
Cu	33.25	33.46	33.84	33.35	33.27	33.61	33.86	31.73	33.80	34.14
Pb	0.27	0.22	0.00	0.32	0.17	0.29	0.22	0.15	0.19	0.00
Fe	30.32	30.28	29.06	30.49	30.25	30.09	30.27	31.90	29.63	30.06
Bi	0.12	0.17	0.00	0.00	0.12	0.00	0.16	0.00	0.00	0.00
Co	0.00	0.00	0.00	0.00	0.00	0.00	0.00	0.00	0.00	0.00
Ni	0.00	0.00	0.00	0.00	0.00	0.00	0.00	0.00	0.00	0.00
Zn	0.00	0.15	0.12	0.00	0.13	0.00	0.14	0.15	0.09	0.10
Total	99.02	99.39	98.62	99.47	98.91	99.64	99.84	99.43	99.12	99.90
Lithology	trc To-rich									
Texture	between to patches									
	Calculated formulae (Ideal formula: $CuFeS_2$)									
S	1.09	1.09	1.11	1.10	1.09	1.11	1.10	1.10	1.10	1.11
Cu	0.52	0.53	0.53	0.52	0.52	0.53	0.53	0.50	0.53	0.54
Pb	0.00	0.00	0.00	0.00	0.00	0.00	0.00	0.00	0.00	0.00
Fe	0.54	0.54	0.52	0.55	0.54	0.54	0.54	0.57	0.53	0.54
Bi	0.00	0.00	0.00	0.00	0.00	0.00	0.00	0.00	0.00	0.00
Co	0.00	0.00	0.00	0.00	0.00	0.00	0.00	0.00	0.00	0.00
Ni	0.00	0.00	0.00	0.00	0.00	0.00	0.00	0.00	0.00	0.00
Zn	0.00	0.00	0.00	0.00	0.00	0.00	0.00	0.00	0.00	0.00
Total Metals	1.07	1.07	1.05	1.07	1.07	1.07	1.08	1.07	1.06	1.08
Metal/S	0.98	0.98	0.95	0.97	0.98	0.96	0.98	0.97	0.97	0.97

Chalcopyrite in Trc, Bc and Phosc.										
	GC1811A_A_4	GC1811A_A_5	GC1811A_A_6	GC1811A_A_7	GC1811A_A_8	GC1811A_A_9	GC1811A_A_10	GC1811A_B_4	GC1811A_B_5	GC1811A_B_6
S	34.98	35.76	35.08	35.62	35.53	35.26	34.80	35.38	35.52	35.27
Cu	34.00	34.27	33.96	34.11	34.36	34.37	34.15	33.50	34.48	34.05
Pb	0.19	0.14	0.15	0.00	0.25	0.32	0.15	0.27	0.00	0.24
Fe	30.09	30.16	30.07	30.54	30.30	30.19	30.17	30.27	29.95	30.09
Bi	0.00	0.00	0.00	0.00	0.00	0.18	0.00	0.15	0.00	0.00
Co	0.00	0.00	0.00	0.00	0.00	0.00	0.00	0.00	0.00	0.00
Ni	0.00	0.00	0.00	0.00	0.00	0.00	0.00	0.00	0.00	0.00
Zn	0.11	0.00	0.19	0.16	0.00	0.09	0.00	0.12	0.20	0.00
Total	99.46	100.47	99.60	100.57	100.57	100.42	99.38	99.71	100.32	99.81
Lithology	Trc bo-rich									
Texture	rim/spindles in mass.bo									
	Calculated formulae (Ideal formula: $CuFeS_2$)									
S	1.09	1.12	1.09	1.11	1.11	1.10	1.09	1.10	1.11	1.10
Cu	0.54	0.54	0.53	0.54	0.54	0.54	0.54	0.53	0.54	0.54
Pb	0.00	0.00	0.00	0.00	0.00	0.00	0.00	0.00	0.00	0.00
Fe	0.54	0.54	0.54	0.55	0.54	0.54	0.54	0.54	0.54	0.54
Bi	0.00	0.00	0.00	0.00	0.00	0.00	0.00	0.00	0.00	0.00
Co	0.00	0.00	0.00	0.00	0.00	0.00	0.00	0.00	0.00	0.00
Ni	0.00	0.00	0.00	0.00	0.00	0.00	0.00	0.00	0.00	0.00
Zn	0.00	0.00	0.00	0.00	0.00	0.00	0.00	0.00	0.00	0.00
Total Metals	1.08	1.08	1.08	1.09	1.08	1.09	1.08	1.07	1.08	1.08
Metal/S	0.99	0.97	0.98	0.98	0.98	0.99	0.99	0.97	0.98	0.98

Chalcopyrite in Trc, Bc and Phosc.										
	GC1811A_B_11	GC1811A_SEMB_4	GC1811A_SEMB_5	GC1811A_SEMB_6	GC1611_B2_1	GC1611_B2_2	GC1611_B2_3	GC1611_B2_11	GC1611_B_1	GC1611_B_2
S	35.63	34.93	35.31	35.01	35.25	35.11	35.04	35.59	34.89	35.21
Cu	33.74	34.53	34.45	34.48	34.27	34.17	34.13	33.79	33.83	33.76
Pb	0.25	0.22	0.00	0.25	0.00	0.00	0.25	0.00	0.18	0.19
Fe	29.95	30.03	30.05	30.22	30.05	30.15	30.19	30.20	29.64	29.99
Bi	0.00	0.00	0.00	0.00	0.00	0.00	0.00	0.00	0.16	0.00
Co	0.00	0.00	0.00	0.00	0.00	0.00	0.00	0.00	0.00	0.00
Ni	0.00	0.00	0.00	0.00	0.00	0.00	0.00	0.00	0.19	0.00
Zn	0.11	0.22	0.00	0.18	0.00	0.11	0.11	0.00	0.08	0.00
Total	99.80	99.93	100.02	100.19	99.68	99.73	99.77	99.84	98.97	99.21
Lithology	Trc bo-rich				trc chp-bo network					
Texture	rim/spindles in mass.bo				chp-bo network ex/repl					
	Calculated formulae (Ideal formula: $CuFeS_2$)									
S	1.11	1.09	1.10	1.09	1.10	1.09	1.09	1.11	1.09	1.10
Cu	0.53	0.54	0.54	0.54	0.54	0.54	0.54	0.53	0.53	0.53
Pb	0.00	0.00	0.00	0.00	0.00	0.00	0.00	0.00	0.00	0.00
Fe	0.54	0.54	0.54	0.54	0.54	0.54	0.54	0.54	0.53	0.54
Bi	0.00	0.00	0.00	0.00	0.00	0.00	0.00	0.00	0.00	0.00
Co	0.00	0.00	0.00	0.00	0.00	0.00	0.00	0.00	0.00	0.00
Ni	0.00	0.00	0.00	0.00	0.00	0.00	0.00	0.00	0.00	0.00
Zn	0.00	0.00	0.00	0.00	0.00	0.00	0.00	0.00	0.00	0.00
Total Metals	1.07	1.09	1.08	1.09	1.08	1.08	1.08	1.07	1.07	1.07
Metal/S	0.96	1.00	0.98	1.00	0.98	0.99	0.99	0.97	0.98	0.97

Chalcopyrite in Trc, Bc and Phosc.										
	GC1611_D2_6	PTC3_C6	PTC3_C7	PTC3_C8	PTC3_C10	PTC3_B5	PTC3_B6	PTC3_B7	PTC3_2B_3	PTC3_2B_4
S	35.16	35.52	35.14	35.58	35.14	35.04	35.26	35.26	35.41	35.43
Cu	32.67	32.95	33.61	33.64	32.65	33.66	33.83	33.76	33.14	33.31
Pb	0.24	0.22	0.20	0.22	0.23	0.25	0.24	0.00	0.22	0.00
Fe	30.34	29.69	30.22	29.33	29.95	29.69	29.96	29.81	29.75	29.85
Bi	0.00	0.00	0.00	0.00	0.00	0.00	0.00	0.00	0.00	0.00
Co	0.00	0.00	0.00	0.00	0.00	0.00	0.00	0.00	0.00	0.00
Ni	0.00	0.00	0.00	0.12	1.14	0.11	0.00	0.00	0.72	0.00
Zn	0.00	0.00	0.00	0.00	0.00	0.00	0.00	0.00	0.00	0.00
Total	98.59	98.45	99.24	98.89	99.13	98.75	99.29	98.96	99.24	98.74
Lithology	trc chp-bo network	trc chp-bo								
Texture	chp-bo network ex/repl	chp with extensive bo								
					Calculated formulae (Ideal formula: $CuFeS_2$)					
S	1.10	1.11	1.10	1.11	1.10	1.09	1.10	1.10	1.10	1.10
Cu	0.51	0.52	0.53	0.53	0.51	0.53	0.53	0.53	0.52	0.52
Pb	0.00	0.00	0.00	0.00	0.00	0.00	0.00	0.00	0.00	0.00
Fe	0.54	0.53	0.54	0.53	0.54	0.53	0.54	0.53	0.53	0.53
Bi	0.00	0.00	0.00	0.00	0.00	0.00	0.00	0.00	0.00	0.00
Co	0.00	0.00	0.00	0.00	0.00	0.00	0.00	0.00	0.00	0.00
Ni	0.00	0.00	0.00	0.00	0.02	0.00	0.00	0.00	0.01	0.00
Zn	0.00	0.00	0.00	0.00	0.00	0.00	0.00	0.00	0.00	0.00
Total Metals	1.06	1.05	1.07	1.06	1.07	1.06	1.07	1.07	1.07	1.06
Metal/S	0.97	0.95	0.98	0.95	0.98	0.97	0.97	0.97	0.97	0.96

Chalcopyrite in Trc, Bc and Phosc.										
	PTC3_2B_8	PTC3_2C_9	PTC3_2C_10	Pa15_A5	GC1811A_A_4	GC1524A_A1	GC1524A_A4	GC1524A_A5	GC1524A_B4	GC1524A_B5
S	35.16	35.15	35.20	35.25	34.98	34.82	34.88	34.65	35.00	34.63
Cu	32.91	33.77	33.33	33.29	34.00	33.49	33.90	33.75	33.91	33.91
Pb	0.16	0.17	0.20	0.35	0.19	0.19	0.27	0.17	0.00	0.28
Fe	29.61	29.98	30.21	29.85	30.09	29.85	29.36	29.96	29.81	29.71
Bi	0.00	0.00	0.00	0.00	0.09	0.21	0.00	0.00	0.00	0.00
Co	0.00	0.00	0.00	0.00	0.00	0.00	0.00	0.00	0.00	0.00
Ni	0.61	0.19	0.29	0.00	0.00	0.00	0.00	0.00	0.00	0.00
Zn	0.00	0.00	0.00	0.00	0.11	0.00	0.00	0.00	0.00	0.00
Total	98.46	99.26	99.23	98.74	99.46	98.62	98.56	98.59	98.87	98.60
Lithology	Trc chp-bo			Trc-chp rich	Trc bo-rich					
Texture	chp with extensive bo			massive	rim/splindles in mass.bo					
Calculated formulae (Ideal formula: $CuFeS_2$)										
S	1.10	1.10	1.10	1.10	1.09	1.09	1.09	1.08	1.09	1.08
Cu	0.52	0.53	0.52	0.52	0.54	0.53	0.53	0.53	0.53	0.53
Pb	0.00	0.00	0.00	0.00	0.00	0.00	0.00	0.00	0.00	0.00
Fe	0.53	0.54	0.54	0.53	0.54	0.53	0.53	0.54	0.53	0.53
Bi	0.00	0.00	0.00	0.00	0.00	0.00	0.00	0.00	0.00	0.00
Co	0.00	0.00	0.00	0.00	0.00	0.00	0.00	0.00	0.00	0.00
Ni	0.01	0.00	0.00	0.00	0.00	0.00	0.00	0.00	0.00	0.00
Zn	0.00	0.00	0.00	0.00	0.00	0.00	0.00	0.00	0.00	0.00
Total Metals	1.06	1.07	1.07	1.06	1.08	1.06	1.06	1.07	1.07	1.07
Metal/S	0.97	0.98	0.98	0.96	0.99	0.98	0.98	0.99	0.98	0.99

Chalcopyrite in Trc, Bc and Phosc. X										
	2/gc1611_B2_1	2/gc1611_B2_2	2/gc1611_B2_3	GC808_Ext1_2	GC808_Ext1_3	GC808_Ext1_3b	GC808_B1	GC808_B3	GC808_2ext_A1	GC808_2ext_A2
S	34.69	34.75	34.88	34.71	34.59	34.51	34.73	34.75	34.34	34.60
Cu	33.92	33.88	33.90	34.01	33.97	33.79	34.25	33.65	33.86	34.10
Pb	0.29	0.31	0.00	0.23	0.22	0.16	0.14	0.00	0.25	0.32
Fe	30.17	29.72	30.09	30.24	30.14	30.36	29.87	30.39	30.25	29.39
Bi	0.00	0.00	0.00	0.00	0.00	0.22	0.00	0.00	0.00	0.00
Co	0.00	0.00	0.00	0.00	0.00	0.00	0.00	0.00	0.00	0.00
Ni	0.00	0.00	0.00	0.00	0.00	0.00	0.00	0.00	0.00	0.00
Zn	0.00	0.00	0.00	0.00	0.00	0.00	0.00	0.00	0.00	0.00
Total	99.14	98.70	99.11	99.19	99.01	99.04	99.02	98.89	98.85	98.47
Lithology	Trc bo-chp			Trc-chp rich						
Texture	chp-bo network ex/repl			prim. Interst						
	Calculated formulae (Ideal formula: $CuFeS_2$)									
S	1.08	1.08	1.09	1.08	1.08	1.08	1.08	1.08	1.07	1.08
Cu	0.53	0.53	0.53	0.54	0.53	0.53	0.54	0.53	0.53	0.54
Pb	0.00	0.00	0.00	0.00	0.00	0.00	0.00	0.00	0.00	0.00
Fe	0.54	0.53	0.54	0.54	0.54	0.54	0.53	0.54	0.54	0.53
Bi	0.00	0.00	0.00	0.00	0.00	0.00	0.00	0.00	0.00	0.00
Co	0.00	0.00	0.00	0.00	0.00	0.00	0.00	0.00	0.00	0.00
Ni	0.00	0.00	0.00	0.00	0.00	0.00	0.00	0.00	0.00	0.00
Zn	0.00	0.00	0.00	0.00	0.00	0.00	0.00	0.00	0.00	0.00
Total Metals	1.08	1.07	1.07	1.08	1.08	1.08	1.07	1.07	1.08	1.06
Metal/S	0.99	0.98	0.99	1.00	1.00	1.00	0.99	0.99	1.00	0.99

Chalcopyrite in Trc, Bc and Phosc. XI.							
	GC808_2ext_B	GC808_2ext_B2	GC808_2ext_C1	P03_phosc_semL1	P03_phosc_semL3	P03_phosc_semLc_3	P03_phosc_semLc_4
S	34.62	34.81	34.62	34.25	34.41	34.35	34.52
Cu	34.07	34.01	33.68	33.77	34.10	34.11	33.82
Pb	0.28	0.18	0.30	0.34	0.23	0.33	0.23
Fe	29.91	30.03	29.88	30.12	29.59	29.89	29.95
Bi	0.21	0.21	0.00	0.00	0.23	0.00	0.20
Co	0.00	0.00	0.00	0.00	0.00	0.00	0.00
Ni	0.00	0.00	0.00	0.00	0.00	0.00	0.00
Zn	0.00	0.00	0.00	0.00	0.00	0.00	0.00
Total	99.12	99.26	98.58	98.57	98.61	98.73	98.74
Lithology	Trc-chp rich			phosc			
Texture	prim. Interst			dissem/CuFeS assembl			
Calculated formulae (Ideal formula: $CuFeS_2$)							
S	1.08	1.09	1.08	1.07	1.07	1.07	1.08
Cu	0.54	0.54	0.53	0.53	0.54	0.54	0.53
Pb	0.00	0.00	0.00	0.00	0.00	0.00	0.00
Fe	0.54	0.54	0.54	0.54	0.53	0.54	0.54
Bi	0.00	0.00	0.00	0.00	0.00	0.00	0.00
Co	0.00	0.00	0.00	0.00	0.00	0.00	0.00
Ni	0.00	0.00	0.00	0.00	0.00	0.00	0.00
Zn	0.00	0.00	0.00	0.00	0.00	0.00	0.00
Total Metals	1.07	1.07	1.07	1.07	1.07	1.07	1.07
Metal/S	1.00	0.99	0.99	1.00	1.00	1.00	0.99

Cubanite in Trc												
	Pa2a_7	Pa2a_1	Pa2a_10	PA25_B7	PA25_B8	GC1610_A_4	GC1610_A_5	GC1610_A_6	GC1610_B_4	GC1610_B_5	GC1610_D_3	GC1610_D_4
S	36.01	35.94	36.12	35.81	35.86	35.26	35.83	35.48	35.83	35.79	35.50	35.90
Cu	22.31	22.35	22.68	22.55	22.86	22.63	21.94	22.09	22.63	22.69	22.56	22.33
Fe	40.49	40.77	40.73	40.38	40.50	40.88	41.00	40.75	40.51	40.25	40.30	40.60
Bi	0.14	0.00	0.00	0.00	0.00	0.13	0.00	0.20	0.00	0.16	0.00	0.18
Zn	0.19	0.00	0.14	0.00	0.09	0.08	0.00	0.00	0.10	0.15	0.00	0.28
Total	99.40	99.20	99.86	98.93	99.51	99.26	98.97	98.71	99.54	99.18	98.64	99.50
Lithology	Trc-sheard sample			Trc To-rich								
Texture	thick lamellae in massive chp			Lamellae in massive chp		exsolution in chp near po						
	Calculated Formulae (Ideal formulae: $CuFe_2S_3$)											
S	3.37	3.36	3.38	3.35	3.35	3.30	3.35	3.32	3.35	3.35	3.32	3.36
Cu	1.05	1.06	1.07	1.06	1.08	1.07	1.04	1.04	1.07	1.07	1.07	1.05
Pb	0.00	0.00	0.00	0.00	0.00	0.00	0.00	0.00	0.01	0.00	0.00	0.00
Fe	2.17	2.19	2.19	2.17	2.18	2.20	2.20	2.19	2.18	2.16	2.16	2.18
Zn	0.01	0.00	0.01	0.00	0.00	0.00	0.00	0.00	0.00	0.01	0.00	0.01
Total Metals	3.24	3.25	3.27	3.24	3.26	3.27	3.24	3.24	3.25	3.24	3.23	3.25
Metal/S	0.96	0.97	0.97	0.97	0.97	0.99	0.97	0.98	0.97	0.97	0.97	0.97

Cubanite in Trc						
	GC1610_D_4	GC1610_D_5	GC1610_D_6	GC1610_C_1	GC1610_C_2	GC1610_A2_7
S	35.90	35.45	35.55	35.70	35.55	35.38
Cu	22.33	22.72	22.75	22.22	22.51	22.01
Fe	40.60	40.83	40.75	40.43	40.43	40.94
Bi	0.18	0.16	0.19	0.00	0.00	0.00
Zn	0.28	0.13	0.00	0.00	0.11	0.22
Total	99.50	99.49	99.44	98.58	98.93	98.89
Lithology	Trc-To-rich					
Texture	exsolution in chp near troilite					
	Calculated formuale (Ideal formulae: $CuFe_2S_3$)					
S	3.36	3.32	3.33	3.34	3.33	3.31
Cu	1.05	1.07	1.07	1.05	1.06	1.04
Fe	2.18	2.19	2.19	2.17	2.17	2.20
Zn	0.01	0.01	0.00	0.00	0.01	0.01
Total Metals	3.25	3.28	3.27	3.22	3.24	3.25
Metal/S	0.97	0.99	0.98	0.97	0.98	0.98

Bornite compositions in Trc, Bc and Phosc.I.										
Element wt%	PTC3_B3	PTC3_B8	PTC3_2B_5	PTC3_2B_6	PTC3_2B_7	Pb1_Bo1	Pb1_Bo2	Pb1_Bo3	Pb1_Bo4	Pb1_Bo5
S	26.41	26.75	26.30	26.28	26.09	26.34	26.08	26.37	26.12	26.35
Cu	61.74	61.85	61.96	62.10	61.68	62.93	62.81	62.33	62.38	62.65
Pb	0.13	0.15	0.27	0.00	0.22	0.14	0.00	0.22	0.00	0.13
Fe	11.18	10.99	10.87	11.10	11.06	11.39	11.24	11.15	11.22	11.17
Bi	0.00	0.00	0.00	0.00	0.00	0.00	0.00	0.00	0.00	0.00
Co	0.00	0.00	0.00	0.00	0.00	0.00	0.00	0.00	0.00	0.00
Ni	0.00	0.00	0.00	0.00	0.00	0.00	0.00	0.00	0.00	0.00
Zn	0.00	0.00	0.00	0.00	0.00	0.00	0.00	0.00	0.00	0.00
Total	**99.47**	**99.75**	**99.40**	**99.60**	**99.04**	**100.85**	**100.23**	**100.13**	**99.80**	**100.33**
Lithology	Trc chp-bo					Trc bo rich				
Texture	extensive with Chp					massive with chp at edges				
					Calculated Formulae (Ideal formula: Cu_5FeS_4)					
S	4.13	4.16	4.12	4.11	4.10	4.07	4.06	4.10	4.08	4.09
Cu	4.87	4.85	4.90	4.90	4.89	4.91	4.94	4.90	4.92	4.91
Pb	0.00	0.00	0.01	0.00	0.01	0.00	0.00	0.01	0.00	0.00
Fe	1.00	0.98	0.98	1.00	1.00	1.01	1.00	1.00	1.01	1.00
Bi	0.00	0.00	0.00	0.00	0.00	0.00	0.00	0.00	0.00	0.00
Co	0.00	0.00	0.00	0.00	0.00	0.00	0.00	0.00	0.00	0.00
Ni	0.00	0.00	0.00	0.00	0.00	0.00	0.00	0.00	0.00	0.00
Zn	0.00	0.00	0.00	0.00	0.00	0.00	0.00	0.00	0.00	0.00
Total Metals	**5.87**	**5.84**	**5.88**	**5.89**	**5.90**	**5.93**	**5.94**	**5.90**	**5.92**	**5.91**
Metals/S (Ideal: 1.5)	**1.42**	**1.40**	**1.43**	**1.44**	**1.44**	**1.45**	**1.46**	**1.44**	**1.45**	**1.44**

Bornite compositions in Trc, Bc and Phosc. II									
Element wt%	2Pb5_bo1	2Pb5_bo2	2Pb5_bo3	2Pb5_bo4	2Pb5_bo5	2Pb5_bo6	2Pb5_bo7	2Pb5_bo8	2Pb5_bo8
S	26.11	25.62	25.96	25.96	25.81	26.08	26.16	26.55	26.77
Cu	61.63	62.15	62.15	61.05	62.49	62.88	62.63	62.40	62.84
Pb	0.15	0.14	0.13	0.00	0.00	0.20	0.30	0.18	0.00
Fe	11.09	10.89	11.25	11.39	11.17	11.12	10.98	11.13	11.28
Bi	0.00	0.00	0.00	0.00	0.00	0.00	0.00	0.00	0.00
Co	0.00	0.00	0.00	0.00	0.00	0.00	0.00	0.00	0.00
Ni	0.00	0.00	0.00	0.00	0.00	0.00	0.00	0.00	0.00
Zn	0.00	0.00	0.00	0.00	0.00	0.00	0.00	0.00	0.00
Total	**99.03**	**98.83**	**99.55**	**98.48**	**99.48**	**100.28**	**100.10**	**100.31**	**100.97**
Lithology	Trc bo rich								
Texture	massive with chp at edges								
					Calculated Formulae (Ideal formula: Cu_5FeS_4)				
S	4.10	4.05	4.07	4.10	4.05	4.06	4.08	4.12	4.12
Cu	4.89	4.96	4.92	4.87	4.95	4.94	4.93	4.89	4.88
Pb	0.00	0.00	0.00	0.00	0.00	0.00	0.01	0.00	0.00
Fe	1.00	0.99	1.01	1.03	1.01	0.99	0.98	0.99	1.00
Bi	0.00	0.00	0.00	0.00	0.00	0.00	0.00	0.00	0.00
Co	0.00	0.00	0.00	0.00	0.00	0.00	0.00	0.00	0.00
Ni	0.00	0.00	0.00	0.00	0.00	0.00	0.00	0.00	0.00
Zn	0.00	0.00	0.00	0.00	0.00	0.00	0.00	0.00	0.00
Total Metals	**5.90**	**5.95**	**5.93**	**5.90**	**5.95**	**5.94**	**5.92**	**5.88**	**5.88**
Metals/S (Ideal: 1.5)	**1.44**	**1.47**	**1.46**	**1.44**	**1.47**	**1.46**	**1.45**	**1.43**	**1.43**

Bornite compositions in Trc, Bc and Phosc. III.										
Element wt%	2PB3_C2_1	2PB3_C2_4	Pa23_2	26B_A24	26B_A211	26B_A_1	26B_A_2	26B_A_3	26B_SE12	26B_SE13
S	26.36	26.09	25.91	26.39	26.29	26.49	26.15	25.94	25.93	26.38
Cu	60.76	60.92	60.93	62.06	62.40	62.25	62.46	62.14	61.66	60.57
Pb	0.00	0.00	0.00	0.00	0.20	0.18	0.00	0.19	0.16	0.26
Fe	11.19	10.98	11.88	11.38	11.23	11.23	11.22	11.26	11.08	11.49
Bi	0.00	0.13	0.00	0.00	0.00	0.00	0.00	0.00	0.00	0.00
Co	0.00	0.00	0.00	0.00	0.00	0.00	0.00	0.00	0.00	0.00
Ni	0.00	0.00	0.00	0.00	0.00	0.00	0.00	0.00	0.00	0.00
Zn	0.16	0.26	0.20	0.21	0.00	0.17	0.11	0.16	0.00	0.10
Total	**98.56**	**98.50**	**99.03**	**100.23**	**100.24**	**100.32**	**100.02**	**99.76**	**98.99**	**98.82**
Lithology	Trc bo rich		trc-chp rich	BC						
Texture	massive with chp at edges		irreg. Exsolution lam. In chp	CuFeS assemblag2						
				Calculated Formulae (Ideal formula: Cu_5FeS_4)						
S	4.15	4.12	4.08	4.10	4.09	4.11	4.08	4.06	4.09	4.15
Cu	4.83	4.86	4.84	4.87	4.90	4.87	4.91	4.91	4.91	4.80
Pb	0.00	0.00	0.00	0.00	0.00	0.00	0.00	0.00	0.00	0.01
Fe	1.01	1.00	1.07	1.02	1.00	1.00	1.00	1.01	1.00	1.04
Bi	0.00	0.00	0.00	0.00	0.00	0.00	0.00	0.00	0.00	0.00
Co	0.00	0.00	0.00	0.00	0.00	0.00	0.00	0.00	0.00	0.00
Ni	0.00	0.00	0.00	0.00	0.00	0.00	0.00	0.00	0.00	0.00
Zn	0.01	0.02	0.02	0.02	0.00	0.01	0.01	0.01	0.00	0.01
Total Metals	**5.85**	**5.88**	**5.92**	**5.90**	**5.91**	**5.89**	**5.92**	**5.94**	**5.91**	**5.85**
Metals/S (Ideal: 1.5)	**1.41**	**1.43**	**1.45**	**1.44**	**1.44**	**1.43**	**1.45**	**1.46**	**1.45**	**1.41**

Bornite compositions in Trc, Bc and Phosc. IV.										
Element wt%	26B_SE14	GC1811A_A_1	GC1811A_A_2	GC1811A_A_3	GC1811A_B_1	GC1811A_B_2	GC1811A_B_3	GC1811A_SEMB_1	GC1811A_SEMB_2	GC1811A_SEMB_3
S	25.54	26.26	26.27	26.04	26.40	25.85	25.91	25.21	26.17	26.25
Cu	61.46	61.57	61.91	61.72	61.82	62.34	62.68	62.86	62.82	62.97
Pb	0.18	0.14	0.14	0.00	0.14	0.14	0.00	0.16	0.00	0.15
Fe	11.19	10.56	10.96	11.22	11.21	11.23	10.82	11.02	11.03	11.52
Bi	0.00	0.12	0.00	0.12	0.00	0.00	0.14	0.00	0.00	0.00
Co	0.00	0.00	0.00	0.00	0.00	0.00	0.00	0.00	0.00	0.00
Ni	0.00	0.00	0.00	0.00	0.00	0.00	0.00	0.00	0.09	0.00
Zn	0.13	0.22	0.18	0.00	0.17	0.22	0.21	0.17	0.00	0.00
Total	**98.63**	**98.88**	**99.49**	**99.30**	**99.82**	**99.78**	**99.87**	**99.47**	**100.26**	**101.02**
Lithology	BC	trc bo-rich								
Texture	CuFeS assemblag2									
					Calculated Formulae (Ideal formula: Cu_5FeS_4)					
S	4.05	4.13	4.11	4.09	4.12	4.05	4.06	3.98	4.07	4.06
Cu	4.92	4.89	4.89	4.89	4.86	4.92	4.95	5.01	4.93	4.91
Pb	0.00	0.00	0.00	0.00	0.00	0.00	0.00	0.00	0.00	0.00
Fe	1.02	0.95	0.98	1.01	1.00	1.01	0.97	1.00	0.99	1.02
Bi	0.00	0.00	0.00	0.00	0.00	0.00	0.00	0.00	0.00	0.00
Co	0.00	0.00	0.00	0.00	0.00	0.00	0.00	0.00	0.00	0.00
Ni	0.00	0.00	0.00	0.00	0.00	0.00	0.00	0.00	0.01	0.00
Zn	0.01	0.02	0.01	0.00	0.01	0.02	0.02	0.01	0.00	0.00
Total Metals	**5.95**	**5.87**	**5.89**	**5.91**	**5.88**	**5.95**	**5.94**	**6.02**	**5.93**	**5.94**
Metals/S (Ideal: 1.5)	**1.47**	**1.42**	**1.43**	**1.44**	**1.43**	**1.47**	**1.47**	**1.51**	**1.46**	**1.46**

Bornite compositions in Trc, Bc and Phosc. V.										
	GC1611_B2_6	GC1611_B2_7	GC1611_B2_8	GC1611_B2_9	GC1611_B2_10	GC1611_B_6	GC1611_B_7	GC1611_B_8	GC1611_B_9	GC1611_SEMD2_3
S	26.49	26.28	25.95	26.35	26.33	25.74	26.14	25.79	25.62	26.28
Cu	62.45	63.02	62.77	62.36	62.94	61.98	61.86	62.01	62.48	62.00
Pb	0.00	0.20	0.00	0.00	0.00	0.00	0.23	0.13	0.14	0.00
Fe	11.32	10.88	11.27	11.16	11.05	10.81	11.23	10.94	11.06	11.04
Bi	0.00	0.00	0.15	0.00	0.00	0.00	0.00	0.21	0.14	0.00
Co	0.00	0.00	0.00	0.00	0.00	0.00	0.00	0.00	0.00	0.00
Ni	0.00	0.00	0.00	0.00	0.00	0.00	0.00	0.00	0.00	0.00
Zn	0.00	0.18	0.16	0.12	0.19	0.15	0.25	0.00	0.18	0.00
Total	**100.38**	**100.56**	**100.32**	**100.06**	**100.59**	**98.83**	**99.79**	**99.08**	**99.62**	**99.58**
Lithology	Trc chp-bo network									
Texture	Bo-Chp network									
	Calculated Formulae (Ideal formula: Cu_5FeS_4)									
S	4.11	4.08	4.04	4.10	4.08	4.07	4.09	4.07	4.03	4.11
Cu	4.89	4.93	4.93	4.90	4.92	4.94	4.88	4.93	4.96	4.90
Pb	0.00	0.00	0.00	0.00	0.00	0.00	0.01	0.00	0.00	0.00
Fe	1.01	0.97	1.01	1.00	0.98	0.98	1.01	0.99	1.00	0.99
Bi	0.00	0.00	0.00	0.00	0.00	0.00	0.00	0.01	0.00	0.00
Co	0.00	0.00	0.00	0.00	0.00	0.00	0.00	0.00	0.00	0.00
Ni	0.00	0.00	0.00	0.00	0.00	0.00	0.00	0.00	0.00	0.00
Zn	0.00	0.01	0.01	0.01	0.01	0.01	0.02	0.00	0.01	0.00
Total Metals	**5.89**	**5.92**	**5.96**	**5.90**	**5.92**	**5.93**	**5.91**	**5.93**	**5.97**	**5.89**
Metals/S (Ideal: 1.5)	**1.44**	**1.45**	**1.47**	**1.44**	**1.45**	**1.46**	**1.45**	**1.46**	**1.48**	**1.43**

Bornite compositions in Trc, Bc and Phosc. VI										
	GC1611_SEMD2_4	GC1611_SEMD2_5	GC1611_D2_5	GC1524A_A6	GC1524A_B1	GC1524A_B2	GC1524A_B3	2/GC813/5_A2b_5	2/GC813/5_SEMA_3	GC815_D2_1
S	26.34	26.19	26.34	25.48	25.50	25.57	26.07	25.80	25.29	25.64
Cu	61.67	62.23	62.89	62.21	62.30	61.74	61.72	61.55	62.11	61.62
Pb	0.17	0.00	0.00	0.00	0.00	0.00	0.22	0.18	0.00	0.17
Fe	11.50	11.13	11.29	11.11	10.70	11.15	11.16	11.70	11.28	11.26
Bi	0.00	0.00	0.00	0.00	0.00	0.19	0.00	0.00	0.00	0.26
Co	0.00	0.00	0.00	0.00	0.00	0.00	0.00	0.00	0.00	0.00
Ni	0.00	0.00	0.00	0.00	0.00	0.00	0.00	0.00	0.00	0.00
Zn	0.00	0.11	0.12	0.00	0.00	0.00	0.00	0.00	0.00	0.00
Total	**99.87**	**99.69**	**100.75**	**98.94**	**98.58**	**98.68**	**99.25**	**99.23**	**98.68**	**98.98**
Lithology	Trc chp-bo network							carb		
Texture	Bo-Chp network			chp-Bo				CuFeS assemblage		
					Calculated Formulae (Ideal formula: Cu_5FeS_4)					
S	4.11	4.09	4.08	4.03	4.04	4.05	4.09	4.06	4.01	4.05
Cu	4.86	4.90	4.91	4.96	4.98	4.93	4.89	4.88	4.97	4.92
Pb	0.00	0.00	0.00	0.00	0.00	0.00	0.01	0.00	0.00	0.00
Fe	1.03	1.00	1.00	1.01	0.97	1.01	1.01	1.06	1.03	1.02
Bi	0.00	0.00	0.00	0.00	0.00	0.00	0.00	0.00	0.00	0.01
Co	0.00	0.00	0.00	0.00	0.00	0.00	0.00	0.00	0.00	0.00
Ni	0.00	0.00	0.00	0.00	0.00	0.00	0.00	0.00	0.00	0.00
Zn	0.00	0.01	0.01	0.00	0.00	0.00	0.00	0.00	0.00	0.00
Total Metals	**5.89**	**5.91**	**5.92**	**5.97**	**5.96**	**5.95**	**5.91**	**5.94**	**5.99**	**5.95**
Metals/S (Ideal: 1.5)	**1.43**	**1.45**	**1.45**	**1.48**	**1.47**	**1.47**	**1.44**	**1.47**	**1.50**	**1.47**

Bornite compositions in Trc, Bc and Phosc. VII.										
	GC815_D_2	GC808_B4	GC808_B5	GC808_B6	GC808_2ext_C2	GC808_sema_1	GC808_sema_2	GC808_sema_3	GC817_semB_1	GC817_semB2_1
S	25.63	25.57	25.44	25.90	25.56	25.62	25.81	26.20	25.49	25.84
Cu	61.80	61.51	61.46	60.68	61.84	60.53	60.50	60.83	62.83	62.75
Pb	0.16	0.13	0.19	0.00	0.14	0.00	0.23	0.20	0.00	0.14
Fe	10.74	11.78	12.45	12.09	11.63	12.80	13.40	13.01	10.85	10.84
Bi	0.25	0.00	0.00	0.00	0.00	0.00	0.00	0.18	0.00	0.00
Co	0.00	0.00	0.00	0.00	0.00	0.00	0.00	0.00	0.00	0.00
Ni	0.00	0.00	0.00	0.00	0.00	0.00	0.00	0.00	0.00	0.00
Zn	0.00	0.00	0.00	0.00	0.00	0.00	0.00	0.00	0.00	0.00
Total	**98.58**	**99.07**	**99.73**	**98.81**	**99.30**	**99.16**	**100.00**	**100.45**	**99.27**	**99.65**
Lithology	Carb	Trc-chp rich							Carb	
Texture	CuFeS assemblage	irreg exsol in chp							Dissem	
	Calculated Formulae (Ideal formula: Cu_5FeS_4)									
S	4.06	4.03	4.00	4.08	4.03	4.03	4.03	4.07	4.02	4.05
Cu	4.95	4.90	4.87	4.83	4.92	4.81	4.77	4.77	5.00	4.97
Pb	0.00	0.00	0.00	0.00	0.00	0.00	0.01	0.00	0.00	0.00
Fe	0.98	1.07	1.12	1.09	1.05	1.16	1.20	1.16	0.98	0.98
Bi	0.01	0.00	0.00	0.00	0.00	0.00	0.00	0.00	0.00	0.00
Co	0.00	0.00	0.00	0.00	0.00	0.00	0.00	0.00	0.00	0.00
Ni	0.00	0.00	0.00	0.00	0.00	0.00	0.00	0.00	0.00	0.00
Zn	0.00	0.00	0.00	0.00	0.00	0.00	0.00	0.00	0.00	0.00
Total Metals	**5.94**	**5.97**	**6.00**	**5.92**	**5.97**	**5.97**	**5.97**	**5.93**	**5.98**	**5.95**
Metals/S (Ideal: 1.5)	**1.46**	**1.48**	**1.50**	**1.45**	**1.48**	**1.48**	**1.48**	**1.46**	**1.49**	**1.47**

Bornite compositions in Trc, Bc and Phosc. VIII						
	P03_phosc_F3_1	P03_phosc_ext1_1	P03_phosc_ext1_2	P03_phosc_semLb_2	P03_phosc_semLc_1	P03_phosc_semLc_2
S	26.03	25.58	26.21	27.52	26.50	26.82
Cu	61.26	61.85	60.59	58.87	60.36	60.04
Pb	0.22	0.00	0.00	0.00	0.22	0.00
Fe	11.94	11.20	11.43	11.90	11.43	11.43
Bi	0.00	0.16	0.17	0.00	0.17	0.00
Co	0.00	0.00	0.00	0.00	0.00	0.00
Ni	0.00	0.00	0.00	0.00	0.00	0.00
Zn	0.00	0.00	0.00	0.00	0.00	0.00
Total	**99.45**	**98.88**	**98.51**	**98.54**	**98.68**	**98.55**
Lithology	phoscorite					
Texture	CuFeS assemblage					
	Calculated Formulae (Ideal formula: Cu_5FeS_4)					
S	4.08	4.04	4.14	4.30	4.17	4.21
Cu	4.84	4.94	4.82	4.64	4.79	4.76
Pb	0.01	0.00	0.00	0.00	0.01	0.00
Fe	1.07	1.02	1.04	1.07	1.03	1.03
Bi	0.00	0.00	0.00	0.00	0.00	0.00
Co	0.00	0.00	0.00	0.00	0.00	0.00
Ni	0.00	0.00	0.00	0.00	0.00	0.00
Zn	0.00	0.00	0.00	0.00	0.00	0.00
Total Metals	**5.92**	**5.96**	**5.86**	**5.70**	**5.83**	**5.79**
Metals/S (Ideal: 1.5)	**1.45**	**1.47**	**1.42**	**1.33**	**1.40**	**1.37**

Troilite compositions of the transgressive carbonatite I.										
	PA25_E4	PA25_E5	PA25_E1	PA25_E2	PA25_E3	GC1610_A_1	GC1610_A_2	GC1610_A_3	GC1610_D_7	GC1610_D_8
S	36.54	36.55	36.38	36.49	36.60	36.50	36.71	36.60	36.57	36.60
Cu	0.00	0.00	0.00	0.00	0.00	0.00	0.00	0.00	0.00	0.00
Pb	0.22	0.00	0.00	0.16	0.36	0.27	0.24	0.18	0.16	0.36
Fe	62.31	62.08	56.07	55.73	55.36	62.56	62.93	62.92	63.01	62.64
Bi	0.00	0.00	0.00	0.00	0.00	0.00	0.00	0.00	0.20	0.00
Co	0.00	0.00	5.18	5.53	5.38	0.00	0.00	0.00	0.00	0.00
Ni	0.00	0.00	0.63	0.58	0.91	0.00	0.00	0.00	0.00	0.00
Zn	0.09	0.00	0.00	0.00	0.00	0.00	0.00	0.21	0.00	0.00
Total	99.31	98.96	98.56	98.73	98.76	99.40	100.00	100.03	100.07	99.75
Lithology	trc-chp	trc-chp	trc-chp	trc-chp	trc-chp	trc-chp	trc-chp	trc-chp	trc-chp	trc-chp
Texture	flames at carbonate contact		stringers in massive chp			extensive anhedral patches in massive chp				
	Calculated formulae ($Fe_{1-x}S$; x=0 - 0.17)									
S	1.14	1.14	1.13	1.14	1.14	1.14	1.14	1.14	1.14	1.14
Cu	0.00	0.00	0.00	0.00	0.00	0.00	0.00	0.00	0.00	0.00
Pb	0.00	0.00	0.00	0.00	0.00	0.00	0.00	0.00	0.00	0.00
Fe	1.12	1.11	1.00	1.00	0.99	1.12	1.13	1.13	1.13	1.12
Bi	0.00	0.00	0.00	0.00	0.00	0.00	0.00	0.00	0.00	0.00
Co	0.00	0.00	0.09	0.09	0.09	0.00	0.00	0.00	0.00	0.00
Ni	0.00	0.00	0.01	0.01	0.02	0.00	0.00	0.00	0.00	0.00
Zn	0.00	0.00	0.00	0.00	0.00	0.00	0.00	0.00	0.00	0.00
Total Metals	1.12	1.11	1.10	1.10	1.10	1.12	1.13	1.13	1.13	1.12
Metal/S	0.98	0.98	0.97	0.97	0.96	0.99	0.99	0.99	0.99	0.98

Troilite compositions of the transgressive carbonatite					
	GC1610_D_9	GC1610_A2_3	GC1610_A2_4	GC1610_A2_5	GC1610_semD_5
S	36.89	36.63	36.72	36.90	36.73
Cu	0.00	0.00	0.00	0.00	0.00
Pb	0.19	0.00	0.15	0.00	0.00
Fe	62.18	62.73	62.30	61.77	63.87
Bi	0.00	0.00	0.00	0.21	0.13
Co	0.00	0.00	0.00	0.00	0.00
Ni	0.00	0.00	0.00	0.00	0.00
Zn	0.00	0.10	0.18	0.08	0.21
Total	99.39	99.57	99.48	99.08	101.01
Lithology	trc-chp	trc-chp	trc-chp	trc-chp	trc-chp
Texture	extensive anhedral patches in massive chp				
	Calculated formulae ($Fe_{1-x}S$; x=0 - 0.17)				
S	1.15	1.14	1.14	1.15	1.15
Cu	0.00	0.00	0.00	0.00	0.00
Pb	0.00	0.00	0.00	0.00	0.00
Fe	1.11	1.12	1.12	1.11	1.14
Bi	0.00	0.00	0.00	0.00	0.00
Co	0.00	0.00	0.00	0.00	0.00
Ni	0.00	0.00	0.00	0.00	0.00
Zn	0.00	0.00	0.00	0.00	0.00
Total Metals	1.11	1.12	1.12	1.11	1.15
Metal/S	0.97	0.98	0.98	0.96	1.00

Sphalerite in transgressive carbonatite I.									
	Pb2_sphl1	Pb2_sphl2	Pb2_sphl3	Pb2_sphl4	Pb1_sphl1	Pb1_sphl2	Pb1_sphl3	Pb1_sphl4	Pb1_sphl5
S	34.09	34.11	33.59	33.92	33.87	33.51	33.85	33.76	33.53
Cu	0.00	0.00	0.00	0.00	0.00	0.00	0.00	0.00	0.00
Pb	0.17	0.00	0.00	0.14	0.15	0.00	0.00	0.00	0.00
Fe	0.74	1.50	0.71	1.41	0.57	0.79	0.87	0.69	0.83
Bi	0.00	0.00	0.00	0.00	0.00	0.00	0.00	0.00	0.00
Co	0.14	0.12	0.16	0.08	0.14	0.18	0.21	0.14	0.20
Ni	0.00	0.00	0.00	0.00	0.00	0.00	0.00	0.00	0.00
Zn	65.55	64.90	64.83	65.31	65.73	65.94	64.30	65.21	65.95
Total	100.75	100.73	99.28	100.91	100.48	100.48	99.32	100.00	100.58
Lithology	trc-chp block	trc-chp block	trc-chp block	trc-chp block	trc- bo rich	trc- bo rich	trc- bo rich	trc- bo rich	trc- bo rich
Texture	Large, anhedral sphalerite grains at chp contact towards non-silicate phases.				Large anhedral sphalerites at edges				
	Calculated Formulae (Ideal formulae: (Zn,Fe)S)								
S	1.06	1.06	1.05	1.06	1.06	1.04	1.06	1.05	1.05
Cu	0.00	0.00	0.00	0.00	0.00	0.00	0.00	0.00	0.00
Pb	0.00	0.00	0.00	0.00	0.00	0.00	0.00	0.00	0.00
Fe	0.01	0.03	0.01	0.03	0.01	0.01	0.02	0.01	0.01
Bi	0.00	0.00	0.00	0.00	0.00	0.00	0.00	0.00	0.00
Co	0.00	0.00	0.00	0.00	0.00	0.00	0.00	0.00	0.00
Ni	0.00	0.00	0.00	0.00	0.00	0.00	0.00	0.00	0.00
Zn	1.00	0.99	0.99	1.00	1.01	1.01	0.98	1.00	1.01
Total Metals	1.02	1.02	1.01	1.03	1.02	1.03	1.00	1.01	1.03
Metal/S	0.96	0.96	0.96	0.97	0.96	0.98	0.95	0.96	0.98

Sphalerite in transgressive carbonatite										
	Pb1_sphl6	PA25_B1	PA25_B2	PA25_B3	PA25_B4	PA15_A2_2	GC1610_B_6	GC1610_B_7	GC1611_D2_1	GC1611_D2_2
S	33.61	33.98	33.68	34.05	33.58	33.84	33.93	33.78	34.07	34.07
Cu	0.00	0.13	0.15	0.20	0.29	0.00	0.00	0.22	1.07	1.06
Pb	0.17	0.25	0.18	0.00	0.23	0.00	0.00	0.00	0.15	0.00
Fe	0.78	6.95	6.87	7.39	7.04	6.86	7.01	7.87	2.27	2.14
Bi	0.00	0.13	0.00	0.21	0.18	0.13	0.00	0.15	0.00	0.00
Co	0.20	0.00	0.00	0.00	0.00	1.20	0.00	0.00	0.00	0.00
Ni	0.09	0.00	0.00	0.00	0.00	0.20	0.00	0.00	0.00	0.00
Zn	65.27	58.44	58.34	57.46	58.22	56.25	58.66	57.25	63.79	63.87
Total	100.24	100.00	99.42	99.49	99.59	98.51	99.95	99.45	101.43	101.28
Lithology	trc- bo rich	trc-chp	trc-chp	trc-chp	trc-chp	trc-chp	trc-chp	trc-chp	trc chp-bo network	trc chp-bo network
Texture	Large anhedral sphalerites at edges	Myrmekite-res./star sphalerite in masive chp				Sphalerite grain in euhedral Co-ptl in massive chp	Small anhedral grain in massive chp- exsolution ~ 100 µm		Small anhedral grain in masisve chp- exsolution ~ 100 µm	
	Calculated Formulae (Ideal formulae: (Zn,Fe)S)									
S	1.05	1.06	1.05	1.06	1.05	1.06	1.06	1.05	1.06	1.06
Cu	0.00	0.00	0.00	0.00	0.00	0.00	0.00	0.00	0.02	0.02
Pb	0.00	0.00	0.00	0.00	0.00	0.00	0.00	0.00	0.00	0.00
Fe	0.01	0.12	0.12	0.13	0.13	0.12	0.13	0.14	0.04	0.04
Bi	0.00	0.00	0.00	0.00	0.00	0.00	0.00	0.00	0.00	0.00
Co	0.00	0.00	0.00	0.00	0.00	0.02	0.00	0.00	0.00	0.00
Ni	0.00	0.00	0.00	0.00	0.00	0.00	0.00	0.00	0.00	0.00

Zn	1.00	0.89	0.89	0.88	0.89	0.86	0.90	0.88	0.98	0.98
Total Metals	1.02	1.02	1.02	1.02	1.02	1.01	1.02	1.02	1.03	1.03
Metal/S	0.97	0.96	0.97	0.96	0.98	0.95	0.97	0.97	0.97	0.97

Cu-S phases in Trc and Phosc														
	2Pb5_di4	ε	2Pb5_di5	ε	2PB3_C2_7	ε	2/GC813/5_A2b_1	ε	2/GC813/5_A3	ε	GC815_D_4	ε	6A_SEMc_2	ε
S (wt%)	22.80	1.32	22.92	1.32	22.96	2.14	21.86	1.35	20.41	1.40	21.09	1.37	22.52	1.35
Cu (wt%)	76.80	0.58	76.92	0.58	75.63	0.86	76.98	0.55	78.23	0.54	77.51	0.54	75.91	0.55
Error cor. Total	99.60		99.84		98.59		98.84		98.64		98.60		98.43	
Lithology	TRc-Bo-rich		TRc-Bo-rich		TRc-Bo-rich		Phosc		Phosc		Phosc		BC	
Texture	Thick lamellae		Thick lamellae		Thick lamellae		Thick lamellae		Thinner irregular network in assemblage		Lamellae		Grain near Bo	
Calculated formulae (Ideal formulae: Cu_9S_5, Ideal Metal/S=1.8)														
S	5.18		5.20		5.26		5.04		4.77		4.90		5.18	
Cu	8.82		8.80		8.74		8.96		9.23		9.10		8.82	
Metal/S	1.70		1.69		1.66		1.78		1.93		1.85		1.70	

Cobalt pentlandite in Trc											
	PTC3_C1	PTC3_C2	PTC3_C3	PTC3_C4	PTC3_C5	PTC3_C9	PTC3_B1	PTC3_B2	PTC3_2B_1	PTC3_2B_2	PTC3_2B_9
S	33.76	33.69	33.39	33.41	33.57	33.75	33.46	33.21	33.43	33.44	32.91
Pb	0.23	0.00	0.20	0.18	0.28	0.13	0.00	0.33	0.22	0.28	0.14
Fe	18.94	18.47	17.63	16.42	19.48	19.32	16.96	18.04	18.73	18.13	16.83
Bi	0.00	0.00	0.00	0.00	0.00	0.00	0.00	0.00	0.00	0.00	0.00
Co	26.50	27.30	28.17	29.78	26.22	27.44	28.96	29.20	27.98	29.34	28.48
Ni	20.49	20.21	20.46	19.58	19.74	19.80	19.89	18.38	18.89	18.45	20.54
Zn	0.00	0.00	0.00	0.00	0.00	0.00	0.00	0.00	0.00	0.00	0.00
Total	99.92	99.80	99.85	99.37	99.28	100.44	99.40	99.14	99.25	99.64	98.91
Error corrected totals	99.69	99.80	99.65	99.19	99.00	100.31	99.40	98.82	99.03	99.36	98.77
Calculated Formulae (ideal formulae $(Fe,Ni,Co)_9S_8$											
S	8.2	8.2	8.1	8.1	8.2	8.1	8.1	8.1	8.1	8.1	8.1
Cu	0.0	0.0	0.0	0.0	0.0	0.0	0.0	0.0	0.0	0.0	0.0
Pb	0.0	0.0	0.0	0.0	0.0	0.0	0.0	0.0	0.0	0.0	0.0
Fe	2.6	2.6	2.5	2.3	2.7	2.7	2.4	2.5	2.6	2.5	2.4
Co	3.5	3.6	3.7	3.9	3.5	3.6	3.8	3.9	3.7	3.9	3.8
Ni	2.7	2.7	2.7	2.6	2.6	2.6	2.6	2.5	2.5	2.5	2.8
Sum Cations	8.8	8.8	8.9	8.9	8.8	8.9	8.9	8.9	8.9	8.9	8.9

Cobalt pentlandite in Trc										
	PTC3_2B_10	PTC3_2C_1	PTC3_2C_2	PTC3_2C_3	PTC3_2C_11	PTC3_2C_12	GC1611_B_5	2/GC813/5_A2b_9	Pa2a_4	Pa2a_5
S	33.83	33.84	33.56	33.37	33.17	33.48	33.30	32.74	33.71	34.00
Pb	0.18	0.20	0.28	0.00	0.00	0.24	0.30	0.00	0.15	0.29
Fe	17.19	18.93	20.01	18.74	18.77	18.72	18.48	17.46	23.25	21.79
Bi	0.00	0.00	0.00	0.00	0.00	0.00	0.00	0.00	0.00	0.24
Co	28.48	27.64	25.49	27.22	27.55	28.03	30.61	33.76	24.34	24.20
Ni	20.11	19.21	20.90	19.78	19.26	18.97	17.21	14.37	18.87	20.53
Zn	0.00	0.00	0.00	0.00	0.00	0.00	0.00	0.00	0.00	0.00
Total	99.80	99.83	100.24	99.23	98.89	99.44	99.99	98.57	100.39	101.09
Error corrected totals	99.62	99.63	99.96	99.23	98.89	99.20	99.70	98.57	100.24	100.56
				Type I				Type III	Type I	
					Calculated Formulae (ideal formulae $(Fe,Ni,Co)_9S_8$					
S	8.2	8.2	8.1	8.1	8.1	8.1	8.1	8.1	8.1	8.1
Cu	0.0	0.0	0.0	0.0	0.0	0.0	0.0	0.0	0.0	0.0
Pb	0.0	0.0	0.0	0.0	0.0	0.0	0.0	0.0	0.0	0.0
Fe	2.4	2.6	2.8	2.6	2.6	2.6	2.6	2.5	3.2	3.0
Co	3.8	3.6	3.4	3.6	3.7	3.7	4.0	4.5	3.2	3.2
Ni	2.7	2.5	2.8	2.6	2.6	2.5	2.3	1.9	2.5	2.7
Sum Cations	8.8	8.8	8.9	8.9	8.9	8.9	8.9	8.9	8.9	8.9

Cobalt pentlandite in Trc											
	Pa2a_6	Pa15_A1	Pa15_A2	Pb2_ptl1	Pb2_ptl2	Pb2_ptl3	Pb2_ptl4	Pb2_ptl5	Pb2_ptl6	Pb2_ptl7	Pb1_ptl4
S	33.92	33.37	33.23	33.54	33.56	33.27	33.38	33.43	33.85	33.45	33.35
Pb	0.15	0.19	0.00	0.23	0.13	0.16	0.14	0.22	0.18	0.23	0.15
Fe	23.82	9.62	8.10	14.25	13.87	14.12	13.90	14.44	14.31	13.98	13.16
Bi	0.00	0.00	0.00	0.00	0.00	0.00	0.00	0.00	0.00	0.00	0.00
Co	23.79	47.55	49.36	34.06	34.92	34.08	34.90	33.41	33.50	34.34	29.94
Ni	18.93	8.13	7.81	18.33	18.37	19.22	18.49	19.37	19.53	18.94	24.20
Zn	0.00	0.00	0.00	0.00	0.00	0.00	0.00	0.00	0.00	0.00	0.00
Total	100.69	98.87	98.60	100.42	100.91	100.85	100.83	100.88	101.44	100.94	100.80
Error corrected totals	100.55	98.68	98.60	100.19	100.78	100.69	100.69	100.65	101.26	100.71	100.65
Type I											
Calculated Formulae (ideal formulae $(Fe,Ni,Co)_9S_8$											
S	8.1	8.2	8.2	8.1	8.1	8.0	8.1	8.1	8.1	8.1	8.0
Cu	0.0	0.0	0.0	0.0	0.0	0.0	0.0	0.0	0.0	0.0	0.0
Pb	0.0	0.0	0.0	0.0	0.0	0.0	0.0	0.0	0.0	0.0	0.0
Fe	3.3	1.4	1.1	2.0	1.9	2.0	1.9	2.0	2.0	1.9	1.8
Co	3.1	6.4	6.6	4.5	4.6	4.5	4.6	4.4	4.4	4.5	3.9
Ni	2.5	1.1	1.1	2.4	2.4	2.5	2.4	2.6	2.6	2.5	3.2
Sum Cations	8.9	8.8	8.8	8.9	8.9	9.0	8.9	8.9	8.9	8.9	9.0

Cobalt pentlandite in Trc											
	Pb1_ptl5	Pb1_ptl6	Pb1_ptl7	Pb1_ptl8	Pb1_ptl9	Pb1_ptl10	Pb1_ptl14	GC1610_A_7	GC1610_A_8	GC1610_A_9	GC1610_B2_1
S	33.34	33.33	33.32	33.53	33.51	33.88	33.44	33.26	33.24	33.10	33.06
Pb	0.23	0.15	0.16	0.23	0.21	0.00	0.14	0.17	0.19	0.00	0.00
Fe	12.87	12.75	12.73	12.42	12.75	14.39	14.27	17.39	17.34	17.68	16.97
Bi	0.00	0.00	0.00	0.00	0.00	0.00	0.00	0.16	0.21	0.00	0.00
Co	31.28	31.59	32.03	32.24	31.89	31.28	30.46	40.46	40.69	39.07	41.42
Ni	22.68	22.94	22.52	22.58	22.74	21.37	22.41	8.66	8.83	9.42	8.07
Zn	0.00	0.00	0.00	0.00	0.00	0.00	0.00	0.00	0.00	0.00	0.00
Total	100.40	100.85	100.80	101.02	101.10	101.05	100.72	100.12	100.52	99.53	99.75
Error corrected totals	100.17	100.71	100.63	100.79	100.89	101.05	100.58	99.80	100.13	99.53	99.75
				Type I						Type II	
				Calculated Formulae (ideal formulae $(Fe,Ni,Co)_9S_8$							
S	8.1	8.0	8.0	8.1	8.1	8.1	8.1	8.1	8.0	8.1	8.1
Cu	0.0	0.0	0.0	0.0	0.0	0.0	0.0	0.0	0.0	0.0	0.0
Pb	0.0	0.0	0.0	0.0	0.0	0.0	0.0	0.0	0.0	0.0	0.0
Fe	1.8	1.8	1.8	1.7	1.8	2.0	2.0	2.4	2.4	2.5	2.4
Co	4.1	4.2	4.2	4.2	4.2	4.1	4.0	5.3	5.4	5.2	5.5
Ni	3.0	3.0	3.0	3.0	3.0	2.8	3.0	1.1	1.2	1.3	1.1
Sum Cations	8.9	9.0	9.0	8.9	8.9	8.9	8.9	8.9	9.0	8.9	8.9

Cobalt pentlandite in Trc								
	GC1610_D_1	GC1610_D_2	GC1610_A2_1	GC1610_A2_2	GC1610_semD_1	GC1610_semD_2	GC1811A_B_10	GC1611_B_3
S	33.62	33.19	32.92	33.37	33.41	33.46	33.66	33.56
Pb	0.24	0.14	0.26	0.17	0.23	0.16	0.21	0.15
Fe	17.10	17.62	15.84	13.29	14.09	16.12	22.98	12.34
Bi	0.00	0.00	0.15	0.14	0.00	0.00	0.00	0.00
Co	40.09	39.46	42.38	46.96	44.72	42.21	13.04	44.75
Ni	9.44	9.45	7.20	5.76	7.08	8.33	30.60	9.90
Zn	0.10	0.00	0.00	0.20	0.00	0.11	0.00	0.00
Total	100.70	99.89	98.83	99.89	99.62	100.44	100.58	100.80
Error corrected totals	100.36	99.75	98.42	99.38	99.40	100.17	100.37	100.66
				Type II				
				Calculated Formulae/ Ideal formula: $(Fe,Ni,Co)_9S_8$				
S	8.1	8.1	8.1	8.1	8.1	8.1	8.1	8.1
Cu	0.0	0.0	0.0	0.0	0.0	0.0	0.0	0.0
Pb	0.0	0.0	0.0	0.0	0.0	0.0	0.0	0.0
Fe	2.4	2.5	2.2	1.9	2.0	2.2	3.2	1.7
Co	5.3	5.2	5.7	6.2	5.9	5.6	1.7	5.9
Ni	1.2	1.3	1.0	0.8	0.9	1.1	4.0	1.3
Sum Cations	8.9	8.9	8.9	8.9	8.9	8.9	8.9	8.9

Appendix 2: The results of the LA-ICPMS standard analyses during the two analysis days

Standard ID:		Mem Po724	Mem Po724b	UQAC FeS	UQAC FeS-b	uqac_FeS_1	Mem Po724T2	Mem Po724T2b	UQAC FEs1	UQAC FEs2	UQAC_FEs3error	UQAC_FEs3
		Measurements during analysis day 1					Measurements during analysis day 2					
33S	wt%	38.0	38.0	40.0	40.0	40.0	38.0	38.0	40.0	40.0	40.0	40.0
57Fe	wt%	61.88	59.82	43.69	44.25	43.68	61.55	60.49	45.79	45.20	44.48	44.88
59Co	ppm	8	8	728	710	668	8	8	761	704	693	647
60Ni	wt%	<0.005	<0.005	2.616	2.650	2.595	<0.005	<0.005	2.562	2.761	2.983	2.790
65Cu	wt%	<0.005	<0.005	2.441	2.354	2.205	<0.005	<0.005	2.392	2.303	2.260	2.166
66Zn	ppm	<9	<9	226	287	315	<10	<10	330	270	259	315
75As	ppm	<1.5	<1.5	1077.5	1167.3	980.7	<1.8	<1.8	1080.9	1154.8	979.0	1106.5
77Se	ppm	<9	<9	305	336	292	<9	<9	264	285	270	329
99Ru*	ppm	32.23	30.81	70.63	76.70	68.57	33.62	30.02	64.38	71.05	76.94	71.29
101Ru*	ppm	31.38	29.75	70.03	76.26	68.14	32.71	29.56	63.53	70.24	76.92	69.67
103Rh*	ppm	37.54	35.46	70.12	66.98	63.20	36.34	34.71	62.19	69.44	72.18	68.11
105Pd*	ppm	50.61	47.31	61.40	60.77	63.02	48.06	46.04	57.68	59.19	51.99	59.29
106Pd*	ppm	51.81	47.48	62.74	58.71	62.76	48.75	46.22	55.57	58.24	56.79	57.37
108Pd*	ppm	51.24	47.26	61.91	60.68	63.00	48.70	46.91	59.77	60.92	58.08	60.33
109Ag	ppm	<0.21	<0.21	155.67	162.05	161.36	<0.26	<0.26	163.81	154.69	177.65	154.57
111Cd	ppm	<0.29	<0.29	1.23	1.81	1.26	<0.35	<0.35	1.88	2.10	2.06	2.09
121Sb	ppm	<0.17	<0.17	103.87	93.26	93.43	<0.19	<0.19	104.31	119.18	119.93	100.76
125Te	ppm	<0.20	<0.20	158.99	149.62	159.84	<0.22	<0.22	159.31	139.64	150.05	157.87
185Re	ppm	<0.02	<0.02	78.85	80.09	79.04	<0.03	<0.03	77.18	74.62	70.30	77.81
189Os	ppm	35.08	32.82	90.07	90.47	89.38	37.16	38.94	108.91	103.85	101.06	98.97
193Ir	ppm	35.40	33.56	63.24	65.05	61.03	37.09	36.17	67.92	64.83	63.67	67.71
195Pt	ppm	36.56	34.70	55.64	61.04	52.43	40.50	41.13	58.58	58.07	49.60	60.95
197Au	ppm	48.91	42.82	68.81	67.90	66.68	42.31	47.43	72.96	70.36	56.51	76.06
206Pb	ppm	<2.8	<2.8	76.9	88.8	82.6	<3.9	<3.9	79.6	79.5	60.6	75.3
209Bi	ppm	<0.04	<0.04	117.59	123.57	120.66	<0.04	<0.04	117.53	118.84	123.03	120.91

Standard ID:		PO724-T expected	UQAC expected	PO724-T expected	UQAC expected
		Measurements during analysis day 1		Measurements during analysis day 2	
33S	wt%	38.0	40.0	38.0	40.0
57Fe	wt%	62.00	45.00	62.00	45.00
59Co	ppm	nda	637	nda	637
60Ni	wt%	0.00	2.50	0.00	2.50
65Cu	wt%	nda	2.30	nda	2.30
66Zn	ppm	nda	275	nda	275
75As	ppm	nda	1050.0	nda	1050.0
77Se	ppm	nda	310.0	nda	310.0
99Ru*	ppm	31.00	65.00	31.00	65.00
101Ru*	ppm	31.00	65.00	31.00	65.00
103Rh*	ppm	35.80	64.00	35.80	64.00
105Pd*	ppm	48.90	60.00	48.90	60.00
106Pd*	ppm	48.90	60.00	48.90	60.00
108Pd*	ppm	48.90	60.00	48.90	60.00
109Ag	ppm	nda	155.0	nda	155.0
111Cd	ppm	nda	2.0	nda	2.0
121Sb	ppm	nda	88.00	nda	88.00
125Te	ppm	nda	170.00	nda	170.00
185Re	ppm	nda	70.00	nda	70.00
189Os	ppm	36.50	75.00	36.50	75.00
193Ir	ppm	34.00	60.00	34.00	60.00
195Pt	ppm	38.70	50.00	38.70	50.00
197Au	ppm	45.80	65.00	45.80	65.00
206Pb	ppm	nda	90.0	nda	90.0
209Bi	ppm	nda	120.00	nda	120.00

Appendix 3: Mantle melting models: Major element modelling: Starting and melt fraction compositions

1. Phlogopite wehrlite melt fraction compositions

1.a: The table shows the starting compositions (bold-blue) and the calculated compositions of the individual melt fractions.

Veined-phlogopite wehrlite model compositions (PW_M) (for major element modelling)										
	Dolomite	Apatite	Phlogopite	Clinopyroxene	Olivine	Cpx/Ol	S	M	C	$CO_2(+P_2O_5)$
	modal%						weight%			
1	**2.5**	**2.5**	**5**	**50**	**40**	**1.3**	**48.40**	**34.82**	**14.52**	**2.26**
F1=0.01	1.00						0.00	20.20	32.37	47.43
F2=0.06	1.50	2.50	1.00				9.40	13.91	39.36	37.33
F3=0.11			4.30	0.70			30.51	21.07	26.90	21.51
F4=0.16				5.00			39.31	20.45	25.74	14.50
F5=0.21				5.00			43.79	20.13	25.15	10.94
F6=0.26				5.00			46.49	19.93	24.79	8.78
F7=0.31				5.00			48.31	19.81	24.55	7.33
F8=0.36				5.00			49.61	19.71	24.38	6.30
F9=0.41				5.00			50.59	19.64	24.25	5.52
F10=0.46				5.00			51.36	19.59	24.15	4.91
F11=0.51				5.00			51.97	19.54	24.07	4.42
2	**2.5**	**2.5**	**5**	**30**	**60**	**0.5**	**45.20**	**42.69**	**9.83**	**2.28**
F1=0.01	1.00						0.00	20.20	32.37	47.43
F2=0.06	1.50	2.50	1.00				9.40	13.91	39.36	37.33
F3=0.11			4.30	0.70			30.51	21.07	26.90	21.51
F4=0.16				5.00			39.31	20.45	25.74	14.50

F5=0.21				5.00			43.79	20.13	25.15	10.94
F6=0.26				5.00			46.49	19.93	24.79	8.78
F7=0.31				5.00			48.31	19.81	24.55	7.33
F8=0.36				5.00			49.61	19.71	24.38	6.30
F9=0.41				5.00			50.59	19.64	24.25	5.52
F10=0.46				5.00			51.36	19.59	24.15	4.91
F11=0.51				5.00			51.97	19.54	24.07	4.42
3	**2.5**	**2.5**	**5**	**10**	**80**	**0.1**	**41.96**	**50.66**	**5.09**	**2.29**
F1=0.01	1.00						0.00	20.20	32.37	47.43
F2=0.06	1.50	2.50	1.00				9.40	13.91	39.36	37.33
F3=0.11			4.30	0.70			30.51	21.07	26.90	21.51
F4=0.16				5.00			39.31	20.45	25.74	14.50
F5=0.21				5.00			43.79	20.13	25.15	10.94
F6=0.26				5.00			46.49	19.93	24.79	8.78
F7=0.31				5.00			48.31	19.81	24.55	7.33
F8=0.36				3.50	1.50		48.95	21.33	23.41	6.30
F9=0.41					50.00		44.74	42.75	9.86	2.65
F10=0.46					50.00		43.62	48.46	6.25	1.68
F11=0.51					50.00		43.10	51.10	4.58	1.23
4	**2.5**	**2.5**	**15**	**40**	**40**	**1.0**	**48.44**	**36.27**	**12.98**	**2.30**
F1=0.01	1.00						0	20.2	32.37	47.43
F2=0.06	1.50	2.50	1.00				9.4	13.91	39.36	37.33
F3=0.11			5.00				30.37	21.9	26.01	21.72
F4=0.16			5.00				38.97	25.18	20.53	15.32
F5=0.21			5.00				43.65	26.97	17.55	11.83
F6=0.26			1.00	4.00			46.57	25.87	18.16	9.4
F7=0.31				5.00			48.48	24.7	19.06	7.76
F8=0.36				5.00			49.82	23.87	19.7	6.61

F9=0.41				5.00			50.82	23.26	20.17	5.75
F10=0.46				5.00			51.58	22.79	20.53	5.1
F11=0.51				5.00			52.19	22.42	20.82	4.57
5	**2.5**	**2.5**	**15**	**20**	**60**	**0.3**	**45.19**	**44.28**	**8.22**	**2.31**
F1=0.01	1.00						0.00	20.20	32.37	47.43
F2=0.06	1.50	2.50	1.00				9.40	13.91	39.36	37.33
F3=0.11			5.00				30.37	21.90	26.01	21.72
F4=0.16			5.00				38.97	25.18	20.53	15.32
F5=0.21			5.00				43.65	26.97	17.55	11.83
F6=0.26			4.00	1.00			46.59	27.53	16.31	9.58
F7=0.31				5.00			48.53	26.04	17.55	7.88
F8=0.36				5.00			49.88	25.01	18.42	6.70
F9=0.41				5.00			50.88	24.24	19.06	5.82
F10=0.46				5.00			51.65	23.65	19.56	5.15
F11=0.51				5.00			52.25	23.19	19.95	4.61
6	**2.5**	**2.5**	**10**	**15**	**70**	**0.2**	**43.57**	**47.48**	**6.65**	**2.30**
F1=0.01	1.00						0.00	20.20	32.37	47.43
F2=0.06	1.50	2.50	1.00				9.40	13.91	39.36	37.33
F3=0.11			5.00				30.37	21.90	26.01	21.72
F4=0.16			5.00				38.97	25.18	20.53	15.32
F5=0.21				5.00			43.72	23.64	21.25	11.40
F6=0.26				5.00			46.53	22.72	21.67	9.07
F7=0.31				5.00			48.39	22.12	21.95	7.54
F8=0.36				2.70	2.30		48.67	24.24	20.64	6.46
F9=0.41					5.00		47.81	28.45	18.09	5.66
F10=0.46					5.00		47.13	31.74	16.10	5.04
F11=0.51					5.00		46.59	34.37	14.50	4.54
7	**5**		**5**	**10**	**80**	**0.1**	**41.81**	**51.09**	**4.51**	**2.59**

F1=0.01	1.00						0	20.2	32.37	47.43
F2=0.06	4.00		1.00				8.25	21.98	28.91	40.86
F3=0.11			4.30	0.70			29.4	25.64	21.06	23.9
F4=0.16				5.00			38.44	23.56	21.78	16.22
F5=0.21				5.00			43.07	22.49	22.16	12.28
F6=0.26				0.80	4.20		43.31	28.13	18.64	9.92
F7=0.31					5.00		43.04	32.97	15.65	8.34
F8=0.36					5.00		42.86	36.48	13.49	7.17
F9=0.41					5.00		42.71	39.13	11.86	6.3
F10=0.46					5.00					
F11=0.51					5.00		42.6	41.2	10.57	5.63
8	**10**		**10**	**20**	**60**	**0.3**	**41.95**	**43.90**	**8.98**	**5.17**
F1=0.01	1.00						0.00	20.20	32.37	47.43
F2=0.06	5.00						0.00	20.20	32.37	47.43
F3=0.11	4.40		0.60				2.64	20.77	31.26	45.33
F4=0.16			5.00				18.00	24.08	24.83	33.09
F5=0.21			5.00				26.83	25.98	21.13	26.06
F6=0.26				5.00			32.93	24.62	21.57	20.88
F7=0.31				5.00			37.01	23.72	21.86	17.42
F8=0.36				5.00			39.92	23.07	22.07	14.94
F9=0.41				5.00			42.11	22.58	22.23	13.08
F10=0.46				5.00			43.82	22.20	22.35	11.63
F11=0.51				3.10	1.90		44.59	23.34	21.59	10.48
9	**10**	**10**	**5**	**5**	**70**	**0.1**	**34.78**	**45.26**	**10.87**	**9.10**
F1=0.01	1.00						0.00	20.20	32.37	47.43
F2=0.06	5.00						0.00	20.20	32.37	47.43
F3=0.11	4.30	0.70					0.12	19.04	33.88	46.96
F4=0.16		5.00					0.69	13.52	41.06	44.74

F5=0.21		5.00					1.00	10.51	44.96	43.53
F6=0.26		0.80	4.20				9.20	13.35	40.13	37.33
F7=0.31			1.80	3.20			16.80	14.95	36.72	31.53
F8=0.36				3.20	1.80		21.70	17.47	33.70	27.14
F9=0.41					5.00		24.11	22.39	29.64	23.86
F10=0.46					5.00		26.00	26.25	26.45	21.30
F11=0.51					5.00		27.52	29.36	23.88	19.23
10	**20**		**5**	**5**	**70**	**0.1**	**34.27**	**47.00**	**8.50**	**10.23**
F1=0.01	1.00						0	20.2	32.37	47.43
F2=0.06	5.00						0	20.2	32.37	47.43
F3=0.11	5.00						0	20.2	32.37	47.43
F4=0.16	5.00						0	20.2	32.37	47.43
F5=0.21	5.00						0	20.2	32.37	47.43
F6=0.26	1.00		4.00				7.6	21.84	29.19	41.37
F7=0.31			2.30	2.70			15.12	22.31	27.32	35.25
F8=0.36				4.00	1.00		20.48	22.92	26.16	30.44
F9=0.41					5.00		22.97	27.08	23.08	26.87
F10=0.46					5.00		24.94	30.37	20.66	24.03
F11=0.51					5.00		26.54	33.03	18.69	21.74
11	**10**	**10**	**10**	**10**	**60**	**0.2**	**36.35**	**42.07**	**12.44**	**9.14**
F1=0.01	1.00						0	20.2	32.37	47.43
F2=0.06	5.00						0	20.2	32.37	47.43
F3=0.11	4.30	0.70					0.12	19.04	33.88	46.96
F4=0.16		5.00					0.69	13.52	41.06	44.73
F5=0.21		5.00					1	10.51	44.96	43.53
F6=0.26		0.80	4.20				9.2	13.35	40.13	37.32
F7=0.31			5.00				16.37	16.15	35.47	32.01
F8=0.36			3.00	2.00			21.94	17.57	32.69	27.8

F9=0.41				5.00			26.43	17.77	31.51	24.29
F10=0.46				5.00			29.91	17.93	30.59	21.57
F11=0.51				3.00	2.00		32.04	19.58	28.96	19.42
12	**20**		**10**	**10**	**60**	**0.2**	**35.82**	**43.85**	**10.05**	**10.28**
F1=0.01	1.00						0	20.2	32.37	47.43
F2=0.06	5.00						0	20.2	32.37	47.43
F3=0.11	5.00						0	20.2	32.37	47.43
F4=0.16	5.00						0	20.2	32.37	47.43
F5=0.21	5.00						0	20.2	32.37	47.43
F6=0.26	1.00		4.00				7.6	21.84	29.19	41.37
F7=0.31			5.00				14.75	23.38	26.19	35.68
F8=0.36			4.00	1.00			20.27	24.19	24.3	31.24
F9=0.41				5.00			24.86	23.57	24.18	27.39
F10=0.46				5.00			28.44	23.08	24.09	24.39
F11=0.51				4.00	1.00		31	23.45	23.57	21.98
13	**20**		**10**	**20**	**50**	**0.4**	**37.44**	**39.92**	**12.39**	**10.25**
F1=0.01	1.00						0	20.2	32.37	47.43
F2=0.06	5.00						0	20.2	32.37	47.43
F3=0.11	5.00						0	20.2	32.37	47.43
F4=0.16	5.00						0	20.2	32.37	47.43
F5=0.21	5.00						0	20.2	32.37	47.43
F6=0.26	1.00		4.00				7.6	21.84	29.19	41.37
F7=0.31			5.00				14.75	23.38	26.19	35.68
F8=0.36			4.00	1.00			20.27	24.19	24.3	31.24
F9=0.41				5.00			24.86	23.57	24.18	27.39
F10=0.46				5.00			28.44	23.08	24.09	24.39
F11=0.51				5.00			31.32	22.69	24.02	21.97
14	**10**	**10**	**10**	**20**	**50**	**0.4**	**37.98**	**38.11**	**14.79**	**9.12**

F1=0.01	1.00							0	20.2	32.37	47.43
F2=0.06	5.00							0	20.2	32.37	47.43
F3=0.11	4.30	0.70						0.12	19.04	33.88	46.96
F4=0.16		5.00						0.69	13.52	41.06	44.73
F5=0.21		5.00						1	10.51	44.96	43.53
F6=0.26		0.80	4.20					9.2	13.35	40.13	37.32
F7=0.31			5.00					16.37	16.15	35.47	32.01
F8=0.36			4.00	1.00				21.85	17.91	32.33	27.91
F9=0.41				5.00				26.36	18.07	31.2	24.37
F10=0.46				5.00				29.86	18.19	30.31	21.64
F11=0.51				5.00				32.65	18.29	29.61	19.45
15	**10**	**10**	**10**	**30**	**40**	**0.8**	**39.61**	**34.17**	**17.13**	**9.09**
F1=0.01	1.00							0	20.2	32.37	47.43
F2=0.06	5.00							0	20.2	32.37	47.43
F3=0.11	4.30	0.70						0.12	19.04	33.88	46.96
F4=0.16		5.00						0.69	13.52	41.06	44.73
F5=0.21		5.00						1	10.51	44.96	43.53
F6=0.26		0.80	4.20					9.2	13.35	40.13	37.32
F7=0.31			5.00					16.37	16.15	35.47	32.01
F8=0.36			4.00	1.00				21.85	17.91	32.33	27.91
F9=0.41				5.00				26.36	18.07	31.2	24.37
F10=0.46				5.00				29.86	18.19	30.31	21.64
F11=0.51				5.00				32.65	18.29	29.61	19.45
16	**20**		**10**	**30**	**40**	**0.8**	**39.05**	**36.01**	**14.72**	**10.22**
F1=0.01	1.00							0	20.2	32.37	47.43
F2=0.06	5.00							0	20.2	32.37	47.43
F3=0.11	5.00							0	20.2	32.37	47.43
F4=0.16	5.00							0	20.2	32.37	47.43

F5=0.21	5.00							0	20.2	32.37	47.43
F6=0.26	1.00		4.00					7.6	21.84	29.19	41.37
F7=0.31			5.00					14.75	23.38	26.19	35.68
F8=0.36			4.00	1.00				20.27	24.19	24.3	31.24
F9=0.41				5.00				24.86	23.57	24.18	27.39
F10=0.46				5.00				28.44	23.08	24.09	24.39
F11=0.51				5.00				31.32	22.69	24.02	21.97
17	**15**		**5**	**40**	**40**	**1.0**		**42.13**	**35.28**	**14.95**	**7.64**
F1=0.01	1.00							0.00	20.20	32.37	47.43
F2=0.06	5.00							0.00	20.20	32.37	47.43
F3=0.11	5.00							0.00	20.20	32.37	47.43
F4=0.16	5.00							0.00	20.20	32.37	47.43
F5=0.21			5.00					11.96	22.78	27.36	37.90
F6=0.26			1.00	4.00				20.48	22.56	26.09	30.87
F7=0.31				5.00				26.42	22.01	25.65	25.92
F8=0.36				5.00				30.72	21.62	25.33	22.33
F9=0.41				5.00				33.97	21.32	25.09	19.62
F10=0.46				5.00				36.52	21.08	24.90	17.50
F11=0.51				5.00				38.58	20.89	24.74	15.79
18	**10**	**5**	**5**	**40**	**40**	**1.0**		**42.42**	**34.37**	**16.15**	**7.06**
F1=0.01	1.00							0	20.2	32.37	47.43
F2=0.06	5.00							0	20.2	32.37	47.43
F3=0.11	4.30	0.70						0.12	19.04	33.88	46.96
F4=0.16		5.00						0.69	13.52	41.06	44.73
F5=0.21			5.00					12.8	17.53	34.14	35.53
F6=0.26			1.00	4.00				21.33	18.3	31.56	28.81
F7=0.31				5.00				27.23	18.44	30.22	24.11
F8=0.36				5.00				31.47	18.54	29.26	20.73

F9=0.41				5.00			34.67	18.61	28.53	18.19
F10=0.46				5.00			37.17	18.67	27.96	16.2
F11=0.51				5.00			39.18	18.72	27.5	14.6
19	**15**	**5**	**30**	**25**	**25**	**1.0**	**41.64**	**32.02**	**16.44**	**9.91**
F1=0.01	1.00						0	20.2	32.37	47.43
F2=0.06	5.00						0	20.2	32.37	47.43
F3=0.11	5.00						0	20.2	32.37	47.43
F4=0.16	5.00						0	20.2	32.37	47.43
F5=0.21		5.00					0.46	15.78	38.12	45.64
F6=0.26		0.90	4.10				8.4	17.56	34.69	39.35
F7=0.31			5.00				15.56	19.73	30.88	33.83
F8=0.36			5.00				20.96	21.36	28	29.68
F9=0.41			5.00				25.18	22.64	25.75	26.43
F10=0.46			5.00				28.57	23.66	23.94	23.83
F11=0.51			5.00				31.35	24.5	22.46	21.69

1.b. The phlogopite wehrlite starting compositions and the individual melt fraction compositions depicted in pseudoquaternary phasediagrams.

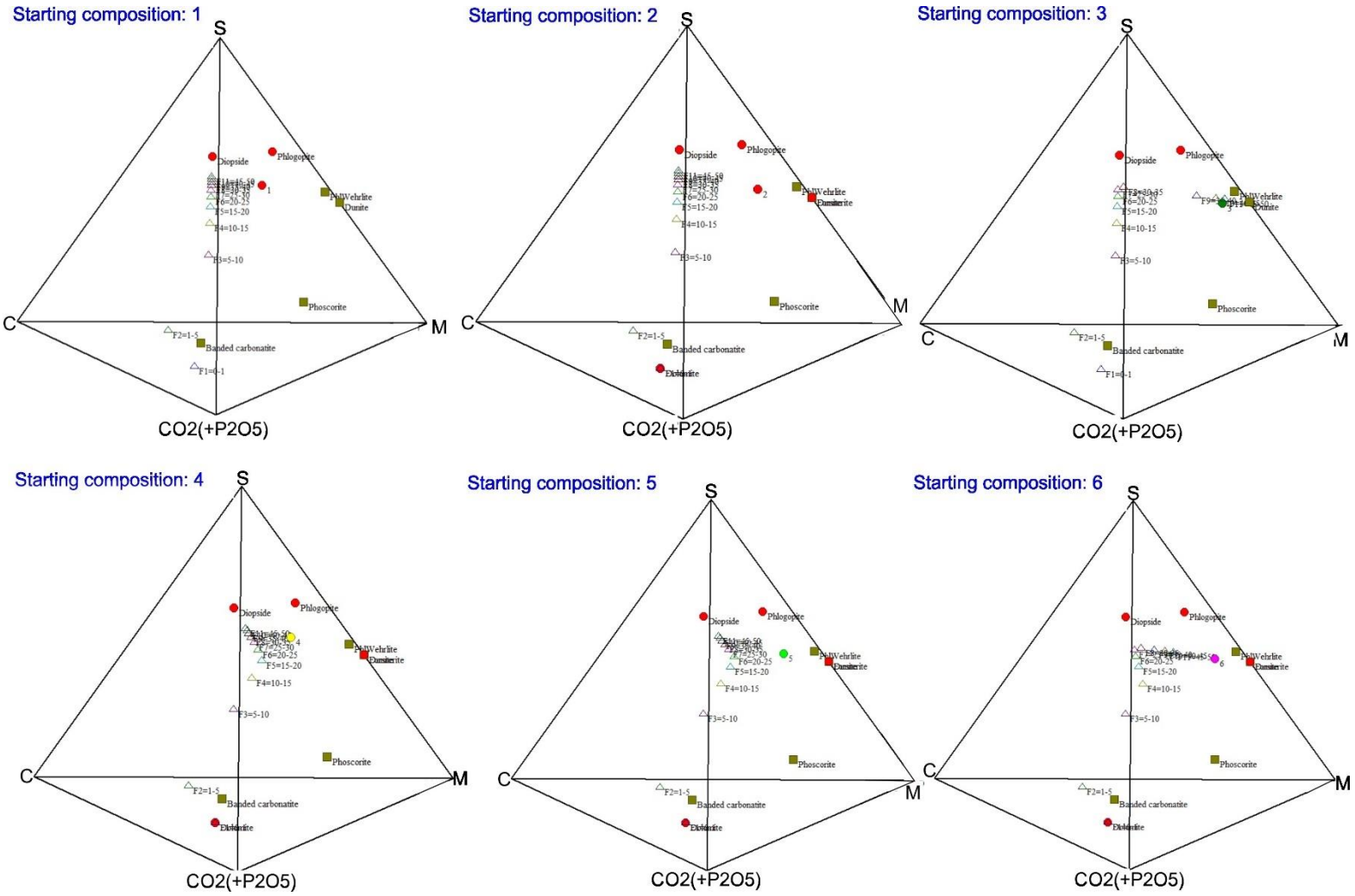

Starting composition: 7

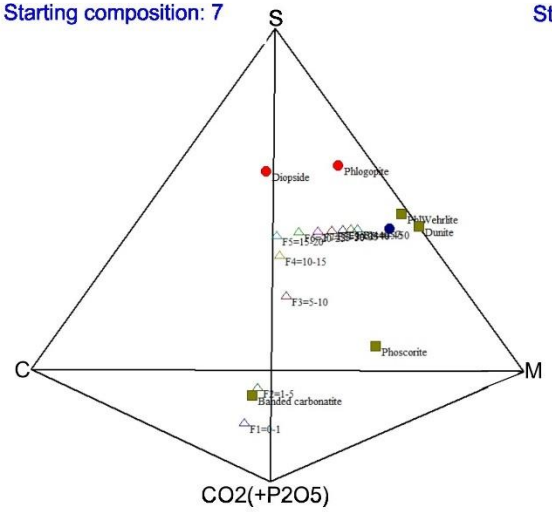

Starting composition: 8

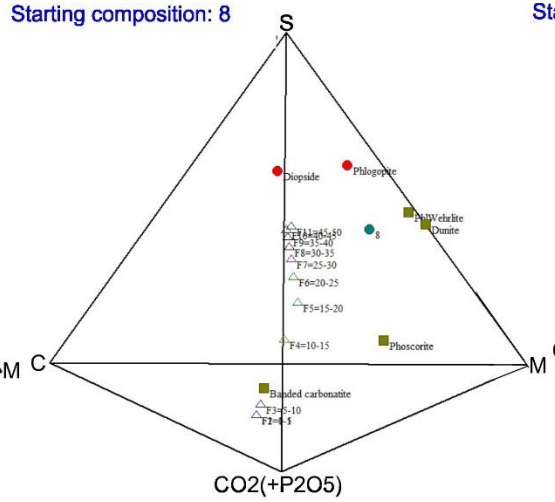

Starting composition: 9

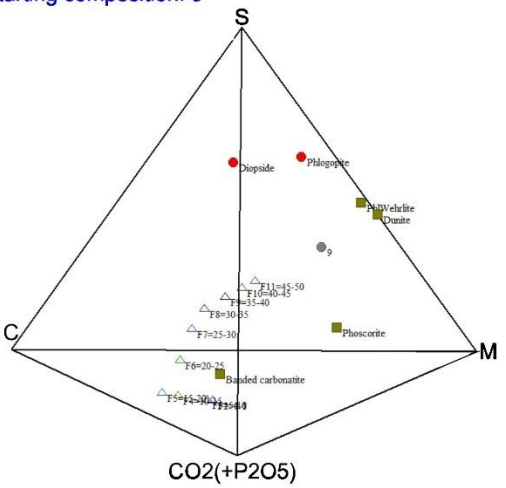

Starting composition: 10

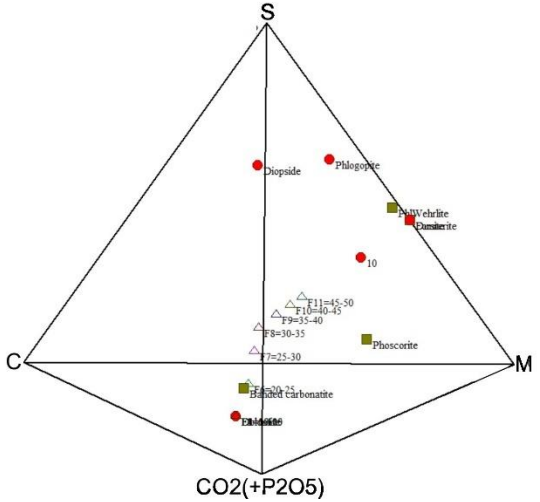

Starting composition: 11

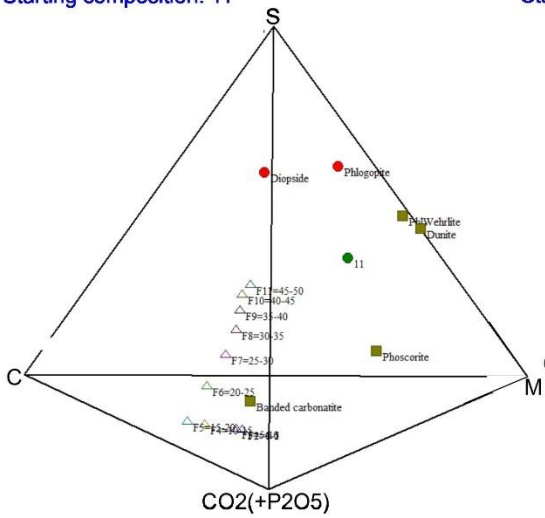

Starting composition: 13

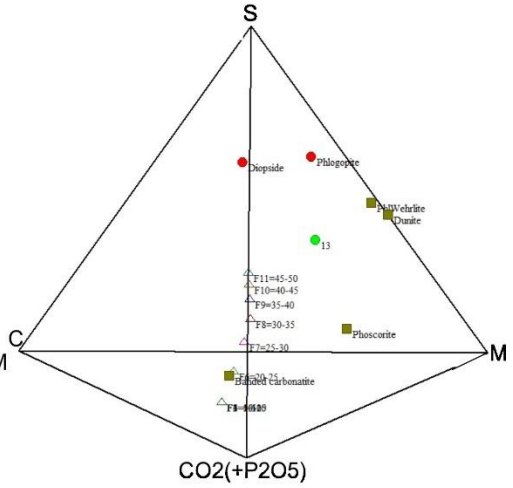

Starting composition: 14

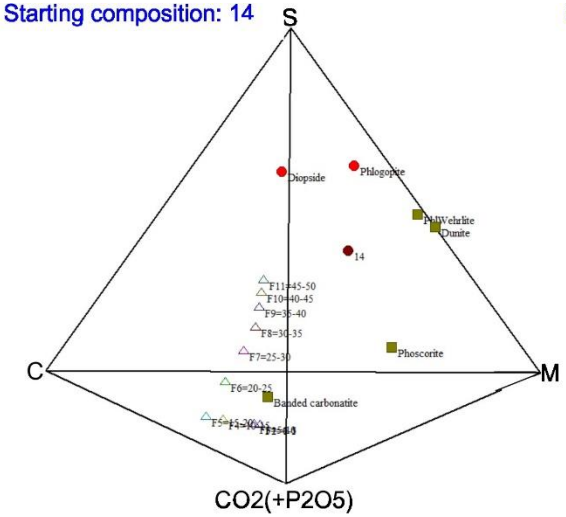

Starting composition: 15

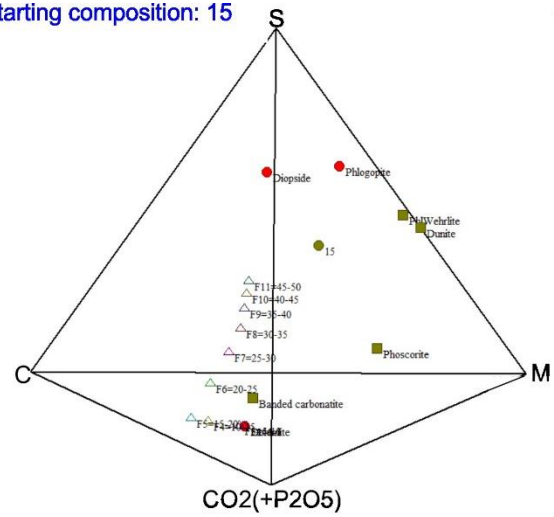

Starting composition: 16

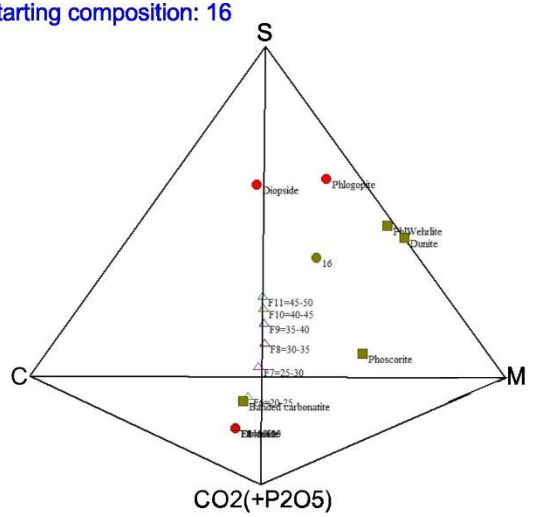

Starting composition: 17

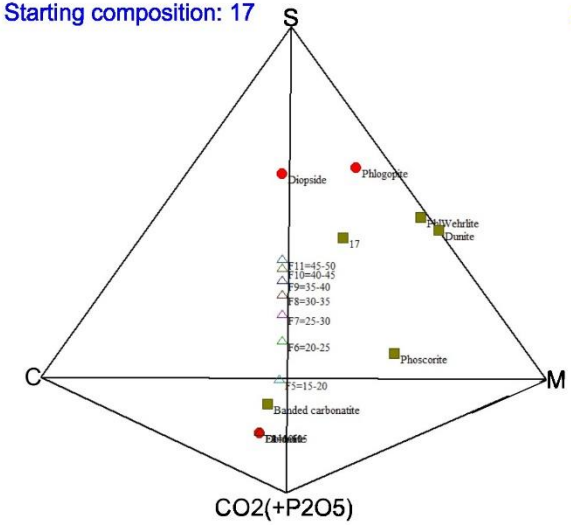

Starting composition: 18

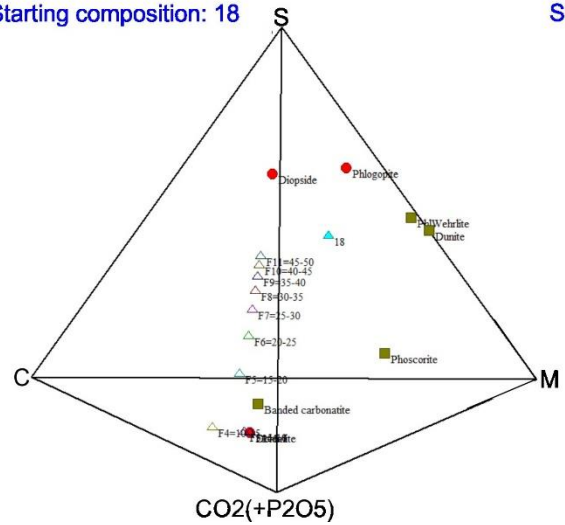

Starting composition: 19

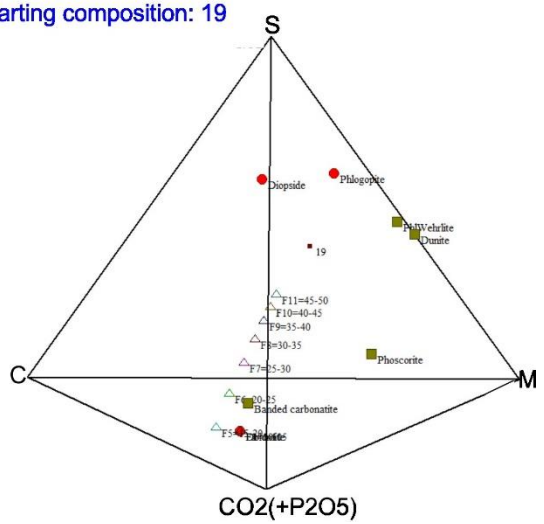

2. Ecglogite melt fraction compositions

2.a: The table shows the starting compositions (bold-blue) and the calculated compositions of the individual melt fractions.

Veined Eclogite model compositions (E_M) (for major element modelling)										
	Dolomite	Apatite	Garnet	Diopside	Rutile	Phlogopite	S	M	C	CO2(+P2O5)
	Modal%						Weight%			
4	**2.4**	**2.4**	**26.7**	**66.7**	**1.9**		**60.09**	**19.62**	**17.97**	**2.32**
F1=0.01	1.00						0.00	20.20	32.37	47.43
F2=0.06	1.40	2.50			1.10		19.28	8.56	36.67	35.48
F3=0.11				4.10	0.90		41.73	10.80	27.65	19.82
F4=0.16				5.00			48.20	12.64	25.36	13.80
F5=0.21				5.00			51.66	13.62	24.13	10.59
F6=0.26				5.00			53.81	14.23	23.36	8.60
F7=0.31				5.00			55.28	14.65	22.84	7.23
F8=0.36			0.50	4.50			56.35	15.10	22.30	6.25
F9=0.41			0.50	4.50			57.17	15.45	21.89	5.49
F10=0.46			1.00	4.00			57.82	15.83	21.43	4.92
F11=0.51			1.00	4.00			58.34	16.15	21.06	4.45
5	**4.5**	**4.5**	**25.5**	**63.6**	**1.8**		**57.11**	**19.17**	**19.32**	**4.40**
F1=0.01	1.00						0.00	20.20	32.37	47.43
F2=0.06	3.60	1.40					0.45	15.87	38.00	45.68
F3=0.11		4.00			1.00		10.15	9.00	41.55	39.30
F4=0.16				4.00	1.00		28.51	10.29	33.77	27.43
F5=0.21				5.00			36.44	11.80	30.63	21.13

F6=0.26				5.00		41.41	12.74	28.66	17.19
F7=0.31				5.00		44.81	13.39	27.31	14.49
F8=0.36			0.50	4.50		47.29	14.01	26.17	12.53
F9=0.41			0.50	4.50		49.17	14.48	25.30	11.05
F10=0.46			1.00	4.00		50.66	14.97	24.49	9.88
F11=0.51			1.00	4.00		51.86	15.36	23.83	8.95
6	**8.3**	**8.3**	**23.3**	**58.3**	**1.7**	**51.96**	**18.40**	**21.65**	**8.00**
F1=0.01	1.00					0.00	20.20	32.37	47.43
F2=0.06	5.00					0.00	20.20	32.37	47.43
F3=0.11	2.60	2.40				0.42	16.15	37.63	45.80
F4=0.16		5.00				0.91	11.44	43.75	43.90
F5=0.21		2.75			2.20	11.56	8.83	40.93	38.68
F6=0.26				5.00		20.99	10.30	37.11	31.60
F7=0.31				5.00		27.50	11.32	34.47	26.71
F8=0.36			0.50	4.50		32.24	12.20	32.40	23.16
F9=0.41			0.50	4.50		35.87	12.88	30.81	20.44
F10=0.46			1.00	4.00		38.72	13.53	29.43	18.32
F11=0.51			1.00	4.00		41.03	14.05	28.32	16.60
9	**16.7**		**23.3**	**58.3**	**1.7**	**51.38**	**20.14**	**19.49**	**9.00**
F1=0.01	1.00					0.00	20.20	32.37	47.43
F2=0.06	5.00					0.00	20.20	32.37	47.43
F3=0.11	5.00					0.00	20.20	32.37	47.43
F4=0.16	5.00					0.00	20.20	32.37	47.43
F5=0.21	2.00			1.00	2.00	12.00	18.18	28.84	40.98
F6=0.26				5.00		21.05	17.95	27.28	33.72
F7=0.31				5.00		27.38	17.78	26.20	28.64
F8=0.36			0.50	4.50		32.02	17.81	25.24	24.93

F9=0.41			0.50	4.50			35.60	17.83	24.51	22.06
F10=0.46			1.00	4.00			38.43	17.96	23.80	19.81
F11=0.51			1.00	4.00			40.73	18.07	23.22	17.98
15	**5**	**5**	**31.5**	**36**	**4.5**	**18**	**55.27**	**20.34**	**19.42**	**4.97**
F1=0.01	1.00						0.00	20.20	32.37	47.43
F2=0.06	4.00	1.00					0.32	17.12	36.37	46.19
F3=0.11		4.30				0.70	4.54	10.96	43.73	40.77
F4=0.16						5.00	20.89	13.49	37.43	28.19
F5=0.21						5.00	29.53	14.82	34.11	21.54
F6=0.26						5.00	34.87	15.65	32.05	17.43
F7=0.31						5.00	38.50	16.21	30.65	14.64
F8=0.36				2.10	0.90	2.00	42.49	15.99	28.88	12.64
F9=0.41				5.00			44.90	16.09	27.85	11.16
F10=0.46				5.00			46.80	16.17	27.04	9.99
F11=0.51			1.00	4.00			48.33	16.45	26.16	9.06
16	**10**	**10**	**28**	**32**	**4**	**16**	**48.51**	**19.14**	**22.57**	**9.78**
F1=0.01	1.00					0.00	0.00	20.20	32.37	47.43
F2=0.06	5.00					0.00	0.00	20.20	32.37	47.43
F3=0.11	4.70	0.70				0.00	0.12	19.08	33.83	46.97
F4=0.16		5.00				0.00	0.67	13.68	40.85	44.80
F5=0.21		5.00					0.98	10.70	44.72	43.60
F6=0.26		0.90				4.10	9.66	11.65	41.89	36.80
F7=0.31						5.00	17.18	12.83	38.97	31.02
F8=0.36						5.00	22.66	13.69	36.85	26.81
F9=0.41						5.00	26.82	14.34	35.23	23.60
F10=0.46					1.00	4.00	31.05	14.44	33.44	21.07
F11=0.51				1.00	4.00		37.10	13.34	30.55	19.01

2.b. The eclogite starting compositions and the individual melt fraction compositions depicted in pseudoquaternary phasediagrams.

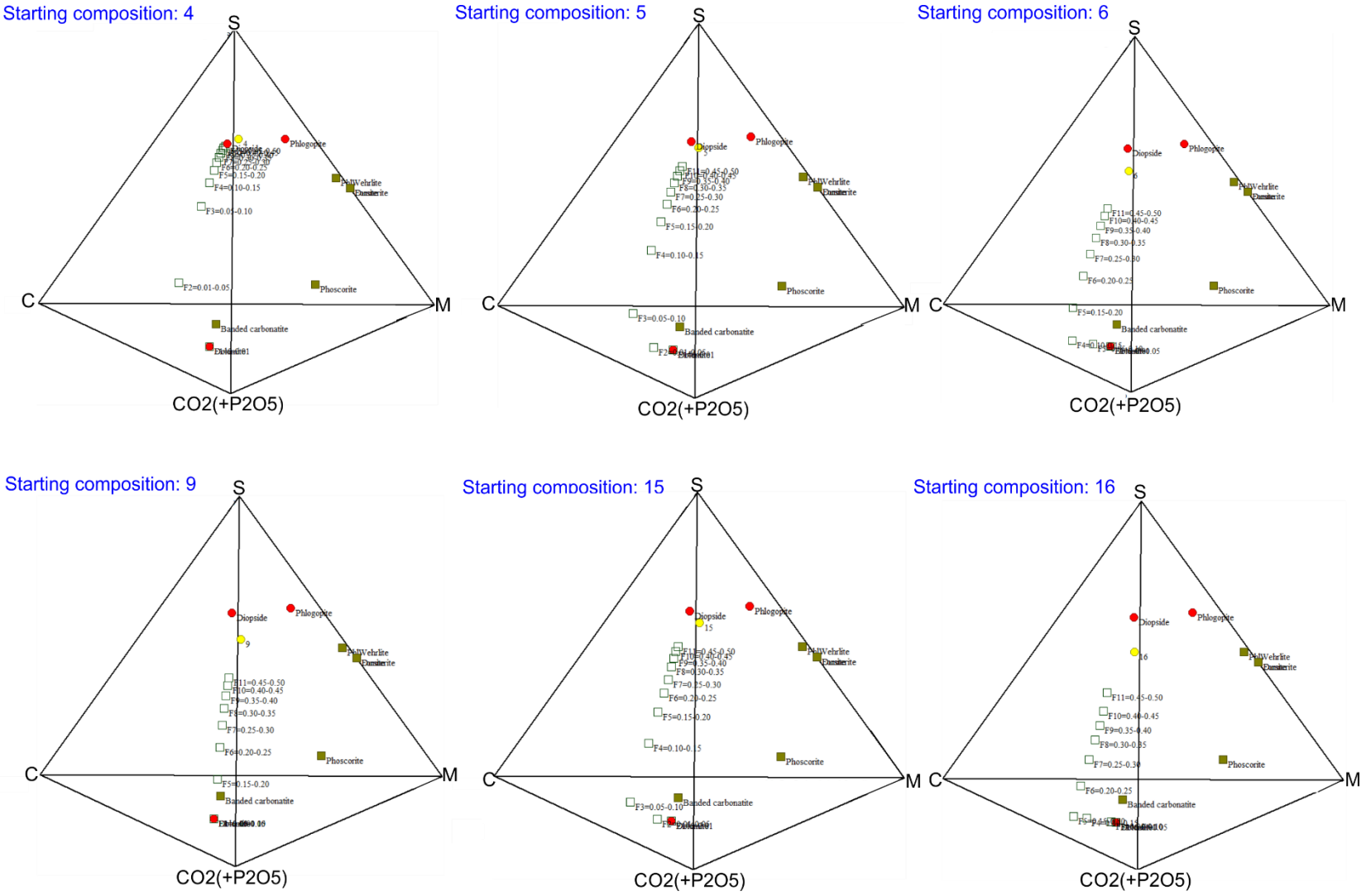

3. MARID melt fraction compositions

3.a: The table shows the starting compositions (bold-blue) and the calculated compositions of the individual melt fractions.

MARID (Samples AJE281 and AJE288) model compositions										
	Carbonate	Apatite	Phlogopite	Clinopyroxene	Amphibole	Ilmenite	S	M	C	CO2(+P2O5)
	Modal %						Weight %			
AJE281	**0.00**	**0.00**	**44.50**	**21.00**	**31.00**	**3.50**	**45.03**	**45.20**	**9.77**	**0.00**
F1=0.01			0.01				59.59	33.10	7.31	0.00
F2=0.05			0.04				59.59	33.10	7.31	0.00
F3=0.10			0.04		0.01		56.23	36.20	7.57	0.00
F4=0.15			0.035		0.01	0.005	54.98	37.58	7.44	0.00
F5=0.20			0.03		0.015	0.005	53.65	38.91	7.44	0.00
F6=0.25			0.025	0.005	0.015	0.005	52.25	40.08	7.67	0.00
F7=0.30			0.025	0.005	0.015	0.005	51.37	40.82	7.81	0.00
F8=0.35			0.025	0.005	0.015	0.005	50.75	41.34	7.91	0.00
F9=0.40			0.025	0.005	0.019	0.001	50.13	41.82	8.05	0.00
F10=0.45			0.025	0.006	0.019		49.61	42.19	8.20	0.00
F11=0.50			0.025	0.006	0.019		49.20	42.48	8.32	0.00
AJE281_5%	**0.08**	**0.08**	**46.73**	**19.95**	**29.45**	**3.72**	**45.47**	**44.76**	**9.71**	**0.06**
F1=0.01	0.01						0.00	20.20	32.37	47.43
F2=0.05	0.001	0.001	0.038				59.36	33.05	7.41	0.18
F3=0.10			0.045		0.005		57.54	34.89	7.50	0.07
F4=0.15			0.045		0.005		57.06	35.37	7.52	0.05
F5=0.20			0.04		0.005	0.005	56.65	35.95	7.37	0.03
F6=0.25			0.035		0.01	0.005	55.75	36.89	7.33	0.03

F7=0.30			0.03	0.005	0.01	0.005	54.58	37.88	7.52	0.02
F8=0.35			0.025	0.005	0.015	0.005	53.37	38.93	7.68	0.02
F9=0.40			0.025	0.005	0.015	0.005	52.51	39.69	7.79	0.01
F10=0.45			0.025	0.005	0.015	0.005	51.86	40.25	7.88	0.01
F11=0.50			0.025	0.005	0.015	0.005	51.36	40.69	7.94	0.01
AJE281_10%	**0.16**	**0.16**	**48.96**	**18.90**	**27.90**	**3.93**	**45.92**	**44.31**	**9.65**	**0.12**
F1=0.01	0.01						0.00	20.20	32.37	47.43
F2=0.05	0.001	0.001	0.038				59.36	33.05	7.41	0.18
F3=0.10		0.001	0.045		0.004		57.89	34.55	7.48	0.08
F4=0.15			0.045		0.005		57.27	35.17	7.51	0.05
F5=0.20			0.04		0.005	0.005	56.80	35.80	7.36	0.04
F6=0.25			0.035		0.01	0.005	55.86	36.78	7.33	0.03
F7=0.30			0.03	0.005	0.01	0.005	54.67	37.80	7.51	0.02
F8=0.35			0.025	0.005	0.015	0.005	53.44	38.87	7.67	0.02
F9=0.40			0.025	0.005	0.015	0.005	52.56	39.64	7.78	0.02
F10=0.45			0.025	0.005	0.015	0.005	51.90	40.21	7.88	0.01
F11=0.50			0.025	0.005	0.015	0.005	51.40	40.65	**7.94**	**0.01**
AJE281_20%	**0.31**	**0.31**	**53.42**	**16.80**	**24.80**	**4.36**	**46.86**	**43.38**	**9.52**	**0.24**
F1=0.01	0.01						0.00	20.20	32.37	47.43
F2=0.05	0.003	0.003	0.034				59.26	33.01	7.48	0.25
F3=0.10			0.045	0	**0.005**		57.41	34.96	7.53	0.10
F4=0.15			0.045	0	0.005		56.97	35.43	7.54	0.06
F5=0.20			0.04	0	0.005	0.005	56.57	36.00	7.38	0.05
F6=0.25			0.035	0	0.01	0.005	55.68	36.94	7.34	0.04
F7=0.30			0.03	0.005	0.01	0.005	54.51	37.93	7.53	0.03
F8=0.35			0.025	0.005	0.015	0.005	53.30	38.99	7.69	0.02
F9=0.40			0.025	0.005	0.015	0.005	52.44	39.74	7.80	0.02
F10=0.45			0.025	0.005	0.015	0.005	51.79	40.30	7.89	0.02

F11=0.50			0.025	0.005	0.015	0.005	51.30	40.74	7.94	0.02
AJE281_5%CarbAp	**2.38**	**2.38**	**42.38**	**20.00**	**29.52**	**3.33**	**43.23**	**43.79**	**11.20**	**1.78**
F1=0.01	0.01						0.00	20.20	32.37	47.43
F2=0.05	0.02	0.02					0.62	14.21	40.15	45.02
F3=0.10		0.01	0.04				58.62	32.76	7.89	0.73
F4=0.15			0.05	0.00	0.01		57.28	34.69	7.71	0.32
F5=0.20			0.04	0.00	0.01	0.01	56.65	35.71	7.44	0.20
F6=0.25			0.04	0.00	0.01	0.01	55.54	36.94	7.37	0.15
F7=0.30			0.03	0.01	0.01	0.01	54.20	38.10	7.59	0.11
F8=0.35			0.03	0.01	0.02	0.01	52.87	39.28	7.76	0.09
F9=0.40			0.03	0.01	0.02	0.01	51.98	40.07	7.87	0.08
F10=0.45			0.03	0.01	0.02	0.01	51.34	40.64	7.95	0.07
F11=0.50			0.03	0.01	0.02	0.01	50.85	41.07	8.02	0.06
AJE281_10%CarbAp	**4.55**	**4.55**	**40.45**	**19.09**	**28.18**	**3.18**	**41.57**	**42.49**	**12.51**	**3.42**
F1=0.01	0.01						0.00	20.20	32.37	47.43
F2=0.05	0.04						0.00	20.20	32.37	47.43
F3=0.10	0.006	0.044					0.86	11.88	43.18	44.08
F4=0.15		0.004	0.046				58.07	32.54	8.25	1.14
F5=0.20			0.04	0	0.005	0.005	56.73	35.18	7.56	0.53
F6=0.25			0.035	0	0.01	0.005	55.24	36.98	7.43	0.35
F7=0.30			0.03	0.005	0.01	0.005	53.69	38.38	7.68	0.25
F8=0.35			0.025	0.005	0.015	0.005	52.25	39.70	7.86	0.19
F9=0.40			0.025	0.005	0.015	0.005	51.35	40.52	7.97	0.16
F10=0.45			0.025	0.005	0.015	0.005	50.73	41.09	8.05	0.13
F11=0.50			0.025	0.005	0.015	0.005	50.28	41.51	8.10	0.11
AJE281_20%CarbAp	**8.33**	**8.33**	**37.08**	**17.50**	**25.83**	**2.92**	**38.62**	**40.18**	**14.86**	**6.35**

F1=0.01	0.01						0.00	20.20	32.37	47.43
F2=0.05	0.04						0.00	20.20	32.37	47.43
F3=0.10	0.045	0.005					0.09	19.29	33.56	47.06
F4=0.15		0.05					0.71	13.31	41.33	44.65
F5=0.20		0.038	0.012				50.52	29.65	13.08	6.75
F6=0.25			0.035	0	0.01	0.005	52.18	38.07	8.39	1.36
F7=0.30			0.03	0.005	0.01	0.005	51.02	39.90	8.35	0.73
F8=0.35			0.025	0.005	0.015	0.005	49.82	41.29	8.39	0.50
F9=0.40			0.025	0.005	0.015	0.005	49.22	42.00	8.41	0.37
F10=0.45			0.025	0.005	0.015	0.005	48.85	42.43	8.42	0.30
F11=0.50			0.025	0.005	0.015	0.005	48.61	42.72	8.42	0.25
AJE281_10%carb	**9.09**	**0.00**	**40.45**	**19.09**	**28.18**	**3.18**	**41.36**	**43.16**	**11.61**	**3.87**
F1=0.01	0.01						0.00	20.20	32.37	47.43
F2=0.05	0.04						0.00	20.20	32.37	47.43
F3=0.10	0.05						0.00	20.20	32.37	47.43
F4=0.15	0.003	0	0.047				58.04	32.77	7.96	1.23
F5=0.20			0.04	0	0.005	0.005	56.73	35.26	7.43	0.58
F6=0.25			0.035	0	0.01	0.005	55.25	37.02	7.35	0.38
F7=0.30			0.03	0.005	0.01	0.005	53.70	38.41	7.62	0.27
F8=0.35			0.025	0.005	0.015	0.005	52.27	39.71	7.81	0.21
F9=0.40			0.025	0.005	0.015	0.005	51.37	40.53	7.93	0.17
F10=0.45			0.025	0.005	0.015	0.005	50.75	41.10	8.01	0.14
F11=0.50			0.025	0.005	0.015	0.005	50.29	41.51	8.07	0.13
AJE288	**0.00**	**0.00**	**87.50**	**0.00**	**9.70**	**2.80**	**58.70**	**33.53**	**7.76**	**0.00**
F1=0.01			0.01				58.70	33.97	7.33	0.00
F2=0.05			0.04				58.70	33.97	7.33	0.00
F3=0.10			0.05				58.70	33.97	7.33	0.00
F4=0.15			0.05				58.70	33.97	7.33	0.00

F5=0.20			0.045		0.005		58.75	33.76	7.49	0.00
F6=0.25			0.04		0.01		58.82	33.46	7.72	0.00
F7=0.30			0.04		0.01		58.87	33.26	7.87	0.00
F8=0.35			0.03		0.02		58.96	32.88	8.16	0.00
F9=0.40			0.025	0	0.024	0.001	59.03	32.55	8.42	0.00
F10=0.45			0.025	0	0.024	0.001	59.09	32.30	8.61	0.00
F11=0.50			0.025	0	0.024	0.001	59.13	32.10	8.77	0.00
AJE288_5%	**0.08**	**0.08**	**87.52**	**0.00**	**9.26**	**3.06**	**58.57**	**33.57**	**7.79**	**0.08**
F1=0.01	0.01						0.00	20.20	32.37	47.43
F2=0.05	0.00	0.00	0.04				58.48	33.91	7.43	0.18
F3=0.10			0.05				58.60	33.95	7.37	0.08
F4=0.15			0.05				58.64	33.96	7.36	0.05
F5=0.20			0.05	0.00	0.01		58.71	33.73	7.52	0.04
F6=0.25			0.04		0.01		58.79	33.43	7.75	0.03
F7=0.30			0.03		0.02		58.92	32.94	8.12	0.02
F8=0.35			0.03	0.00	0.02	0.00	59.01	32.54	8.43	0.02
F9=0.40			0.03	0.00	0.02	0.00	59.08	32.24	8.66	0.02
F10=0.45			0.03	0.00	0.02	0.00	59.13	32.02	8.84	0.01
F11=0.50			0.03	0.00	0.02	0.00	59.17	31.84	8.98	0.01
AJE288_10%	**0.16**	**0.16**	**87.60**	**0.00**	**8.77**	**3.31**	**58.44**	**33.60**	**7.81**	**0.16**
F1=0.01	**0.01**						0.00	20.20	32.37	47.43
F2=0.05	**0.00**	**0.00**	**0.04**				58.45	33.90	7.45	0.20
F3=0.10			**0.05**				58.59	33.94	7.38	0.09
F4=0.15			**0.05**				58.63	33.95	7.36	0.06
F5=0.20			**0.05**	**0.00**	**0.01**		58.71	33.73	7.52	0.04
F6=0.25			**0.04**		**0.01**		58.79	33.42	7.75	0.04
F7=0.30			**0.03**		**0.02**		58.92	32.93	8.12	0.03
F8=0.35			**0.03**	**0.00**	**0.02**	**0.00**	59.01	32.53	8.44	0.02

F9=0.40			**0.03**	**0.00**	**0.02**	**0.00**	59.08	32.24	8.66	0.02
F10=0.45			**0.03**	**0.00**	**0.02**	**0.00**	59.13	32.01	8.84	0.02
F11=0.50			**0.03**	**0.00**	**0.01**	**0.01**	58.99	32.28	8.72	0.01
AJE288_20%	**0.31**	**0.31**	**87.77**	**0.00**	**7.79**	**3.82**	**58.17**	**33.67**	**7.85**	**0.32**
F1=0.01	0.01						0.00	20.20	32.37	47.43
F2=0.05	0.00	0.00	0.03				58.37	33.87	7.50	0.26
F3=0.10			0.05				58.57	33.93	7.40	0.10
F4=0.15			0.05				58.62	33.95	7.37	0.06
F5=0.20			0.05				58.64	33.95	7.36	0.05
F6=0.25			0.04		0.01		58.74	33.59	7.63	0.04
F7=0.30			0.03		0.02		58.88	33.07	8.02	0.03
F8=0.35			0.03		0.02	0.00	58.98	32.64	8.35	0.03
F9=0.40			0.03		0.02	0.00	59.05	32.33	8.60	0.02
F10=0.45			0.03		0.02	0.00	59.10	32.09	8.78	0.02
F11=0.50			0.03		0.00	0.02	58.72	32.94	8.32	0.02
AJE288_5%CarbAp	**2.38**	**2.38**	**83.33**	**0.00**	**9.24**	**2.67**	**55.51**	**32.27**	**9.81**	**2.41**
F1=0.01	0.01						0.00	20.20	32.37	47.43
F2=0.05	0.024	0.016					0.62	14.21	40.15	45.02
F3=0.10		0.008	0.042				57.76	33.62	7.90	0.72
F4=0.15			0.05				58.27	33.81	7.59	0.33
F5=0.20			0.05				58.42	33.87	7.50	0.21
F6=0.25			0.04		0.01		58.60	33.45	7.79	0.16
F7=0.30			0.03		0.02		58.79	32.87	8.22	0.12
F8=0.35			0.025		0.024	0.001	58.92	32.42	8.56	0.10
F9=0.40			0.025		0.024	0.001	59.01	32.10	8.80	0.09
F10=0.45			0.025		0.024	0.001	59.07	31.87	8.98	0.08
F11=0.50			0.025		0.024	0.001	59.12	31.69	9.12	0.07

AJE288_10%CarbAp	**4.55**	**4.55**	**79.55**	**0.00**	**8.82**	**2.55**	**52.65**	**31.14**	**11.64**	**4.57**
F1=0.01	0.01						0.00	20.20	32.37	47.43
F2=0.05	0.04						0.00	20.20	32.37	47.43
F3=0.10	0.006	0.044					0.86	11.88	43.18	44.08
F4=0.15		0.004	0.046				57.19	33.38	8.28	1.15
F5=0.20			0.05				57.97	33.69	7.79	0.55
F6=0.25			0.05				58.22	33.78	7.63	0.37
F7=0.30			0.025		0.025		58.60	32.76	8.36	0.28
F8=0.35			0.025		0.024	0.001	58.79	32.25	8.74	0.22
F9=0.40			0.025		0.024	0.001	58.92	31.92	8.99	0.18
F10=0.45			0.025		0.024	0.001	59.00	31.68	9.16	0.15
F11=0.50			0.025		0.024	0.001	59.07	31.51	9.29	0.13
AJE288_20%CarbAp	**8.33**	**8.33**	**72.92**	**0.00**	**8.08**	**2.33**	**47.75**	**29.20**	**14.77**	**8.27**
F1=0.01	0.01						0.00	20.20	32.37	47.43
F2=0.05	0.04						0.00	20.20	32.37	47.43
F3=0.10	0.045	0.05					0.67	13.74	40.77	44.82
F4=0.15		0.05					1.01	10.45	45.04	43.50
F5=0.20		0.045	0.005				38.02	24.85	21.75	15.38
F6=0.25			0.05				55.91	32.74	9.28	2.07
F7=0.30			0.05				57.20	33.31	8.37	1.12
F8=0.35			0.05				57.68	33.52	8.04	0.76
F9=0.40			0.045		0.005		57.98	33.42	8.02	0.58
F10=0.45			0.04		0.005	0.005	58.02	33.63	7.88	0.47
F11=0.50			0.04		0.005	0.005	58.05	33.78	**7.79**	**0.38**
AJE288_10%carb	**9.09**	**0.00**	**79.55**	**0.00**	**8.82**	**2.55**	**52.31**	**32.08**	**10.44**	**5.16**
F1=0.01	0.01						0.00	20.20	32.37	47.43
F2=0.05	0.04						0.00	20.20	32.37	47.43

F3=0.10	0.006	0	0.044				57.79	33.76	7.71	0.74
F4=0.15			0.05				58.27	33.87	7.51	0.35
F5=0.20			0.05				58.42	33.91	7.45	0.22
F6=0.25			0.05				58.49	33.92	7.42	0.17
F7=0.30			0.025	0	0.025		58.75	33.07	8.05	0.13
F8=0.35			0.025	0	0.024	0.001	58.88	32.59	8.42	0.11
F9=0.40			0.025	0	0.024	0.001	58.98	32.25	8.68	0.09
F10=0.45			0.025	0	0.024	0.001	59.04	32.00	8.88	0.08
F11=0.50			0.025	0	0.024	0.001	59.10	31.80	9.03	0.07

3.b. The MARID starting compositions and the individual melt fraction compositions depicted in pseudoquaternary phasediagrams.

Starting composition: AJE281

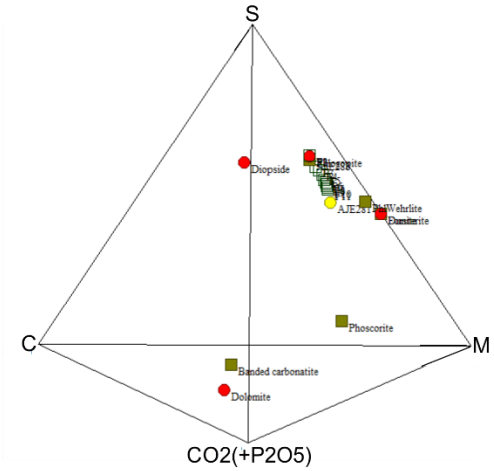

Starting composition: AJE281_5%

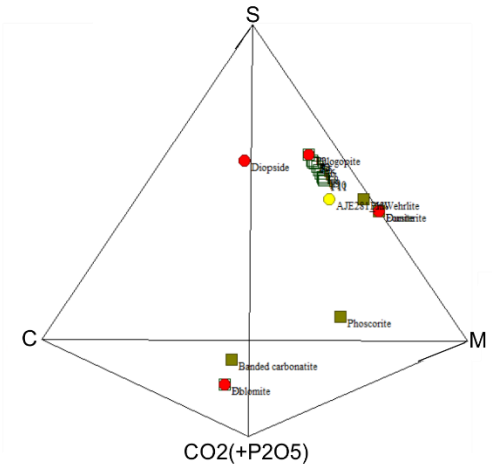

Starting composition: AJE281_10%

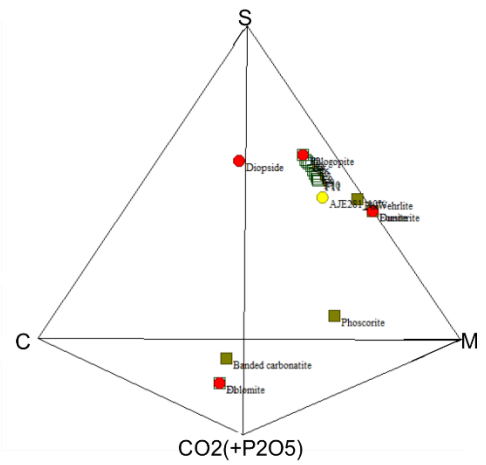

Starting composition: AJE281_20%

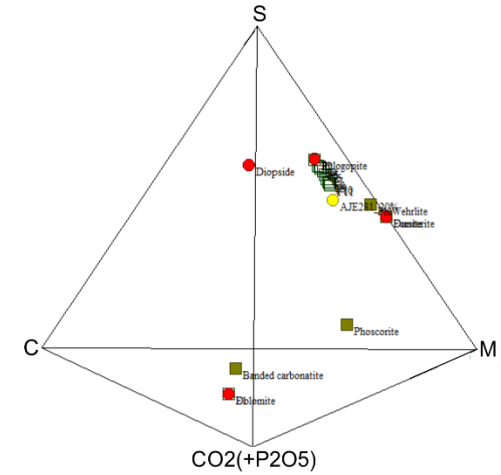

Starting composition: AJE281_5% CarbAp

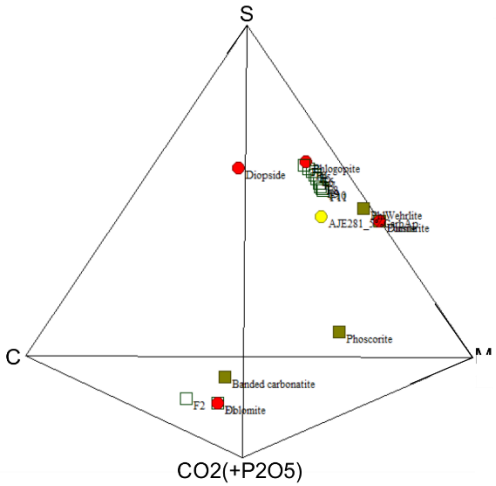

Starting composition: AJE281_10% CarbAp

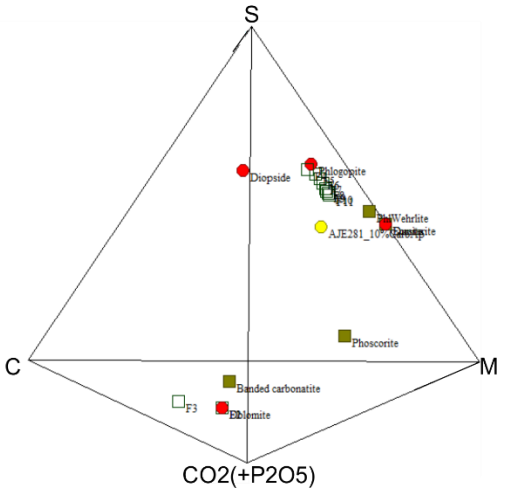

Starting composition: AJE281_10% carb

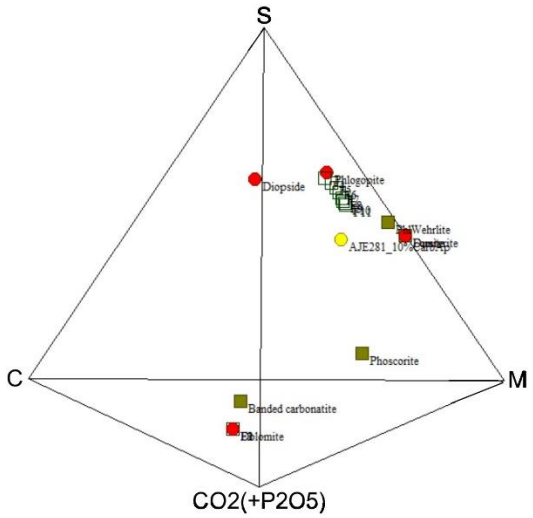

Starting composition: AJE288_5%

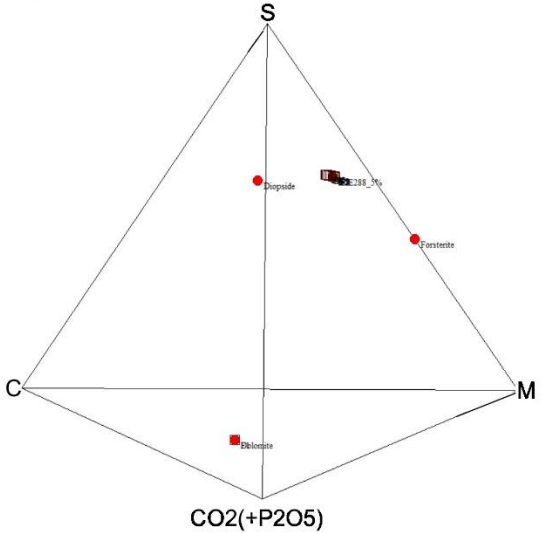

Starting composition: AJE288_10%

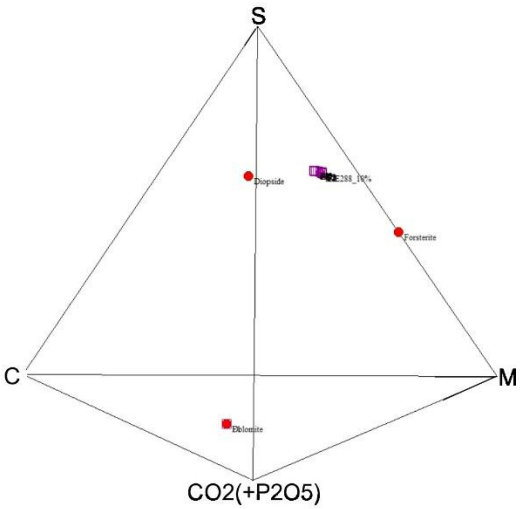

Starting composition: AJE288_20%

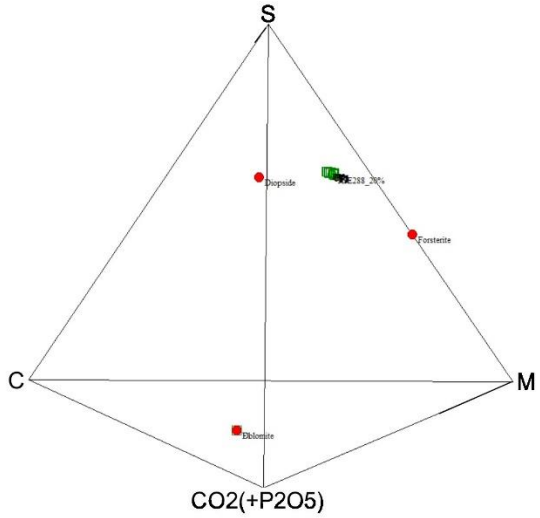

Starting composition: AJE288_5% CarbAp

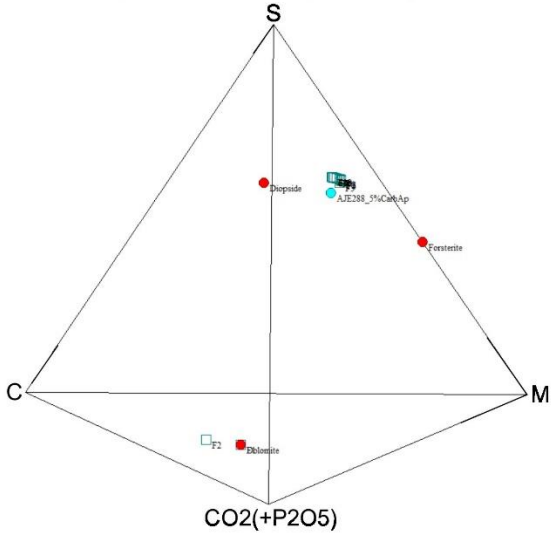

Starting composition: AJE288_10% CarbAp

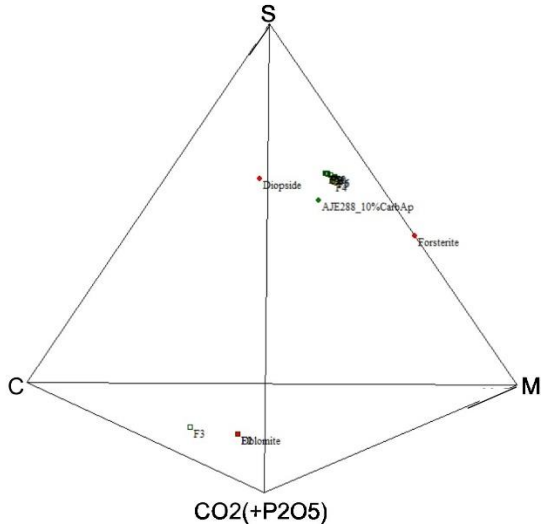

Starting composition: AJE288_20% CarbAp

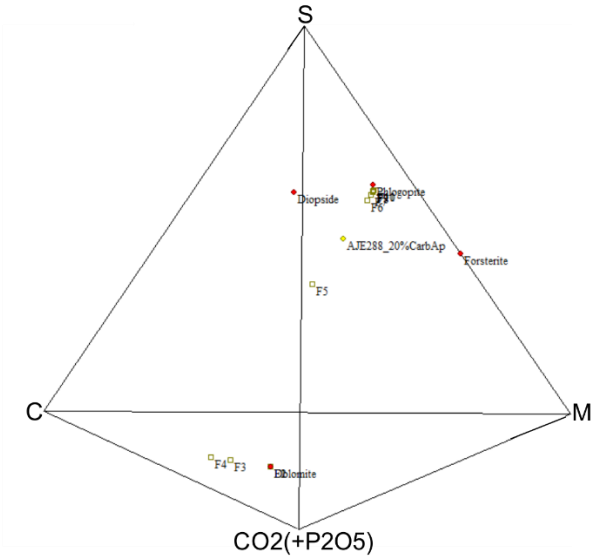

Starting composition: AJE288_10% Carb